APPENDIX A: METHOD FOR LEAKAGE ASSESSMENT FOR THE FINITE ELEMENT ANALYSIS OF PRESTRESSED CONCRETE CONTAINMENT VESSELS

Background and introduction

The SPE Phase 2 Problem Statement describes that Model 4 and adjunct submodels should be planned to estimate crack size and leak area, as this is one of the primary goals of the Phase 2 work. In conjunction with this, the AERB and BARC have researched methodologies for calculating leak rates as a function of crack size, and this has been provided to the SPE participants (we discuss this later in this Appendix).

Since the April 13-14, 2011 Meeting of the SPE, renewed study has been made of the 1:4 Scale Model liner tears, and liner metallurgical properties. The liner and the regions at or near all 26 observed tears were studied in [7]. Some SPE-3 participants may wish to expand on previously used liner failure criterion in their Phase 2 analyses and conclusions about failure and leakage, as for example, a few participants did in Phase 1, considering a fracture mechanics approach. Another approach to both aspects of the problem (the estimation of crack size, and the estimation of probabilistic distribution on leakage and crack size versus pressure) is the methodology developed during the EPRI research in the 1990's. References for more information on this are [8 and 9]. Ref. [8] provides a general description of the methodology, and is publicly available; Ref. [9] provides more detail, but is only available on a limited basis.

Strain-based failure criteria

Based on the existing research of behavior of steel-lined concrete containments, liner-tearing with associated leakage is the failure mode for slow pressurization of the containment. Fracture and tearing of the steel shell is followed by leakage through the tear aperture, and then through cracks in the concrete. Concrete cracks are certain to occur at containment wall strains large enough to tear the steel shell. And even upon unloading of the containment, partial closing of many of these cracks may occur, but test and analysis evidence suggests that residual leak paths will still exist in the concrete.

The state-of-the-art for predicting tearing for steel shells comprised of plates, weld seams, stiffeners and other details, consists of two fundamental types of failure criteria:

1. strain-based failure criteria applied to unflawed steel material and components;
2. fracture-based failure methods applied to postulated flaws, which are commonly found in welded steel shell structures

Both are highly relevant to the steel-lined concrete containments, and are widely used for shell failure predictions of other structure types, but both have different information requirements about the material, the strain state, and the conditions surrounding a potential crack. Failure Criteria Type 1 has been, by far, the most widely used by concrete containment severe accident analysts, and remains a viable option for the SPE work. Failure Criteria type 2 is much more demanding in terms of information required. Gathering this information has three necessary parts: 1) expert review of the structure design and construction documents to assess what location and what type of critical fracture locations exist; 2) material sampling directly from the structure and laboratory testing to obtain fracture toughness data; and 3) fracture prediction

finite element analysis, using J-Integral theory. While some aspects of the first of these activities have been performed over the years of study of the Sandia/NUPEC 1:4 Scale PCCV, the second and third of these activities have not. After searching through the data records, and the special report prepared on metallurgy of the liner, no fracture toughness data is available. Further, the analysis assignment has two types, with two separate objectives – a) analysis to predict fracture, and b) analysis to predict crack propagation (and how far it propagates). The scope of such analyses are proving to be more than the current SPE work can afford in terms of resources and schedule. So the decision has been made to utilize strain-based failure criteria. Significant research has been done by EPRI, Sandia, and other organizations related to developing such criteria, although in most applications, the criteria only focuses on prediction of the onset of tearing. For the SPE we have attempted a key second step methodology, which employs the benefits of these early developments, but also pushes the state-of-the-practice to the new goal of quantifying leakage versus pressure.

Review of leakage basis for concrete containments

EPRI/CTL tests

Experimental evidence supporting the leak-before-break hypothesis for concrete containments is extensive; a summary of it, used to develop a methodology for predicting leakage versus pressure during an EPRI sponsored research program of the late 1980s-1990s is provided here and in [8].

Five examples of liner tearing (or liner distress) are briefly discussed as an overview of the experimental evidence supporting the leakage prediction methodology. The first four are from the EPRI-sponsored containment specimen test program at Construction Technology Laboratories (CTL) in Skokie, Illinois [9]. The test program included full-scale structural specimen tests of special regions of containments, and prestressed as well as reinforced concrete containment types were investigated. This and other test data from CTL has been applied to verification of analytical methods, tabulation of strain concentration factors near discontinuities, and forming conclusions regarding general behavior patterns such as liner tearing and liner-concrete interaction. Figure A-1 shows the locations of the liner tears and distressed areas in several of these specimen tests. The fifth example, the Sandia 1:6 scale reinforced concrete containment model, provided vast information for studying the failure behavior of reinforced concrete containments. An unwrapped view of the cylinder liner surface is shown in Fig. A-2, indicating the many liner tears that occurred near the end of the test. The experimental evidence derived from these five examples is summarized below. The 1:4 Scale PCCV test, chronologically later than the EPRI research, now adds yet another body of data from which we establish our leakage prediction methodology.

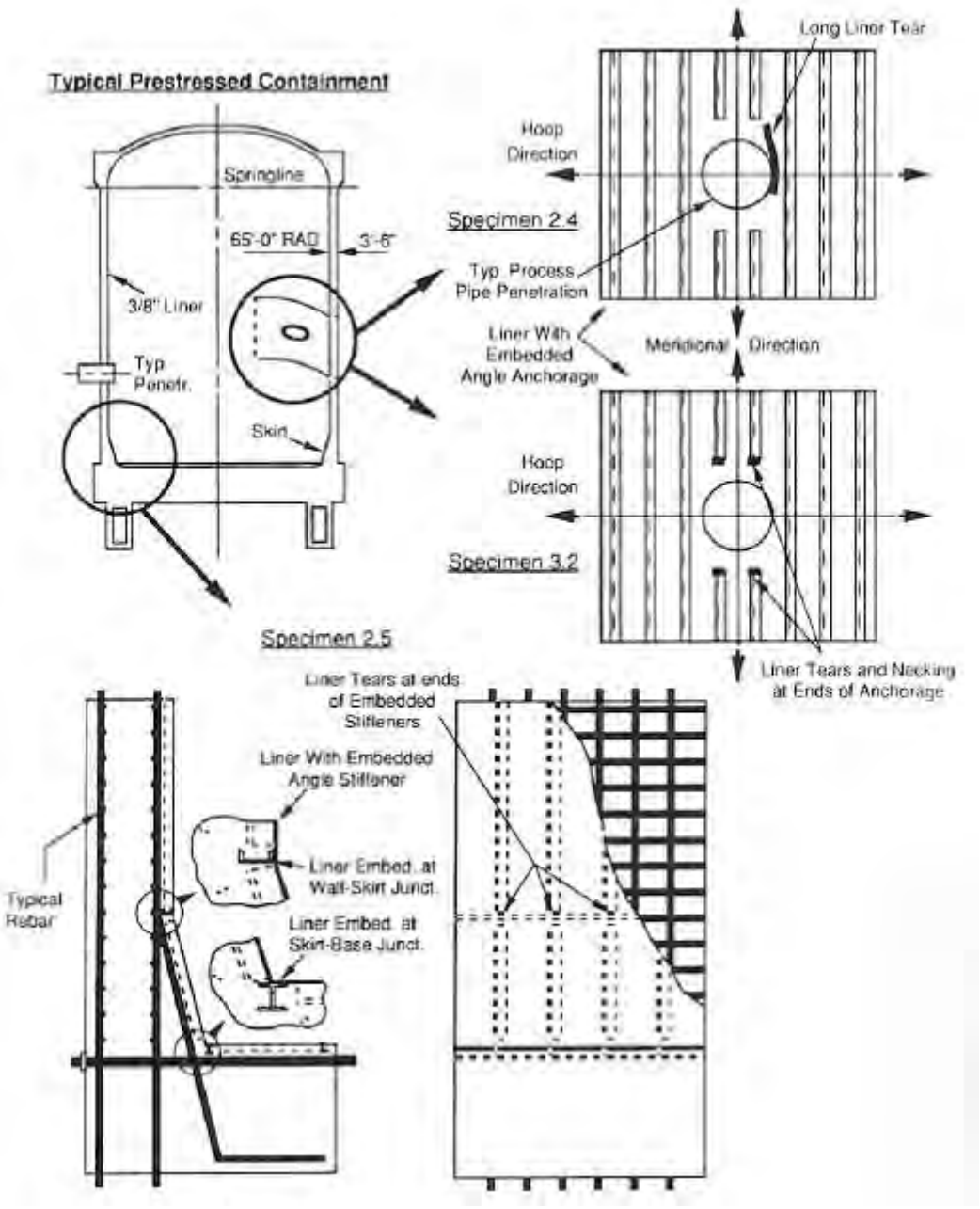

Figure A - 1: Liner tearing examples in EPRI/CTL tests

EPRI/CTL Specimen 2.5. Wall-basemat juncture – prestressed geometry

A full scale model of the wall-skirt-basemat region of a typical prestressed containment was subjected to the meridional force, shear and bending moment that would occur in an actual containment during overpressure. The circumferential liner anchorage at the wall-skirt juncture and the termination of meridional liner stiffeners at this location caused strain concentrations that led to tearing as shown in the figure. Correlation of measured strains to pre- and post-test

analysis has resulted in the development of wall-skirt basemat strain magnification factor curves.

EPRI/CTL Specimen 2.4. Wall specimen with penetration – pre-stressed geometry

The wall specimens with penetrations were designed to represent a square section of the containment wall with a medium sized (30 to 42 inch diameter) process penetration. The presence of a penetration causes severe stiffness discontinuity. Specimen 2.4 was loaded with a hoop to meridional stress ratio of 2:1 plus an outward punch force. The specimen developed a large liner tear at the liner-penetration juncture at a far field strain across the specimen wall below that corresponding to global failure in an actual containment.

EPRI/CTL Specimen 3.2. Prestressed geometry with penetration: inward punch shear force

Similar to 2.4, this specimen utilized the 2:1 applied stress ratio but included a series of increasing inward punch loads. An inward punch force simulates the case of a piping penetration that is restrained against axial motion, thus constraining a point on the containment wall. Liner strain concentrations at the ends of the stiffeners reached peak strain levels large enough to tear the liner, while the global strain was still below global failure levels.

EPRI/CTL Specimen 3.3. Wall with penetration – reinforced geometry

This specimen was loaded in the same way as Specimen 3.2, but for a reinforced concrete geometry. One notable difference was the addition of a thickened liner region around the penetration. This detail was also used for the penetration in the 1:6 scale model. With this detail, the largest liner strain occurs at a radius just beyond the thickened region. Here, as with most of the other specimens, strain measurements and pre- and post-test analyses were used to develop strain concentration factor curves for this type of geometry.

Sandia 1:6 scale RCCV model

The Sandia model was designed with construction details and penetrations that are similar to many existing LWR containments. After maximum pressure was reached and the model was unloaded, many liner tears were visible near various penetrations, as shown in A-2. Post-test efforts using the test's detailed strain measurements were very useful in the further development of strain concentration curves for different types of stiffness discontinuity geometries.

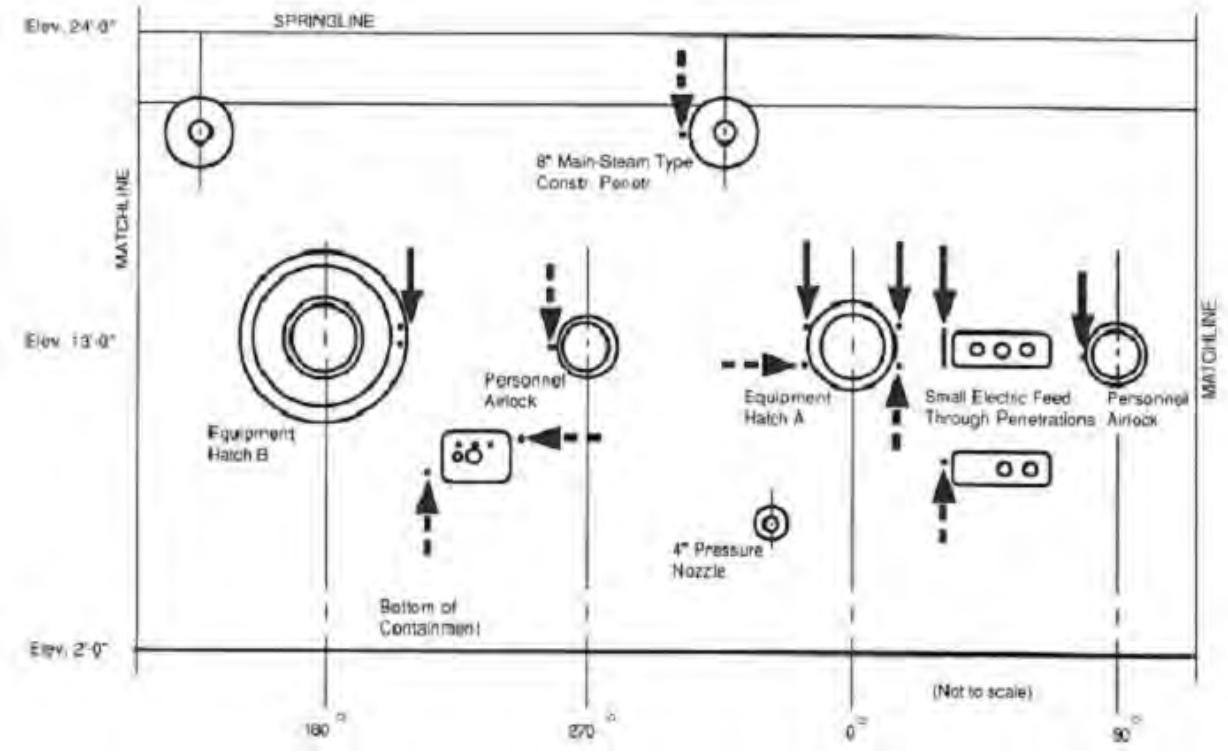

Figure A - 2: Unwrapped view of Sandia 1:6 scale RCCV model cylinder

Sandia/NUPEC 1:4 scale PCCV model

As described in many references [3,4,6], the 1:4 Scale PCCV Model Limit State Test failed by tearing of the liner in many locations as shown in Figure A-3a. Measured strains occurring near a typical penetration are shown in Figure A-3b. Strains as high as 4.6% were measured at pressure of 3.3xPd. As has been found in these and other tests, it is difficult (or impossible) to locate gages exactly at what will be the highest strain concentration location. The fact is further impetus for adopting the approximate procedure described herein. Leak measurements in the 1:4 Scale PCCV Model Test are shown in Figures A-4, A-5, A-6.

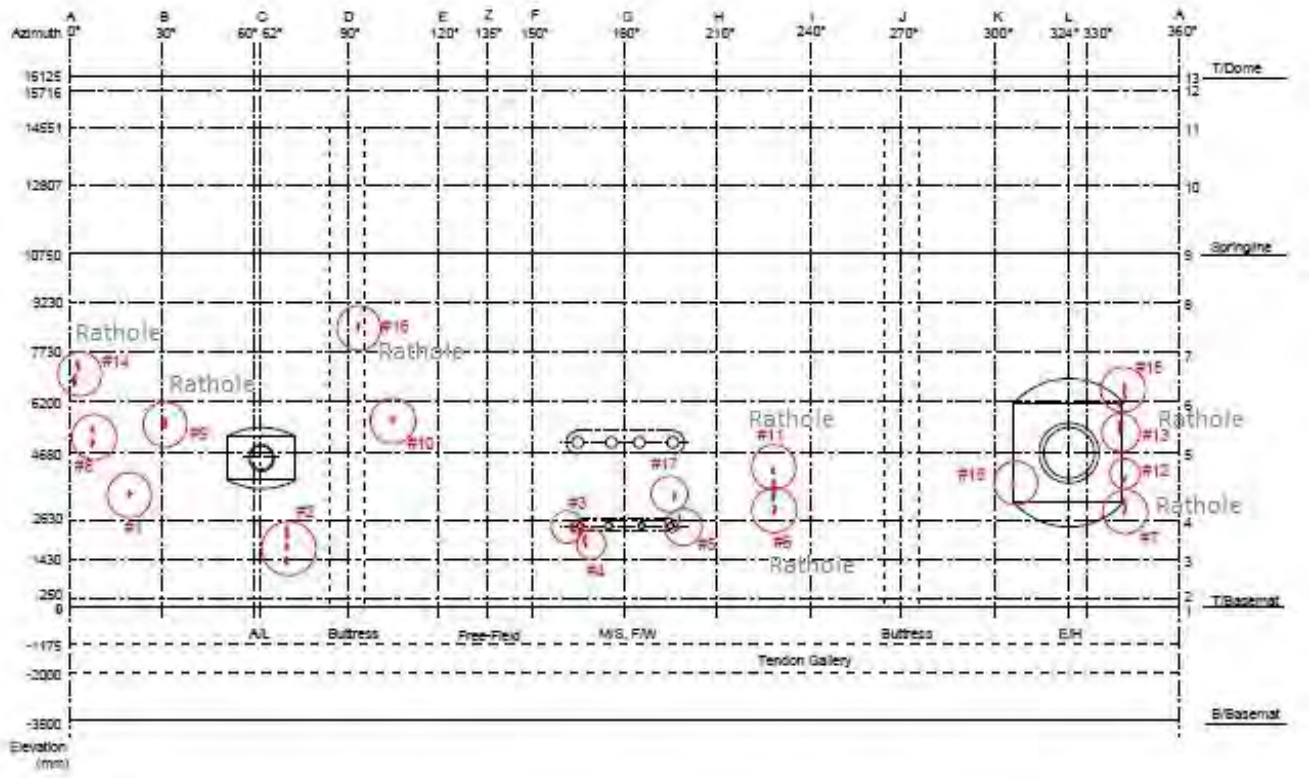

Figure A - 3a: 1:4 Scale PCCV observed liner tear locations

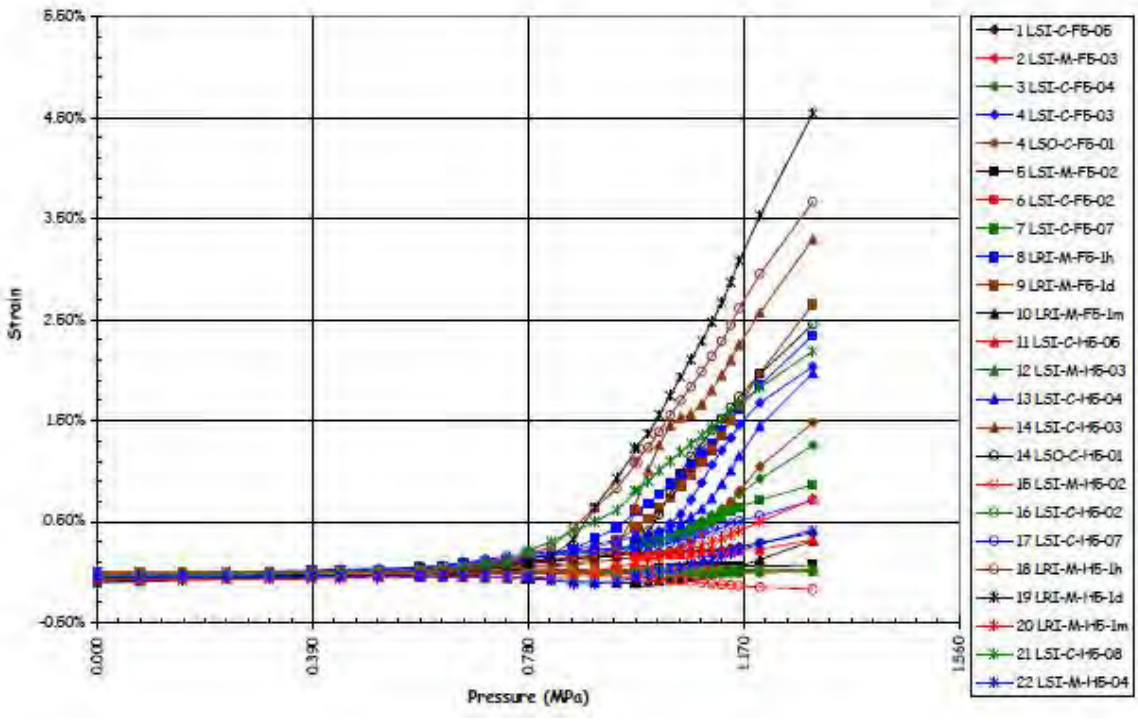

Figure A - 3b: Liner strain gage measurements near M/S penetration (Ref D-SN-P-220)

Plots of leak-rates at different stages of testing are provided for reference in Figures A-4, A-5, and A-6.

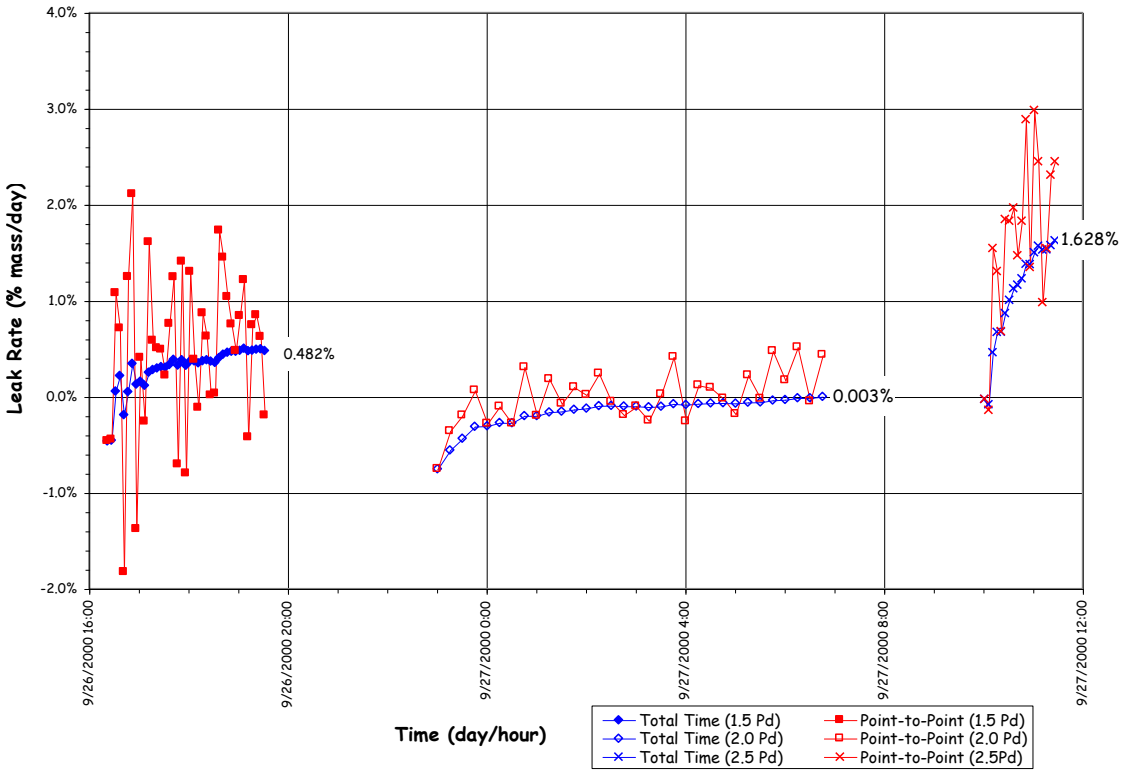

Figure A - 4: LST calculated leak rates at 1.5, 2.0, and 2.5 Pd

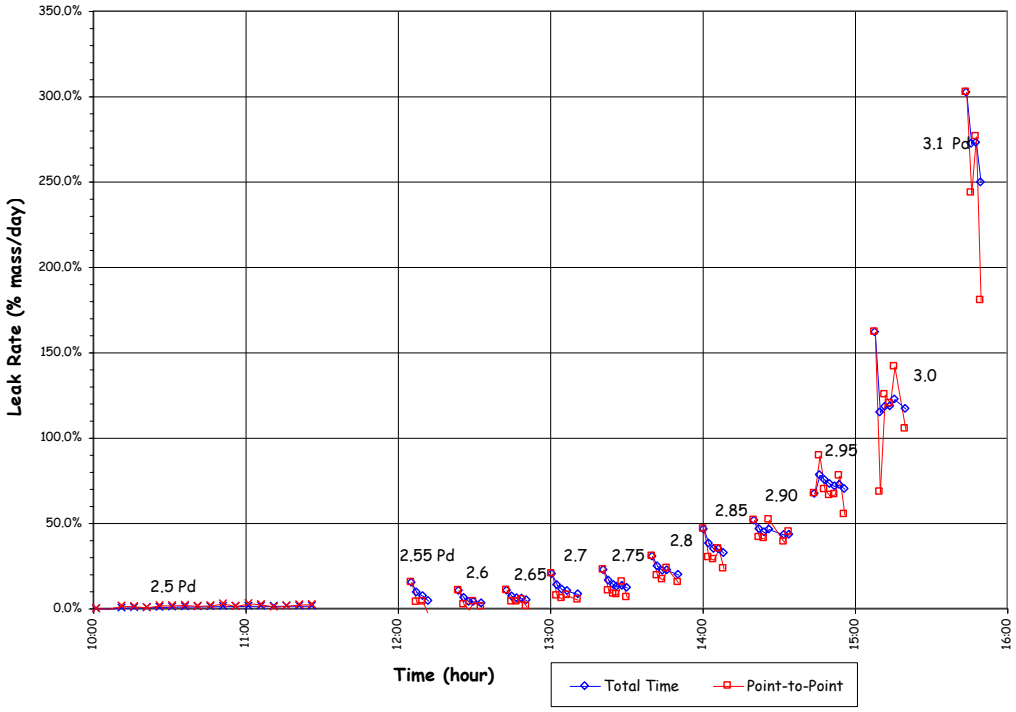

Figure A - 5: LST - estimated leak rates (2.5-3.1 Pd)

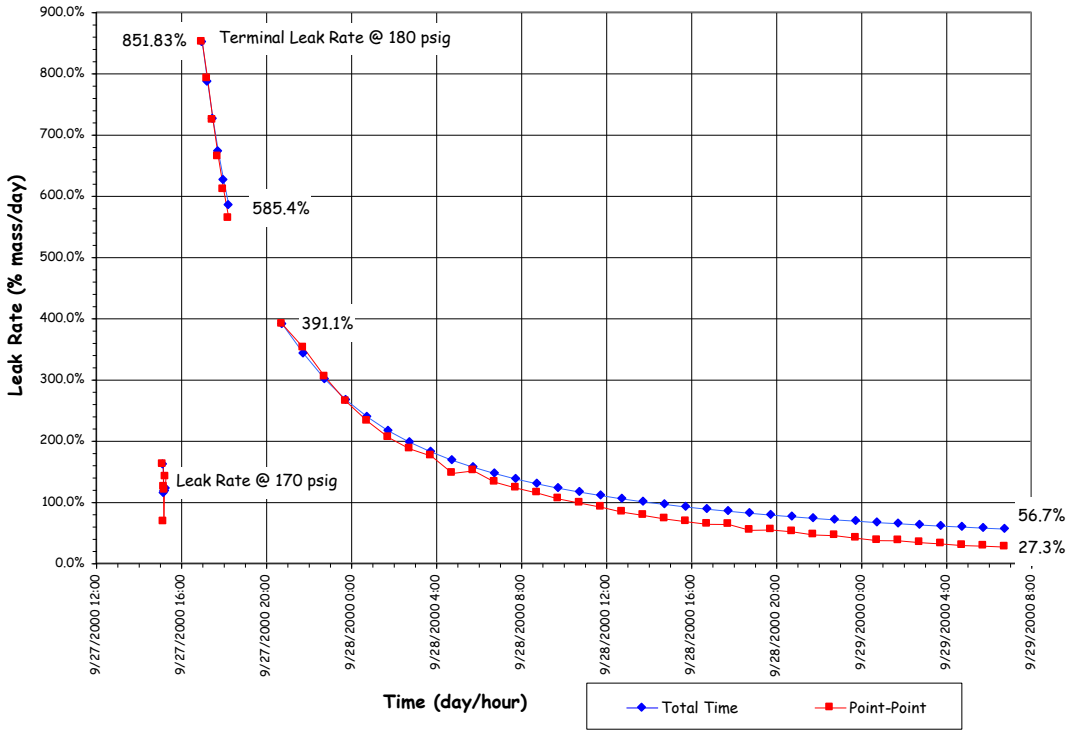

Figure A - 6: LST - estimated terminal leak rates

Leak area prediction method

Liner tearing criteria, strain concentration factors and stress biaxiality factors

The calculation of local strain near discontinuities which cause liner tears requires very localized modeling of the liner, concrete, rebar, and liner anchorage using specialized material and computational models. While these techniques have been developed and extensively utilized, their use is not cost effective for examining all possible tearing locations of individual containments on a case-by-case basis. During the EPRI research program, FEA techniques were used in conjunction with a liner tearing criterion, to develop a database of liner strain concentration factors and thereby construct a simplified analysis procedure for predicting leakage in concrete containments.

Separate sets of strain concentration factor curves (K) versus normalized global strain were developed in the EPRI work. It is based on a coordinated liner tearing criterion of the form:

$$\varepsilon_p = K\, B\, \varepsilon_{global} \qquad (1)$$

Where ε_p is the equivalent peak uniaxial strain at a discontinuity location; this is the strain which is ultimately compared to uniaxial failure strain (max uniaxial elongation) obtained from liner coupon tests. K is the strain concentration factor, B is a stress biaxiality factor and ε_{global} is the global strain quantity that corresponds to the location where the local peak strain is being evaluated, in other words, the "driving strain" behind the concentrated peak strain. A quantity called "normalized global strain" is defined as:

$$\varepsilon_n = (E/\sigma_y)\, \varepsilon_{global} \qquad (2)$$

So it is global strain, normalized to yield strain.
Strain concentration factors versus normalized global strain were published in [8 and 9], and are combined here in Figure A-8, for various geometries of stiffness discontinuities.

The tearing criteria itself is based on a multiaxial stress versus ductility formulation published by Manjoine [11], who cited tests on various ductile materials and proposed the following formula for the ductility ratio μ:

$$\mu = \varepsilon_{eff}/(\text{max uniaxial elongation \%}) \qquad (3)$$

$$\mu = 2^{(1 - TF)} \qquad (4)$$

Where μ is the ductility (reduction) ratio and TF is the Davis triaxiality factor.

$$TF = \frac{\sqrt{2}\,(\sigma_1 \quad \sigma \quad \sigma)}{(\sigma_1 - \sigma) \quad (\sigma - \sigma) \quad (\sigma - \sigma_1)^{1}} \qquad (5)$$

But when the third principal stress is zero or nearly zero, as in the case of the containment liner,

$$TF = \frac{(\sigma_1 \quad \sigma)}{(\sigma_1 \quad - \sigma_1\sigma \quad \sigma)^1} \tag{6}$$

For instance when $\sigma_1 = \sigma_2$, TF = 2 and the ductility ratio is 0.5; i.e., failure strain reduces to half its uniaxial ductility limit. For the last two decades, many containment analysts have used this criteria for predicting onset of liner tearing, but most have concluded that there is also extensive judgment involved in its application. Strains predicted by FE models can be highly dependent on the level of detail (and mesh refinement) included in the model. And, as was seen in the 1:4 Scale PCCV Model, the existence of flaws in the material (especially at weld seams) mean that tears might occur at strains significantly lower than the absolute ductility of the material.

With this formula it is straightforward to calculate ductility ratios at various liner stress states. For example, for uniaxial tension, $\sigma_2 = 0$, TF =1, ductility ratio = 1. For $\sigma_1 = \sigma_2$ (for example the approximate stress condition in the containment dome), TF =2, ductility ratio = 0.5, which means that the liner will tear at an effective plastic strain of only half the uniaxial failure strain. This range of application of Eq. (4) is plotted in Fig. A-7 with additional ductility versus biaxial stress data added from literature surveys. This forms the basis of the tearing criteria and the basis for defining the factor B as well as quantification of its uncertainty bands. Although biaxiality effects are typically characterized as reducing ductility, the approach used for this methodology is a strain magnification approach. Therefore, the reciprocal of the Ductility Ratio is used to magnify the strain. This has been labeled the biaxiality coefficient (B), and for containment liners, under the assumptions of the above discussion it is a number ranging from 1.0 (perfect uniaxial stress state) to .0 (1:1 biaxial stress state, $\sigma_3 = 0$). In other words,

$$B = \frac{1}{\text{ductility ratio}} = \frac{1}{} \tag{7}$$

$1.0 \leq B \leq .0$.

K is then defined to be a strain concentration factor associated with the stiffness discontinuity geometry.

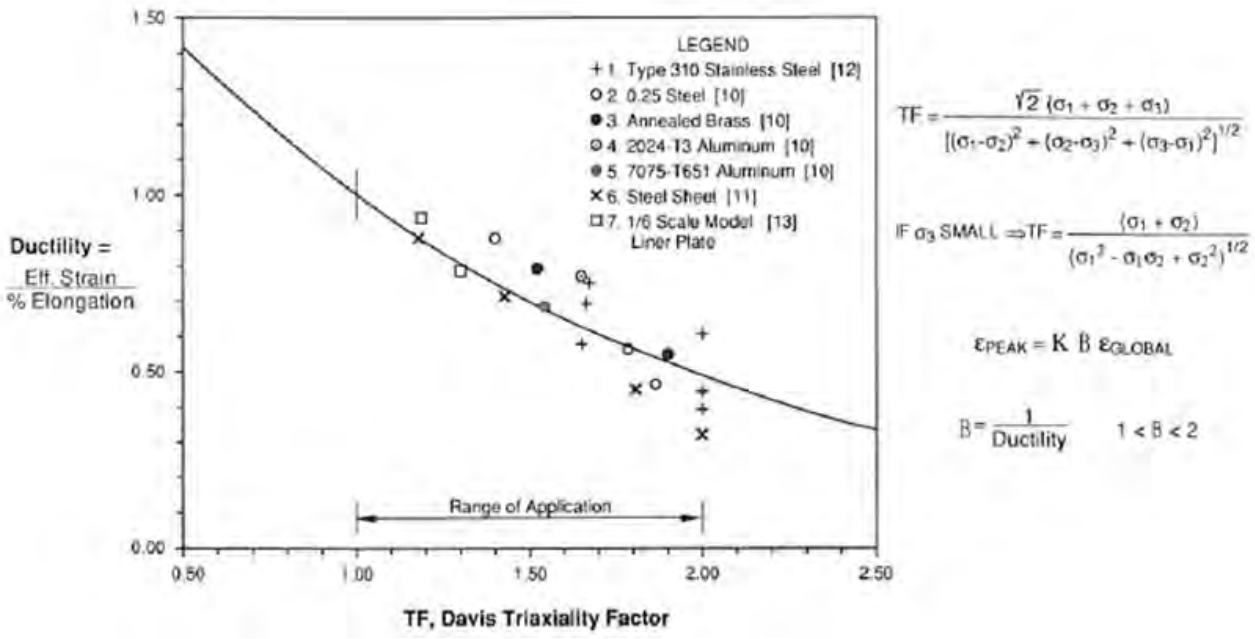

Figure A - 7: Reduced version of Manjoine's multiaxial failure criteria, relating to containment liners

Five fundamental strain concentration factor curves developed in the EPRI program for typical locations of CCV liners are shown in Figure A-8. An additional curve for typical penetrations of an RCCV is also shown in Figure A-8. It can be noted in all these curves that from Global Strain equals zero, out to just past yield, the curves have quite similar shape. Several of the curves begin in the range of K=10, then gradually increase as the locally intensified strain yields and plastifies while the global, driving strain remains elastic. It also should be observed that, as a practical matter, the curves need only be considered out to Normalized Global Strain of approximately 10, i.e., global strain of approximately 1.7%. No tested concrete containment vessel test has survived beyond this level of global strain without tearing the liner. After global strain begins to yield, the strain concentration versus global strain stabilizes within a range of approximately 17 to 30, with an average of approximately K=25. This defines the assumed shape of the K-curve. We now believe that combining the strain concentration factor trends into one curve is within the range of uncertainty appropriate to the data available. It is true that more refined K-curve could be devised for specific containment geometries or specific liner discontinuities, but this is beyond the scope of the current work.

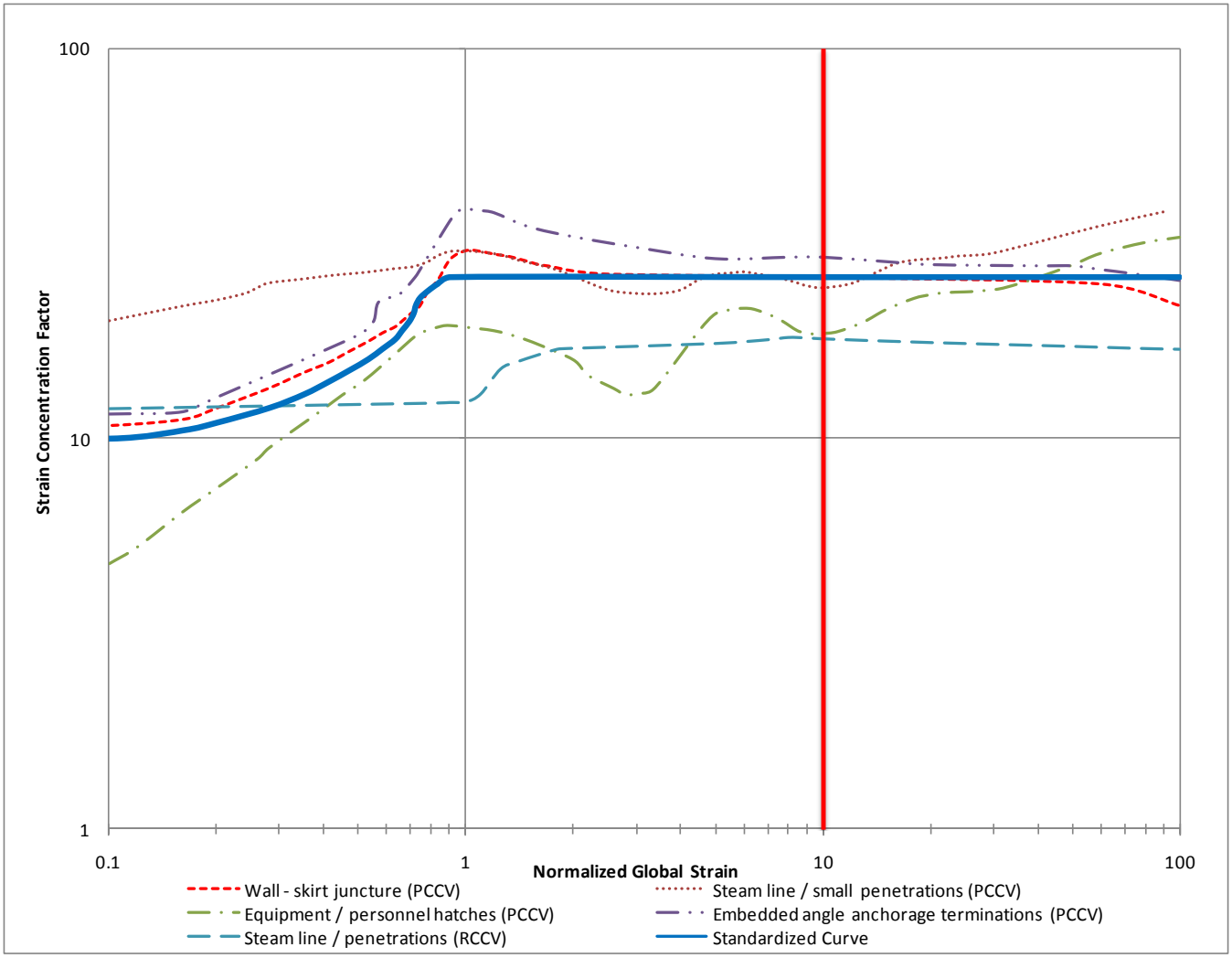

Figure A - 8: Biaxiality and strain concentration factors at various locations around the PCCV

The standardized strain concentration curve proposed for strain concentration locations in the PCCV, is shown in blue in Figure A-8. This curve is proposed for application to all liner strain concentration locations as follows:

1. Vertical weld seams straddled by horizontal stiffeners with a “rat-hole”; based on observations from the PCCV test, the vertical extent of these affected areas will be approximately 8 times the horizontal dimension of the rat-hole. (In the case of the PCCV 1:4 Scale Model, the rathole dimensions is 35 mm., so 8 x 35 mm = 280 mm = the assumed height of “rat-hole” tears.)

2. Vertical weld seams adjacent to E/H, Airlock, Mainsteam, and Electric Feed Penetrations. The tear heights here are defined by the penetration geometry itself; for example at the E H, “k” is applied to global strains along the full height of the stiffness discontinuity formed by the straight vertical edge of the containment wall embossment.

The postulated strain concentration factor curve can also be checked against a very detailed study performed for typical weld seams at the horizontal stiffener rat-holes in Chapter 8 of NUREG/CR-6809 [12]. Some figure excerpts from this work are shown below. Some of the key conclusions from that study are summarized here.
Five groupings of strain gages were placed in locations 1 and 2 (referenced above), as shown in the Figures below (excerpts from [12]). These gages occur at weld seam near a buttress, weld seams near the E/H, and weld seams at general, free-field locations on the liner (e.g., azimuth 135-degrees). Examining these gages shows corroboration of the approximate magnitude of the strain concentrations caused at these locations.

Studies with postulated liner thinning (due to weld-repair grinding) and variations in yield strengths (for base metal, heat-affected zone, and weld metal) explain much of the variability in the measured strains and in the occurrence of liner tears at specific weld locations.

Conclusions from the post-test studies of [12] are as follows.

- Because of competing mechanisms (between the weld zone and the ends of stiffeners), making yield strength and ultimate strength adjustments to the Heat Affected Zone (HAZ) material properties near welds is necessary to correctly predict strain concentration location and intensity.

- Back-up bars should also be modeled. (There are other complications which drives us toward using the simplified “k”-factor approach.)

- Case C6 with back-up bars, nominal geometric properties, and best-estimate material properties is the best predicator of defect-free construction of rat-hole/weld-seam details, as probably occurred in the PCCV model at locations such as D7 and J5; however, even without back-up bars, Case 4, also provides reasonable simulation (and correlation with gages) at these locations.

- Case 10 appears to provide the best simulation of the behavior of tear occurrences in which severe liner thinning (due to weld repair grinding) was present and back-up bars were absent; these conditions existed at tears 7, 8, 10, 12, 13, 14, 15, and 16.

- Case C5 showed the highest strains of all the cases (with a peak over twice as high as Case 10) even though it is analogous to Case 10, which back-up bars added. This shows that in the presence of grinding-caused liner thinning, back-up bars may actually exacerbate the strain concentration in the HAZ. Note, however, that the peak strain in the HAZ was also strongly influenced by the presence of the tear 16 detail. This case appears to reasonably simulate the tears that occurred *with* back-up bars present, namely, tears 1, 2, 6, 9, 11, and 16. The severity of the strain in this case also shows that a tear (ε_{eff} > 20%) at the geometry simulated would have been predicted to occur as early as 3.0 Pd.

- Cases C3 and C4 reasonably simulate tear 16. The lower strain concentration in these models also simulate other tears that appear to have formed at the ends of stiffeners: tears 3, 6, 7, 9, and 11.

- If a section of liner with a rat-hole/liner-seam detail such as that at tear location 7, 12, 13, and 15 is subjected to additionallyelevated strain (i.e. strain across the liner model that is

larger than free-field global strain), a tear even earlier than 3.0 Pd can be justified. In practice, such a prediction could be approximated using a strain concentration factor approach. The strain concentration factors ("k" = peak ε_{eff} divided by global ε_{hoop}) implied by this liner seam study are as follows:

ε_{hoop} = 21mm/5375mm = 0.00391 (radial displacement / R)

Case 4: "k" = 48 (tear at stiffener end, no back-up bar)
Case C6: "k" = 45 (tear at stiffener end, with bacl-up bar)
Case 10: "k" = 59 (tear at HAZ, no back-up bar, and 40% thickness reduction due to grinding)
Case C4: "k" = 91 (tear at Tear 16, if a short segment of horizontal weld seam back-up bar is missing)

- Using the LST pressurization, the rat-hole/seam locations without defects, such as location D-7, still would have developed liner tears by a pressure of 3.4 Pd.

In the post-test report 1 "k" is analogous to KxB defined in the current work. At . Pd, Model 3 analysis indicates B of approximately 1.72 in the zones of most tear locations (midheight of the cylinder). Thus, for the cases cited in [12], the implied Ks are

Case 4 K = 28
Case C6 K = 26
Case 10 K = 34
Case C4 K = 53

These Ks are larger than the generic K = 25 described earlier, because they include various "defects" in the liner, such as over-grinding (reduced thickness) and variations in back-up bar. In total, this information, the biaxial-stress-based liner tearing criteria, and engineering judgment form a reasonable basis for predicting liner tearing occurrence and vertical length of tears in the PCCV model liner.

Additional Strain Gages Near Buttress

	Gage ID	Azimuth (°)	Elevation (m)
1	LSI-C-J5-05	271.9	4.750
2	LSI-C-J5-06	271.9	4.700
3	LSI-C-J5-07	274	4.750
4	LSI-C-J5-08	276	4.750
5	LSI-C-J5-09	278	4.750
6	LSI-C-J5-10	280	4.750

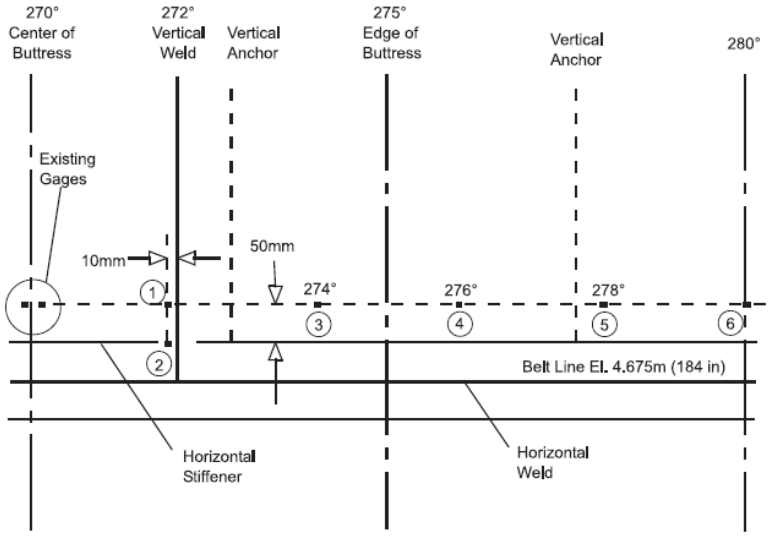

Figure A - 9: Locations of liner strain gages at "J5" (from [12])

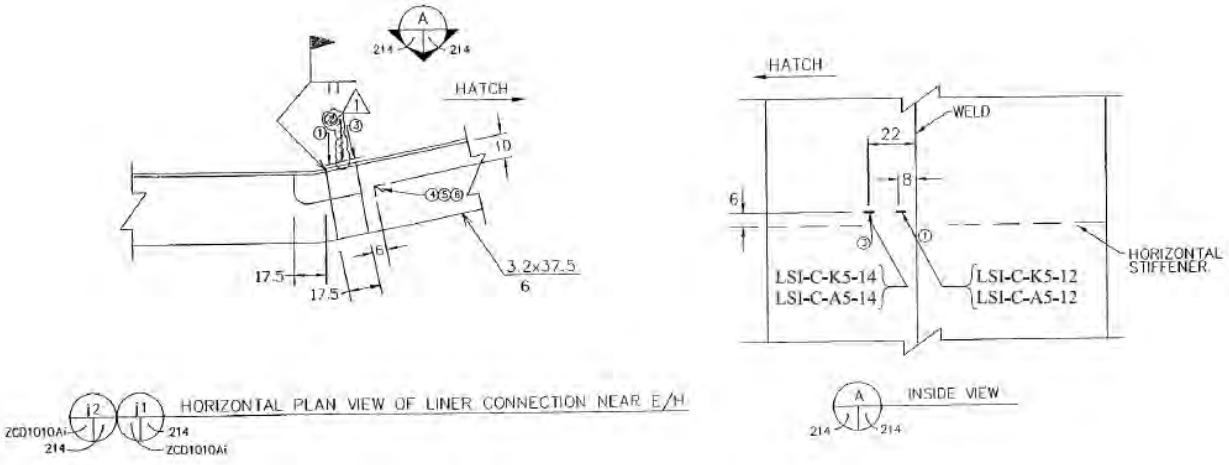

Figure A - 10: Locations of liner strain gages at "K5" & "A5" (Near E/H) (from [12])

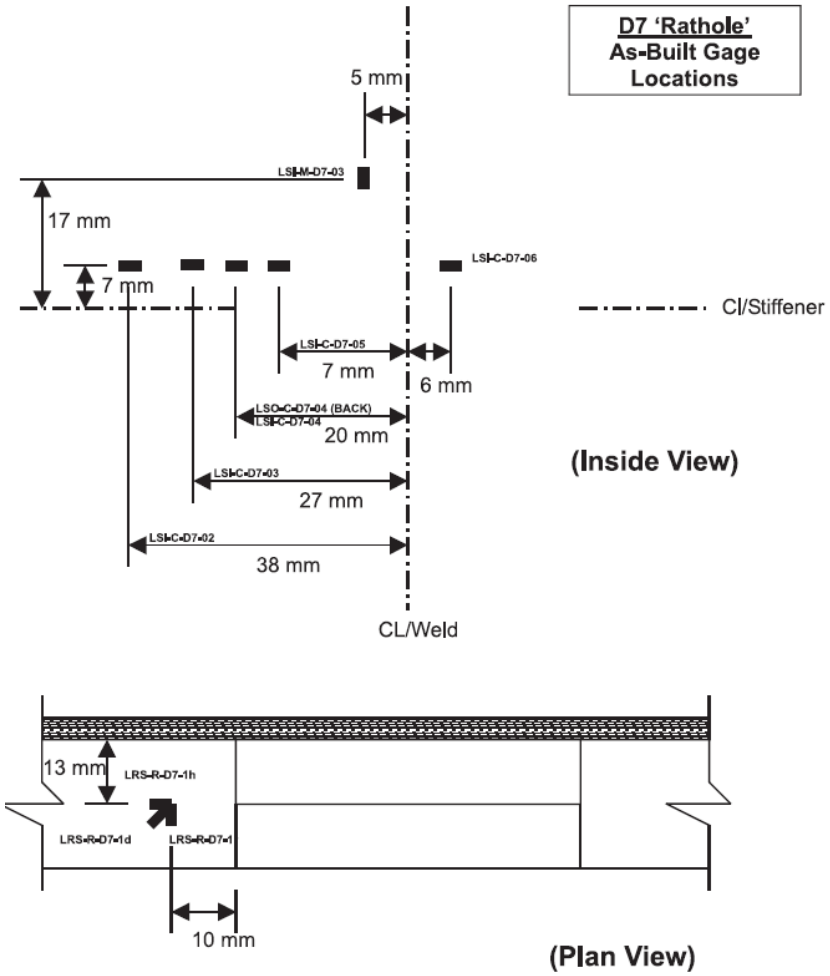

Figure A - 11: Locations of liner strain gages "D5" (near 90-degree buttress) (from [12])

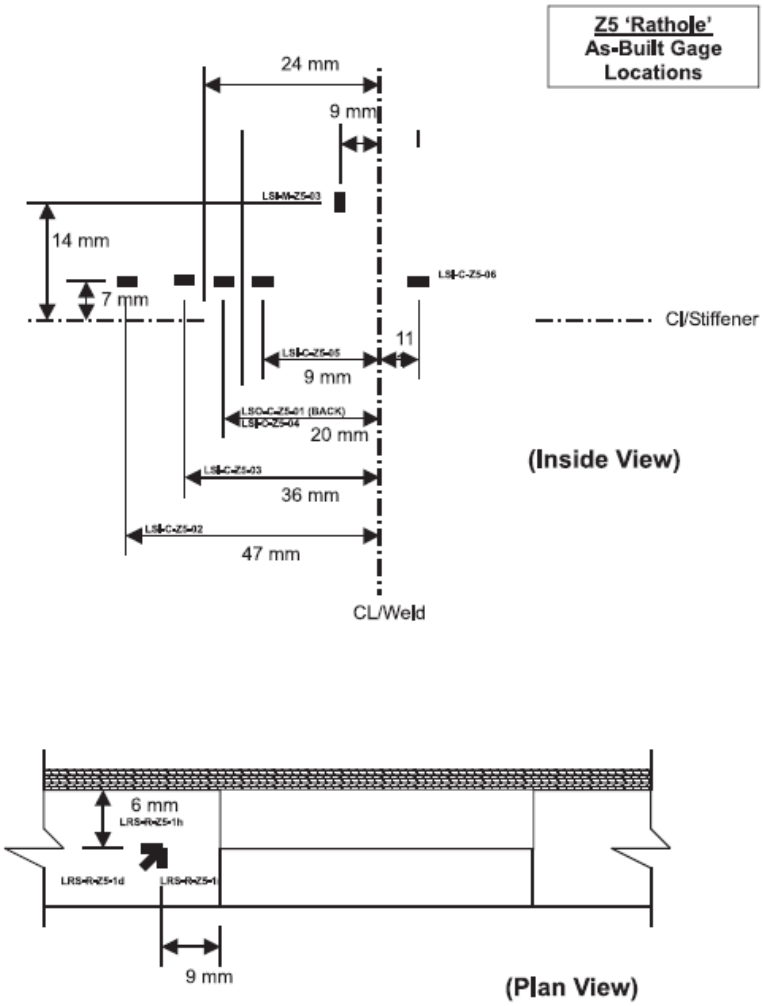

Figure A - 12: Locations of liner strain gages "Z5" (near weld/rat-hole at Azimuth 135-degrees) (from [12])

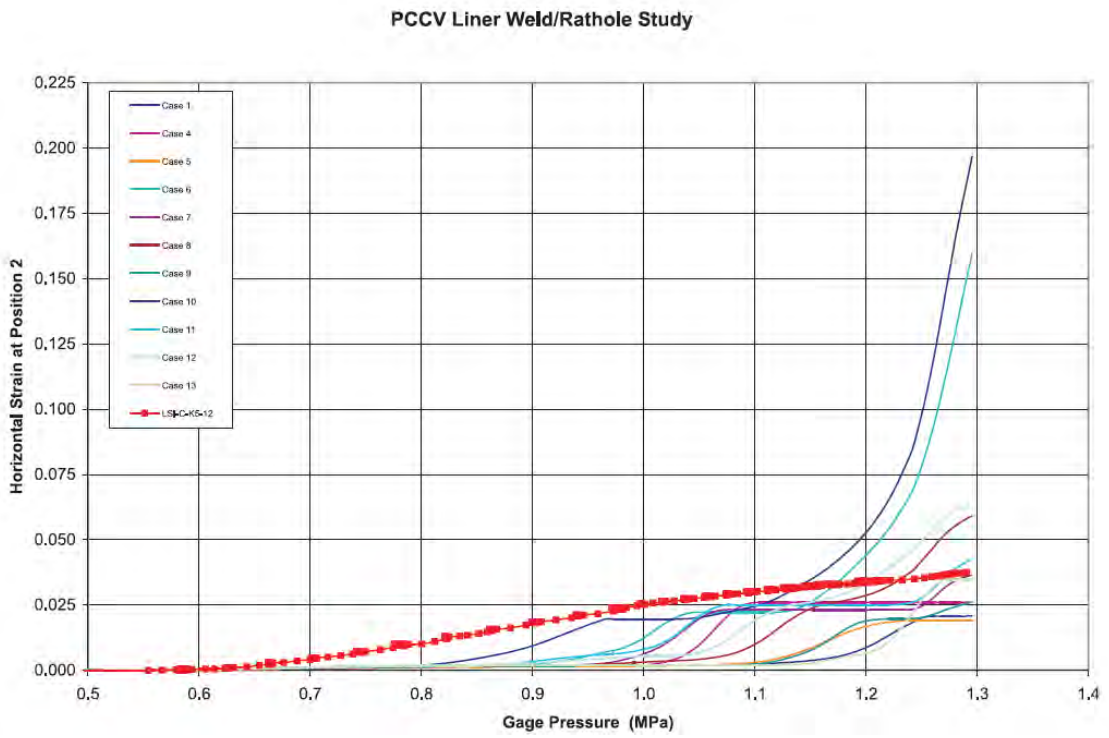

Figure A - 13: PCCV liner weld/rat-hole study mesh sensitivity, horizontal strain comparisons at gage position 2 (from [12])

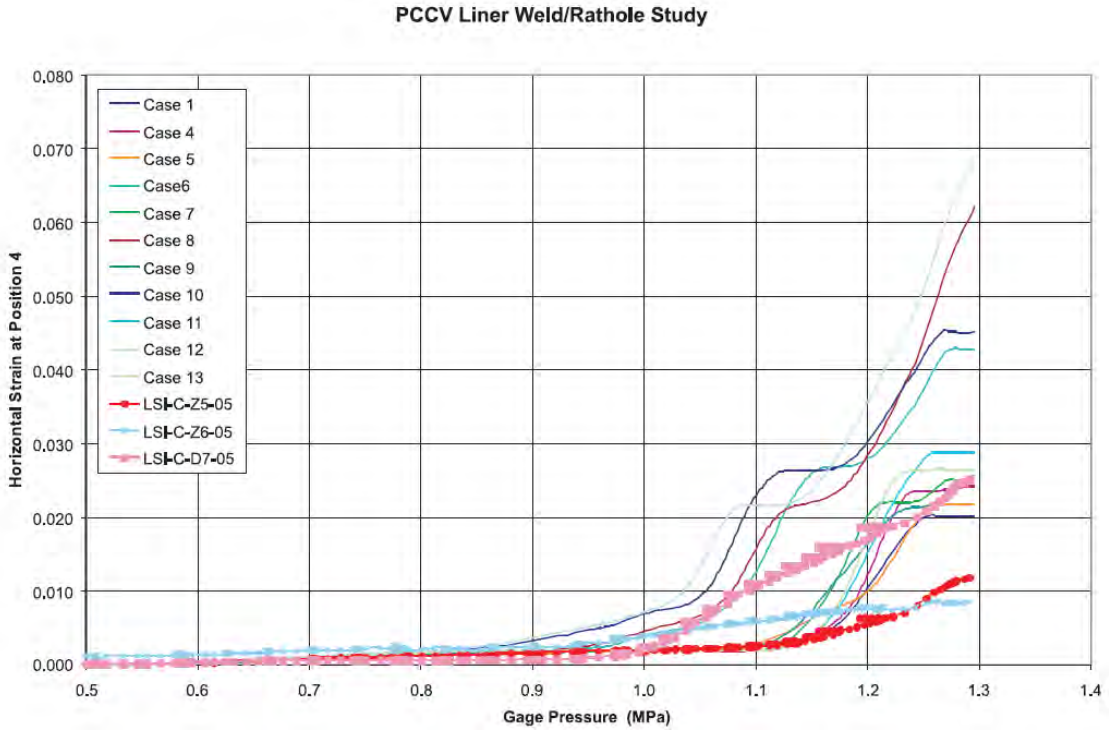

Figure A - 14: PCCV liner weld/rat-hole study mesh sensitivity, horizontal strain comparisons at gage position 4 (from [12])

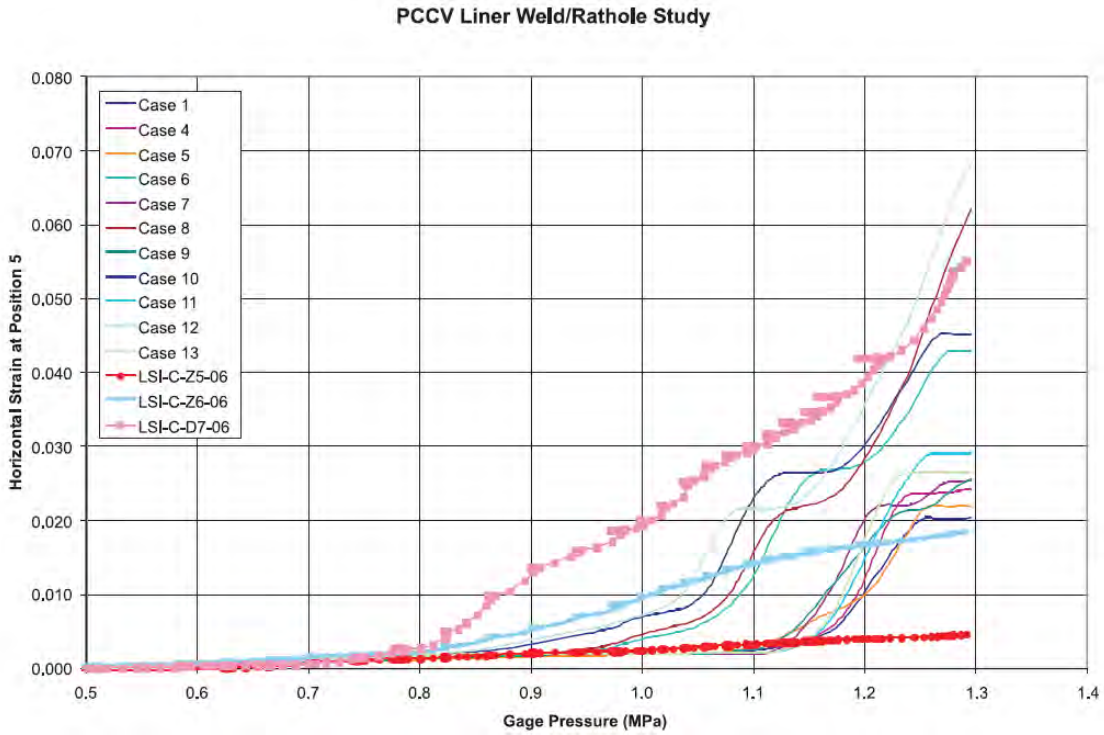

Figure A - 15: **PCCV liner weld/rat-hole study mesh sensitivity, horizontal strain components at gage position 5 (from [12])**

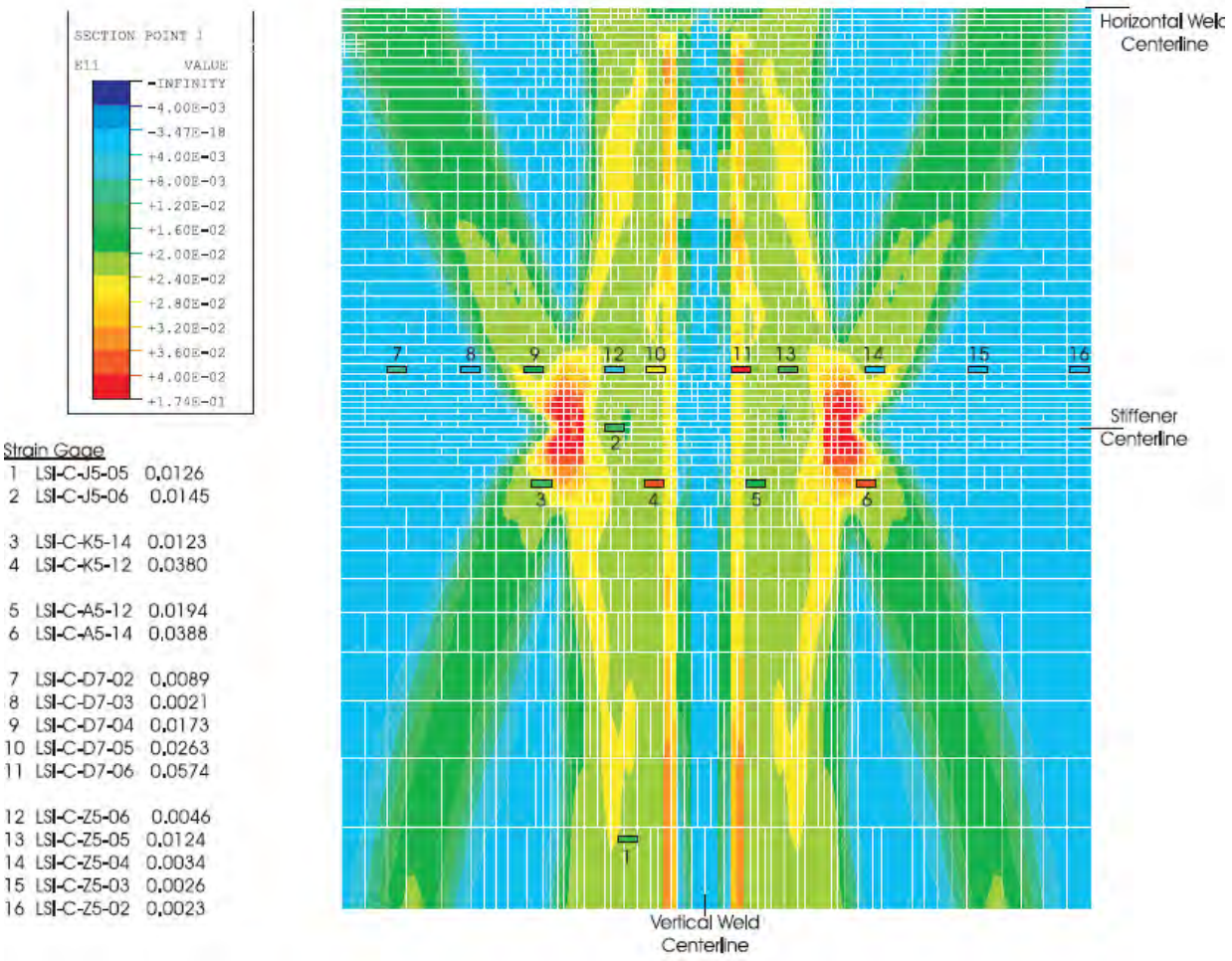

Figure A - 16: **PCCV liner seam rat-hole study, horizontal strain contour, case 4, lst strain gage data superimposed at 3.3 Pd (from [12])**

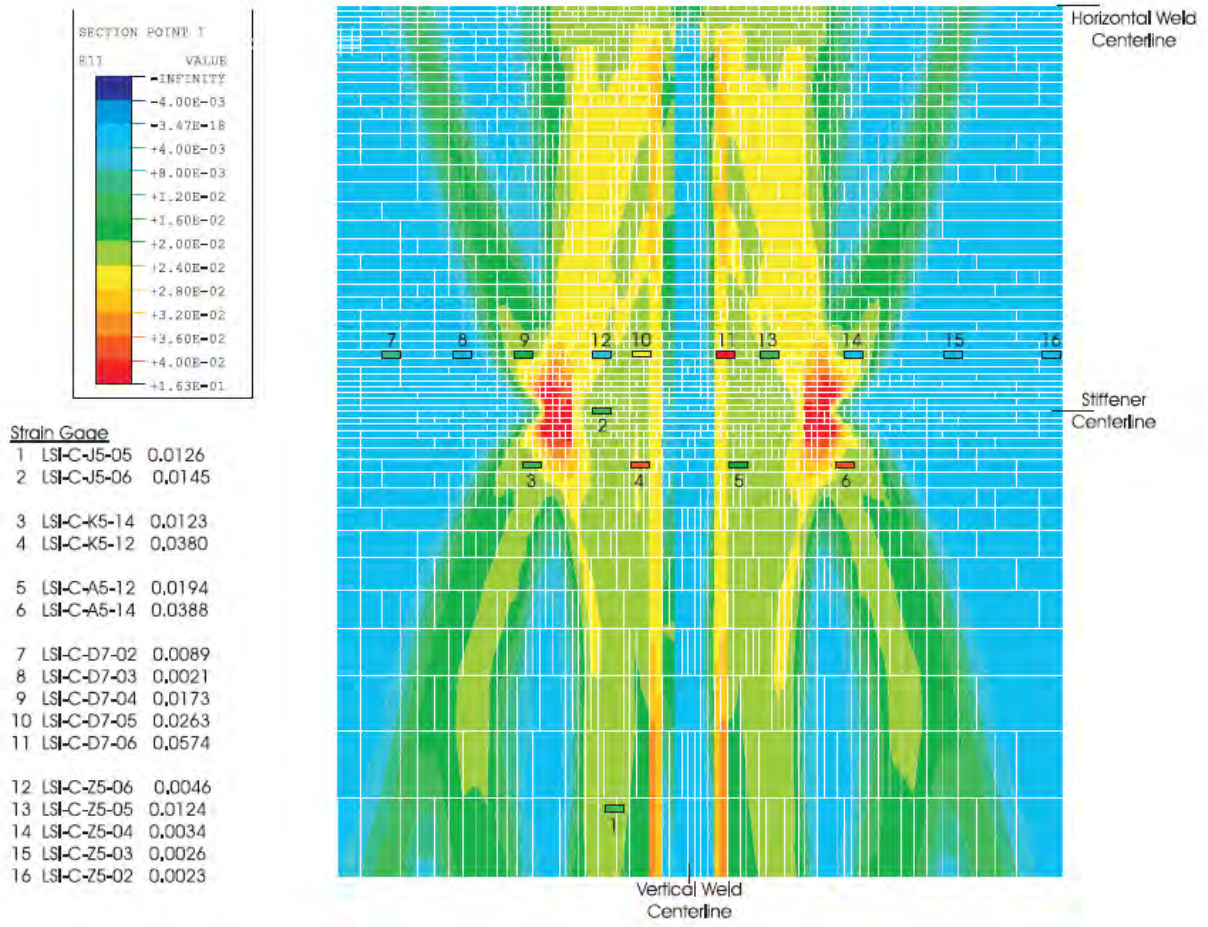

Figure A - 17: PCCV liner seam rat-hole study, horizontal strain contour, case c6, lst strain gage data superimposed at 3.3 Pd (from [12])

Stepwise approach from 'global' strains to tear prediction

To predict tearing of the liner, the strain-based failure criteria is used. 'Global' strains are transformed to an equivalent peak uniaxial strain at a discontinuity location. This conversion of 'global' strain to 'peak' strain allows comparison among the research results mentioned in [12], which states that when the strain at a discontinuous location reaches 21%, a tear is likely to occur. Therefore, using the results obtained from ABAQUS, we can take 'global' strains and convert to an equivalent peak strain at the various discontinuity locations by the strain-based failure criteria method. This conversion is performed by Equation (1).

An example to illustrate this approach is Model 4 - Case 2 at 3.4 x Pd near the E/H.

ε_{global} is the global strain quantity that corresponds to the location where the local peak strain is to be evaluated. Using results obtained from ABAQUS, mechanical strains are

$\varepsilon_{global} = \varepsilon_{hoop} - \varepsilon_{thermal}$.

With a pressure of 3.4 x Pd near the E/H, the hoop strain is 0.0099 and thermal strain is 0.0037. Taking the difference produces a global strain value of 0.0062. Next, the global strain needs to be calculated by the factors K and B, which are the strain concentration and stress biaxiality factors, respectively.

Using Equations (5) with

σ_1 (the maximum in-plane principal stress) = 56627psi and

σ_2 (the minimum in-plane principal stress) = 24130.2psi

TF = 1.64.

Equation (4) gives the ductility ratio of 0.64. As a result, B = 1.56.

Taking the global strain value of 0.0062 and dividing by the normalized yield strain and the K curve illustrated in Figure A-8 (K = 26), the equivalent peak strain at a discontinuity location is 0.251.

In this example, since $\varepsilon_p = 0.251 > 0.21$, tearing of the liner has occurred.

Implementation (computing tear areas)

Continuing with the same example, since $\varepsilon_p > 0.21$, tearing of the liner has occurred.

The next step in the analysis is determining the crack width. Assuming the average crack width occurs over the spacing between anchors,

$W_{avg} = \varepsilon_{global}$ times spacing between anchors.

For this example, the spacing between anchors is 6 inches.

Therefore, $W_{avg} = 0.04$ inches.

Along the Equipment Hatch, the assumed height of the tear is as long as the discontinuity occurs and the strain is of sufficient magnitude for the tear criteria to be satisfied. In this case, that tear height is 13.31 inches, so the tear area at this particular location is 0.5 in^2.

Converting tear area to leak rate

This section summarizes the work documented in “Proposed Formula for Leakage versus Pressure through concrete containment Phase – Study of SPE ,” by Atomic Energy Regulatory Board (Niyamak Bhavan and Anushakti Nagar, Mumbai – 400094, India).

Formulation of leakage through concrete section

There are many models available in the literature for estimating air leakage through a concrete section. Rizkalla et al. [13], Nagano et al [14], Suzuki et al. [15] [16], Greiner and Ramm [17] are a few to be named. In literature, we also find some application and comparative study of these formulae. It is observed that for a general case, where pressure variation and range of crack

width are large, formulae suggested by Rizkalla et al and Suzuki et al [16] give a fair estimation of leakage. It is also observed in literature [18] that formula given by Suzuki estimates reasonable leakage for low pressure difference, where as formula proposed by Rizkalla et al is applicable for wide range of pressure differences. (This is why we have chosen the Rizkalla method.)

General

Description of crack, including parameters that are required to use these formulae stated in this chapter.

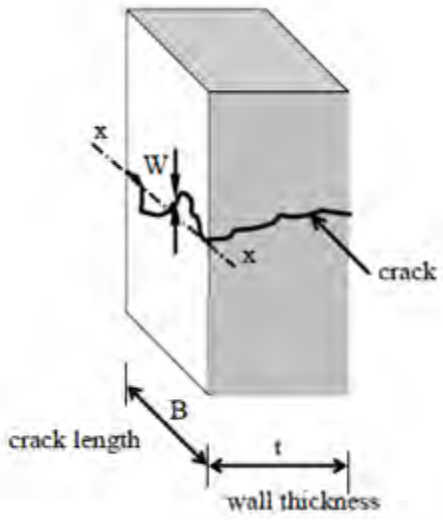

Figure A - 18: **Definition of crack length and crack width**

On the surface of the cracked wall, a straight crack length is defined as in Figure A-18. The straight-line x-x in Figure A-18 is an example of crack length. The crack width W is the direction perpendicular the straight-line x-x on the surface of the wall.

Rizkalla et al.

$$\frac{p_1^2 - p_2^2}{t} = \left(\frac{k^n}{2}\right)\left(\frac{\mu}{2}\right)^n (RT)^{n-1}\left|\frac{p_2 Q}{B}\right|^{2-n} \frac{1}{\sum_{i=1,j} W_j^3},$$

where, $\sum_{i=1,j} W_j^3 = 1.42 N W_{av}^3$ and N = *number of* cracks and W_{av} = average crack width

$$n = \frac{0.133}{\left(\sum W_i^3\right)^{0.81}} = \frac{0.195}{\left(N W_{av}^3\right)^{0.063}} \text{ and } k = 2.907x10^7\left(\sum W_i^3\right)^{0.428} = 8.702x10^6\left(N W_{av}^3\right)^{0.367}$$

Where, Q = flux through the wall (ft^3/s), B = crack length (ft), W = crack width (ft), t = wall thickness, p_1 = upstream pressure (lb/ft^2), p_2 = downstream pressure (lb/ft^2), μ = dynamic viscosity of air or gas used (lb s/ ft^2), T = absolute temperature (°R), R = gas constant ($sqft/s^2$ °R). W_{av} is the average crack width of the total concrete section of interest. Typical values of μ and R are 1.80 x 10^{-5} Pa-s and 1716 $sqft/s^2$ °R respectively.

Suzuki et al. [16]

$$Q^2 = \frac{W^3(p_1^2 - p_2^2)}{2\rho_o p_0 t\left[\bar{a}(W)\frac{12\mu}{\rho_o Q} + b(W)\right]}$$

Where, $\bar{a}(W) = \frac{4.33x10^{-5}}{W^{1.5}} + 1$ and $b(W) = \frac{3.41x10^{-4}}{W}$

This equation is modified to the following equation for $p \cong 1(atm)$ and $\Delta p \le 0.2(atm)$

$$Q = \bar{\alpha}(W)\frac{W^3(p_1 - p_2)}{\mu t}, \text{ where } \bar{\alpha}(W) = 15.3W + 7.56x10^{-3}$$

The units of these parameters are W in m, p1, p_2, p_o in P_a, ρ_o in Kg/m^3, t in m, μ_o in Pa s and Q in $m^3/s/m$. Estimated leakage based on above formula is for unit crack length. To get the total leakage, the Q should be multiplied with crack length (B).

Methodology

A tentative methodology is furnished below for easy reference and understanding. Participants are free to choose methodology for estimating leakage through PCCV with respect to different pressure.

(i) Get strains of rebar/prestress cable in a grid or matrix format of the entire location, wall and dome of containment, for a particular state of internal pressure as suggested in White Paper.

(ii) Calculate crack width and Number of cracks at each matrix element/location using available methodologies in literature.

(iii) Calculate leakage in every matrix element/location

(iv) Get the total leakage by summing up the leakages in every matrix element/location.

(v) Repeat (i) to (iv) for each pressure loading/steps.

This is the procedure we have followed in the Sandia / Moffatt & Nichol analysis work, including the choice of using Rizkalla's method for the leak rate calculation.

STANDARD PROBLEM EXERCISE ON

PERFORMANCE OF CONTAINMENT VESSEL UNDER SEVERE ACCIDENT CONDITIONS

Phase -2 Analysis Report

Part- II: Estimation of Leakage through Containment wall

EXERCISE UNDERTAKEN BY

Siting and Structural Engineering Division
ATOMIC ENERGY REGULATORY BOARD
MUMBAI

MARCH 2012

CONTENT

1.0 INTRODUCTION

The U.S. Nuclear Regulatory Commission (USNRC) and SANDIA National Lab, USA are participating in a round robin analysis, called the Standard Problem Exercise (SPE) No. 3, with the Atomic Energy Regulatory Board (AERB) of India. Phase-1 of the round robin analysis involved structural response of a prestressed concrete containment vessel (PCCV) for pressure loading under severe accident conditions including the local effects due to hatch openings. Phase-2 analysis involves structural responses of PCCV due to temperature and pressure variations as per a specified pseudo time history (case-1) and also for variations corresponding to a specified station black out condition (SBO) (case-2) by USNRC. The phase-2 also includes leakage prediction for pressure loading of phase-1 as well as both the load cases of phase-2 and finally transitions them to probabilistic space. The details of the scope of studies are given in white paper, phase-2. This report contains methodology of leakage estimation, leakage calculations for phase-1 loading as well as for both case studies of phase-2 including probabilistic estimates of the leakages.

2.0 METHODOLOGY OF LEAKAGE ESTIMATION

The air leakage through steel lined prestressed concrete containment is a complex phenomenon. The physics of this type of leakage is still a topic of research studies. An attempt has been made during SPE-3 exercise to estimate leak rate because of internal pressure as well as combined effect of internal pressure and temperature corresponding to severe accident scenario. The methodology is described in three steps, step-1: assumptions, step-2: number of cracks and crack width calculations, step-3: estimation of leakage rate. These steps are explained in detail in this chapter.

2.1 Assumptions

The following assumptions are made while formulating leak rate calculations:

(i) The containment is loaded by prestress, internal pressure and temperature only.

(ii) The crack width and number of cracks in prestressed concrete containment section are functions of strain in prestress cables.

(iii) There will not be any leakage until the prestressed concrete section is cracked.

(iv) Vertical through-the-wall cracks, due to hoop strains in prestressing cables are considered for calculations as contribution of circumferential cracks was seen to be insignificant.

(v) The leak rate through concrete cracks is controlled by the extent of liner damage at co-locations besides the pressure gradient.

(vi) Properties of air are considered constant throughout.

2.2 Number of Cracks and Crack Width Calculation

Number of cracks and crack width are the major parameters for leakage calculation assuming air leakage from inside of the containment to outside through the cracks in concrete section based on differential pressure and temperature inside the containment.

In this study, the number of cracks and the crack width of prestressed concrete section of PCCV are estimated using the methodology suggested by Rizkalla et. al [1]. The formulation for crack width calculation requires estimation of lost bond length and bond transfer length of prestressing steels, strain in prestress cable and mean strain, which is a function of the ratio of cable stress at load step to cable stress at onset of section cracking. In walls containing prestressing tendons parallel to the direction of cracking, through-the-wall cracks will occur at the same spacing as the tendons. Should the tendon spacing exceed twice the wall thickness an additional through-the wall crack will occur midway between the tendons. The number of through-the wall cracks stabilizes, when strain in prestress cable reaches 0.002., i.e. no new crack formation after the cable attains a strain of 0.002. At any given strain less than 0.002, the number of through-the wall cracks can be expressed as

$$N = N_{twc}\left[\frac{\varepsilon_{s2} - \varepsilon_{s2,cr}}{0.002 - \varepsilon_{s2,cr}}\right]$$

Where, N_{twc} = the final number of through-the wall cracks according to assumptions as described above, N= the number of such cracks corresponding to strain, ε_{s2} the strain in prestressing steel perpendicular to the crack and $\varepsilon_{s2,\ cr}$ = average strain in prestressing steel at on-set of concrete section cracking.

The numbers of cracks are rounded off to the nearest whole number.

2.3 Estimation of Leakage Rate

2.3.1 Methodology

Rizkalla et. al [2] suggested correlations for pressurized air leakage through concrete cracks based on experimental studies. The leakage rate calculation is straight forward if crack width and pressure gradient are known. These correlations can be applied directly for unlined concrete containment. The physics of leakage is complex for steel lined containment. Dameron et al [3] attempted leakage rate through lined containment with the assumption that leakage would occur regardless of whether the concrete crack is aligned with the liner tear. So, the leakage was estimated based on liner crack width (average liner strain x anchorage spacing or gauge length) considering a single crack in a particular gauge length/area.

In this study, it is assumed that air will leak through cracked concrete but amount of leakage will be controlled by the degree of damage in the co-located liner. Since the concrete wall is a sub-stratum to the liner in a containment, both will experience the stress severity at identical locations and hence the likely leakage path would be through the co-located parts of concrete and liner as this would also be the path of least resistance for air flow. Thus determination of liner damage at any loading/pressure stage is important in estimating leakage through PCCV.

In absence of detailed fracture mechanics calculations for linear damage based on some assumed initial flaw sizes, it is assumed here that the liner damage permitting leakage initiates when the induced liner stress correspond to the liner fracture toughness, Jcr. The ultimate liner damage, when it will cease to control the leakage through cracked concrete, is assumed to occur when the induced liner strain reaches the failure strain/elongation. This failure strain is a function of the uniaxial rupture strain and the state of strain in the liner. The rupture strain value is thus modified using a triaxiality factor [4] for the biaxial state of strain in the containment wall. Assuming hoop stress to meridional stress ratio of 2.0, the triaxiality factor (TF) works out to be 1.7. This assumption is considered to be reasonable in light of the stress analysis results, which indicate no damage in the dome area. The TF value is kept constant for all cases, variation of TF based on stress variants is not considered.

2.3.2 Leakage Rate Formulation for concrete section

There are many models reported in literature for estimating air leakage through a concrete section viz. Rizkalla et al. [2], Nagano et al. [5], Suzuki et al. [6] [7], Greiner and Ramm [8] and comparative study of these formulae by Riva et. al. [9]. It is observed that for a general case, where pressure variation and range of crack width are large, formula suggested by Rizkalla et al [2] is more appropriate, particularly for higher pressure gradients. In this study, the formulation as suggested by Rizkalla et al is used, which is as follows:

$$\frac{p_1^2 - p_2^2}{t} = \left(\frac{k^n}{2}\right)\left(\frac{\mu}{2}\right)^n (RT)^{n-1} \left|\frac{p_2 Q}{B}\right|^{2-n} \frac{1}{\sum_{i=1,j} W_j^3},$$

where, $\sum_{i=1,j} W_j^3 = 1.42 N W_{av}^3$ and N = *number of* cracks and W_{av} = average crack width

$$n = \frac{0.133}{\left(\sum W_i^3\right)^{0.81}} = \frac{0.195}{\left(N W_{av}^3\right)^{0.063}} \text{ and } k = 2.907x10^7 \left(\sum W_i^3\right)^{0.428} = 8.702x10^6 \left(N W_{av}^3\right)^{0.367}$$

Where, Q = flux through the wall (ft^3/s), B = crack length (ft), W = crack width (ft), t = wall thickness, p_1 = upstream pressure (lb/ft^2), p_2 = downstream pressure (lb/ft^2), μ = dynamic viscosity of air or gas used (lb s/ ft^2), T = absolute temperature (^oR), R = gas constant ($sqft/s^2\ ^oR$). W_{av} is the average crack width of the total concrete section of interest.

Typical values of μ and R are 1.80×10^{-5} Pa-s and 1716 $sqft/s^2\ ^oR$ respectively.

2.3.3 Leakage rate calculations

The leakage rate is estimated as per the note circulated by us (AERB) earlier as a part of phase-2 exercise, incorporating the above stated methodology. The step-wise calculation is explained below:

(i) Strains and stresses of prestress cable in hoop direction (received as output of FE analysis) in each gauge area, (assumed here same as finite element area of 0.2 x 0.2 sqm), for whole containment (13900 elements) for a particular state of internal pressure are captured and stored.

(ii) Strains in hoop direction of steel liner are also captured and stored in similar manner.

(iii) Prestress cable strains are checked against concrete cracking strain to establish on-set of cracking in the element areas.

(iv) Crack widths and number of cracks are calculated for each element/gauge area. Crack height is assumed to be the same as element height.

(v) Leakage is calculated for each element using the formula given in 2.3.2. Temperature histories (case-1 and case-2) are considered during this stage of leakage calculation to provide temperature value in the leakage formula. For pressure alone ambient temperature of 25 ^oC is considered.

(vi) Liner strains are checked in every element for initiation of liner damage based on Jcr.

(vii) If the liner strain is more than initiation strain, damage co-efficient is calculated for each of the three assumed variations of the damage co-efficient from zero to one, viz. linear, parabolic and power variation. Damage co-efficient is 1.0 at failure strain, which is 20% strain, multiplied with ductility factor (ductility factor, $\mu = 2^{(1-TF)}$) [4]. For strains less than the initiation strain, damage coefficient is considered to be zero.

(viii) The damage co-efficient is then multiplied with corresponding element leakage rate to get the effective leakage rate.

(ix) Total leakage rate is calculated by summing up the effective leakage rates in all the elements. This leakage rate is then converted to %volume of containment per day.

(x) Step-(i) to (ix) is repeated for various load steps.

(xi) Finally leakage in % Volume of containment /day is plotted with respect to pressure values in terms of multiples of design pressure.

3.0 RESULTS

The initiation of liner damage is estimated based on critical J-integral values taken from the Model-2 report of phase-1 by Dameron et. al. Typical Jcr value of 350 in-lbs/sq in is considered as mean value. The variation of Jcr values was to be considered as 500, 200 and 800 in-lbs/sq. in as suggested in the white paper. But average strain corresponding to Jcr=800 in-lbs/sq. in could not be calculated from the plot provided in Model-2 report of Dameron et. al. So, three values of Jcr considered for leakage calculations are; 200,350 and 500 in-lbs/sq in. The corresponding average strains for damage initiation are 0.0022, 0.0028 and 0.0034 respectively. For initiation of concrete cracking, composite section of containment wall is considered, which includes reinforcing steel as well as prestressing steel. The cracking strain of the homogenized composite section was calculated to be 0.000629. Crack widths were calculated following the methodology of Rizkalla et al [1] when the induced strain exceeded the cracking strain. Leakage rates were estimated for three cases corresponding to pressure loading (phase-1 study) alone and combination of pressure and temperature histories for two accident scenarios (phase-2 study: case-1 and case-2) .

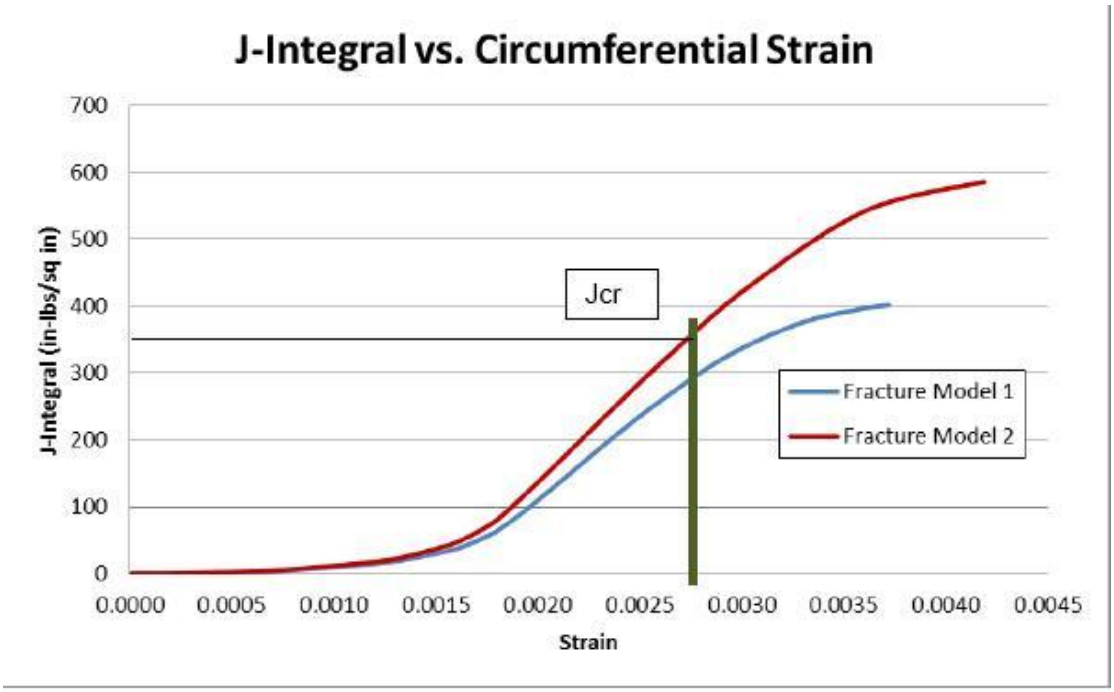

Fig.1 J-integral vs circumferential strain of liner as furnished in Tech Memo of Model-2 by Dameron et. al.

3.1 Leakage Estimation for Phase-1 Exercise

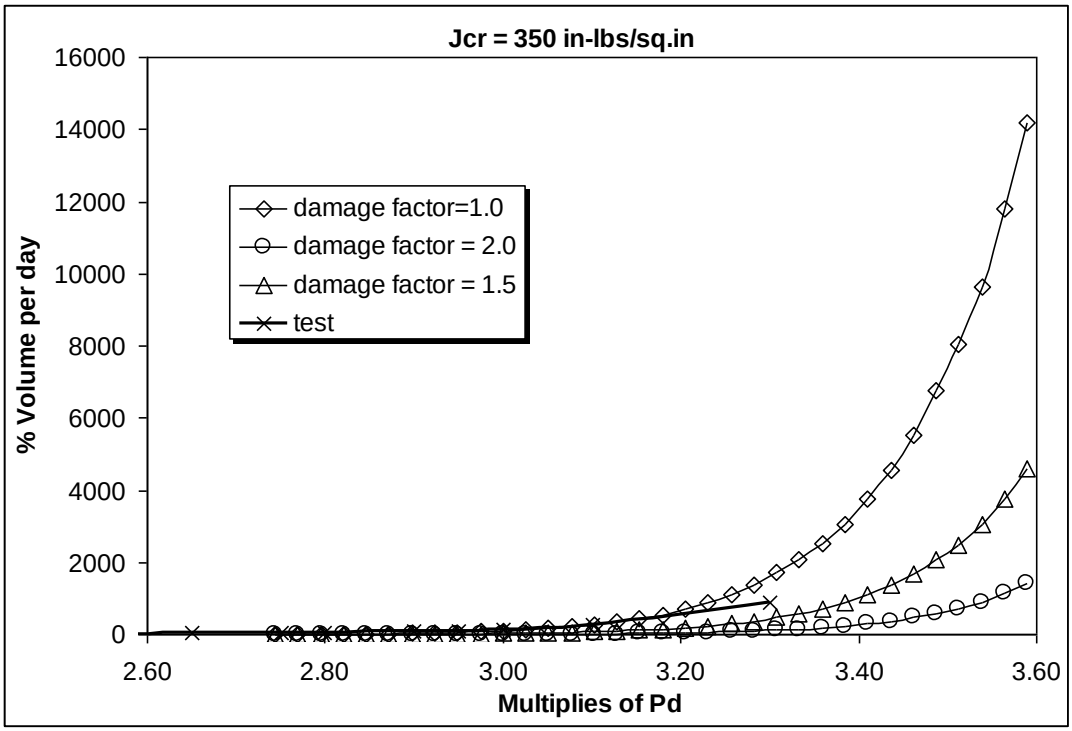

Fig.2 (a) variation of leakage rate w.r.t multiplies of design pressure for Jcr = 350 in-lbs/sq.in

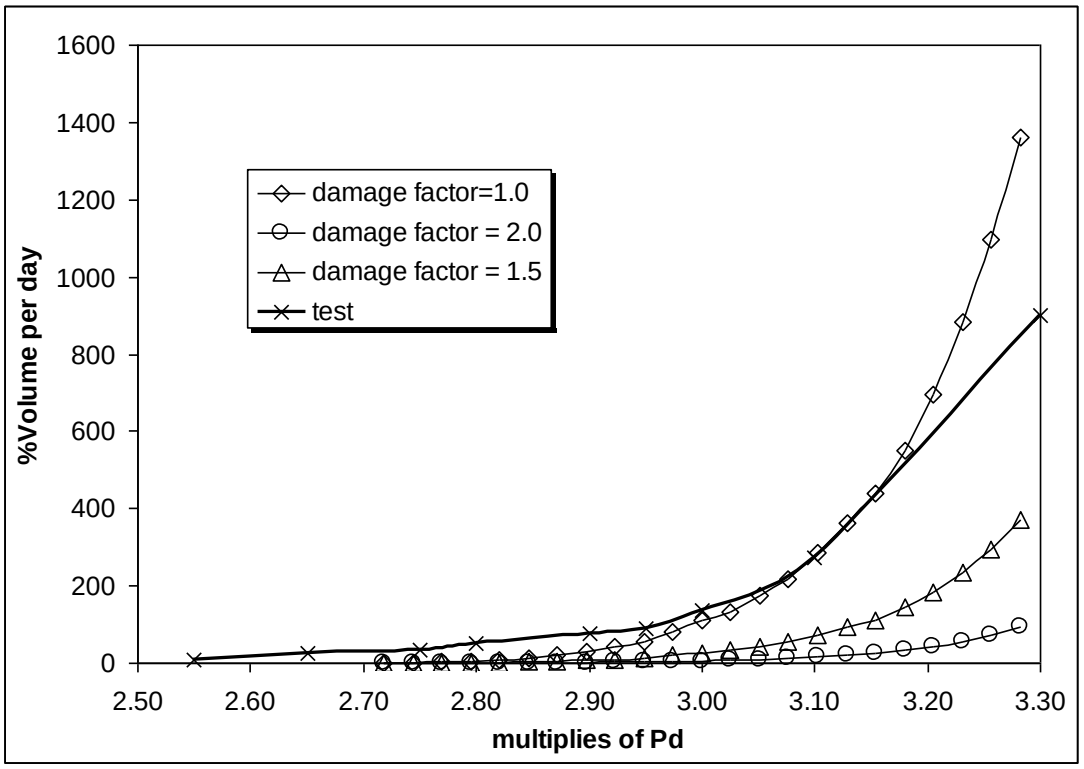

Fig.2 (b) variation of leakage rate w.r.t multiplies of design pressure up to 3.3Pd for Jcr = 350 in-lbs/sq.

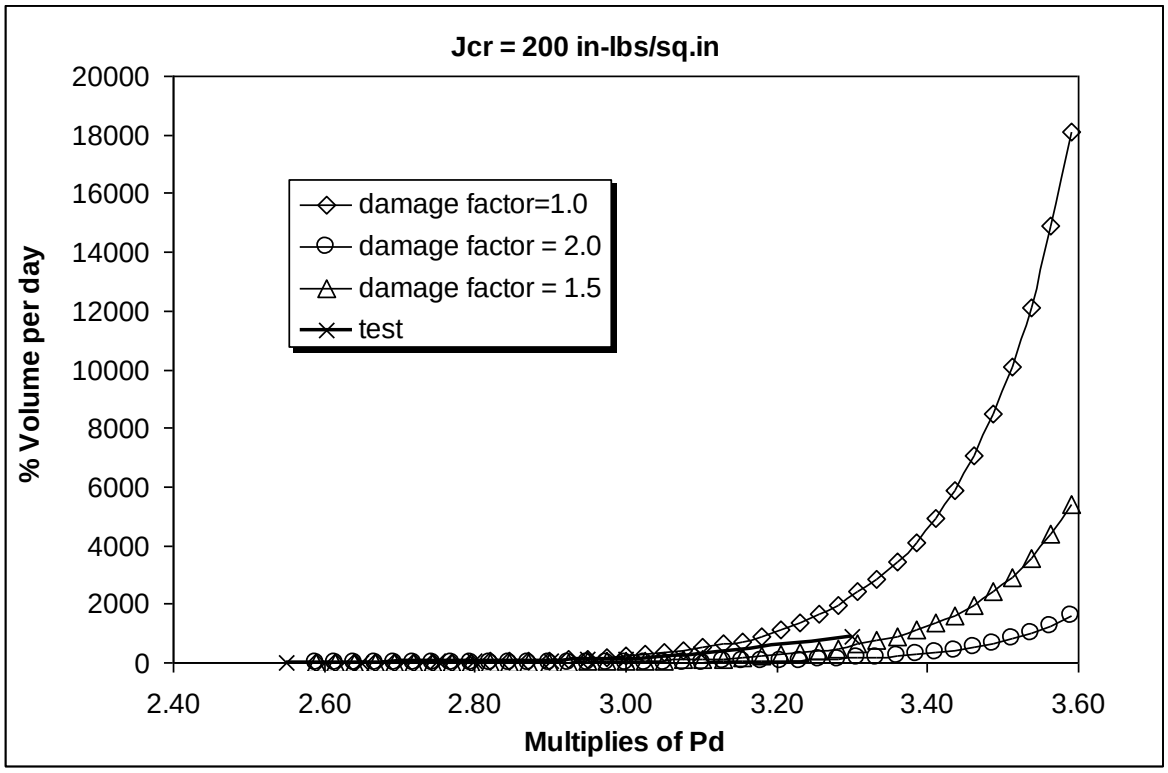

Fig.3(a) variation of leakage rate w.r.t multiplies of design pressure for Jcr = 200 in-lbs/sq.in

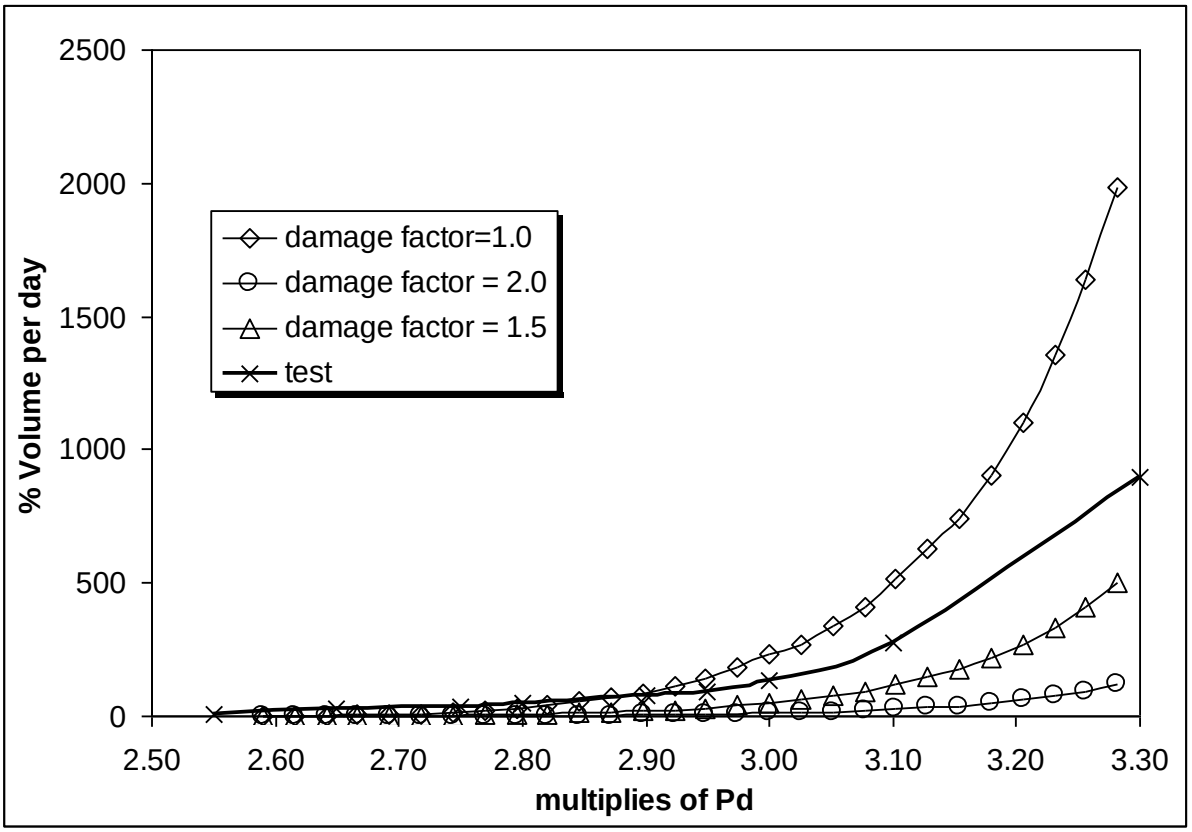

Fig.3(b) variation of leakage rate w.r.t multiplies of design pressure up to 3.3Pd for Jcr = 200 in-lbs/sq.in

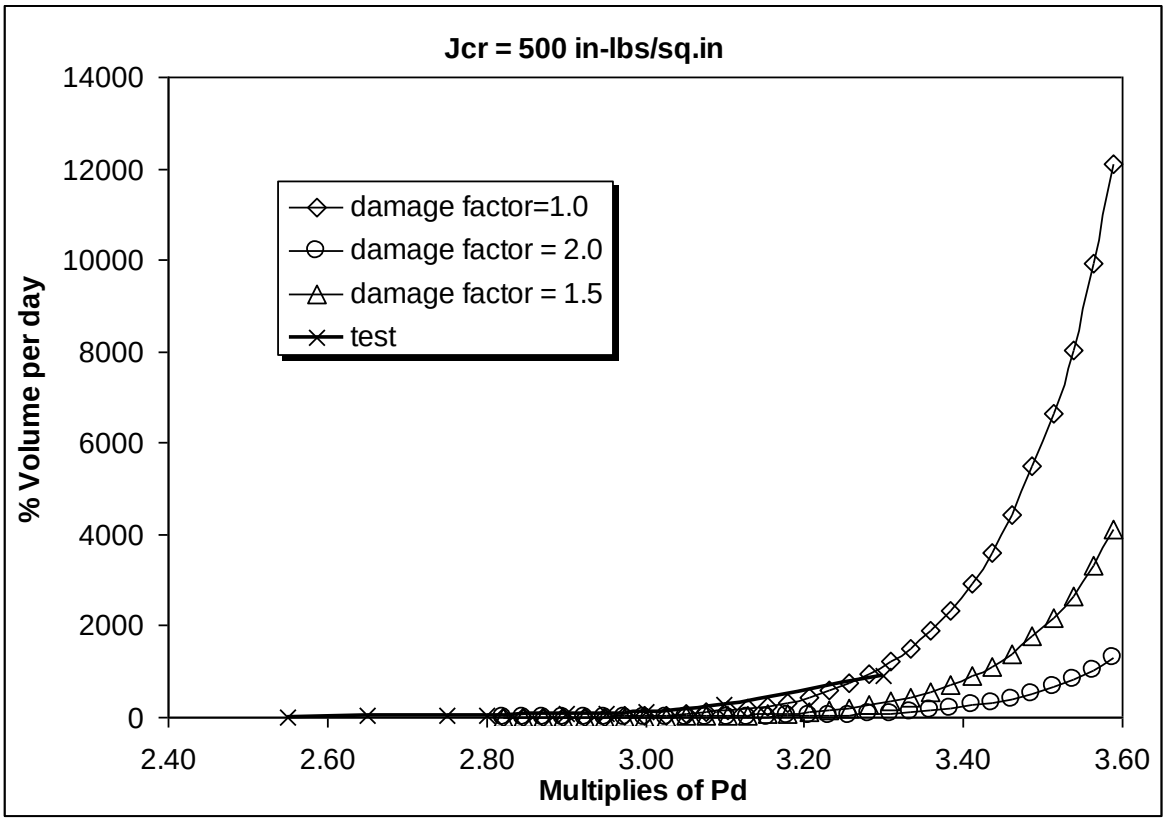

Fig.4(a) variation of leakage rate w.r.t multiplies of design pressure for Jcr = 500 in-lbs/sq.in

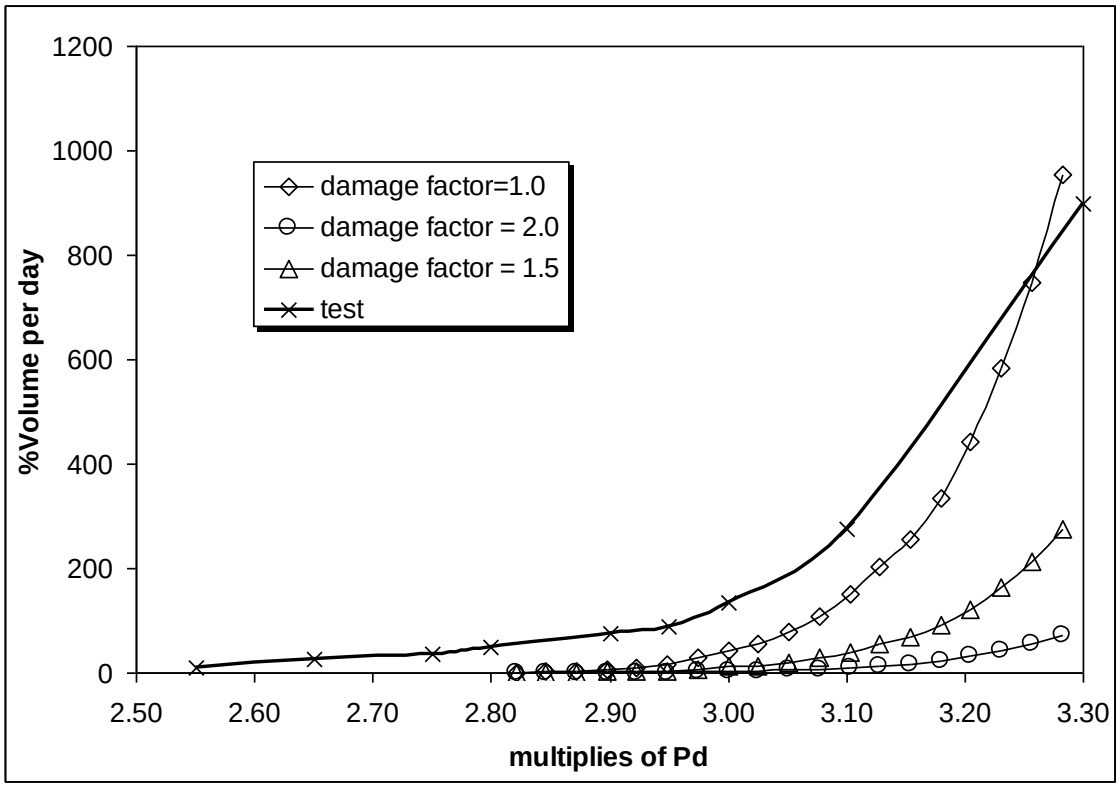

Fig.4(b) variation of leakage rate w.r.t multiplies of design pressure up to 3.3Pd for Jcr = 500 in-lbs/sq.in

3.2 Leakage Estimation for Phase-2: Case-1 Exercise

The Phase-2: Case-1 exercise is done for pressure and temperature loading, saturated pseudo-time history, as given in white paper, furnished here in Fig. 4. Leakage rates are estimated considering stress/strain resultants of 3D global FE model subject to this loading.

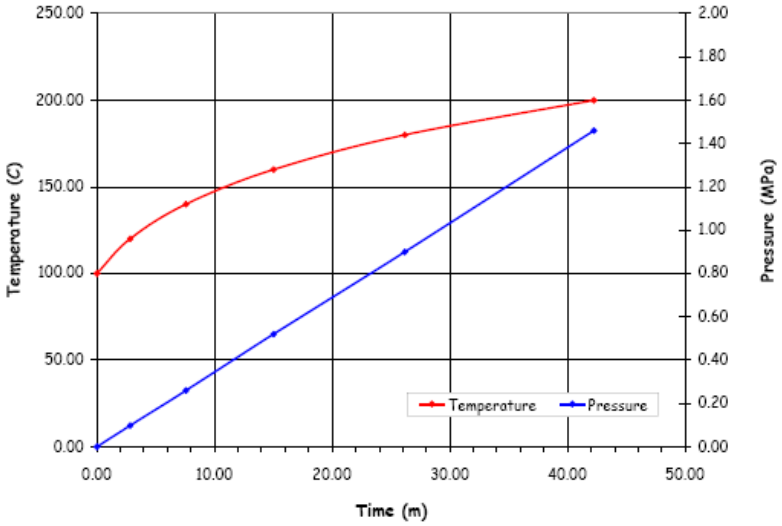

Fig.5 Phase-2: Case-1, saturated pseudo-time history

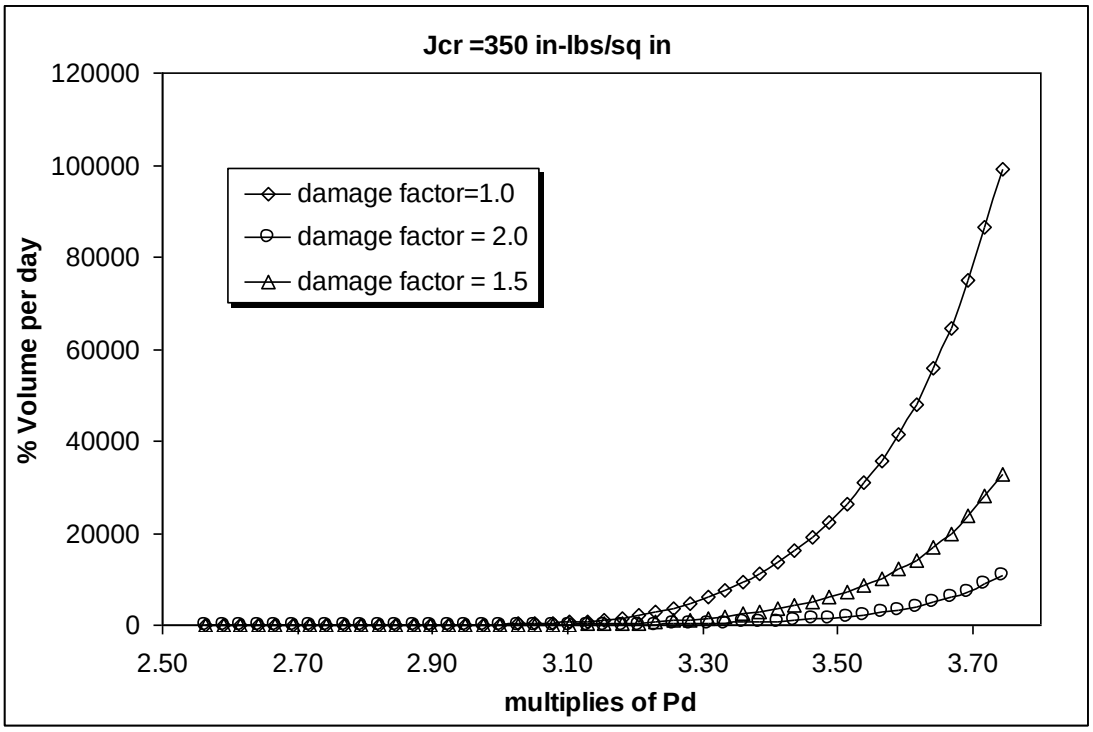

Fig.6 variation of leakage rate w.r.t multiplies of design pressure for Jcr = 350 in-lbs/sq.in

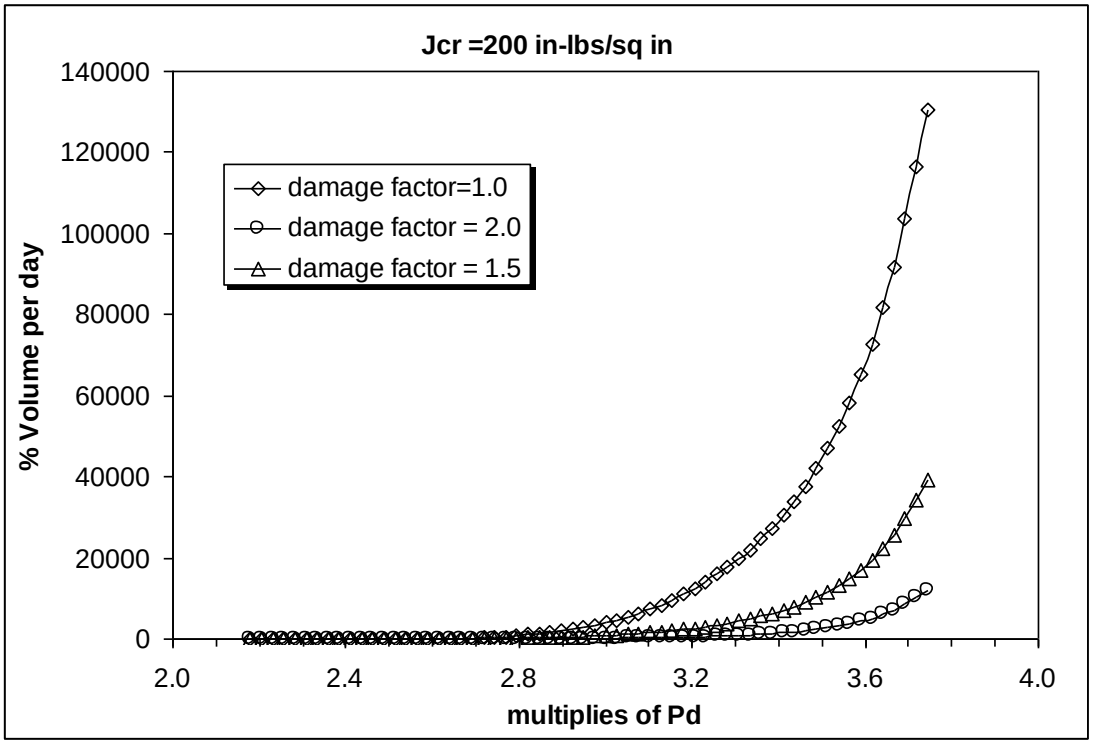

Fig.7 variation of leakage rate w.r.t multiplies of design pressure for Jcr = 200 in-lbs/sq.in

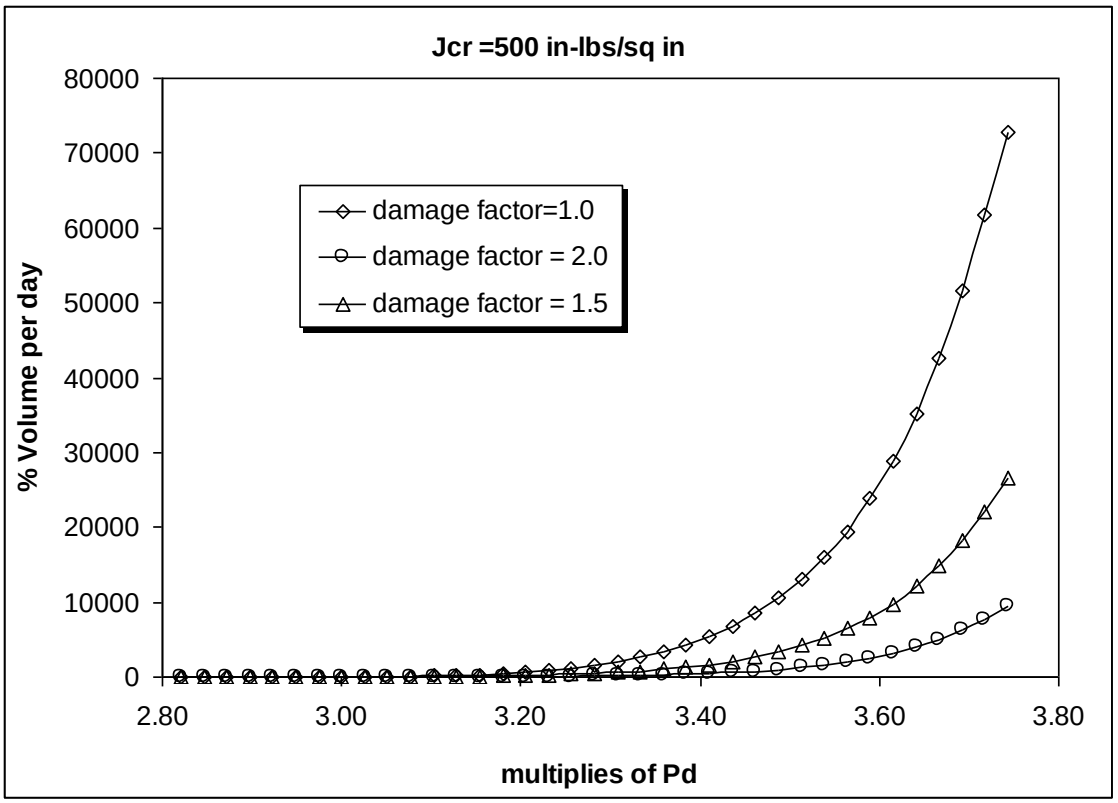

Fig.8 variation of leakage rate w.r.t multiplies of design pressure for Jcr = 500 in-lbs/sq.in

3.3 Leakage Estimation for Phase-2: Case-2 (SBO) Exercise

The Phase-2: Case-2 exercise is done for pressure and temperature loading, for station black-out scenario (SBO), as given in white paper, furnished here in Fig. 8. Leakage rates are calculated considering stress/strain resultants of 3D global FE model subject to this loading.

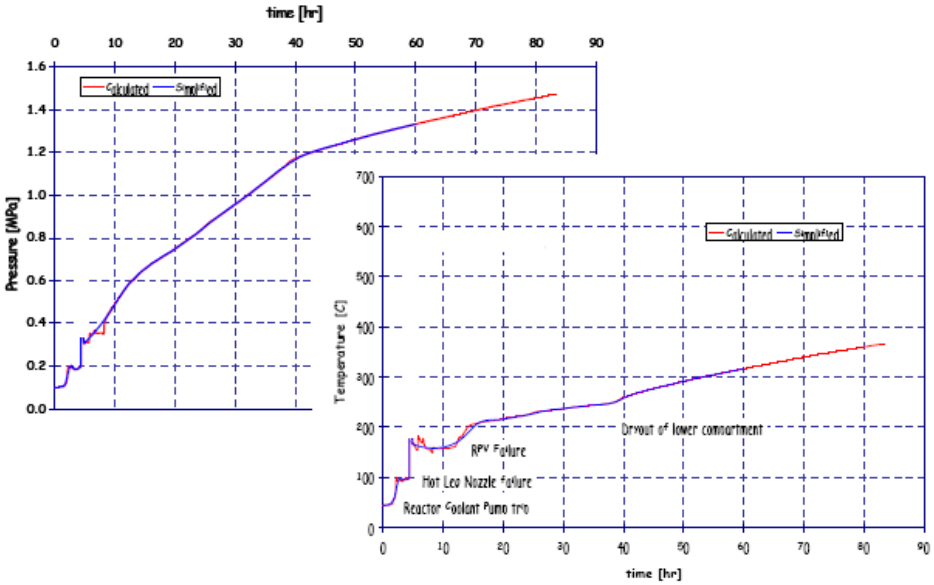

Fig.9 Phase-2: Case-2, station black-out (SBO) time history

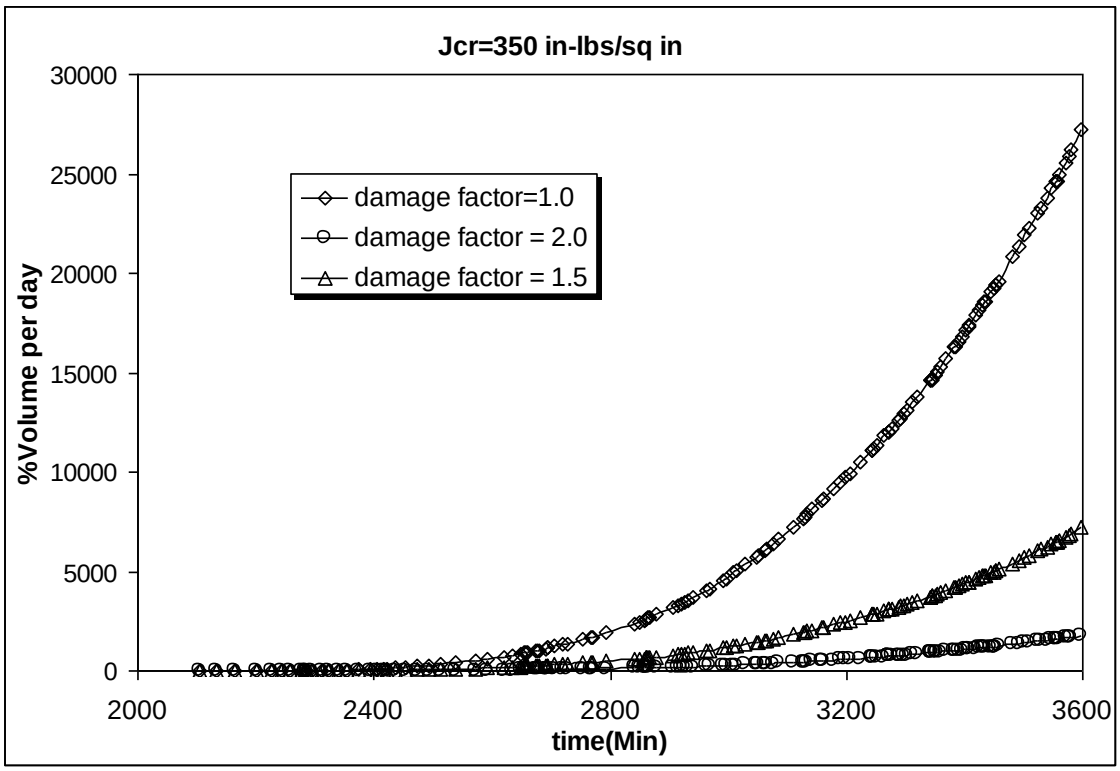

Fig.10(a) variation of leakage rate with time due to SBO condition for Jcr = 350 in-lbs/sq.in

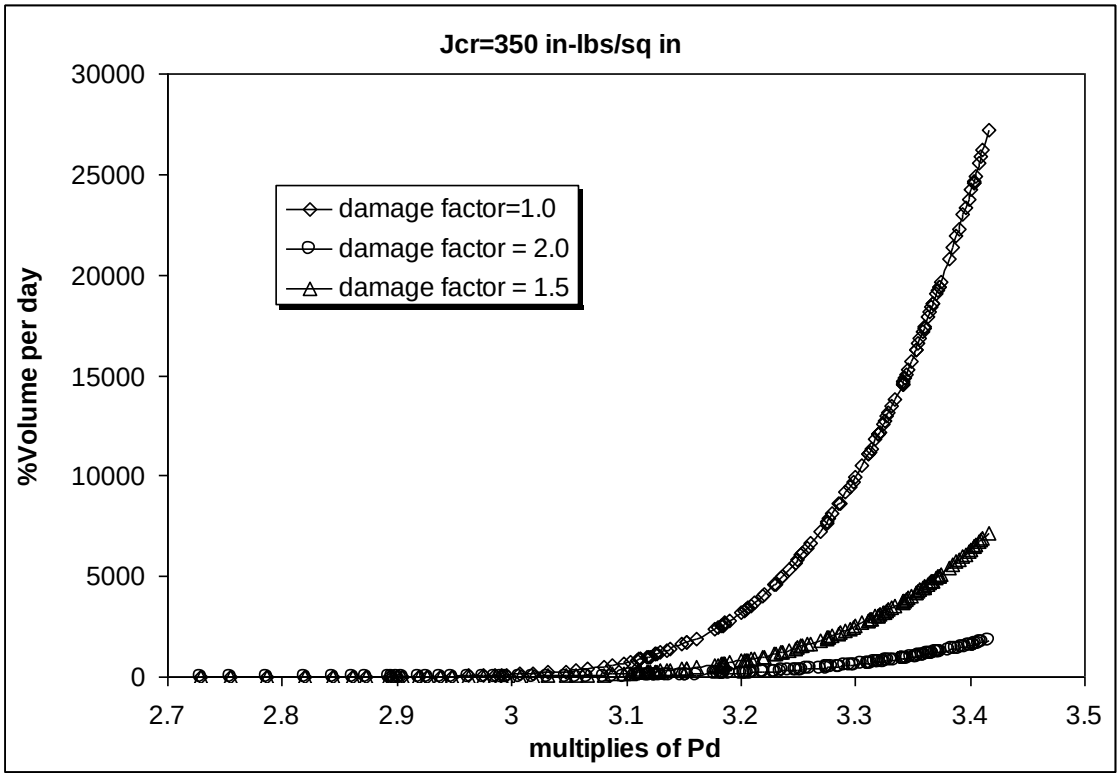

Fig.10(b) variation of leakage rate w.r.t multiplies of design pressure for SBO condition for Jcr = 350 in-lbs/sq.in

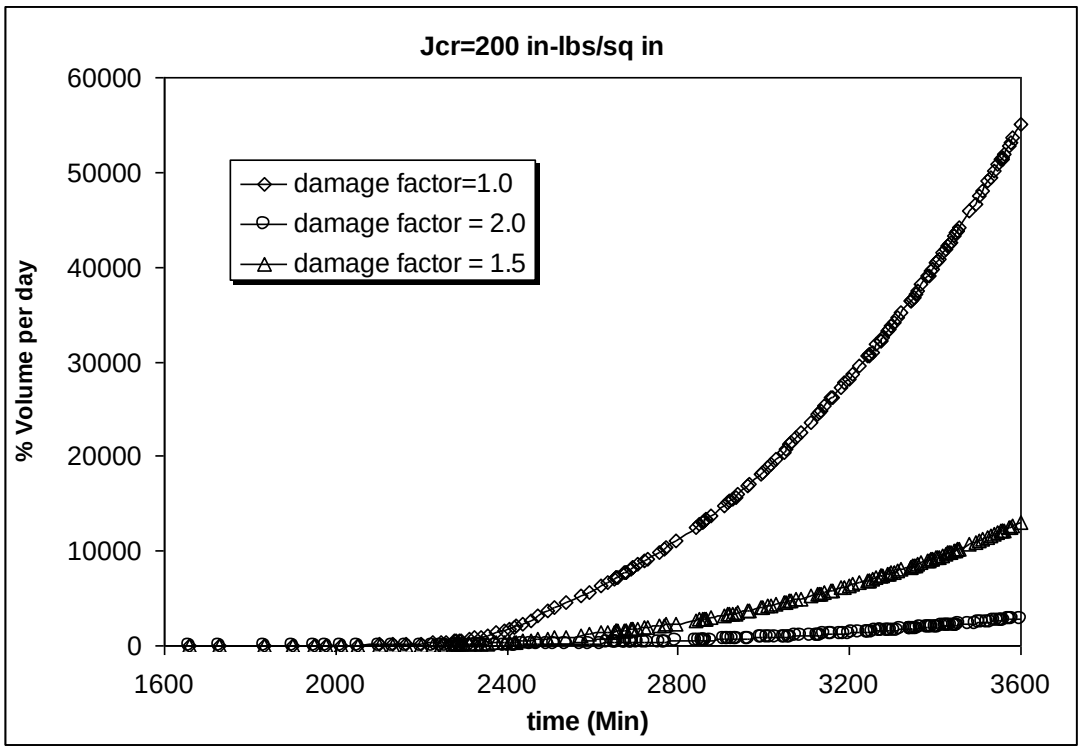

Fig.11(a) variation of leakage rate with time due to SBO condition for Jcr = 200 in-lbs/sq.in

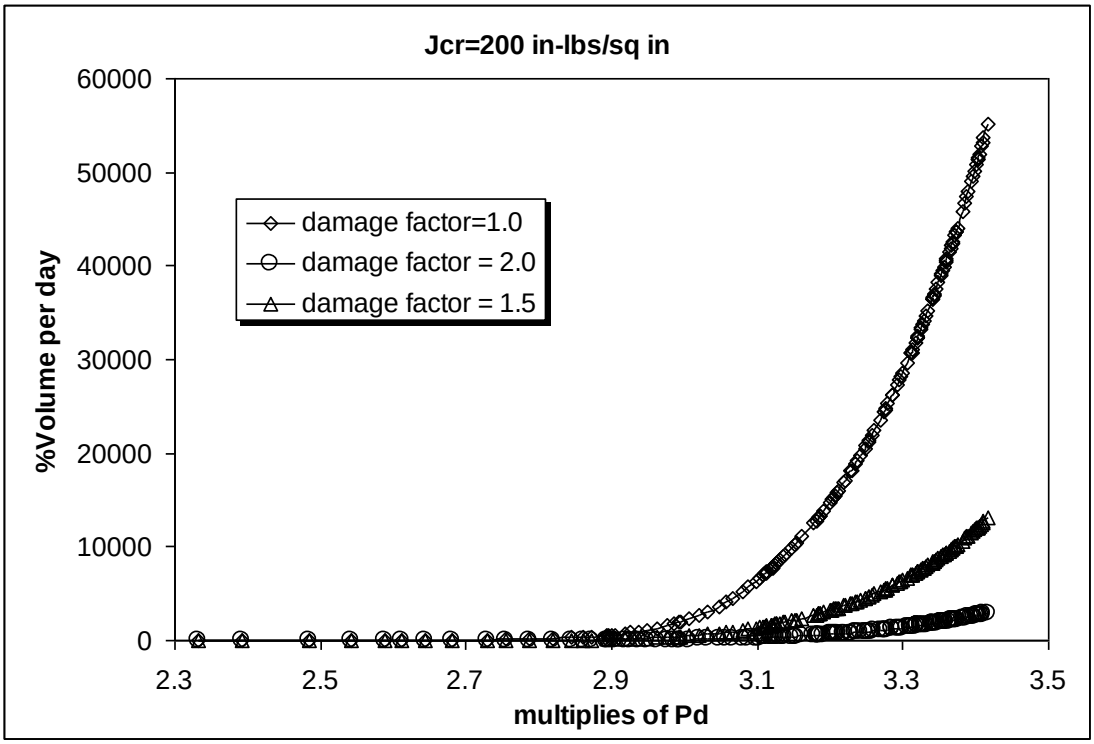

Fig.11(b) variation of leakage rate w.r.t multiplies of design pressure for SBO condition for Jcr = 200 in-lbs/sq.in

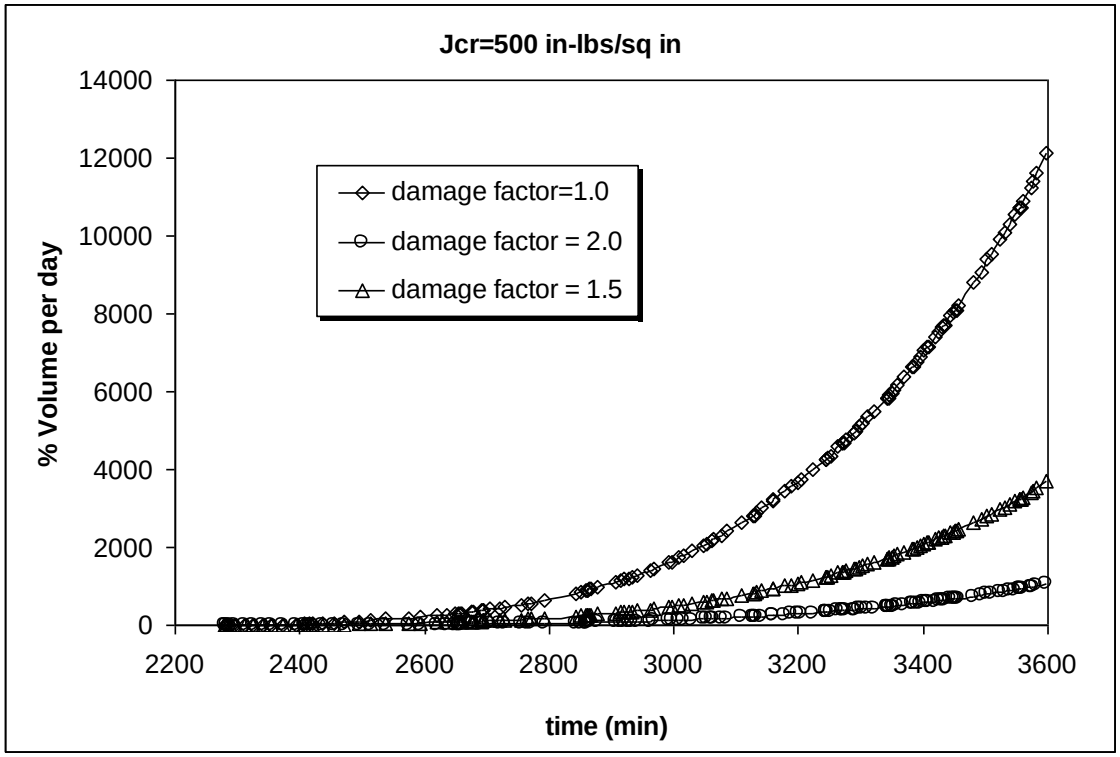

Fig.12(a) variation of leakage rate with time due to SBO condition for Jcr = 500 in-lbs/sq.in

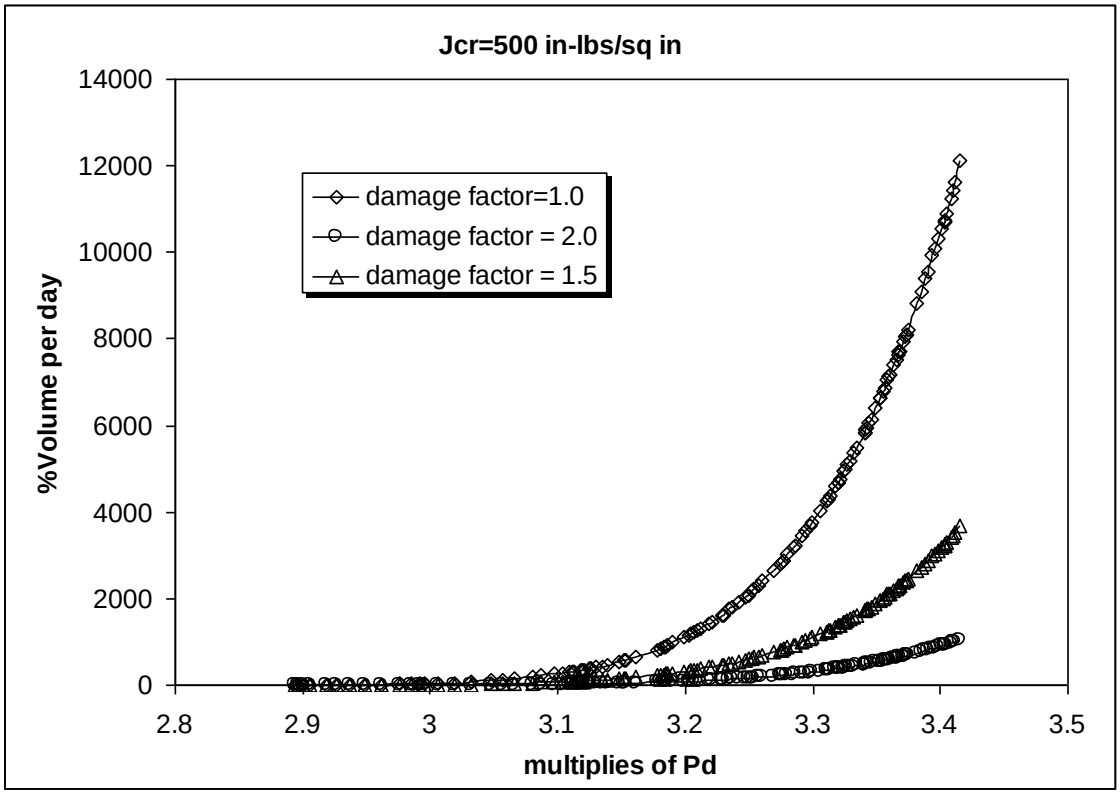

Fig.12(b) variation of leakage rate w.r.t multiplies of design pressure for SBO condition for Jcr = 500 in-lbs/sq.in

4.0 PROBABILISTIC STUDY

Probabilistic estimation of leakage rate is another objective for phase-2 study of SPE-3. An attempt has been made to do this exercise based on variations of liner properties and concrete tensile strength while estimating the leakage rate. To generate data, three basic parameters are varied, viz. liner damage strain based on Jcr value (200, 350 and 500 in-lbs/sq in), damage factor of liner (1.0, 1.25, 1.5, 1.75 and 2.0) and maximum tensile stress of concrete (2.11, 2.48 and 2.85 MPa). Experimental data of concrete compressive strength at different pour/level of containment wall were found to vary $\pm$ 15%. It was assumed the tensile strength of concrete would also vary in similar manner. However, the analysis of 3D FE model was done using the tensile strength of concrete as 2.48MPa only. Five different damage factors of liner were taken to consider the maximum uncertainly in this newly introduced major parameter. The probabilistic analysis is done for phase-1 study only, i.e. without the effect of temperature. Total 36 pressure load steps (from 2.66 Pd) were considered and each load step consisted of 45 values of leakage rate. Based on histogram

plot of variation of data for a particular load step, Weibull distribution was fit. The leakage rate was calculated for mean, 95% and 5% confidence, Fig.12.

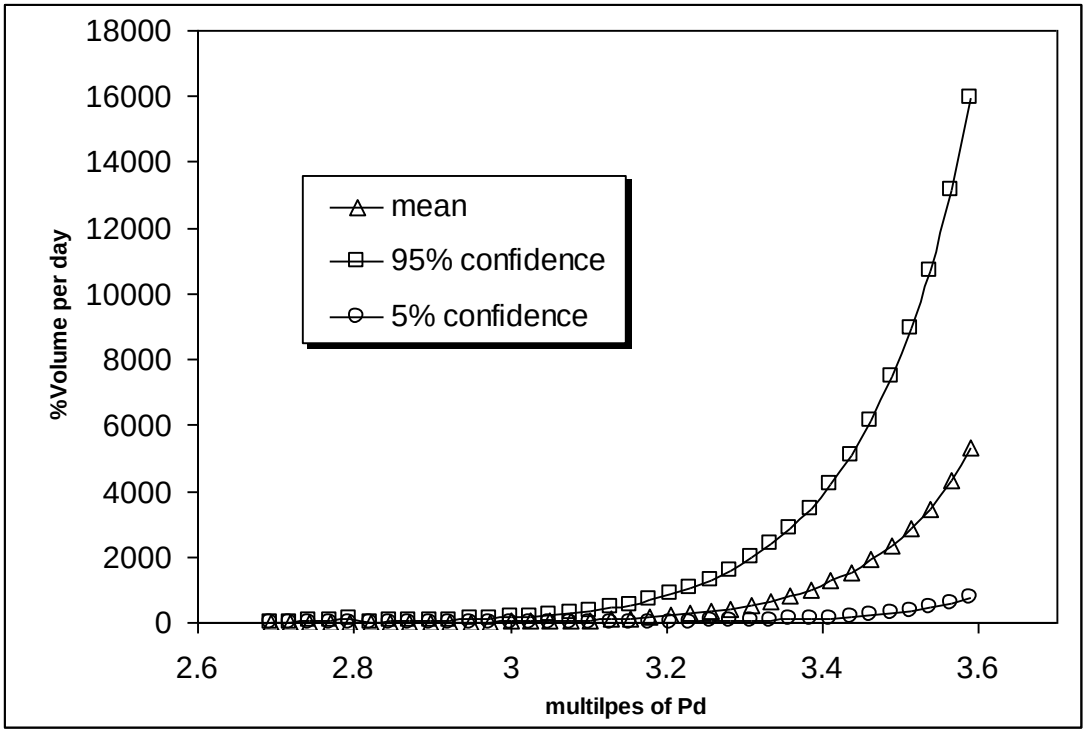

Fig.13 Leakage rate (% Volume per day) with respect to multiplies of design pressure (Pd) for mean, 95% and 5% confidence

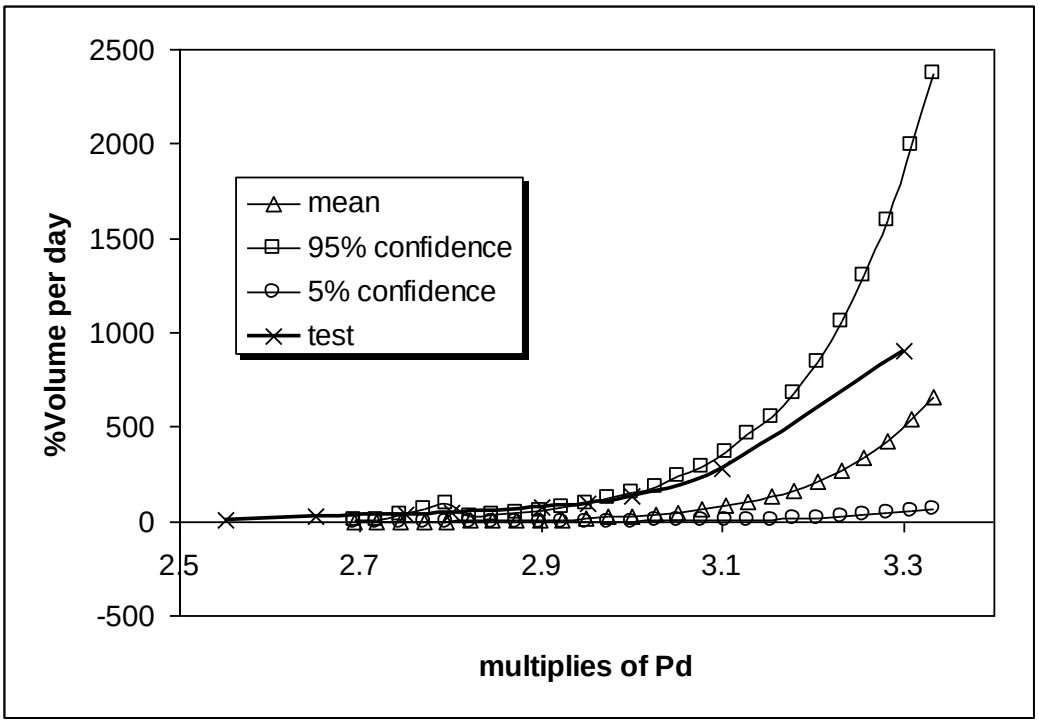

Fig.14 Leakage rate (% Volume per day) with respect to multiplies of design pressure (Pd) for mean, 95% and 5% confidence and PCCV test results

5.0 CONCLUSION

The following conclusion may be drawn from the above study:

(i) Leakage rate increases with increase in internal pressure of containment as expected. The leakage rate follows a power law with respect to internal pressure.

(ii) Initiation of leakage depends on initiation of liner damage, though concrete section cracks much earlier than initiation of liner damage.

(iii) Parabolic damage variation (damage factor = 2.0) of liner produces minimum leakage, whereas linear damage (damage factor = 1.0) produces maximum leakage.

(iv) This exercise shows that temperature has a strong effect on leakage rate. The initiation of leakage starts earlier when temperature is considered with internal pressure. High strain in steel liner due to temperature along with internal pressure triggers the initiation of liner tear at early pressure.

(v) The study shows that saturate pseudo time-history (case-1) produces enhanced leakage compared to SBO condition (case-2) till 3.0Pd. At later stages, case-2 leakages are more than case-1 as the maximum temperature is high for case-2. this could be attributed to the change in temperature profile. For case-1, variation of temperature starts from 100^{o}C to 200^{o}C within a span of 40 min, whereas, in case-2 temperature varies from 25^{o}C to 350^{o}C within a time span of 3600 min.

(vi) A comparison of leakage rates (%volume per day) for three cases considering Jcr=200 in-lbs/sq in and damage factor = 1.5 is given in Table-1 below:

Table-1 Comparison of leakage rate (%volume per day) for three cases

multiplies of Pd	Phase-1	phase2: case-1	phase2: case-2
2.6	0.15	7.56	5.61
2.8	8.36	209.83	48.34
3.0	52.55	840.35	477.94
3.2	268.21	2666.37	3204.39
3.4	1346.28	7093.23	11958.43

6.0 REFERNCES

[1] Rizkalla, S.H., Simmonds, S.H. and MacGregor J.G., 1984. Cracking of P/C Nuclear Containment Structures, *J. Struct. Eng*. *ASCE* 110 (9), pp. 2148 – 2163.

[2] Rizkalla, S.H., Lau, B.L., Simmonds, S.H., 1984. Air leakage characteristics in reinforced concrete. *J. Struct. Eng*. *ASCE* 110 (5), pp. 1149 – 1162.

[3] Dameron R. A., Rashid Y. R. and Tang H. T., 1993. Leak area and leakage rate prediction for probabilistic risk assessment of concrete containments under severe core conditions, *Proc. SMIRT-12*, Session H (H05/6), pp. 181 – 185.

[4] Dameron R. A., Dunham R.S., and Rashid Y.R., 1991. Conclusions of EPRI concrete containment research program, *Nuclear Engineering and Design*, 125, pp. 41-55.

[5] Nagano, T., Kowada, A., Matumura, T., Inada, Y., Yajima, K., 1989. Experimental study of leakage through residual shear cracks on RC walls. *Proc. SMIRT-10*, Session Q, pp. 139 – 144.

[6] Suzuki, T., Takiguchi, K., Hotta, H., Kojima, N., Fukuhara, M., Kimura, K., 1989. Experimental study on the leakage of gas trough cracked concrete walls. *Proc. SMIRT-10*, Session Q, pp. 145 – 150.

[7] Suzuki, T., Takiguchi, K., Hotta, H., 1992. Leakage of gas trough concrete cracks, *Nuclear Engineering and Design*, 133, pp. 121 – 130.

[8] Greiner, U., Ramm, W., 1995. Air leakage characteristics in cracked concrete, *Nuclear Engineering and Design*, 156, pp. 167 – 172.

[9] Riva P., Brusa L.,Contri P. and Imperato L., 1999, Prediction of air and steam leak rate through cracked reinforced concrete panels , *Nuclear Engineering and Design*, 192, pp. 13-30

Leak Rate Estimation of the Standard Problem Exercise Containment

Phase II Final Report

March-16-2012

J. Kahkonen and P. Varpasuo

E-mail: jukka.kahkonen@fortum.com; pentti.varpasuo@fortum.com

Fortum Power and Heat Ltd.

P.O.B. 100, FI-00048 FORTUM, Finland

Keilaniementie 1, Espoo

Table of Contens

List of Figures

1. INTRODUCTION

This paper presents the method we used to estimate leak rates for the ISP-48 Sandia/NRC/NUPEC 1:4 scale pre-stressed concrete containment vessel. The method relays on the pressure measurement data plotted in Ref. [1] and the calculated liner hoop strain data [2] given to the Standard Problem Exercise participants.

The method is parameterized and the leak rate probability densities are determined for different levels of containment over pressure. The leaking gas in this study is N_2. The study is not extended to steam leak rate estimation.

2. THE APPROACH

The basic assumption is that the ideal gas law applies. The assumption is not bad, considering the governing pressure and temperature conditions and that the leaking gas is N_2. Further, we consider that the leaking is happening so slow that the temperature differences between containment internals and the surroundings will have time to even out. Hence, we assume that the N_2 has a constant temperature value of 300 K.

Further we assume that the concrete of the containment experiences the same hoop strain field as the liner.

The approach to estimate leak rates we use can be outlined as follows:

1. Calculation of leak rates from the pressure measurement data presented in Ref. [1].
2. Use of 'Rizkalla' equation [3] and the hoop strain data [2] to create procedure which yields good fit to the calculated leak rate data.
3. Parameterization of the procedure and Monte Carlo simulation to get the probability densities of the leak rates for different containment over pressure levels.

3. INPUT DATA

The input data used in our approach is presented next. From the dimensions shown in Fig. 1 we get the containment volume $V_{cont} \approx 1300\ m^3$. The volume is needed in gas mass calculations when the leak rates are converted to volume rates.

From Fig. 2 we see that the temperature fluctuations are in the range of ~3 centigrade when gauge pressure is > 1 MPa. This justifies our constant temperature assumption. When the pressure reaches the maximum value of 1.3 MPa and the leakage is massive, the constant temperature assumption is no longer valid. Luckily, the nitrogen leakage can be read from the Fig. 3. The leakage rate of 925 %mass/day at over pressure of 1.3 MPa was adopted directly to our study.

The pressure measurement data shown in Fig. 4 was digitized and the leak rates were calculated up to 1.2 MPa over pressure. Method to calculate leak rates is presented in Chapter 4.

The liner (concrete) hoop strain data used in our study is presented in Figs. 5 - 11.

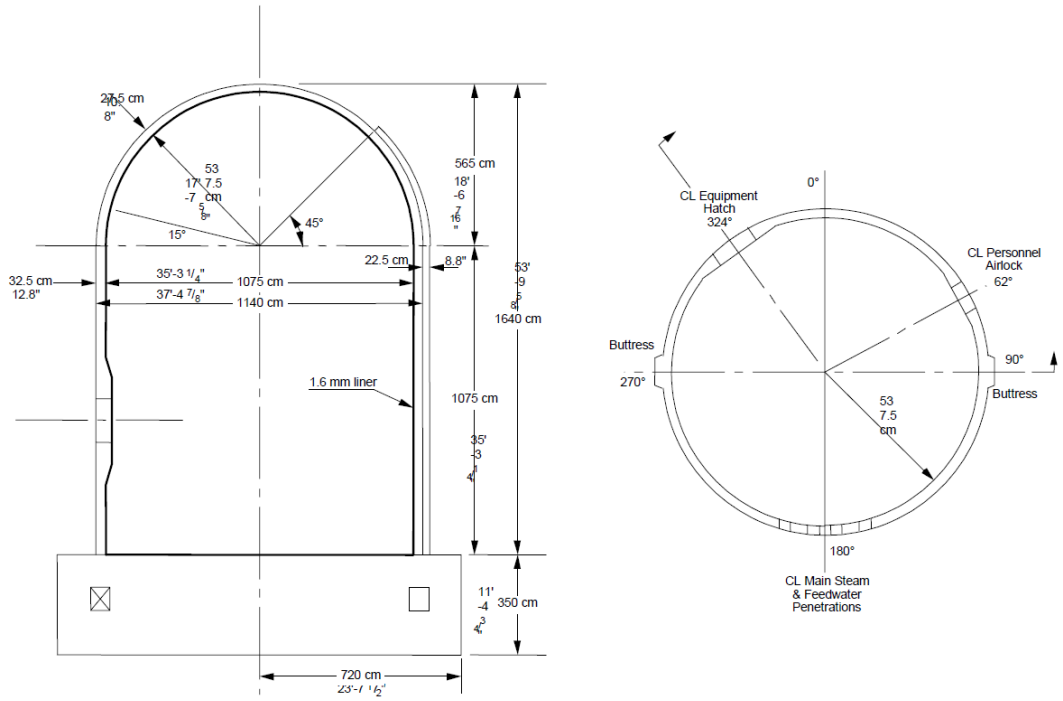

Figure 1. Containment dimensions [1].

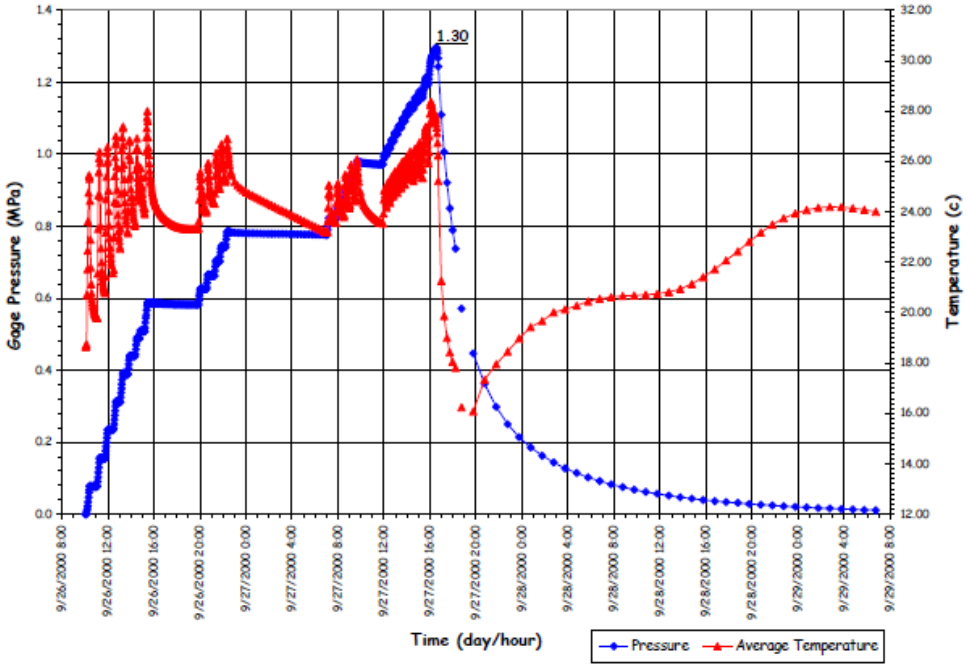

Figure 2. Pressure temeprature data [1].

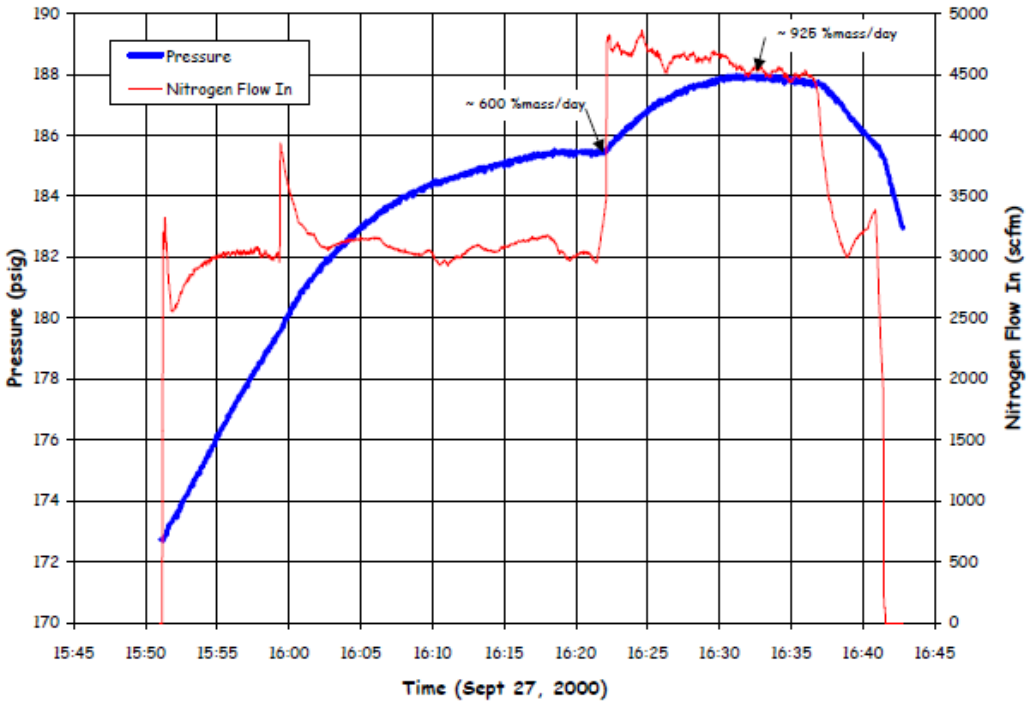

Figure 3. Leak rate at maximum pressure of 1.3 MPa [1].

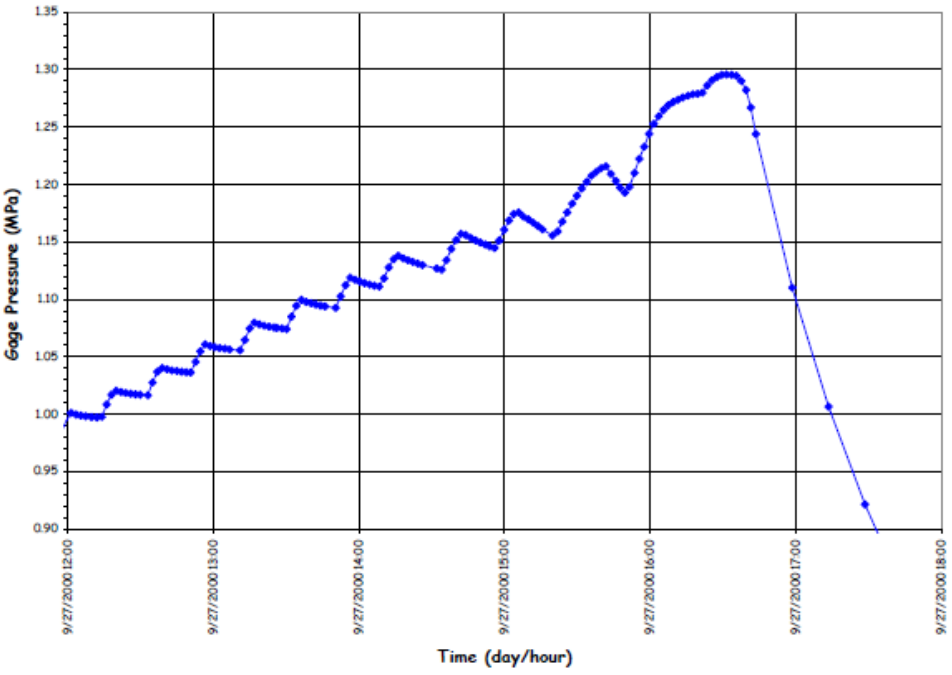

Figure 4. Measured pressure data [1].

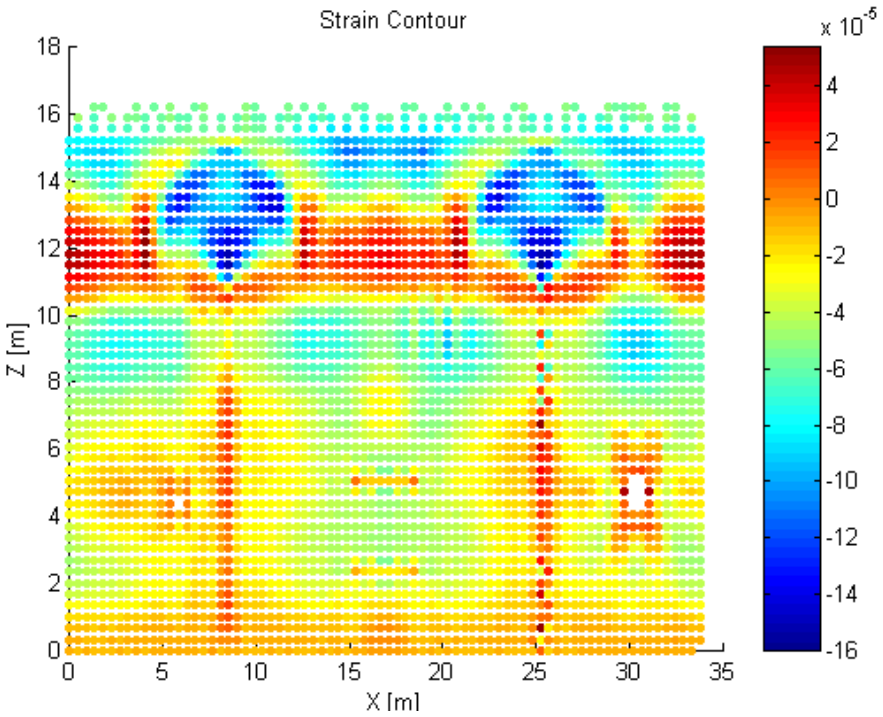

Figure 5. Hoop strain field 1.0xPd [2].

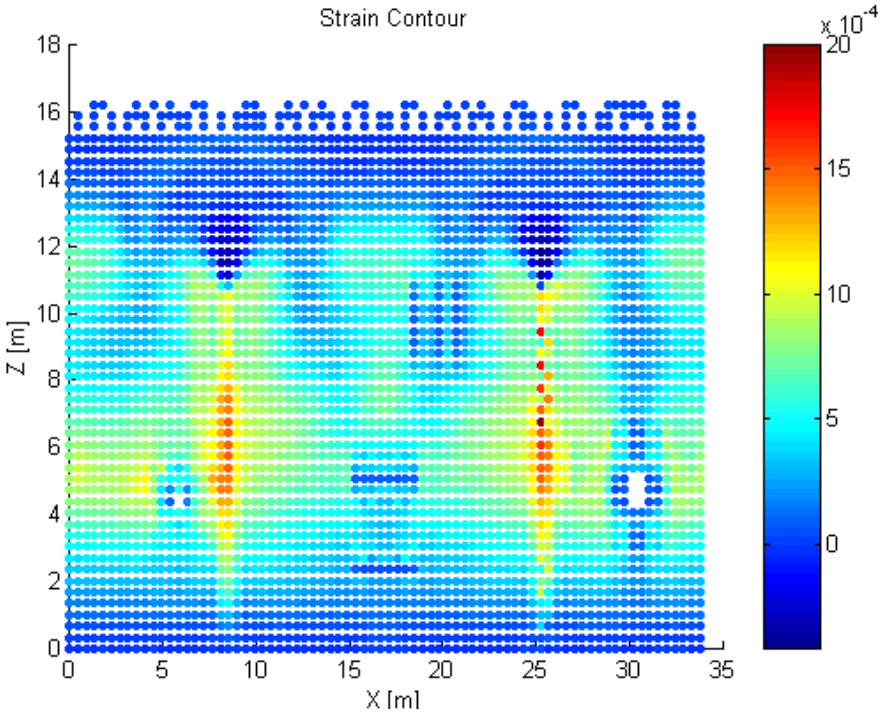

Figure 6. Hoop strain field 2.0xPd [2].

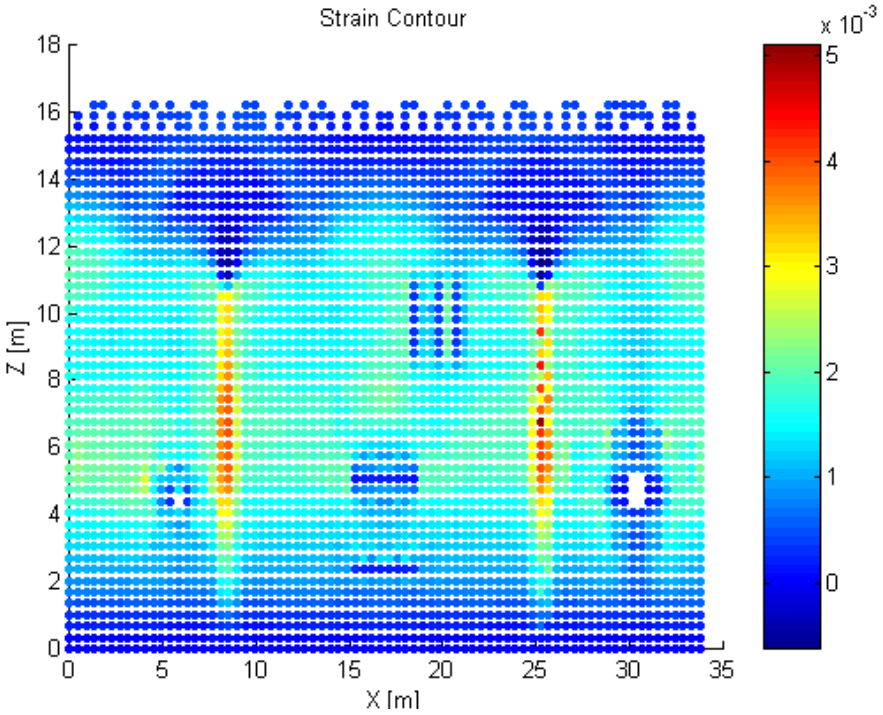

Figure 7. Hoop strain field 2.5xPd [2].

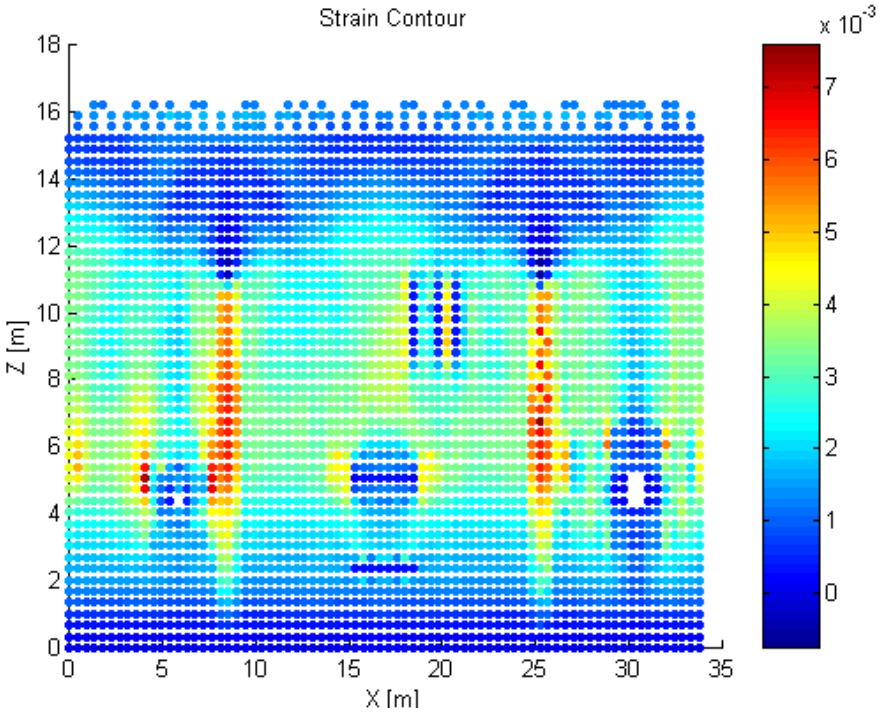

Figure 8. Hoop strain field 3.0xPd [2]

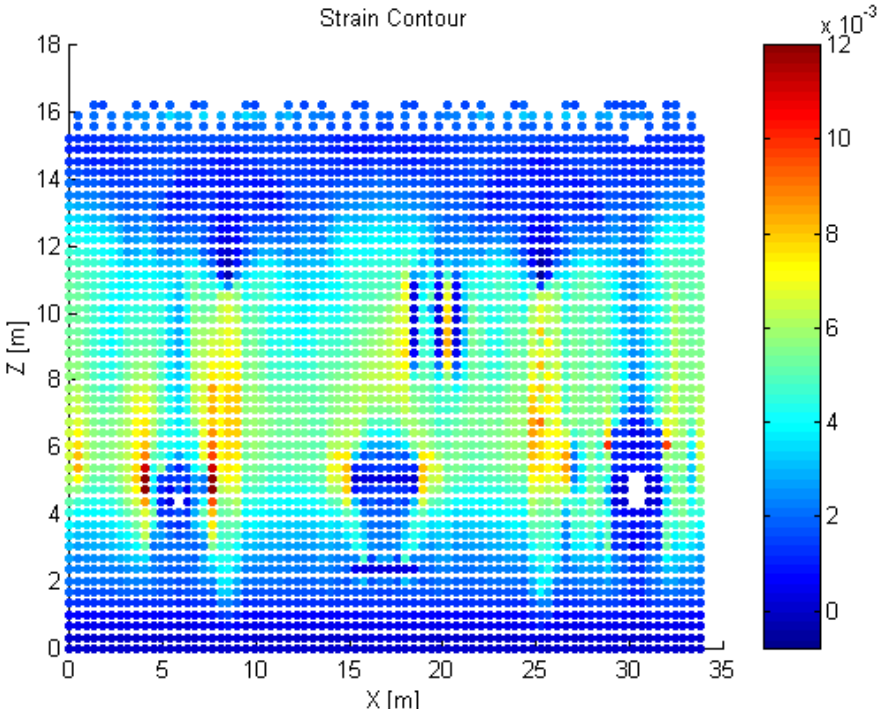

Figure 9. Hoop strain field 3.3xPd [2].

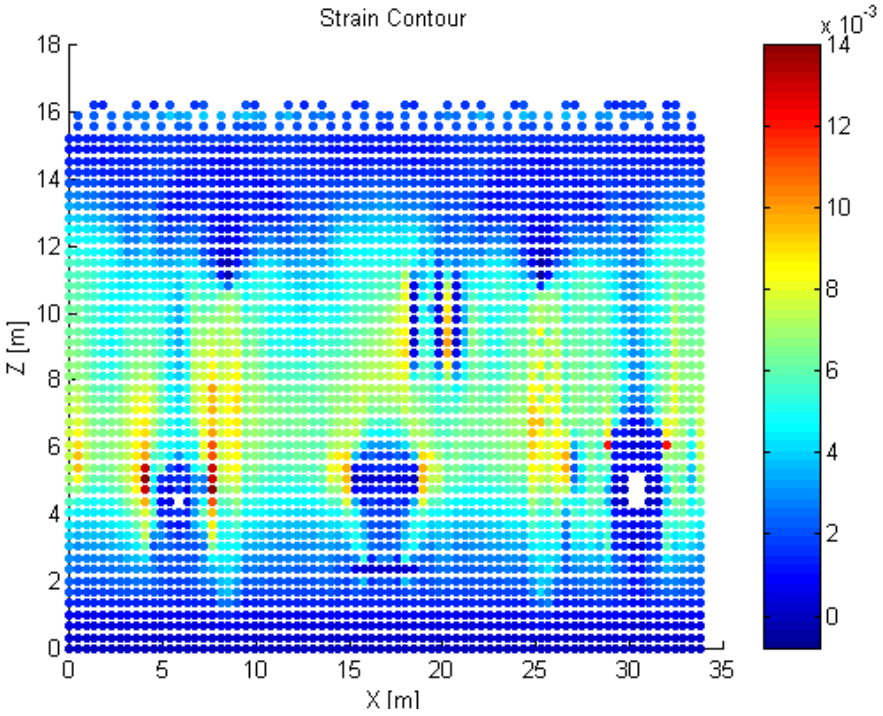

Figure 10. Hoop strain field 3.4xPd [2].

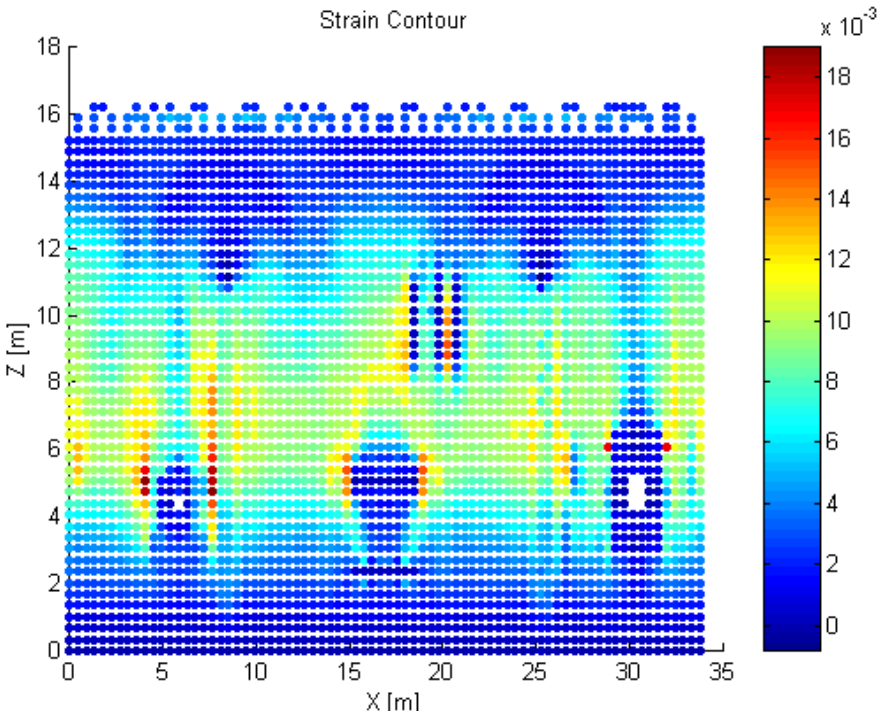

Figure 11. Hoop strain field 3.5xPd [2].

4. LEAK RATE DETERMINATION FROM THE PRESSURE MEASUREMENTS

Fig. 12 illustrates how the pressure drops due to leakage from state 0 to state 1. After time Δt more nitrogen is pumped into the containment and then new depressurization is observed.

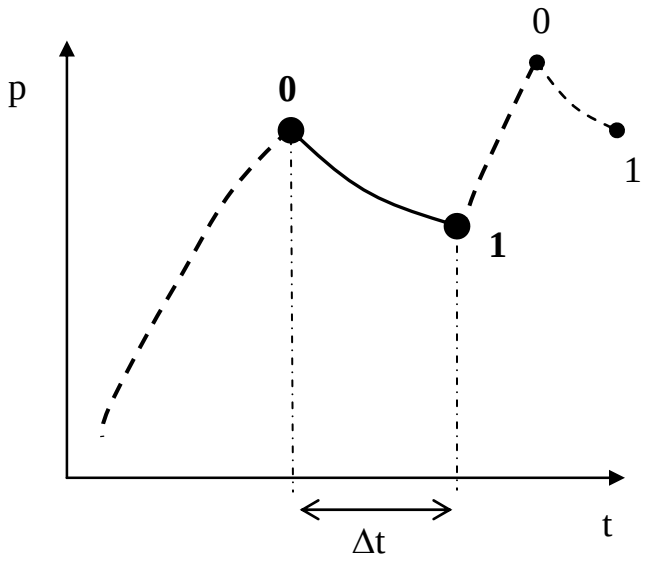

Figure 12. Pressure drop due to leakage.

Based on ideal gas law:

$$p_0 V_{cont} = m_0 R_{N2} T \quad \text{and} \quad p_1 V_{cont} = m_1 R_{N2} T \,, \tag{1}$$

where R_{N2} is gas constant divided by the nitrogen gas molar mass. Form equations 1 we get:

$$m_1/m_0 = p_1/p_0 \tag{2}$$

We approximate the leakage mass rate at p_0 with:

$$dm/dt \approx (p_0 + 1\ \text{atm})\ V_{cont}\ (1 - m_1/m_0)/(\ R_{N2} T \Delta t) \,, \tag{3}$$

To get the leak volume rate at atmospheric conditions (q_2 in Rizkalla eq.) we used conversion:

$$q_2 = dm/dt/1.165\ \text{kg/m}^3 \tag{4}$$

Using presented calculation method we get leak rates presented in Figs. 13 and 14. It should be noted that the last value (p = 1.3 MPa) is adopted directly from Fig. 3.

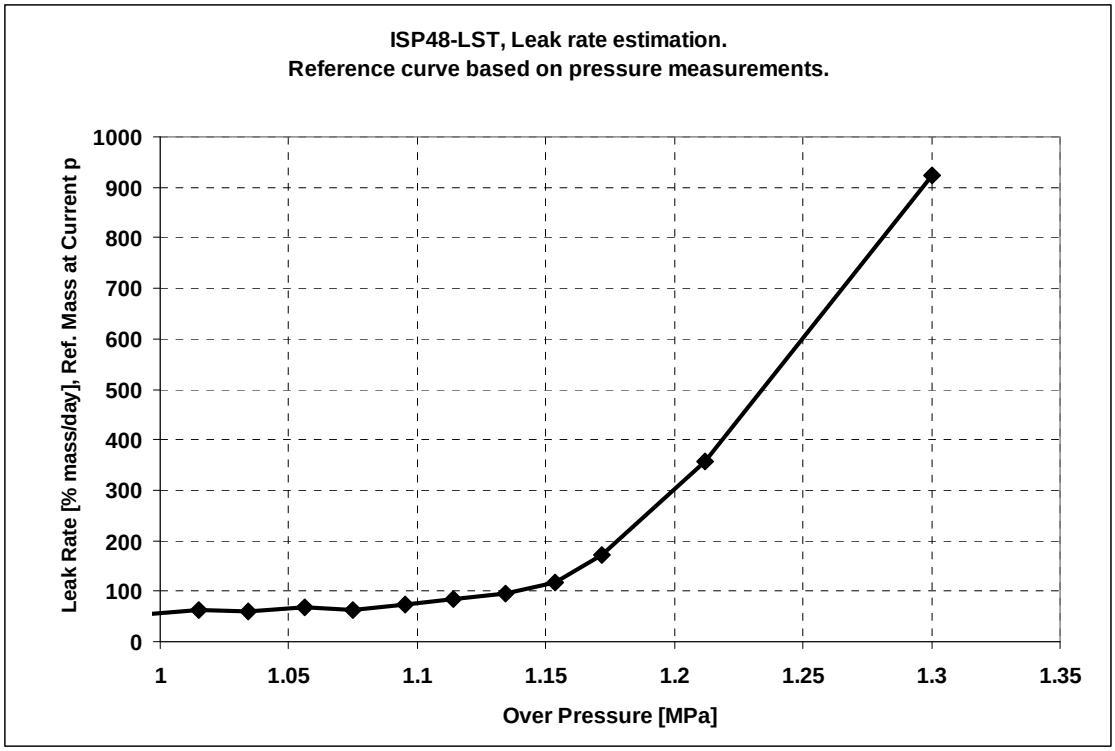

Figure 13. Calculated reference mass rate estimation.

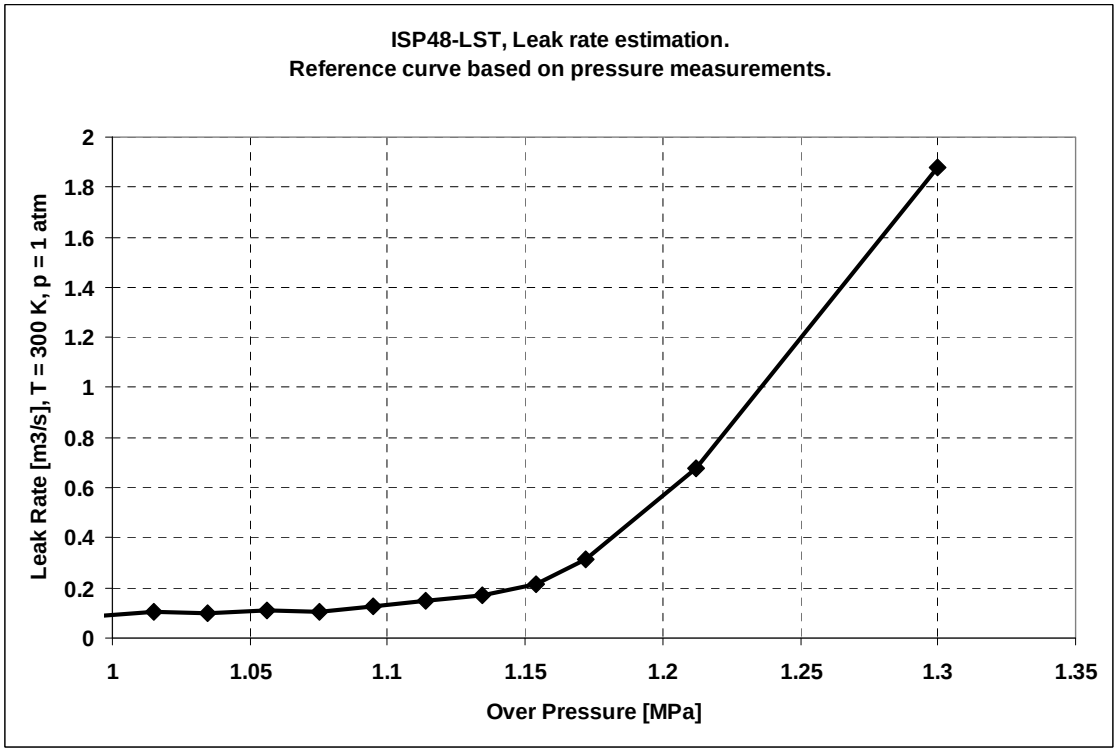

Figure 14. Calculated reference volume rate estimation at atmospheric conditions.

5. LEAK RATE ESTIMATION USING LINER STRAIN DATA

5.1. General

We used the so called Rizkalla equation [3] with the liner hoop strain data to estimate the leak rates. The Rizkalla equation for single reads:

$$\frac{p_1^2 - p_2^2}{L} = \left(\frac{k^n}{2}\right)\left(\frac{\mu}{2}\right)^n (RT)^{n-1}\left(\frac{p_2 q_2}{B}\right)^{2-n} \frac{1}{w^3}, \tag{5}$$

where L is the wall thickness, μ is the gas viscosity, R is the molar gas constant, T is the temperature, B is the crack height, w is the crack width, p_1 is the containment pressure, p_2 is the pressure outside the containment (1 atm) and q_2 is the leak volume rate outside the containment (atmospheric conditions). Entities k an n are dimensionless parameters. The q_2 in equation 5 can be solved following way:

$$\left(\frac{p_2 q_2}{B}\right)^{2-n} = \frac{\left(p_1^2 - p_2^2\right) w^3}{L\left(\frac{k^n}{2}\right)\left(\frac{\mu}{2}\right)^n (RT)^{n-1}} = \alpha \tag{6}$$

$$q_2 = \alpha^{\frac{1}{2-n}} \frac{B}{p_2} \tag{7}$$

The parameters k and n are defined to be:

$$k = 2.907 \cdot 10^7 \cdot \left(w^3\right)^{0.428} \cdot \frac{1}{\left(0.3048^3\right)^{0.428}} \tag{9}$$

$$n = \frac{0.133}{\left(w^3\right)^{0.081}} \cdot \left(0.3048^3\right)^{0.081} \tag{10}$$

For other parameters we used values:

- $R = 8.3145 \frac{\text{J}}{\text{mol} \cdot \text{K}} / 0.02802 \frac{\text{kg}}{\text{mol}} = 296.73 \frac{\text{J}}{\text{kg} \cdot \text{K}}$ (Gas constant for N_2)
- $\mu = 1.76 \cdot 10^{-5} \frac{\text{N} \cdot \text{s}}{\text{m}^2}$
- L = 0.325 m
- B = 0.34 m
- T = 300 K

The crack width w was defined to be:

$$w = w(L_e, \varepsilon_\theta) = L_e(c_1\varepsilon_\theta + c_2{\varepsilon_\theta}^2), \tag{11}$$

where L_e = 0.46m, which is the representative width of the liner element used in hoop strain field analysis. ε_θ is the hoop strain at particular point on the liner. The parameters c_1 and c_2 are tuning parameters to be determined so that the Rizkalla equation yields good match to the reference leak data shown in Fig. 14. The total leak rate is determined as a sum of all the leak rates calculted for the strain value locations. The strain points at the buttress locations were omitted from the procedure.

It should be noted that we use unit system [m, kg, K and s] in our equations. That is why k and n have peculiar additional multipliers.

5.2. Results

After rigorous "optimization" we found that tuning parameter values $c_1 = 7.5 \cdot 10^{-3}$ and $c_2 = 2.25$ yield good estimation of the reference curve. The curve fit can be seen in Figs. 15 and 16.

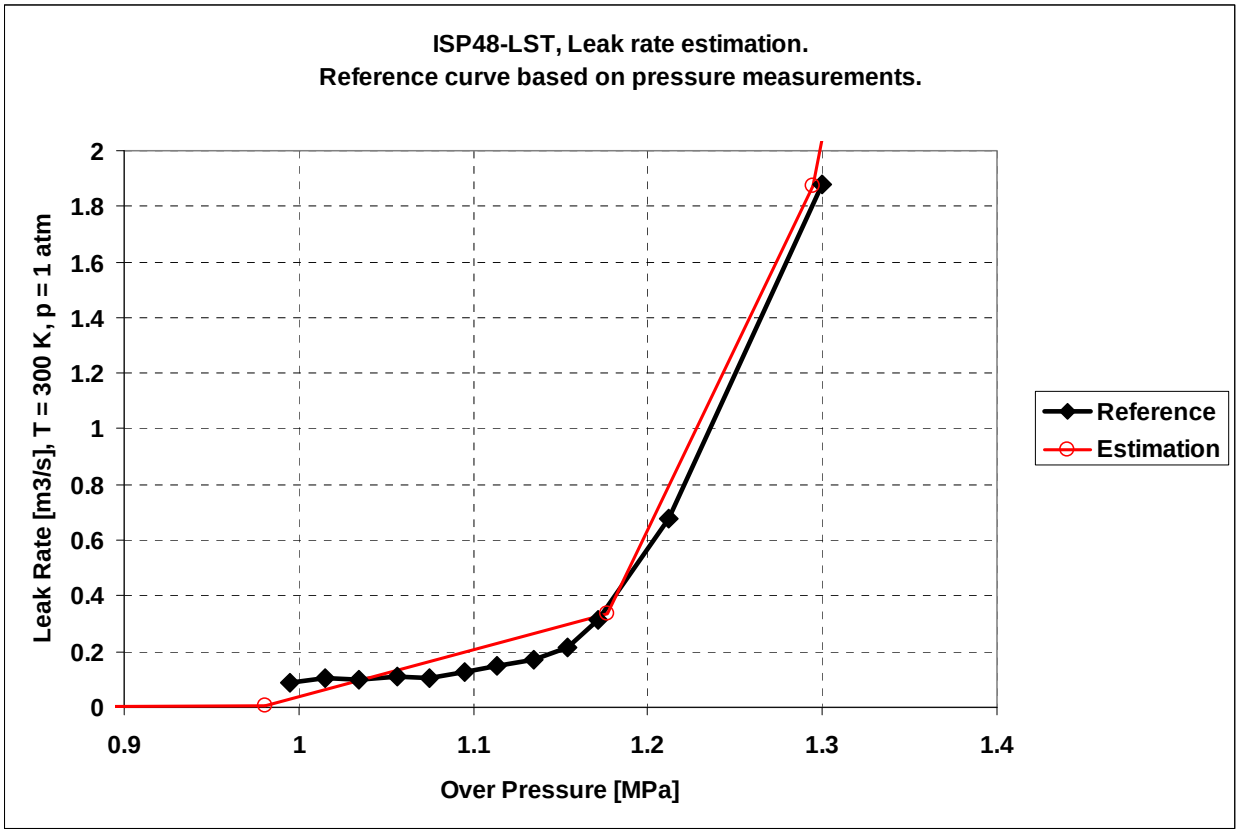

Figure 15. Estimation based on Rizkalla equation vs. reference curve.

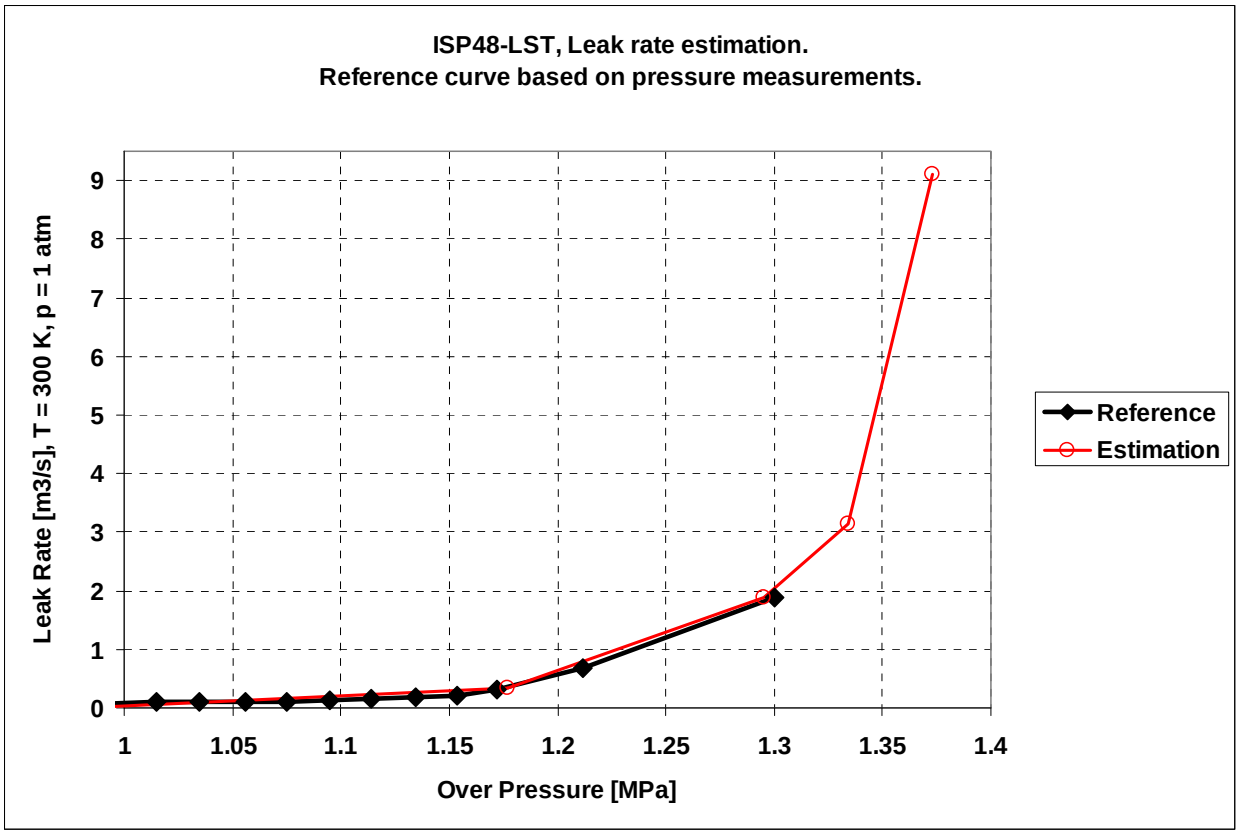

Figure 16. Estimation based on Rizkalla equation vs. reference curve. Extrapolation of leak rate up to 3.5Pd.

6. PROBABILISTIC ESTIMATION

In order to determine leak rate probabilistic densities at different over pressure levels, a Monte Carlo simulation was used. Number of samples generated was 10 000 for each over pressure level.

In the parameterization of Rizkalla equation we used uniformly distributed random number *r*, defined as:

$$r \in [0.5 \ldots 1.5]$$

We selected five representative parameters in Rizkalla equation and they were defined in Monte Carlo simulation as:

$B^* = r \cdot B$, B = 0.34 m

$L_e^* = r \cdot L_e$, L_e = 0.46 m

$c_1^* = r \cdot c_1$, $c_1 = 7.5 \cdot 10^{-3}$

$c_2^* = r \cdot c_2$, $c_2 = 2.25$

$\mu^* = r \cdot \mu$, $\mu = 1.76 \cdot 10^{-5}$ Ns/m^2

When the parameters were determined, they were applied to all of the strain points in the leak rate calculation. After that, a new set of parameters were generated and the leak rate was calculated again. This procedure was repeated 10 000 times for each over pressure levels.

The Monte Carlo procedure produced probability densities shown in Figs. 17 - 21. The Fig. 22 illustrates the cumulative probability distribution of the leak rate at 3.5Pd over pressure level.

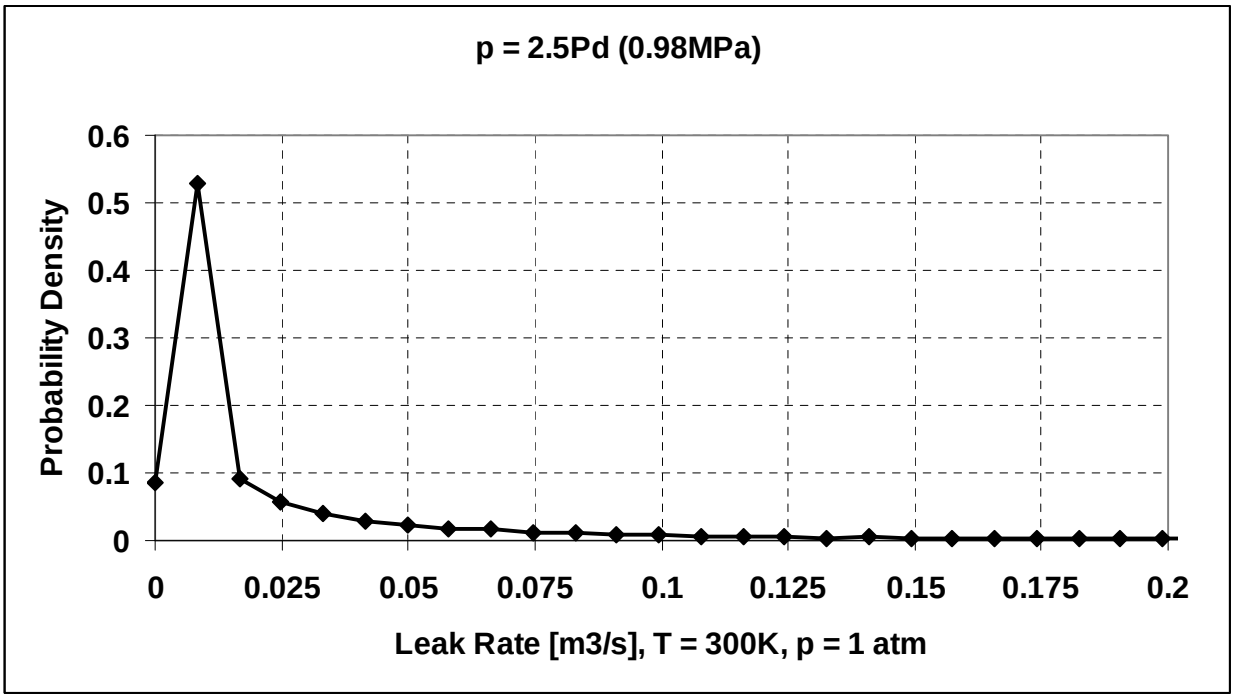

Figure 17. Leak rate probability density at 2.5Pd.

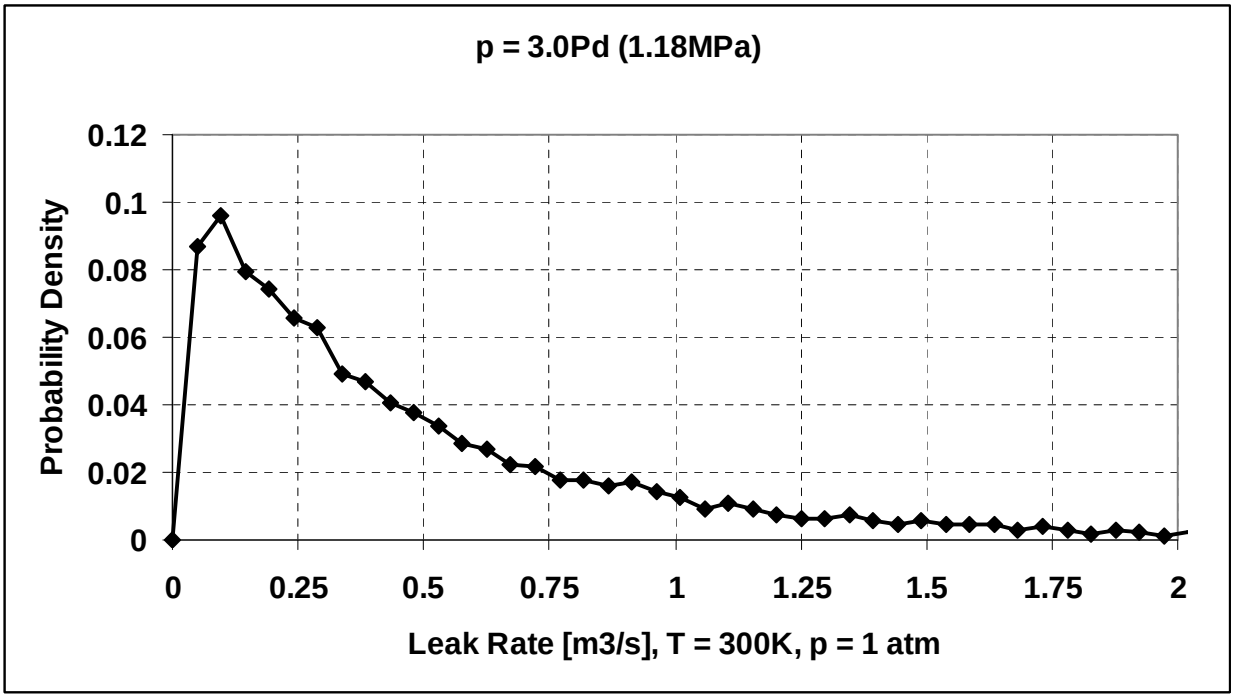

Figure 18. Leak rate probability density at 3.0Pd.

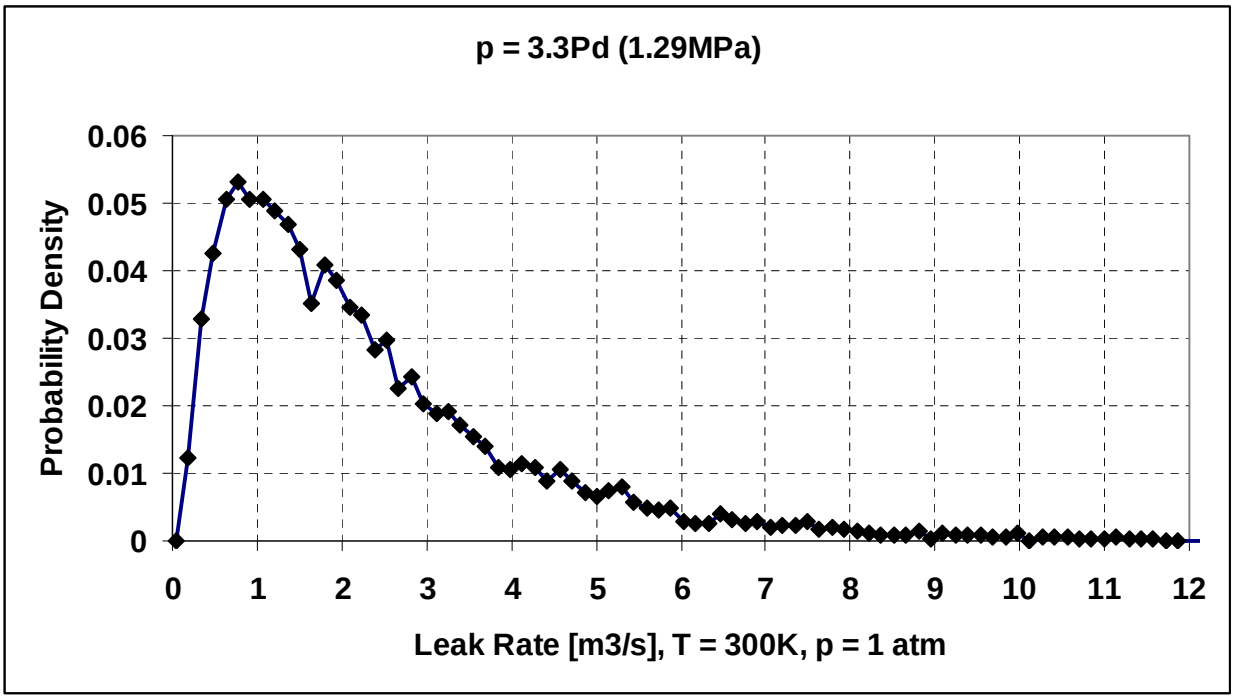

Figure 19. Leak rate probability density at 3.3Pd.

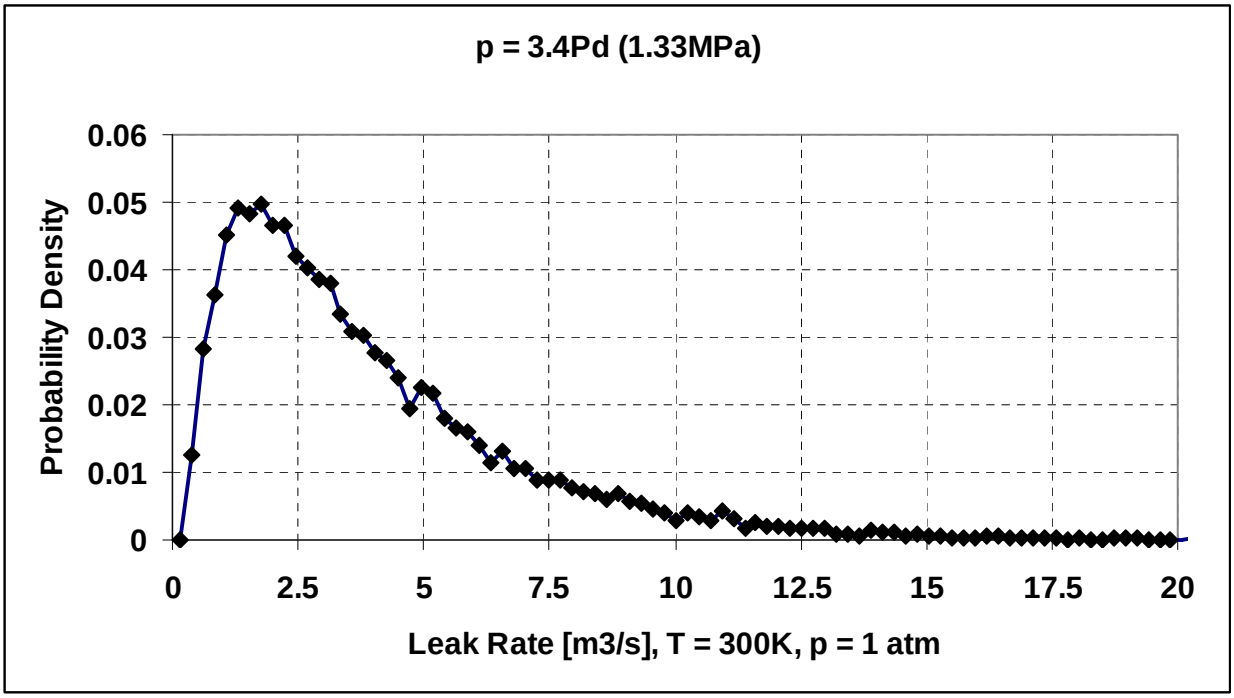

Figure 20. Leak rate probability density at 3.4Pd.

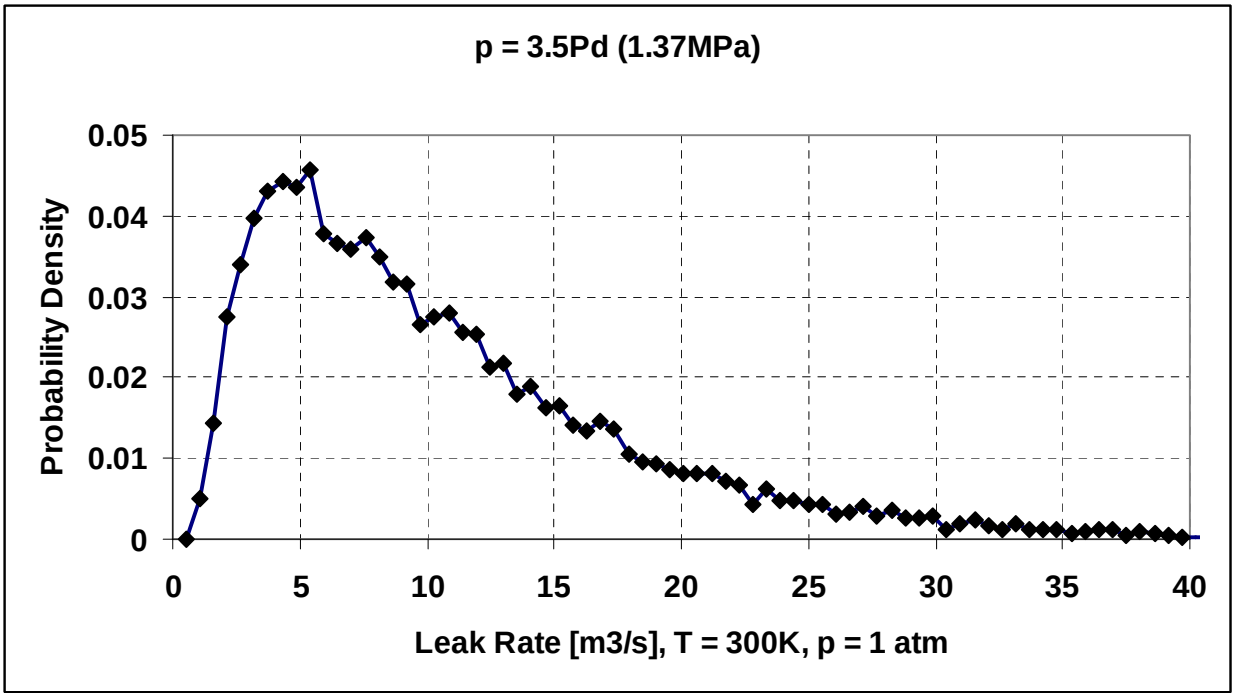

Figure 21. Leak rate probability density at 3.5Pd.

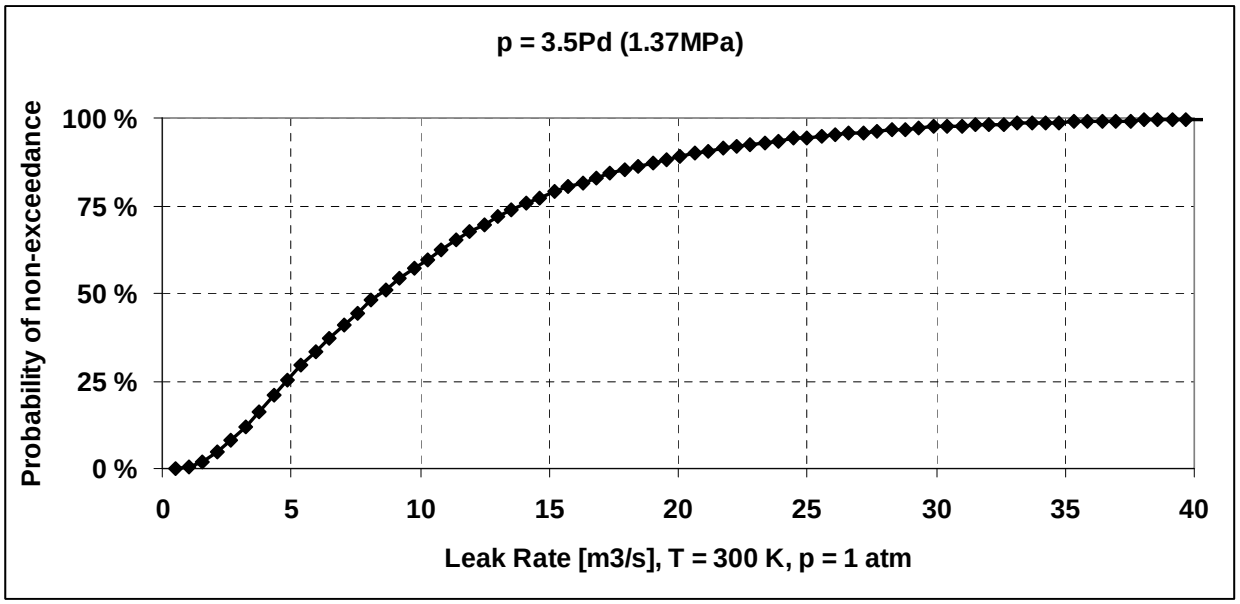

Figure 22. Leak rate cumulative probability at 3.5Pd.

7. SUMMARY AND CONCLUSIONS

A procedure to generate leak rate estimations was presented. Based on Fig. 16 the leak rate at 3.5Pd over pressure level is ca. 9 m^3/s of N_2 gas in atmospheric conditions, which corresponds to $0.1/1.37 \times 9/1300 \times 3600 \times 24 \times 100\% \approx 4\ 400\%$mass/day.

The procedure was parameterized and Monte Carlo simulation was done. At over pressure level 2.5Pd the probability density curve had a "spike" shape at low leak rate region. When the over pressure level goes to higher values, the probability density curve gets wider. Clear log-normal probability distribution shape is observed.

REFERENCES

[1] NEA/CSNI/R(XX), INTERNATIONAL STANDARD PROBLEM NO. 48 CONTAINMENT CAPACITY, Phase 2 Report-Results of Pressure Loading Analysis, Sandia National Laboratories, Albaquerque, New Mexico, USA, May 2004.

[2] strain_mapping_M&N.XLSX, Excel file, R. Dameron E-mail, May-24-2011.

[3] Rizkalla, S.H., Lau, B.L., Simmonds, S.H., 1984. Air leakage characteristics in reinforced concrete. J. Struct. Eng. ASCE 110 (5), pp. 1149 – 1162.

APPENDIX D: NRC

Introduction

Background

The U.S. Nuclear Regulatory Commission (USNRC) and Sandia National Laboratories (with support from Moffatt & Nichol) are participating in a round robin analysis with the Atomic Energy Regulatory Board of India (AERB). This analysis is focused on the Standard Problem Exercise (SPE) No. 3, involving the structural analysis of a prestressed concrete containment vessel (PCCV). Phase 1 examined the local effects of the PCCV. During the first phase, the analysis focused on:

- Effects of containment dilation on prestressing force
- Slippage of prestressing cables
- Steel-concrete interface
- Fracture mechanics behavior
- Scatter in data of prestressed concrete properties

The analysis results for Phase 1 were discussed in a meeting and documented in Tech Memo 1, 2, and 3, so are not discussed here, but are implemented into the global model of the PCCV.

After the SPE Phase 1 Results Discussion meeting for the SPE-3 in Washington DC in April 2011, a consensus was reached on the details for the Phase 2 SPE program.

Objective

Phase 2 requires participants to re-investigate Model 3 from Phase 1, with two distinct objectives. 1) The participants are asked to examine the methods to estimate leakage rate as a function of pressure. These methods will be evaluated relative to the PCCV test results, and incorporate lessons learned from Phase 1 of the round robin analysis. 2) Temperature effects modifications will be implemented into Model 3. SPE refers to this additional investigation as Model 4. It is essentially Model 3, but with all modifications the participant may wish to include based on lessons-learned from Phase 1 and modifications suitable to introducing temperature into the solution. The participants are to apply two different temperature loading cases to the global Model 4. The two thermal analysis cases under consideration in Part 2 were selected based on the participant's agreement to use the ISP-48 cases, which are considered as representative challenges to typical containments:

- Case 1 a "Saturated Steam Condition" case defined by adding a temperature to each pressure step from the original PCCV pressure analysis, and
- Case 2 an accident safety case, known as a "Station Blackout" scenario, but ignoring the hydrogen burn at about 4-1/2 hours into the event due to general consensus on its lack of effect on leak rate.

This report focuses primarily on the application of temperature on the PCCV and the leakage prediction results obtained for Model 3 and 4. The methodology for leakage assessment for

finite element a model of PCCVs is discussed Appendix A. The modeling assumptions, initial conditions, and analysis results are presented herein.

The approach

The ABAQUS Standard FE program was used for the analysis as described herein. The model includes concrete, tendons (hoop and vertical), rebar (hoop, vertical), and liner. Shear reinforcement was not included in the model, since the structure wall was represented by shell elements. Vertical tendons and vertical rebar were included. Concrete was modeled with 4-node shell elements (for which through-wall shear response is approximated by elastic shell theory), and rebar was modeled with embedded subelements, tendons with two-node beam elements, and liner with 4-node shell elements, overlain onto the same nodes as the concrete shell nodes, but offset by the appropriate eccentric dimension.

Model 4 geometry and initial conditions

Overall geometry

Similar to Model 3, the geometry and boundary condition assumptions of Model 4 are shown in Figures 1 through 4. The geometry is as specified in the SPE-3 problem statement, and on the drawings and NUREG/CR-6810. Two sets of predefined temperature loading cases are applied to the global Model 4. These two loading cases are shown in Figures 1 and 2 and are specified in the SPE Phase 2 White Paper [1].

Figure D-1 shows the general outline of the Model 3 FE Mesh. The wall-base juncture occurs at the correct location, geometrically, but since shell elements are aligned with mid-thicknesses of structural elements, the wall-base juncture is separated by half the thickness of the basemat. This juncture is appropriately tied with translational and rotational constraints (“rigid links” as shown in Figure D-4). Figures D-2a and D-2b show the actual element mesh, including color coding of different rebar mesh densities. Figure D-3 shows the Equipment Hatch thickness assigned to each element by the ABAQUS mesh generator.

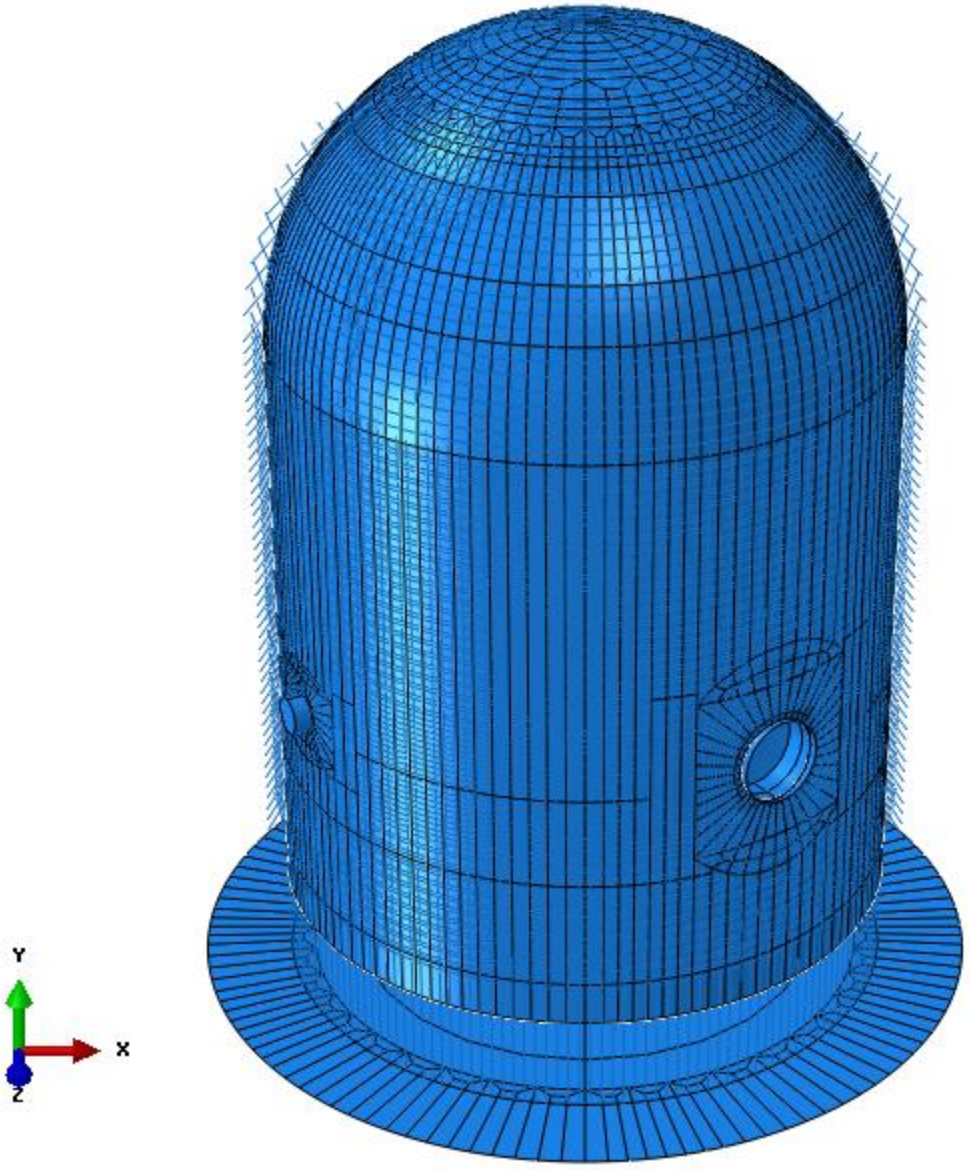

Figure D - 1: Model 3 overview

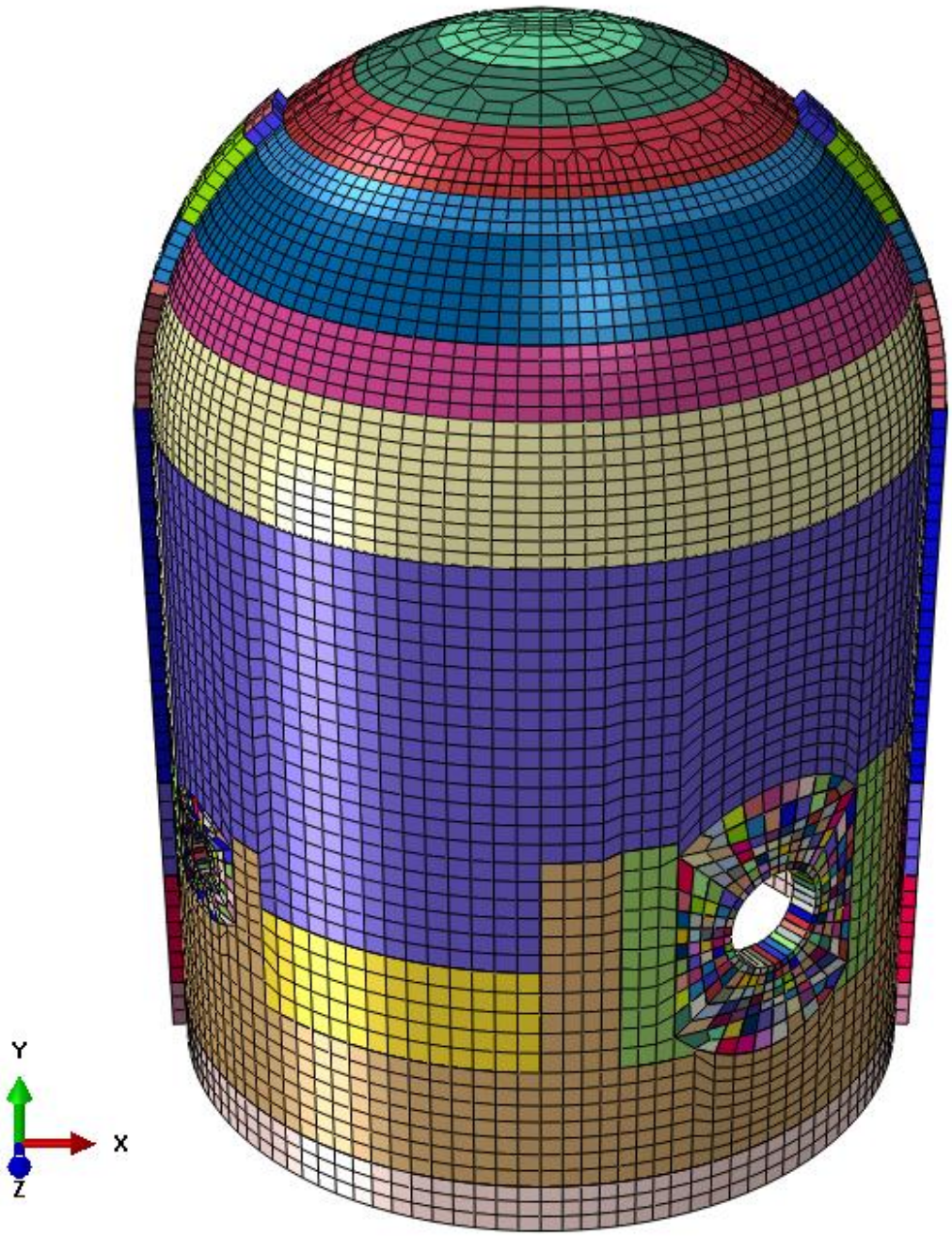

Figure D - 2a: Meshed concrete vessel with various section assignments. (The thickness of shell element was rendered in ABAQUS, and variations are due to rebar layers and concrete thickness.)

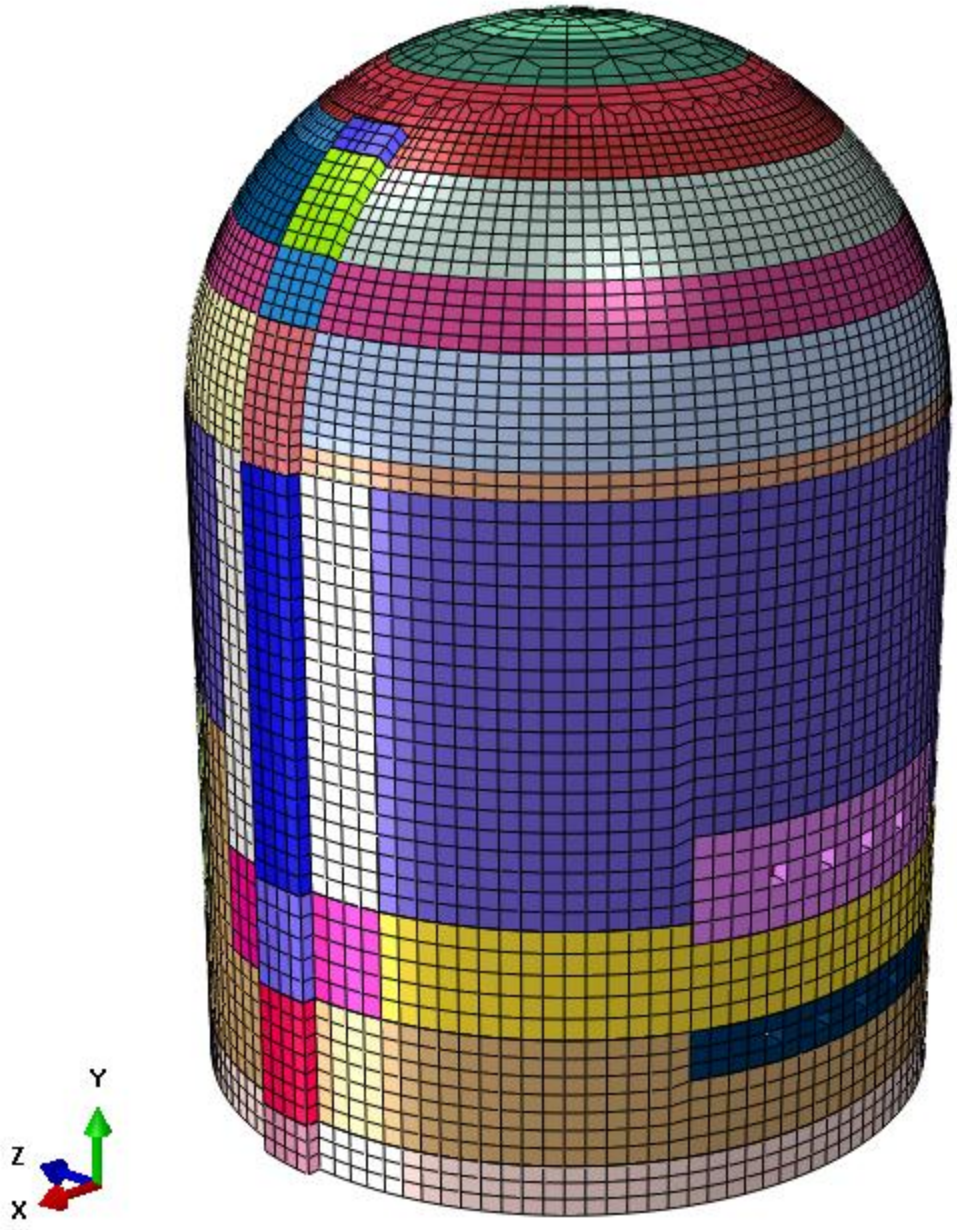

Figure D - 2b: Meshed concrete vessel with various section assignments. View of M/S and F/W penetrations

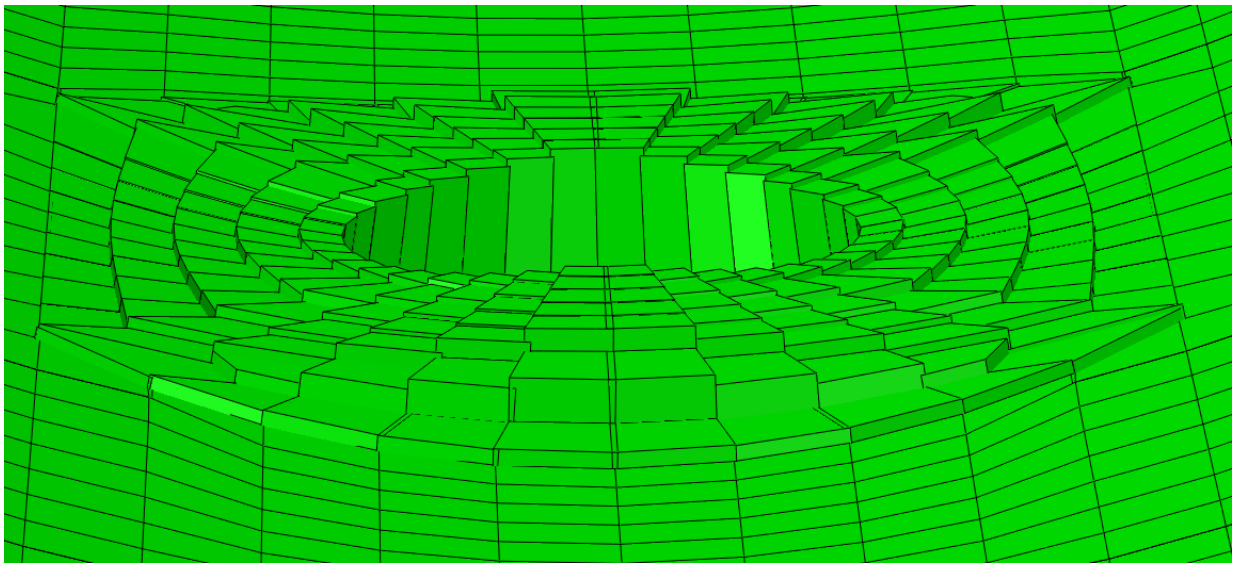

Figure D - 3: Equipment Hatch Thickness Assigned to Center of Each Element. Air-Lock Similar

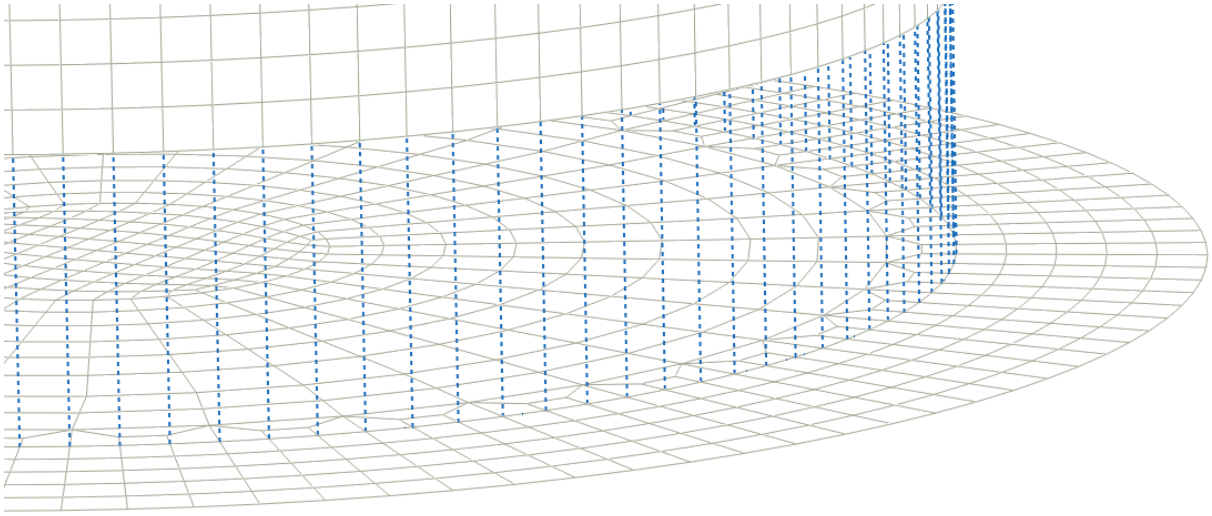

Figure D - 4: Rigid links from bottom of vessel to basemat elements

Temperature loads, case 1, and case 2

For both Loading Cases 1 and 2, a temperature (heat-transfer) solution performed during ISP-48 [2] is referenced to obtain the temperature gradients through-the-thickness of the vessel, which when interpolated, provides temperatures at every node and layer of the 3D shell model (Model 4).

Figure D-5 shows the time history analysis to be applied to Case 1, “Saturated Steam” condition. This case considers a monotonically increasing static pressure and temperature that is based on the pseudo-time history of the 1:4 Scale PCCV Model SFMT pressurization rate (5 psi/min) [3]. Figure D-6 shows the time history analysis to be applied to Case 2, “Station Blackout” condition where the hydrogen burn has been ignored. For both cases, the pressure and temperature curves are imposed only through the thickness of the PCCV cylinder and dome wall. No temperature condition has been set on the basemat foundation since it is so thick, the temperature is not high enough to produce significant changes.

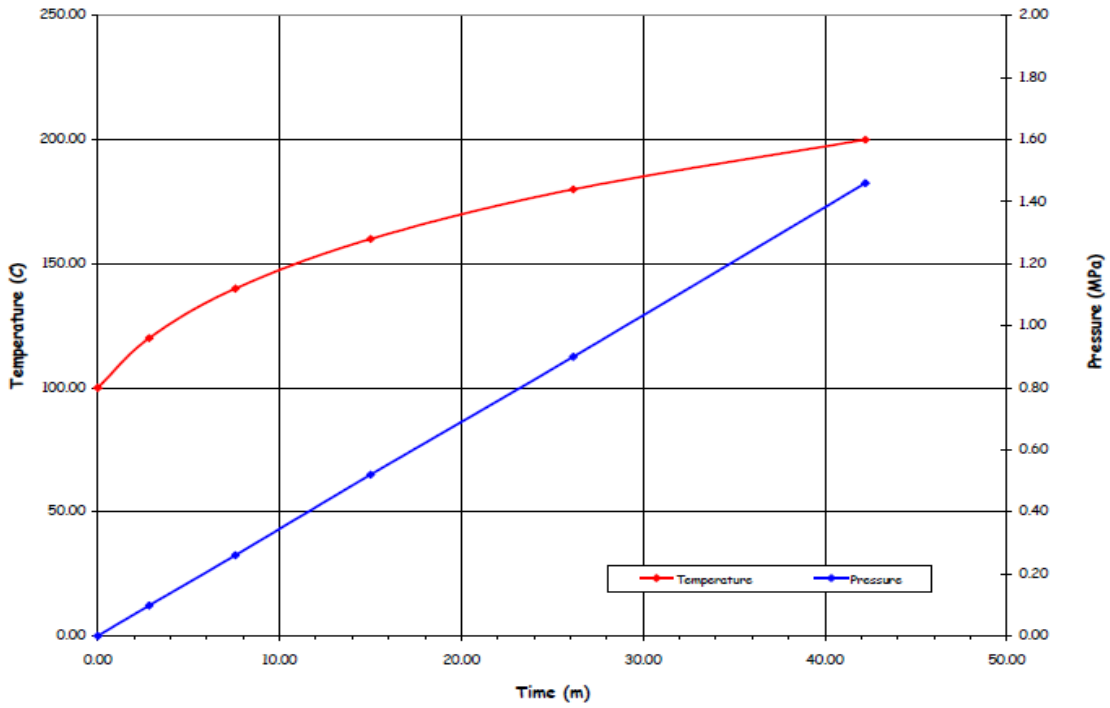

Figure D - 5: Model 4 – case 1 saturated steam pseudo-time history

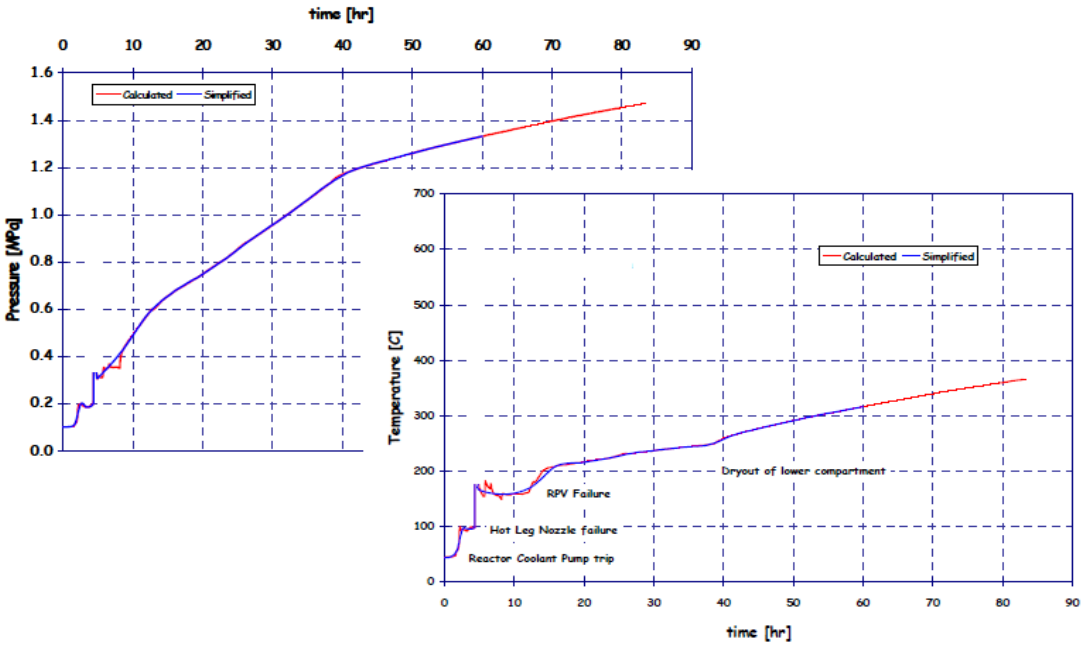

Figure D - 6: Model 4 – case 2 station blackout time history (ignoring hydrogen burn that occurs between time = 260 min. to time = 285 min.)

The temperature solution for Case 1 varies linearly through the thickness. The following graphs illustrate how pressure and temperature were combined together in the analysis. Figure D-7 shows the temperature at the inside face of the vessel at the corresponding pressure. Figure D-8 shows the temperature variation through the thickness of the vessel at different pressure milestones.

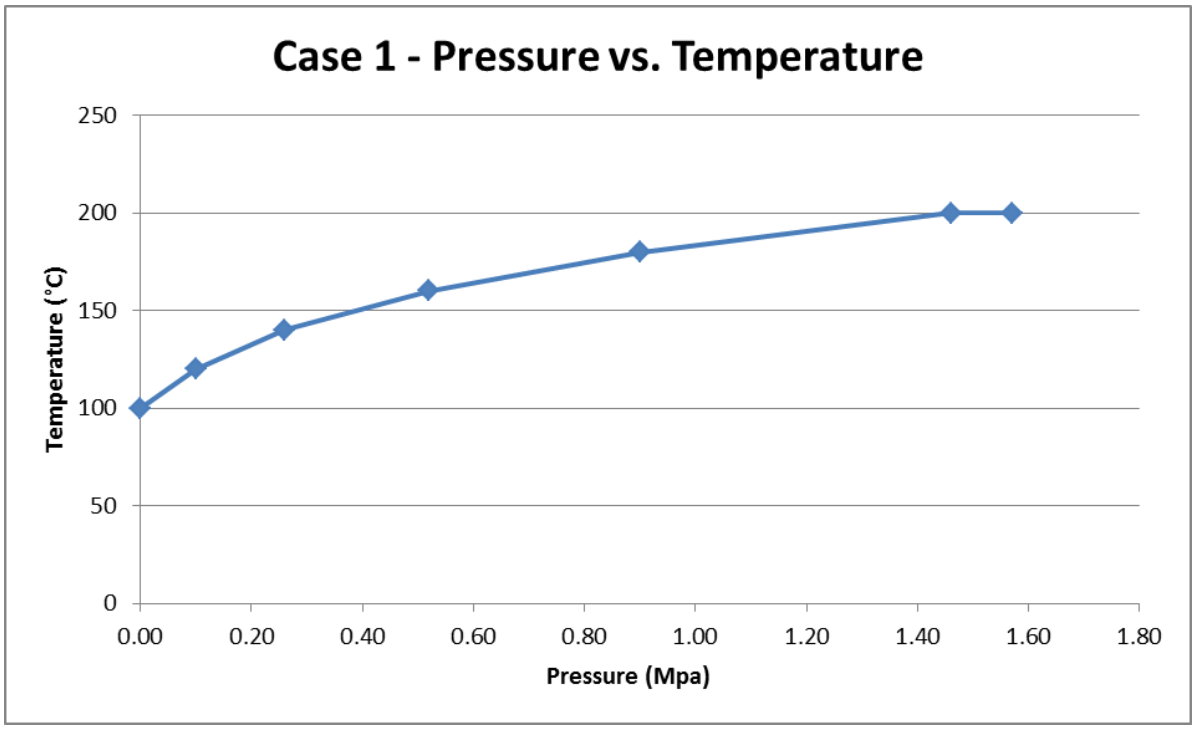

Figure D - 7: Case 1 - Relationship between pressure and temperature

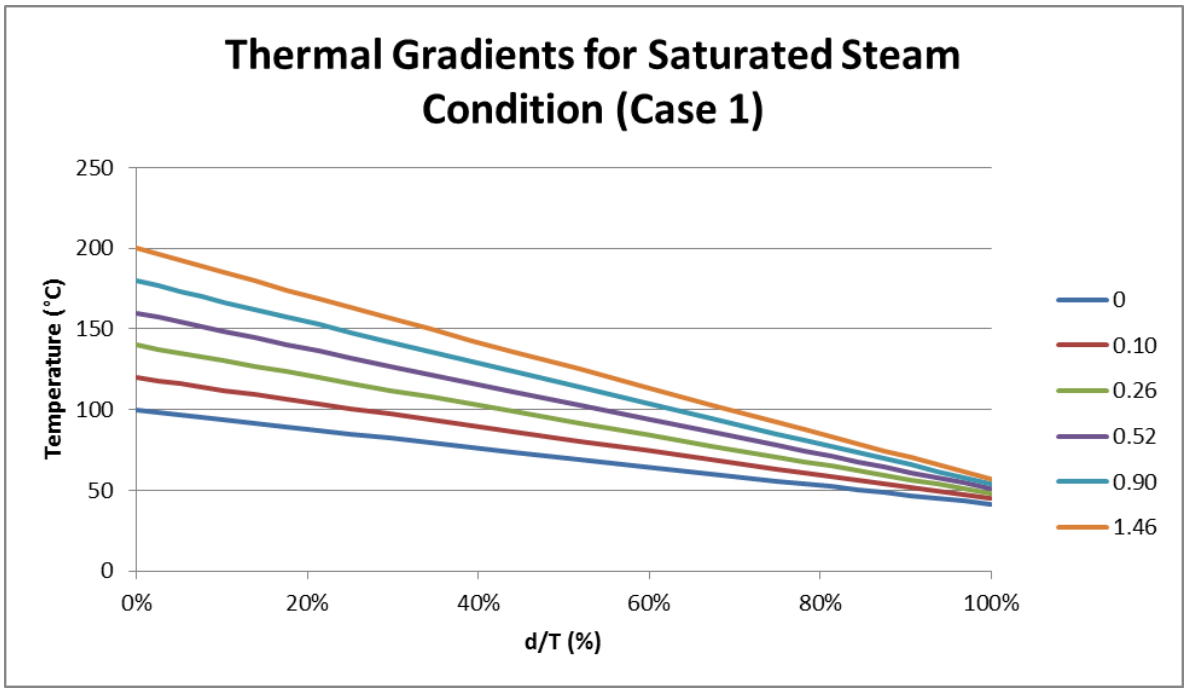

Figure D - 8: Case 1 – Temperature through thickness through time

For Case 2, a different approach was used to accommodate the temperature change. Case 2 has a curved temperature distribution, due to the high temperatures which exist for short time durations within the containment. For shell models, ABAQUS only handles applied temperature

gradients piecewise-linearly using temperature points equally spaced through the thickness. Five temperature values were applied, which follow the number of integration points. Several methods were tried to find the best way to model the temperature gradient with pressure for Case 2. The methods attempted were:

1) Piecewise linear with temperature curves corresponding to pressure time steps (see Figure D-9 and Table D-1)
2) Piecewise linear with one temperature curve corresponding to 3.6 x Pd (see Figure D-10)

The results from the first analyses were discussed in preliminary submittals, which state that Attempt 1 was only able to get to 1.72 x Pd when the solution diverged. Several variations of Attempt 1 were created, based on different combinations of how the temperature and pressure are applied. However, all variations attempted still led to solution divergence before reaching 3.6 x Pd. Attempt 2 ramped up the temperature curve corresponding to the pressure of 3.6, which occurs at time = 3600 minutes in one step, where the solution was able to converge to 3.6 x Pd.

In summary, the final solution strategy that was successfully executed was as follows. Each step has many load increments and equilibrium iterations; the load incrementation within a step is selected by ABAQUS, and cut-backs automatically when convergence becomes different.

- Solution Step 1: Apply Dead Load
- Solution Step 2: Apply Prestress
- Solution Step 3: Apply Anchor-Set
- Solution Step 4: Apply Pressure and Temperature

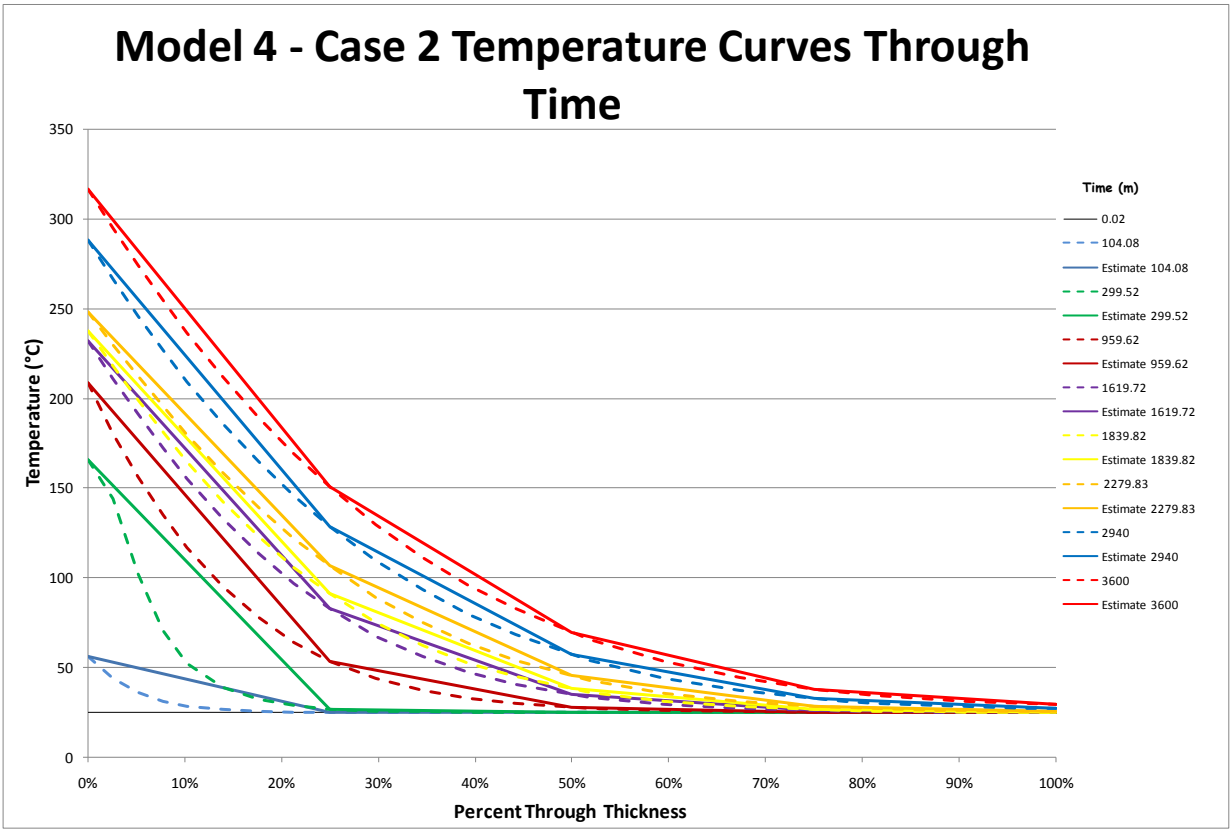

Figure D - 9: Case 2 – temperature through thickness through time. Method 1.

Table D - 1: Method 1 - Temperature Variation through Thickness of Wall (°C)

Temperature Curves with 5 Points Defined				% Through Thickness				
Time (min)	Pressure (MPa)	Pressure (xPd)	Analysis Step 3	0% (liner)	25%	50%	75%	100%
0.02	0.10	0.26	3.06	77.00	77.00	77.00	77.00	77.00
104.08	0.12	0.29	3.07	133.40	77.17	77.00	77.00	77.00
299.52	0.31	0.79	3.20	330.50	80.33	77.02	77.00	77.00
959.62	0.68	1.72	3.43	408.40	128.60	82.02	77.32	77.03
1619.72	0.90	2.28	3.57	450.40	181.20	95.76	79.27	77.41
1839.83	0.97	2.47	3.62	460.40	196.70	101.71	80.49	77.71
2279.83	1.13	2.88	3.72	478.60	224.20	114.64	83.85	78.69
2940.00	1.25	3.19	3.80	550.80	263.80	135.50	91.03	81.23
3600.00	1.33	3.39	3.85	601.90	303.40	157.60	100.30	85.01
3600.00	1.57	4.00	4.00	664.73	330.50	167.25	103.09	85.97

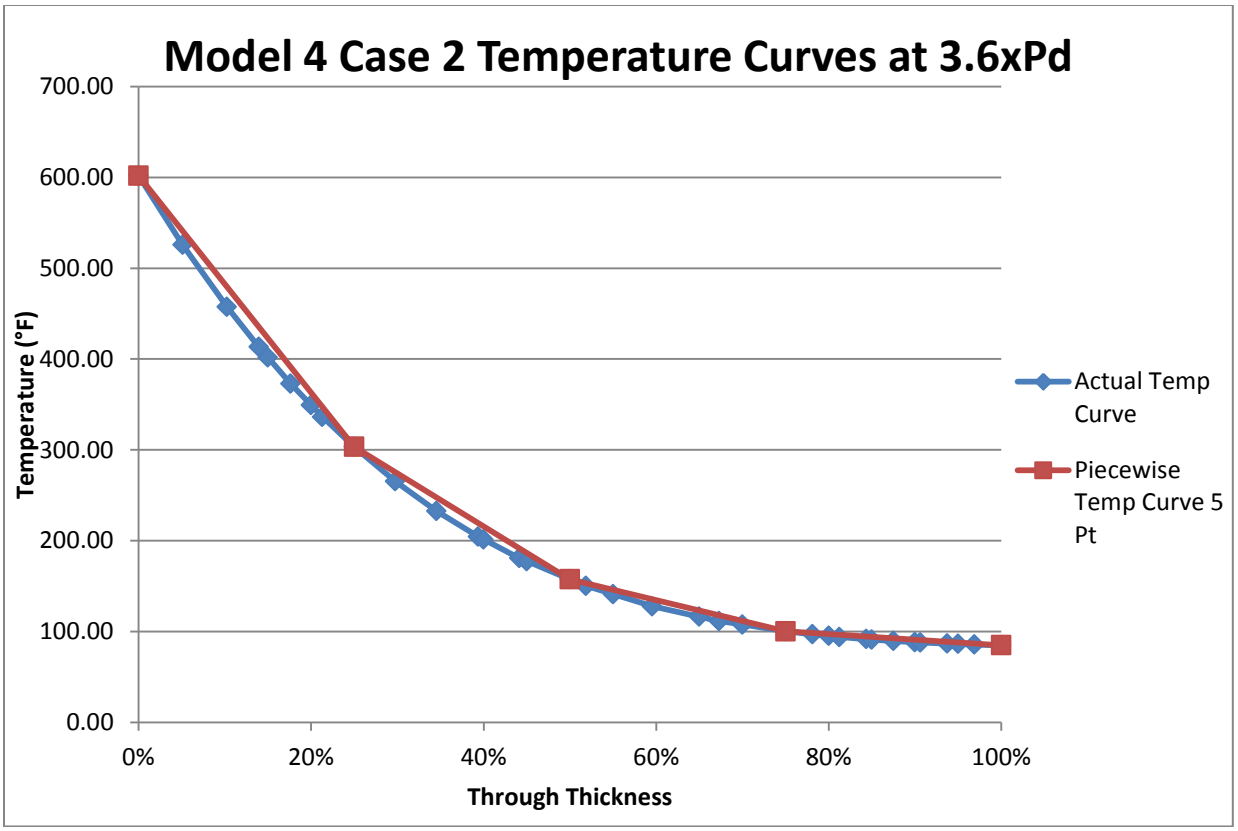

Figure D - 10: Case 2 – Modeling technique method 2.

Table D-2 shows how the temperature is applied at the different pressure milestones. The application of temperature for Model 4 – Case 1 is a true match of the temperature data provided through the time history graph.

Table D - 2: Comparison of temperature applied to case number

Temperature Applied to Inner Face of Liner		
	Case 1 Temp. (°F)	Case 2 Temp. (°F)
0xPd	0	0
1xPd	329	162
1.5xPd	361	247
2.0xPd	382	332
2.5xPd	400	416
3.0xPd	415	502
3.3xPd	423	549
3.4xPd	427	569
3.6xPd	432	590

Model 4 material modeling

From Model 3, concrete and rebar material stress-strain assumptions were implemented which follow the stress-strain curves tabulated in Appendix 1 of NUREG/CR-6810 [4]. Concrete was simulated using the ABAQUS concrete “Damaged Plasticity” constitutive model. This model utilizes a smeared-cracking formulation in tension (where cracking occurs at the element integration points), and a compressive plasticity theory. Steel elements were simulated using ABAQUS Standard Plasticity. The stress-strain inputs to these models consist of effective stress (Mises) and effective strain. The inputs are taken directly from the SPE Appendices, and are shown in the Model 1 report, so are not repeated here. The only difference from previous material models that has been implemented into Model 4 is the modulus of the steel liner.

Implementing temperature dependent property degradation

For Model 4, thermal analysis is considered. As temperature rises to certain thresholds, concrete and steel material strength start to degrade. In the past, the strength of concrete was modified by an assumed strength and modulus degradation based on the peak loading demand the PCCV would experience. The reduction factors held were based on the literature surveys of information available from the 1990’s and earlier. In the ISP-48 analysis, work there was also a limitation of its application in that the amount of reduction was held constant throughout the loading sequence. With recent research advancement in fire-resistance, the effect of temperature on strength is better known (especially for concrete). Material stress-strain curves are defined and implemented for fully-coupled temperature degradation of material properties. The property definitions have one reduction factor for the elastic region and another factor for the inelastic region. In addition, a difference in reduction factor exists for compression and tension. The relationship between temperature and material property was adopted based on the 2005 Euro-code, as is specified in the SPE Phase 2 White Paper. Further, the reductions were implemented in a fully-coupled, temperature dependent fashion for the current analysis.

For concrete under compression, the stress-strain relationships are based on elevated temperature and type of aggregate used, which is outlined in Table D-3. The region prior to peak compressive strength is defined by Equation (1) with a linear descending branch post-peak stress value. Using these relationships, the following stress-strain curves were used in analyses highlighted in Figure D-11.

Table D - 3: Values for parameters of the stress-strain relationships of normal weight concrete with siliceous or calcareous aggregates at elevated temperatures.

Concrete	Siliceous aggregates			Calcareous aggregates		
temp. θ	$f_{c,\theta} / f_{ck}$	$\varepsilon_{c1,\theta}$	$\varepsilon_{cu1,\theta}$	$f_{c,\theta} / f_{ck}$	$\varepsilon_{c1,\theta}$	$\varepsilon_{cu1,\theta}$
[°C]	[-]	[-]	[-]	[-]	[-]	[-]
1	2	3	4	5	6	7
20	1,00	0,0025	0,0200	1,00	0,0025	0,0200
100	1,00	0,0040	0,0225	1,00	0,0040	0,0225
200	0,95	0,0055	0,0250	0,97	0,0055	0,0250
300	0,85	0,0070	0,0275	0,91	0,0070	0,0275
400	0,75	0,0100	0,0300	0,85	0,0100	0,0300
500	0,60	0,0150	0,0325	0,74	0,0150	0,0325
600	0,45	0,0250	0,0350	0,60	0,0250	0,0350
700	0,30	0,0250	0,0375	0,43	0,0250	0,0375
800	0,15	0,0250	0,0400	0,27	0,0250	0,0400
900	0,08	0,0250	0,0425	0,15	0,0250	0,0425
1000	0,04	0,0250	0,0450	0,06	0,0250	0,0450
1100	0,01	0,0250	0,0475	0,02	0,0250	0,0475
1200	0,00	-	-	0,00	-	-

$$\sigma(\theta) = \frac{3\varepsilon f_{c,\theta}}{\varepsilon_{c1,\theta}(2+(\frac{\varepsilon}{\varepsilon_{c1,\theta}})^3)} \text{ for range } \varepsilon \leq \varepsilon_{c1,\theta} \quad (1)$$

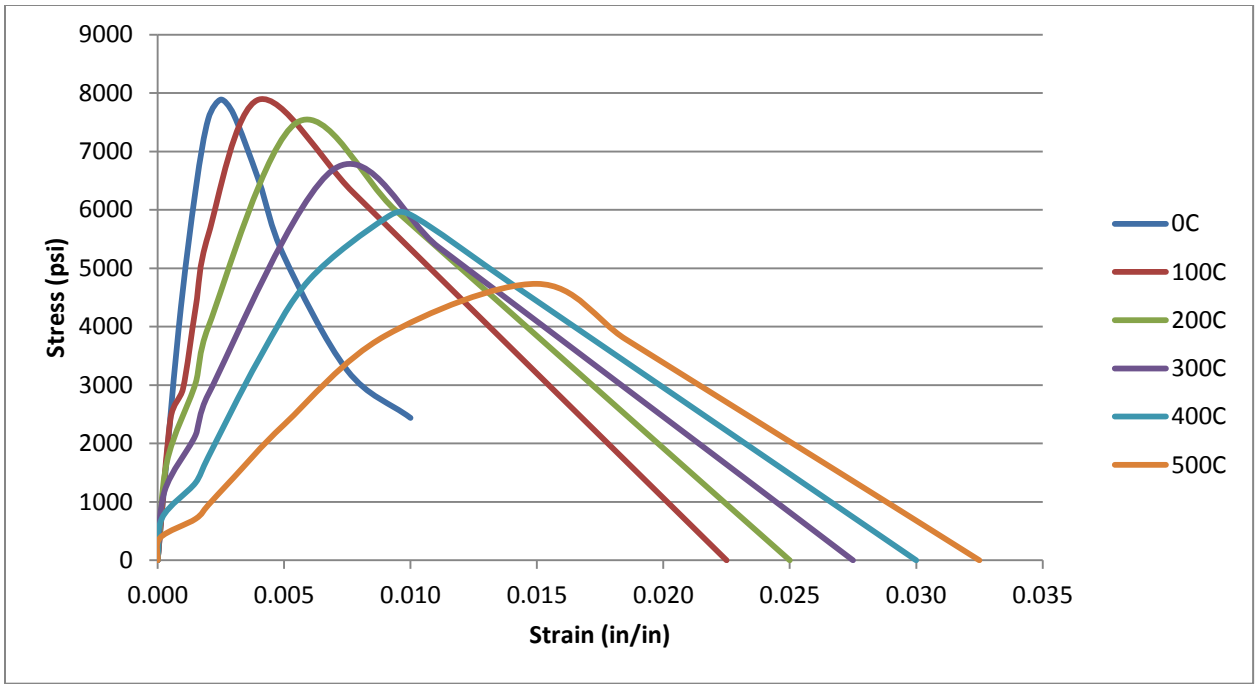

Figure D - 11: Concrete compressive strength at elevated temperatures

For concrete in tension, a reduction factor, $k_{c,t}(\theta)$ based on elevated temperature is used to determine the tensile strength of concrete. Equation 2 highlight the changes.

$$k_{c,t}(\theta) = 1.0 \text{ for } 20°C \leq \theta \leq 100°C$$
$$k_{c,t}(\theta) = 1.0 - 1.0(\theta - 100)/500 \text{ for } 20°C \leq \theta \leq 100°C \quad (2)$$

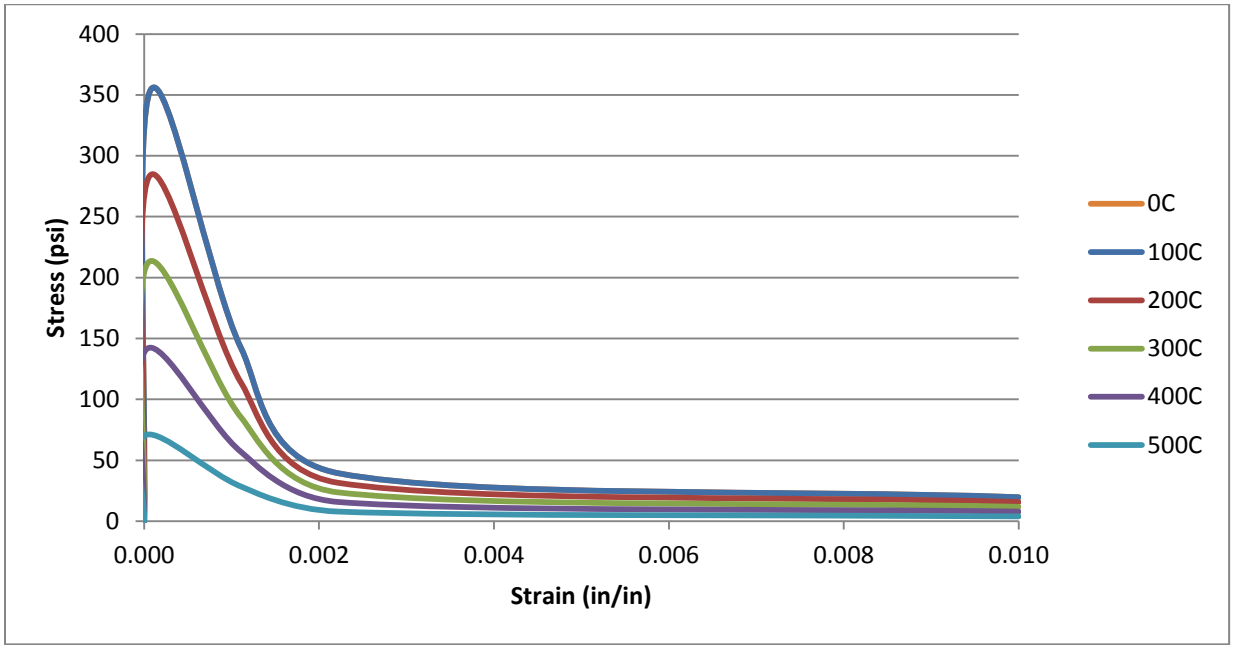

Figure D - 12: Concrete tensile strength at elevated temperatures

Similar to concrete, steel stress-strain relationships vary with elevated temperature by reduction factors in the proportional limit, effective yield strength, and Young's Modulus, highlighted in Table D-4. The region between the proportional limit and effective yield strength is outlined in Figure D-13. The region that is strain-hardened is factored down by the curve's corresponding yield reduction factor. The stress-strain curves at elevated temperatures for all types of rebar and the liner are illustrated in Figures D-14 through D-22.

Table D - 4: Reduction factors for stress-strain relationship

Steel Temperature θ_a	Reduction factors at temperature θ_a relative to the value of f_y or E_a at 20°C		
	Reduction factor (relative to f_y) for effective yield strength $k_{y,\theta} = f_{y,\theta}/f_y$	Reduction factor (relative to f_y) for proportional limit $k_{p,\theta} = f_{p,\theta}/f_y$	Reduction factor (relative to E_a) for the slope of the linear elastic range $k_{E,\theta} = E_{a,\theta}/E_a$
20°C	1,000	1,000	1,000
100°C	1,000	1,000	1,000
200°C	1,000	0,807	0,900
300°C	1,000	0,613	0,800
400°C	1,000	0,420	0,700
500°C	0,780	0,360	0,600
600°C	0,470	0,180	0,310
700°C	0,230	0,075	0,130
800°C	0,110	0,050	0,090
900°C	0,060	0,0375	0,0675
1000°C	0,040	0,0250	0,0450
1100°C	0,020	0,0125	0,0225
1200°C	0,000	0,0000	0,0000

NOTE: For intermediate values of the steel temperature, linear interpolation may be used.

Strain range	Stress σ	Tangent modulus	
$\varepsilon \le \varepsilon_{p,\theta}$	$\varepsilon E_{a,\theta}$	$E_{a,\theta}$	
$\varepsilon_{p,\theta} < \varepsilon < \varepsilon_{y,\theta}$	$f_{p,\theta} - c + (b/a)\left[a^2 - (\varepsilon_{y,\theta} - \varepsilon)^2\right]^{0,5}$	$\frac{b(\varepsilon_{y,\theta} - \varepsilon)}{a\left[a^2 - (\varepsilon_{y,\theta} - \varepsilon)^2\right]^{0,5}}$	
$\varepsilon_{y,\theta} \le \varepsilon \le \varepsilon_{t,\theta}$	$f_{y,\theta}$	0	
$\varepsilon_{t,\theta} < \varepsilon < \varepsilon_{u,\theta}$	$f_{y,\theta}\left[1 - (\varepsilon - \varepsilon_{t,\theta})/(\varepsilon_{u,\theta} - \varepsilon_{t,\theta})\right]$	-	
$\varepsilon = \varepsilon_{u,\theta}$	0,00	-	
Parameters	$\varepsilon_{p,\theta} = f_{p\theta}/E_{a,\theta}$	$\varepsilon_{y,\theta} = 0,02$	$\varepsilon_{t,\theta} = 0,15$ $\varepsilon_{u,\theta} = 0,20$
Functions	$a^2 = (\varepsilon_{y,\theta} - \varepsilon_{p,\theta})(\varepsilon_{y,\theta} - \varepsilon_{p,\theta} + c/E_{a,\theta})$ $b^2 = c(\varepsilon_{y,\theta} - \varepsilon_{p,\theta})E_{a,\theta} + c^2$ $c = \frac{(f_{y,\theta} - f_{p,\theta})^2}{(\varepsilon_{y,\theta} - \varepsilon_{p,\theta})E_{a,\theta} - 2(f_{y,\theta} - f_{p,\theta})}$		

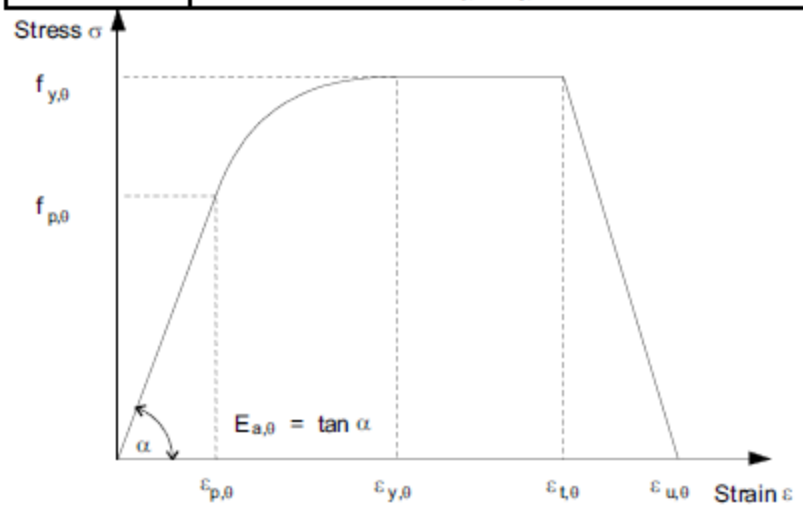

Key:

$f_{y,\theta}$	effective yield strength;
$f_{p,\theta}$	proportional limit;
$E_{a,\theta}$	slope of the linear elastic range;
$\varepsilon_{p,\theta}$	strain at the proportional limit;
$\varepsilon_{y,\theta}$	yield strain;
$\varepsilon_{t,\theta}$	limiting strain for yield strength;
$\varepsilon_{u,\theta}$	ultimate strain.

Figure D - 13: Stress-strain relationship for region between proportional limit and effective yield strength

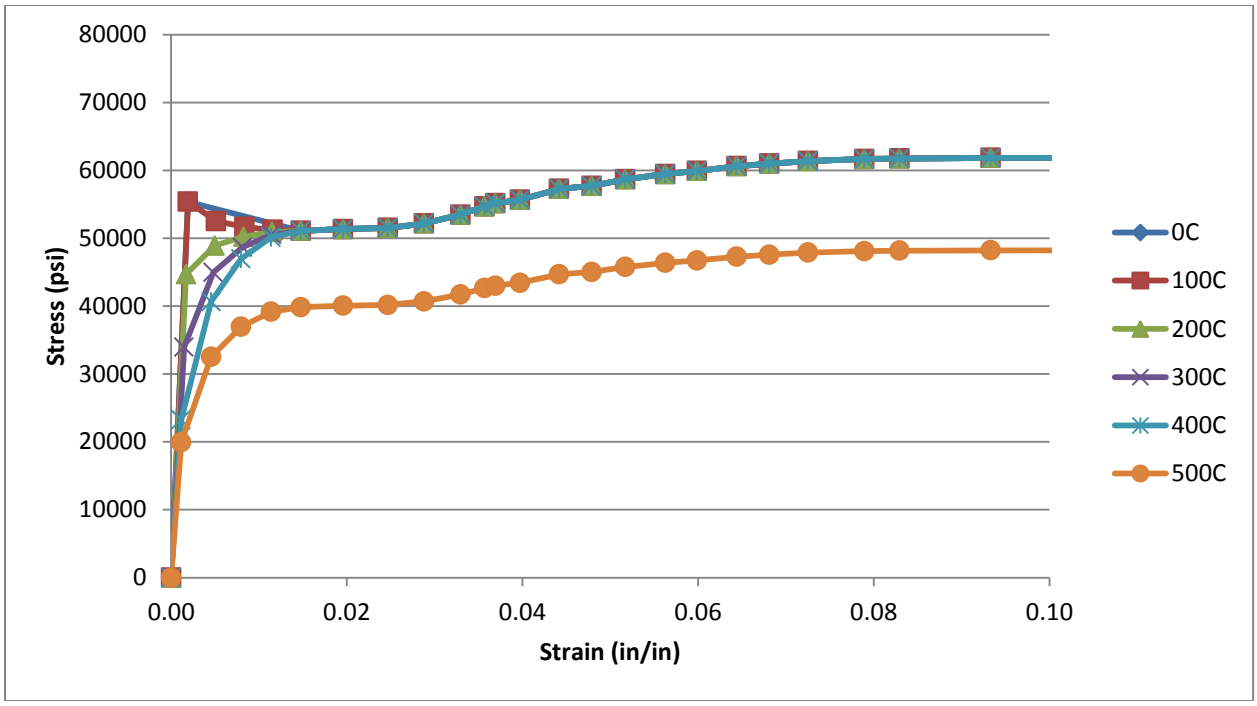

Figure D - 14: Rebar D6SD345 stress-strain curves at elevated temperatures

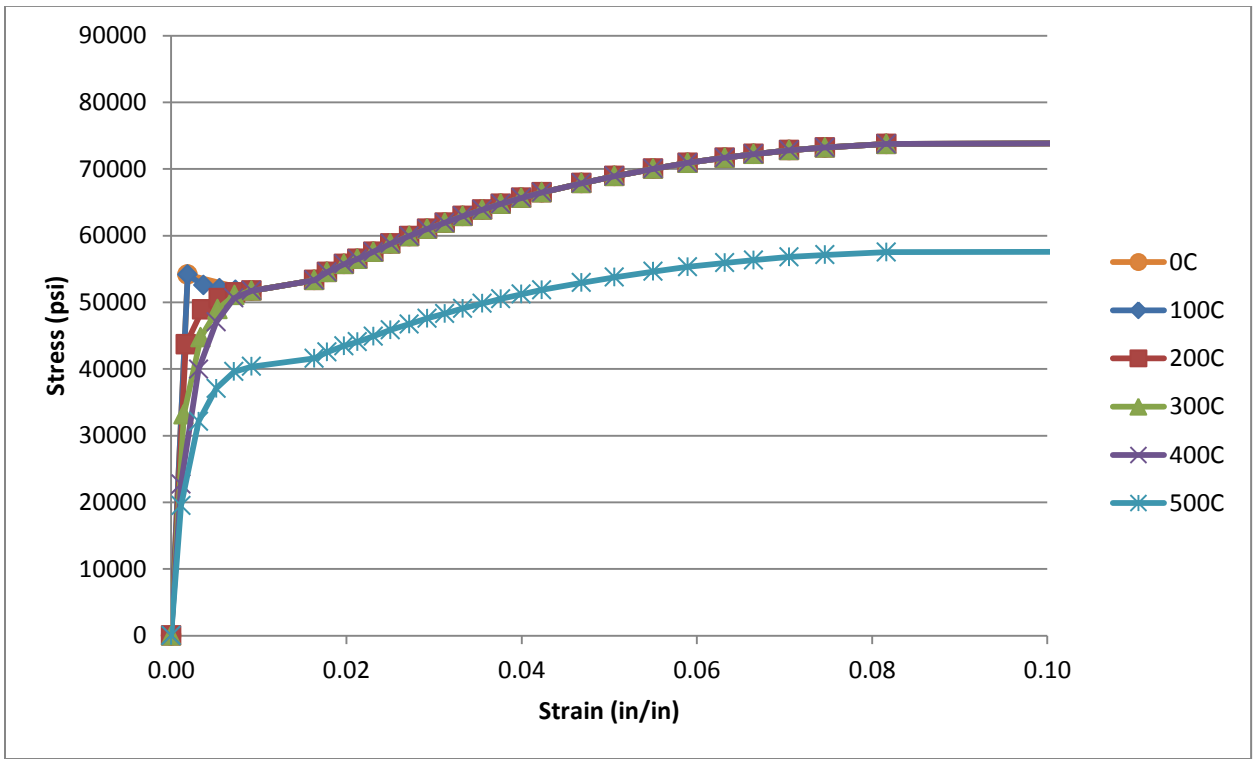

Figure D - 15: Rebar D10SD345 stress-strain curves at elevated temperatures

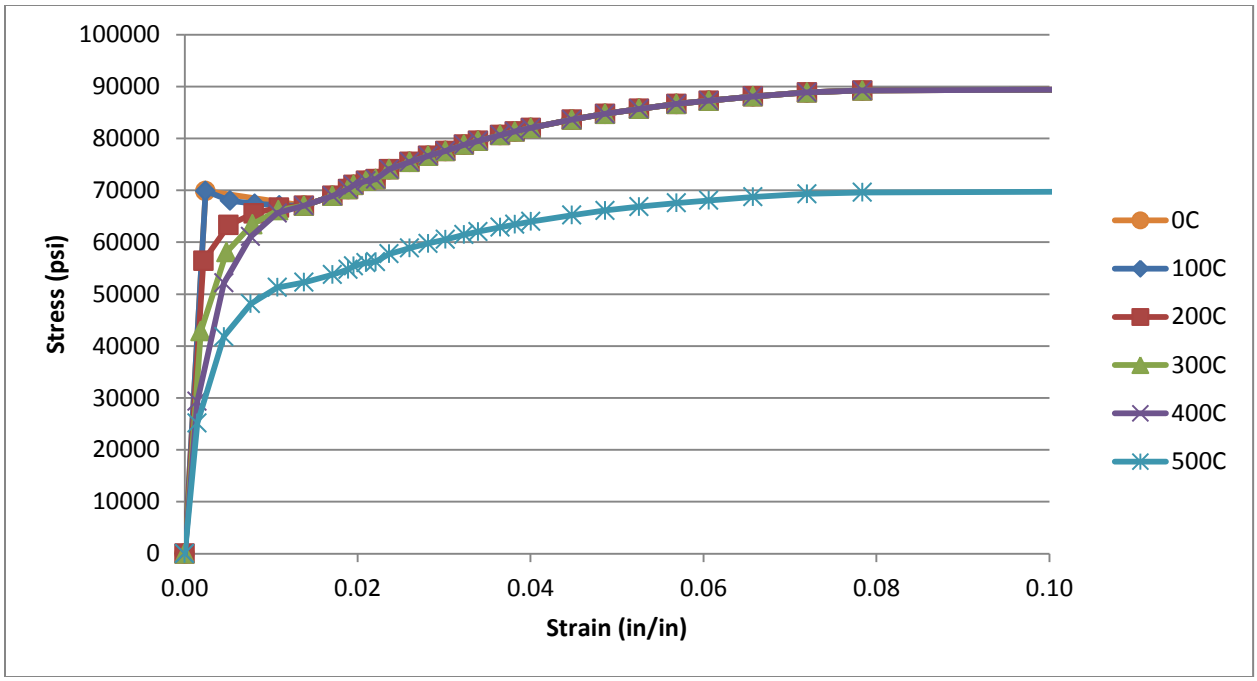

Figure D - 16: Rebar D10SD390 stress-strain curves at elevated temperatures

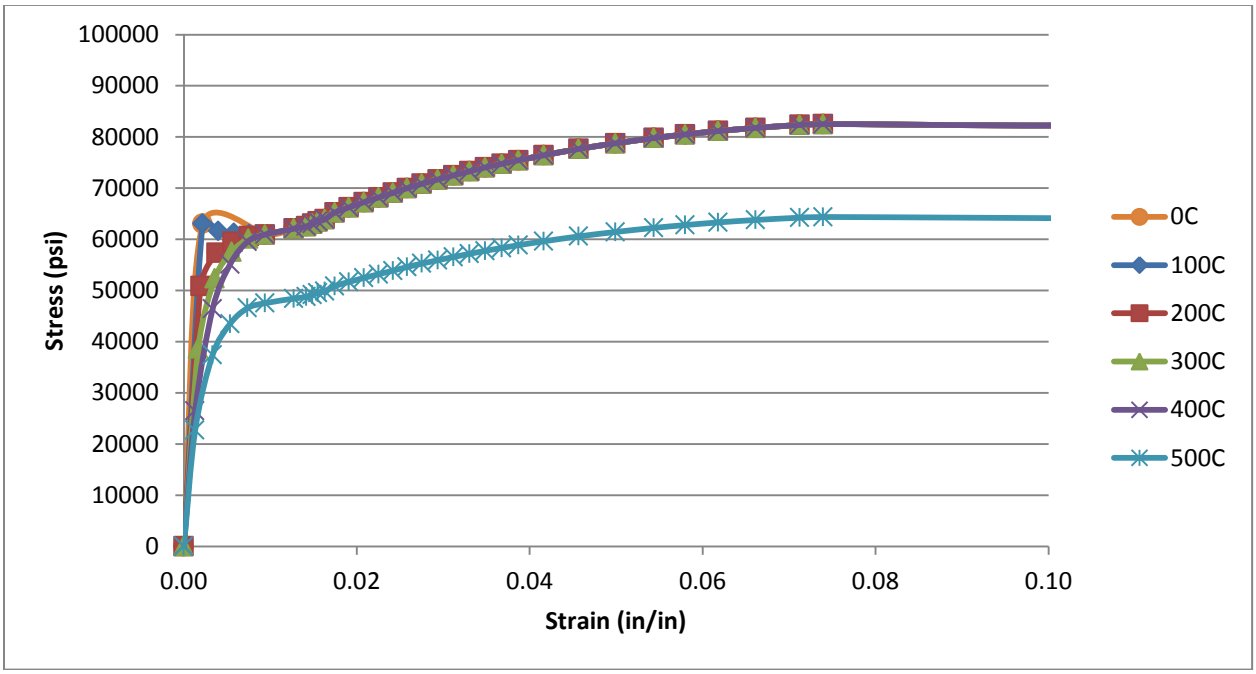

Figure D - 17: Rebar D13SD390 and D16SD390 stress-strain curves at elevated temperatures

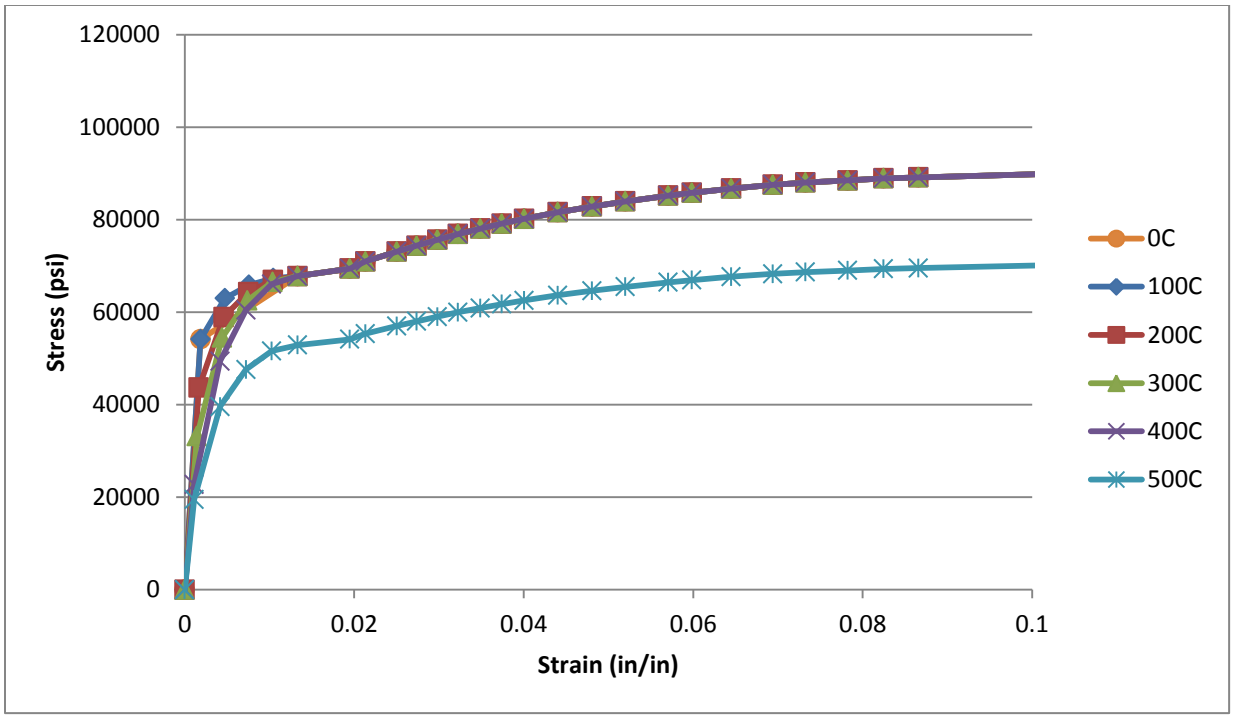

Figure D - 18: Rebar D19SD390 stress-strain curves at elevated temperatures

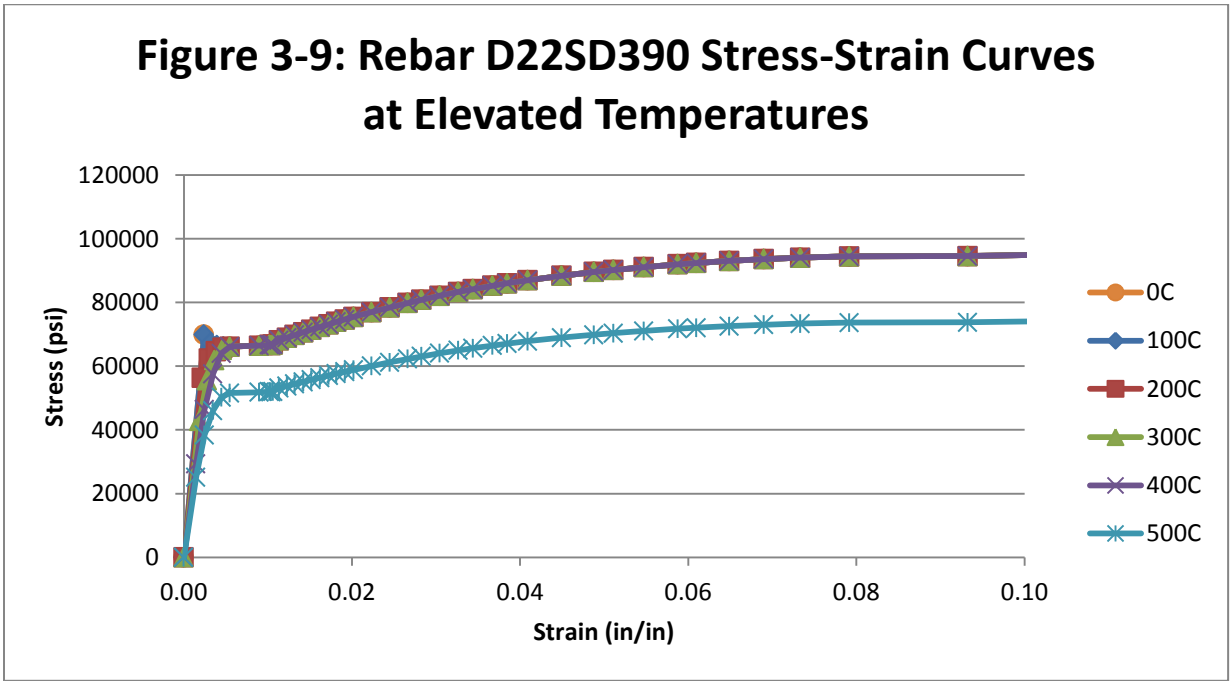

Figure D - 19: Rebar D22SD390 stress-strain curves at elevated temperatures

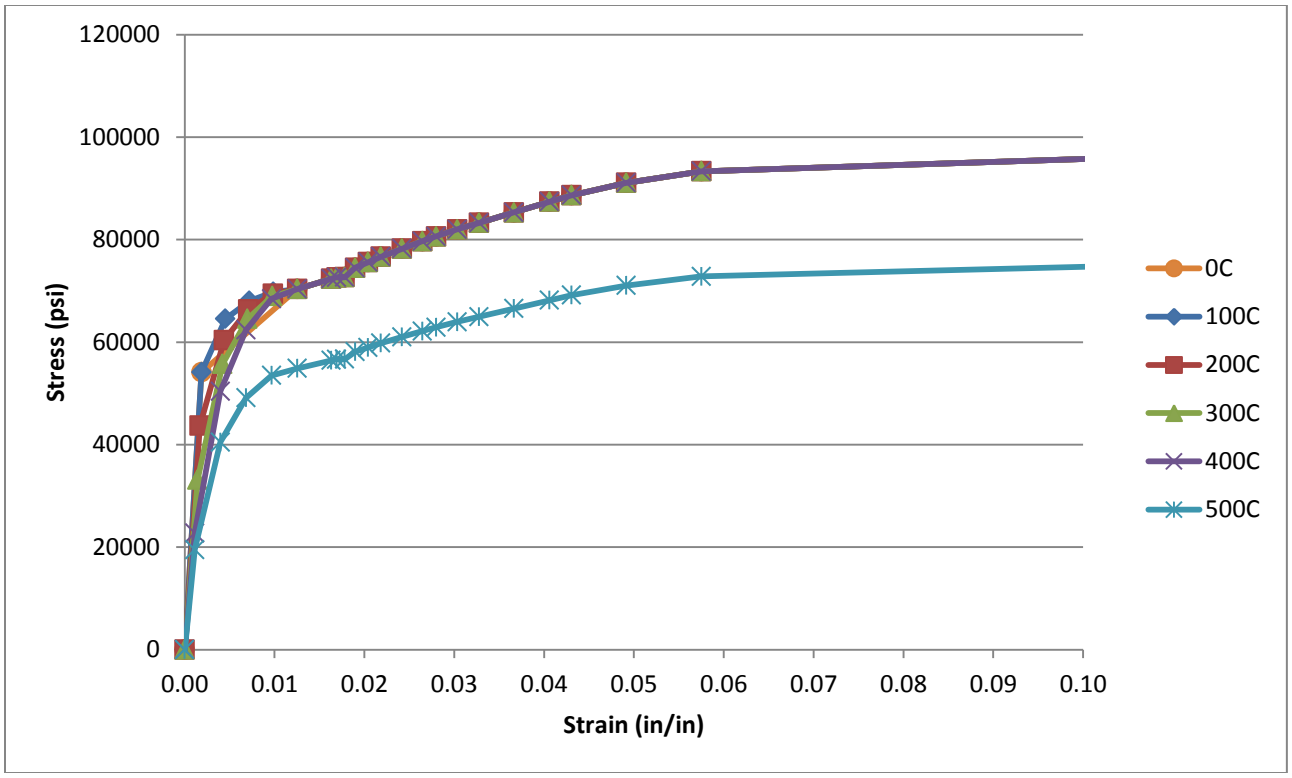

Figure D - 20: Rebar D16SD490 stress-strain curves at elevated temperatures

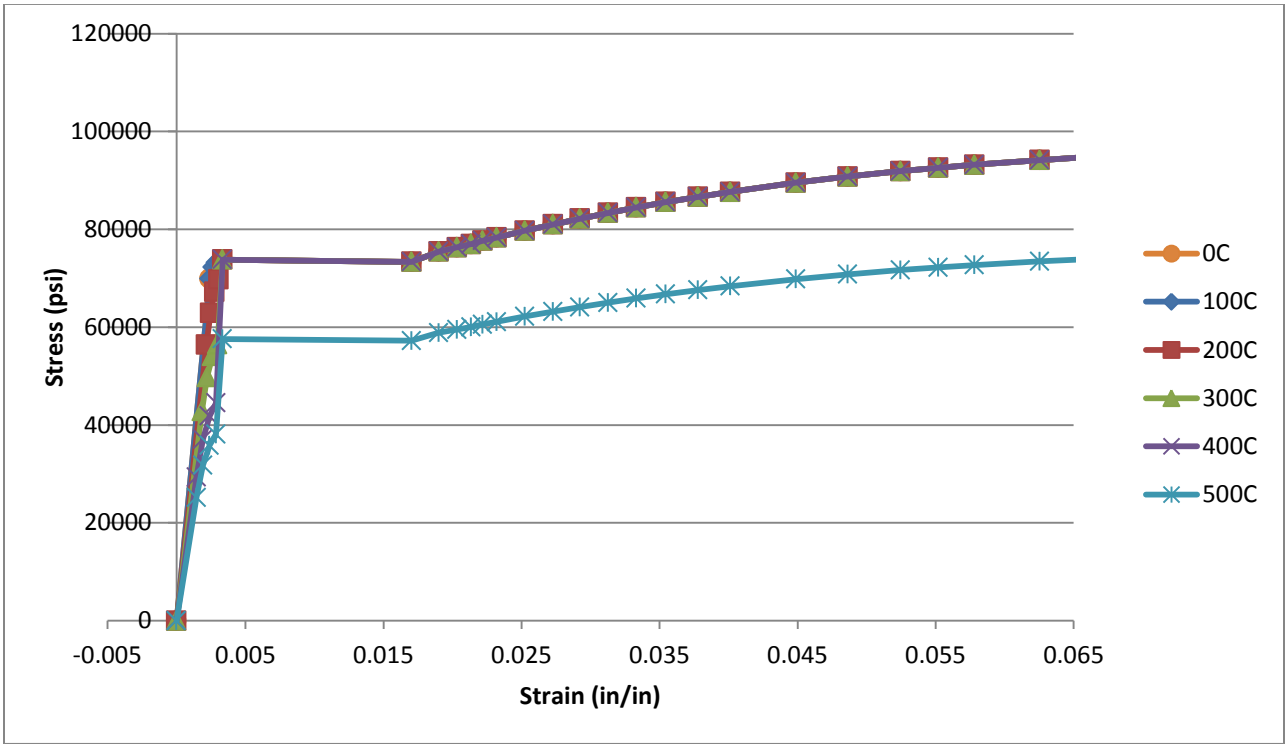

Figure D - 21: Rebar D19SD490 stress-strain curves at elevated temperatures

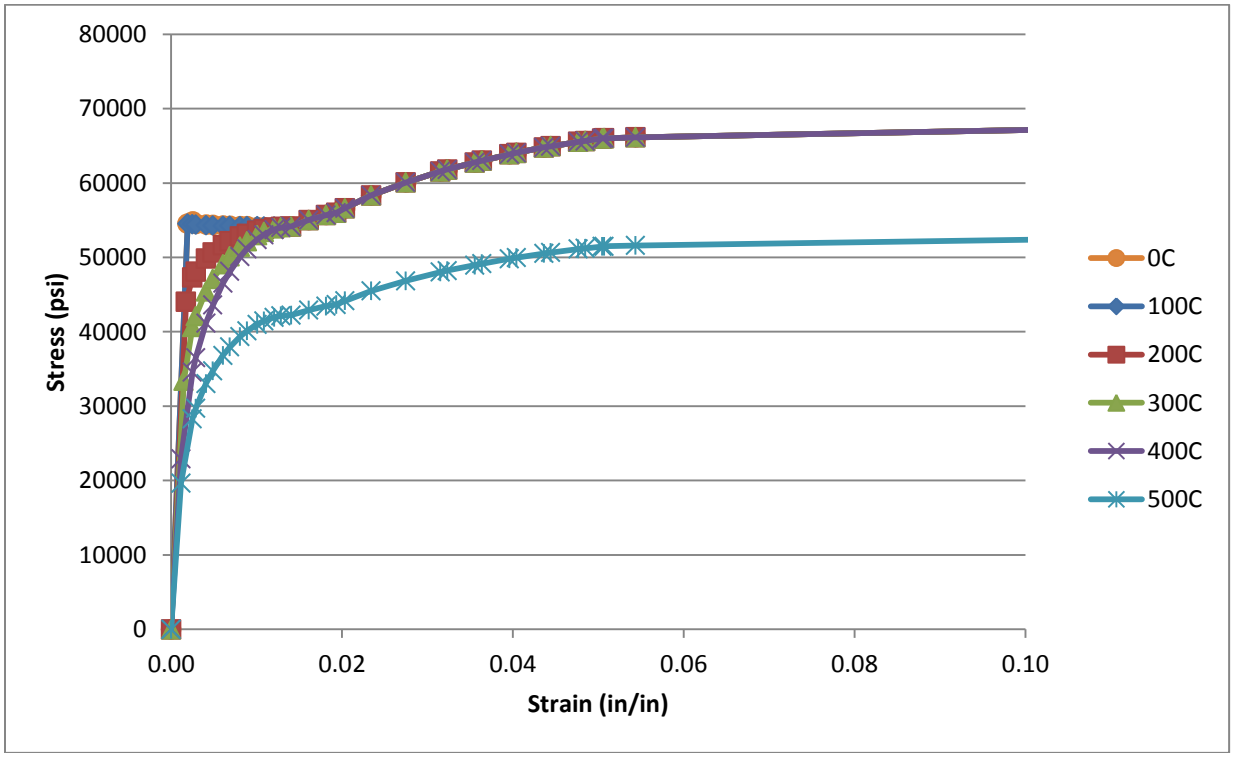

Figure D - 22: Liner stress-strain curves at elevated temperatures

Analysis results

Following the guidelines set forth in the SPE Phase 2 White Paper there are the following Required Outputs/Results for Model 4:

1.1 Description of Failure Prediction Model or Criteria Selected

1.2 Assumptions Made In Geometric Modeling, and Model Description

1.3 A subset of the response information defined by the "55 standard output locations" of the 1:4 Scale PCCV round-robin exercise.

1.4 Contour Plot of Peak Strains in the Liner During the LST at the pressure milestones: P = 0 (prestress applied); 1 x P_d; 1.5 P_d; 2 P_d; 2.5 P_d; 3 P_d; 3.3 P_d; 3.4 P_d; Ultimate Pressure

1.5 A subset of the response information defined by the "55 standard output locations" of the 1:4 Scale PCCV round-robin exercise; see below for the specific list.

1.6 Contour Plots of Peak Strains in the Liner During the LST at the pressure milestones: P=0 (prestress applied); 1 x P_d; 1.5 P_d; 2 P_d; 2.5 P_d; 3 P_d; 3.3 P_d; 3.4 P_d; Ultimate Pressure

1.7 Liner Strain Map of Entire Liner Surface; this was discussed at the April 13-14 Meeting, and an Excel format for this has been developed. Participants are asked to plan for outputting this from their Model 4 Analysis. The "map" has a location format using the azimuths and elevations of the model as shown in Figure 11. It will not matter how fine is the spacing of the data points, because participants' mesh sizes vary, but participants were asked to plan

for a minimum spacing for liner strain data of 450 mm, which corresponds to the liner-anchor spacing.

For direct comparison amongst participants, the following are plotted

- Liner Strain Magnitudes (Hoop Direction) at Locations Indicated in Figure D-23 (of SPE problem statement), versus pressure
- Tendon stress distribution at P = 0 (prestress applied); 1 x P_d; 1.5 P_d; 2 P_d; 2.5 P_d; 3 P_d; 3.3 P_d; 3.4 P_d; Ultimate Pressure for
    - Hoop Tendons # H35, H53, H68
    - Vertical Tendon # V37 and V46
- Plots of response versus pressure for Standard Output Locations:
  1-15 (displacements); 22-29 (rebar strains); 36-42 (liner strains);
  48-55 (tendon strains and stresses)

(see Table 4-1 in NUREG/CR-6809 for exact locations and definitions of SOL's)

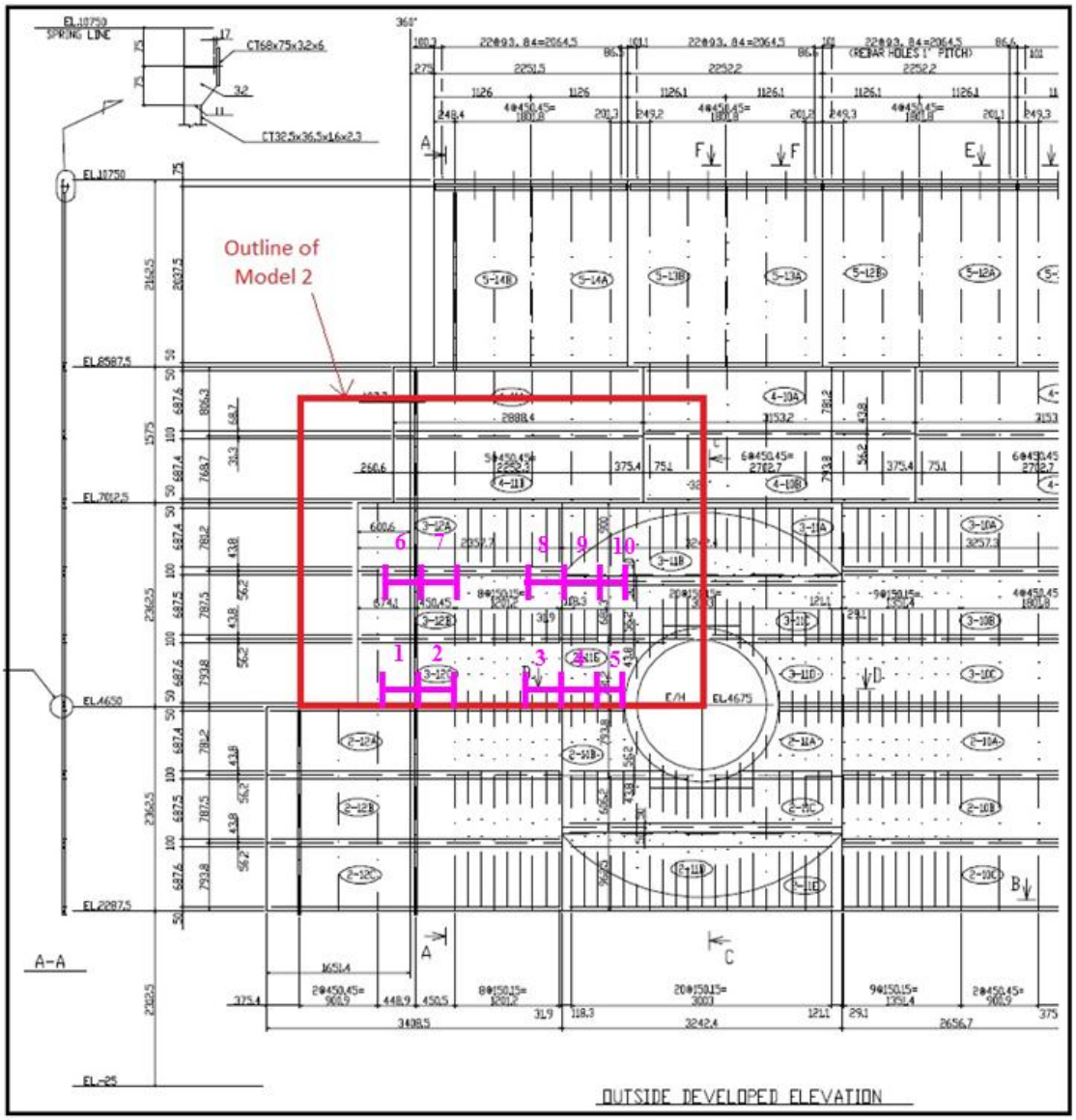

Figure D - 23: Liner (E/H) View Showing Strain Reports (cut from Page A-28 of NUREG/CR-6810)

Case 1 – "Saturated steam" condition

The results of pressure milestones are shown in Table D-5.

Table D - 5: Case 1 results by pressure milestones at 6.2 m

Milestone	Pressure (MPa)	x Pd
Zero Concrete Hoop Stress (at 0^o azimuth)	0.78	2.00
Concrete Hoop Cracking Occurs (at 0^o azimuth)	0.80	2.04
Tendon A Reach approx.1% Strain (at 0^o azimuth)	1.23	3.13

Tendon B Reach approx.1% Strain (at 0^o azimuth)	1.18	3.00

Deformed shapes of the full model are shown in Figures D-24a and D-24b for, respectively, the a) after prestress and tendon anchorage step, b) at pressurization of 3.6 Pd, which is incipient failure of the vessel.

A series of “plan-view” slice deformed shapes are shown in Figures D-25a through D-25i, at a Model Elevation of 4.68 meters. Based on rough comparisons to the results from Model 3, these shapes and the magnitude of the displacements are in reasonably good agreement.

A series of global plots of Maximum Principal Strains are shown for the Liner, and for the Concrete Mid-thickness of the Vessel in the Plot Series, Figures D-26a through D-26i and D-27a through D-27i.

Figures D-28a through D-28d show hoop tendon stresses, D-29a through D-30 show vertical tendon stresses, and Figures D-31a through D-31r show hoop tendon strains.

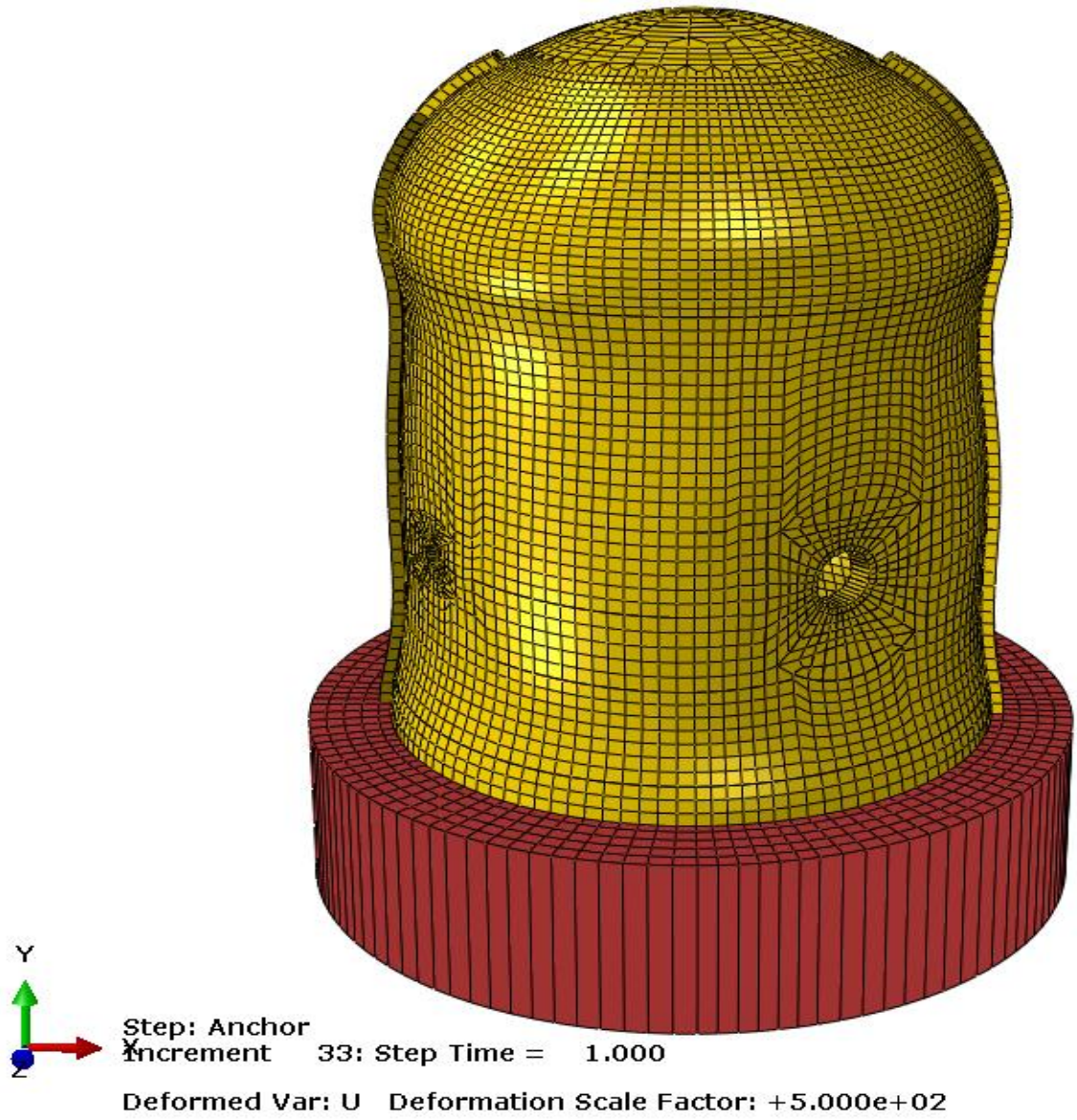

Figure D - 24a: Case 1 deformed shape after tendon anchorage. Deformation scale x 500

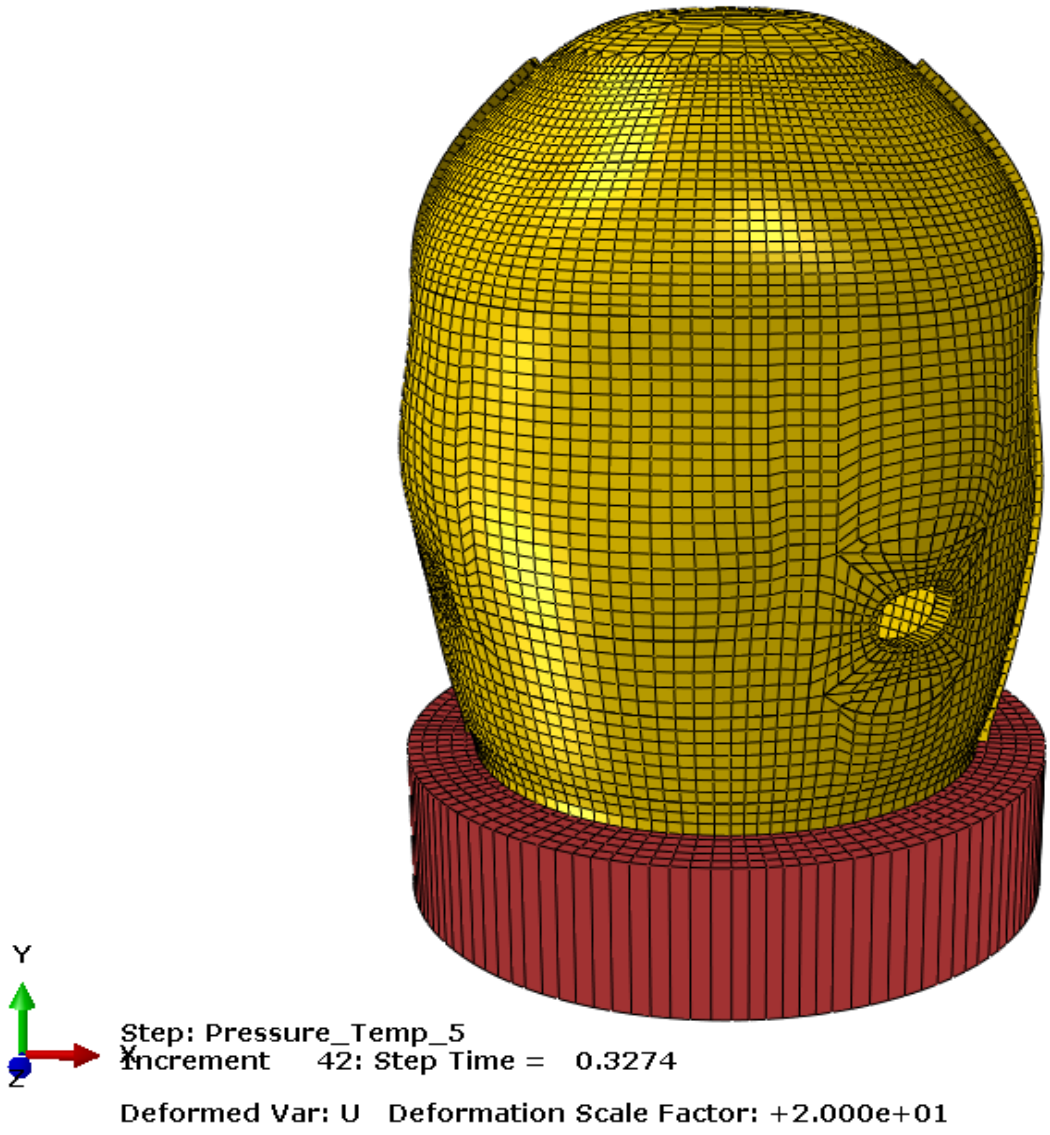

Figure D - 24b: Case 1 deformed shape at 3.6xpd. Deformation scale x 20

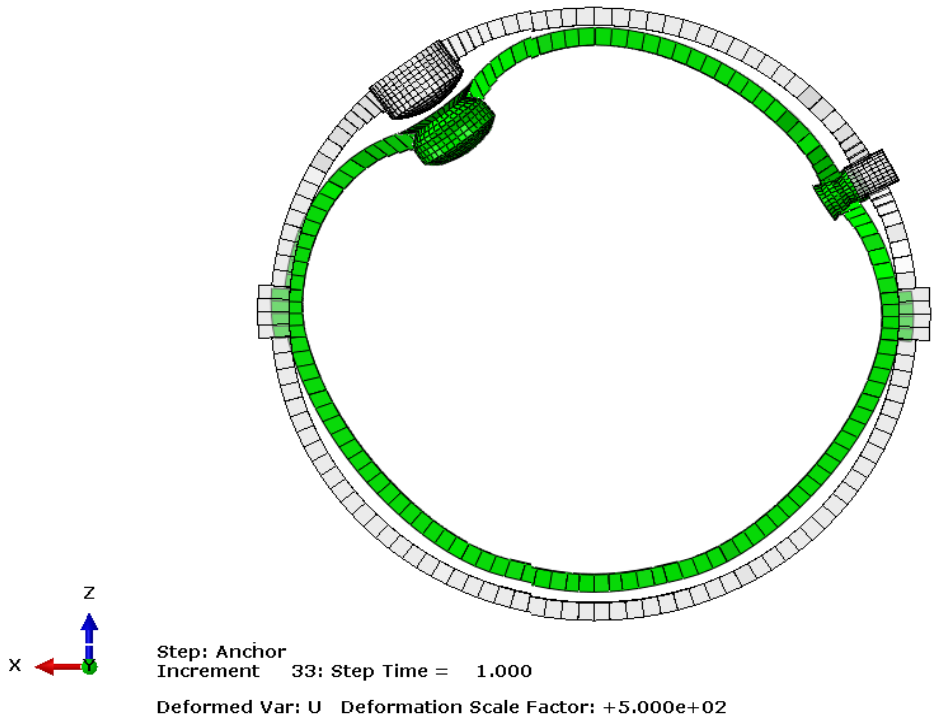

Figure D - 25a: Case 1 deformed shape at anchoring at elev. 4.68 m (15'-4 1/16") (x500)

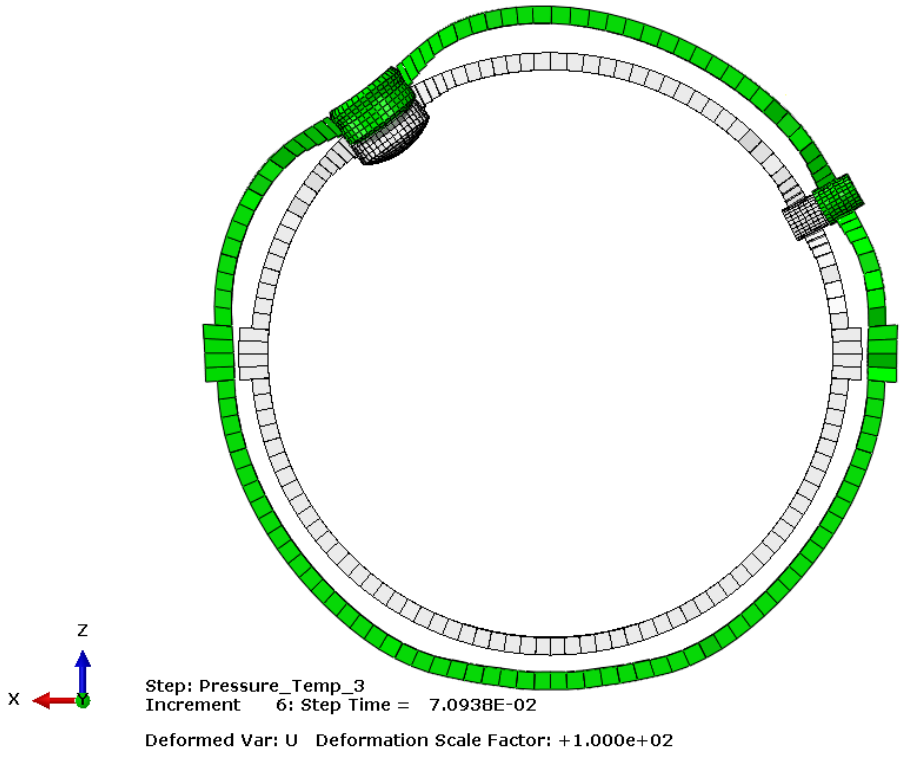

Figure D - 25b: Case 1 deformed shape at 1.0 x design pressure at elev. 4.68 m (15'-4 1/16") (x100)

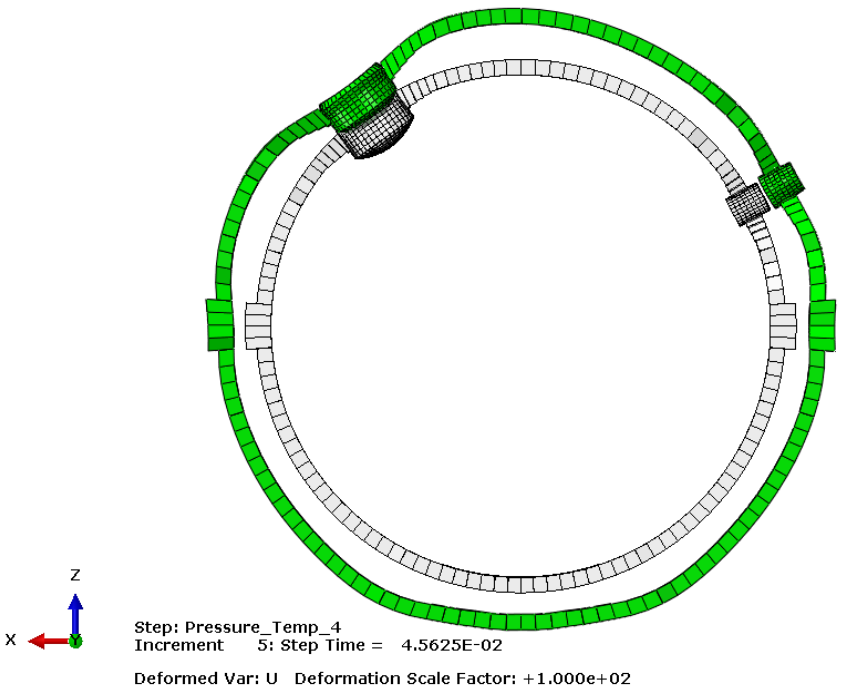

Figure D – 25c: Case 1 deformed shape at 1.5 x design pressure at elev. 4.68 m (15'-4 1/16") (x100)

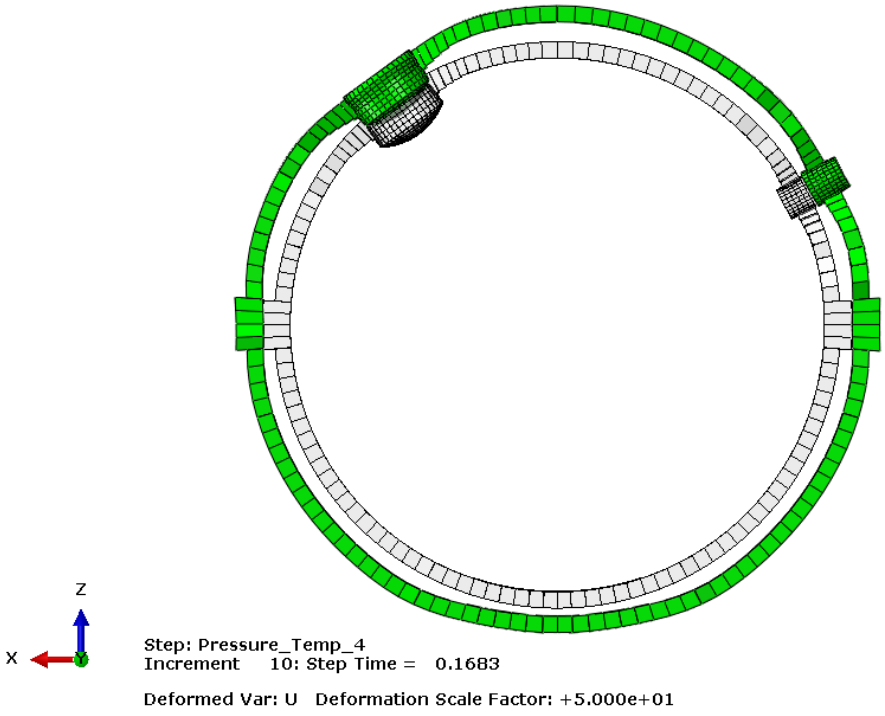

Figure D – 25d: Case 1 deformed shape at 2.0 x design pressure at elev. 4.68 m (15'-4 1/16") (x50)

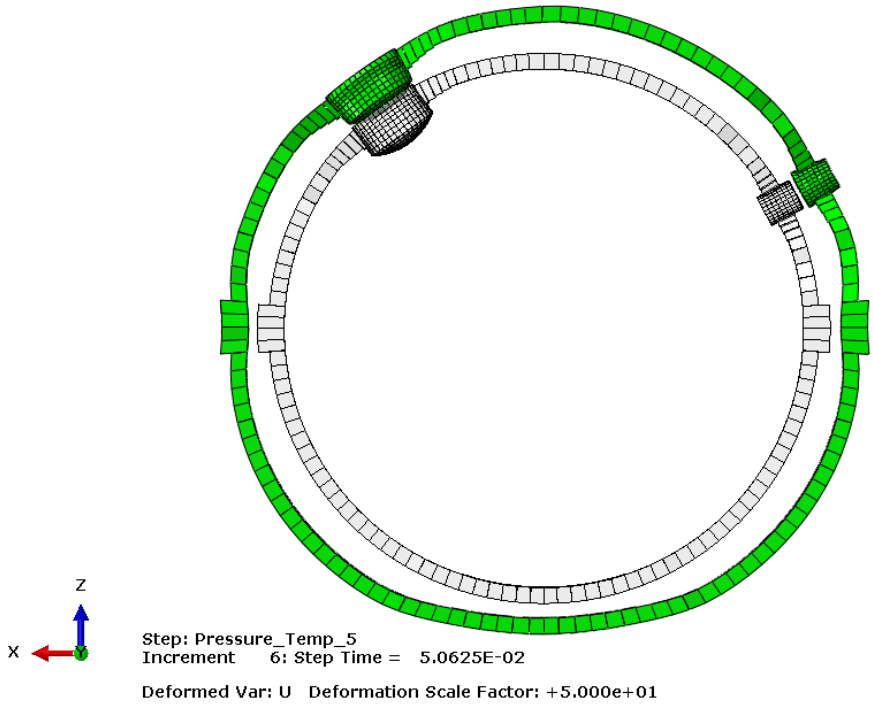

Figure D – 25e: Case 1 deformed shape at 2.5 x design pressure at elev. 4.68 m (15'-4 1/16") (x50)

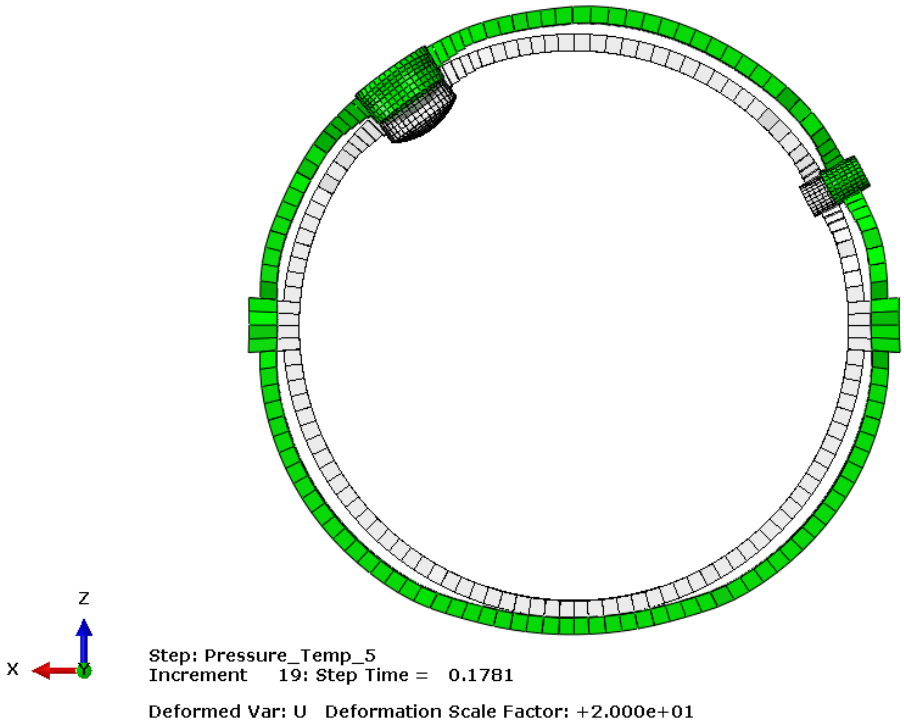

Figure D – 25f: Case 1 Deformed Shape at 3.0 x Design Pressure at Elev. 4.68 m (15'-4 1/16") (x20)

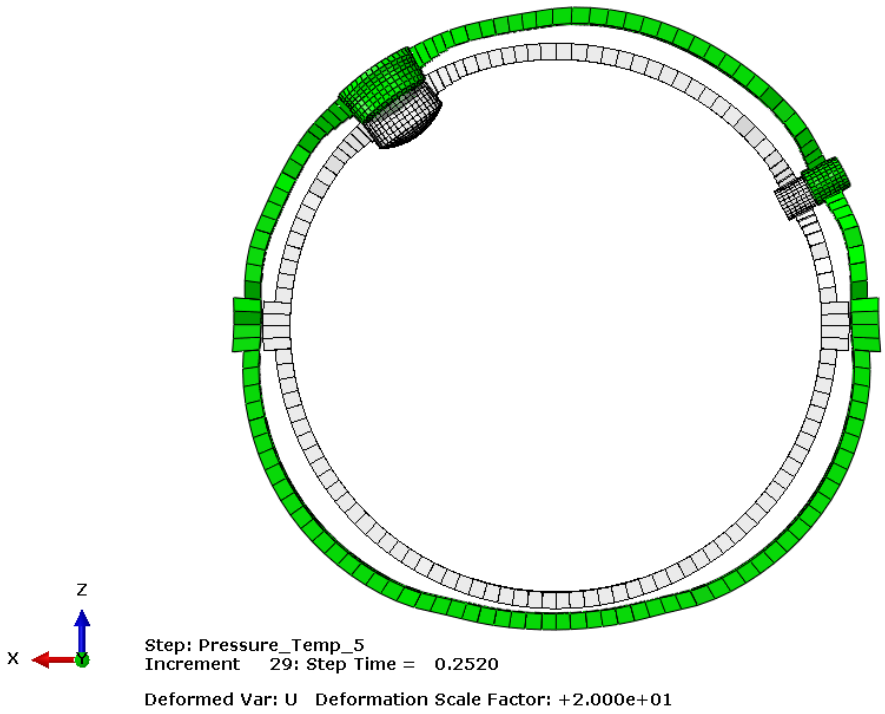

Figure D – 25g: Case 1 deformed shape at 3.3 x design pressure at elev. 4.68 m (15'-4 1/16") (x20)

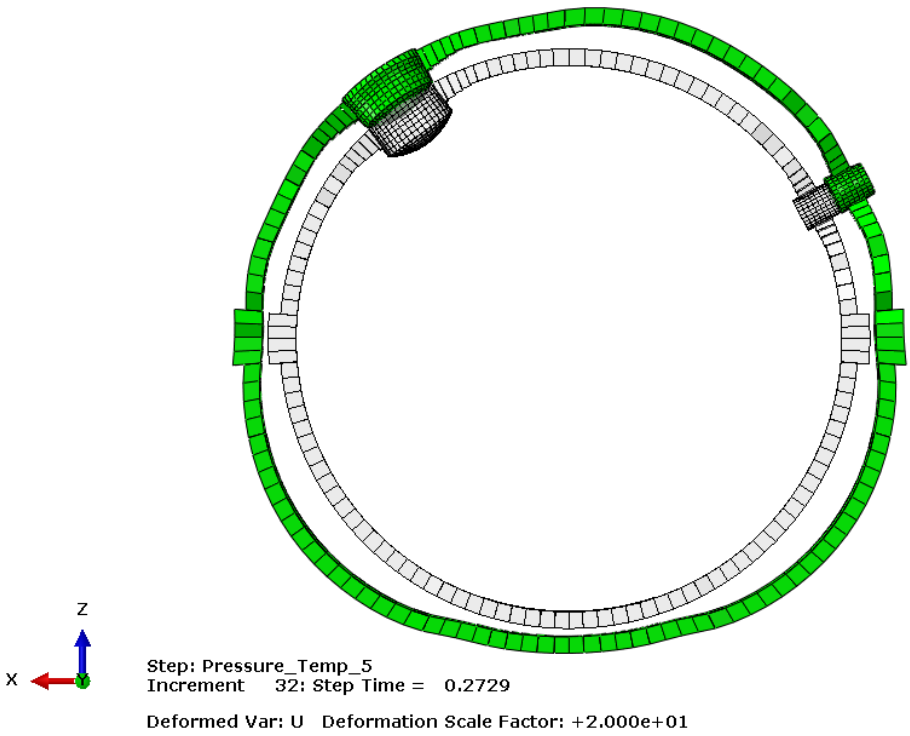

Figure D - 25h: Case 1 deformed shape at 3.4 x design pressure at elev. 4.68 m (15'-4 1/16") (x20)

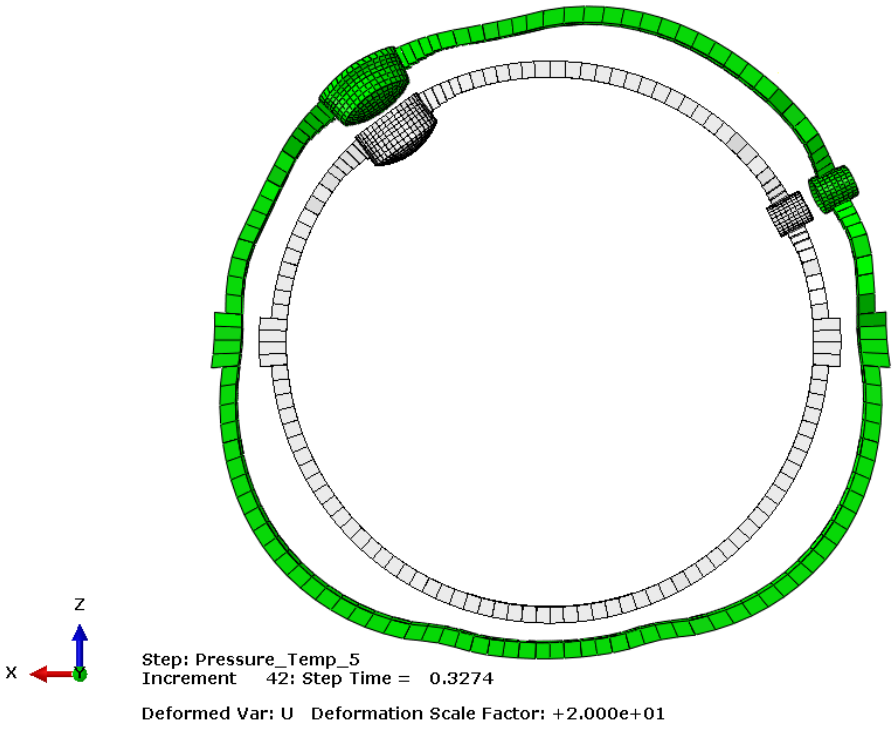

Figure D – 25i: Case 1 deformed shape at 3.6 x design pressure at elev. 4.68 m (15'-4 1/16") (x20)

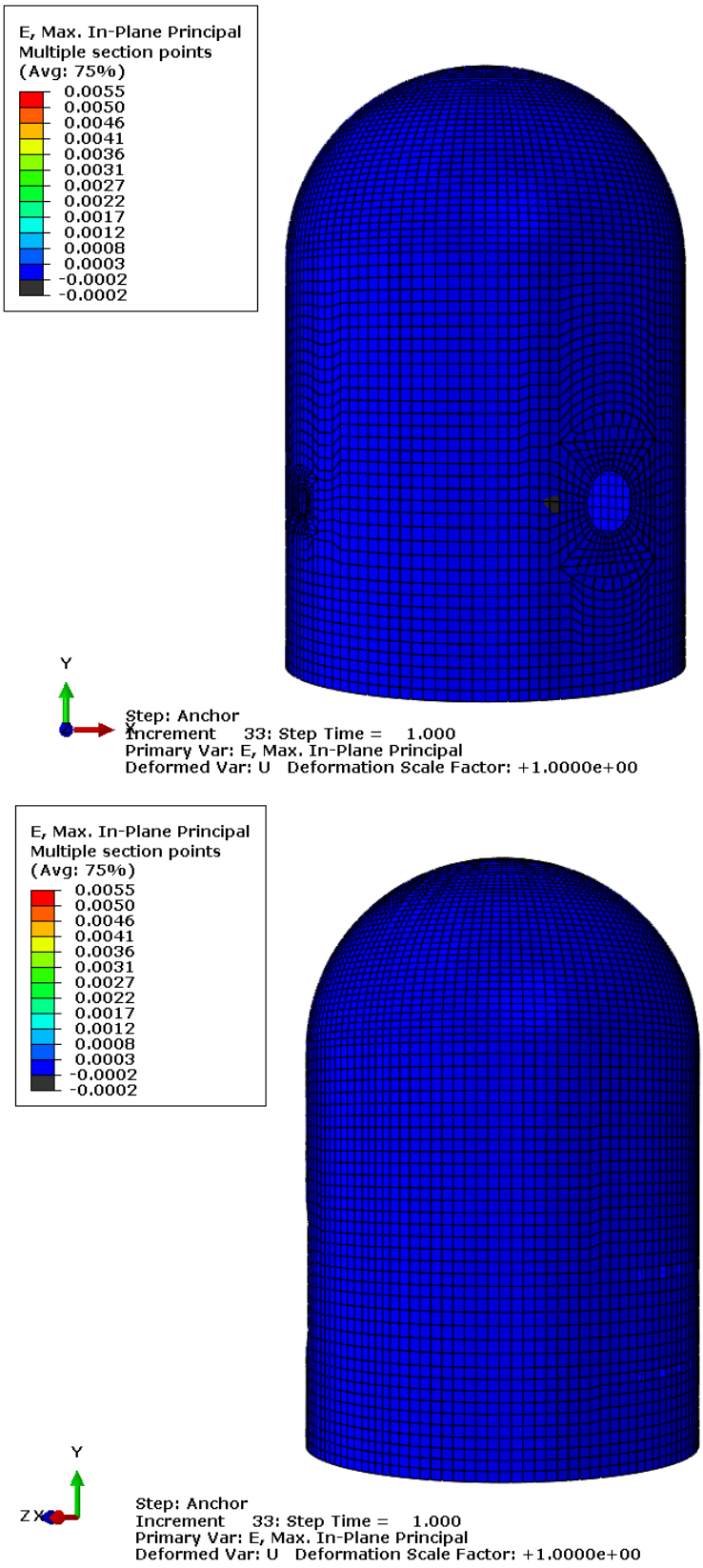

Figure D - 26a: Case 1 max principal strain in liner after tendon anchorage

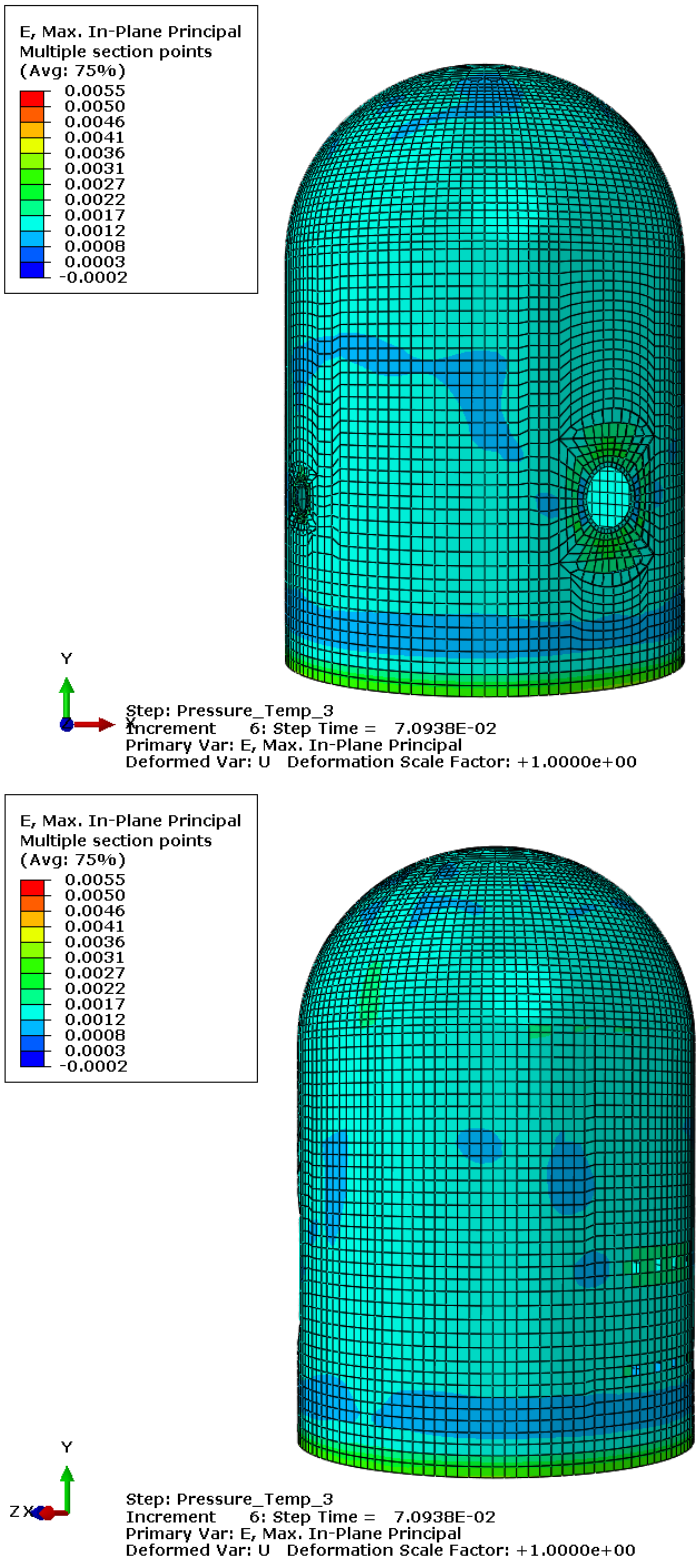

Figure D – 26b: Case 1 max principal strain in liner at 1.0xPd

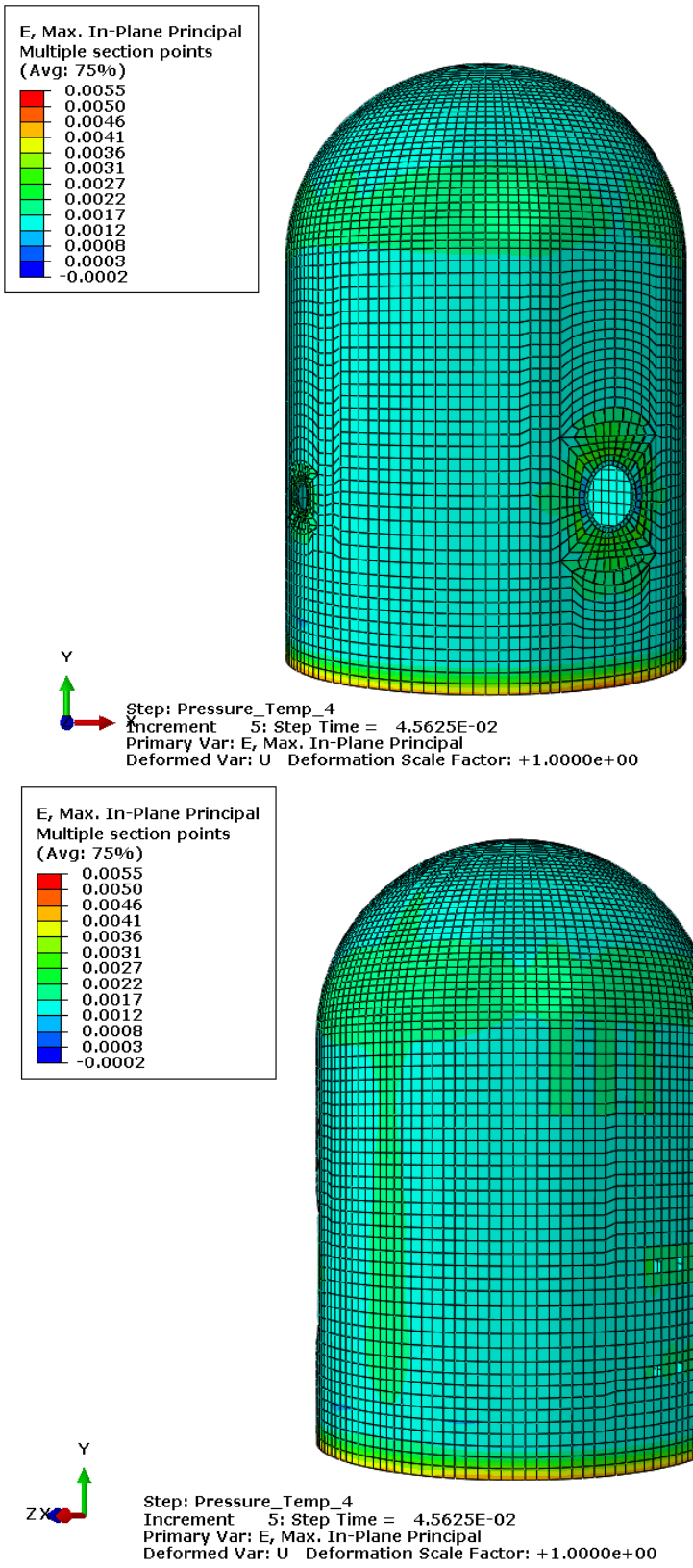

Figure D – 26c: Case 1 max principal strain in liner at 1.5xPd

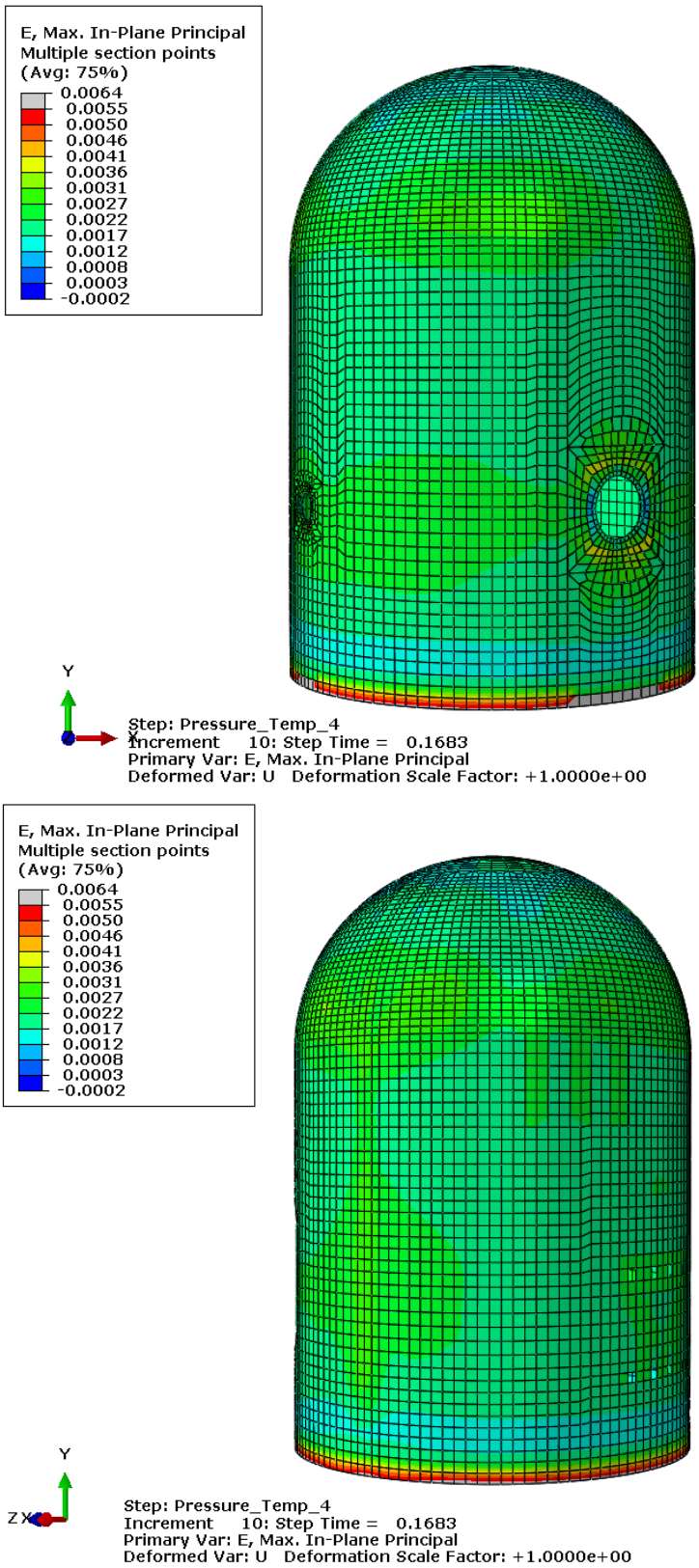

Figure D – 26d: Case 1 max principal strain in liner at 2.0xPd

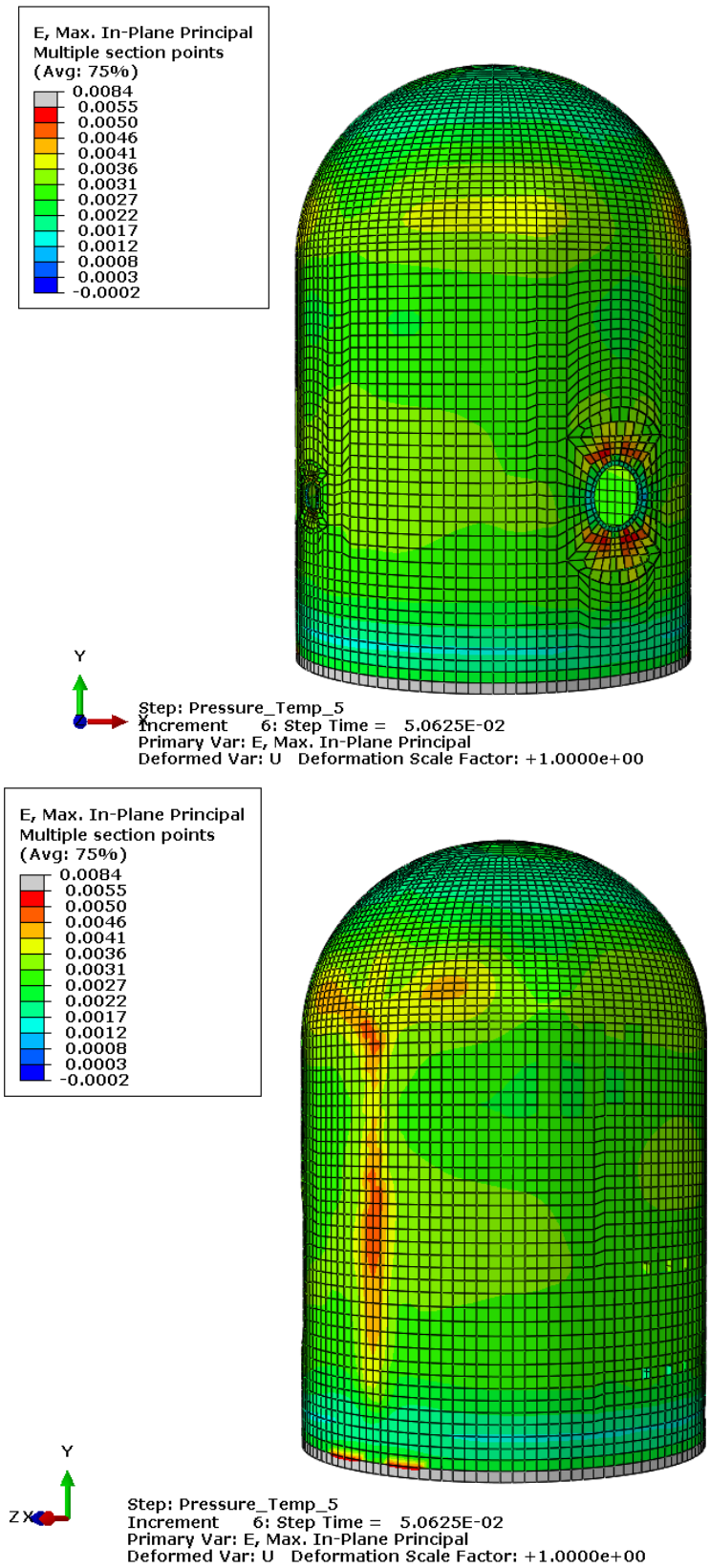

Figure D – 26e: Case 1 max principal strain in liner at 2.5xPd

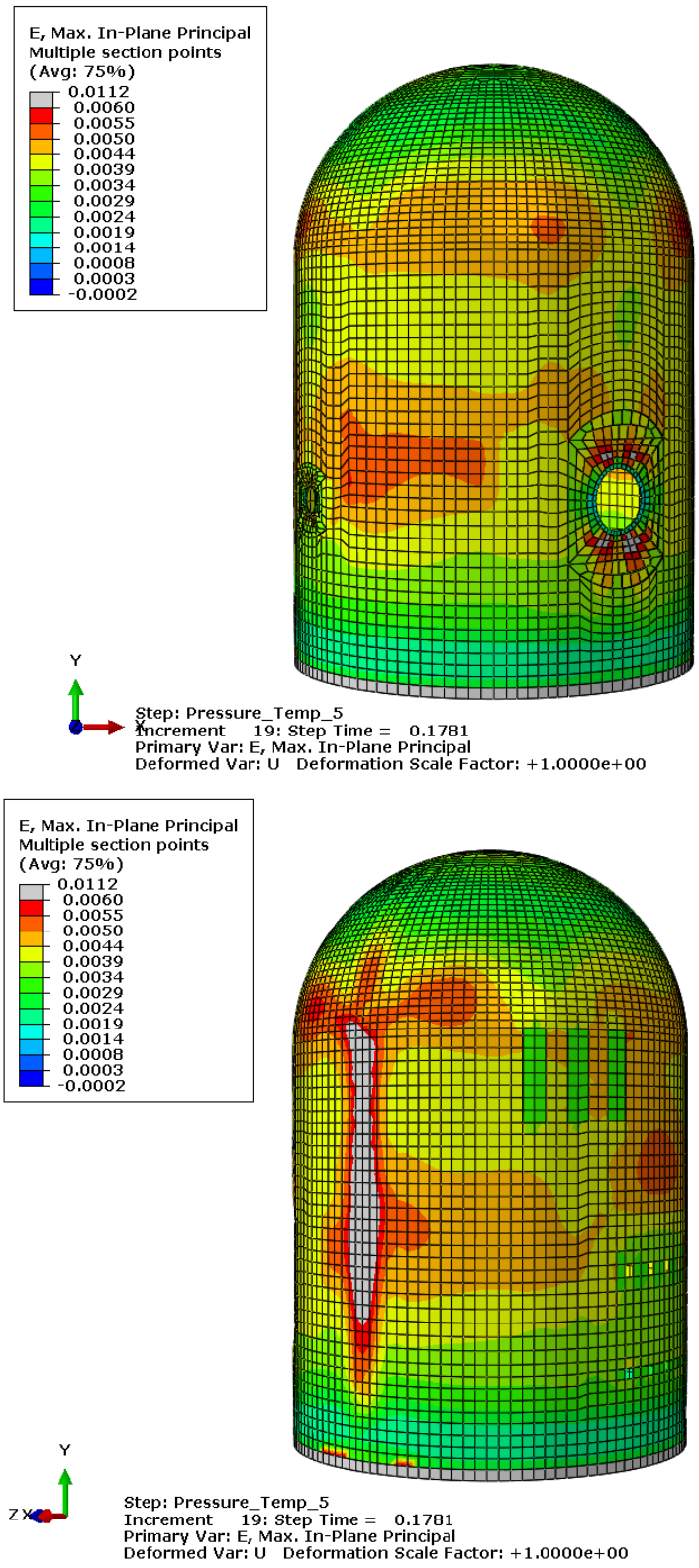

Figure D – 26f: Case 1 max principal strain in liner at 3.0xPd

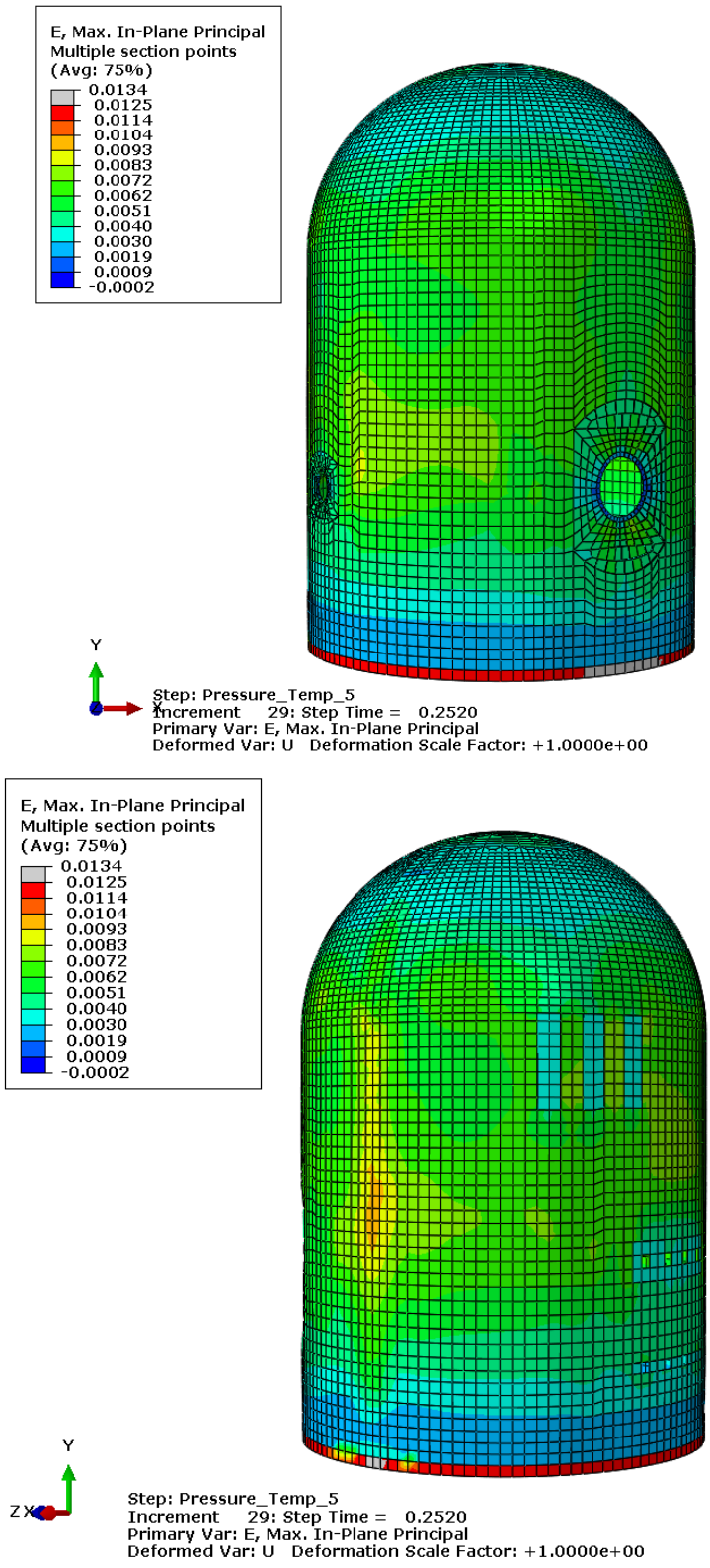

Figure D – 26g: Case 1 max principal strain in liner at 3.3xPd (high contour color limits)

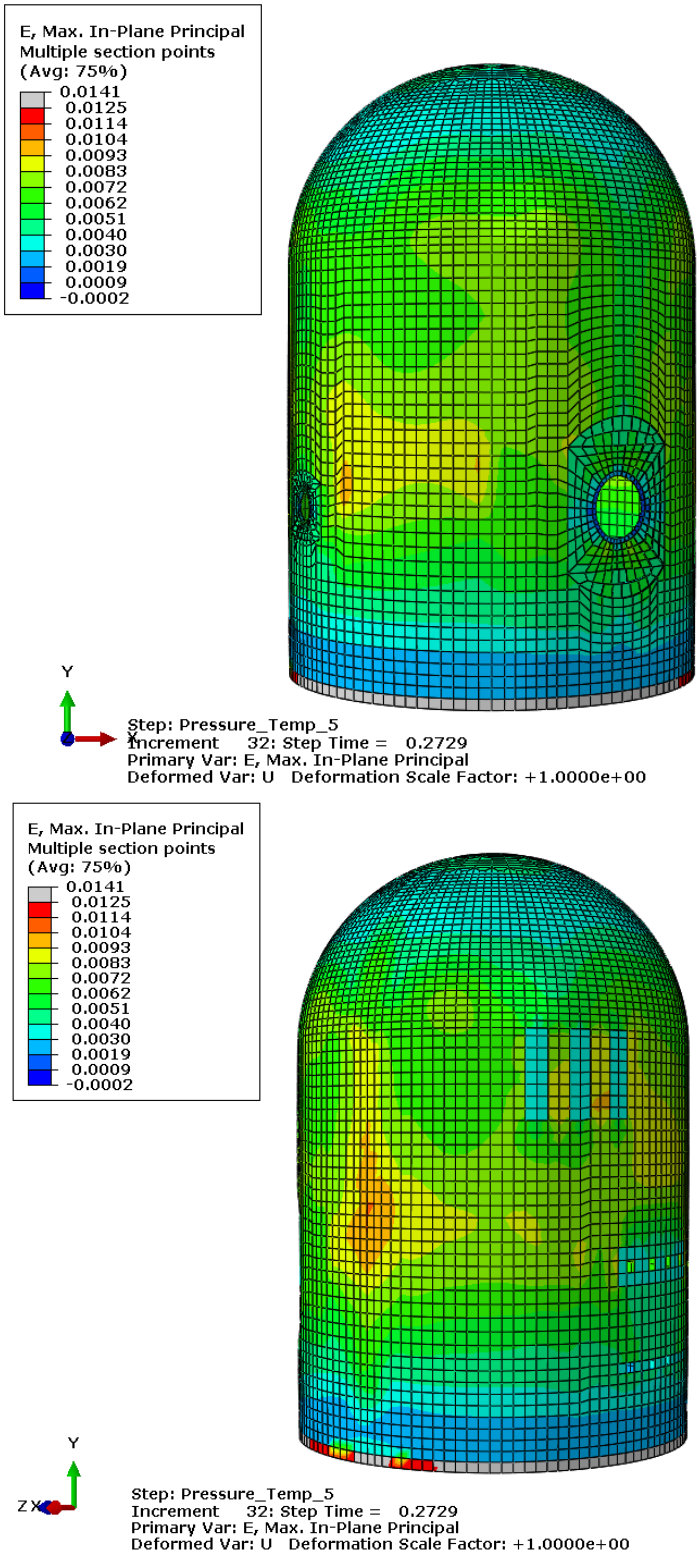

Figure D – 26h: Case 1 Max principal strain in liner at 3.4xPd (high contour color limits)

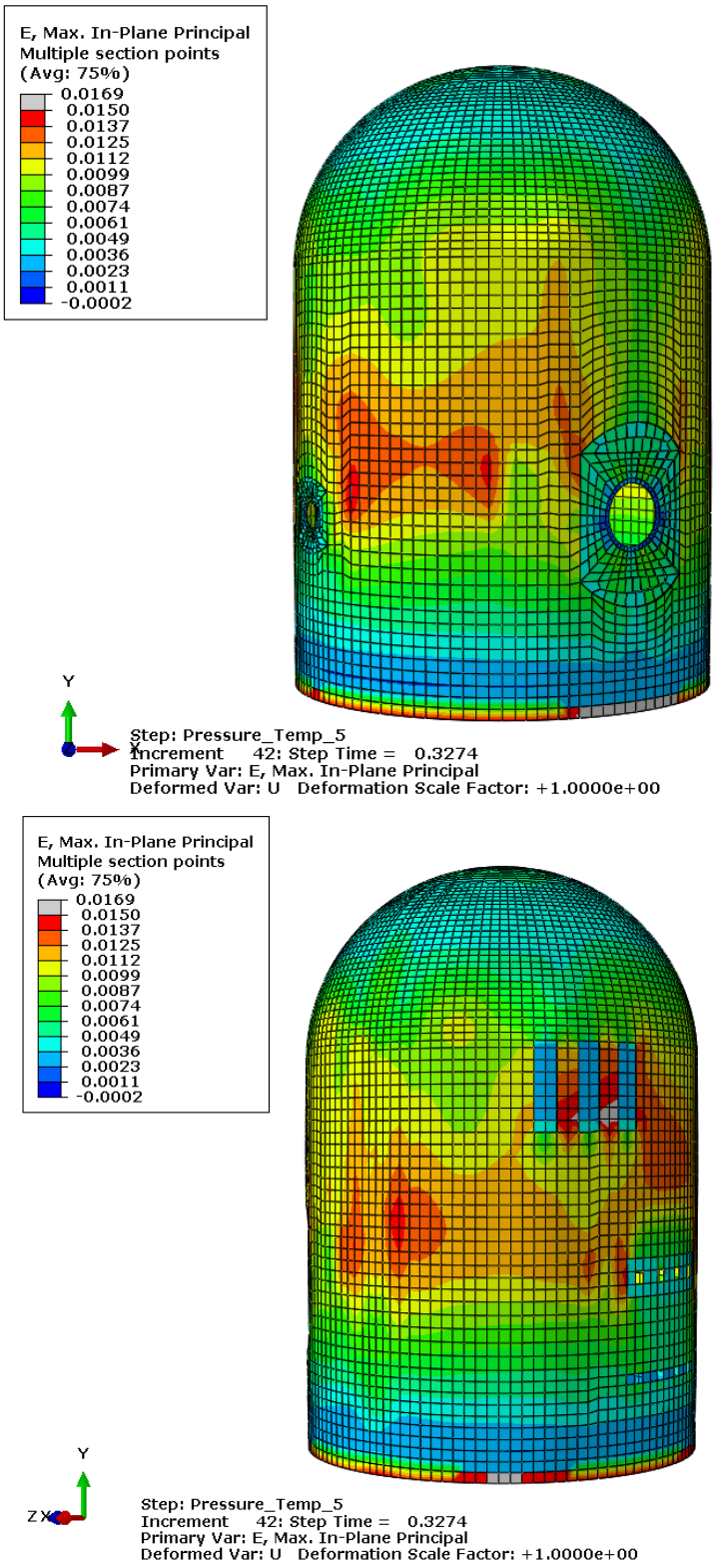

Figure D – 26i: Case 1 max principal strain in liner at 3.6xPd (high contour color limits)

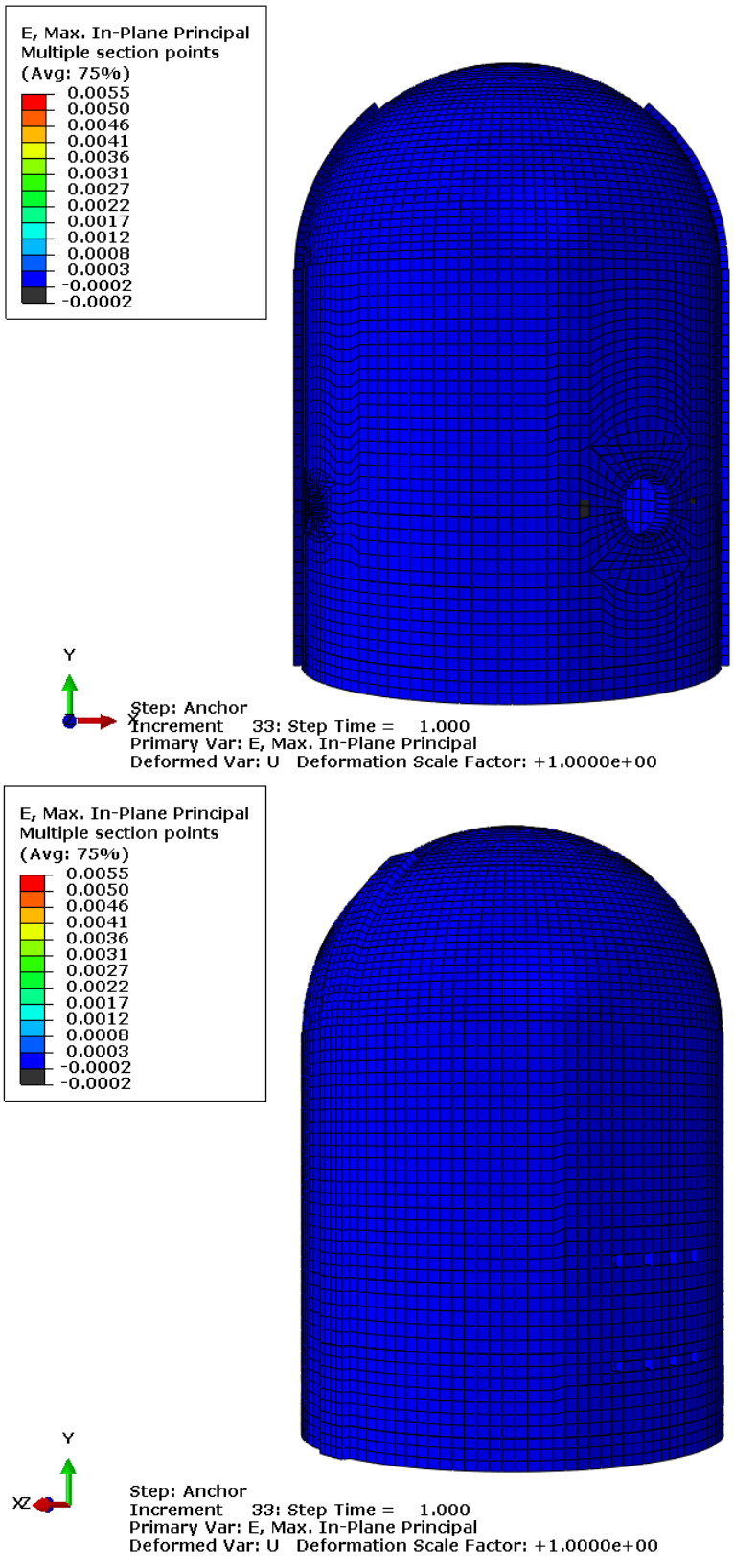

Figure D - 27a: Case 1 max principal membrane strain in concrete after tendon anchorage

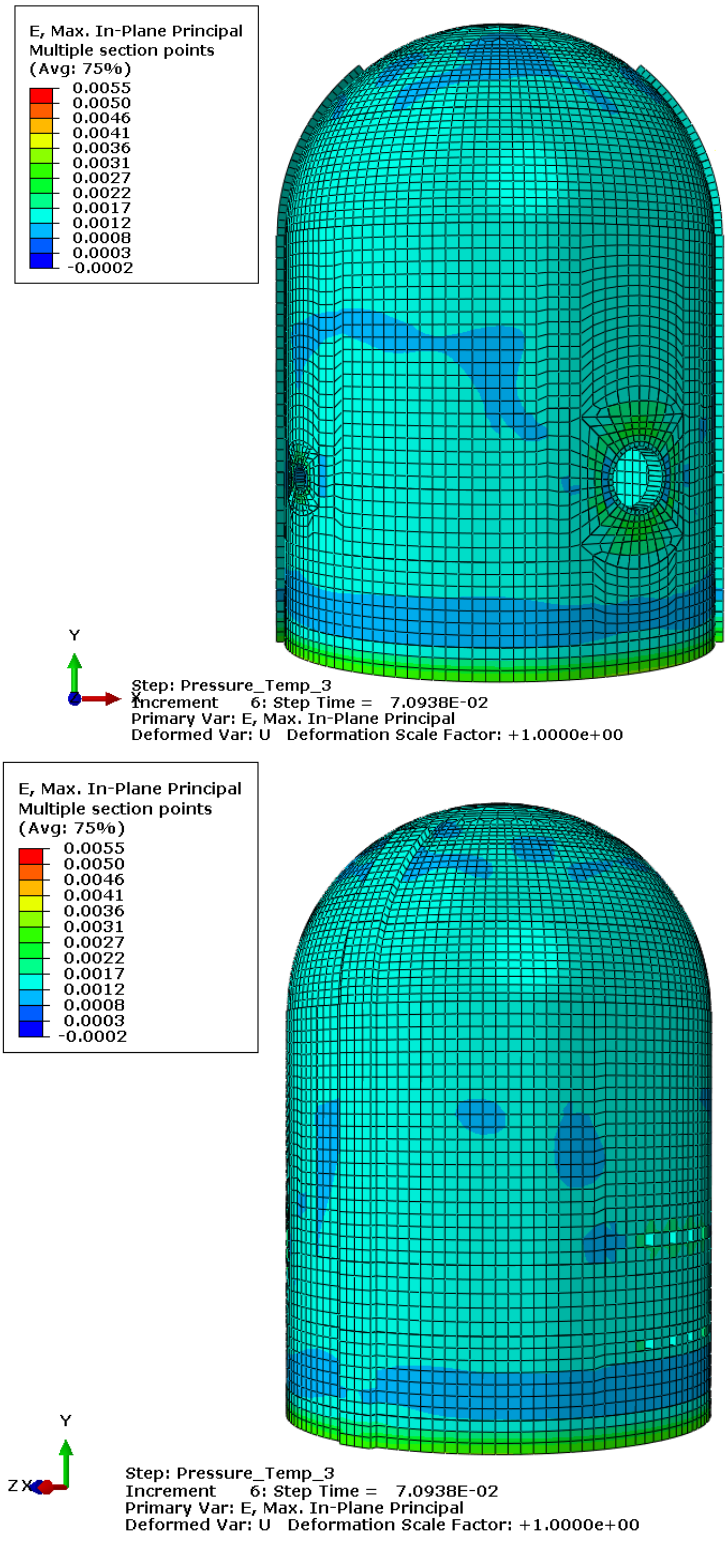

Figure D – 27b: Case 1 max principal membrane strain in concrete at 1.0xPd

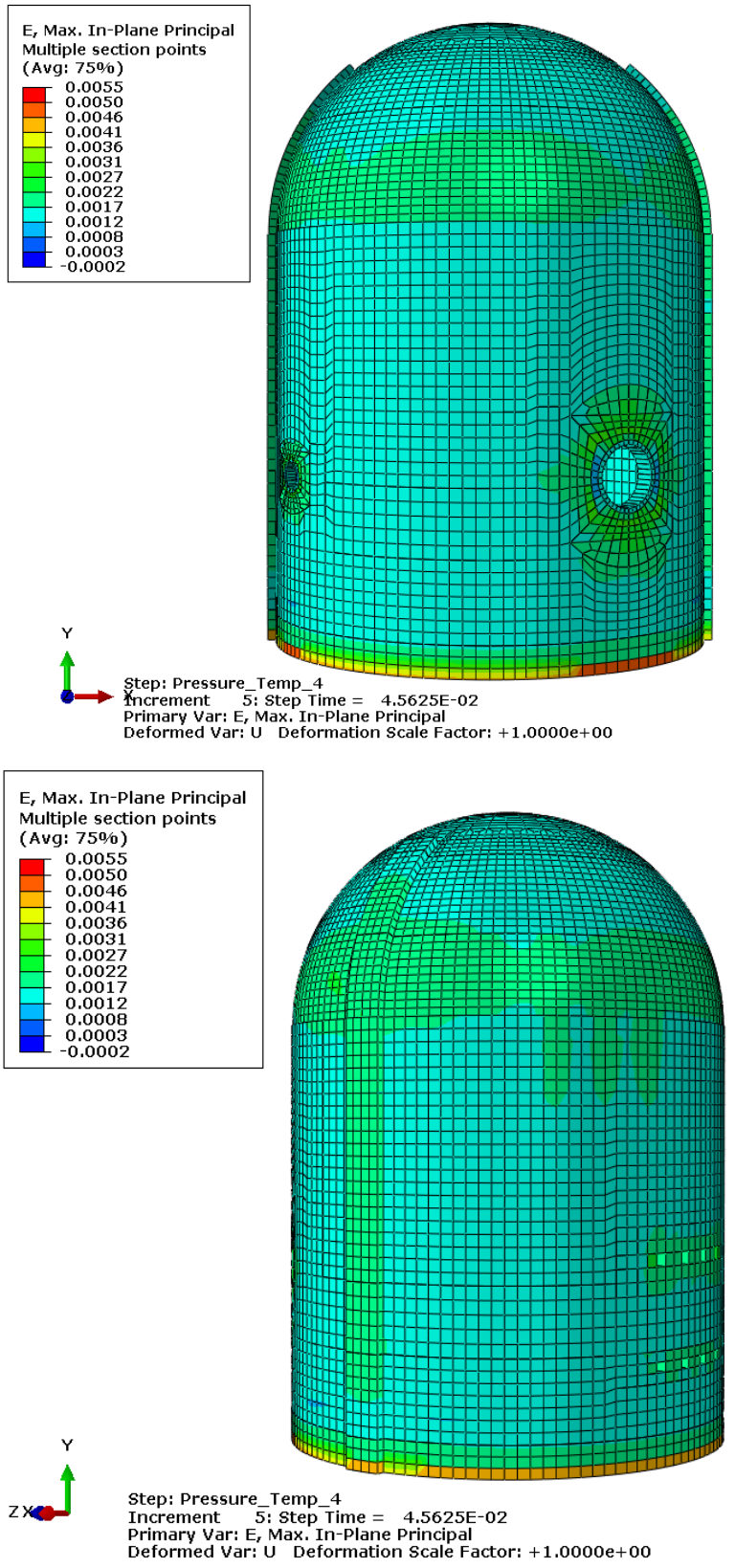

Figure D – 27c: Case 1 max principal membrane strain in concrete at 1.5xPd

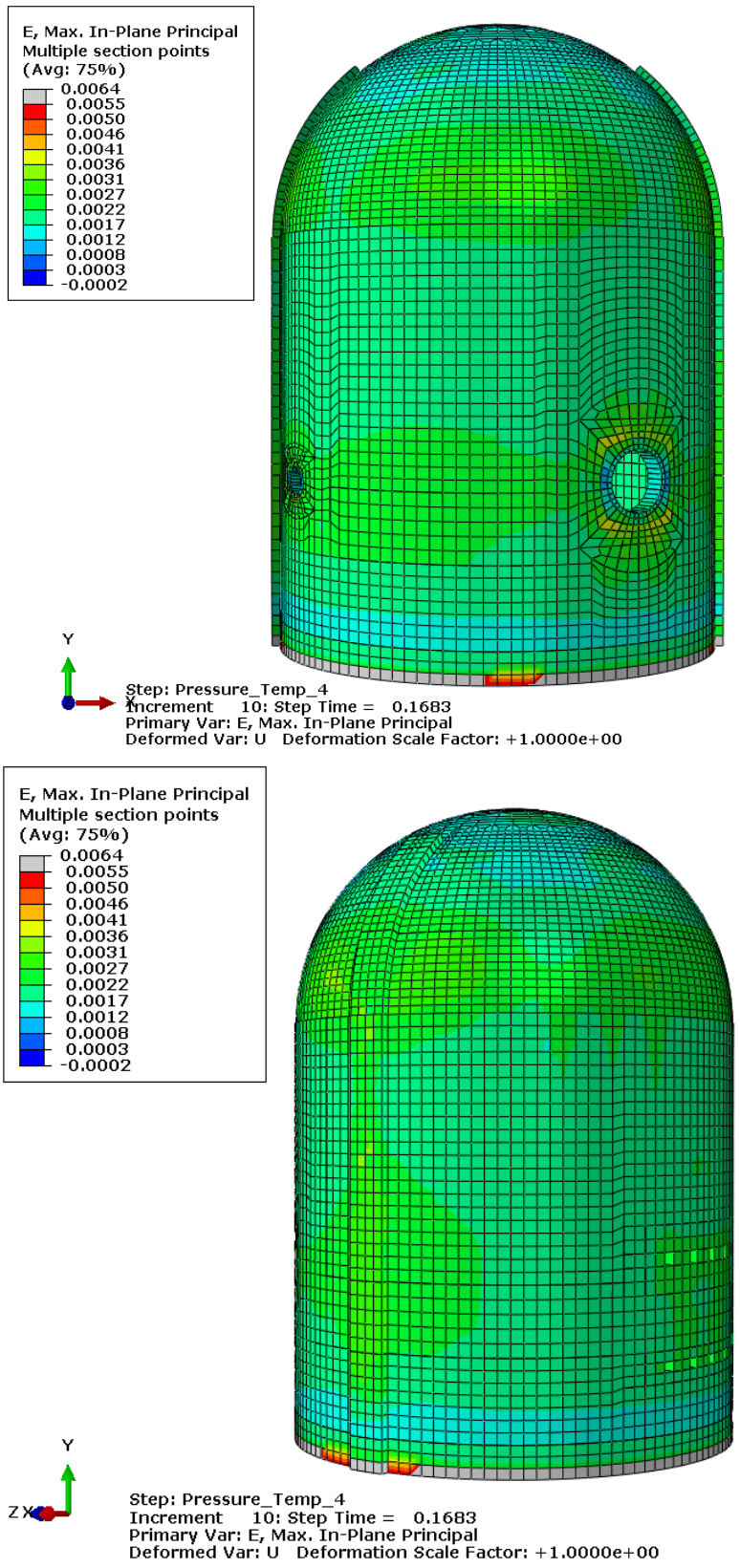

Figure D – 27d: Case 1 max principal membrane strain in concrete at 2.0xPd

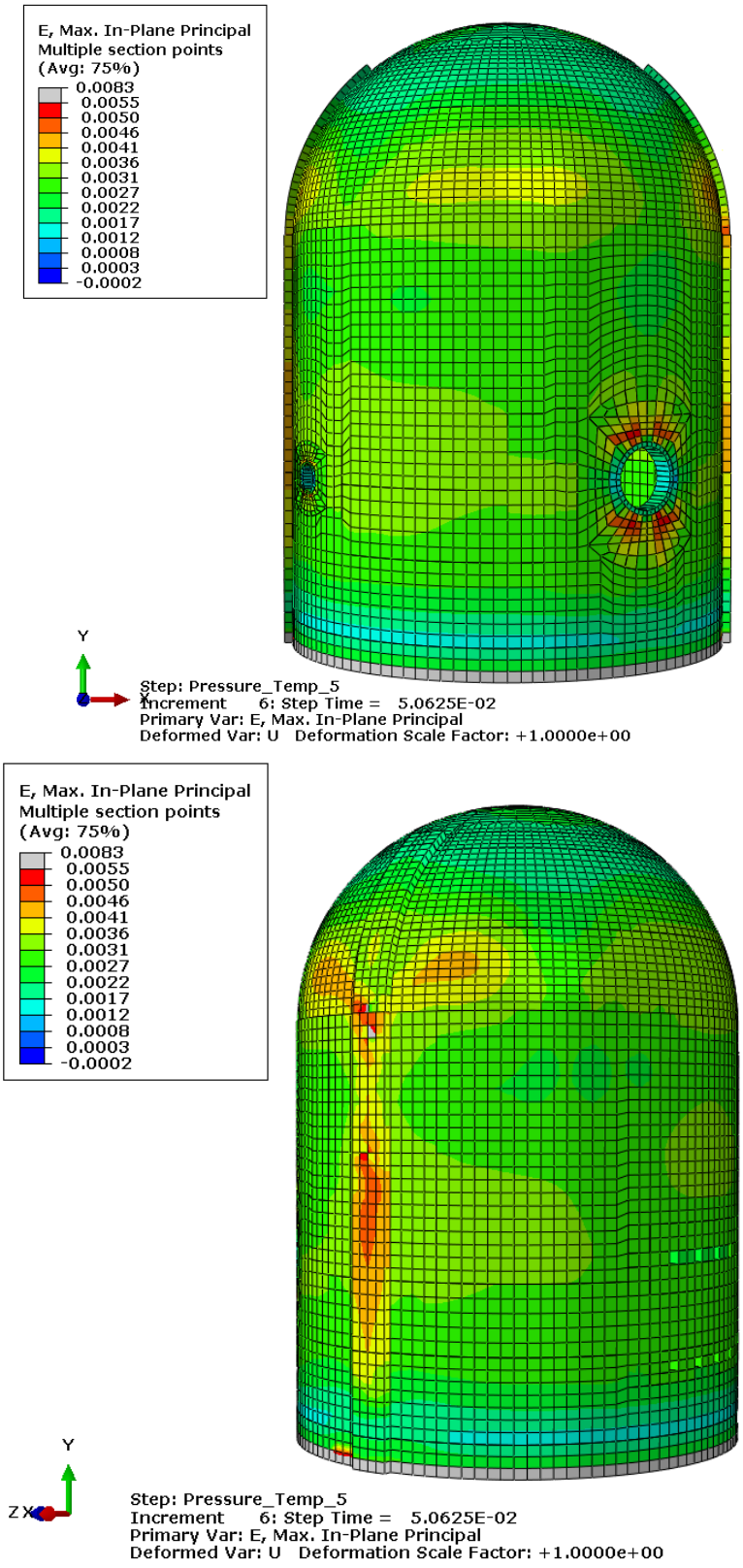

Figure D – 27e: Case 1 max principal membrane strain in concrete at 2.5xPd

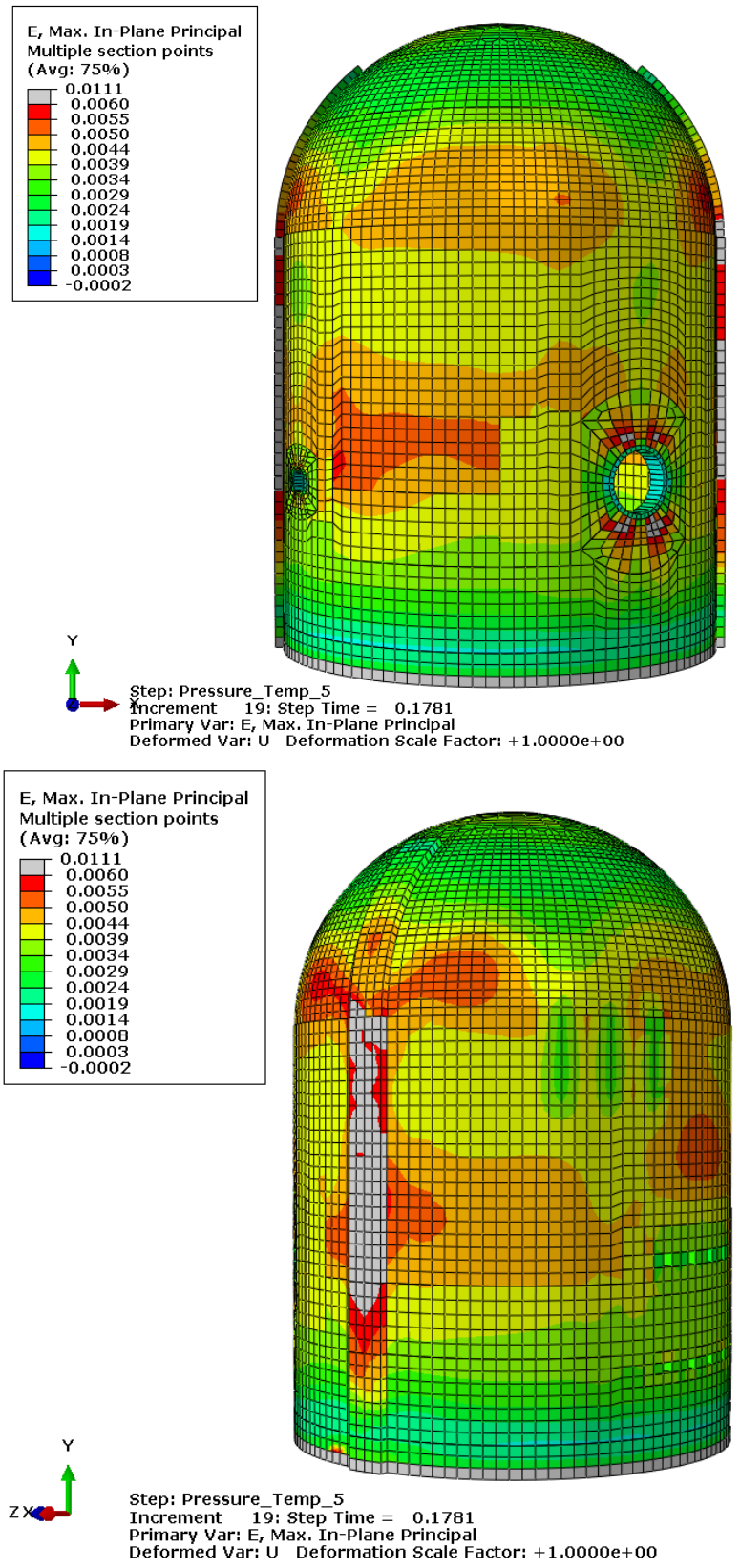

Figure D – 27f: Case 1 max principal membrane strain in concrete at 3.0xPd

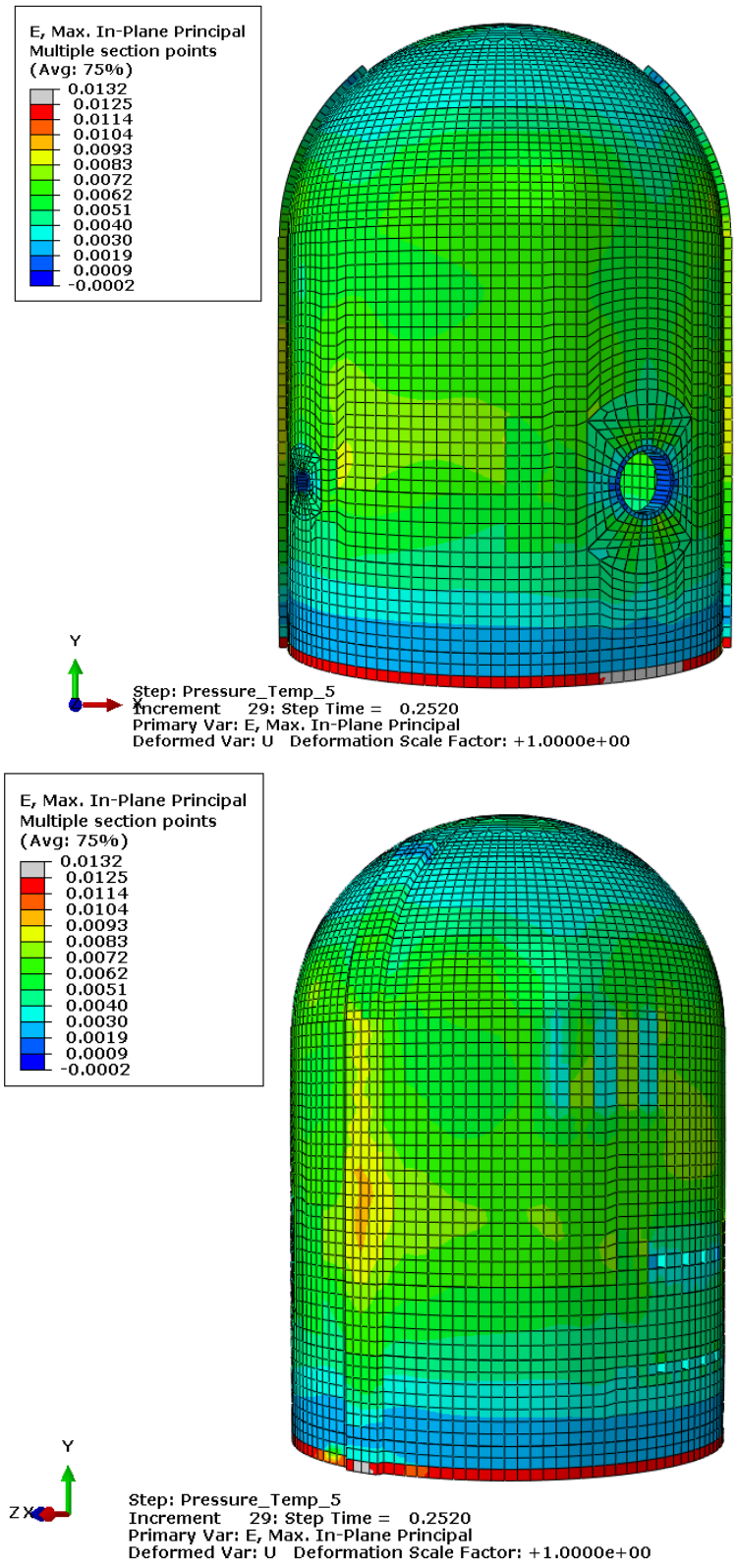

Figure D – 27g: Case 1 max principal membrane strain in concrete at 3.3xPd (high contour color limits)

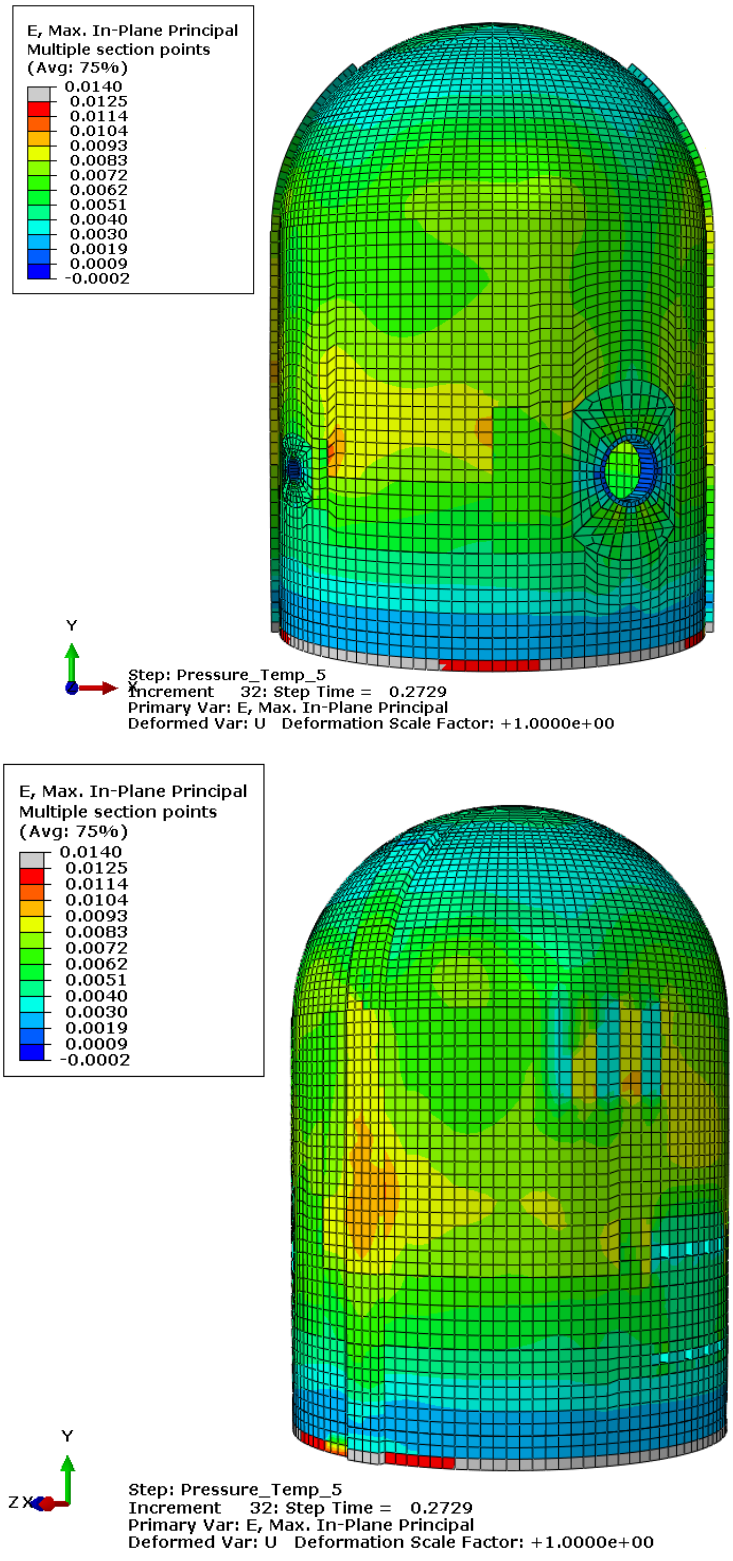

Figure D – 27h: Case 1 max principal membrane strain in concrete at 3.4xPd (high contour color limits)

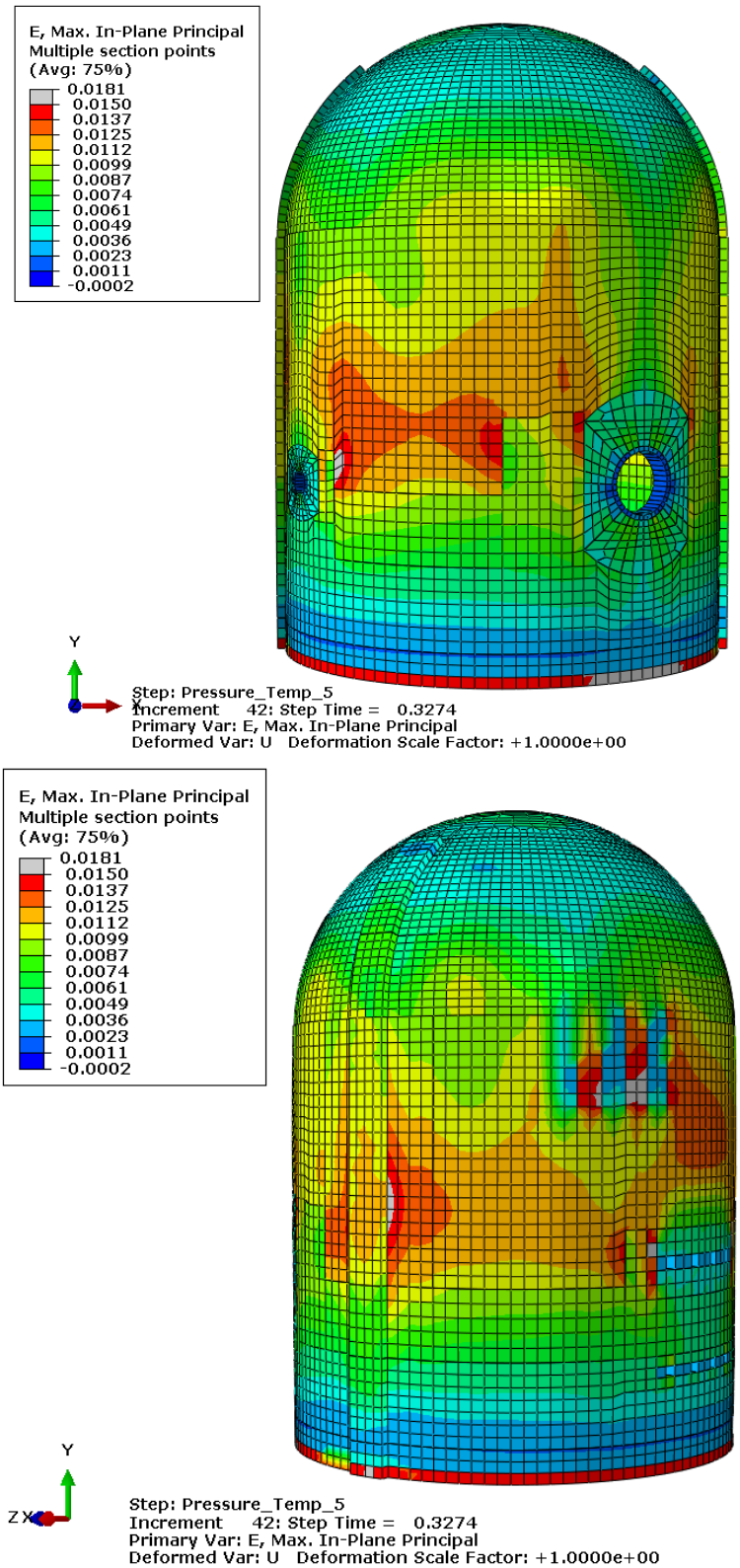

Figure D – 27i: Case 1 max principal membrane strain in concrete at 3.6xPd (high contour color limits)

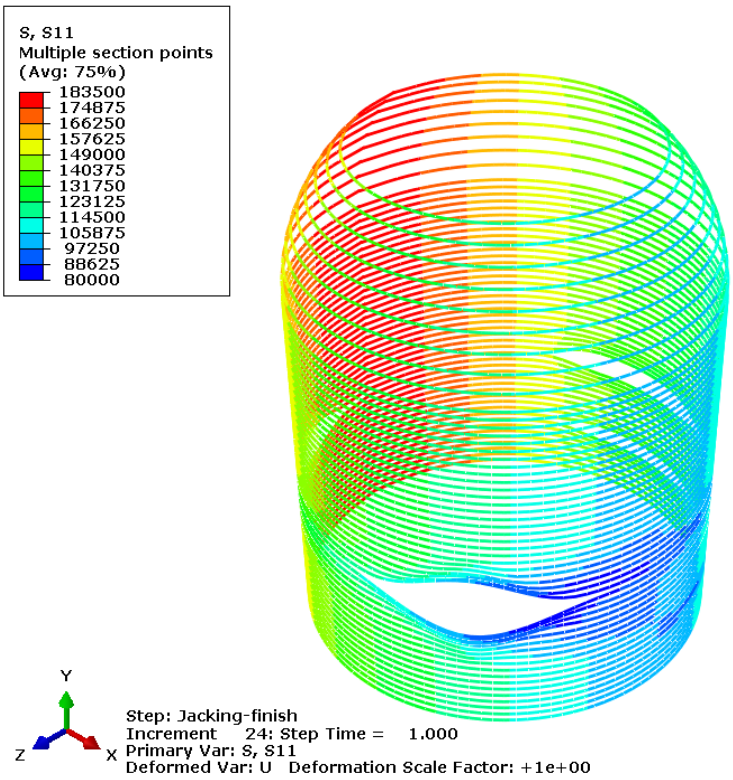

Figure D - 28a: Stress in hoop tendons anchored at 90° after jacking before anchorage

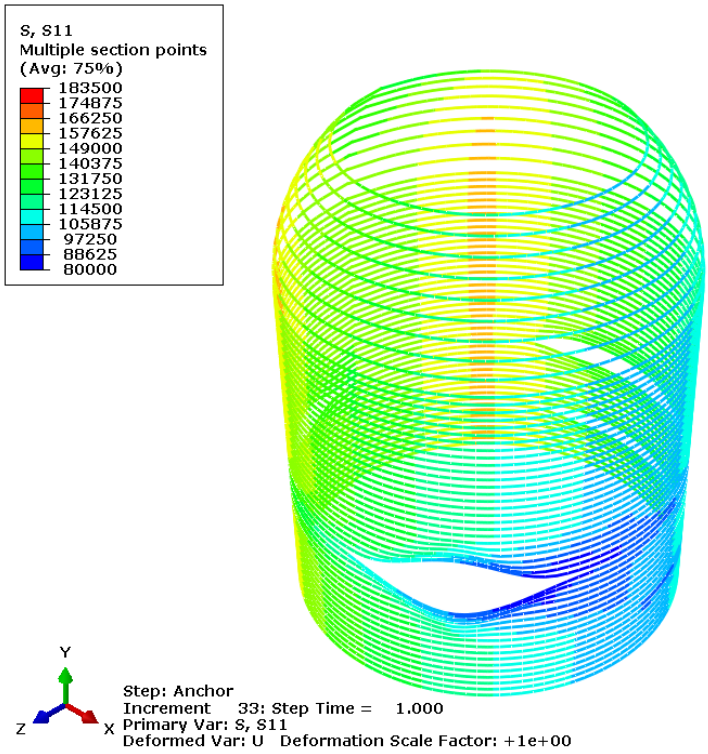

Figure D – 28b: Stress in hoop tendons anchored at 90° after anchorage

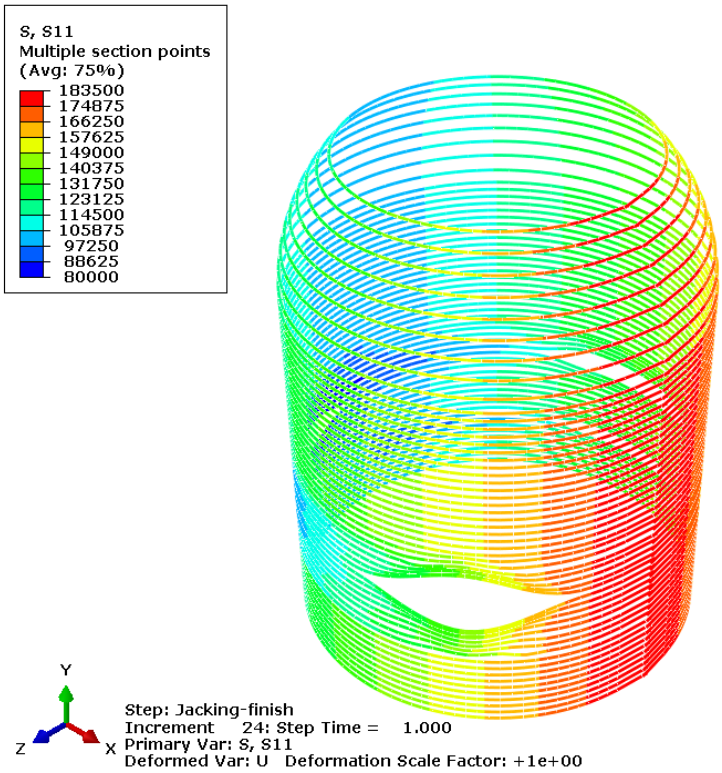

Figure D – 28c: Stress in hoop tendons anchored at 270° after jacking before anchorage

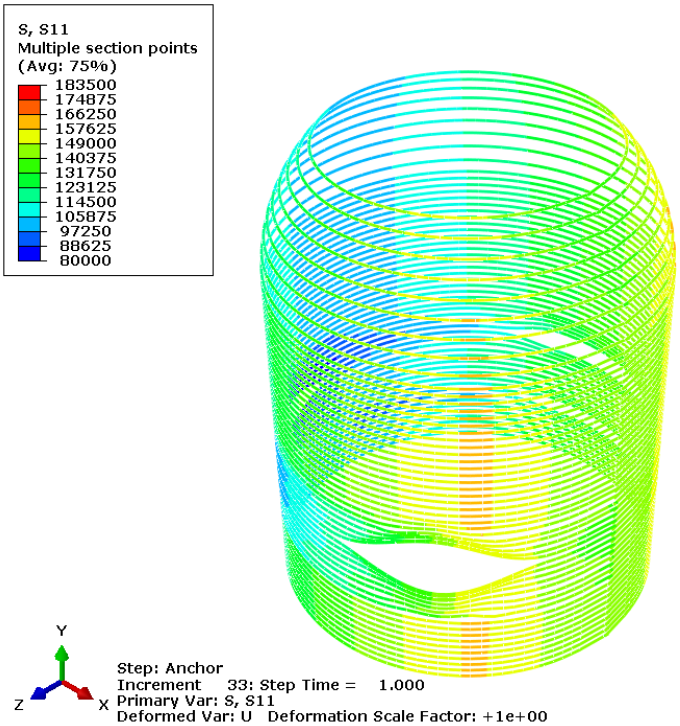

Figure D – 28d: Stress in hoop tendons anchored at 270° after anchorage

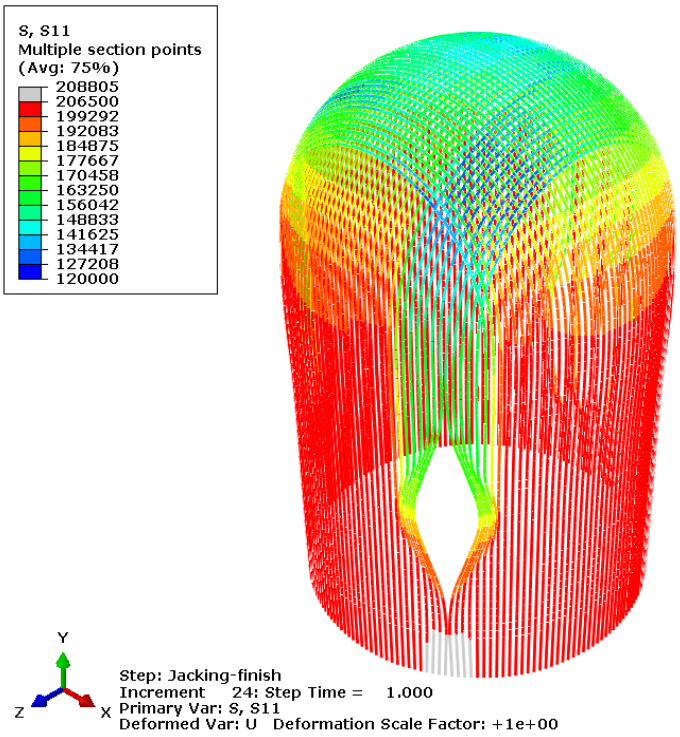

Figure D - 29a: Stress in vertical tendons after jacking before anchorage

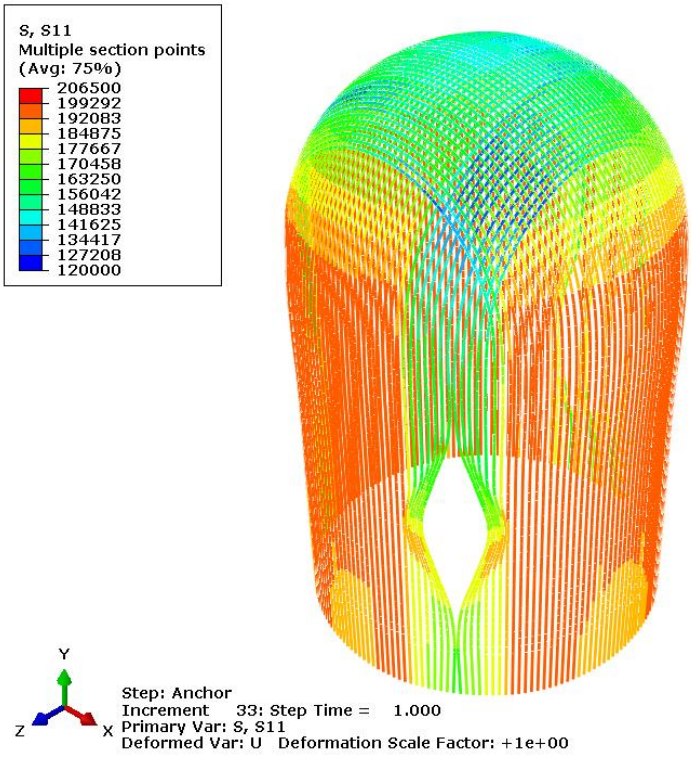

Figure D – 29b: Stress in vertical tendons after anchorage

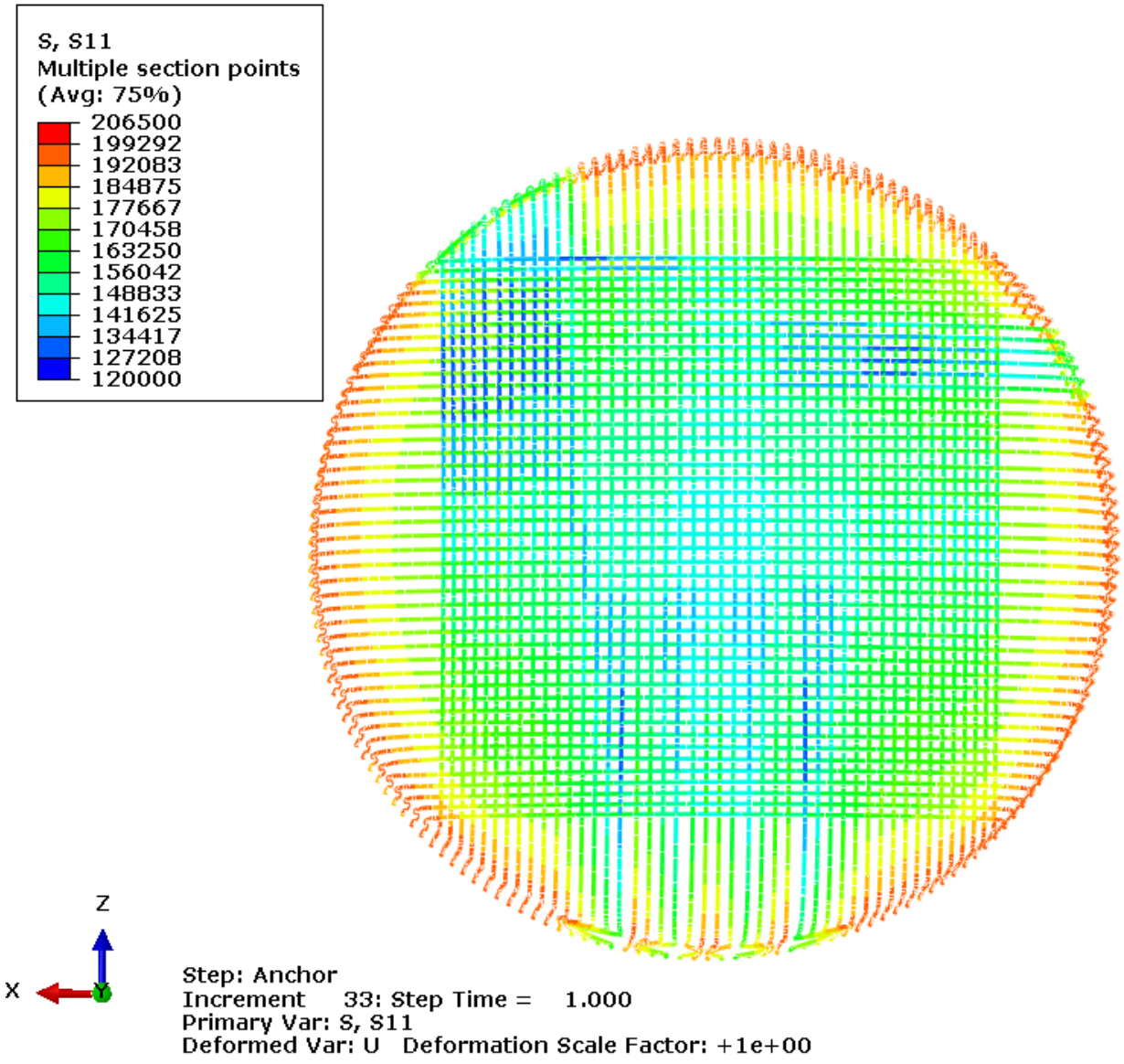

Figure D - 30: Stress in vertical tendons in dome after anchorage

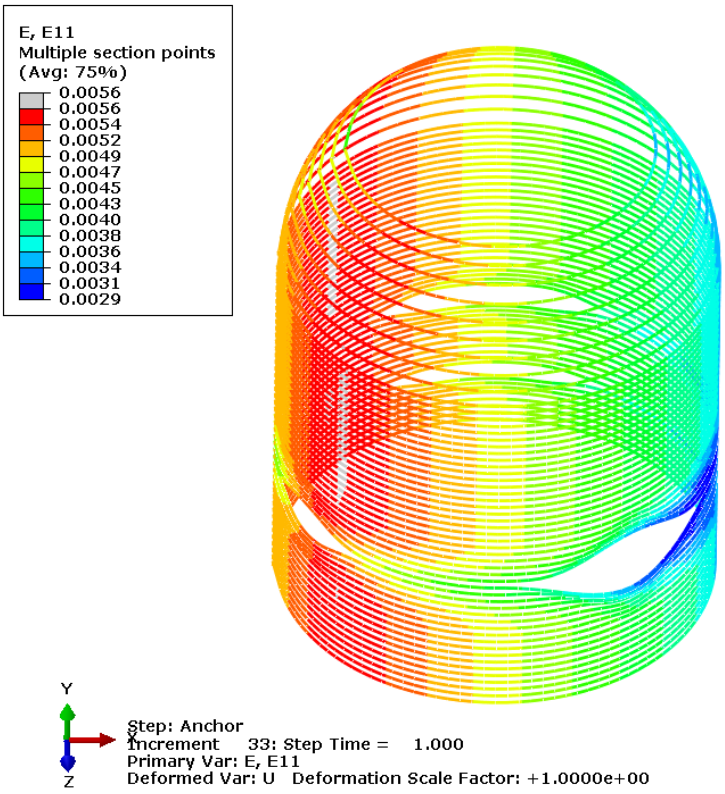

Figure D - 31a: Case 1 strain in hoop tendons anchored at 90° after anchorage

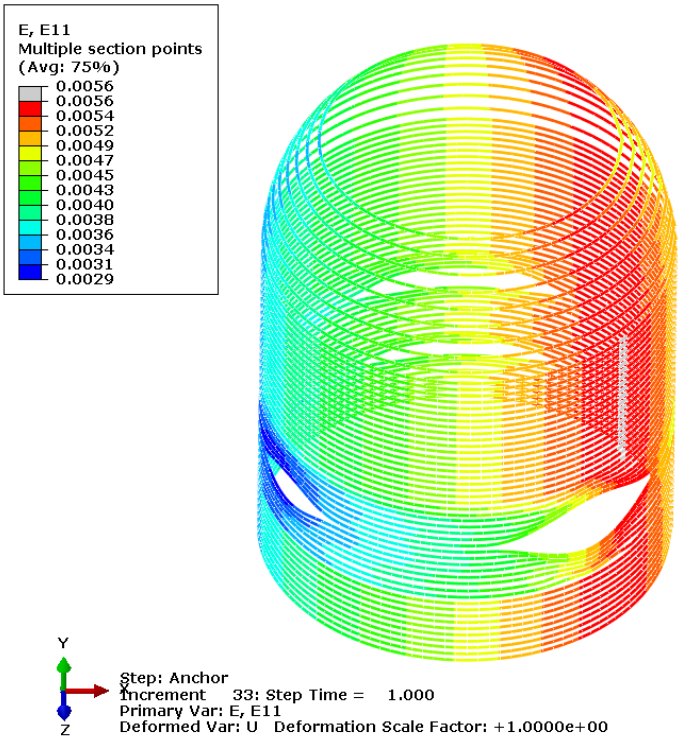

Figure D – 31b: Case 1 strain in hoop tendons anchored at 270° after anchorage

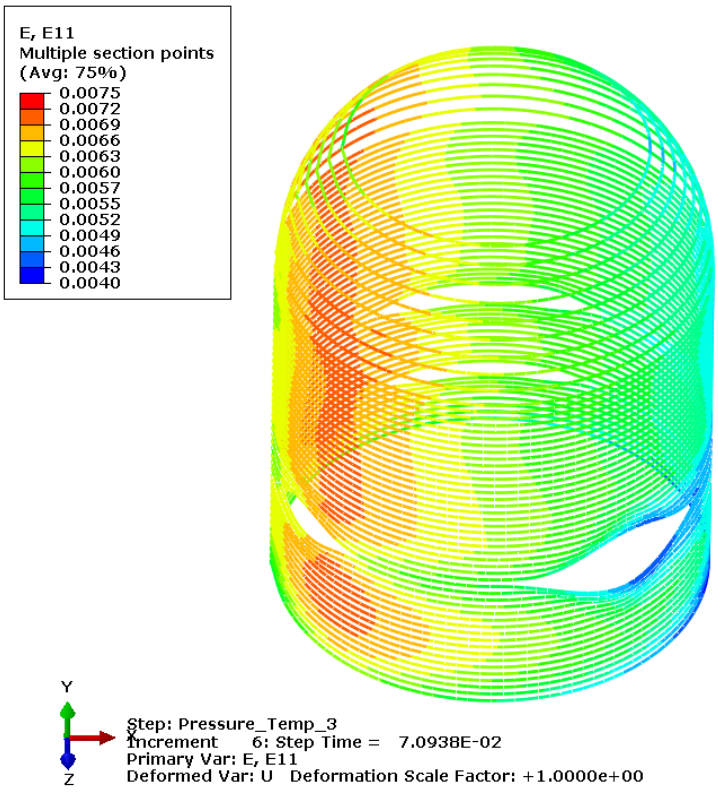

Figure D – 31c: Case 1 strain in hoop tendons anchored at 90° at 1.0 x Pd.

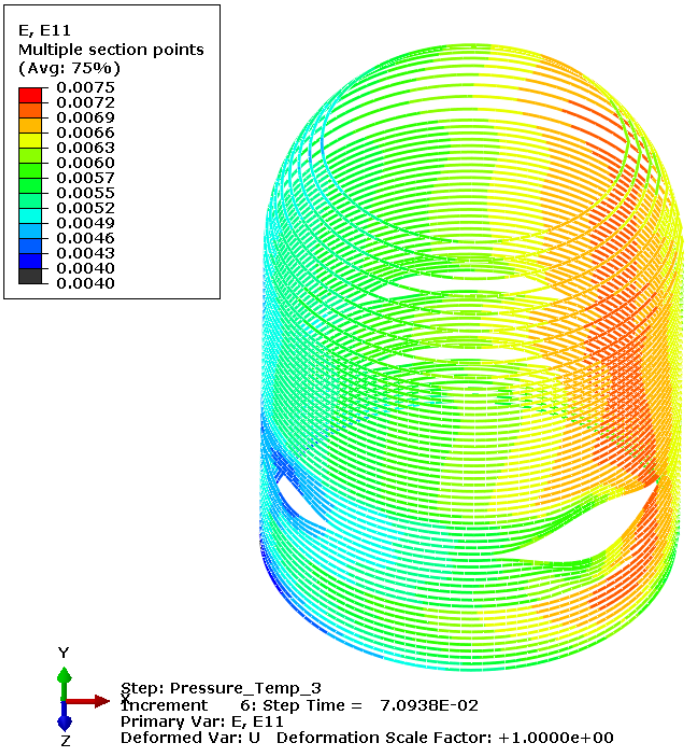

Figure D – 31d: Case 1 strain in hoop tendons anchored at 270° at 1.0 x Pd.

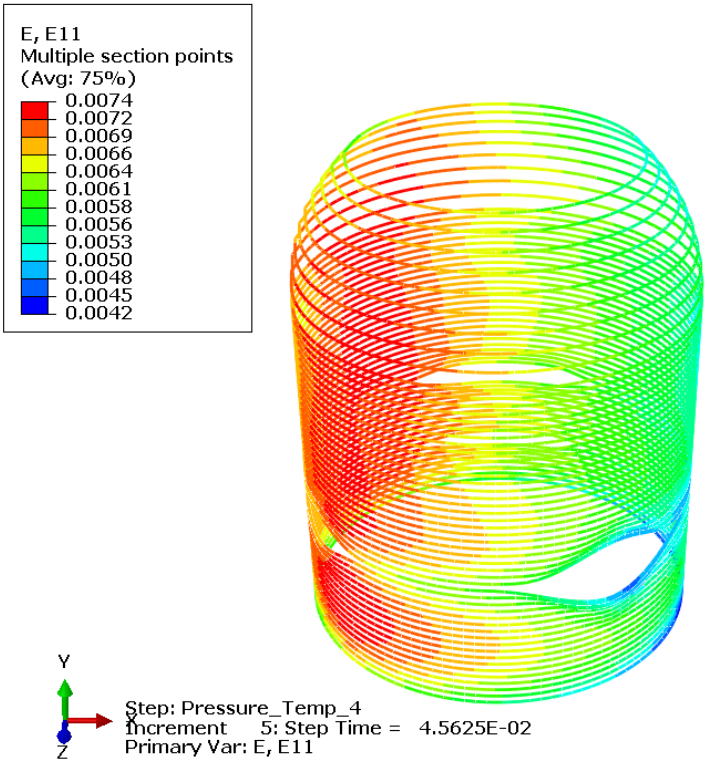

Figure D – 31e: Case 1 strain in hoop tendons anchored at 90° at 1.5 x Pd.

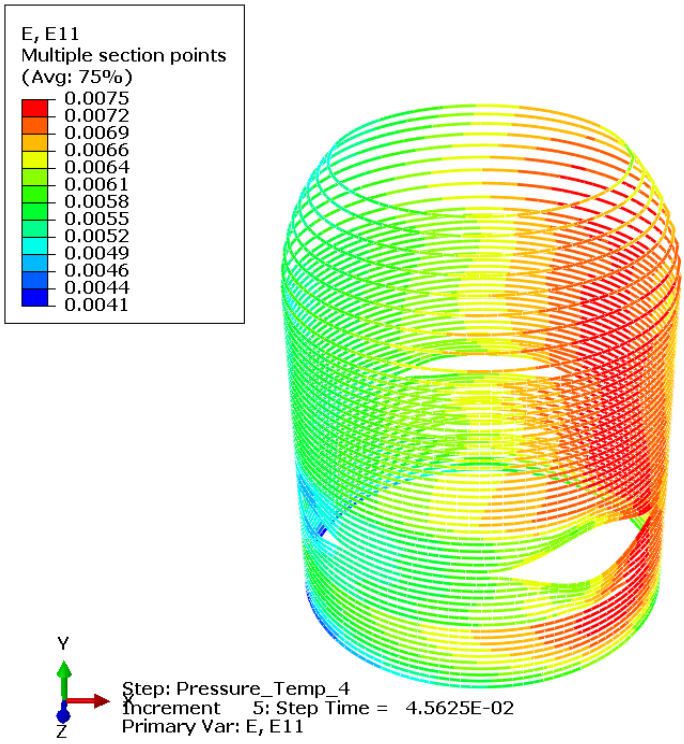

Figure D – 31f: Case 1 strain in hoop tendons anchored at 270° at 1.5 x Pd.

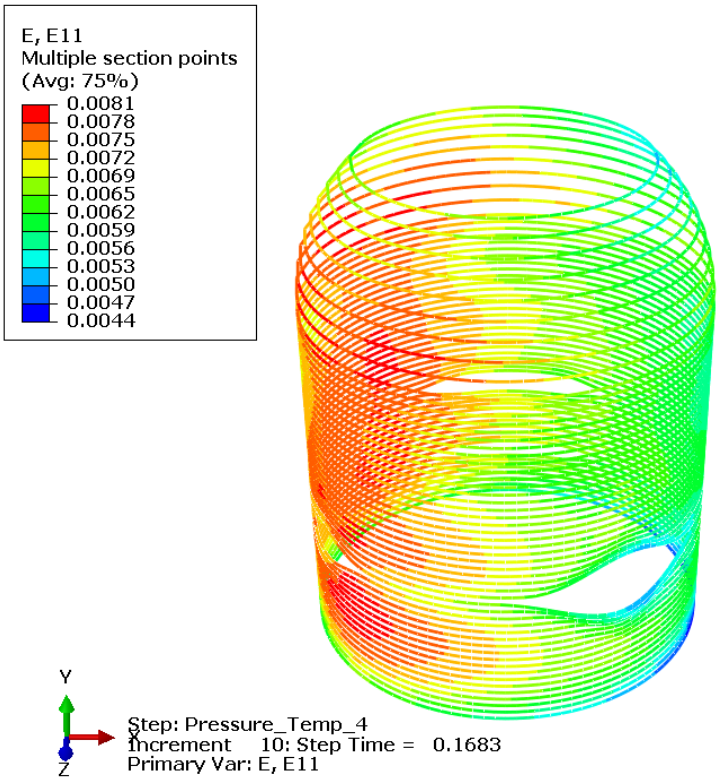

Figure D – 31g: Case 1 strain in hoop tendons anchored at 90° at 2.0 x Pd.

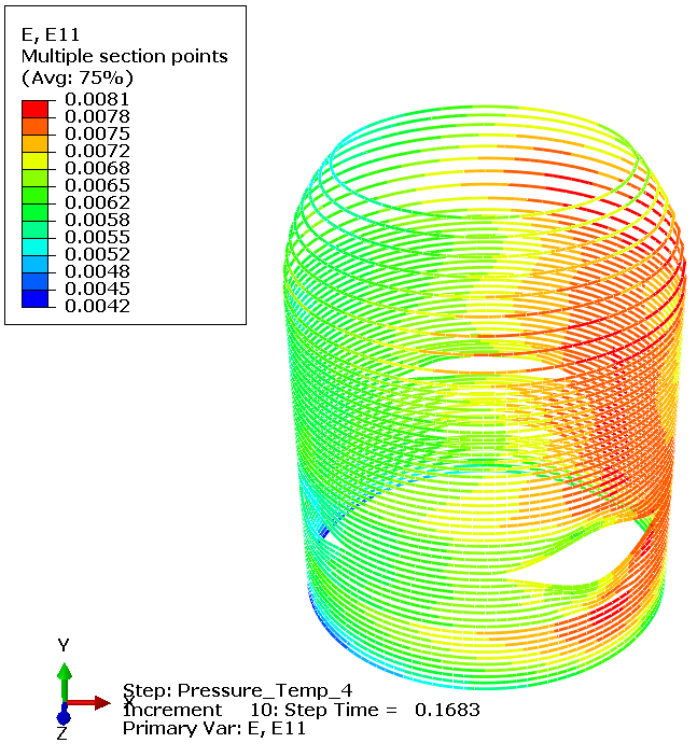

Figure D – 31h: Case 1 strain in hoop tendons anchored at 270° at 2.0 x Pd.

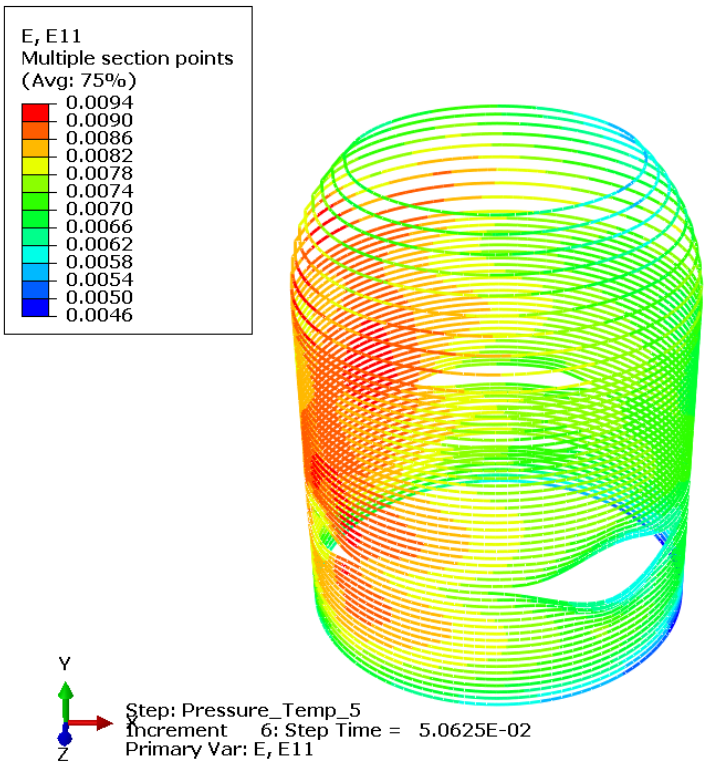

Figure D – 31i: Case 1 strain in hoop tendons anchored at 90° at 2.5 x Pd.

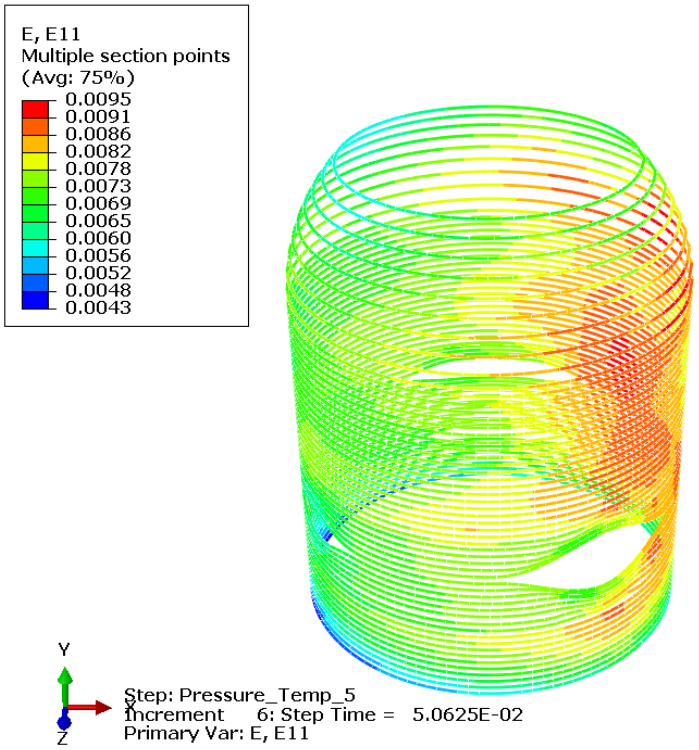

Figure D – 31j: Case 1 strain in hoop tendons anchored at 270° at 2.5 x Pd.

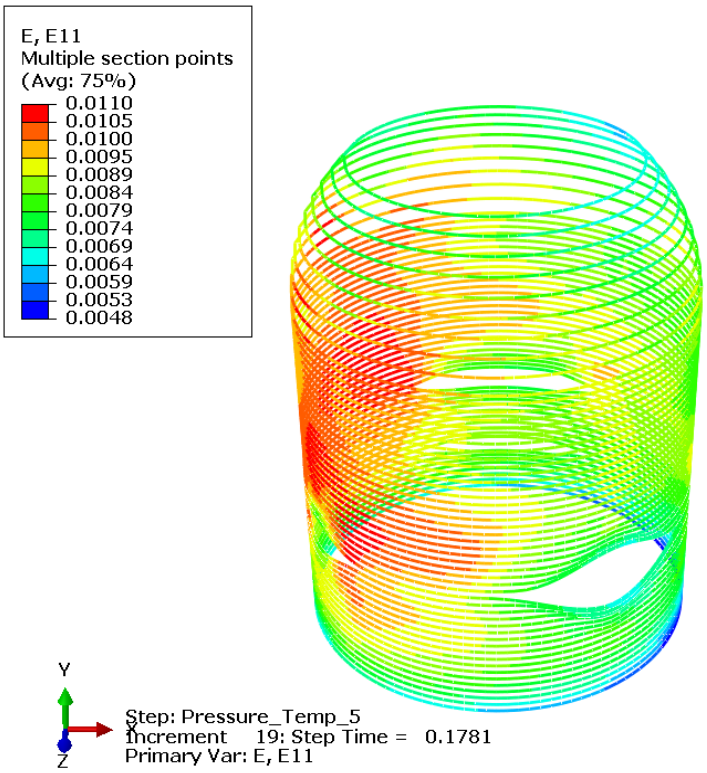

Figure D – 31k: Case 1 strain in hoop tendons anchored at 90° at 3.0 x Pd.

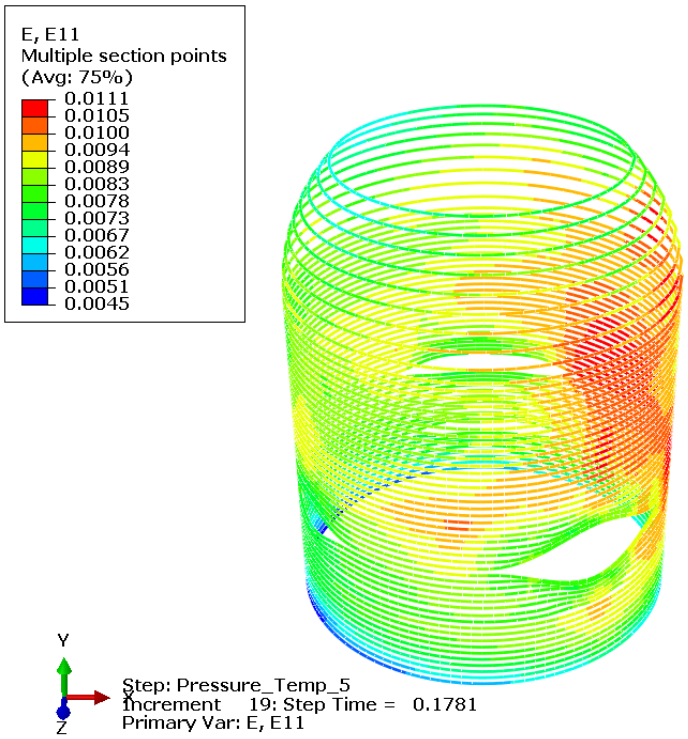

Figure D – 31l: Case 1 Strain in Hoop Tendons Anchored at 270° at 3.0 x Pd.

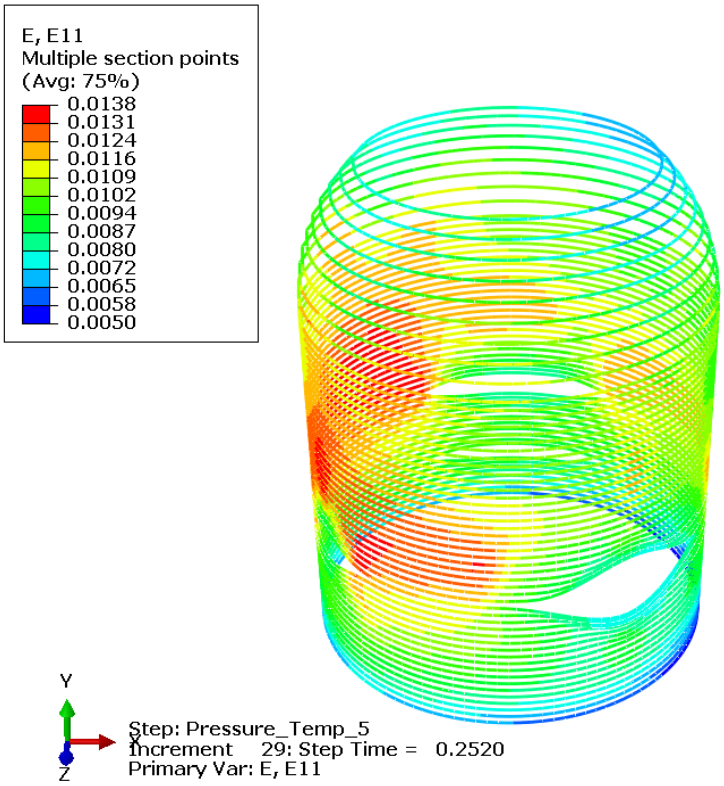

Figure D – 31m: Case 1 strain in hoop tendons anchored at 90° at 3.3 x Pd.

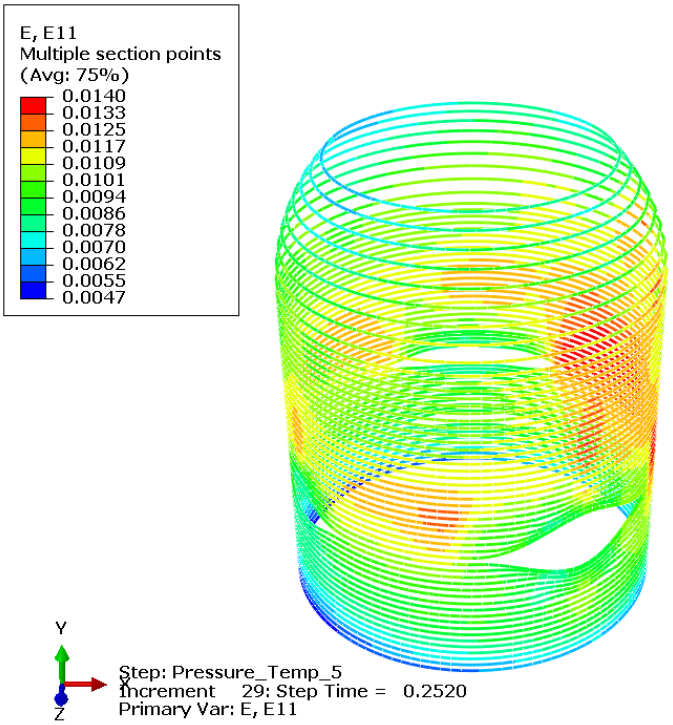

Figure D – 31n: Case 1 Strain in Hoop Tendons Anchored at 270° at 3.3 x Pd.

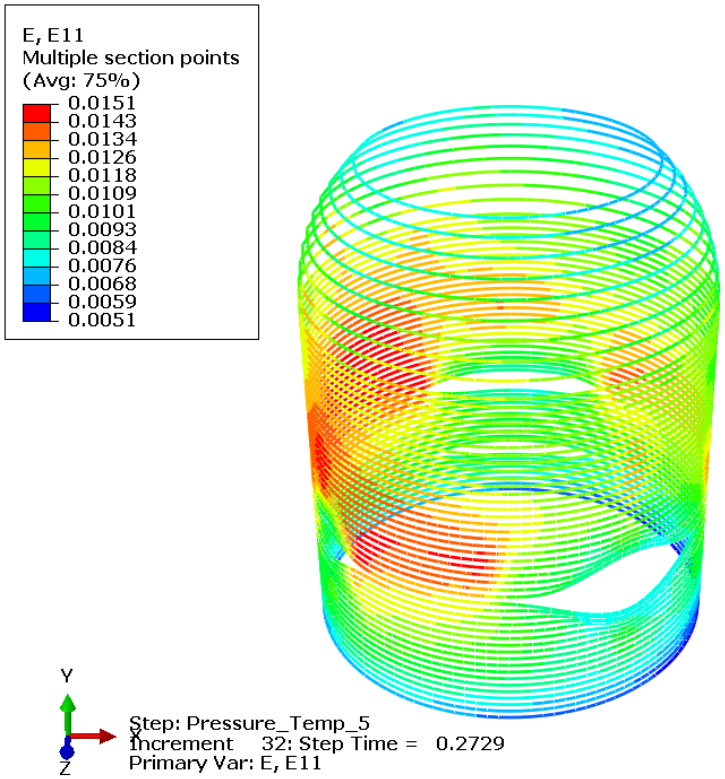

Figure D – 31o: Case 1 strain in hoop tendons anchored at 90° at 3.4 x Pd.

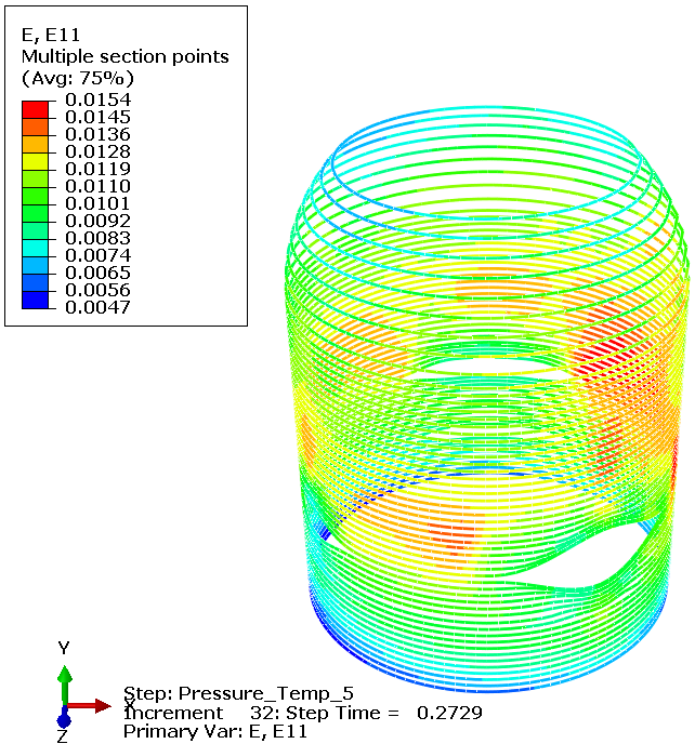

Figure D – 31p: Case 1 strain in hoop tendons anchored at 270° at 3.4 x Pd.

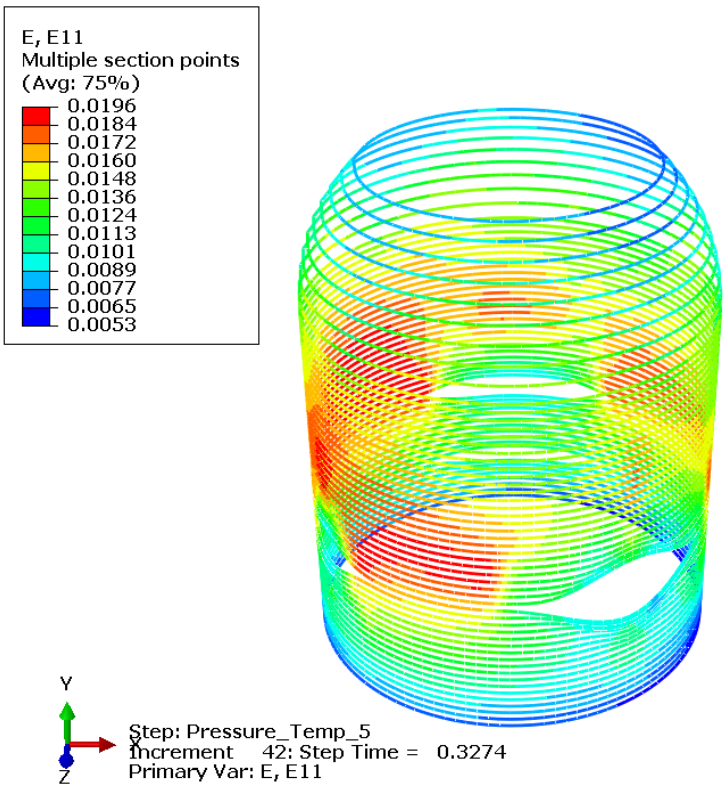

Figure D – 31q: Case 1 strain in hoop tendons anchored at 90° at 3.6 x Pd.

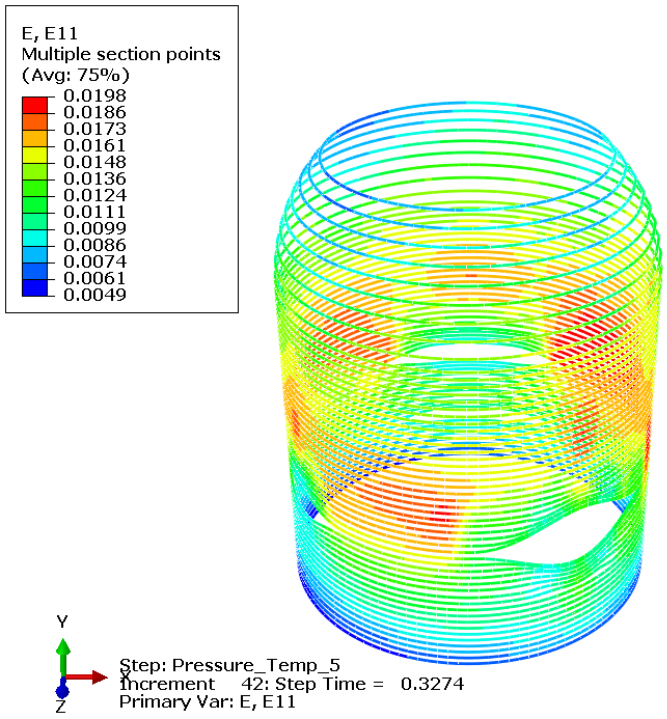

Figure D – 31r: Case 1 strain in hoop tendons anchored at 270° at 3.6 x Pd

Figures D-32 through D-35 show strains over selected gage lengths near the penetrations, as requested of the analysts in the SPE instructions. The reference frame defining these locations was shown in Figure 9 of the Model 2 Report.

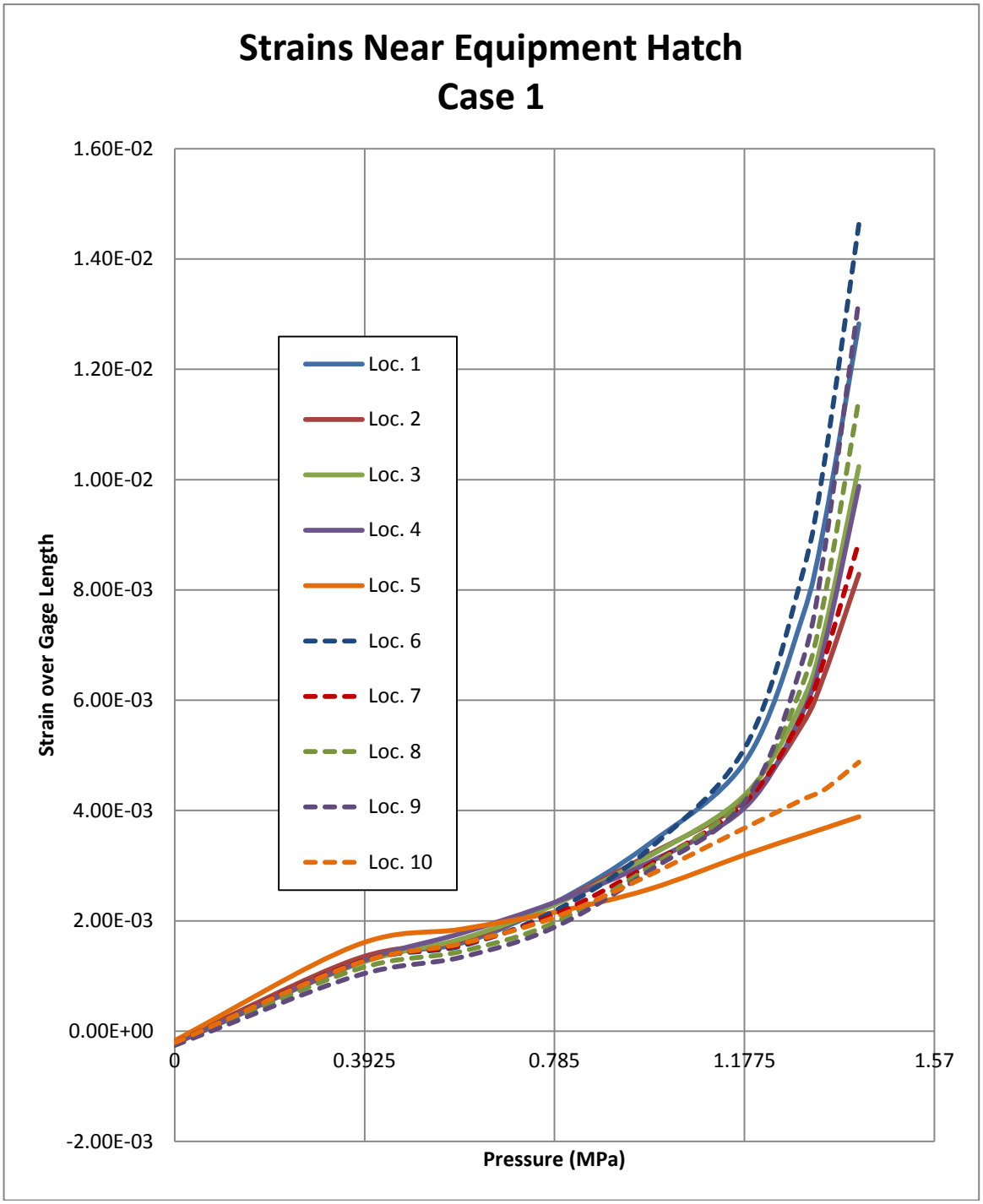

Figure D - 32: Case 1 strains over selected gage length near E/H

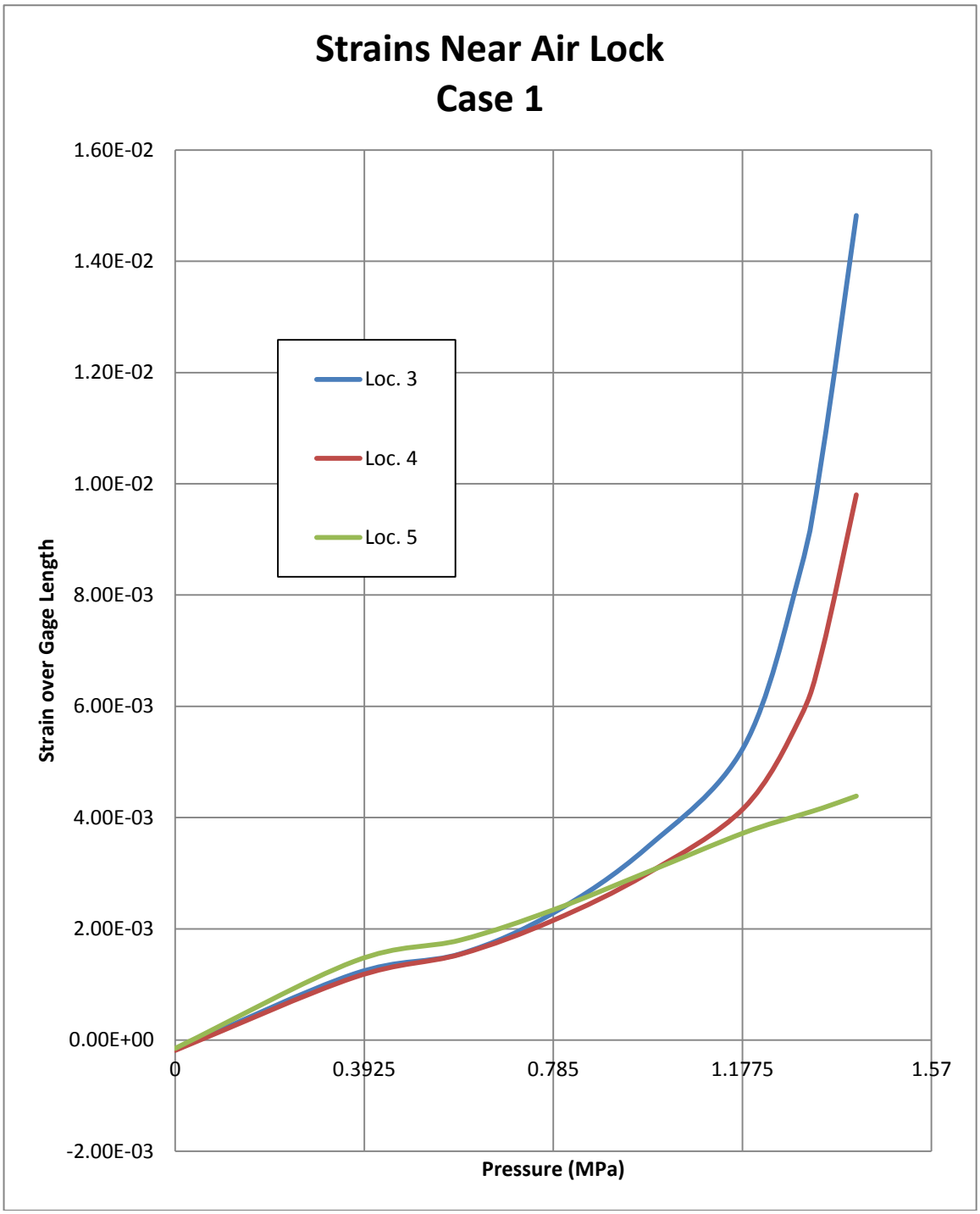

Figure D - 33: Case 1 strains over selected gage length near A/L

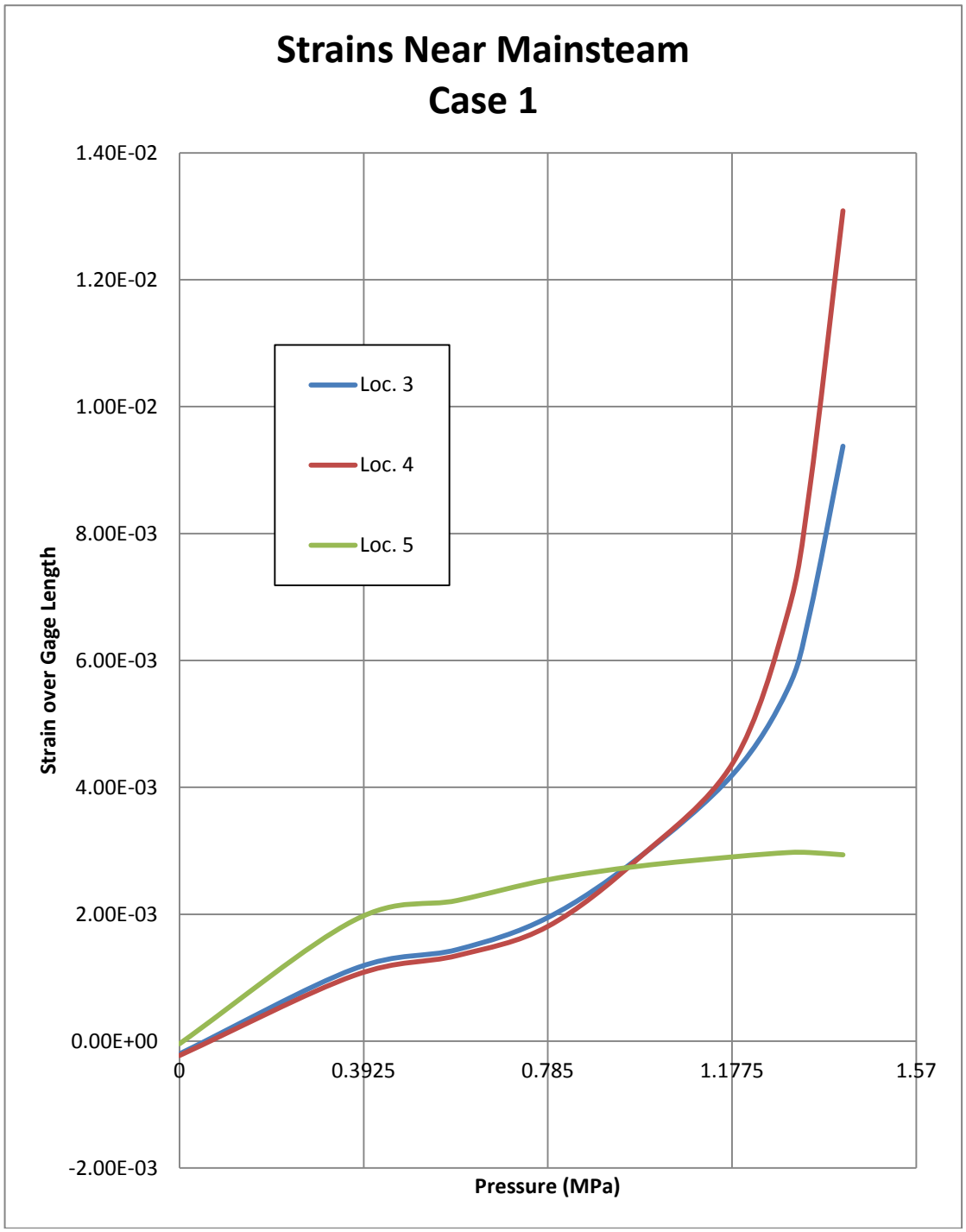

Figure D - 34: Case 1 strains over selected gage length near M/S

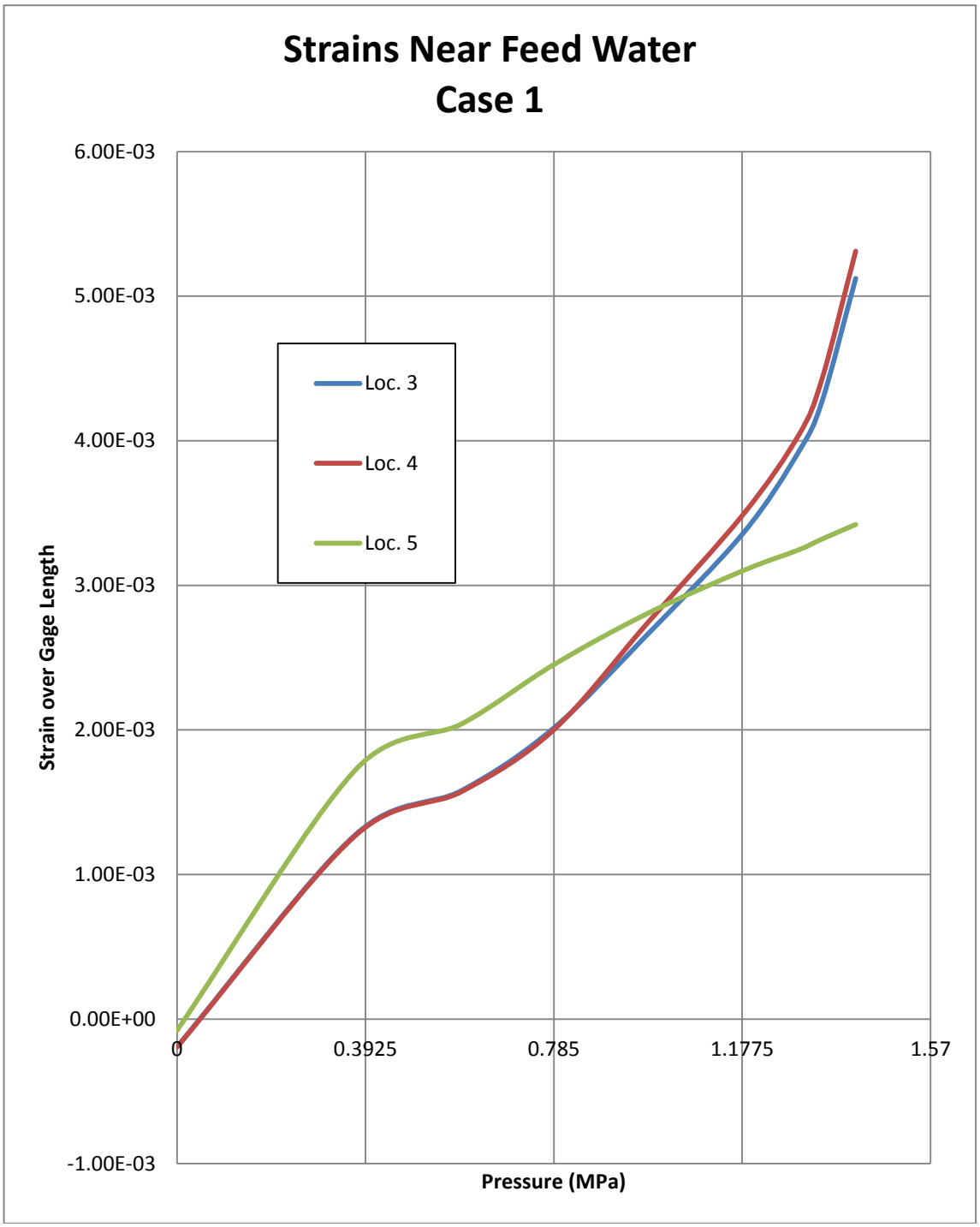

Figure D - 35: Case 1 strains over selected gage length near F/W

Figures D-36a through D-15b show tendon stress profiles for the most comprehensively instrumented tendons in the 1:4 Scale PCCV model test.

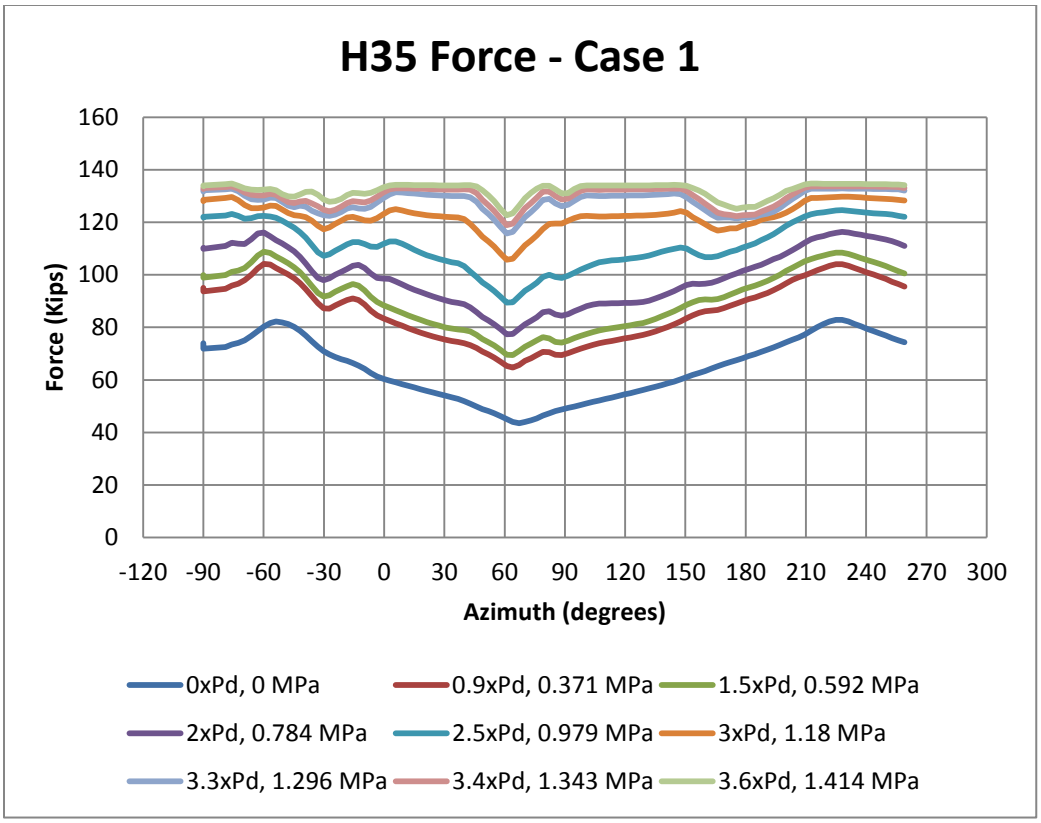

Figure D - 36a: Case 1 Abaqus analysis – hoop tendon H35 force

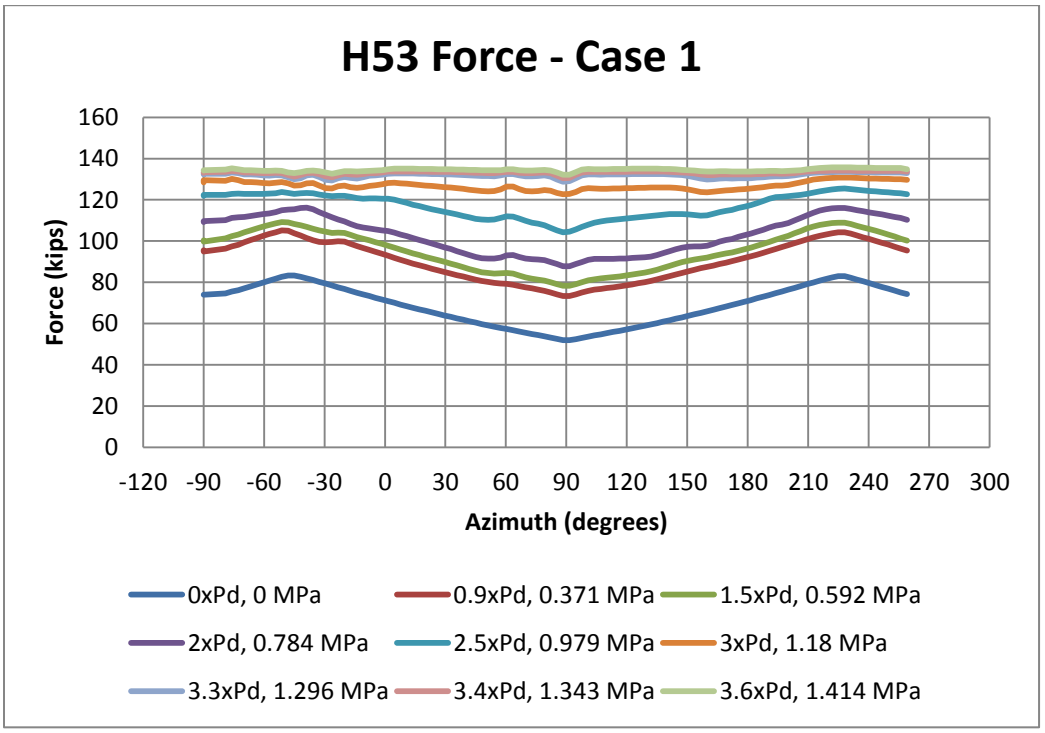

Figure D – 36b: Case 1 Abaqus analysis – hoop tendon H53 force

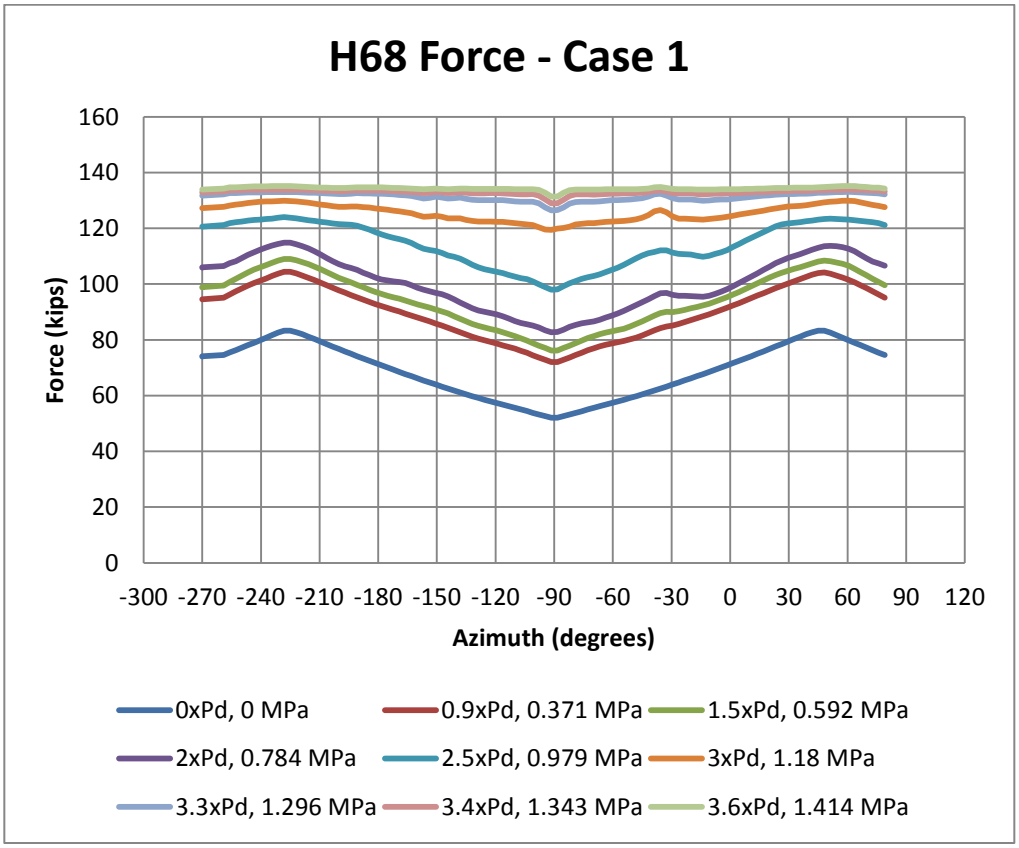

Figure D – 36c: Case 1 Abaqus analysis – hoop tendon H68 force

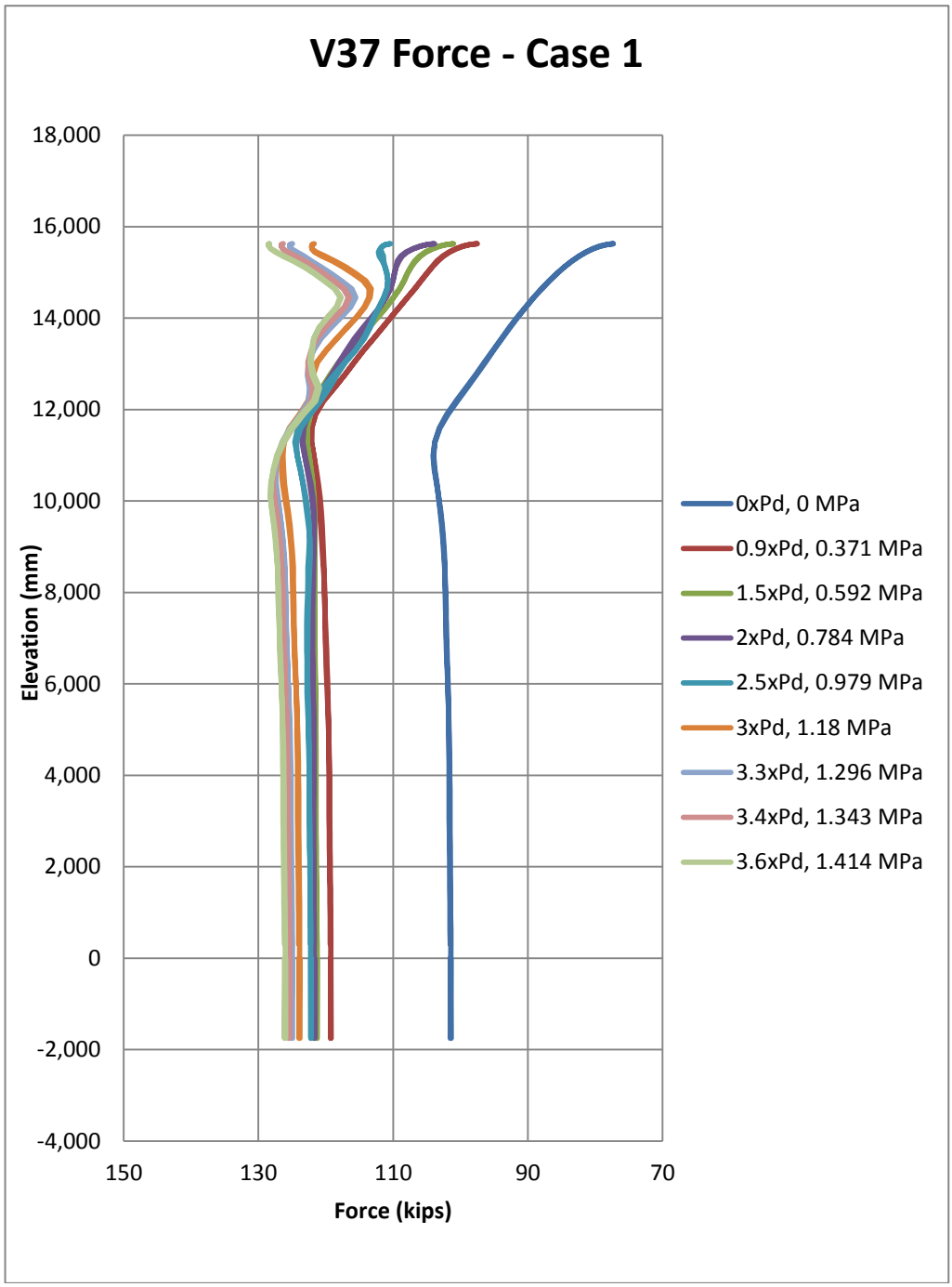

Figure D - 37a: Case 1 Abaqus analysis – hairpin tendon V37 force

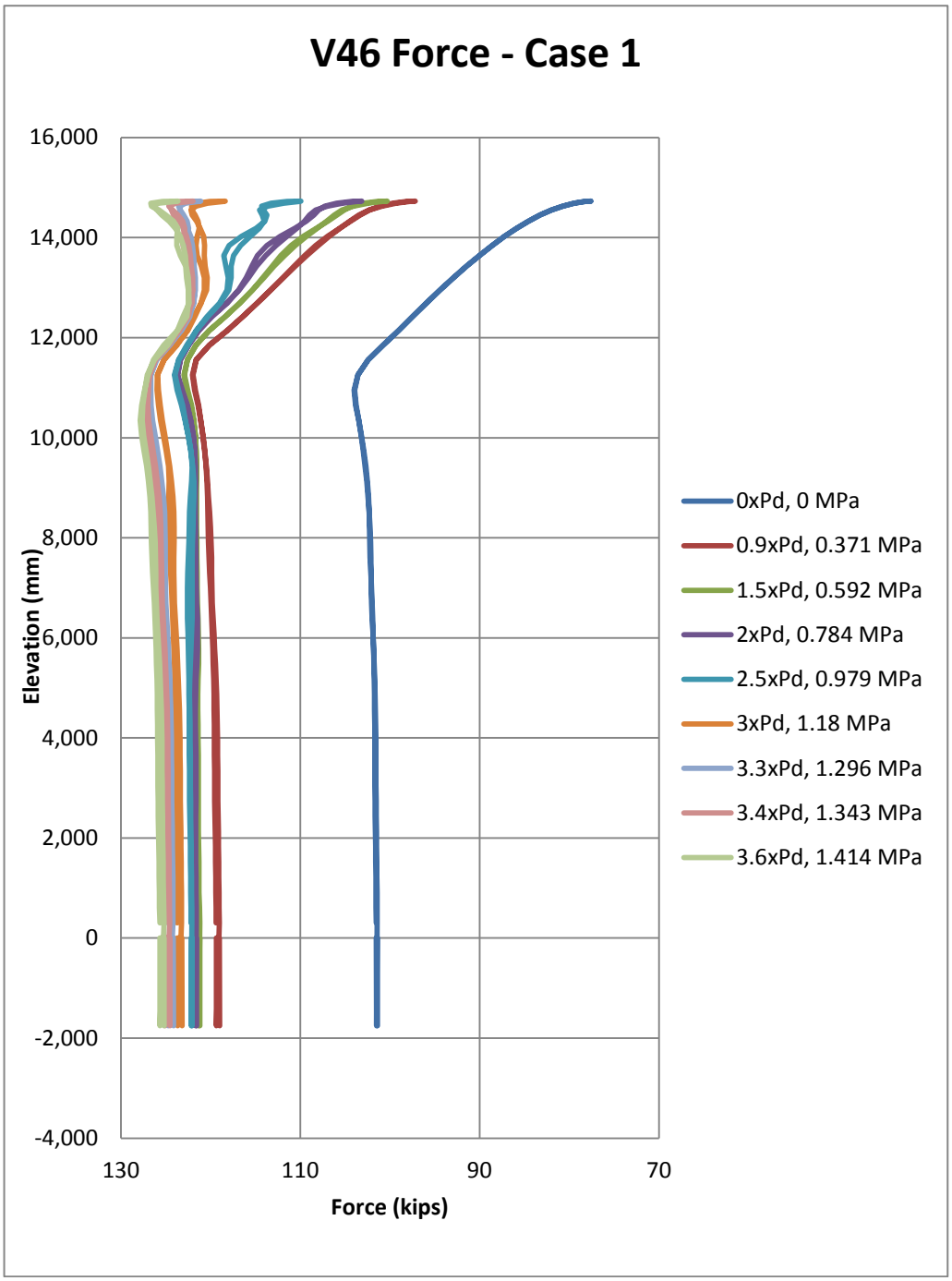

Figure D – 37b: Case 1 Abaqus analysis – hairpin tendon V46 force

Case 2 – "Station blackout" condition

The results of pressure milestones are shown in Table D-6.

Table D - 6: Case 2 results by pressure milestones at 6.2 m

Milestone	Pressure (MPa)	x Pd
Zero Concrete Hoop Stress (at 0^o azimuth)	0.74	1.89
Concrete Hoop Cracking Occurs (at 0^o azimuth)	0.77	1.95
Tendon A Reach approx.1% Strain (at 0^o azimuth)	1.20	3.06
Tendon B Reach approx.1% Strain (at 0^o azimuth)	1.24	3.16

Deformed shapes of the full model are shown in Figures D-38a and D-38b for, respectively, the a) after prestress and tendon anchorage step, b) at pressurization of 3.6 Pd, which is incipient failure of the vessel.

A series of "plan-view" slice deformed shapes are shown in Figures D-39a through D-39i, at a Model Elevation of 4.68 meters. Based on rough comparisons to the results from Model 3, these shapes and the magnitude of the displacements are in reasonably good agreement.

A series of global plots of Maximum Principal Strains are shown for the Liner, and for the Concrete Mid-thickness of the Vessel in the Plot Series, Figures D-40a through D-41i.

Figures D-42a through D-42p show hoop tendon strains.

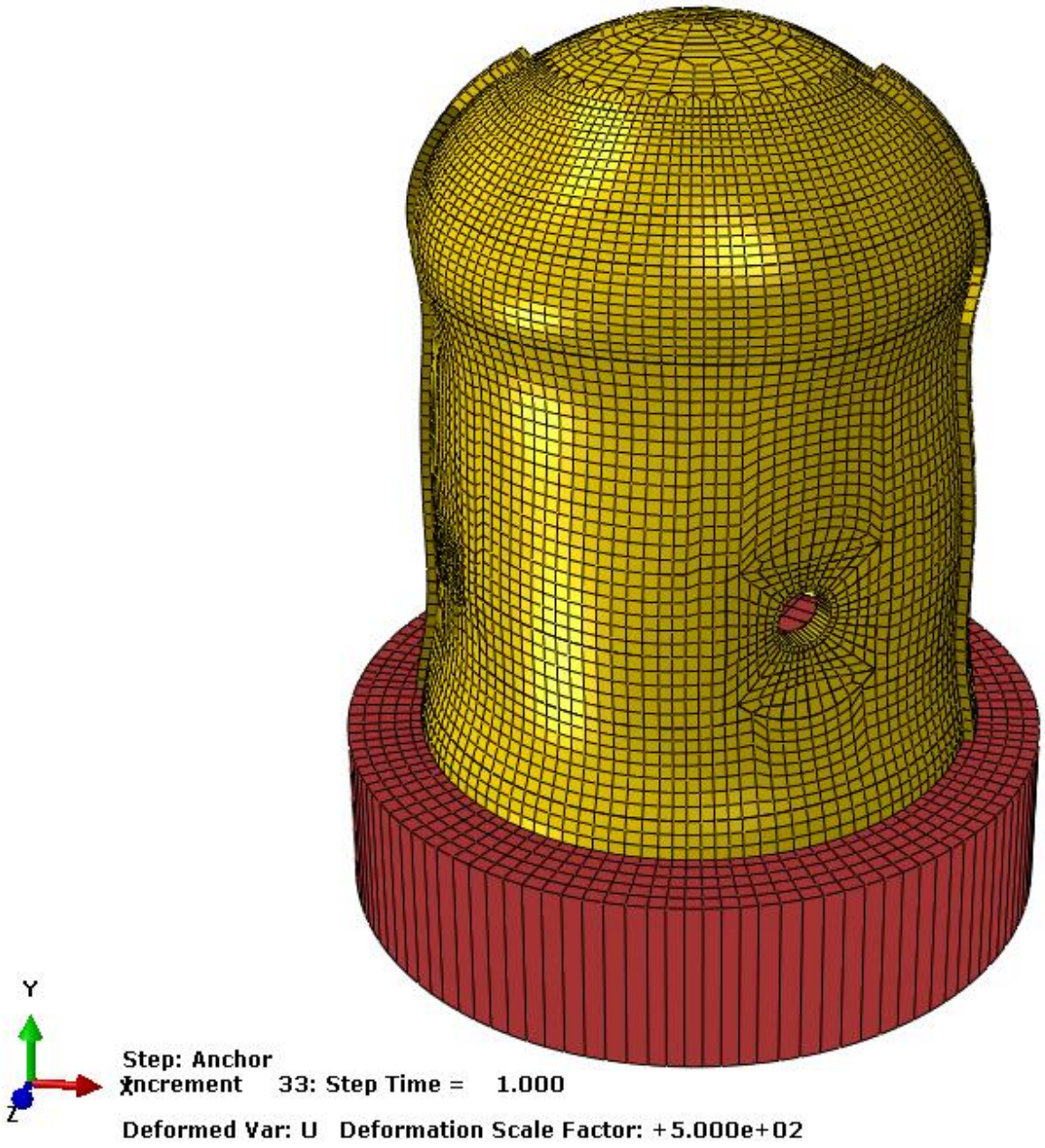

Figure D - 38a: Case 2 deformed shape after tendon anchorage. Deformation scale x 500

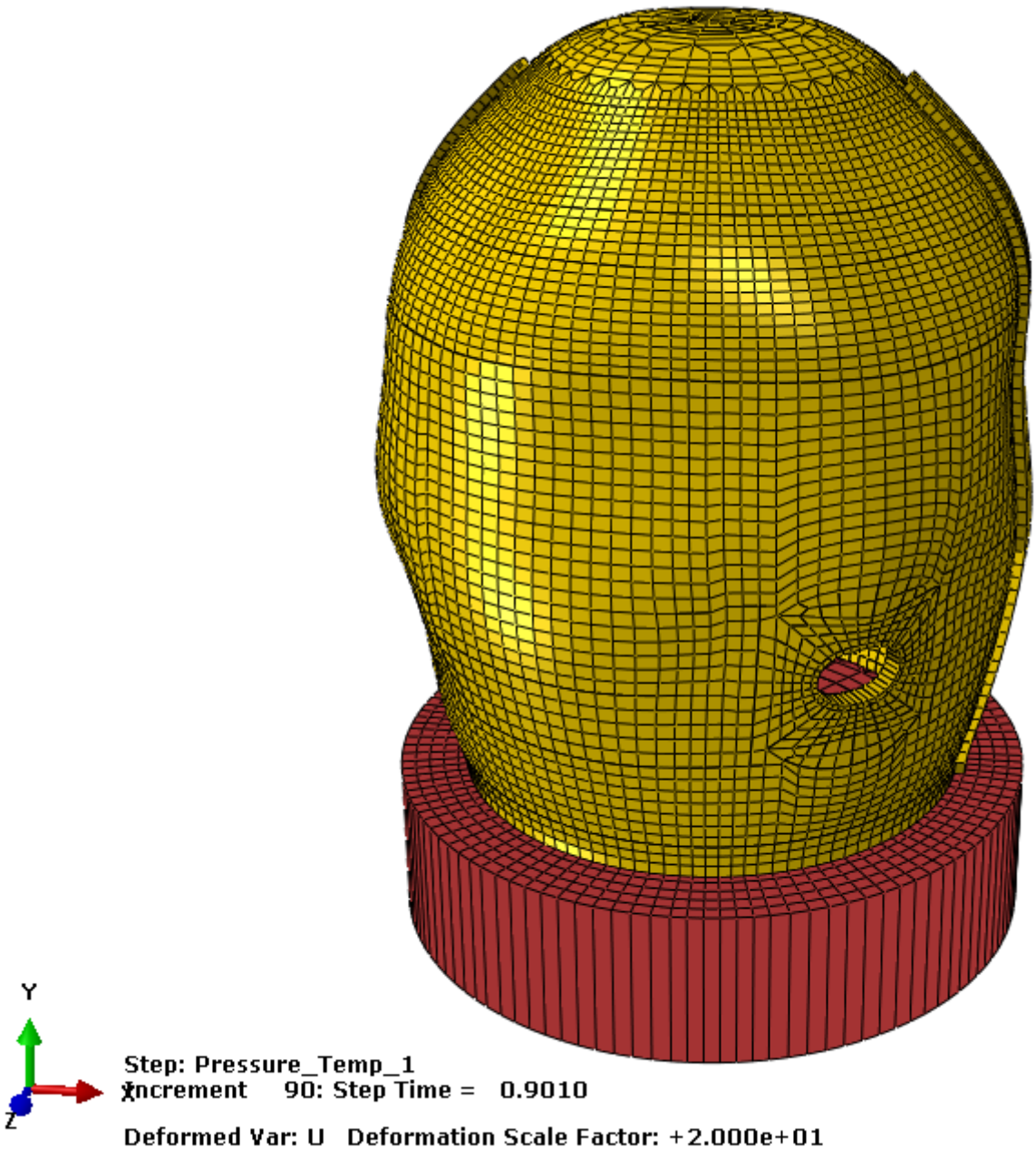

Figure D – 38b: Case 2 deformed shape at 3.6xPd. Deformation scale x 20

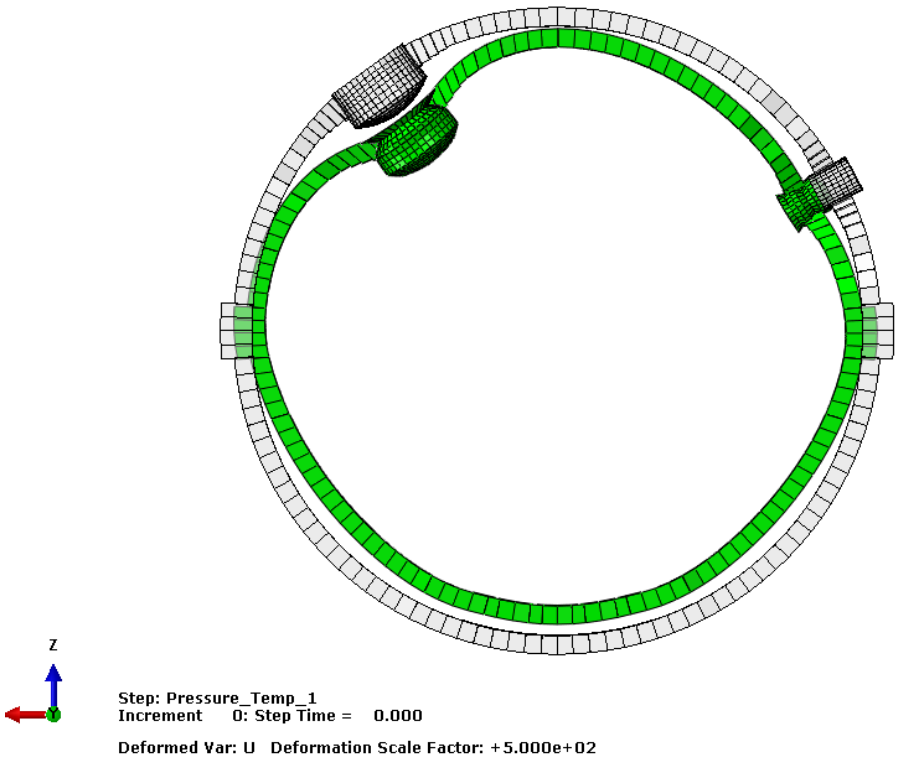

Figure D - 39a: Case 2 deformed shape at anchoring at elev. 4.68 m (15'-4 1/16") (x500)

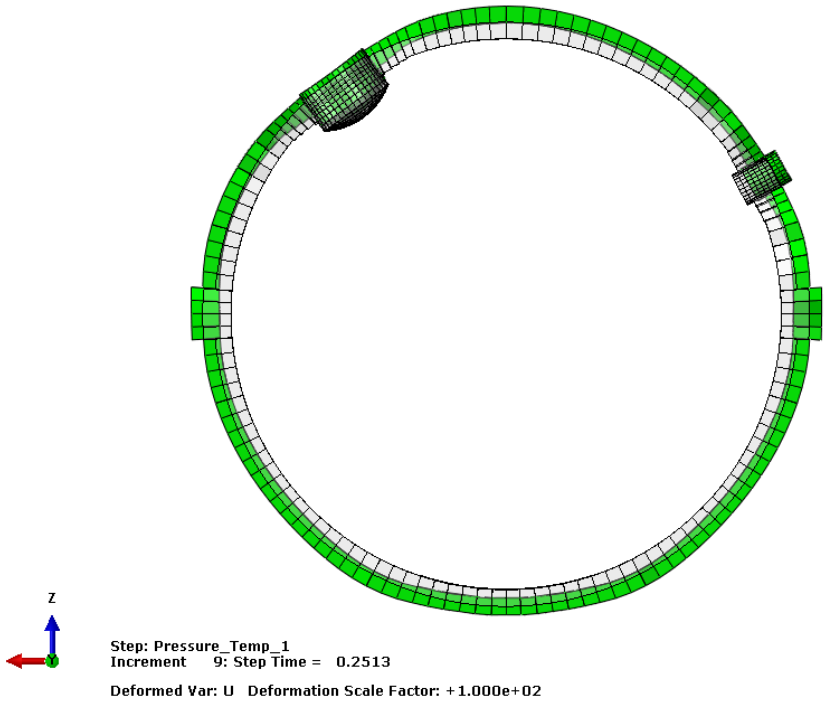

Figure D – 39b: Case 2 deformed shape at 1.0 x design pressure at elev. 4.68 m (15'-4 1/16") (x100)

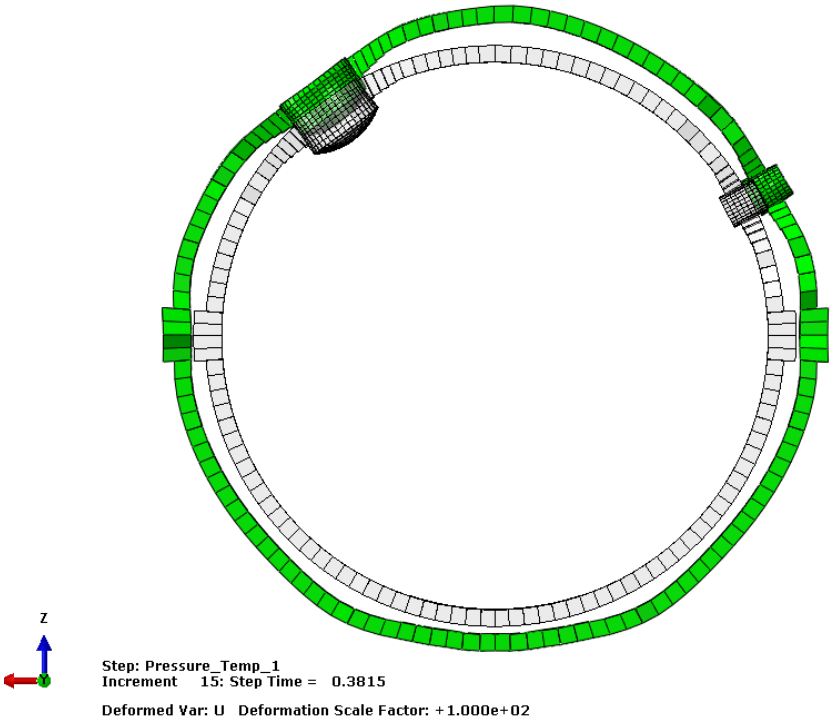

Figure D – 39c: Case 2 deformed shape at 1.5 x design pressure at elev. 4.68 m (15'-4 1/16") (x100)

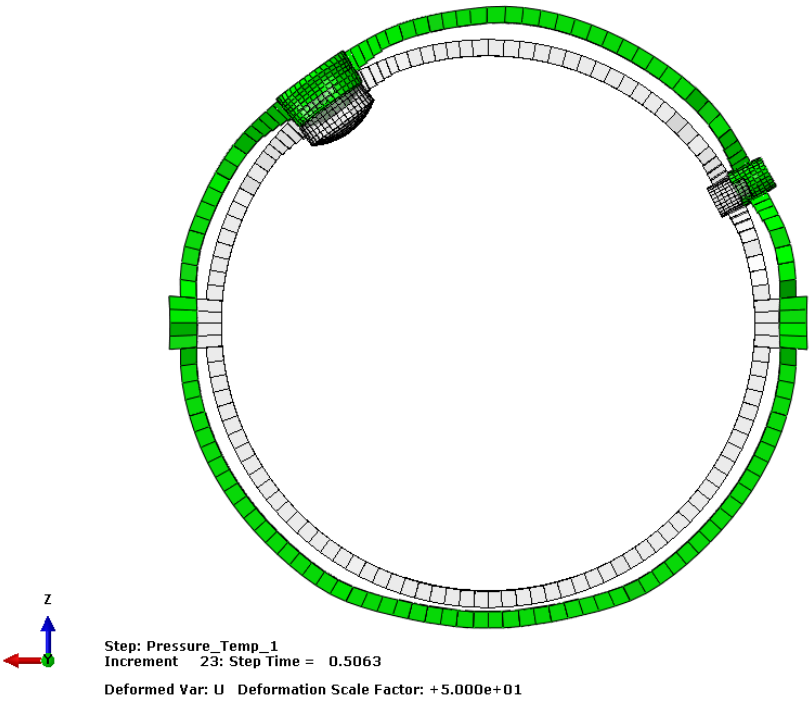

Figure D – 39d: Case 2 deformed shape at 2.0 x design pressure at elev. 4.68 m (15'-4 1/16") (x50)

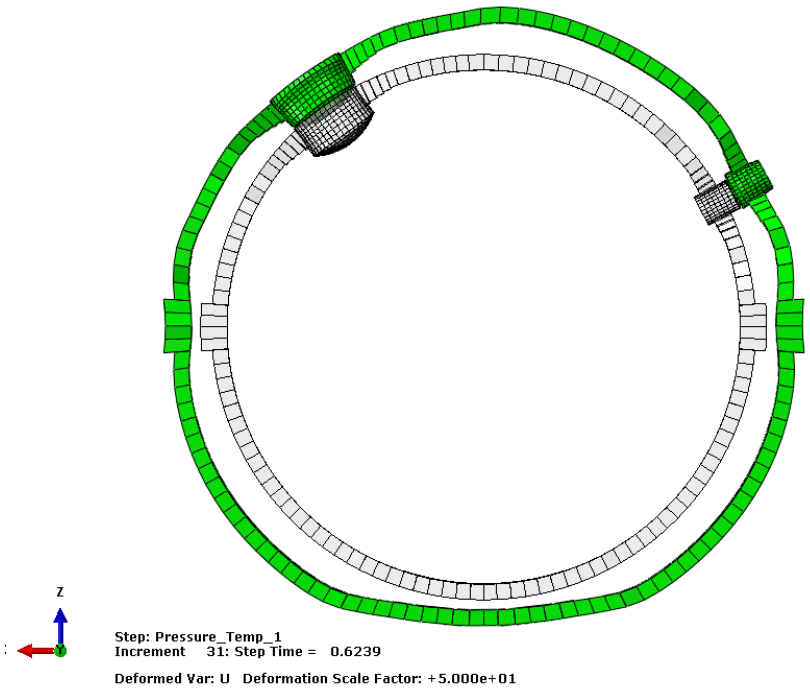

Figure D – 39e: Case 2 deformed shape at 2.5 x design pressure at elev. 4.68 m (15'-4 1/16") (x50)

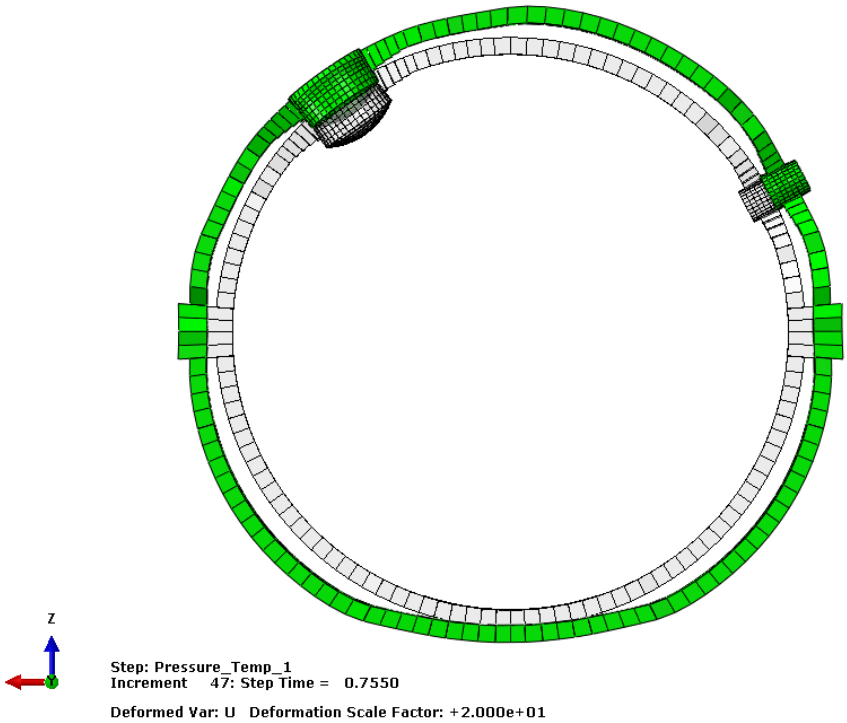

Figure D – 39f: Case 2 deformed shape at 3.0 x design pressure at elev. 4.68 m (15'-4 1/16") (x20)

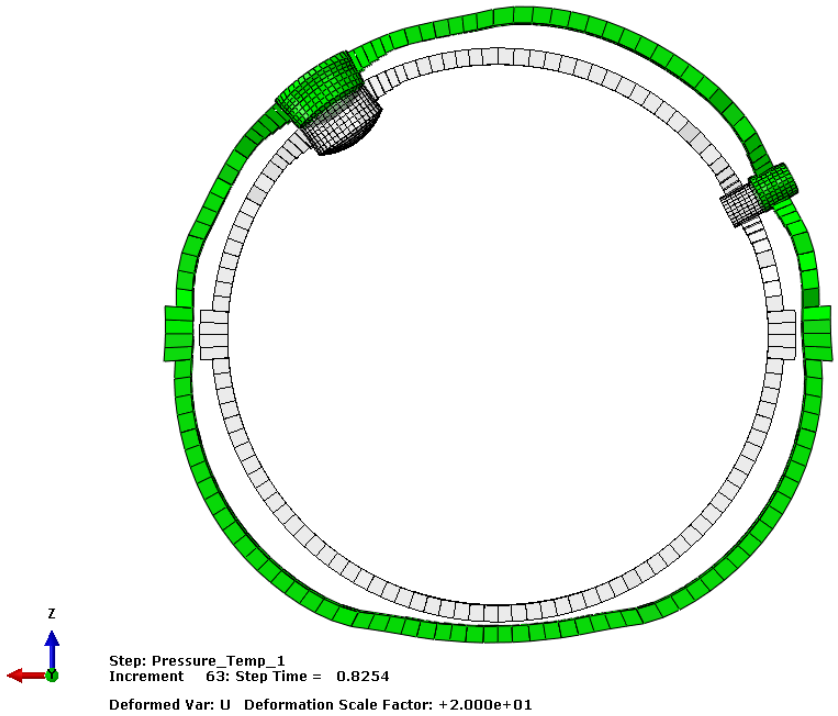

Figure D – 39g: Case 2 deformed shape at 3.3 x design pressure at elev. 4.68 m (15'-4 1/16") (x20)

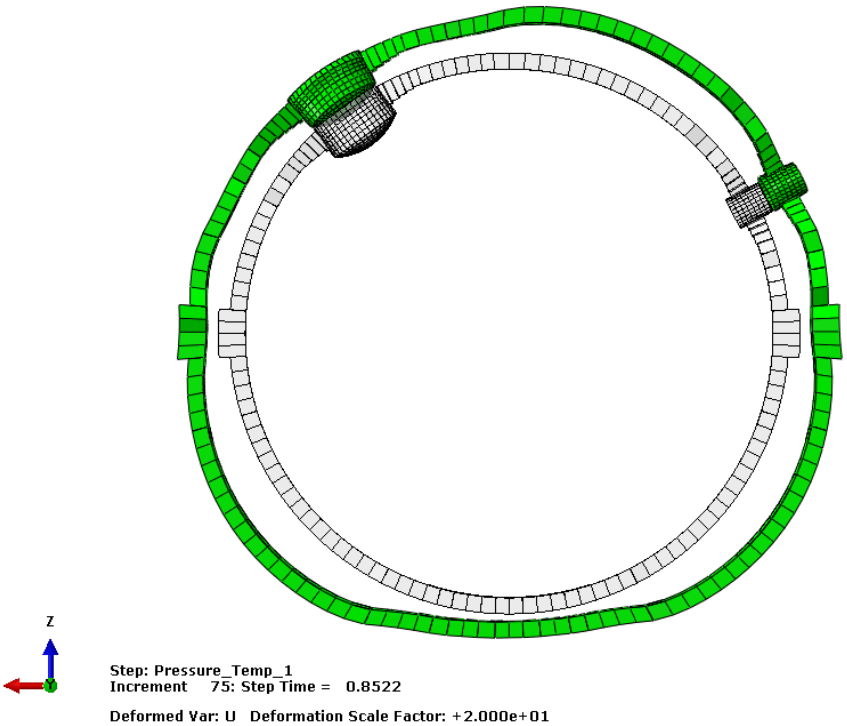

Figure D – 39h: Case 2 deformed shape at 3.4 x design pressure at elev. 4.68 m (15'-4 1/16") (x20)

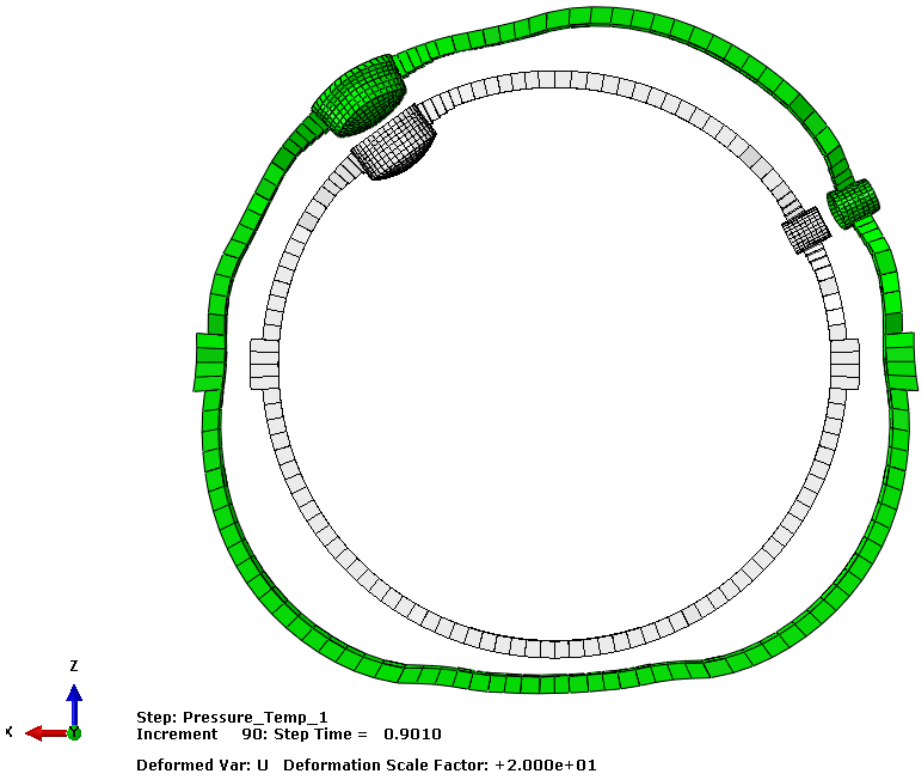

Figure D – 39i: Case 2 deformed shape at 3.6 x design pressure at elev. 4.68 m (15'-4 1/16") (x20)

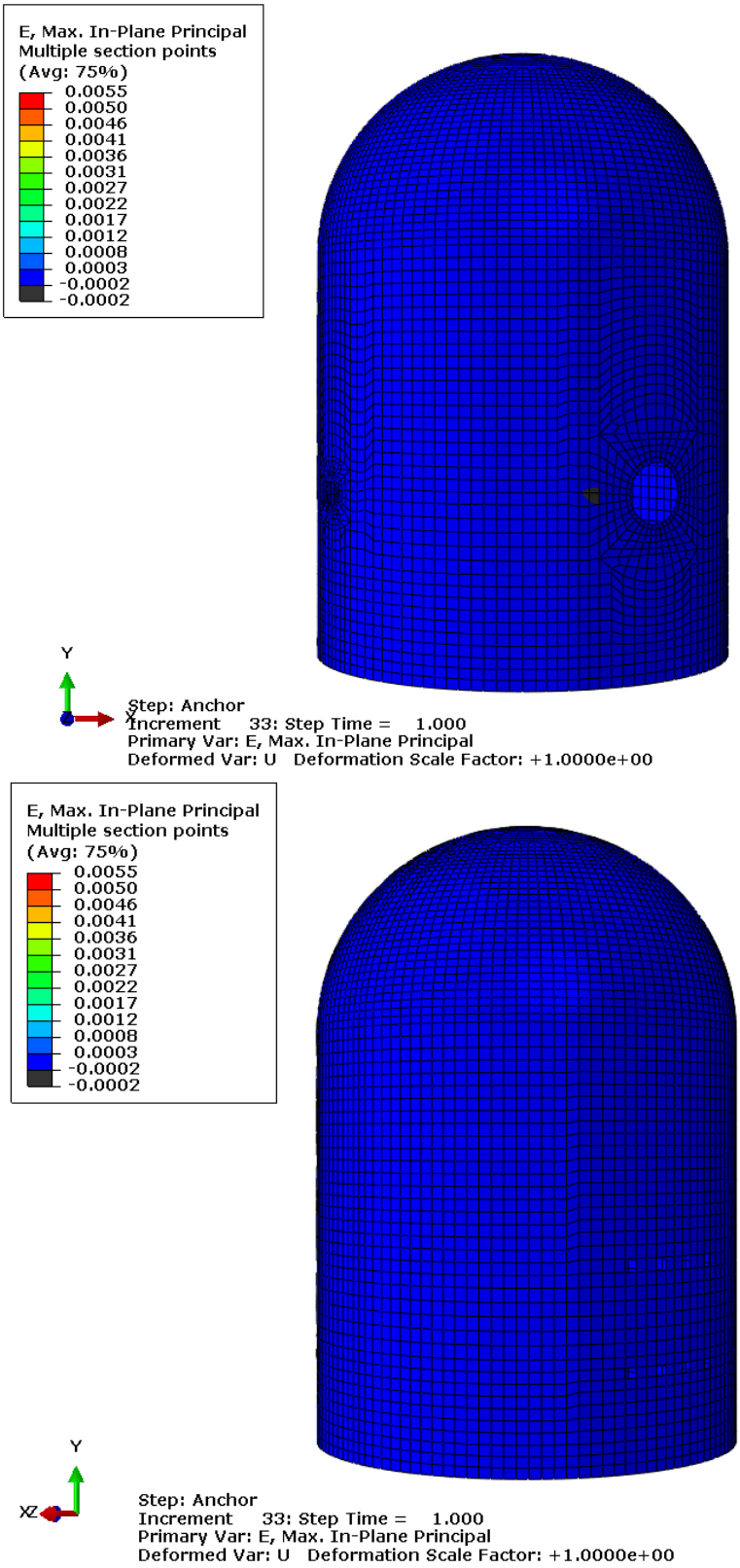

Figure D - 40a: Case 2 max principal strain in liner after tendon anchorage

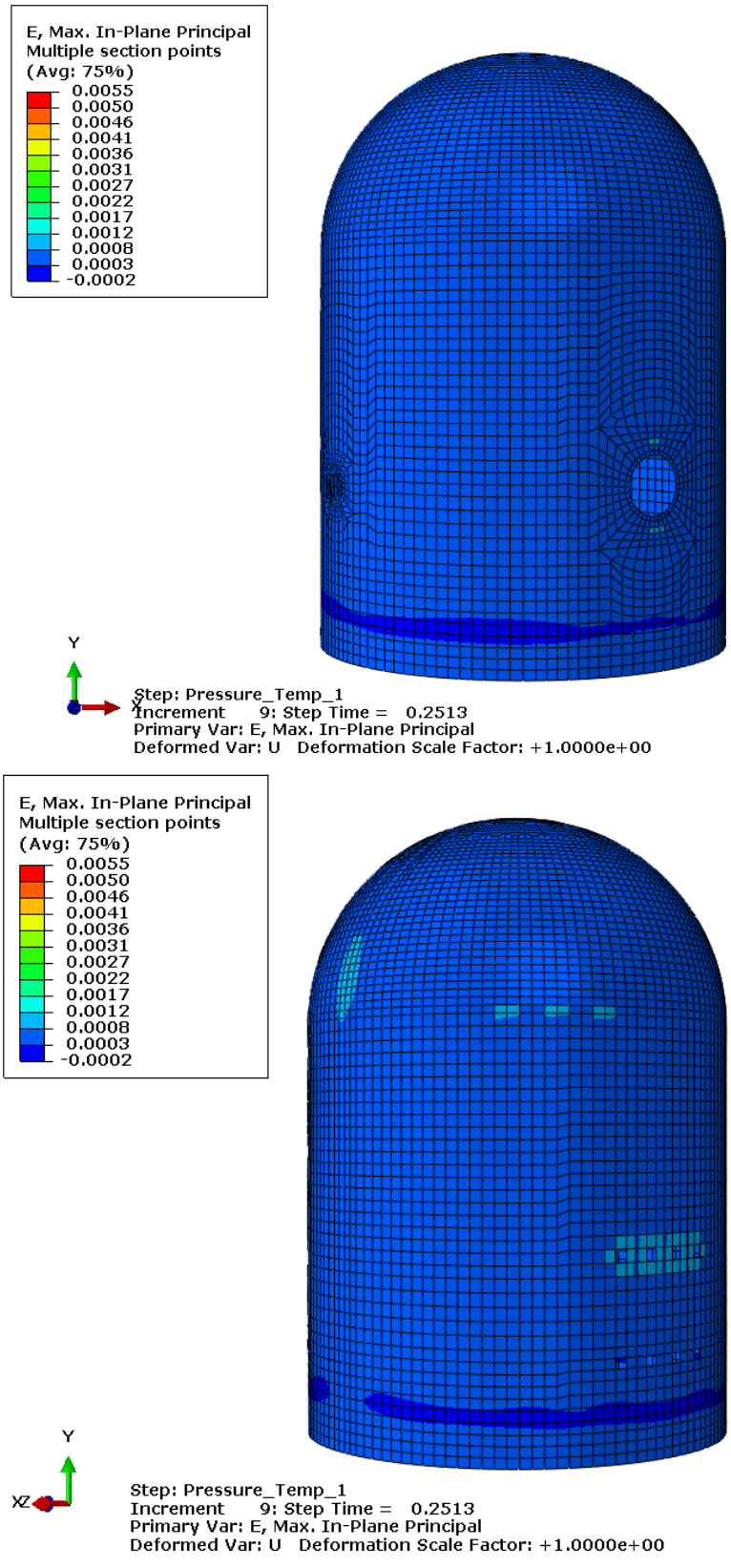

Figure D – 40b: Case 2 max principal strain in liner at 1.0xPd

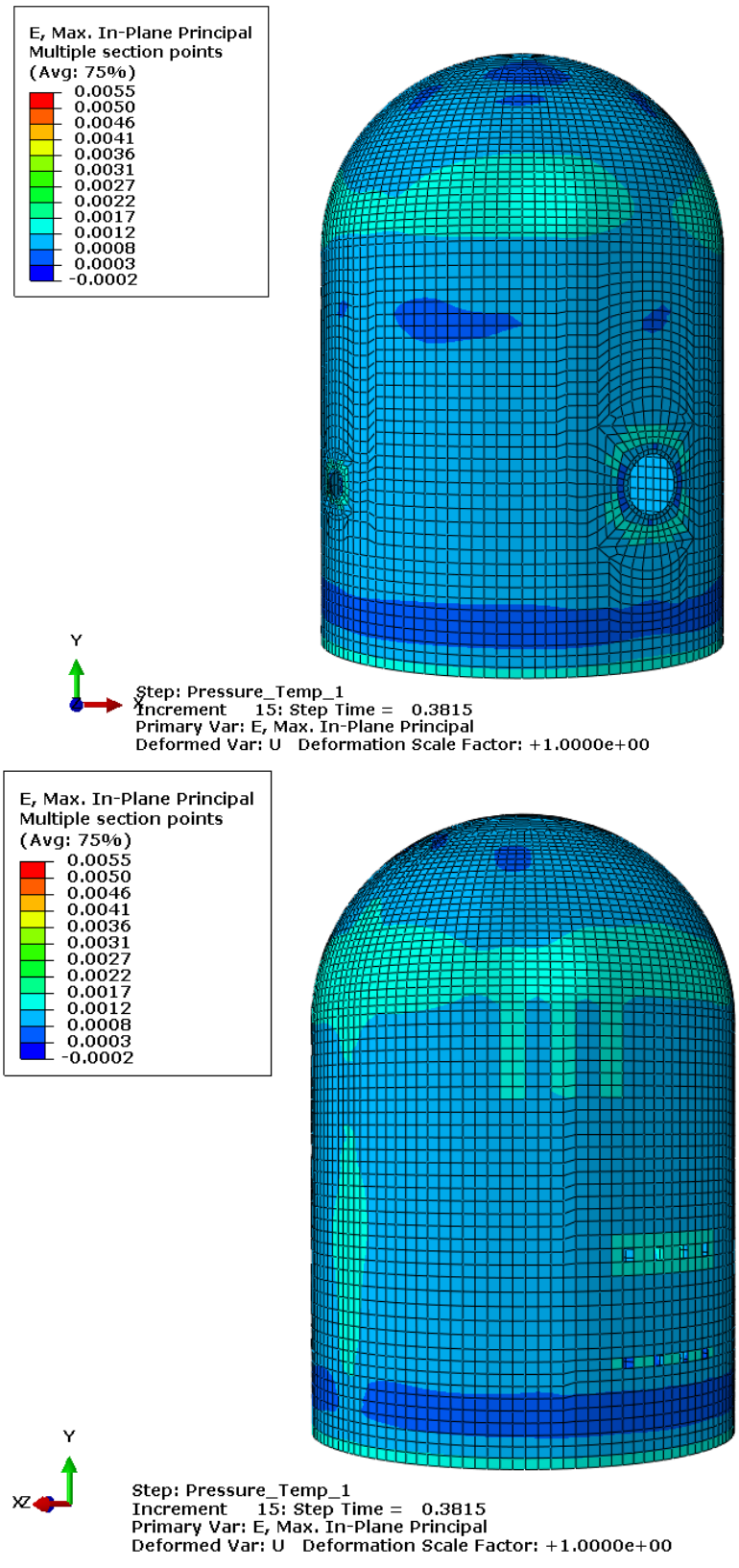

Figure D – 40c: Case 2 max principal strain in liner at 1.5xPd

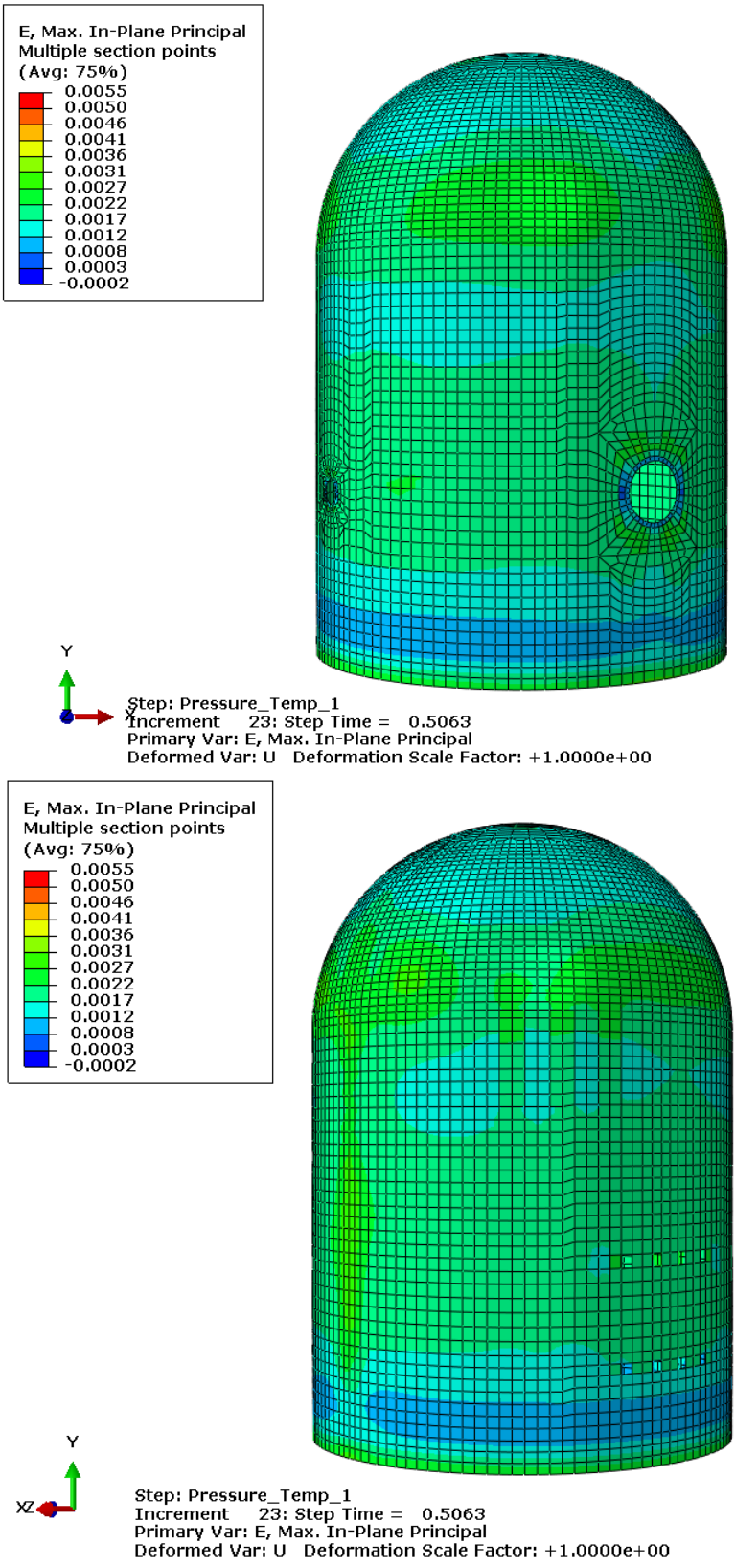

Figure D – 40d: Case 2 max principal strain in liner at 2.0xPd

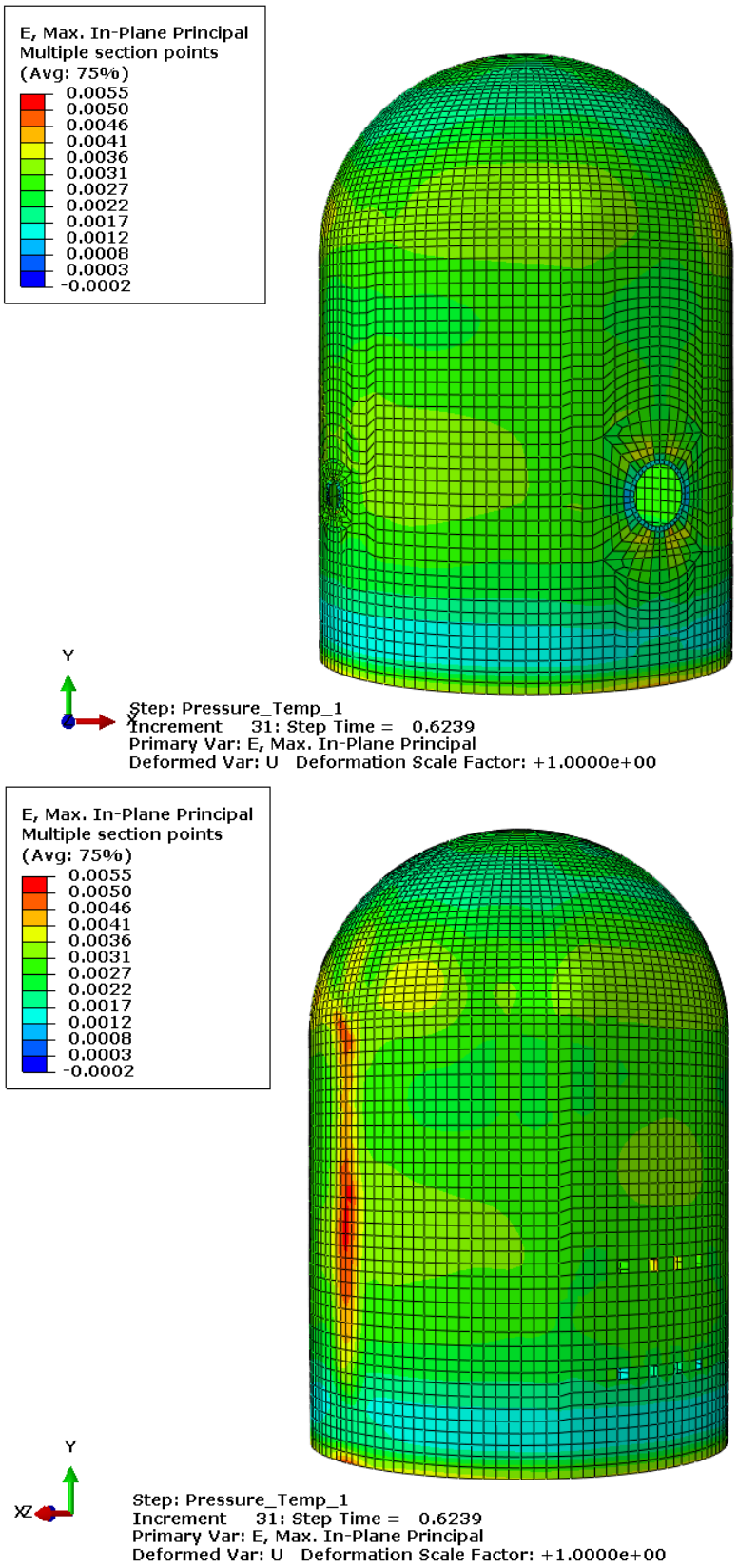

Figure D – 40e: Case 2 max principal strain in liner at 2.5xPd

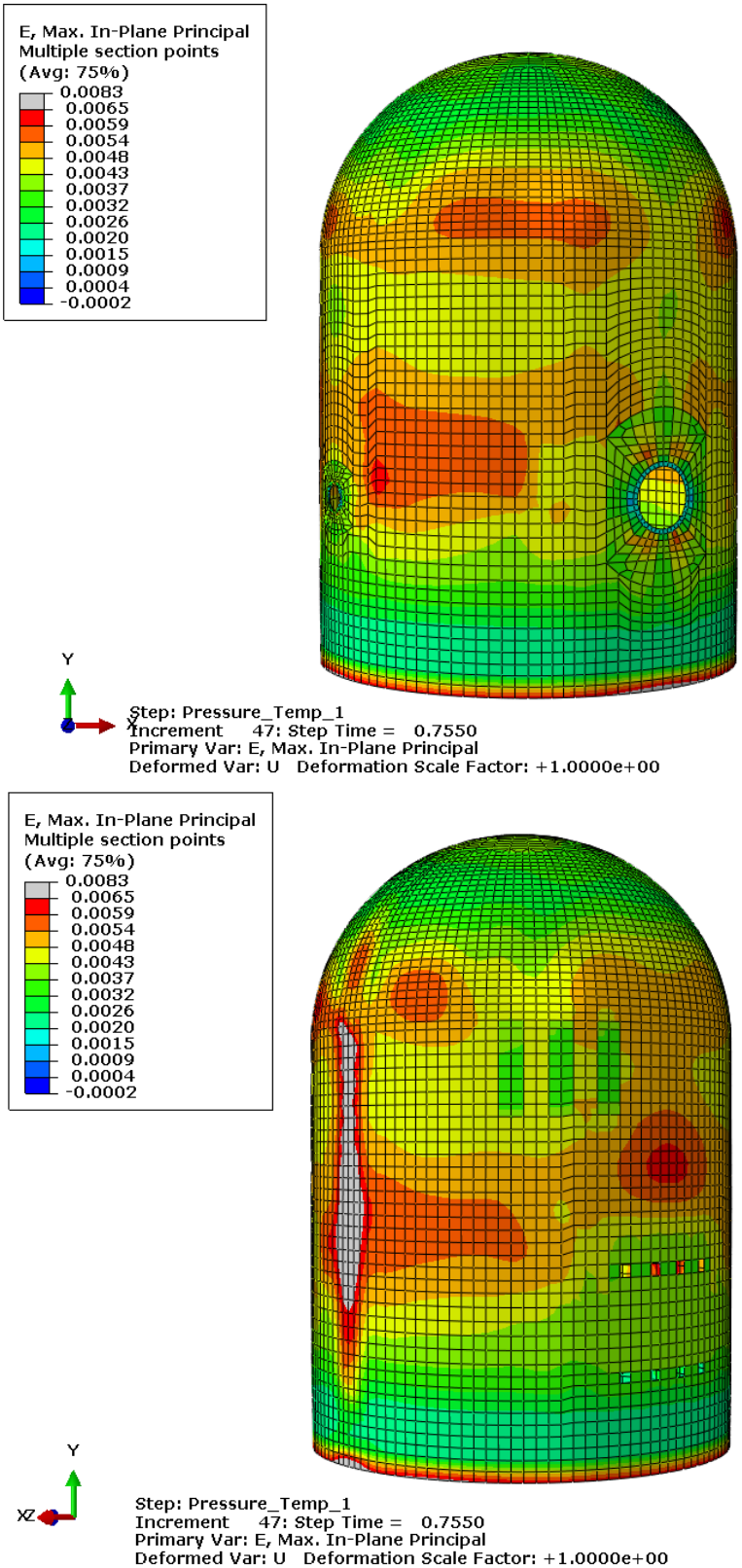

Figure D – 40f: Case 2 max principal strain in liner at 3.0xPd

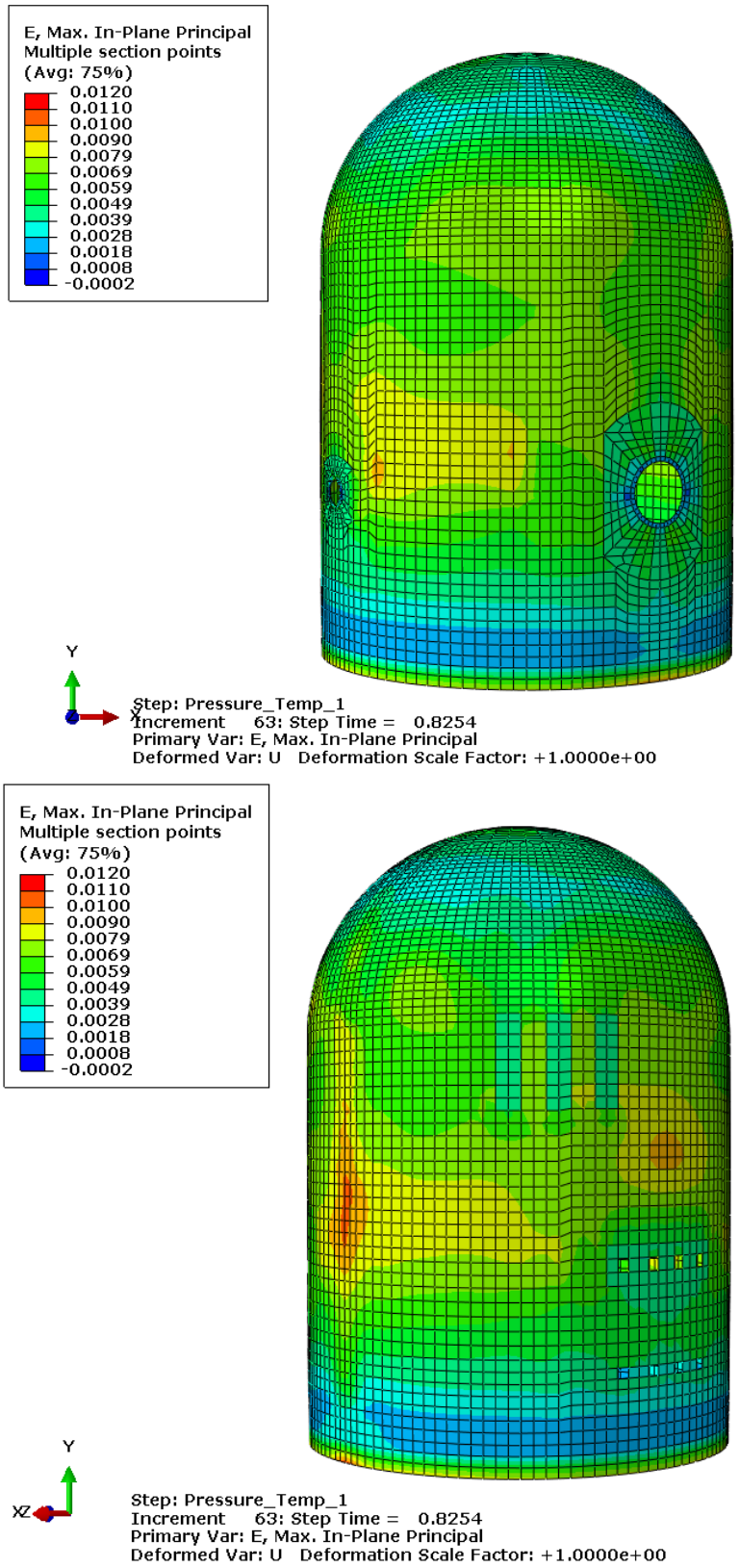

Figure D – 40g: Case 2 max principal strain in liner at 3.3xPd (high contour color limits)

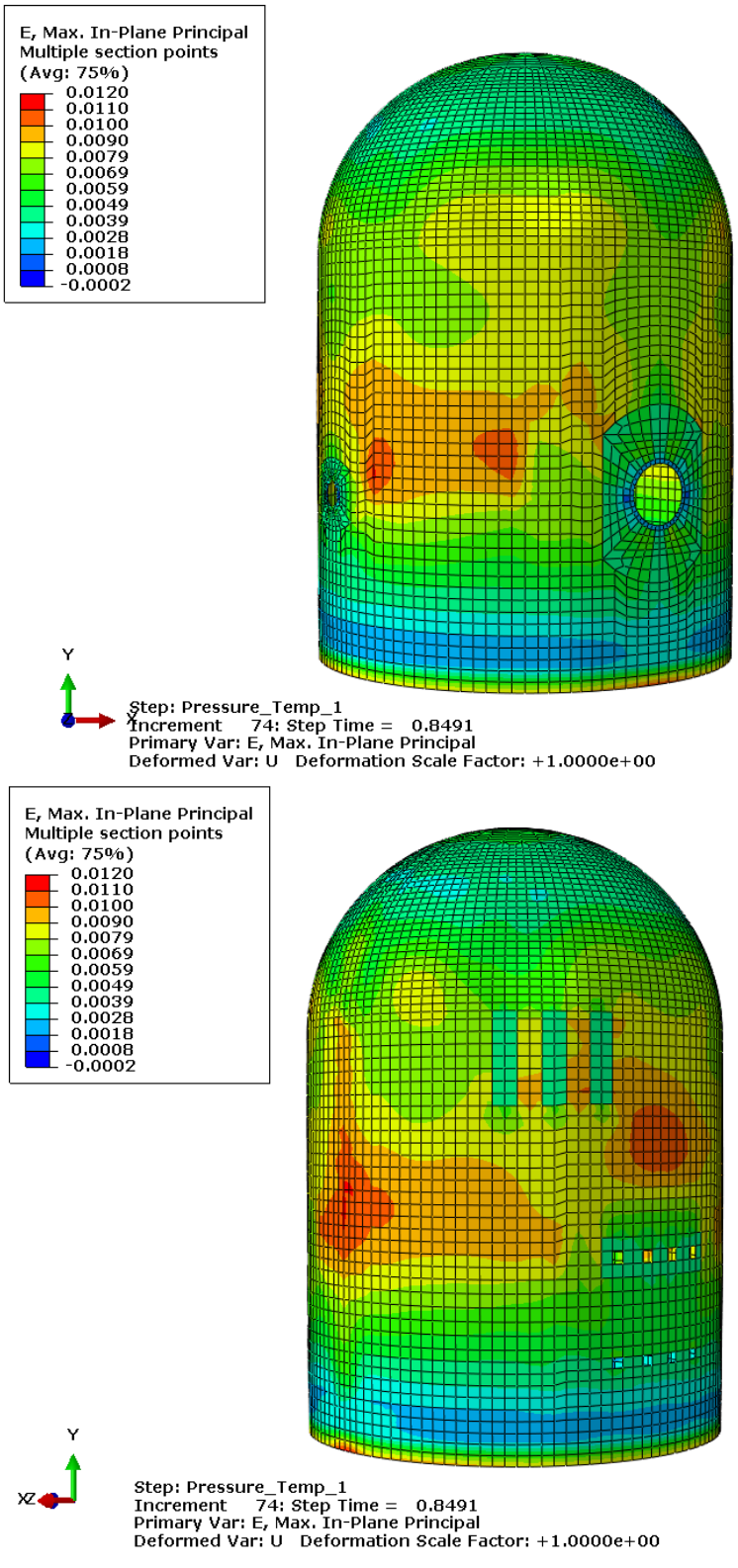

Figure D – 40h: Case 2 max principal strain in liner at 3.4xPd (high contour color limits)

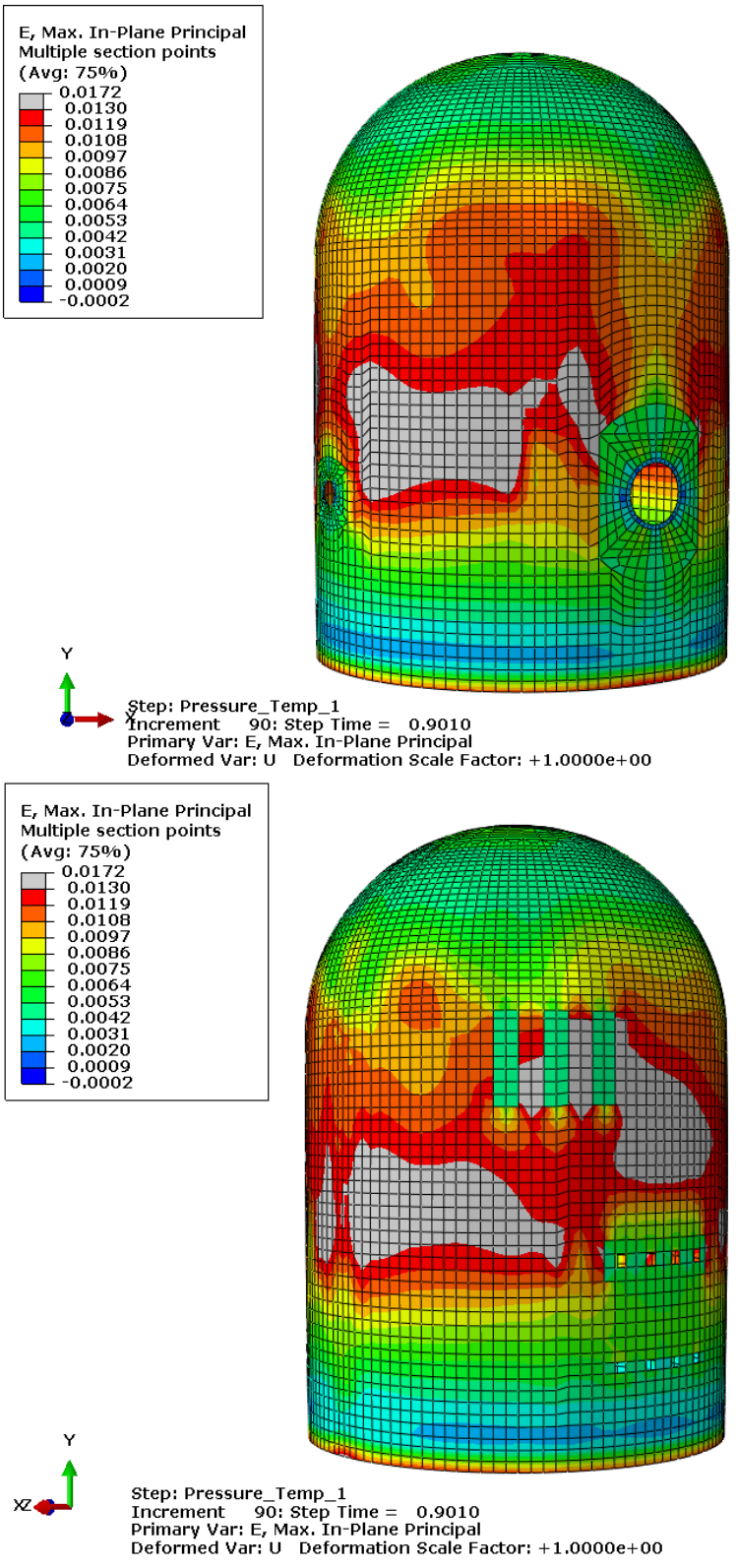

Figure D – 40i: Case 2 max principal strain in liner at 3.6xPd (high contour color limits)

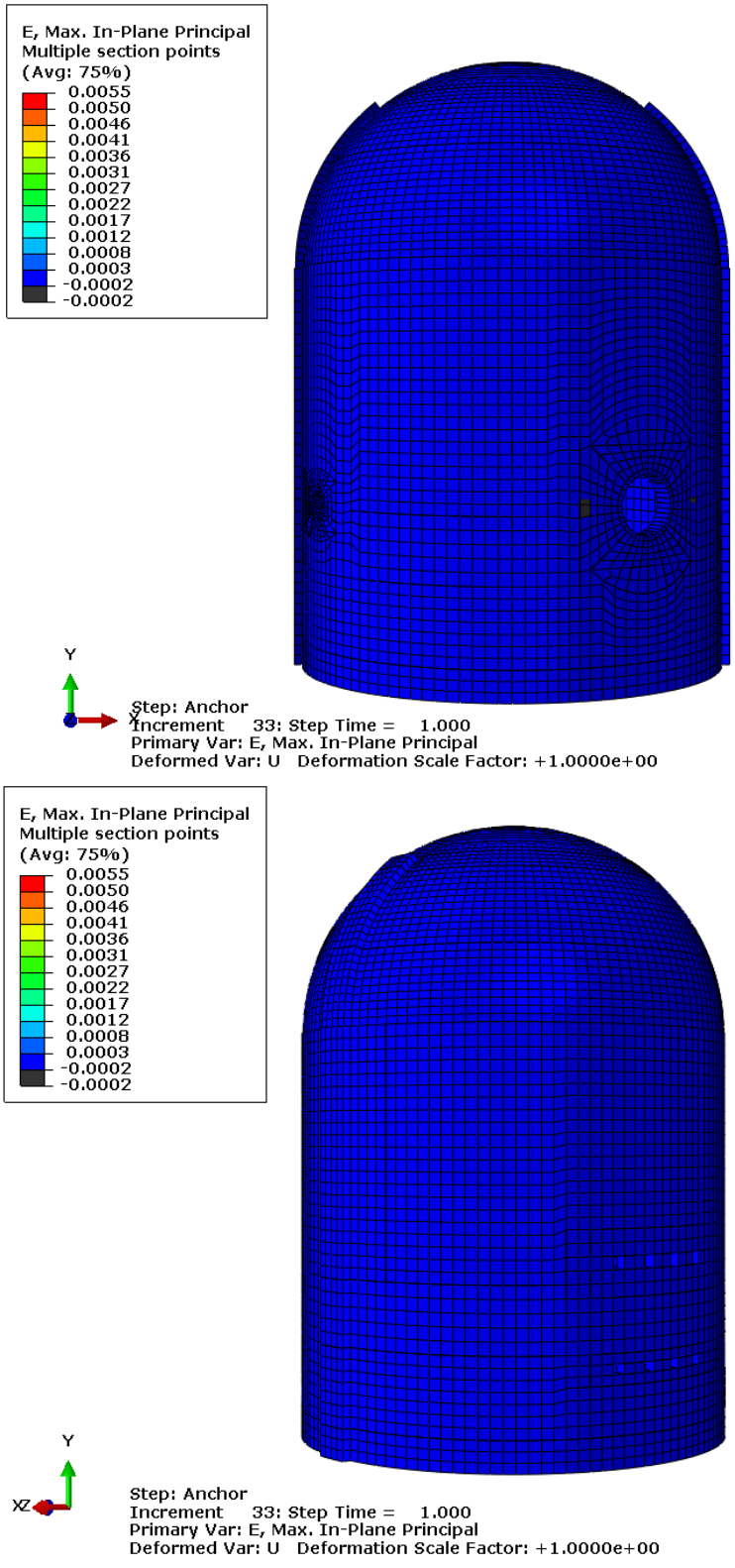

Figure D - 41a: Case 2 max principal membrane strain in concrete after tendon anchorage

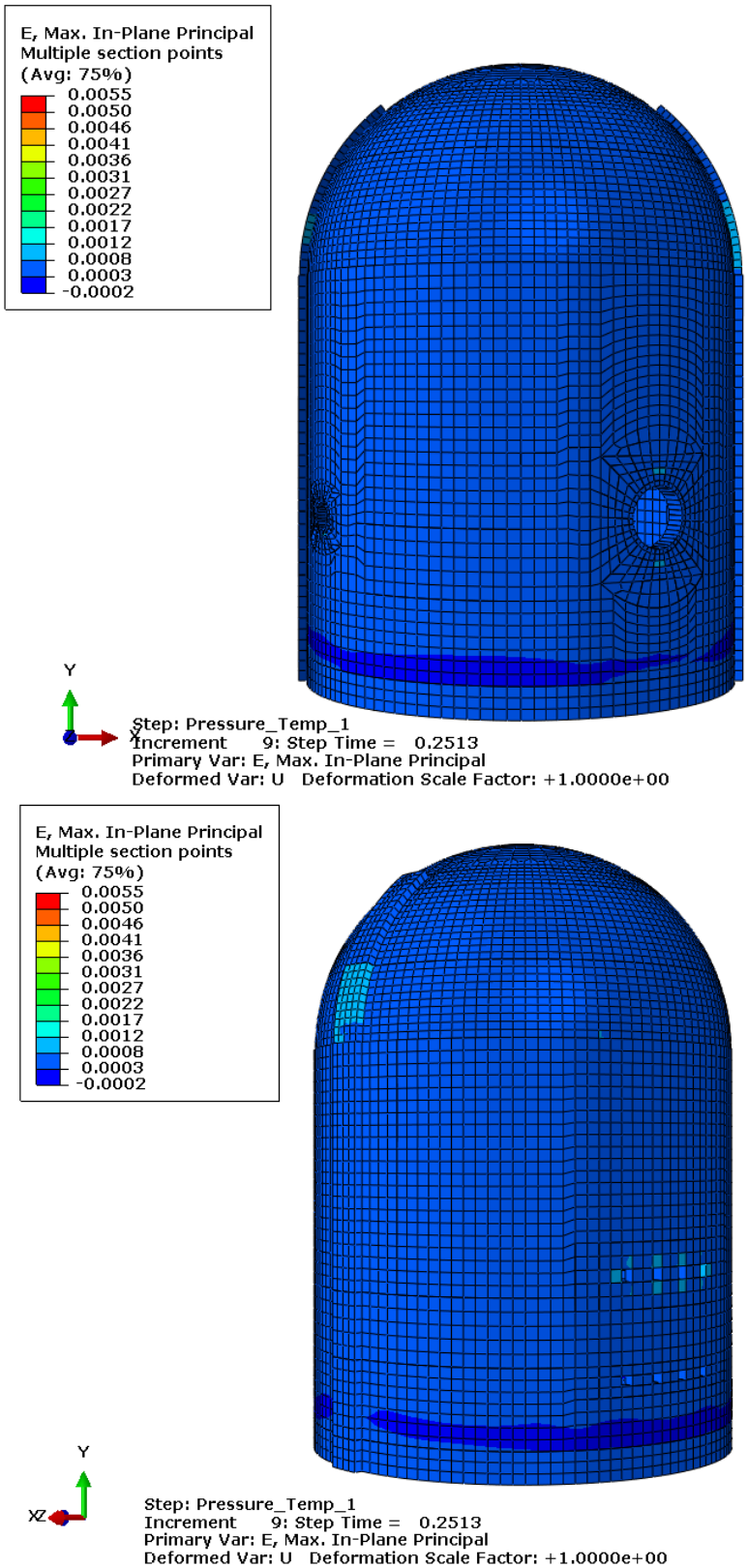

Figure D – 41b: Case 2 max principal membrane strain in concrete at 1.0xPd

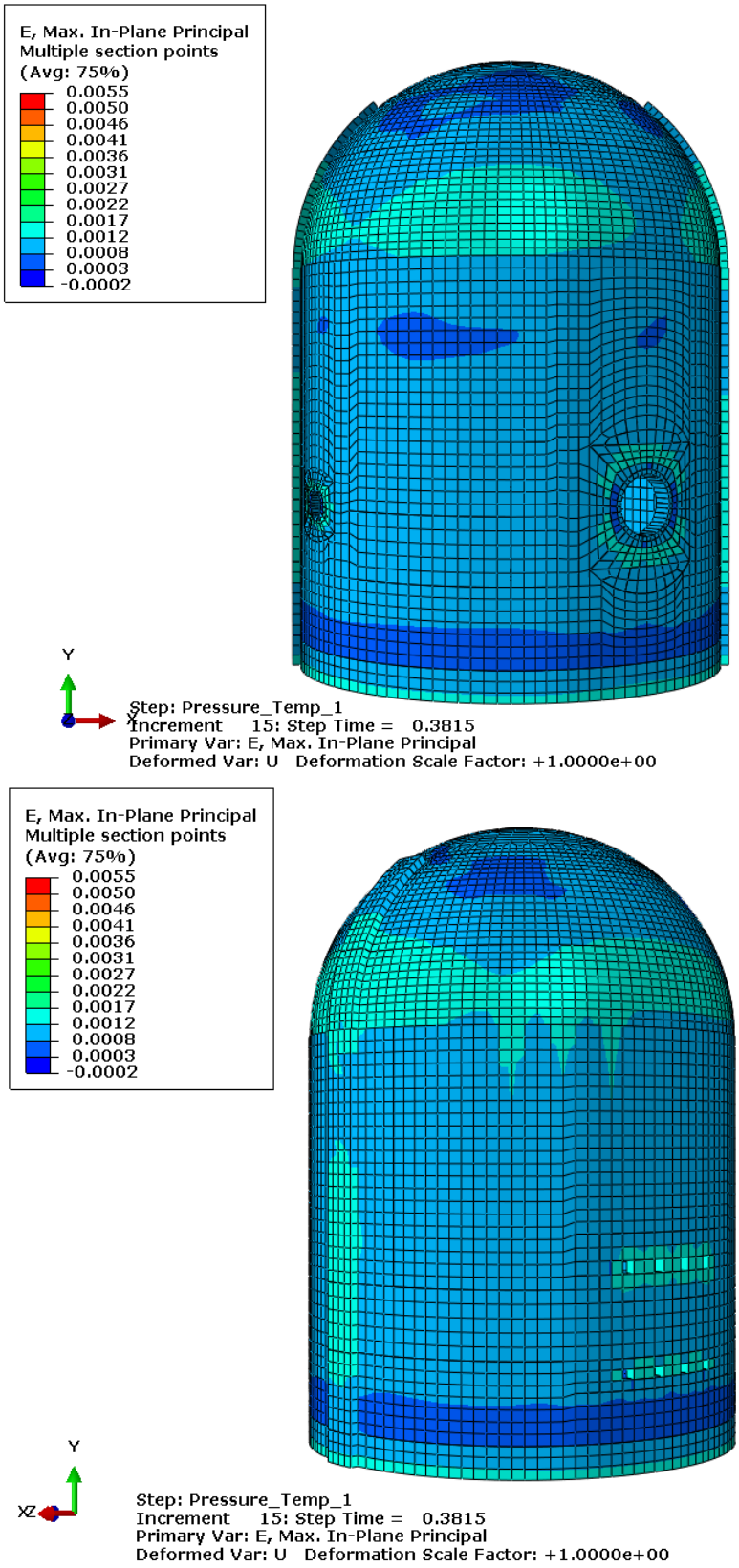

Figure D – 41c: Case 2 max principal membrane strain in concrete at 1.5xPd

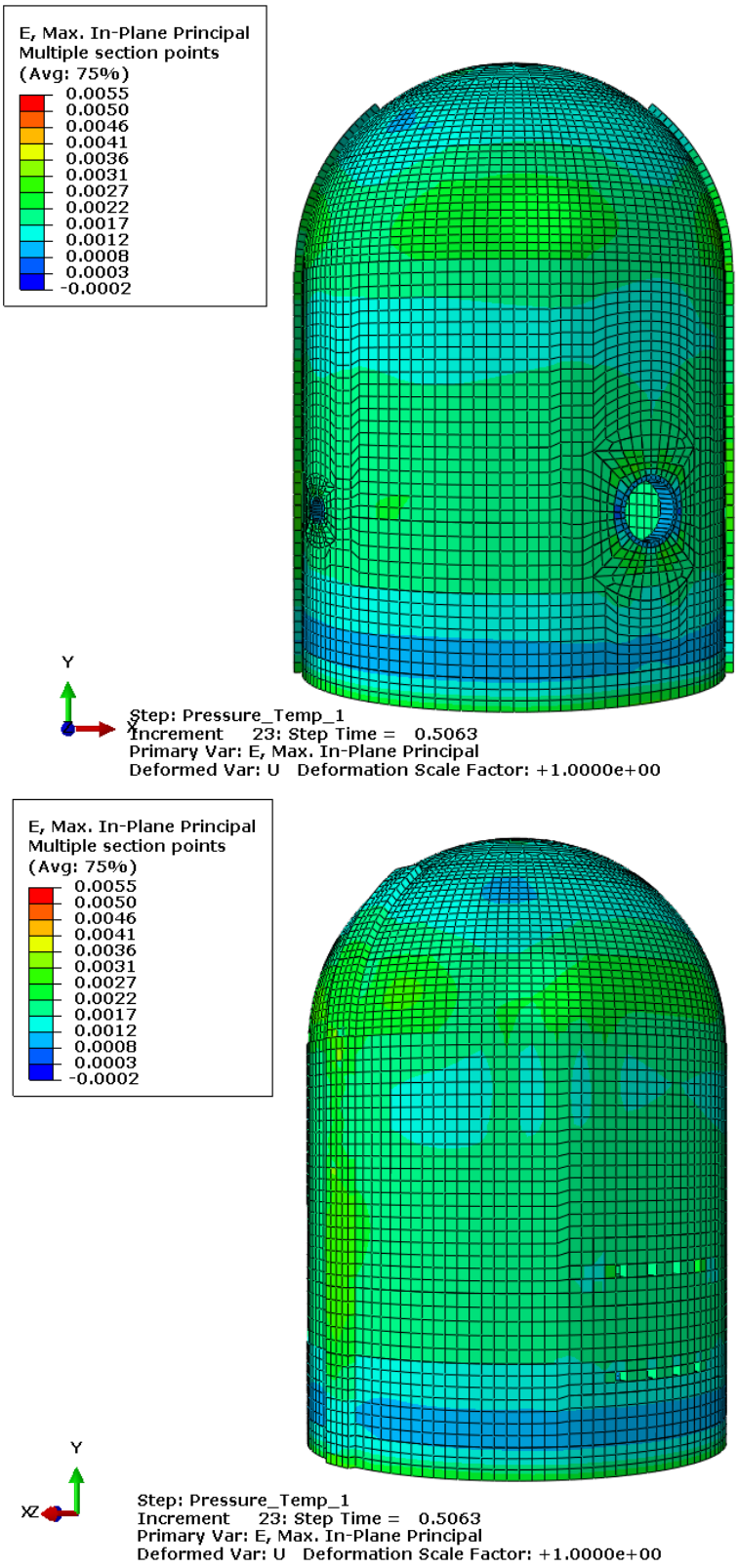

Figure D – 41d: Case 2 max principal membrane strain in concrete at 2.0xPd

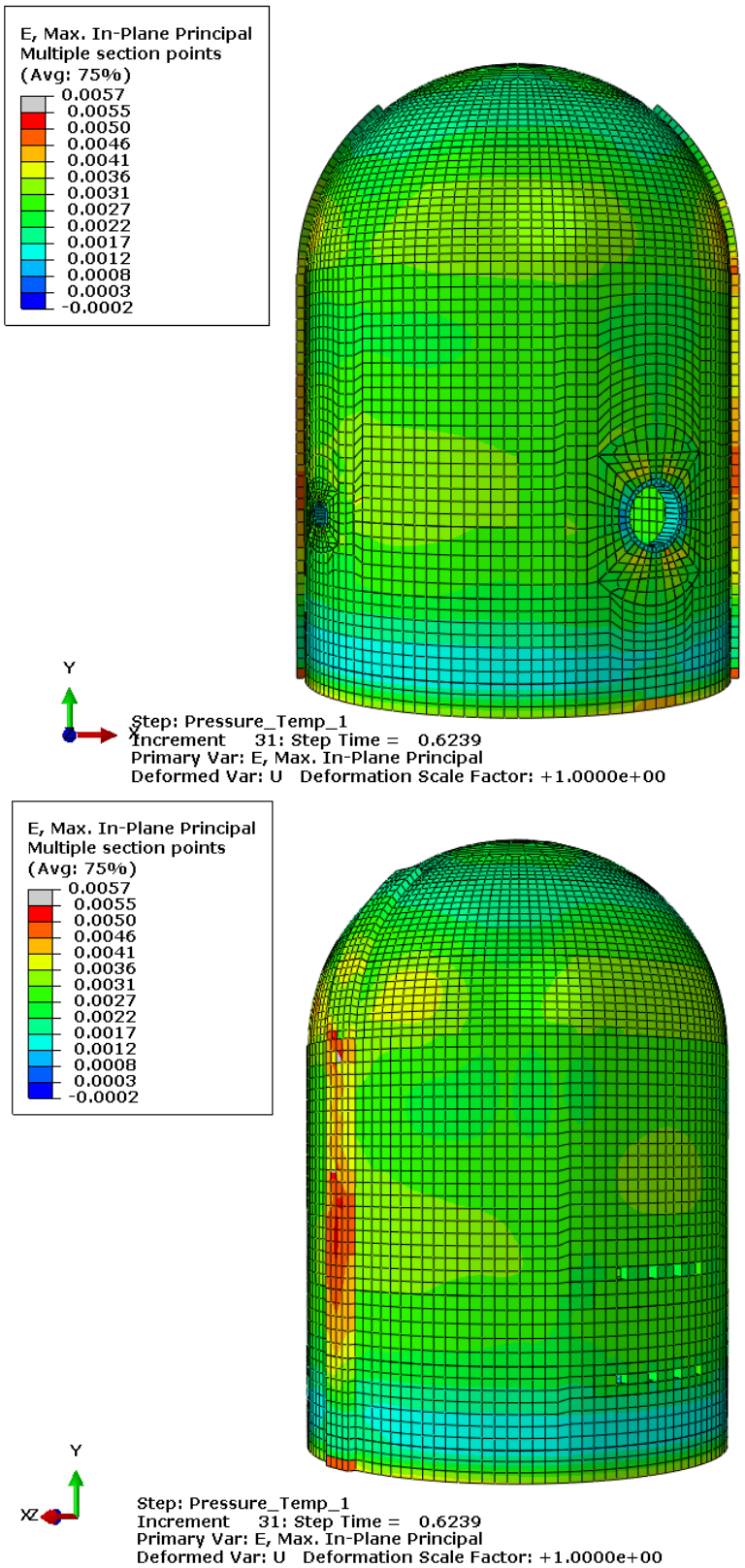

Figure D – 41e: Case 2 max principal membrane strain in concrete at 2.5xPd

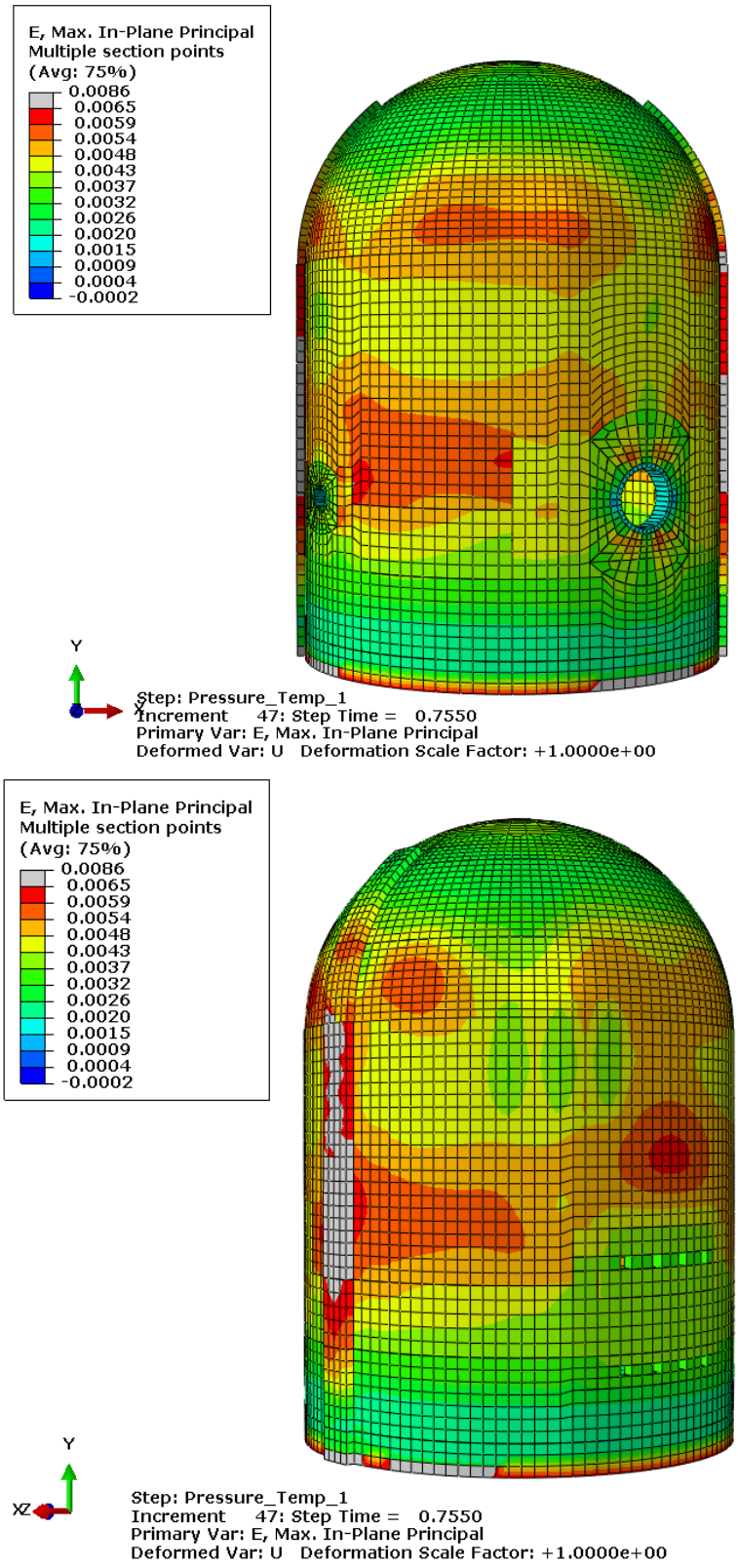

Figure D – 41f: Case 2 max principal membrane strain in concrete at 3.0xPd

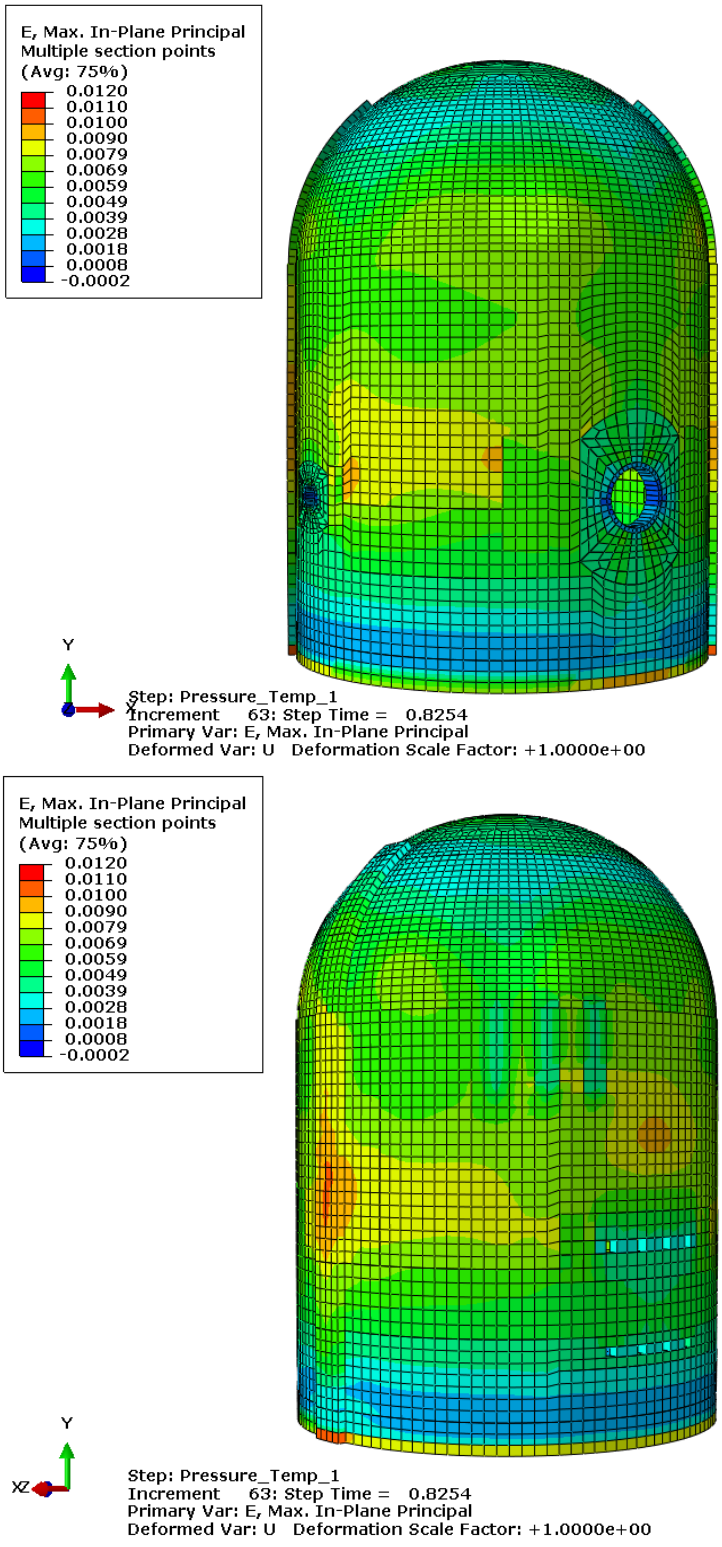

Figure D – 41g: Case 2 max principal membrane strain in concrete at 3.3xPd (high contour color limits)

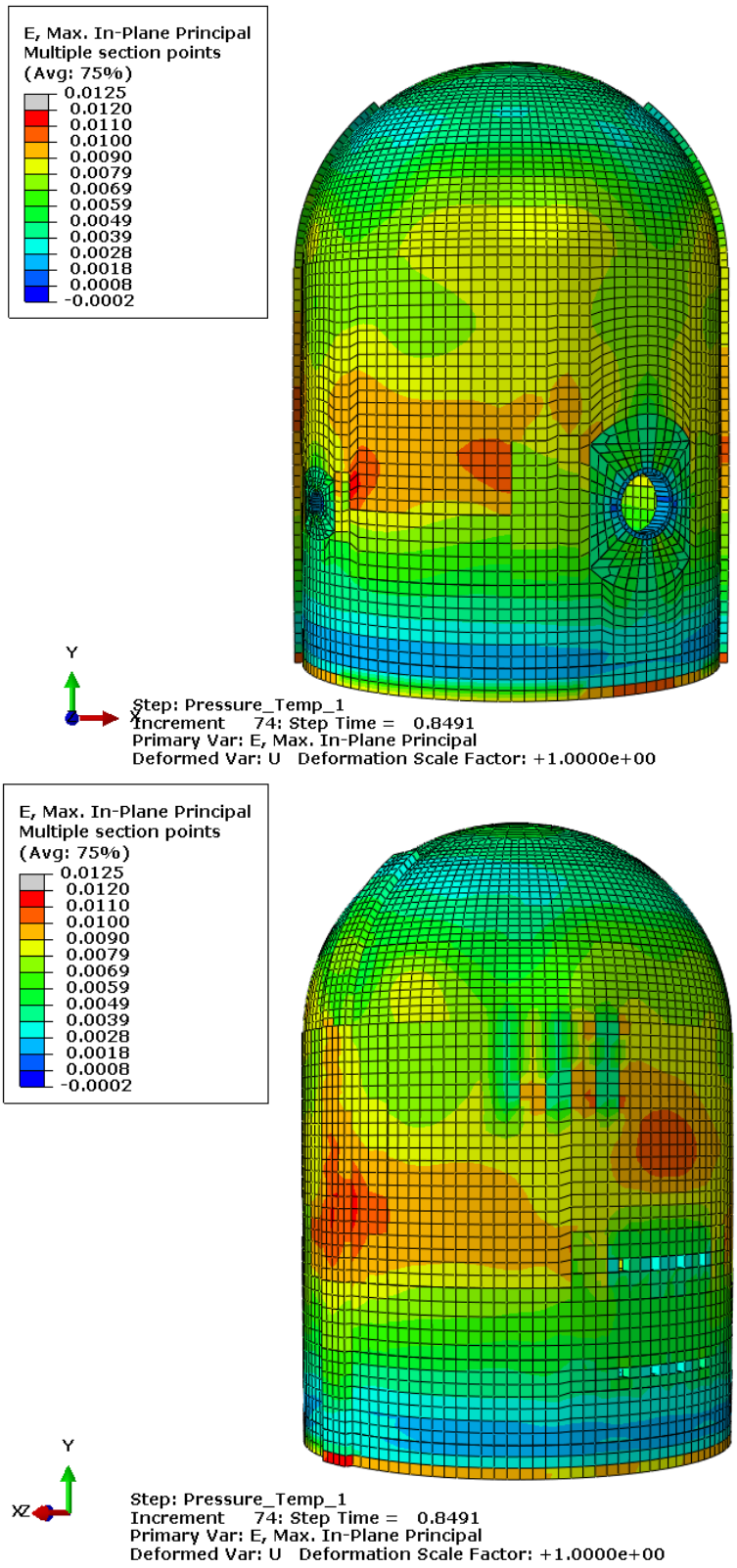

Figure D – 41h: Case 2 max principal membrane strain in concrete at 3.4xPd (high contour color limits)

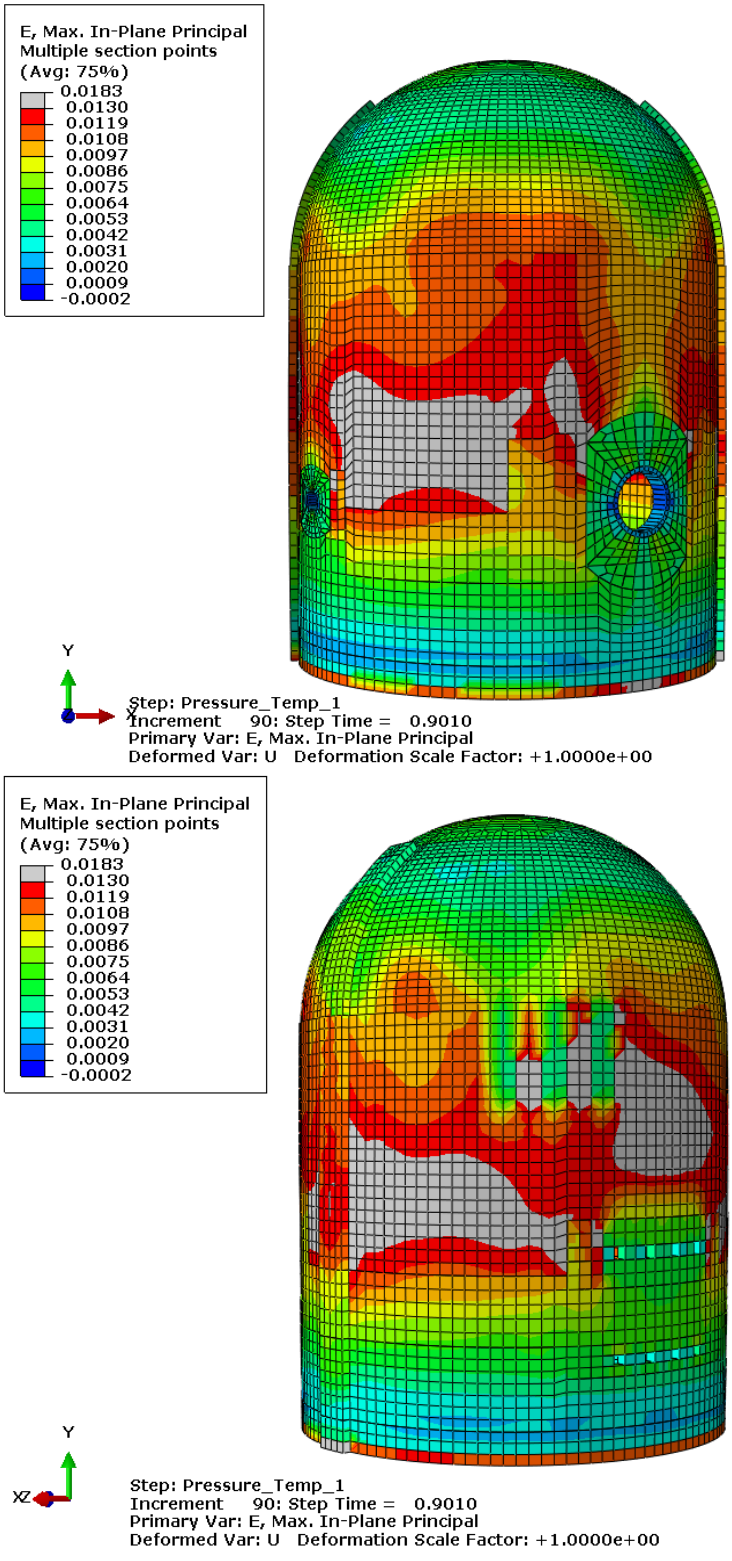

Figure D – 41i: Case 2 max principal membrane strain in concrete at 3.6xPd (high contour color limits)

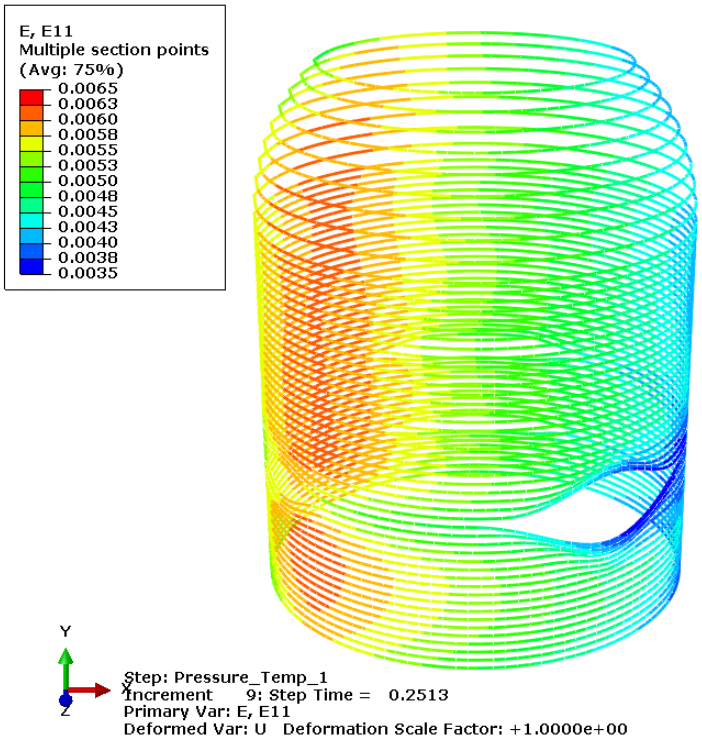

Figure D - 42a: Case 2 strain in hoop tendons anchored at 90° at 1.0 x Pd.

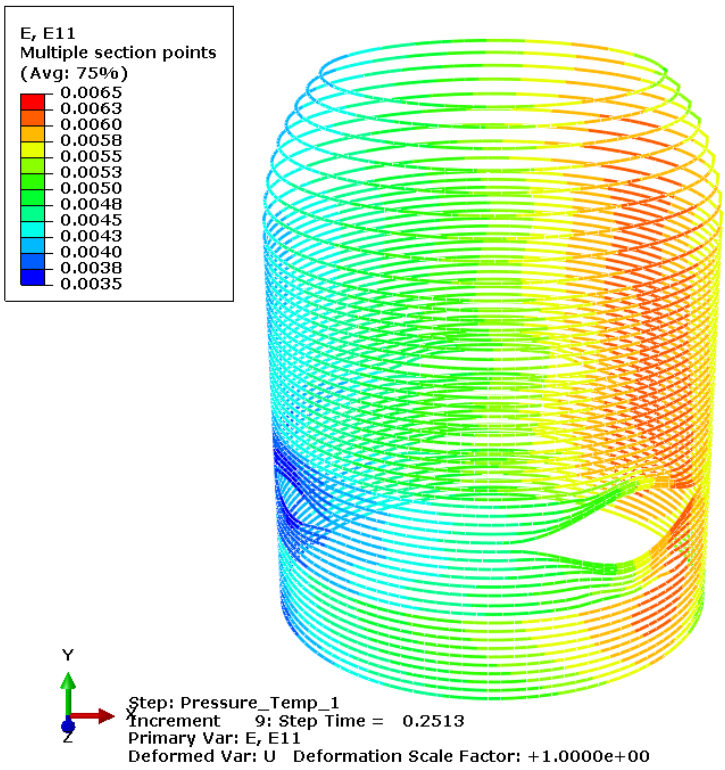

Figure D – 42b: Case 2 strain in hoop tendons anchored at 270° at 1.0 x Pd.

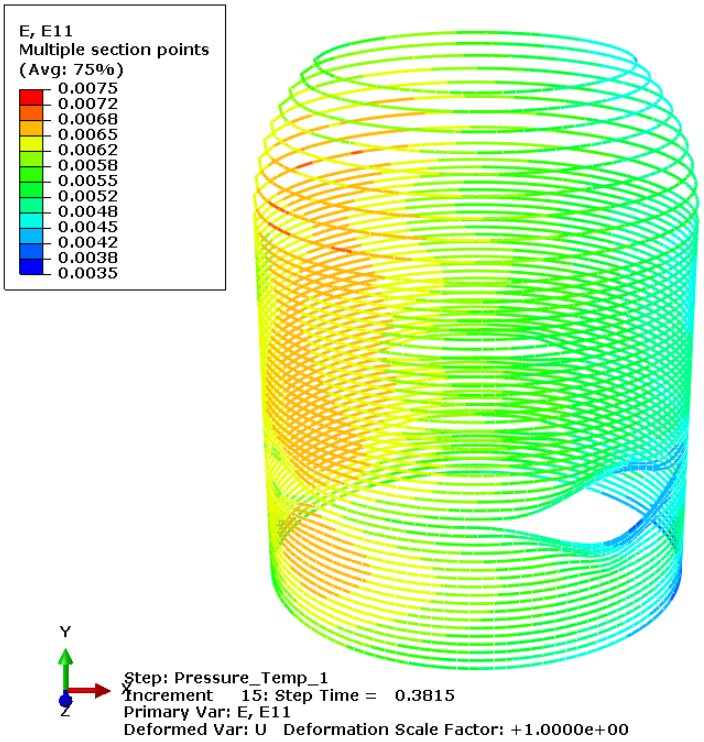

Figure D – 42c: Case 2 strain in hoop tendons anchored at 90° at 1.5 x Pd.

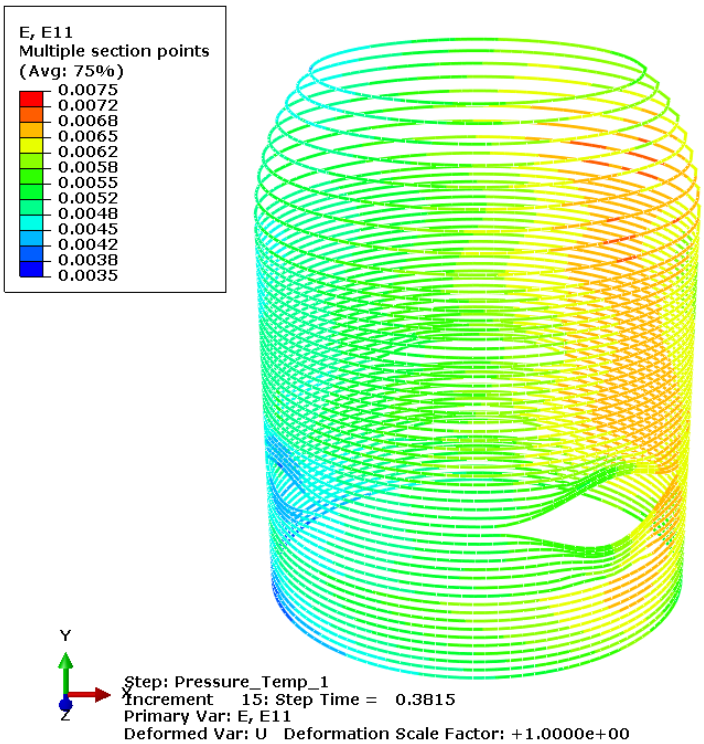

Figure D – 42d: Case 2 strain in hoop tendons anchored at 270° at 1.5 x Pd.

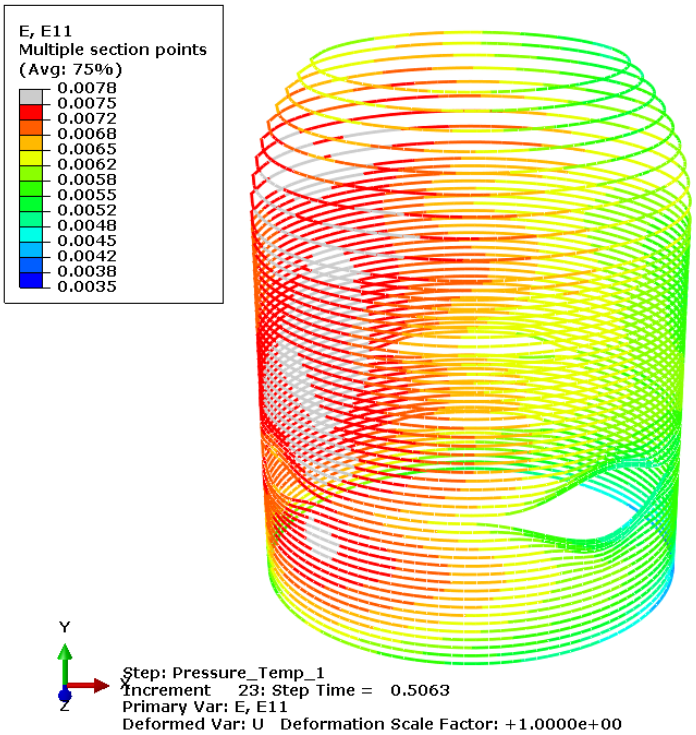

Figure D – 42e: Case 2 strain in hoop tendons anchored at 90° at 2.0 x Pd.

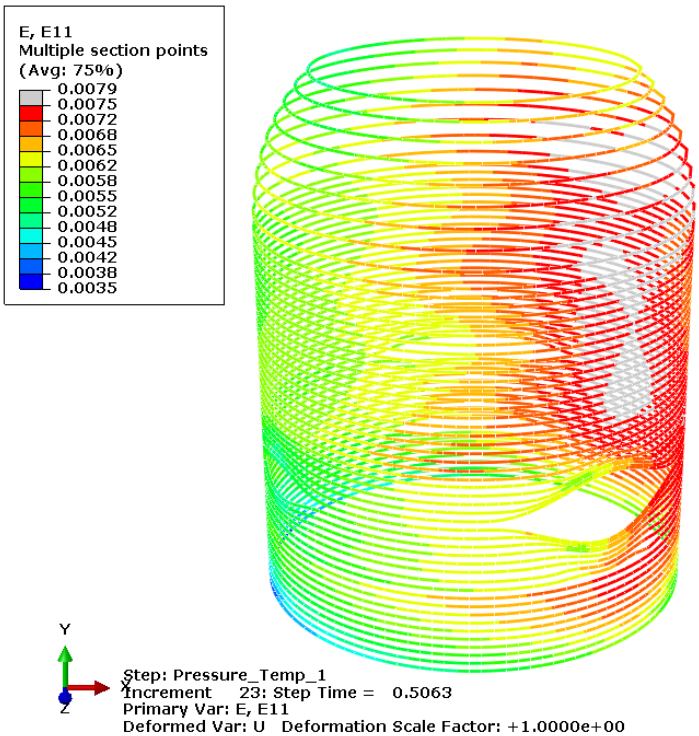

Figure D – 42f: Case 2 strain in hoop tendons anchored at 270° at 2.0 x Pd.

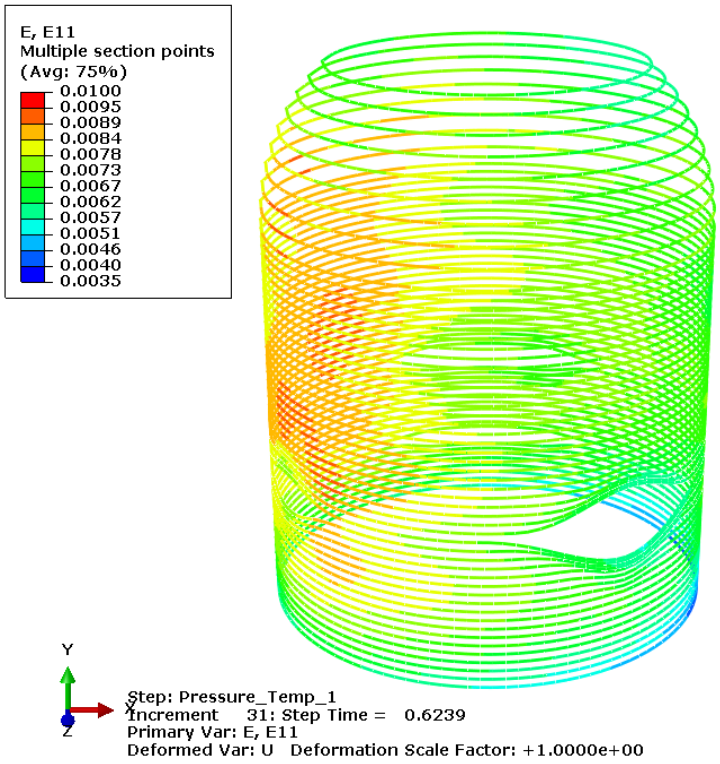

Figure D – 42g: Case 2 strain in hoop tendons anchored at 90° at 2.5 x Pd.

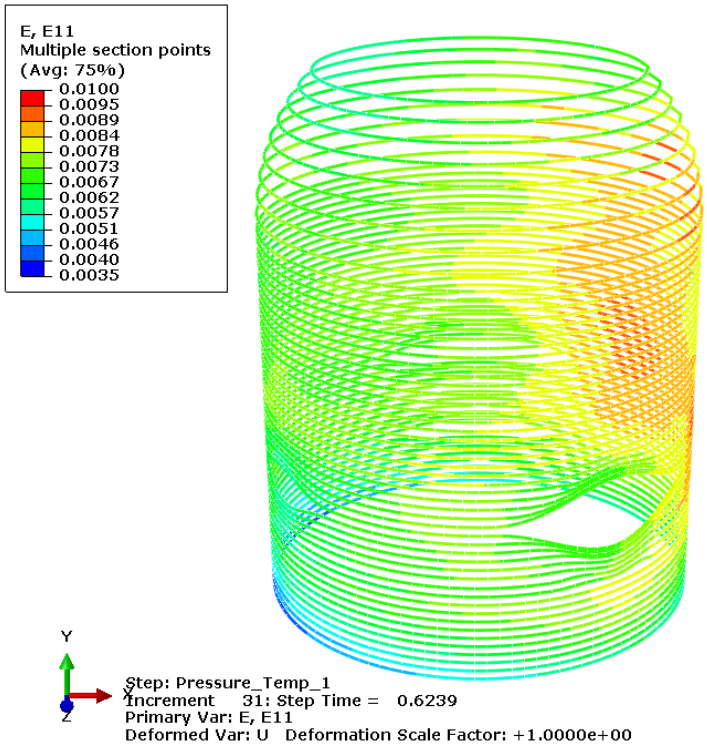

Figure D – 42h: Case 2 strain in hoop tendons anchored at 270° at 2.5 x Pd.

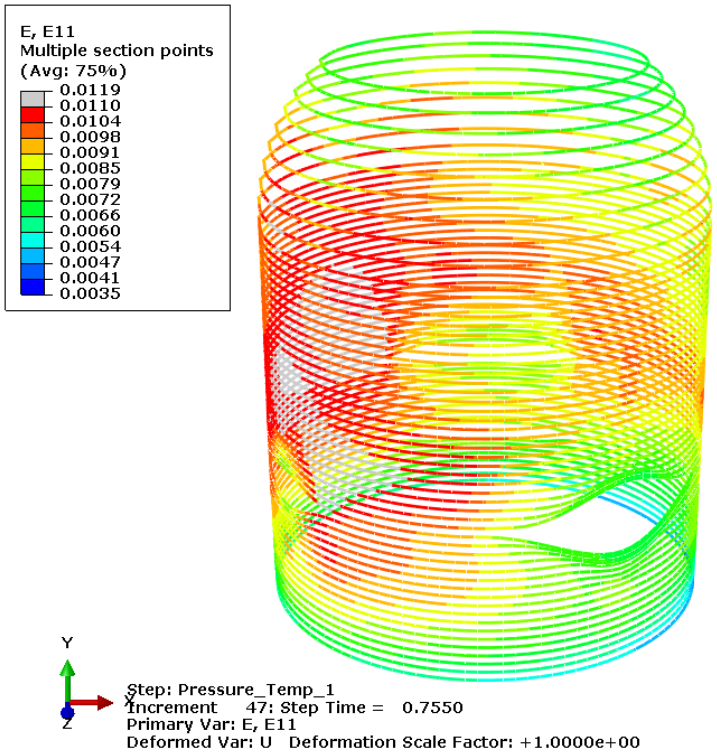

Figure D – 42i: Case 2 strain in hoop tendons anchored at 90° at 3.0 x Pd.

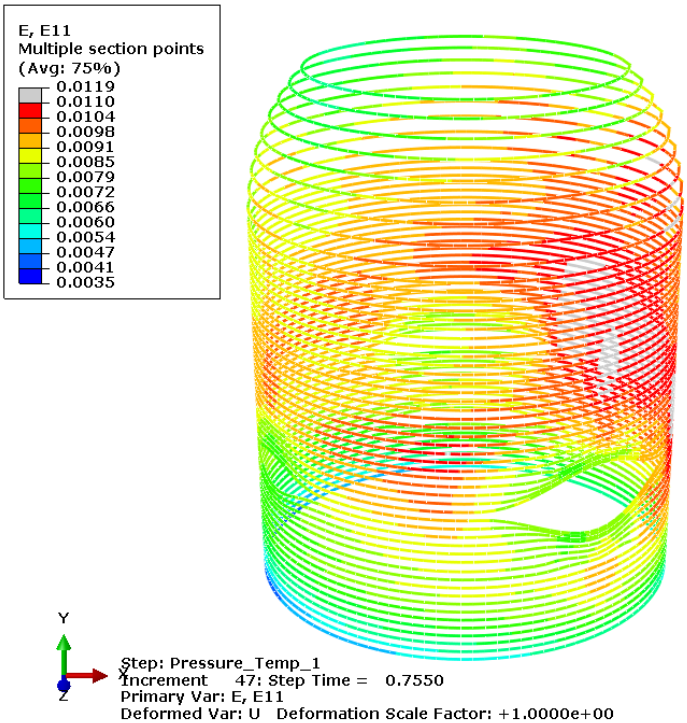

Figure D – 42j: Case 2 strain in hoop tendons anchored at 270° at 3.0 x Pd.

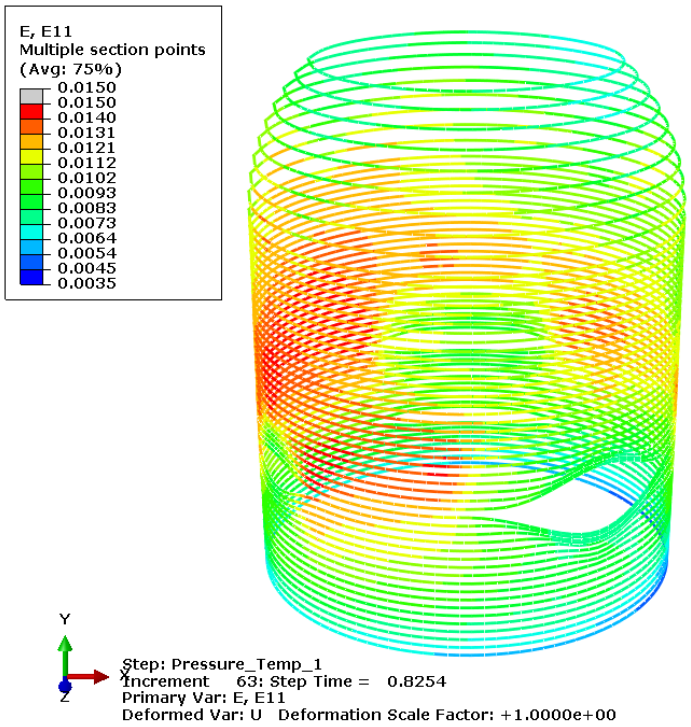

Figure D – 42k: Case 2 strain in hoop tendons anchored at 90° at 3.3 x Pd.

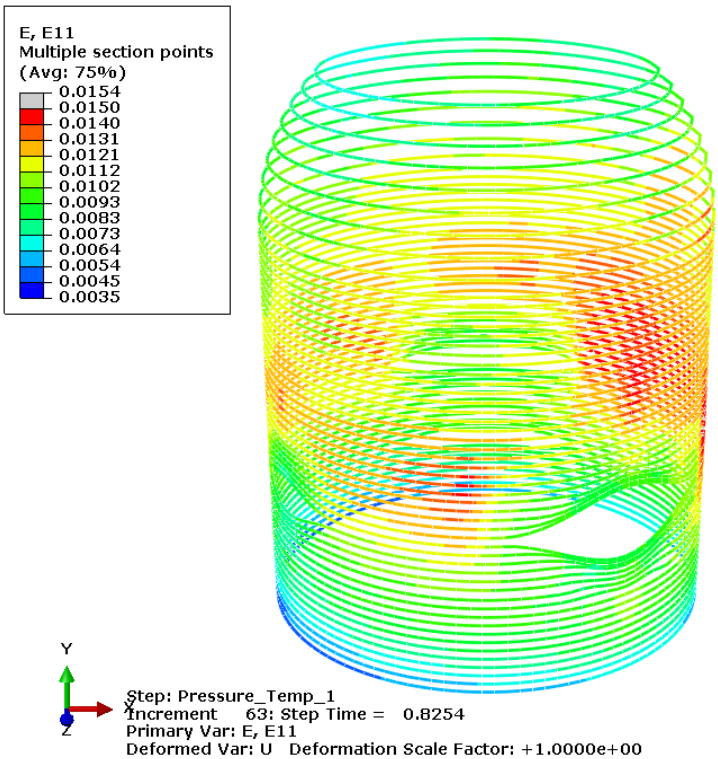

Figure D – 42l: Case 2 strain in hoop tendons anchored at 270° at 3.3 x Pd.

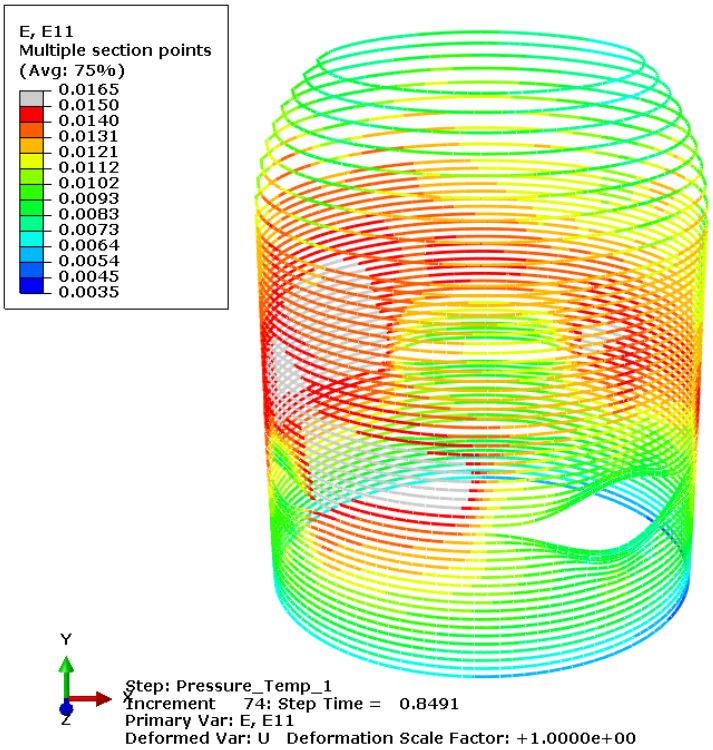

Figure D – 42m: Case 2 strain in hoop tendons anchored at 90° at 3.4 x Pd.

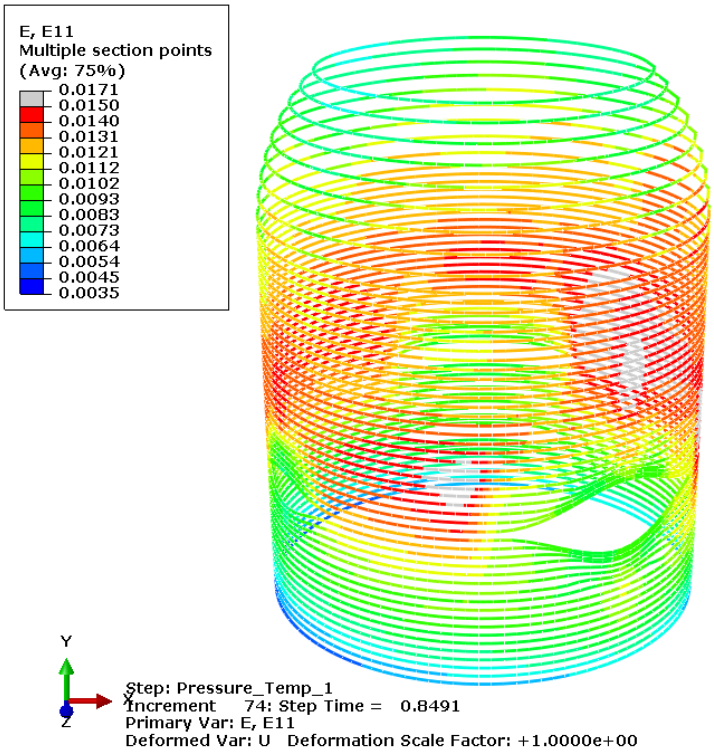

Figure D – 42n: Case 2 strain in hoop tendons anchored at 270° at 3.4 x Pd.

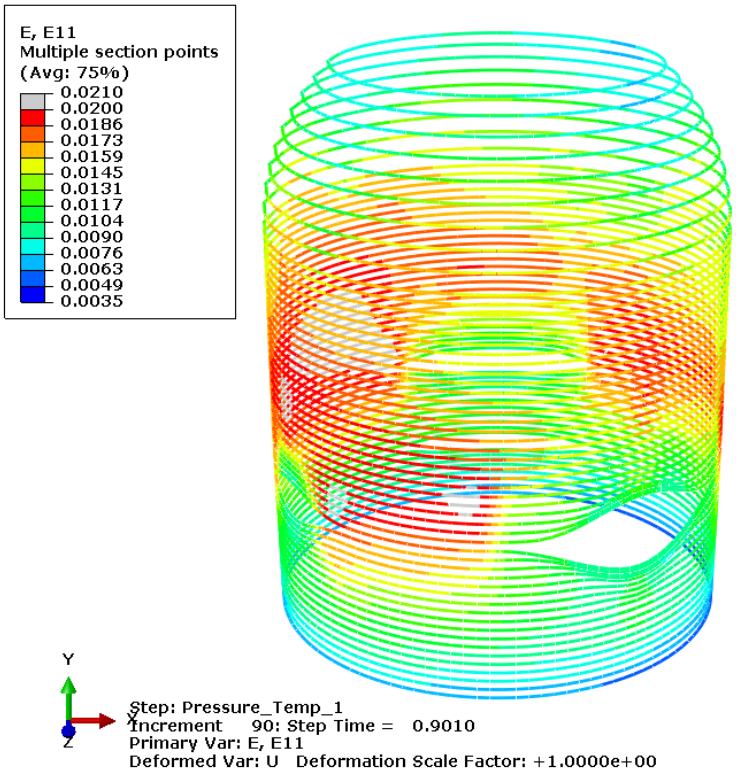

Figure D – 42o: Case 2 strain in hoop tendons anchored at 90° at 3.6 x Pd.

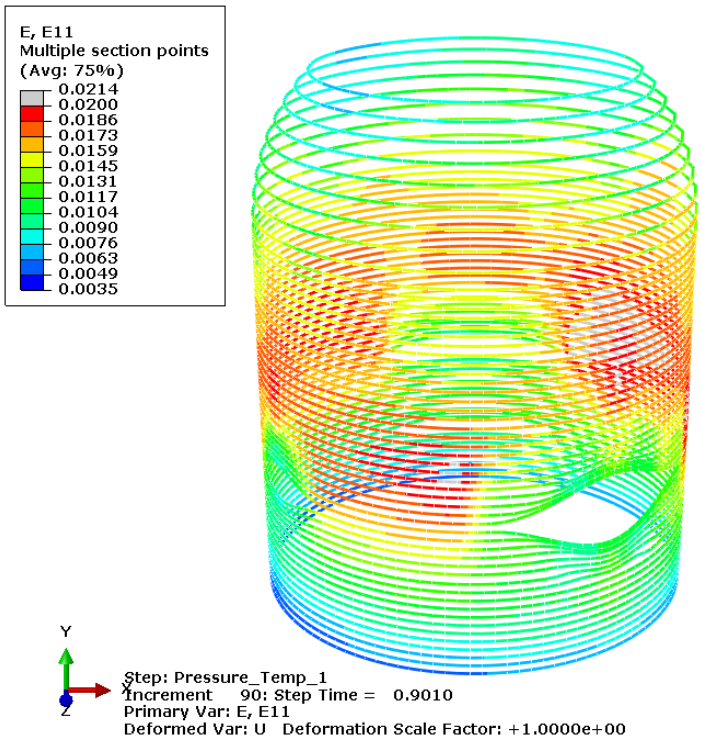

Figure D – 42p: Case 2 strain in hoop tendons anchored at 270° at 3.6 x Pd.

Figures D-43 through D-46 show strains over selected gage lengths near the penetrations, as requested of the analysts in the SPE instructions. The reference frame defining these locations was shown in Figure 9 of the Model 2 Report.

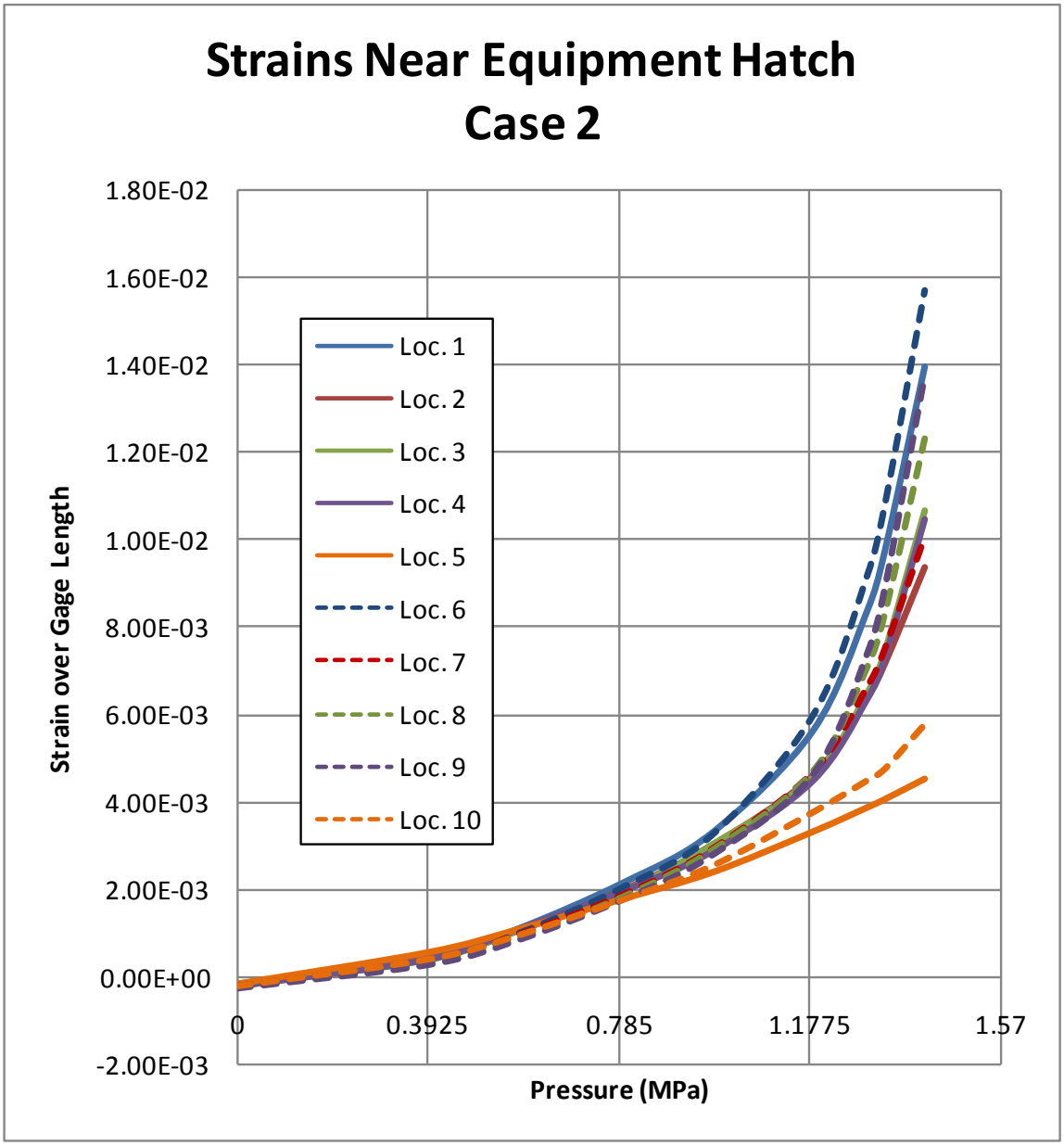

Figure D - 43: Case 2 strains over selected gage length near E/H

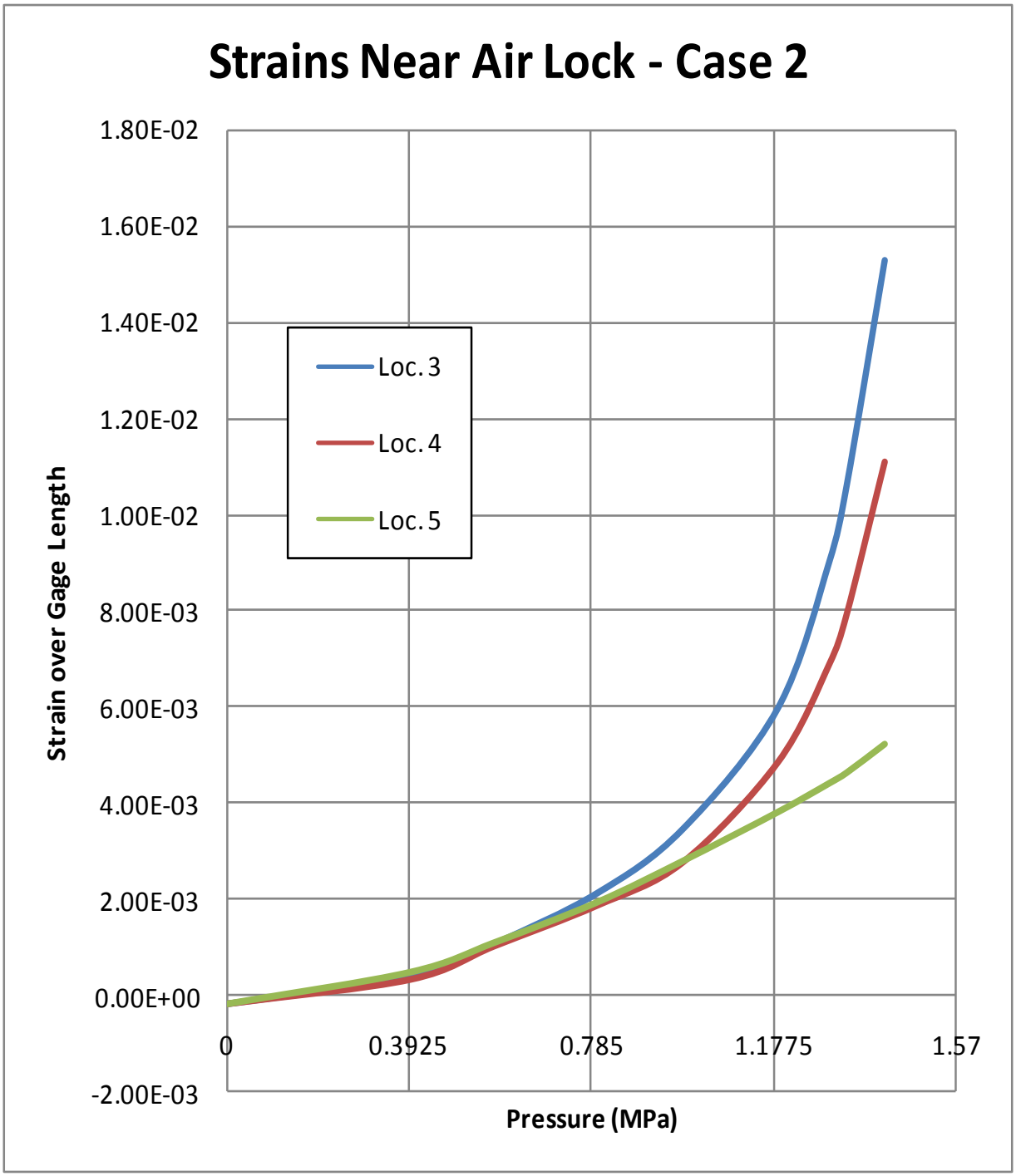

Figure D - 44: Case 2 strains over selected gage length near A/L

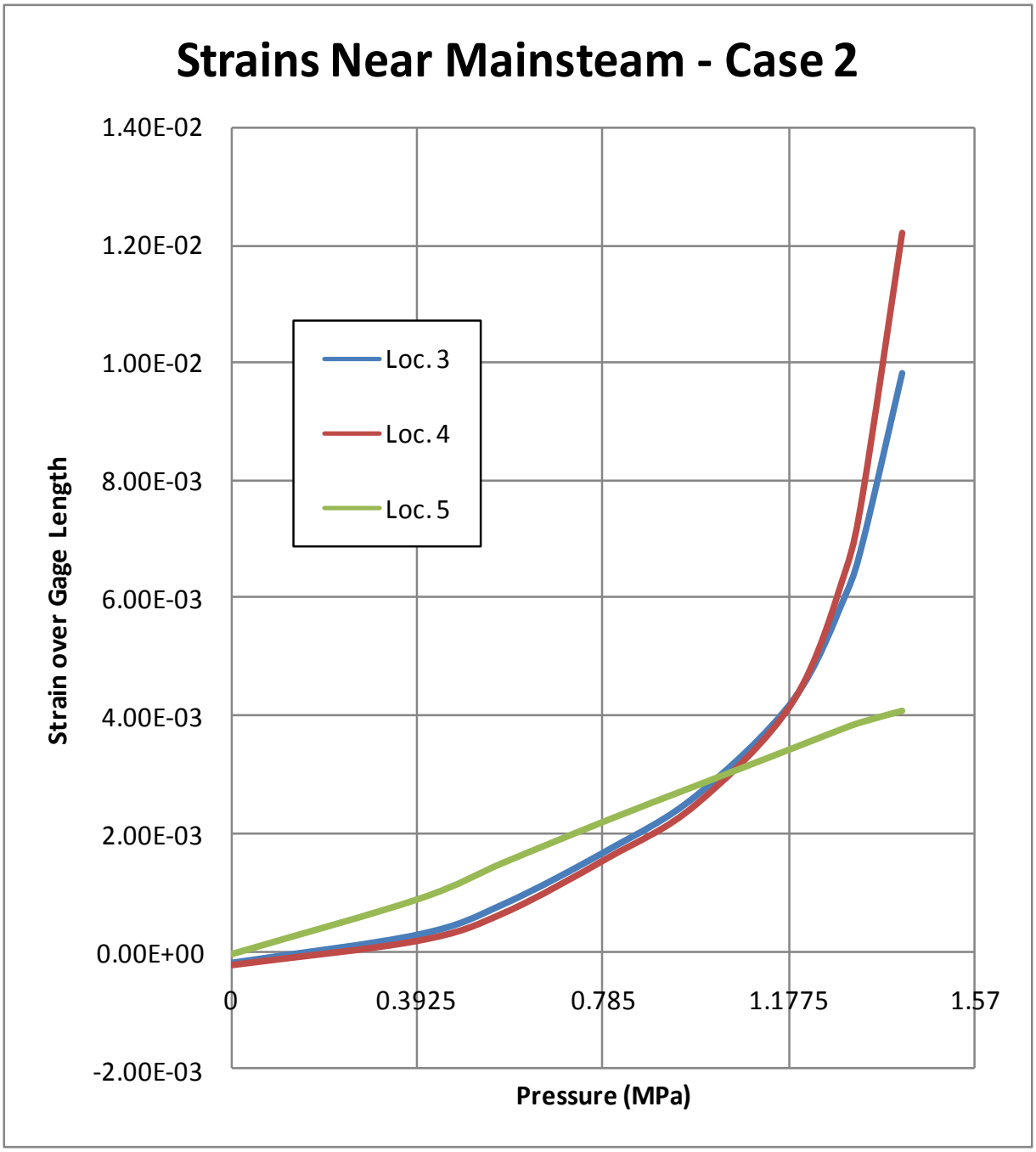

Figure D - 45: Case 2 strains over selected gage length near M/S

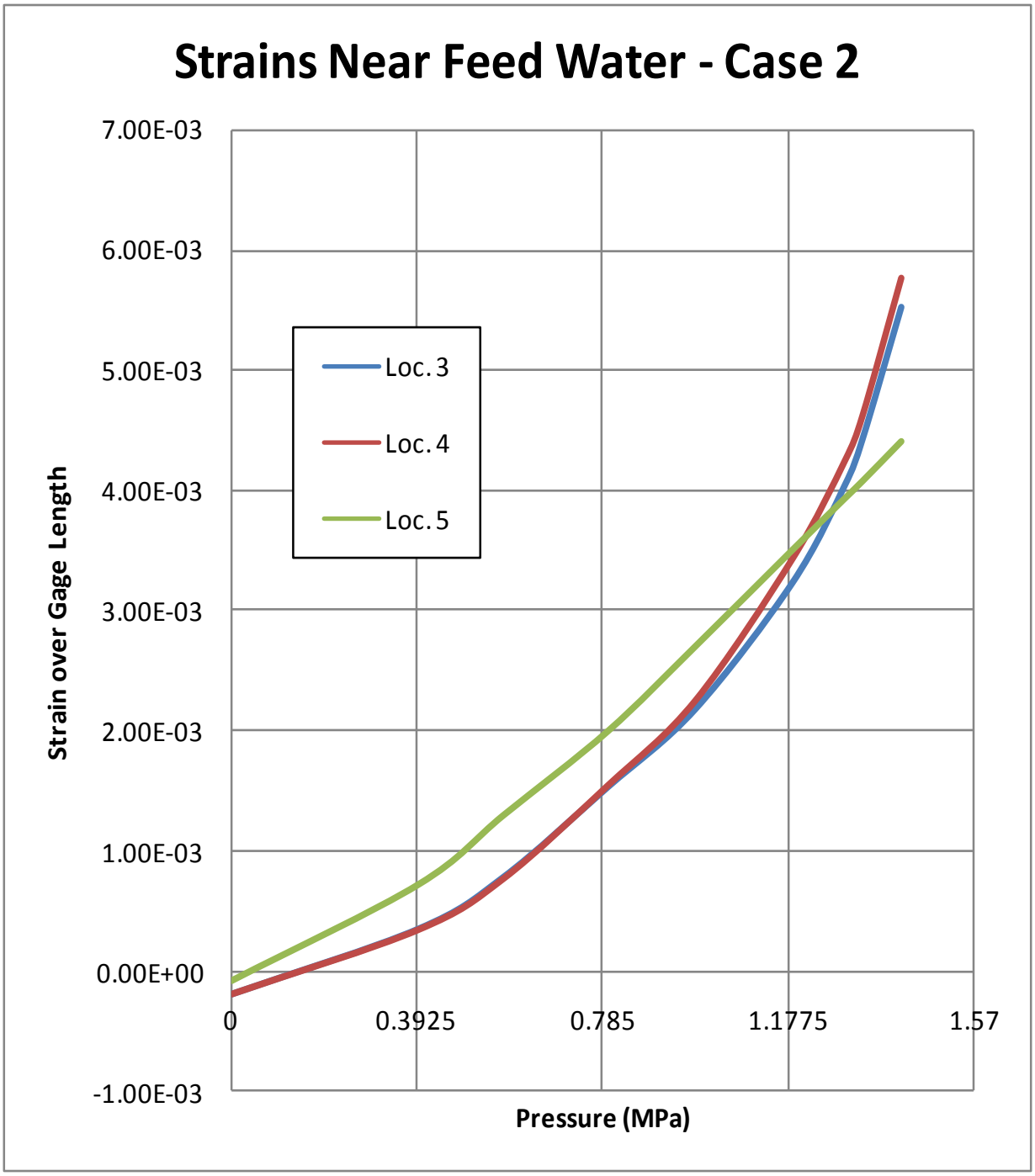

Figure D - 46: Case 2 strains over selected gage length near F/W

Figures D-47a through D-48b show tendon stress profiles for the most comprehensively instrumented tendons in the 1:4 Scale PCCV model test.

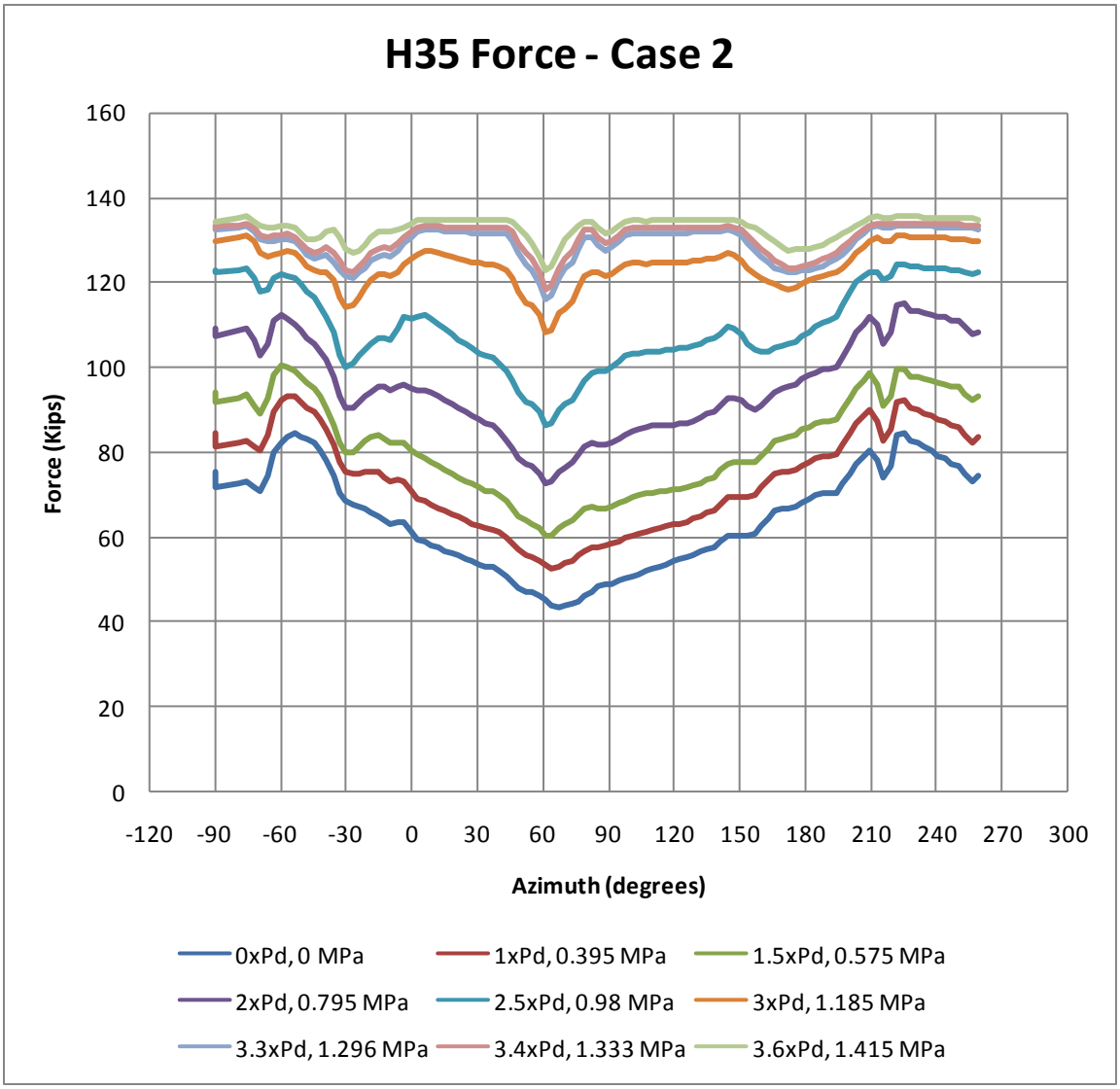

Figure D - 47a: Case 2 Abaqus analysis – hoop tendon H35 force

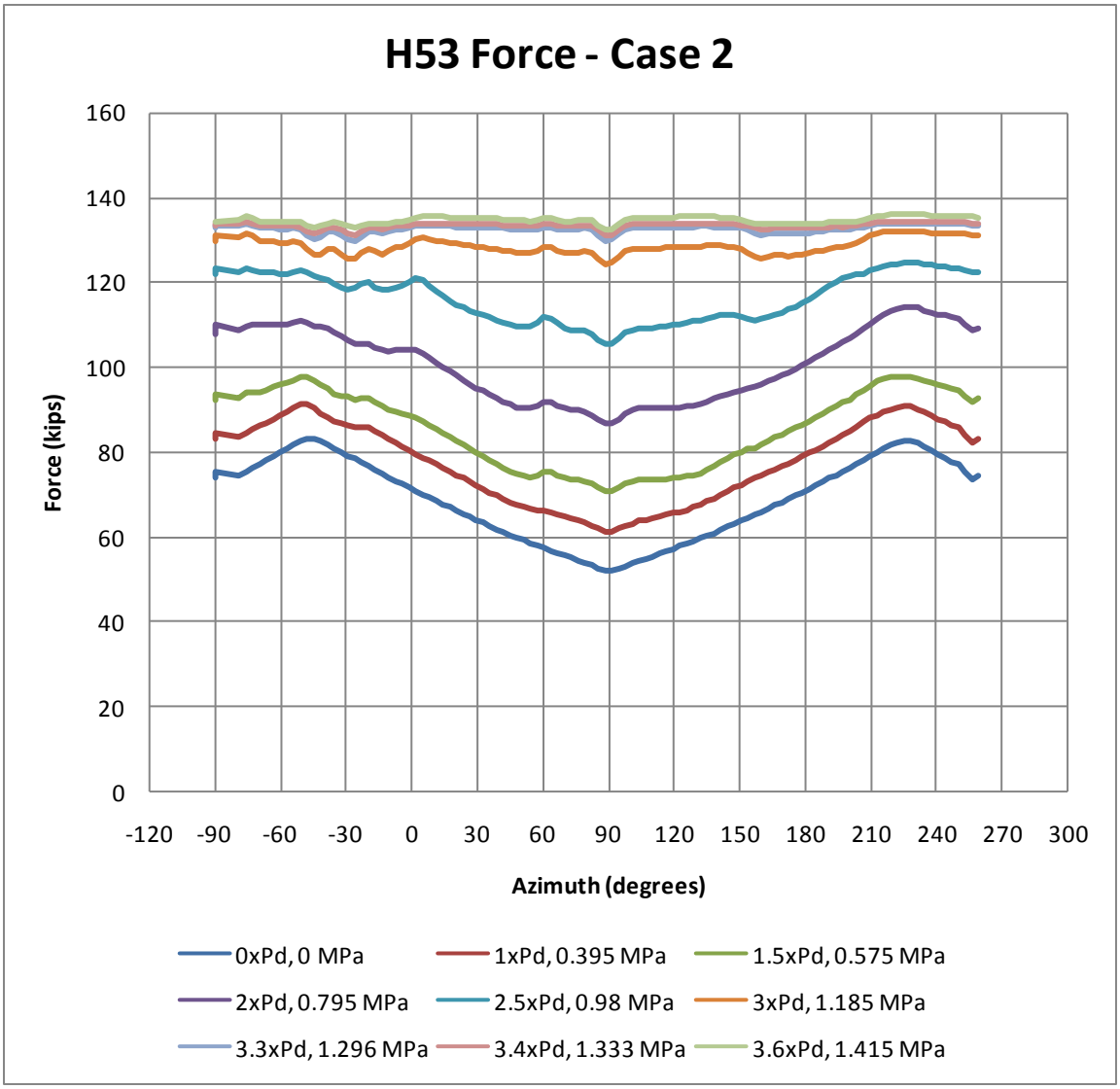

Figure D – 47b: Case 2 Abaqus analysis – hoop tendon H53 force

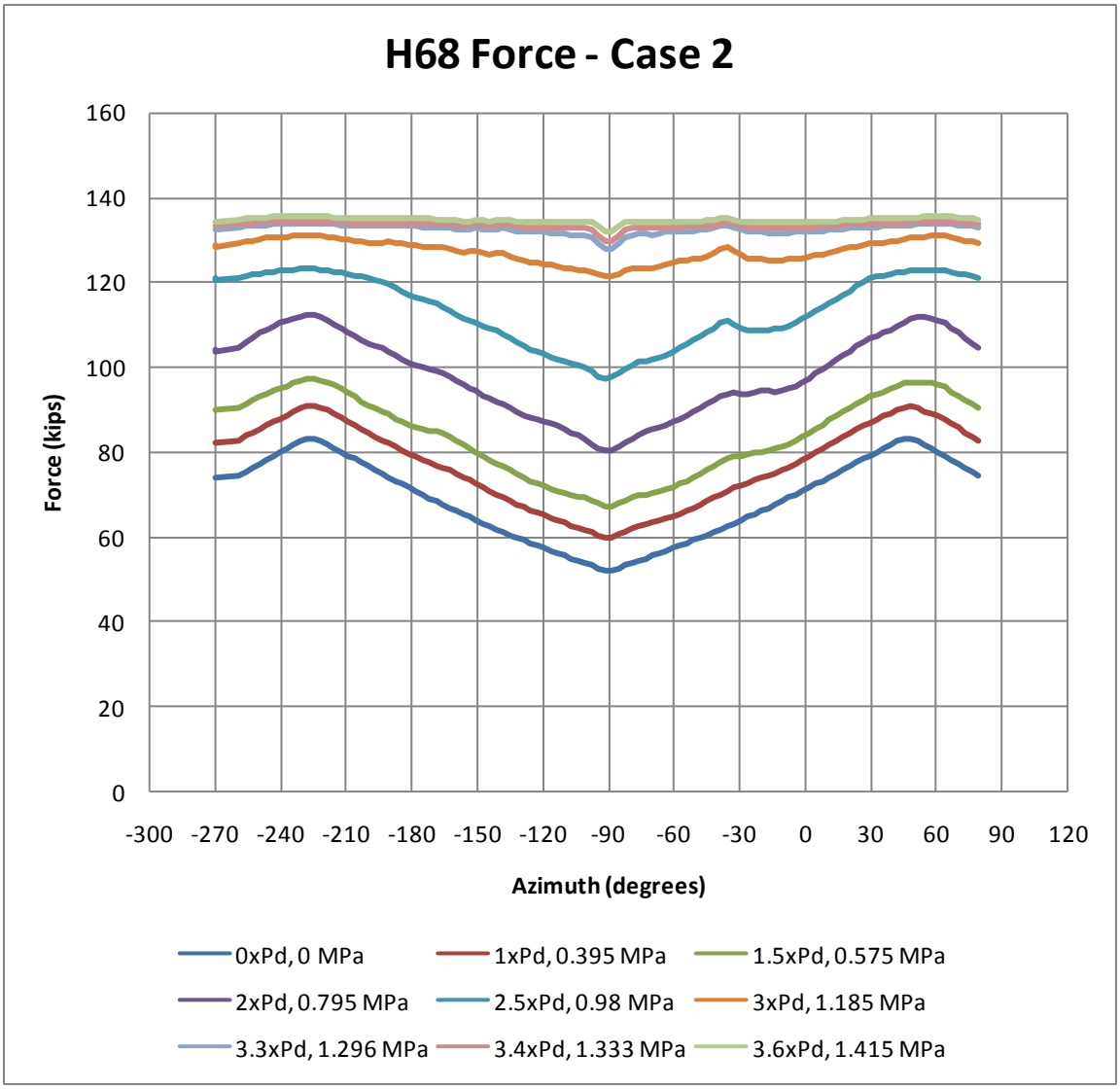

Figure D – 47c: Case 2 Abaqus analysis – hoop tendon H68 force

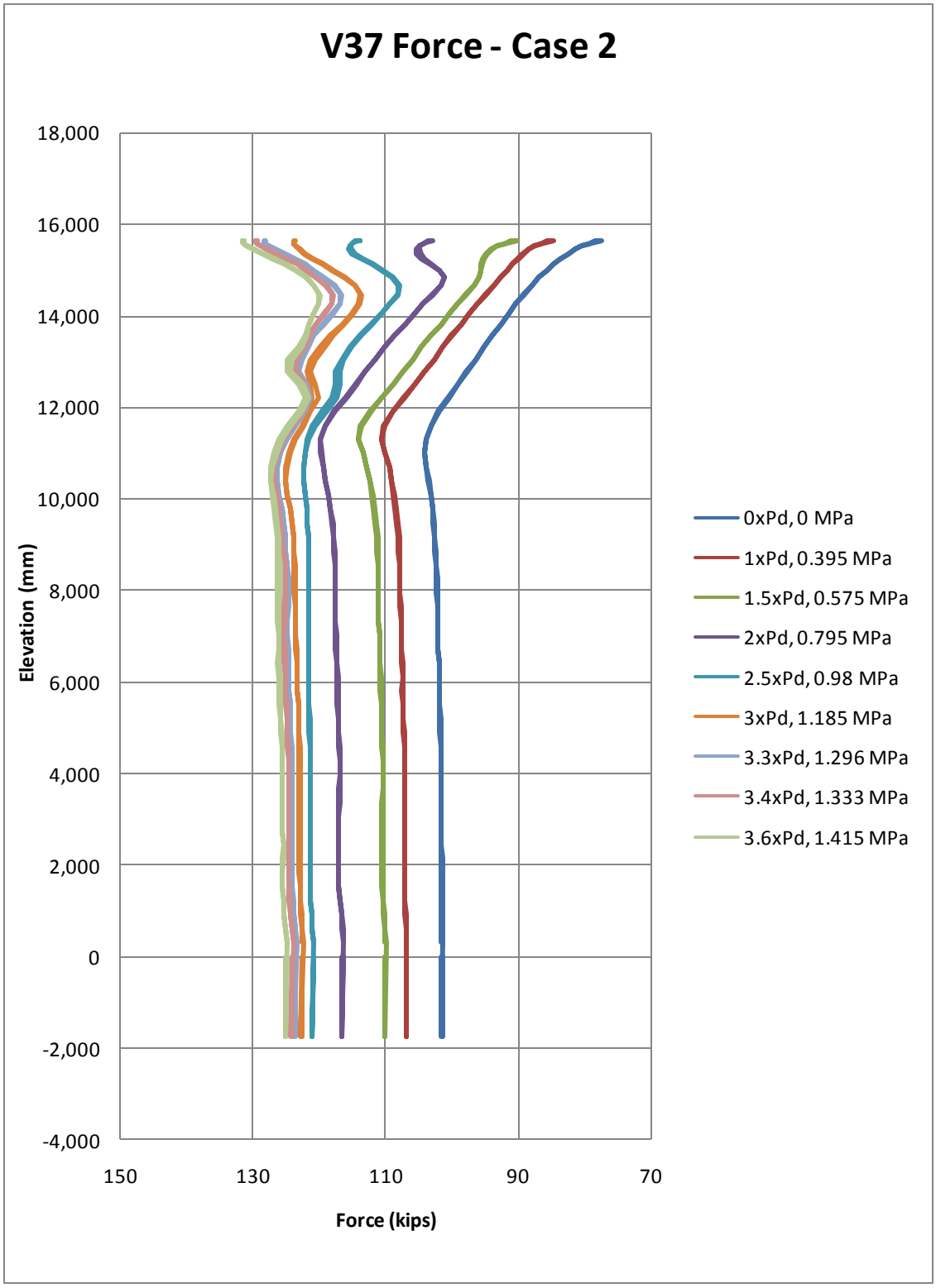

Figure D - 48a: Case 2 Abaqus analysis – hairpin tendon V37 force

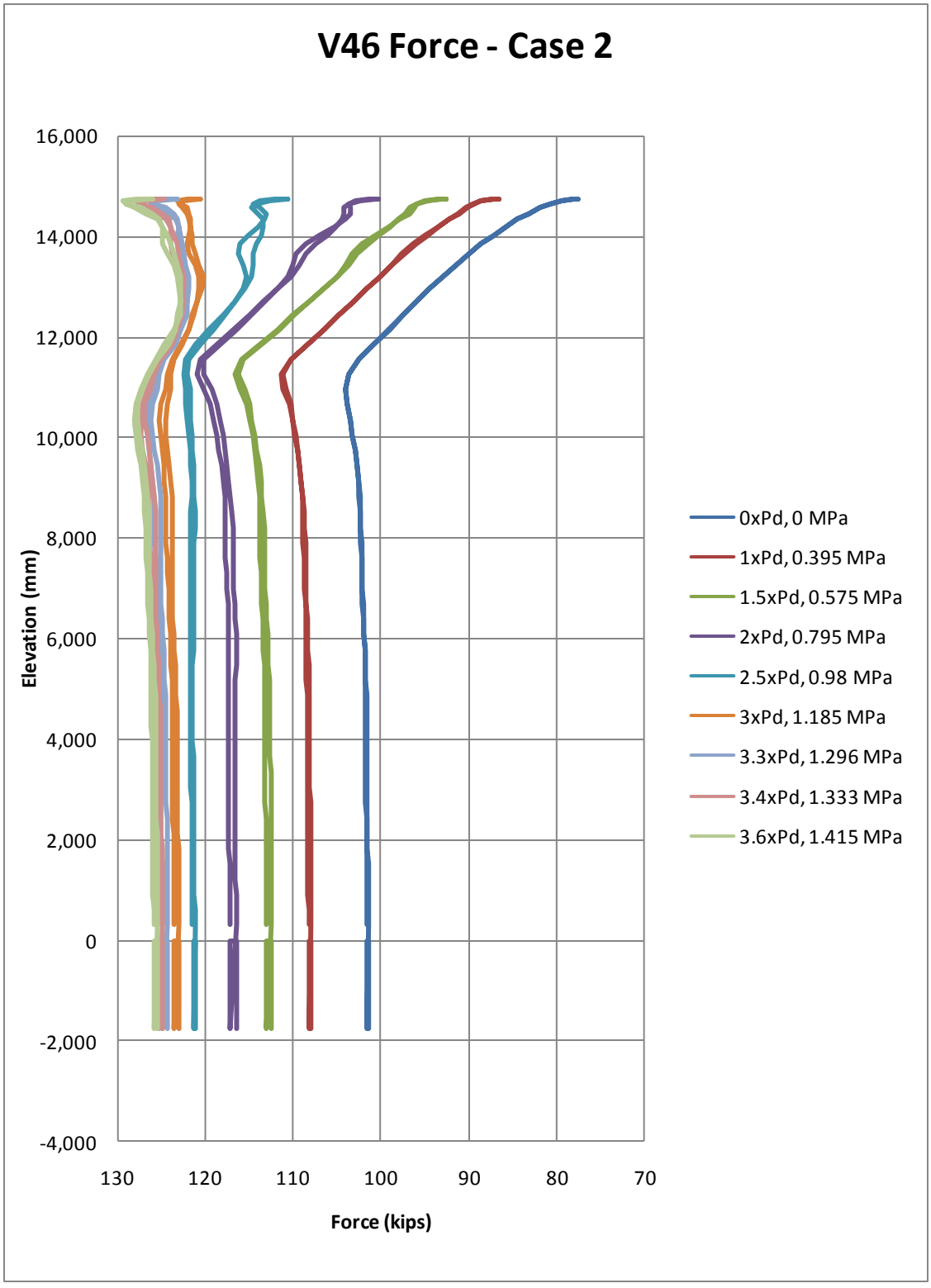

Figure D – 48b: Case 2 Abaqus analysis – hairpin tendon V46 force

Comparison of model 3 and model 4 (case 1 and case 2) at the requested SOLs

The requested Standard Output Locations (SOLs) compare Model 3 and Model 4 (Case 1 and Case 2). These SOLs are displayed in Figure D-49a through D-49s.

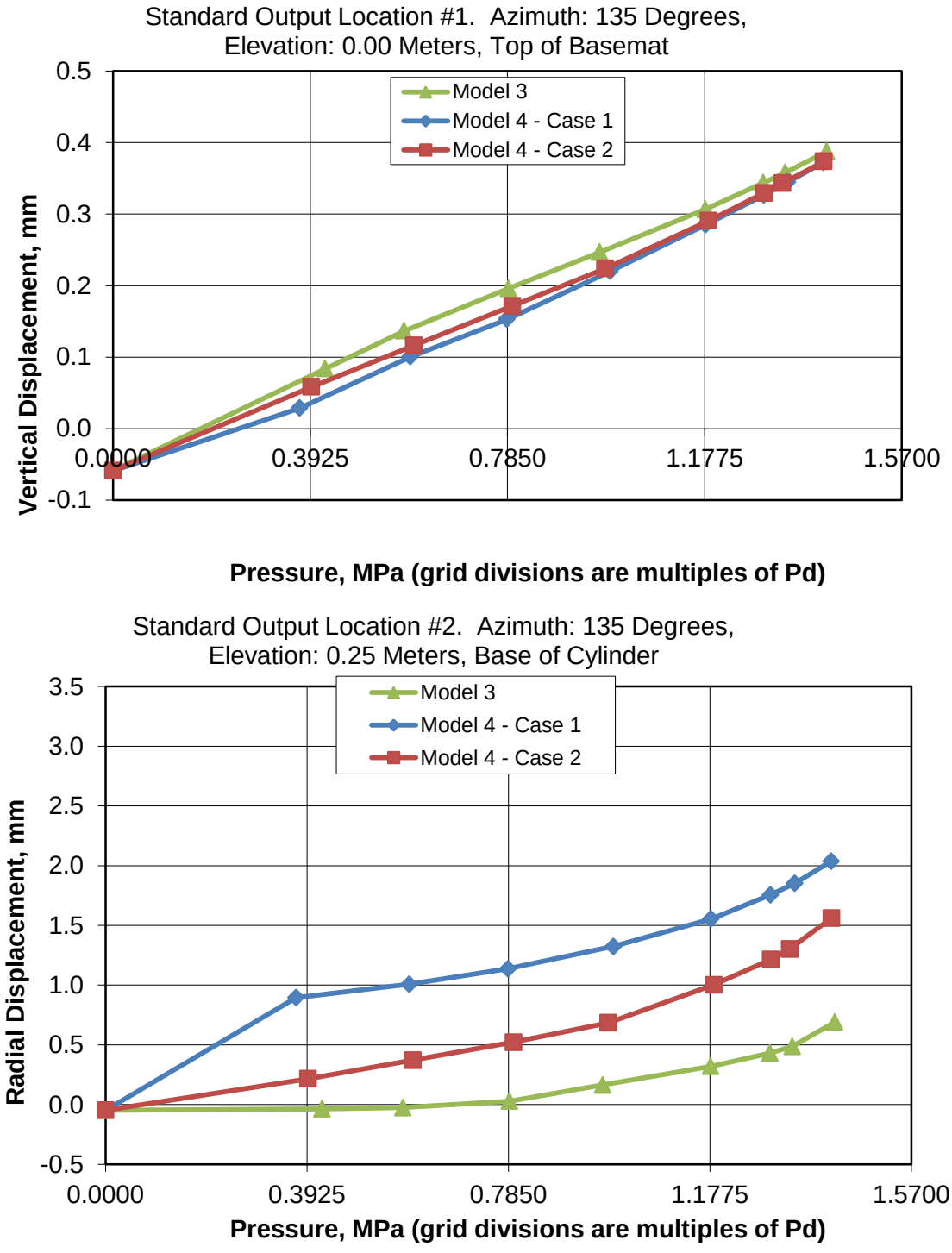

Figure D - 49a: Comparisons at standard output location 1, 2

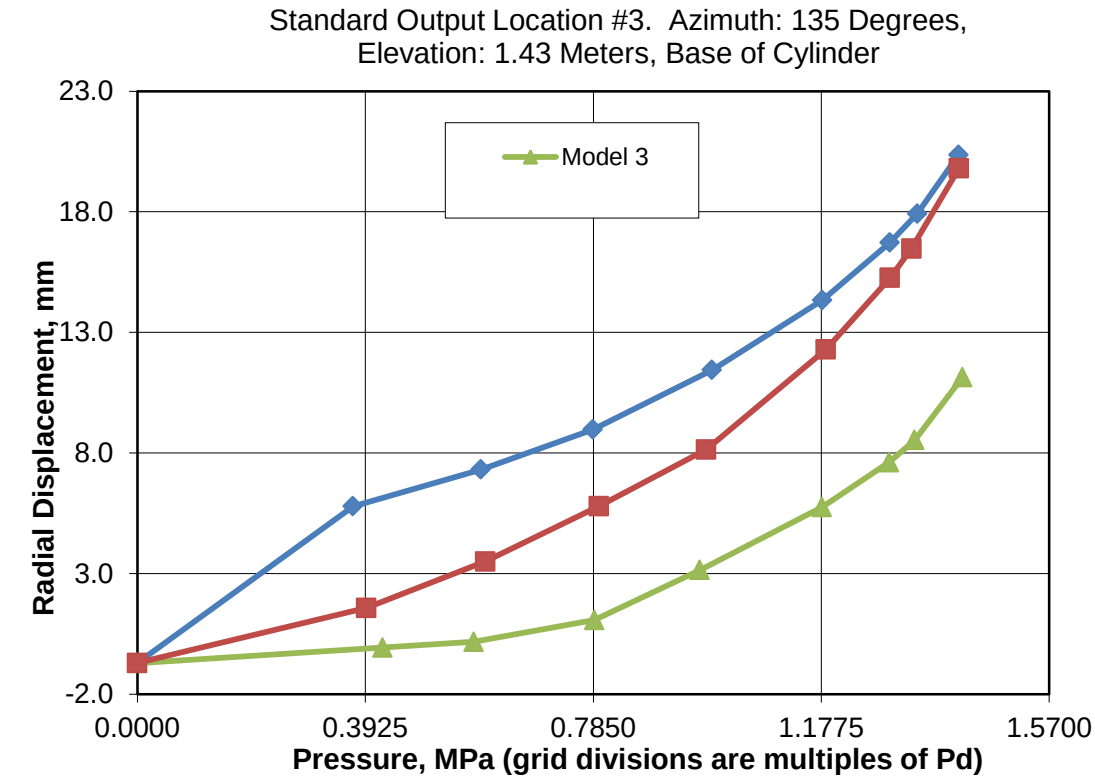

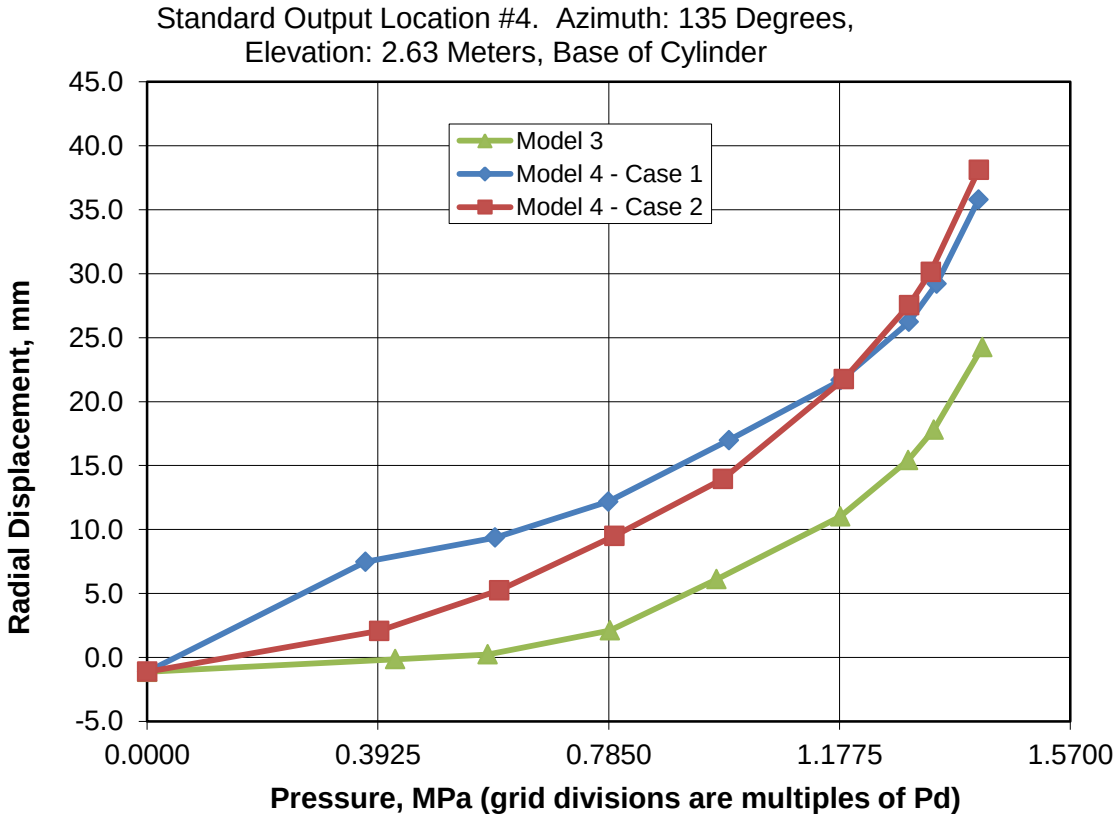

Figure D – 49b: Comparisons at standard output location 3, 4

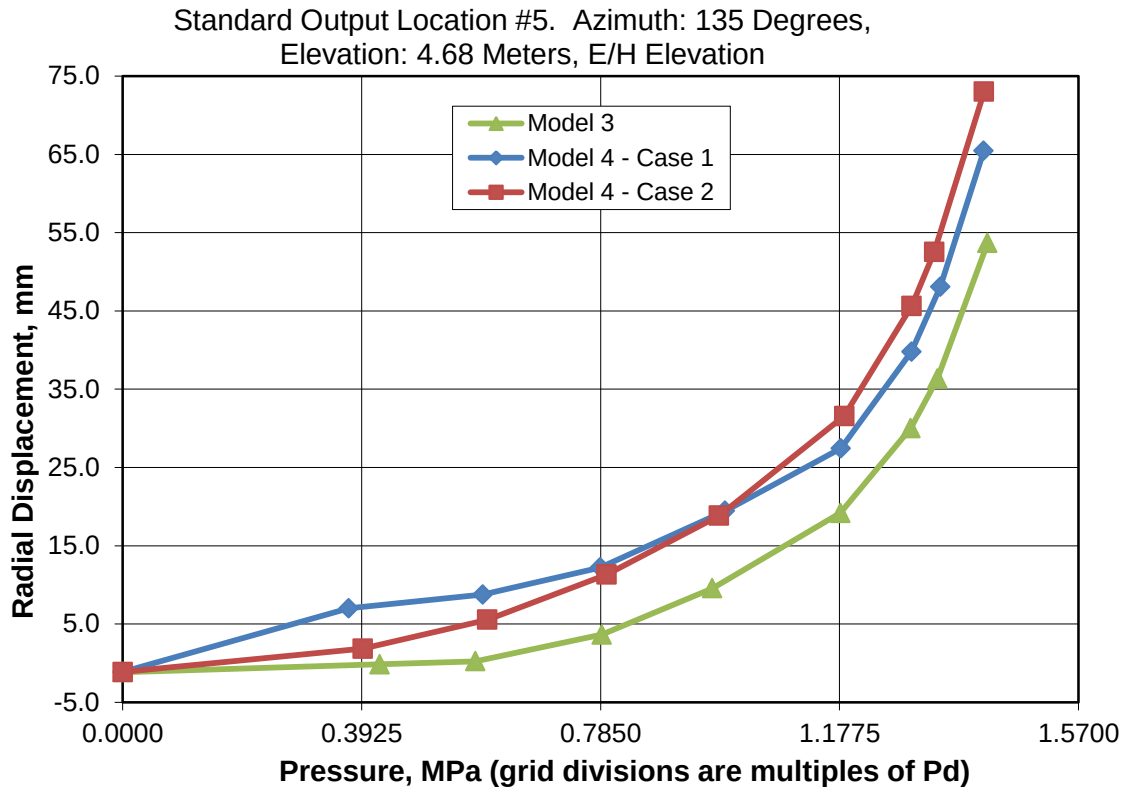

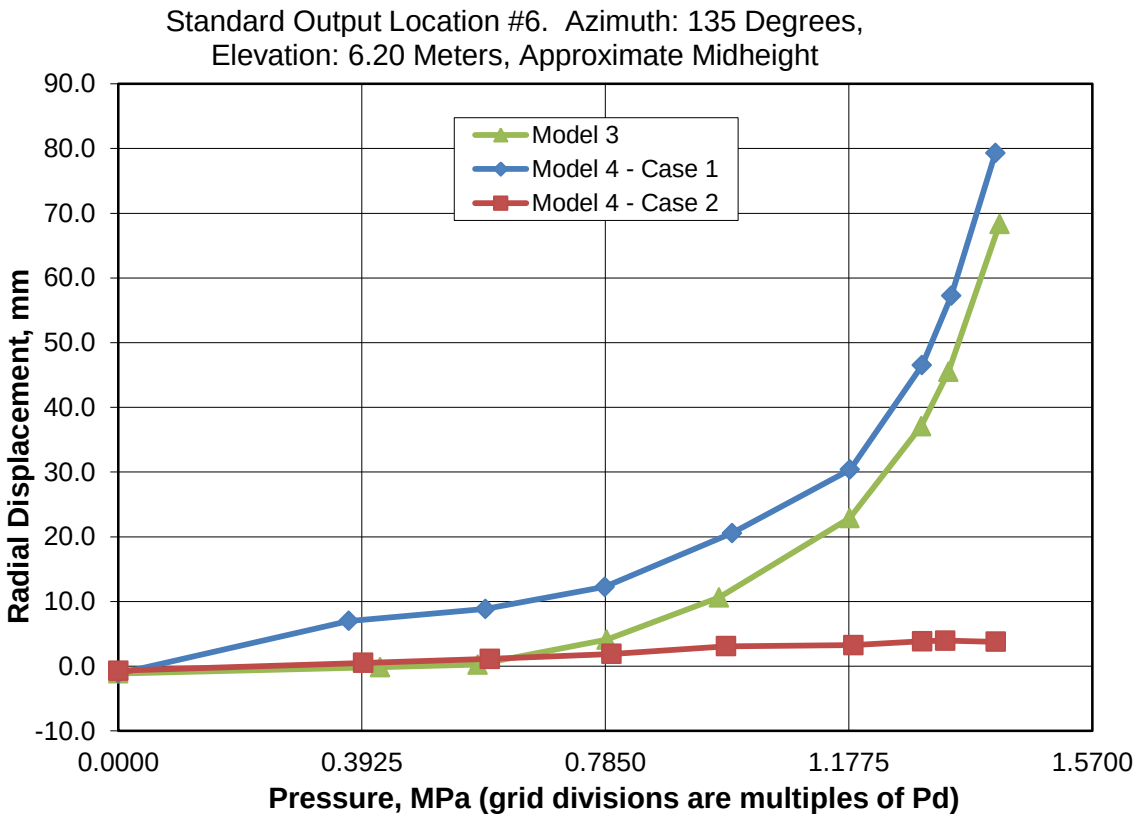

Figure D – 49c: Comparisons at standard output location 5, 6

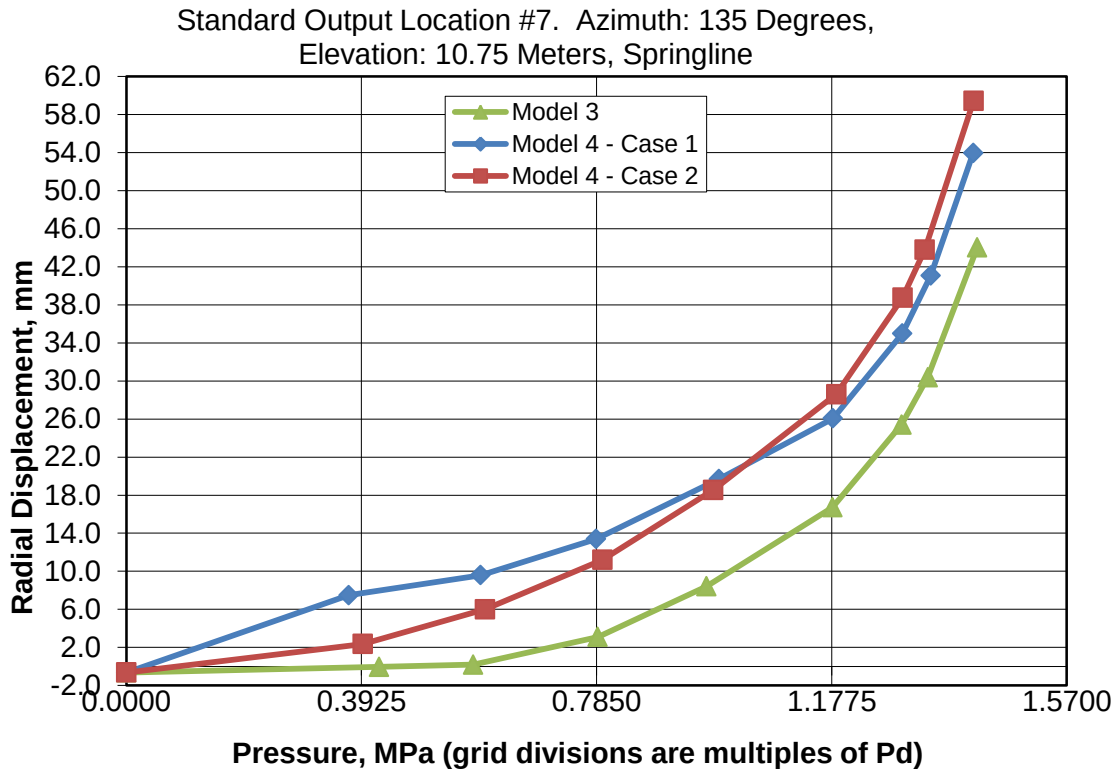

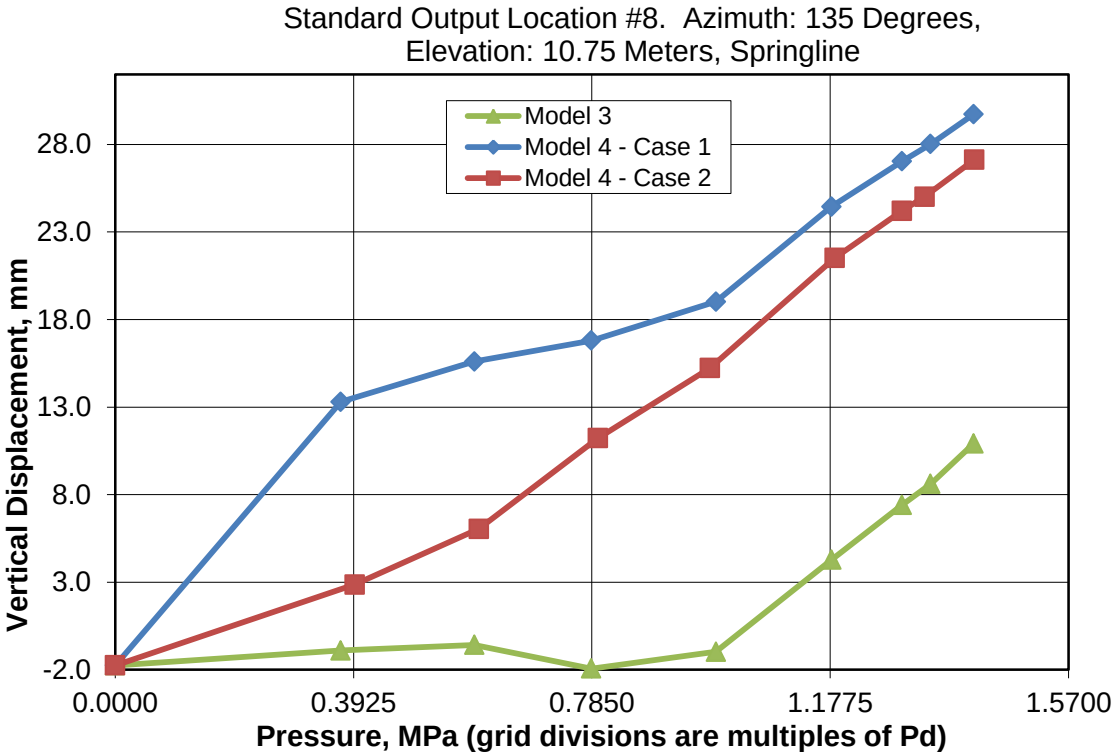

Figure D – 49d: Comparisons at standard output location 7, 8

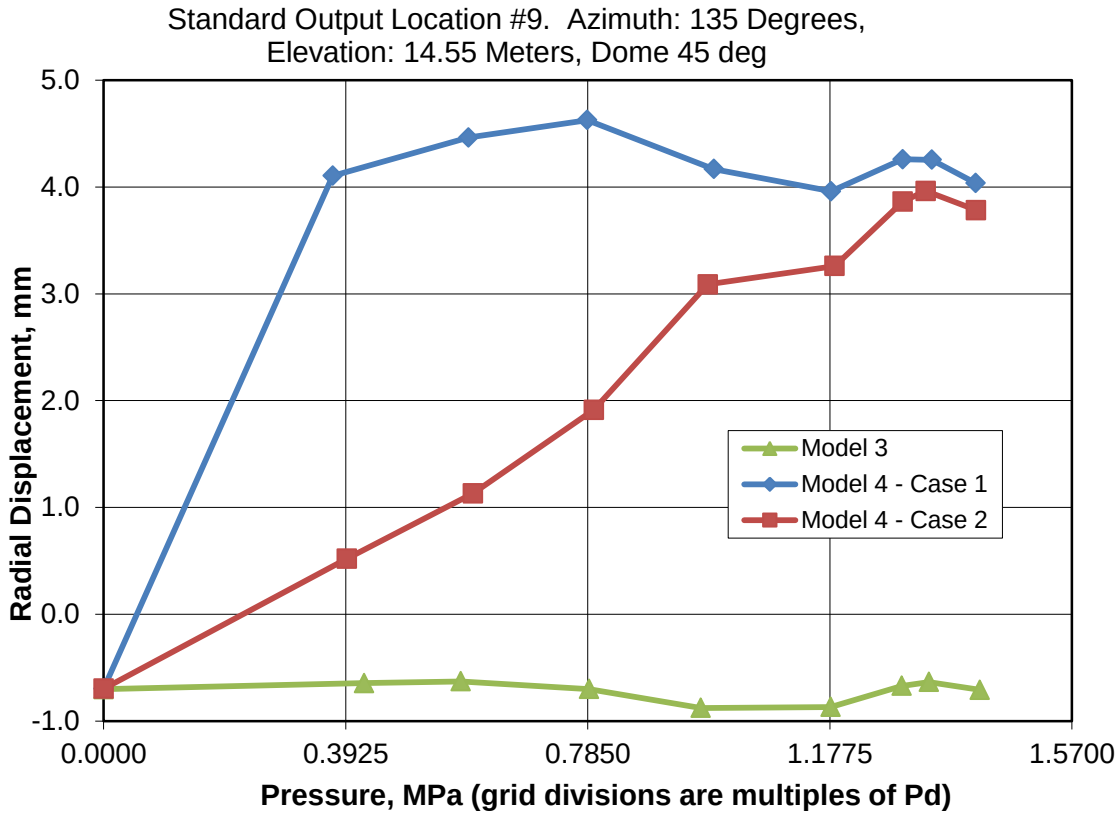

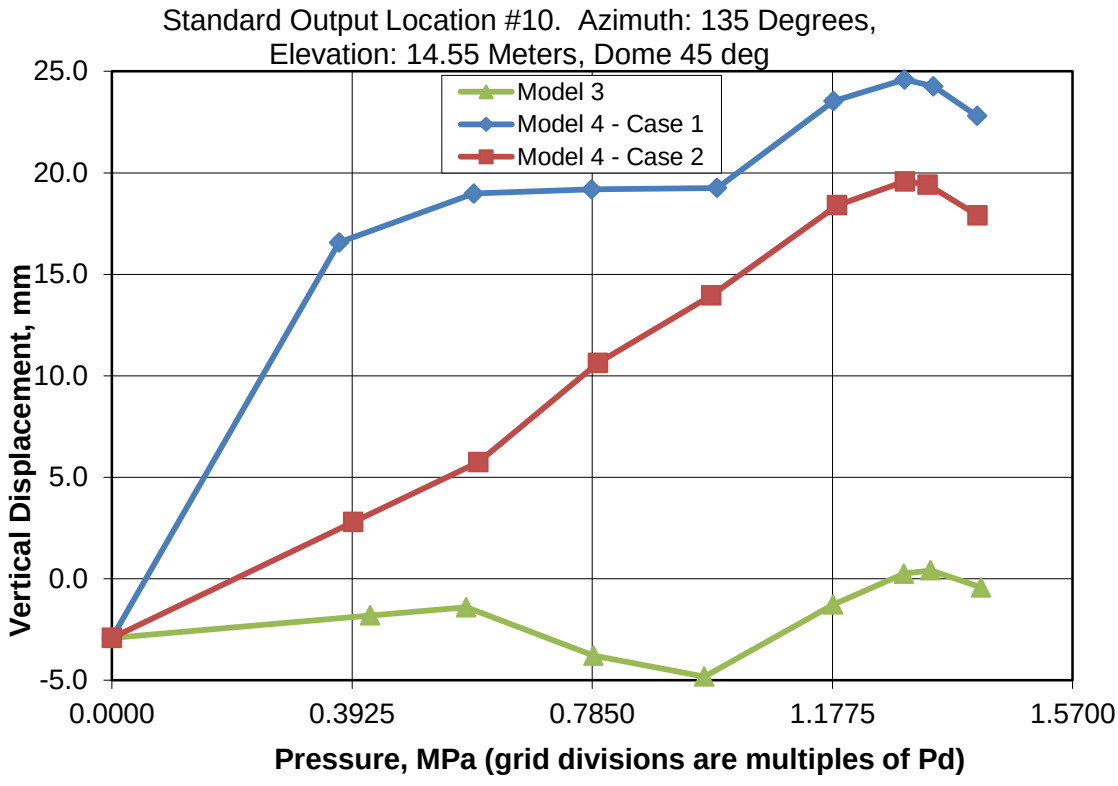

Figure D – 49e: Comparisons at standard output location 9, 10

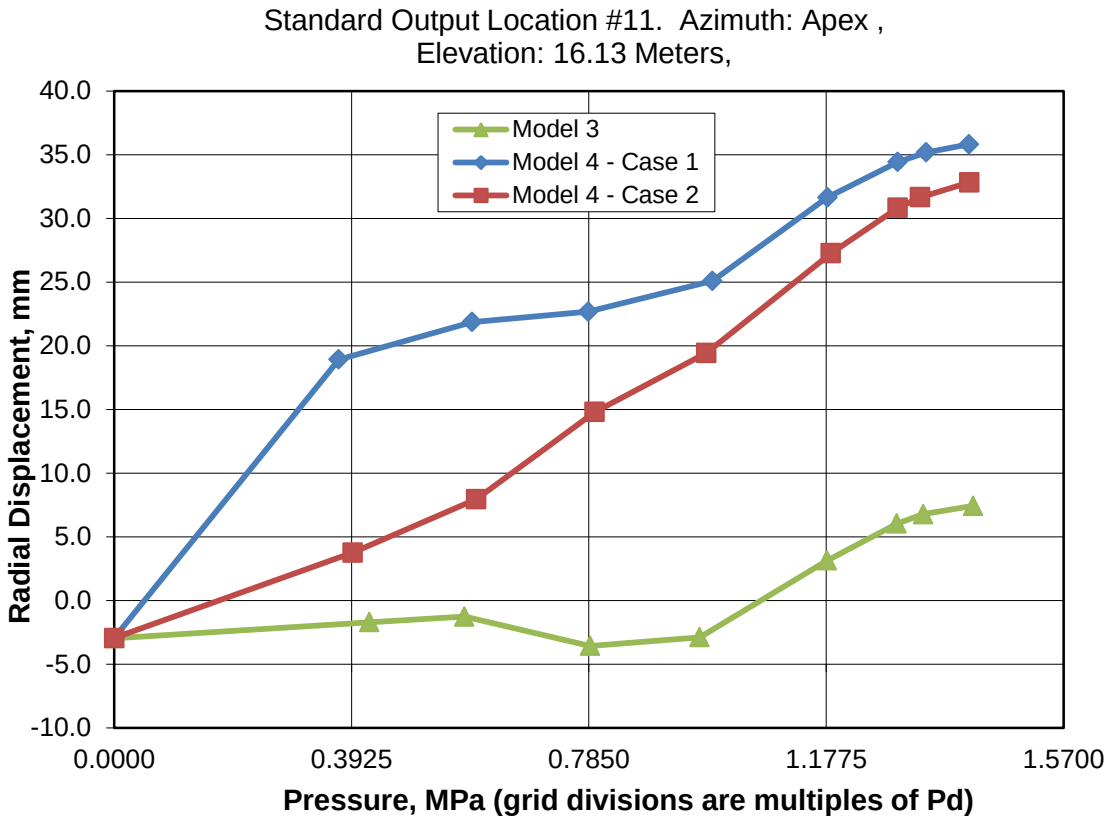

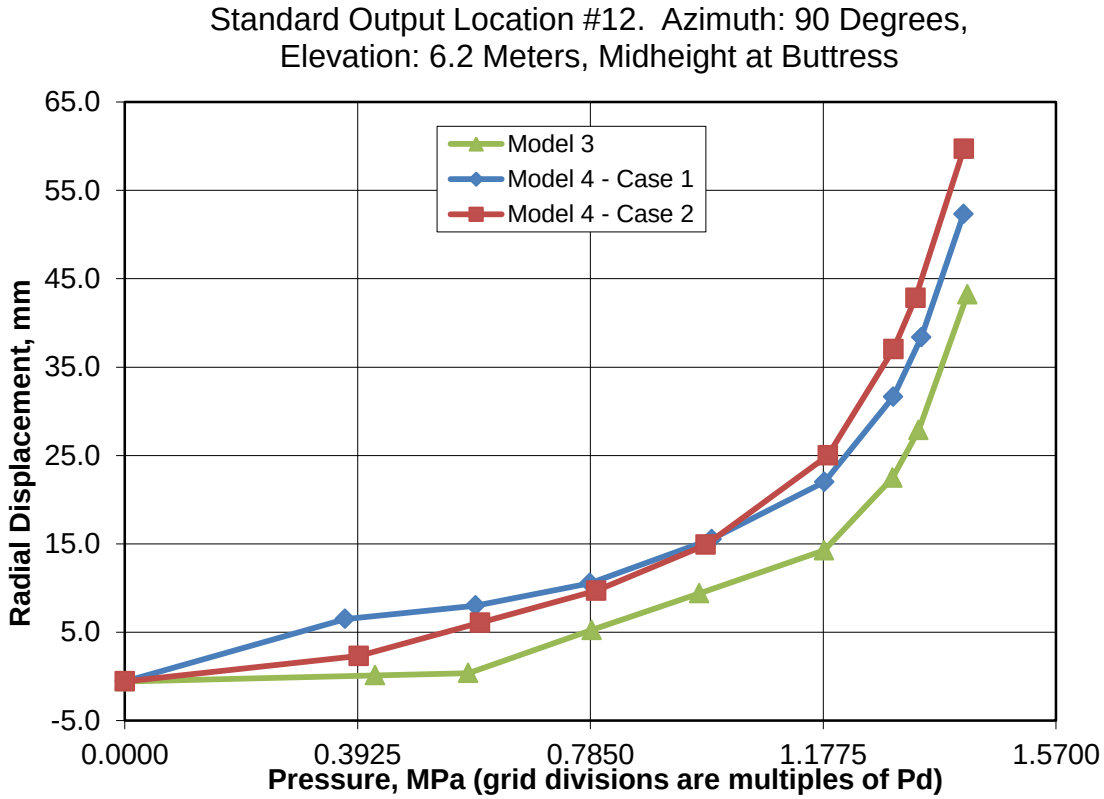

Figure D – 49f: Comparisons at standard output location 11, 12

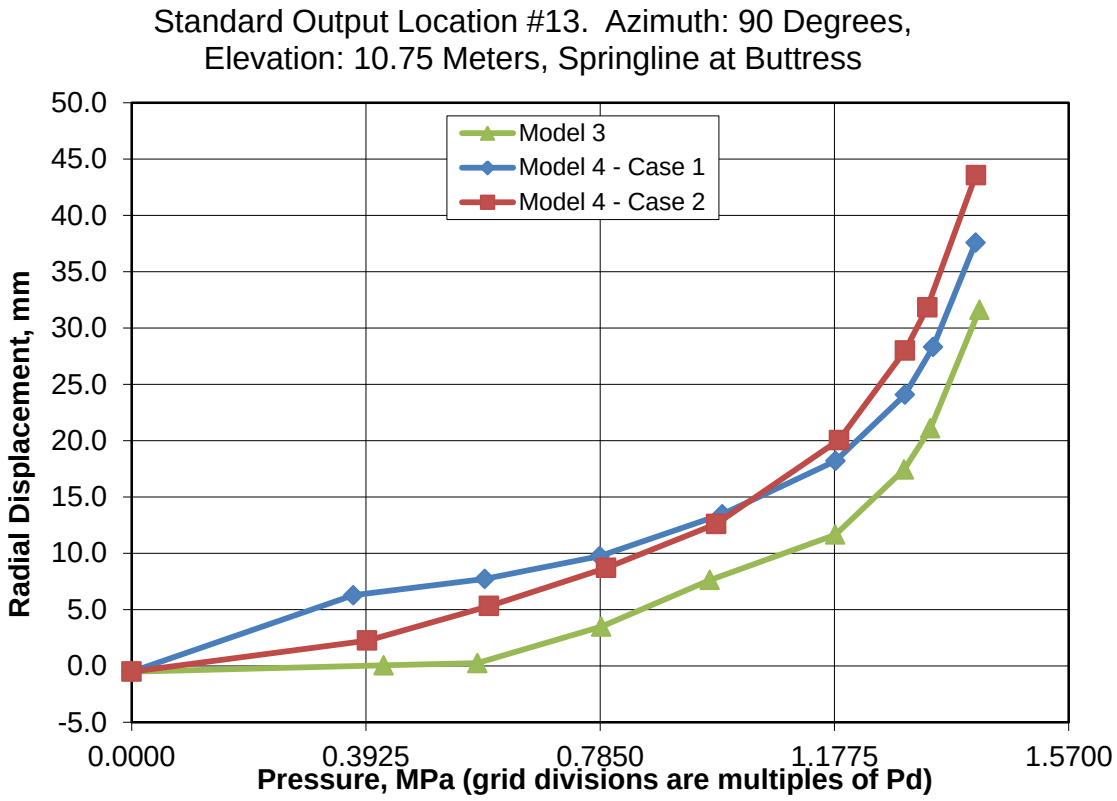

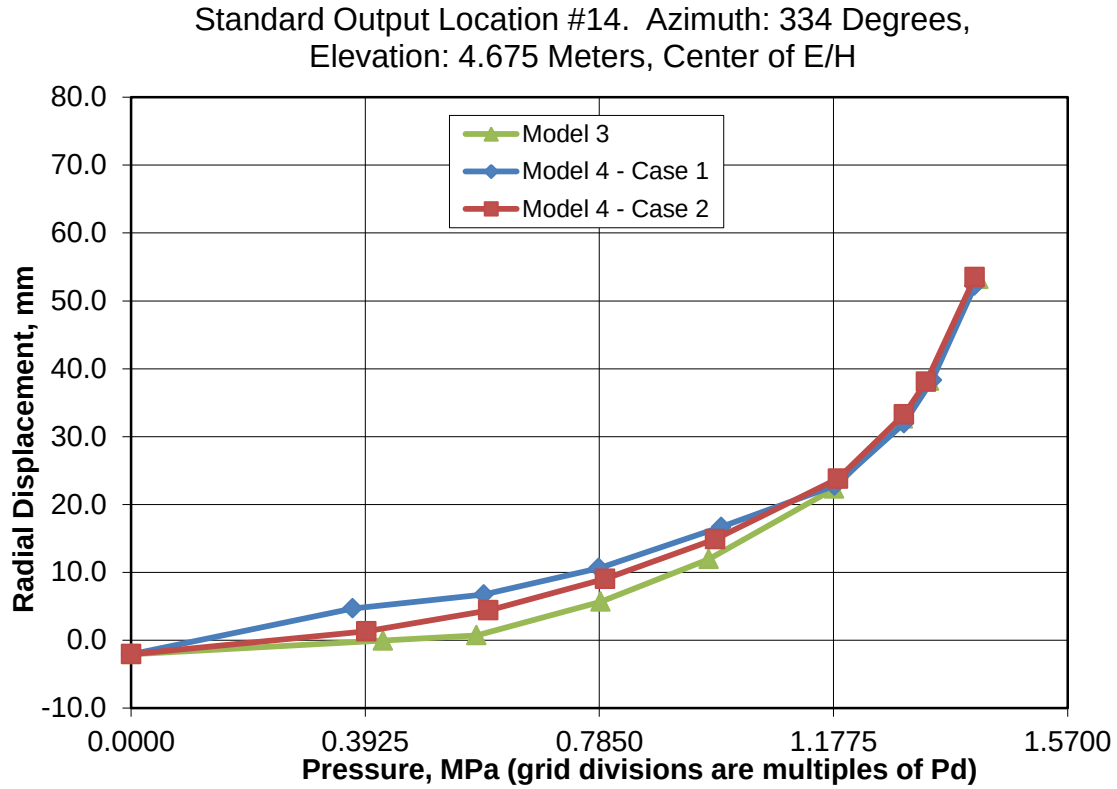

Figure D – 49g: Comparisons at standard output location 13, 14

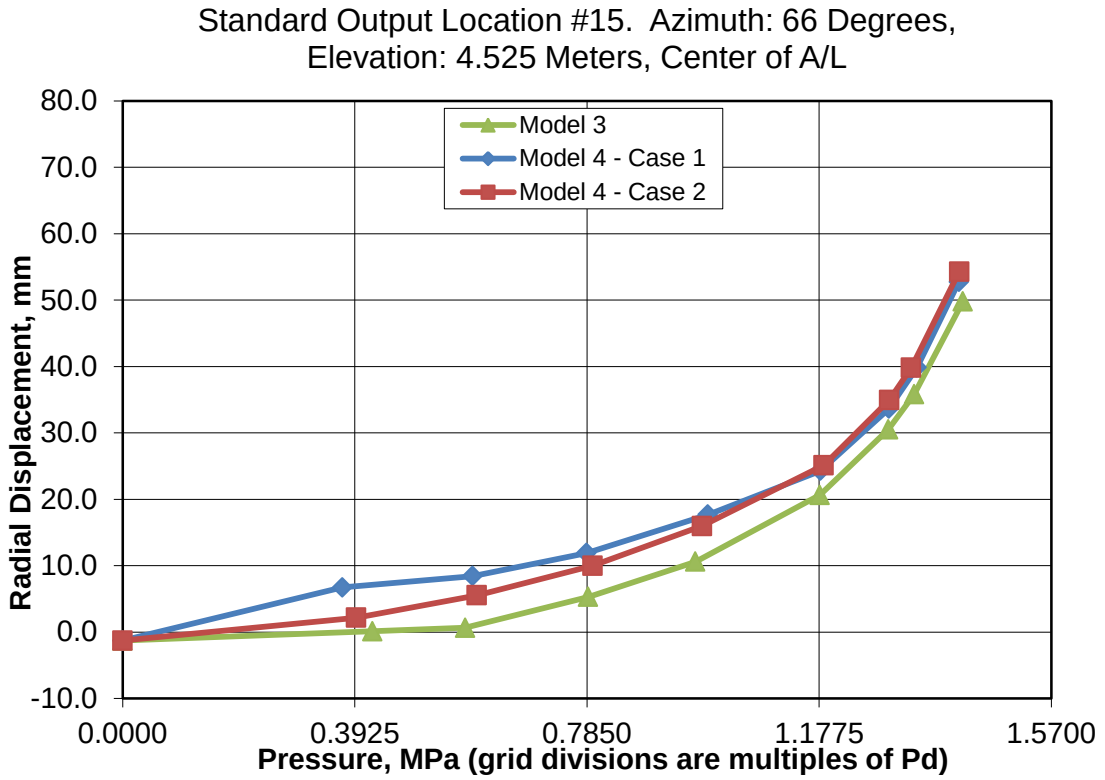

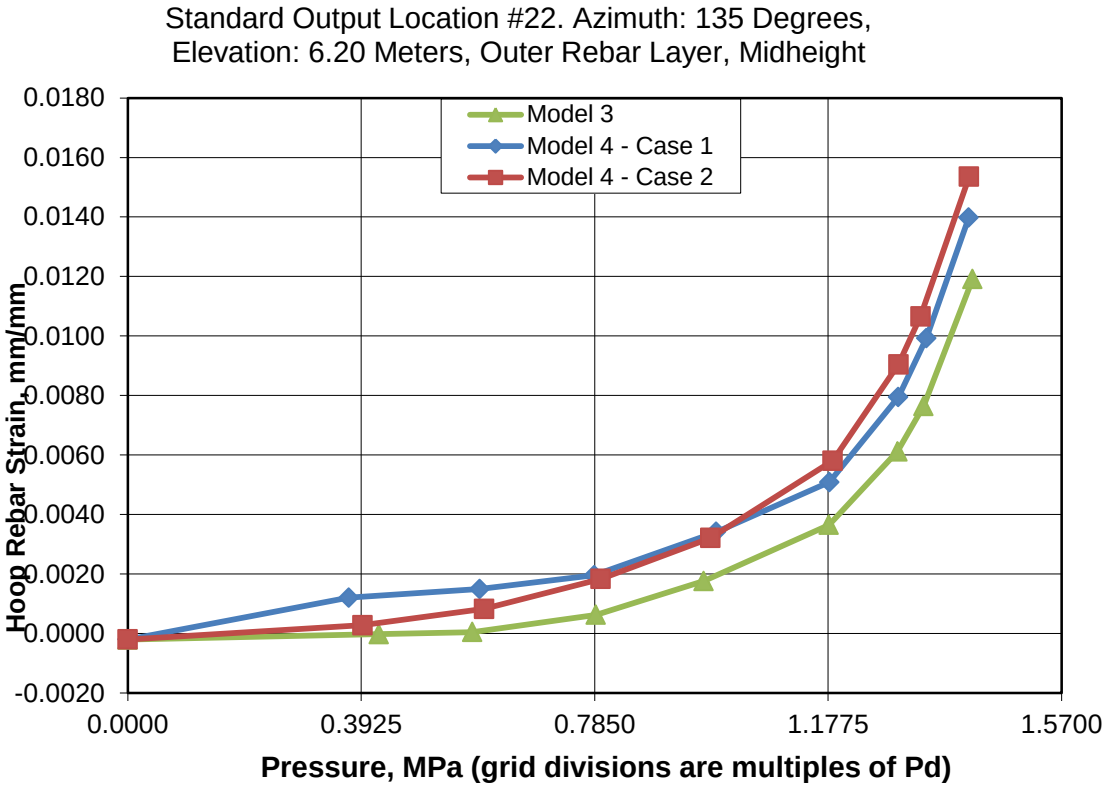

Figure D – 49h: Comparisons at standard output location 15, 22

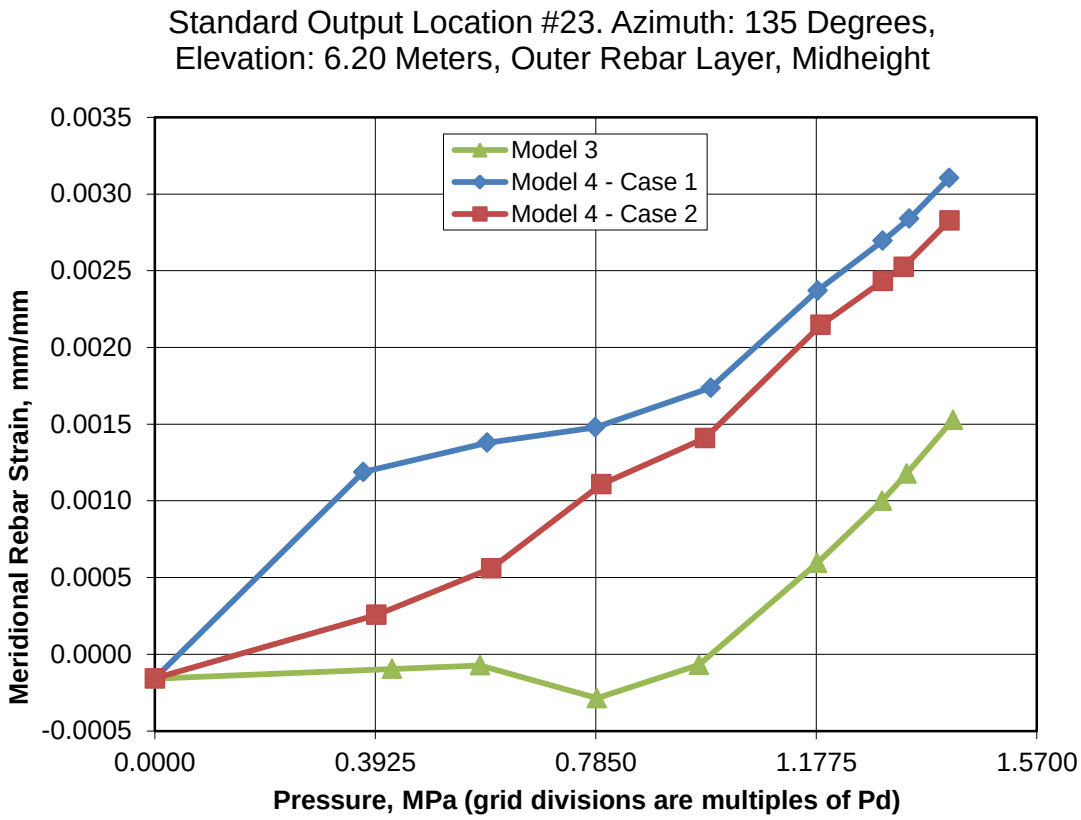

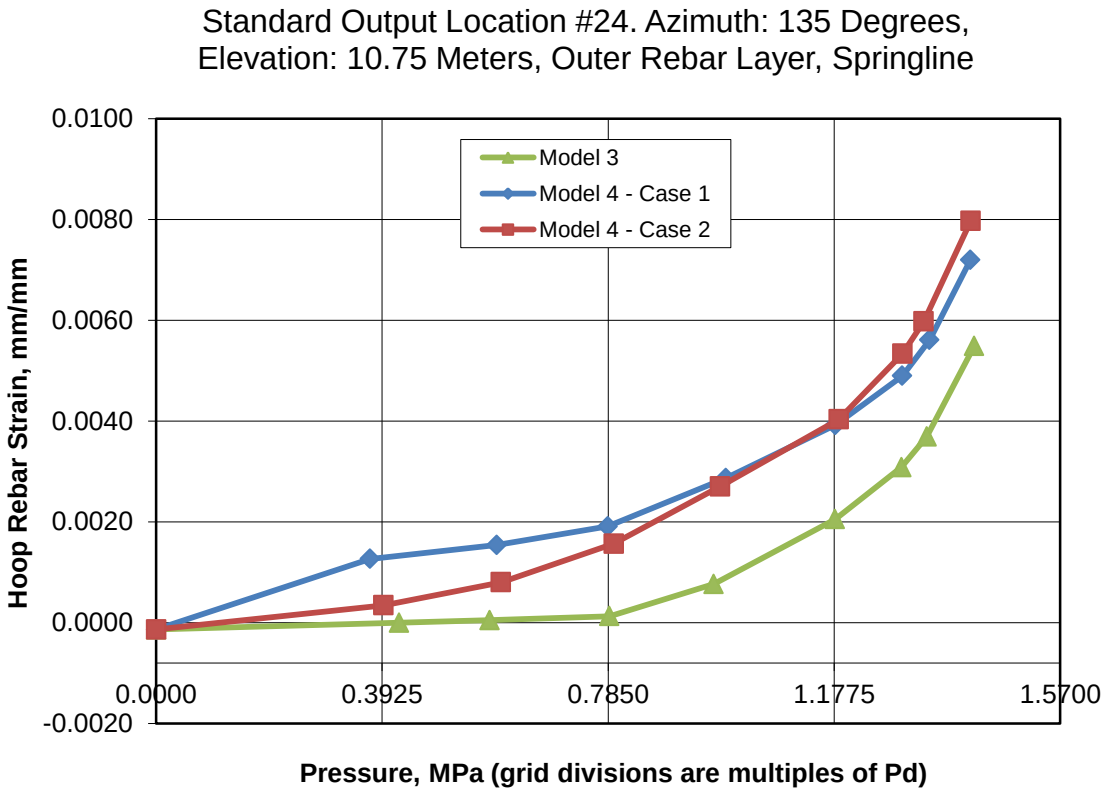

Figure D – 49i: Comparisons at standard output location 23, 24

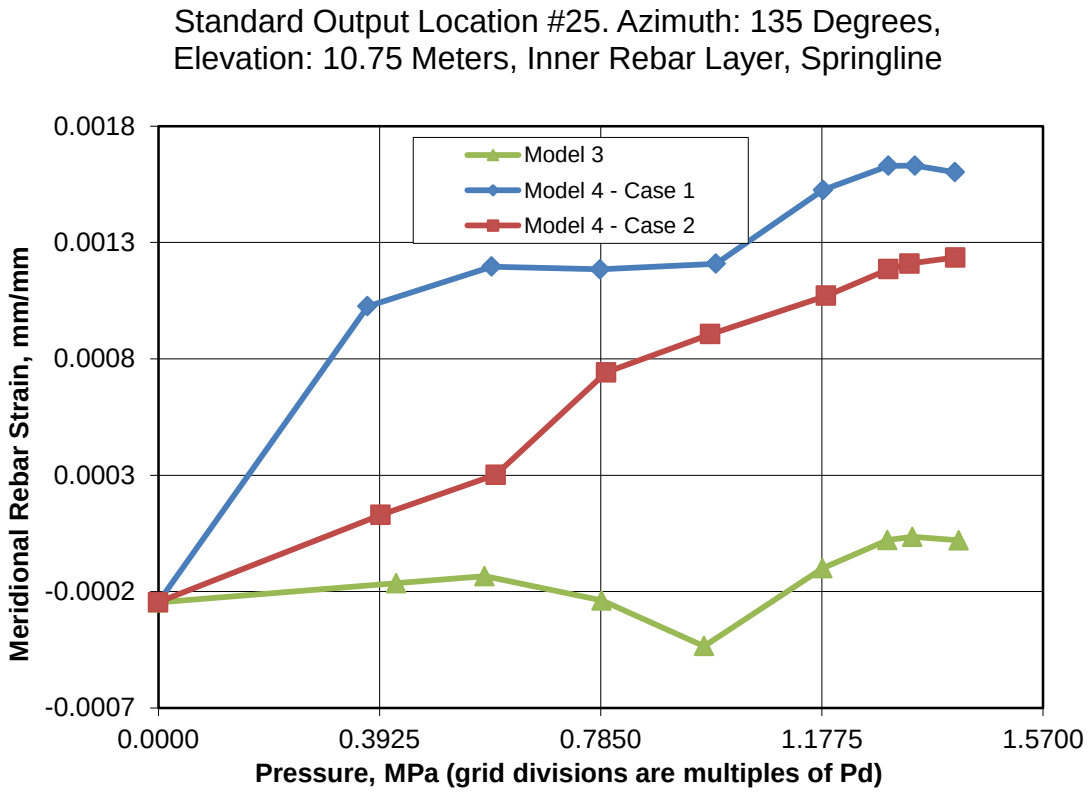

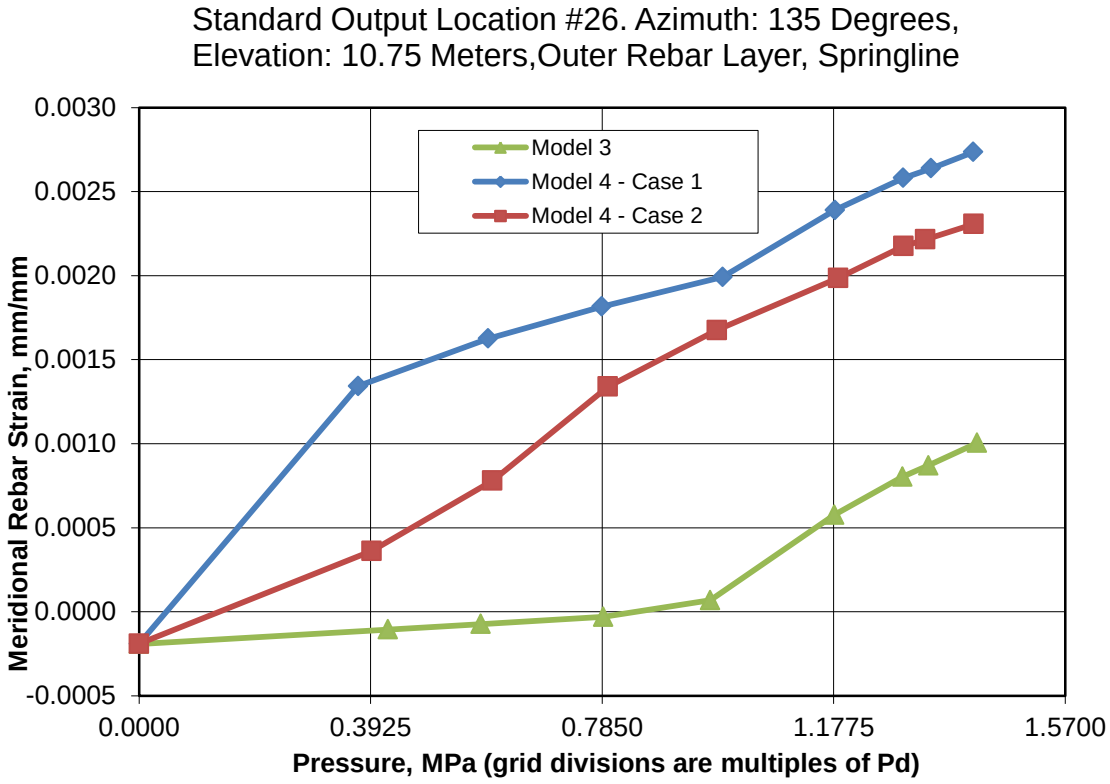

Figure D – 49j: Comparisons at standard output location 25, 26

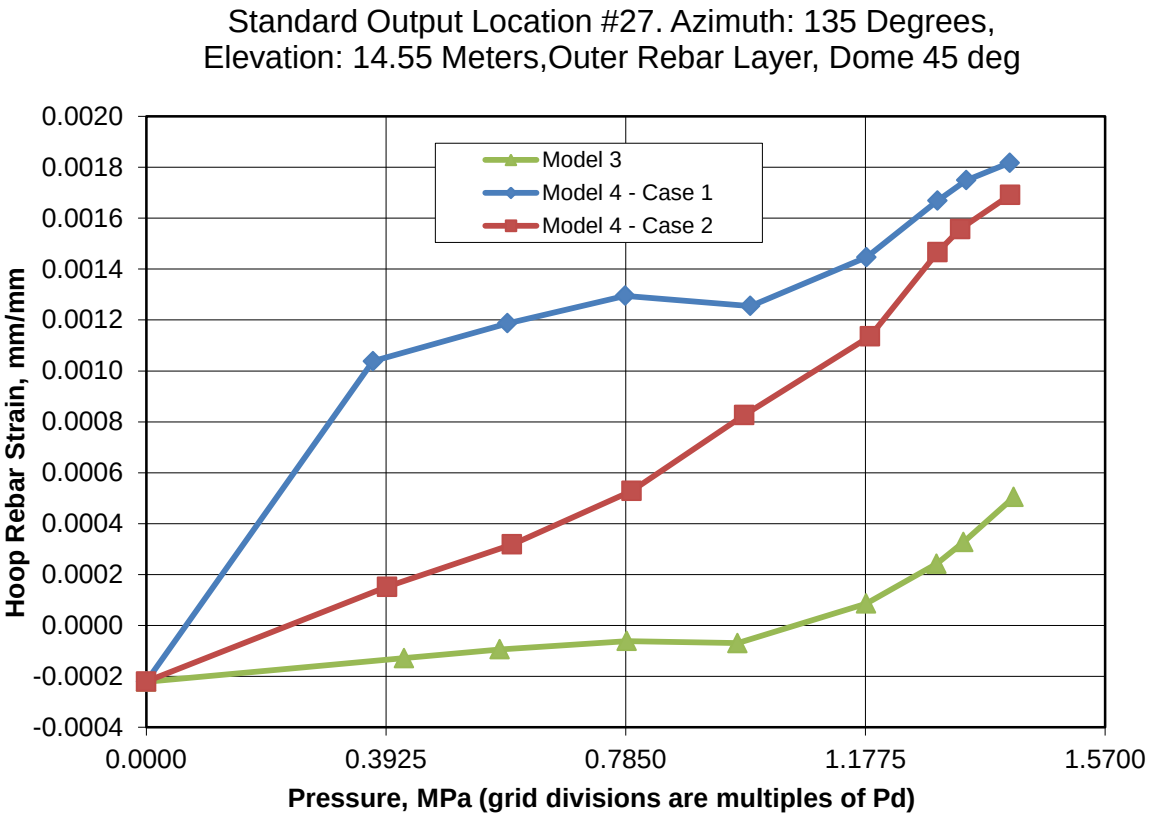

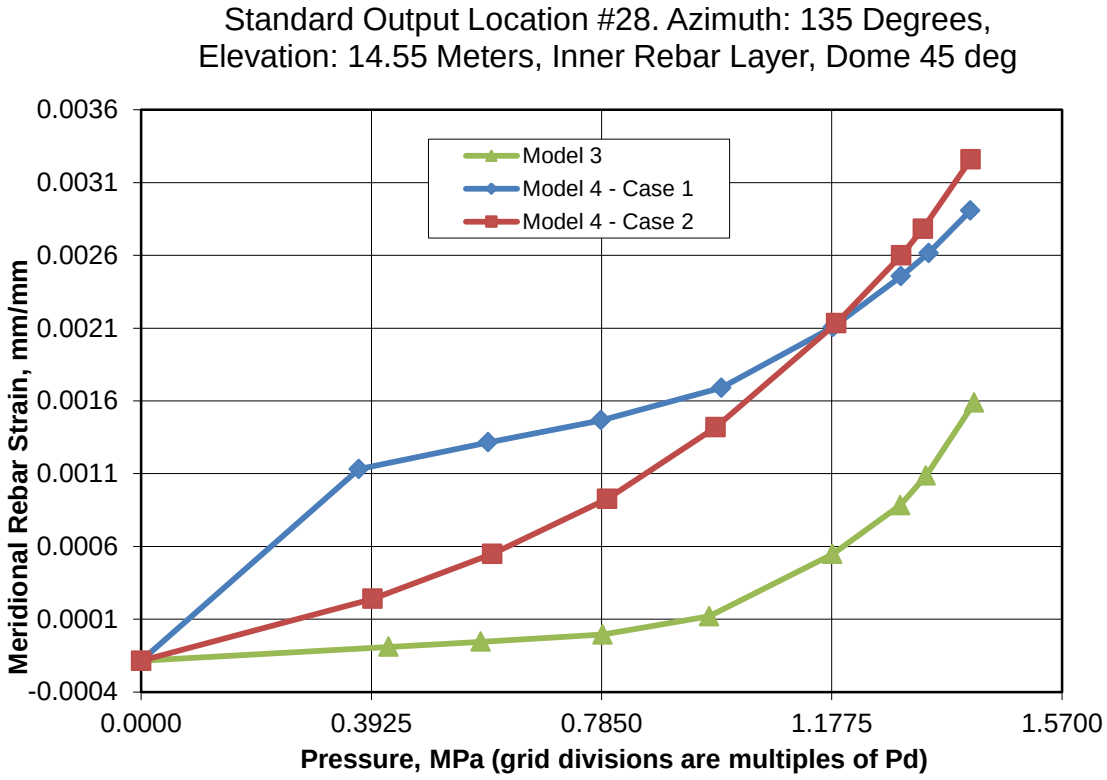

Figure D – 49k: Comparisons at standard output location 27, 28

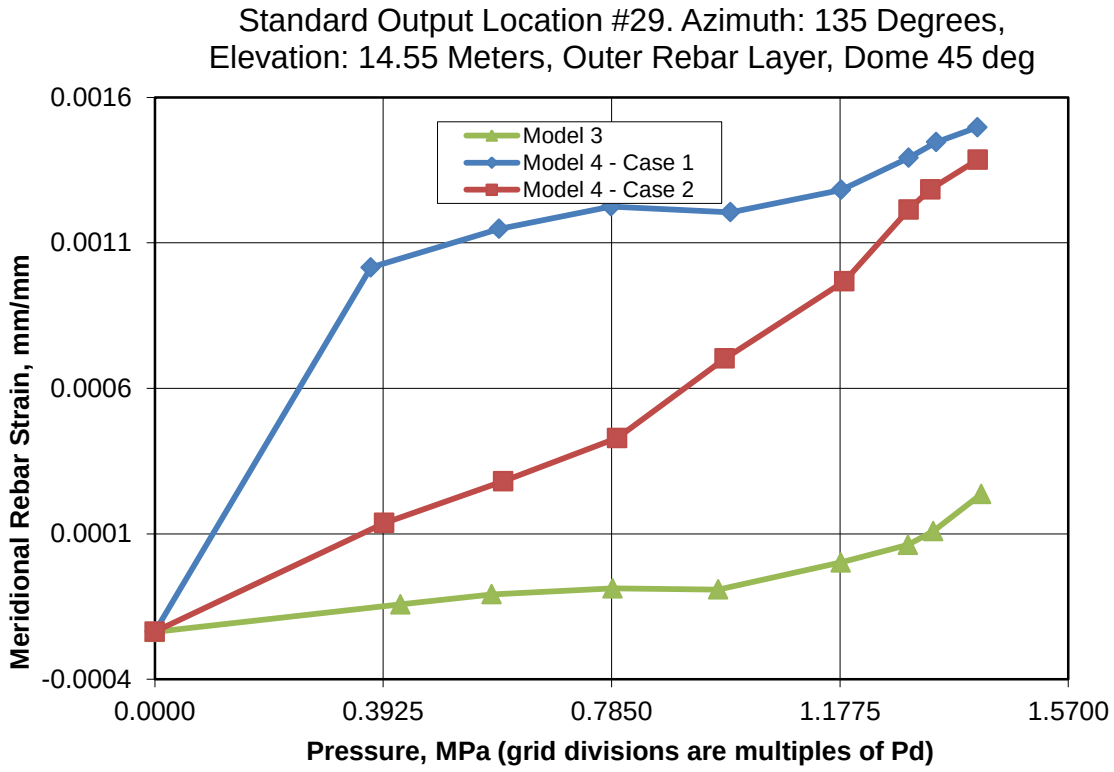

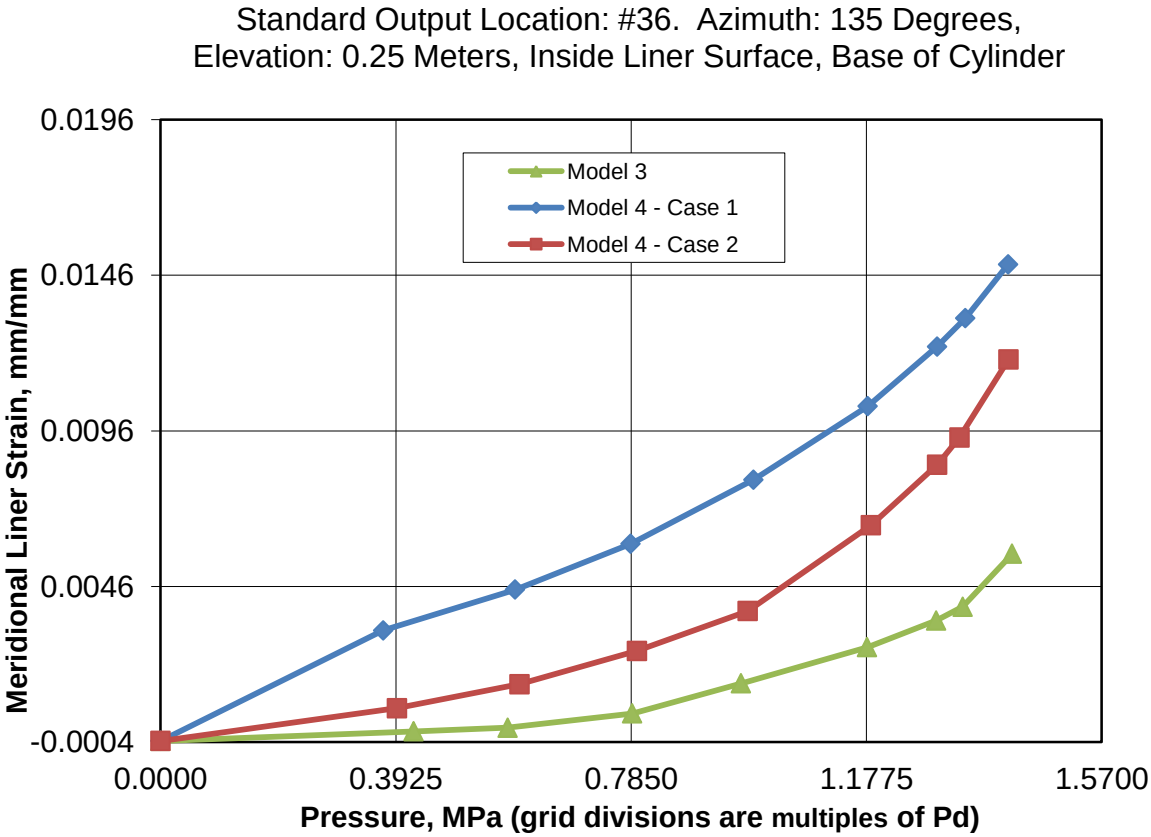

Figure D – 49l: Comparisons at standard output location 29, 36

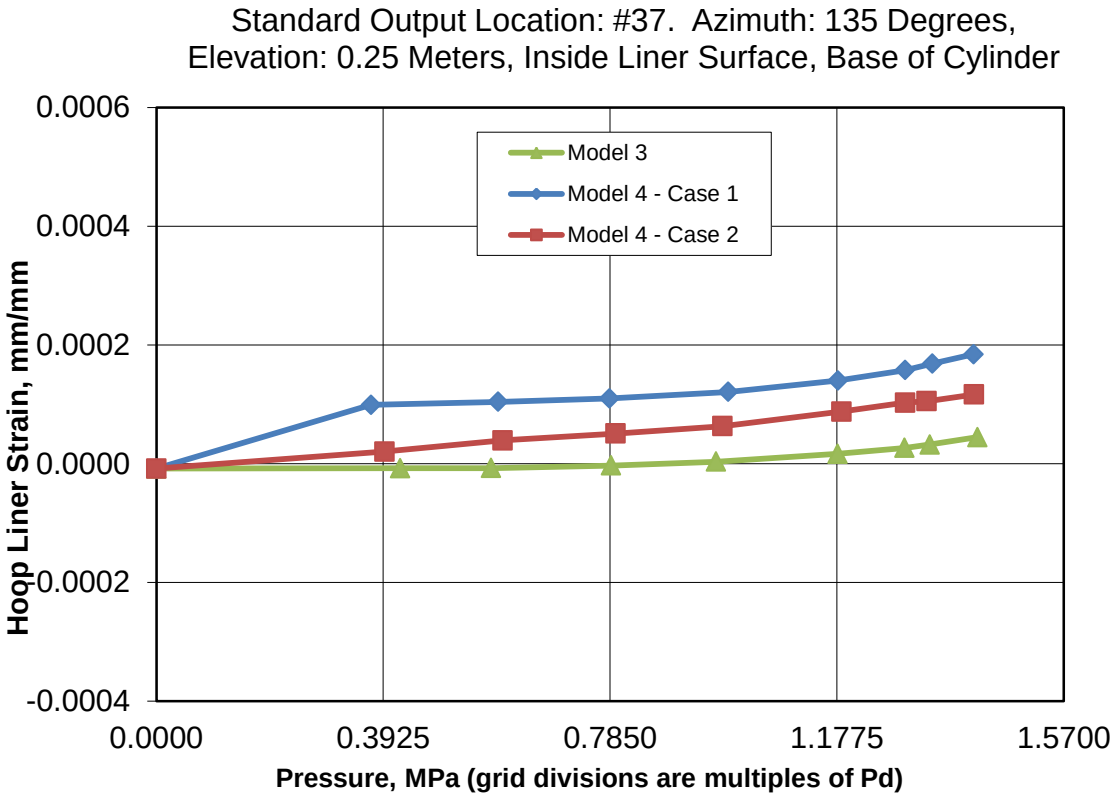

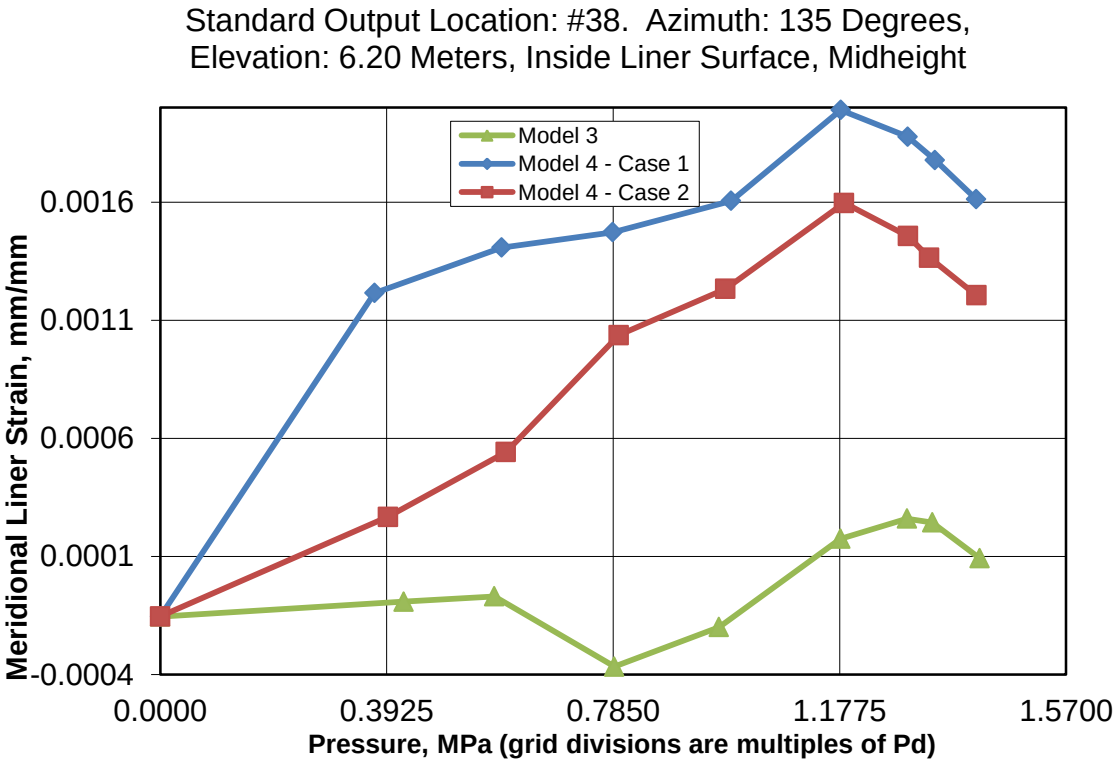

Figure D – 49m: Comparisons at standard output location 37, 38

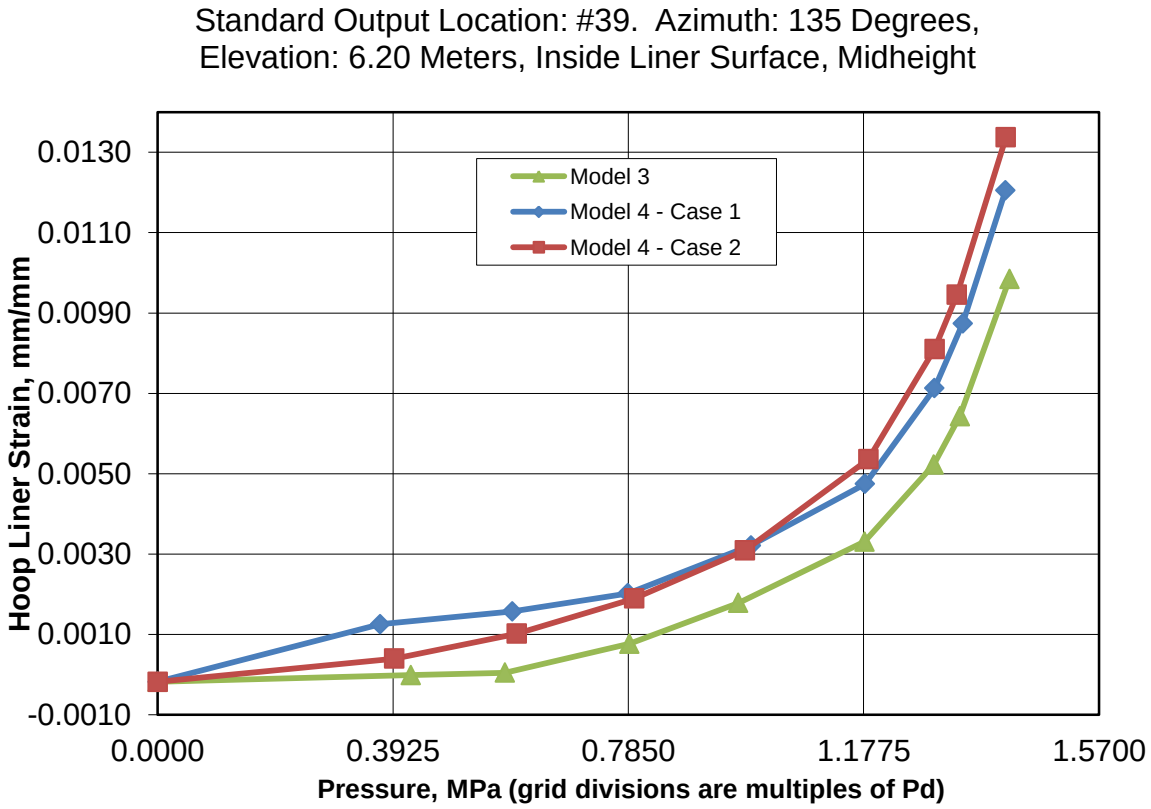

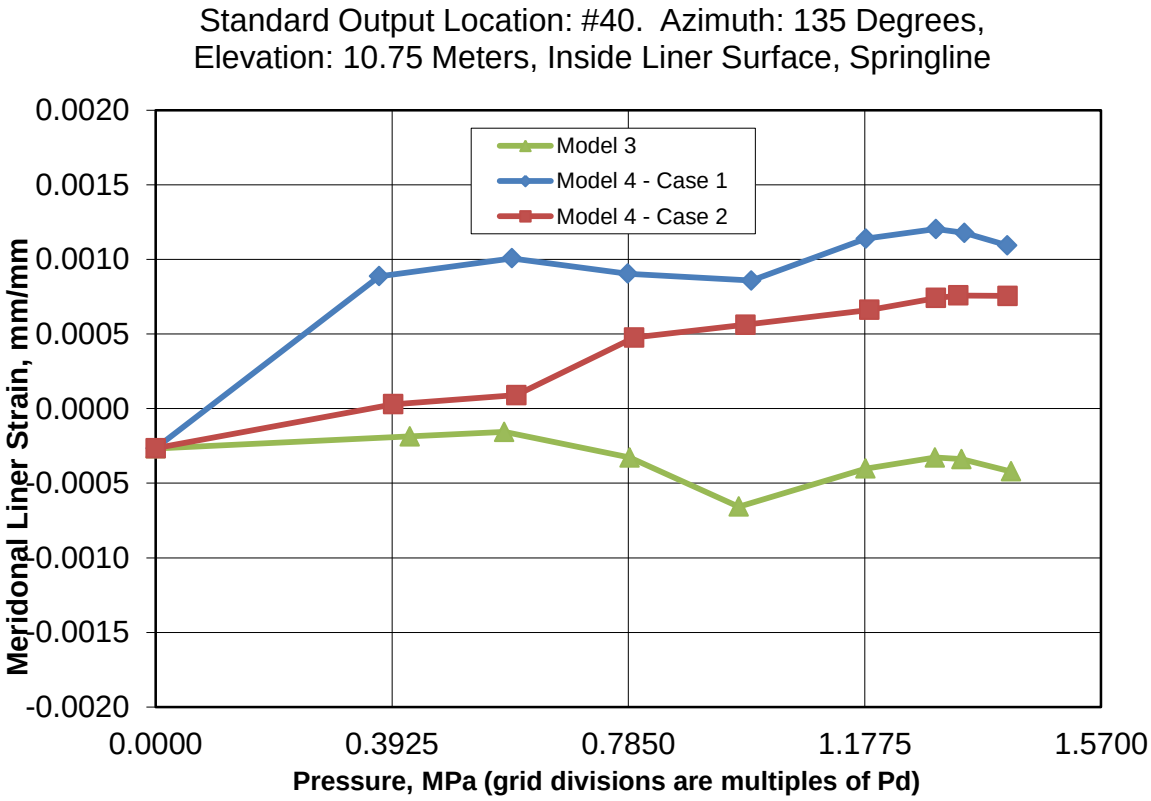

Figure D – 49n: Comparisons at standard output location 39, 40

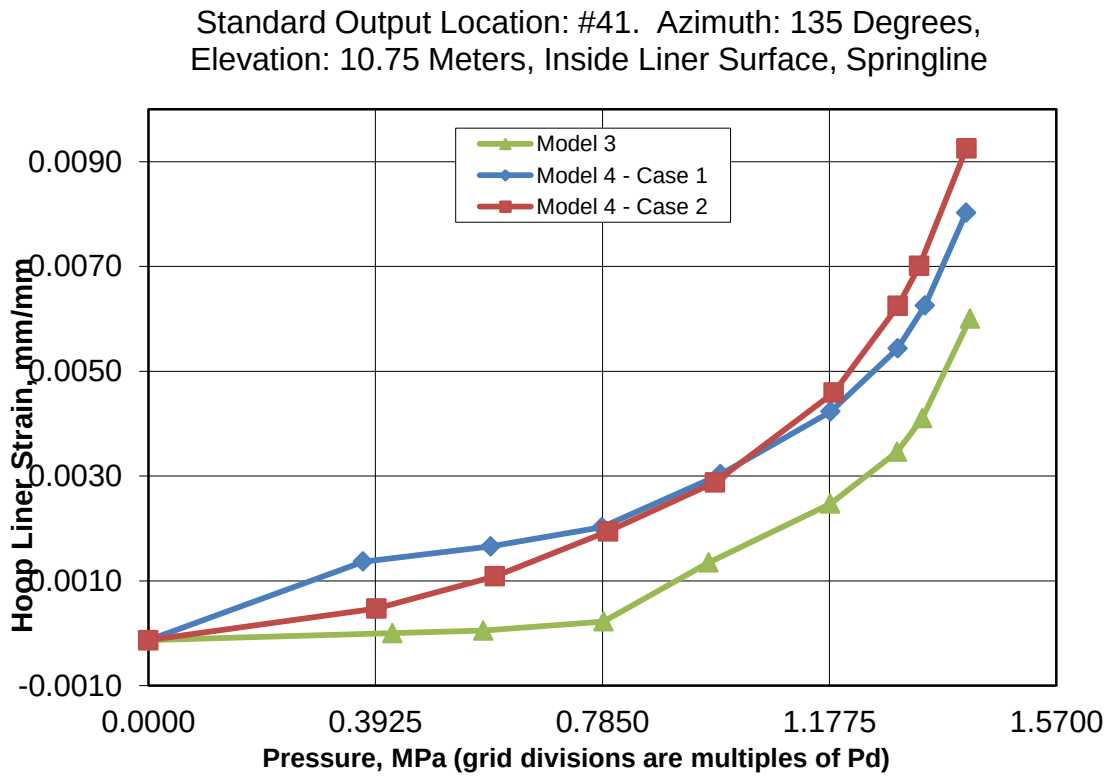

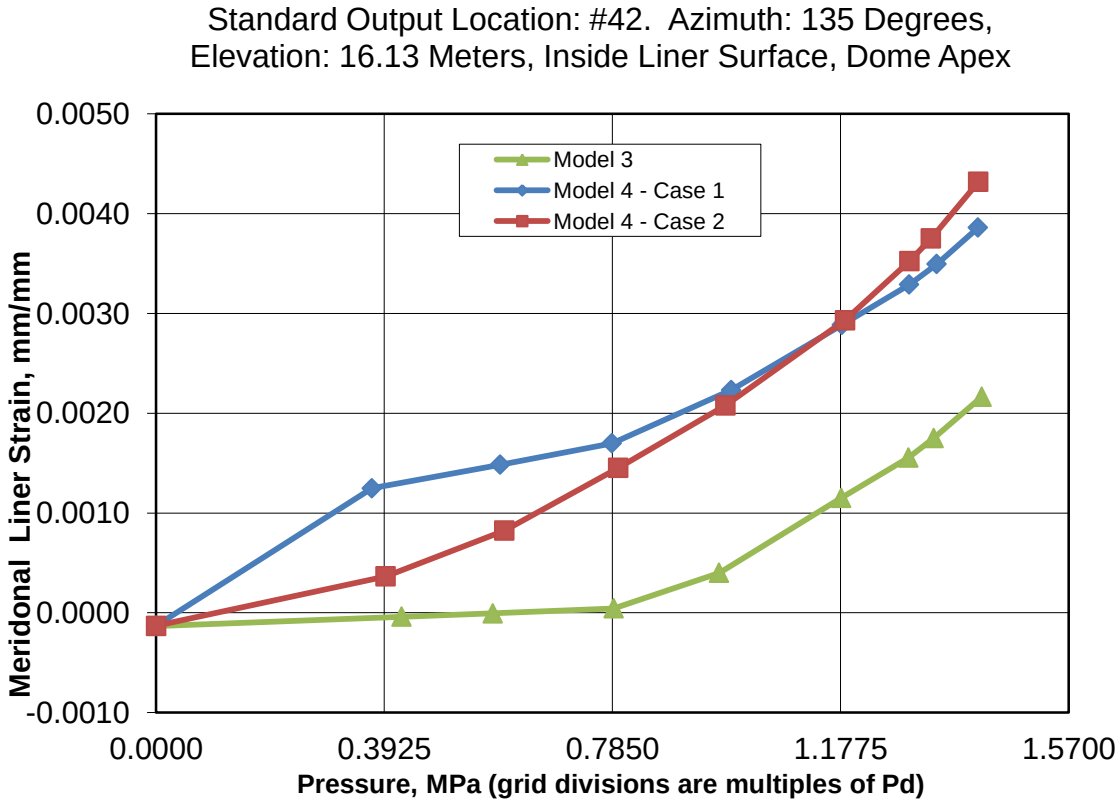

Figure D – 49o: Comparisons at standard output location 41, 42

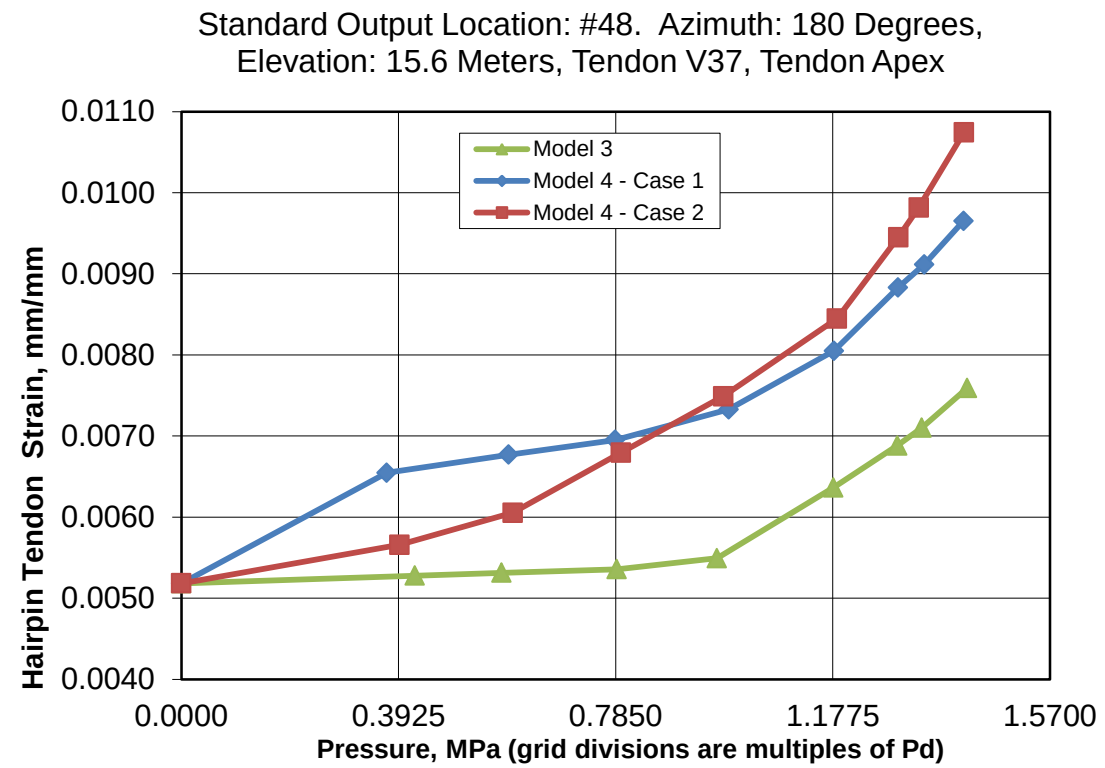

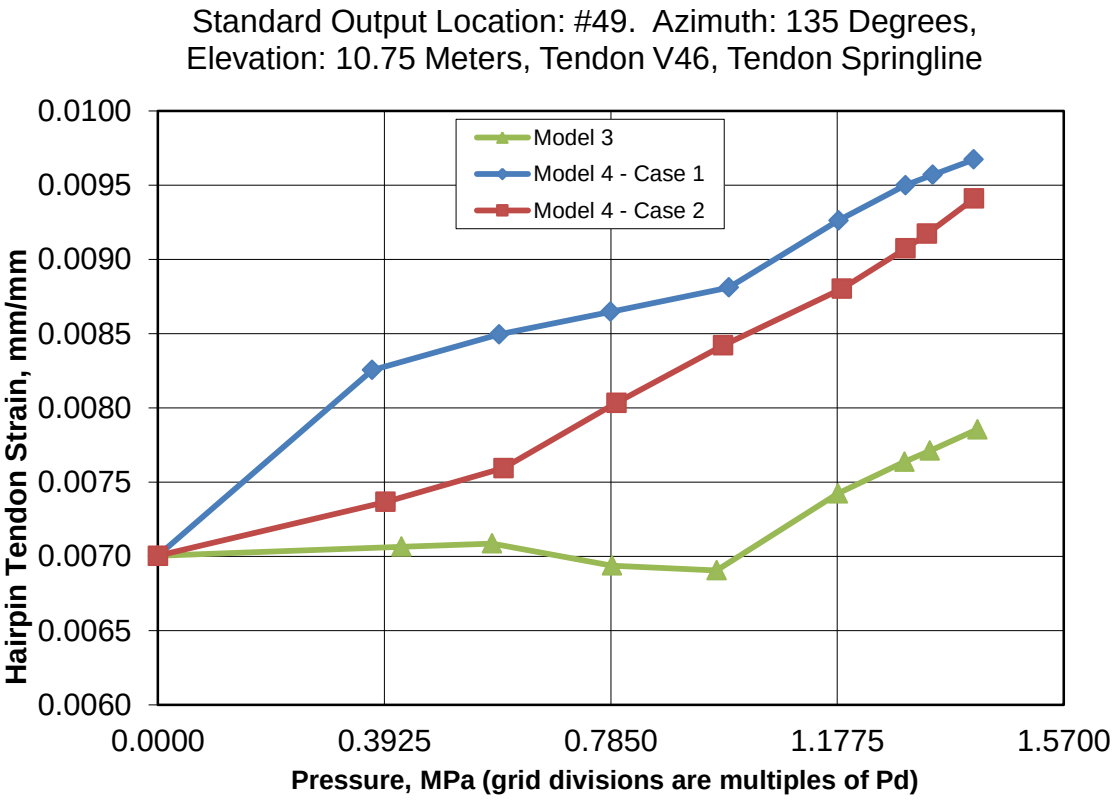

Figure D – 49p: Comparisons at standard output location 48, 49

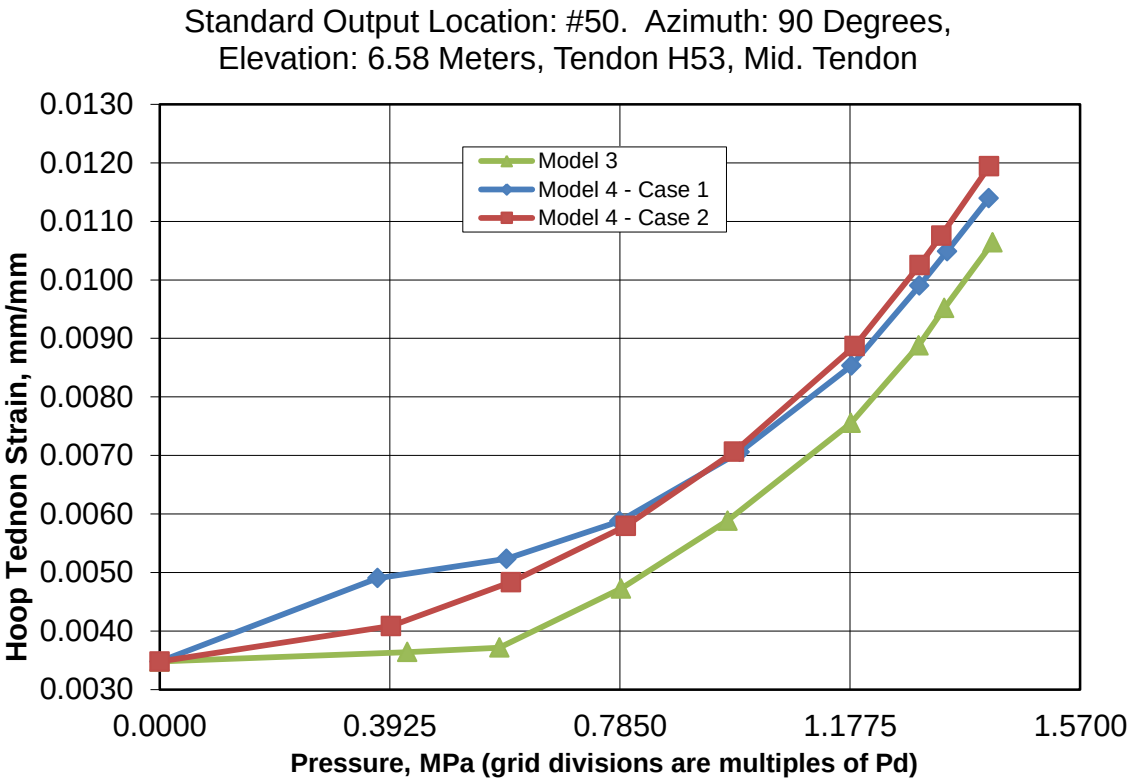

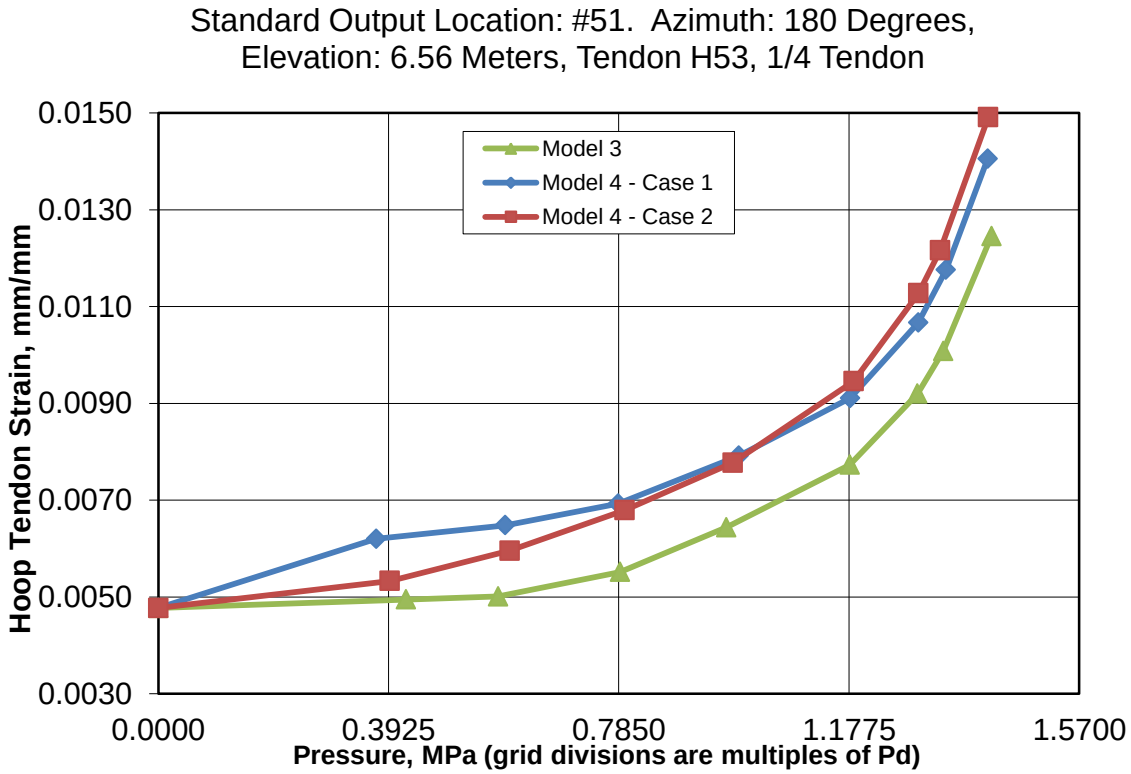

Figure D – 49q: Comparisons at standard output location 50, 51

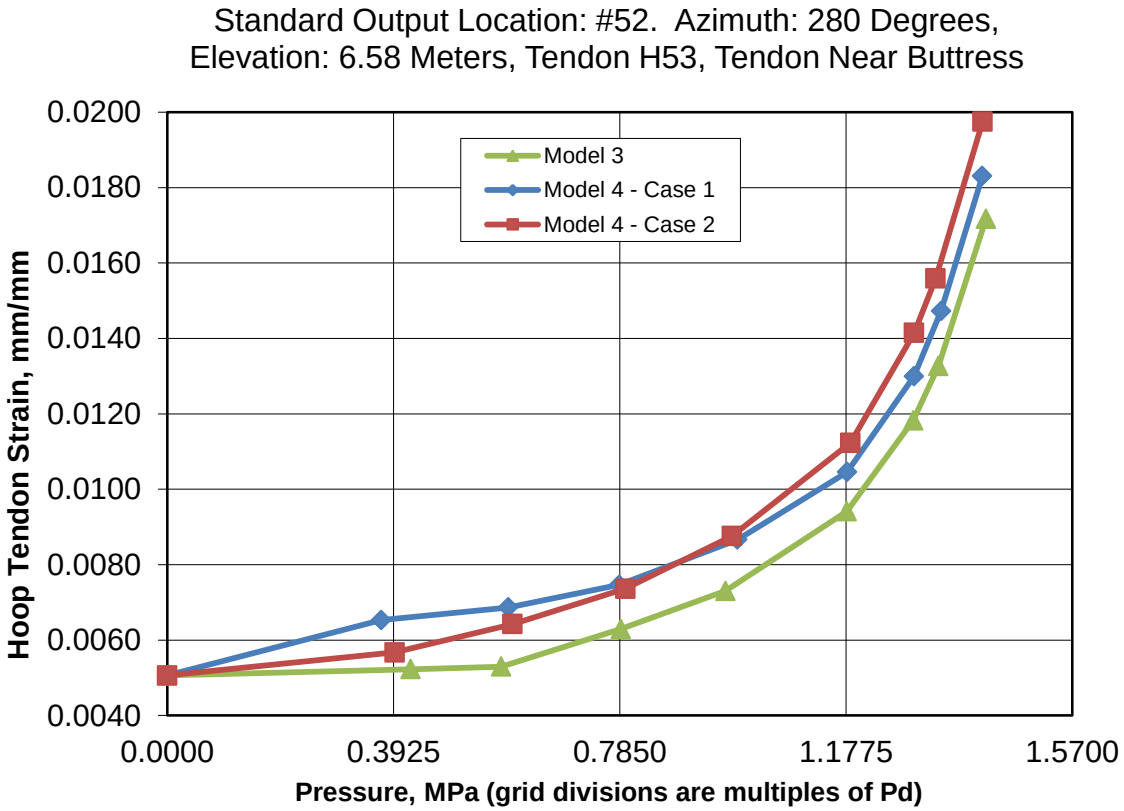

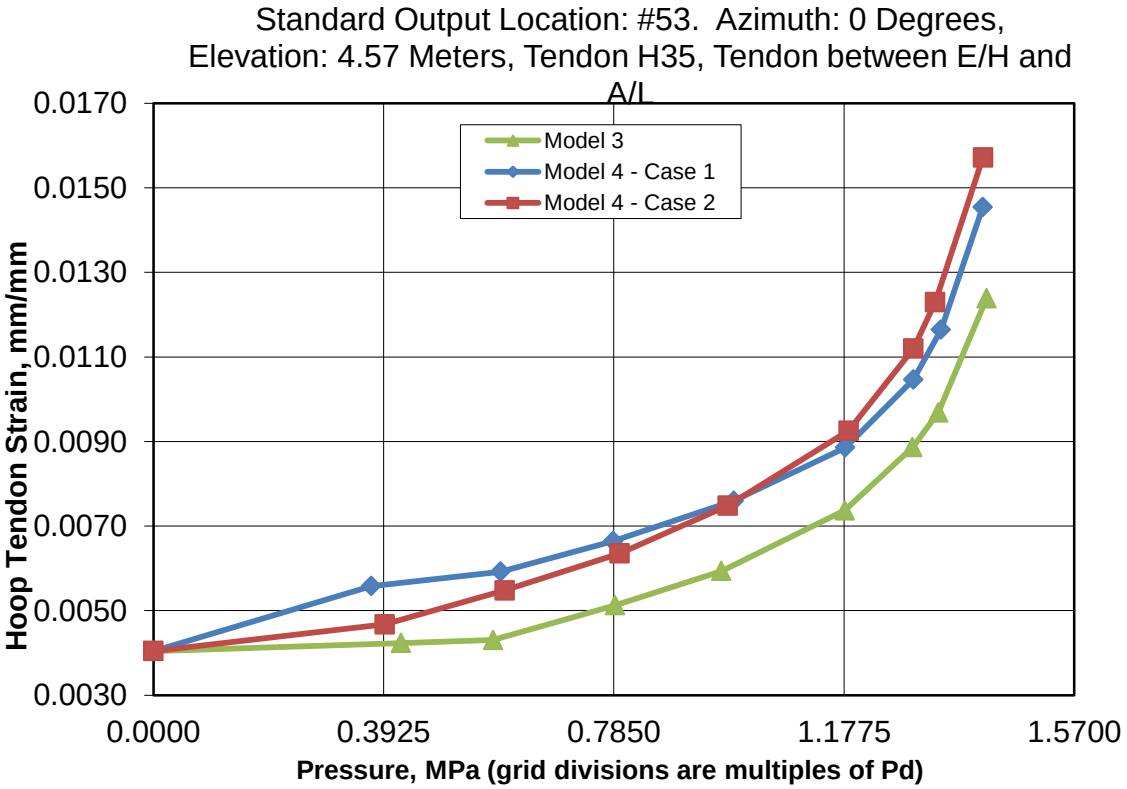

Figure D – 49r: Comparisons at standard output location 52, 53

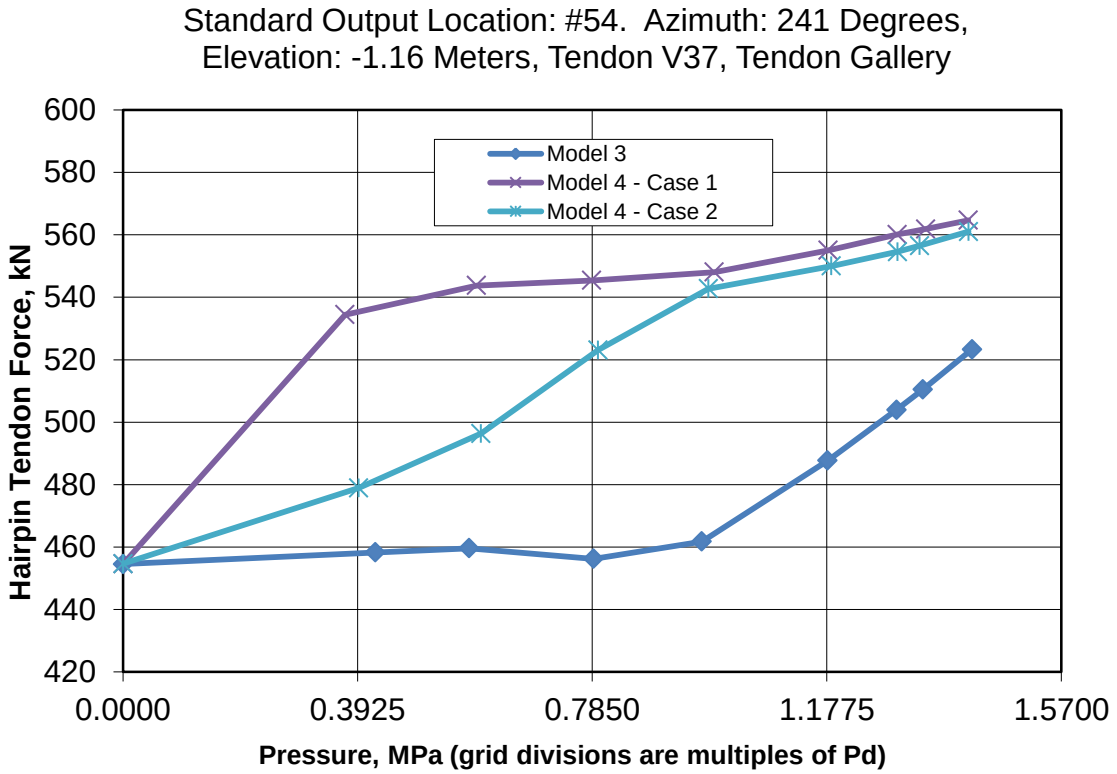

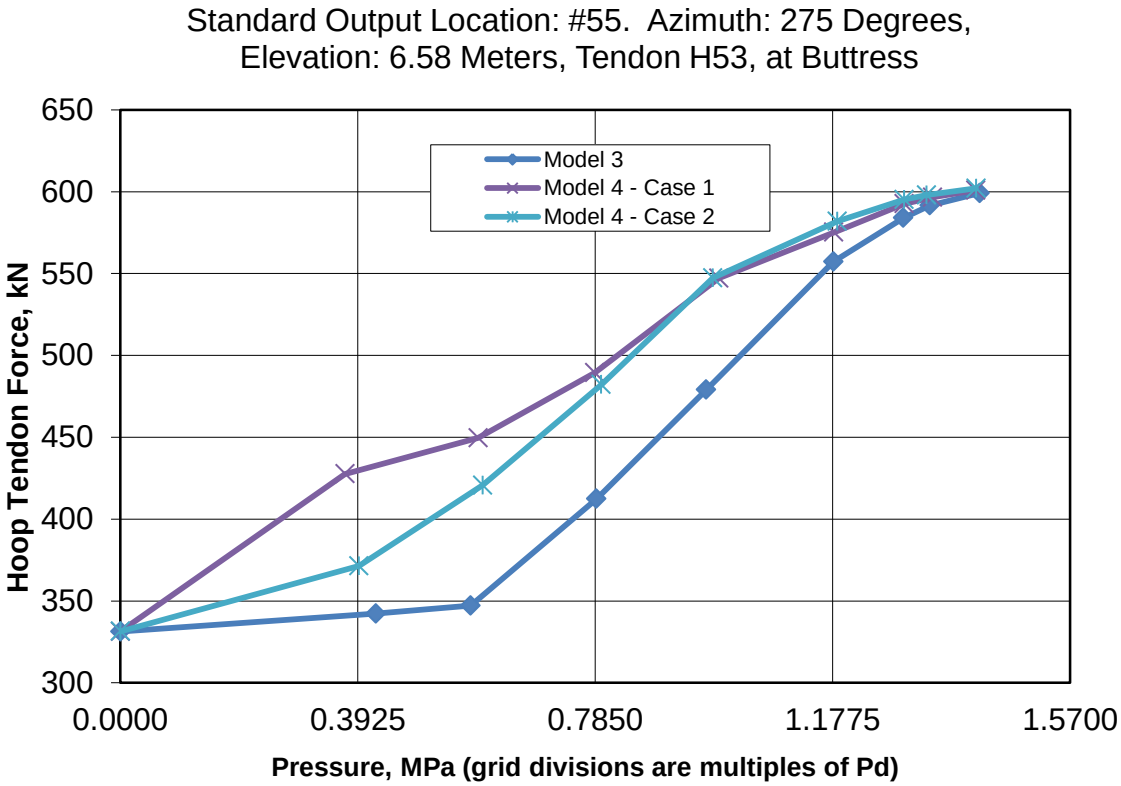

Figure D – 49s: Comparisons at standard output location 54, 55

Failure criteria

From SPE Phase 1, the relevant failure criterion for Model 1 was Tendon failure. The rebar generally has higher ductility than the tendons, so it is not the controlling criteria. For Models 2, 3, and 4, Tendon Failure criteria remains at 3.8% strain as for Model 1. But for Models 3 and 4, liner tearing is the predominate failure mode.

For SPE Phase 2, a key objective of the work is to estimate crack size and leak area. After consideration of alternative methods such as fracture mechanics (some of which were discussed at the April, 2011 SPE participants meeting, it was decided to use the applied methodology developed through EPRI research in the 1990's as the basis for the prediction of crack size and occurrence. This also leads to estimation of leakage versus pressure.

Based on the existing research of behavior of steel-lined concrete containments, liner-tearing with associated leakage is the failure mode for slow pressurization of the containment. Fracture and tearing of the steel shell is followed by leakage through the tear aperture, and then through cracks in the concrete. The strain-failure criterion is the primary method used for this analysis based on its widely used application from previous analysis on concrete containment severe accident studies. Additionally, the Rizkalla formulation provided from the AERB and SNL was used to convert the equivalent peak uniaxial strain at discontinuity locations to the leakage rate. A more detailed description of the leakage prediction method formulated for the current SPE-3 work is provided.

Leakage prediction results – application to SPE model 3 & 4 (3D global analysis)

Liner strain mapping

Liner strain mapping for Model 3 (pressure only) is shown in Figures D-50a through D-50h and for Model 4 (Case 1 and Case 2) in Figures D-51a through D-51h and D-52a through D-52h. The color codes on the strain mapping are shown in Table D-7.

Table D - 7: Strain mapping color codes.

Color codes	
Strain	Color
$0 \le \varepsilon < 0.006$	green
$0.006 \le \varepsilon < 0.012$	yellow
$\varepsilon \ge 0.012$	red

Model 3 – Pressure Only Case:

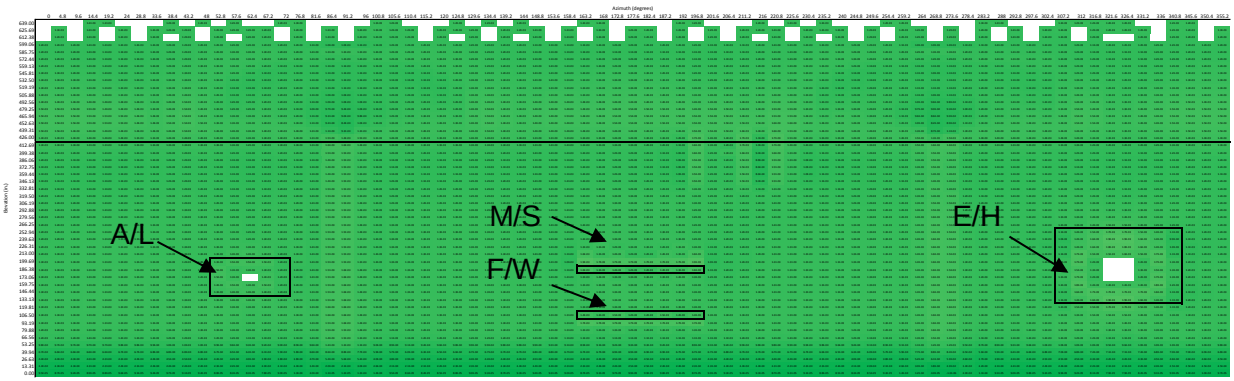

Figure D - 50a: Model 3 liner strain map of entire liner surface at 1.0xPd

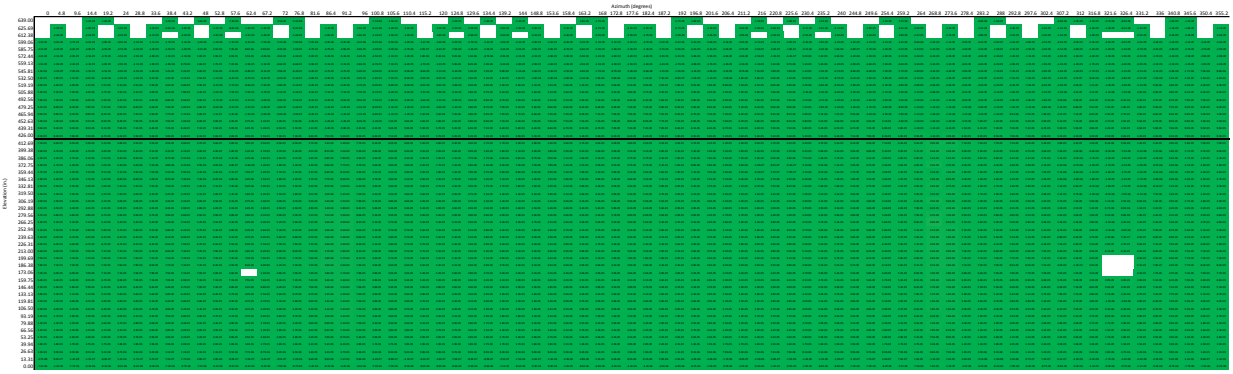

Figure D – 50b: Model 3 liner strain map of entire liner surface at 1.5xPd

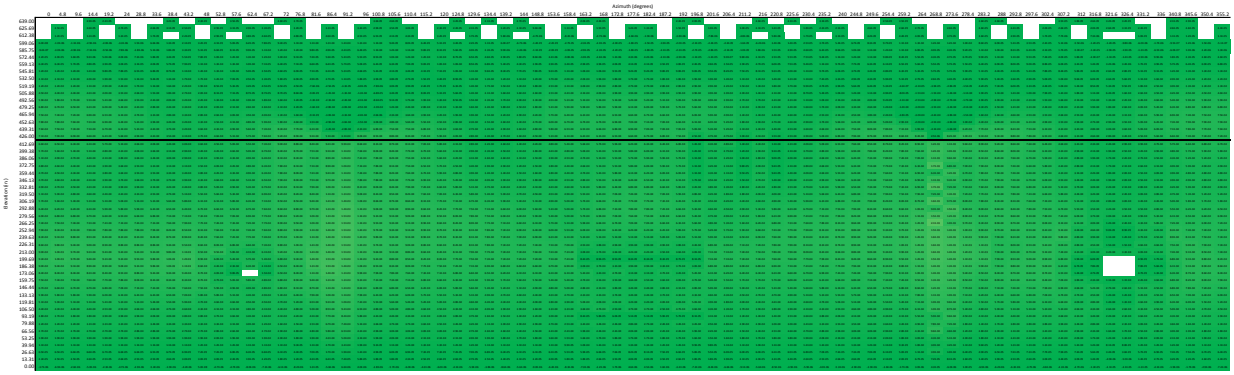

Figure D – 50c: Model 3 liner strain map of entire liner surface at 2.0 xPd

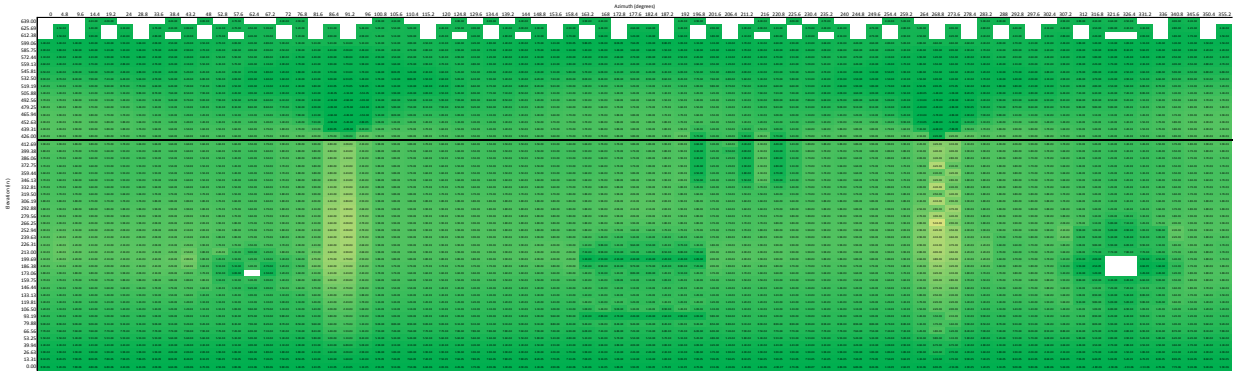

Figure D – 50d: Model 3 Liner Strain Map of Entire Liner Surface at 2.5 xPd

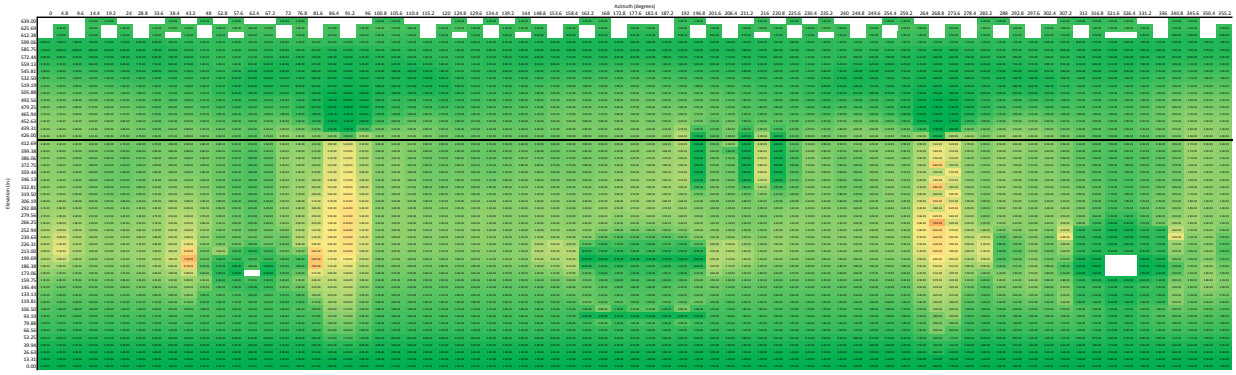

Figure D - 50e: Model 3 liner strain map of entire liner surface at 3.0xPd

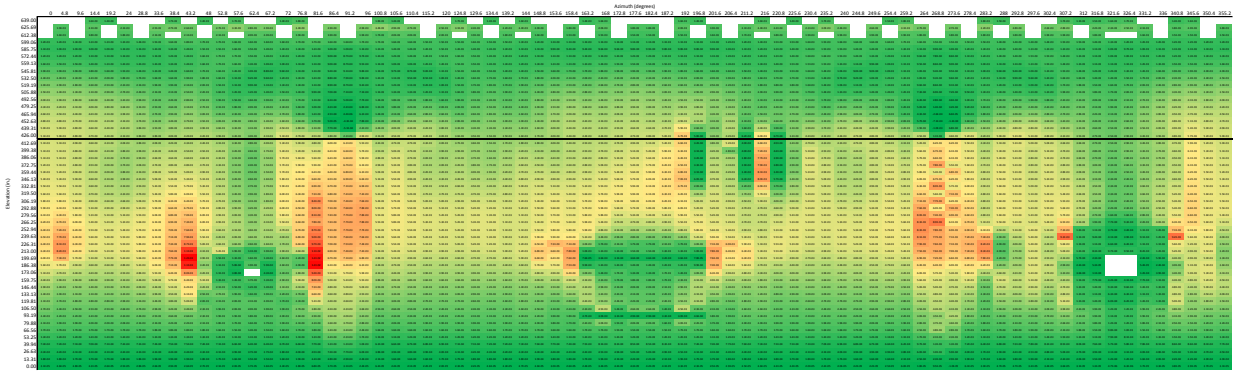

Figure D – 50f: Model 3 liner strain map of entire liner surface at 3.3xPd

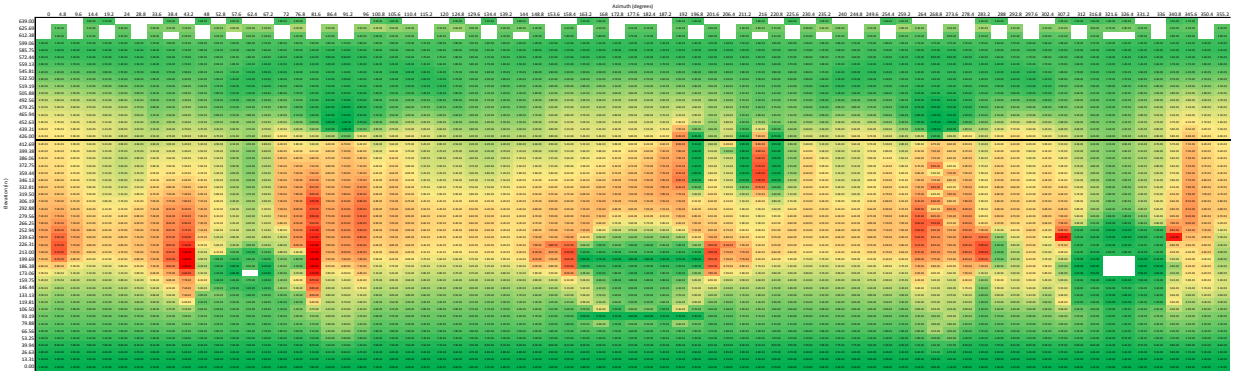

Figure D – 50g: Model 3 liner strain map of entire liner surface at 3.4xPd

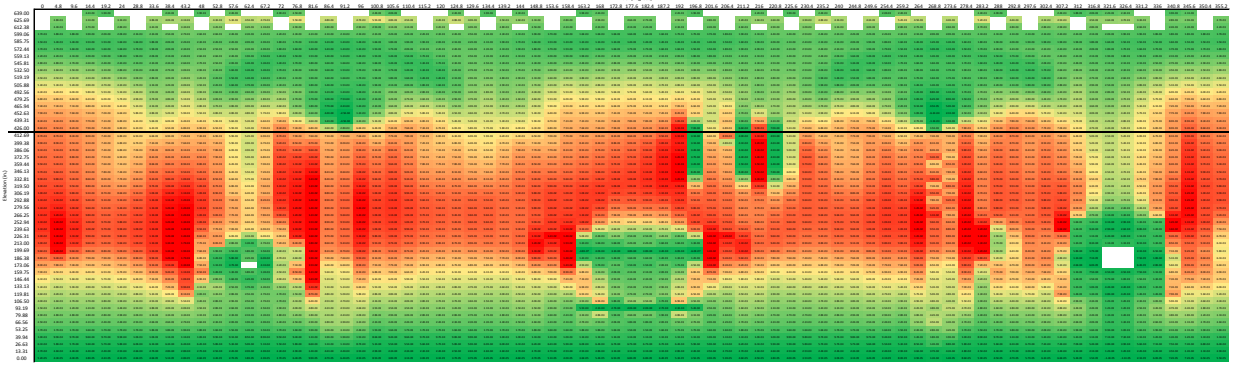

Figure D – 50h: Model 3 liner strain map of entire liner surface at 3.6xPd

Case 1:

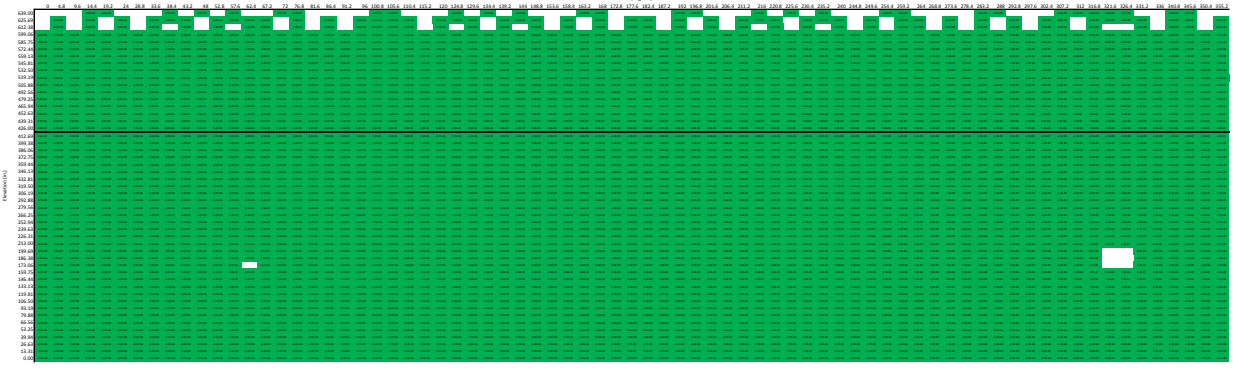

Figure D - 51a: Case 1 liner strain map of entire liner surface at 1.0xPd

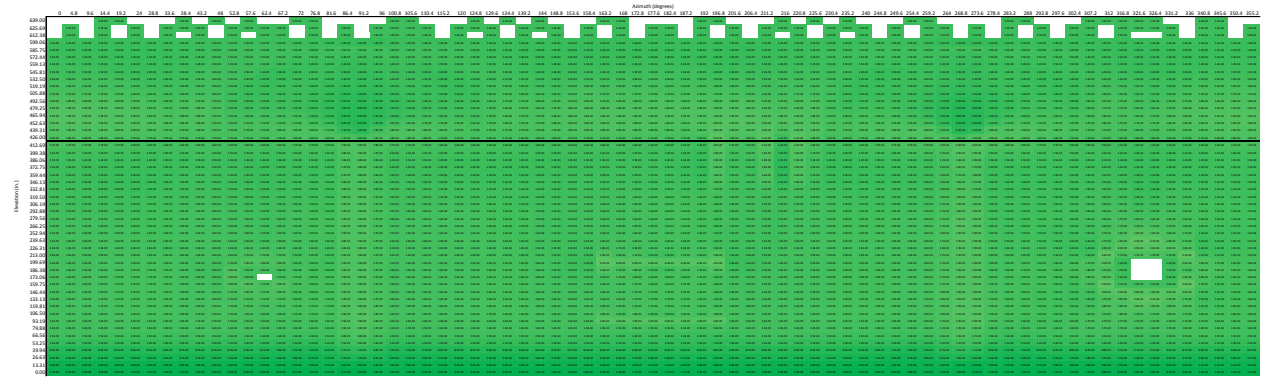

Figure D – 51b: Case 1 liner strain map of entire liner surface at 1.5xPd

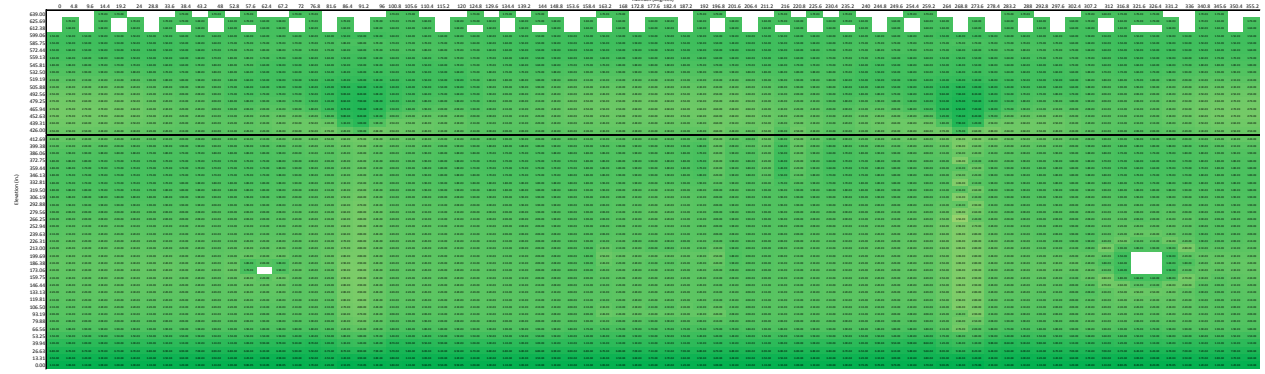

Figure D – 51c: Case 1 liner strain map of entire liner surface at 2.0xPd

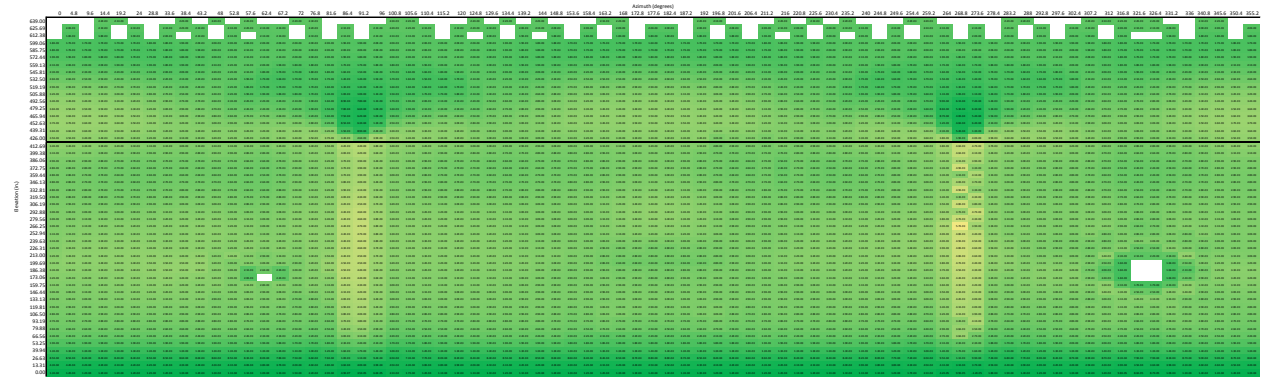

Figure D – 51d: Case 1 liner strain map of entire liner surface at 2.5xPd

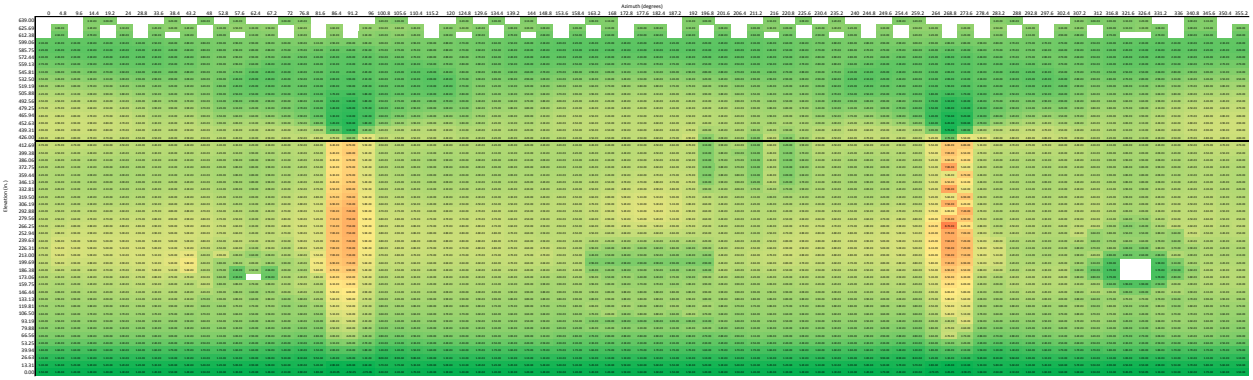

Figure D – 51e: Case 1 liner strain map of entire liner surface at 3.0xPd

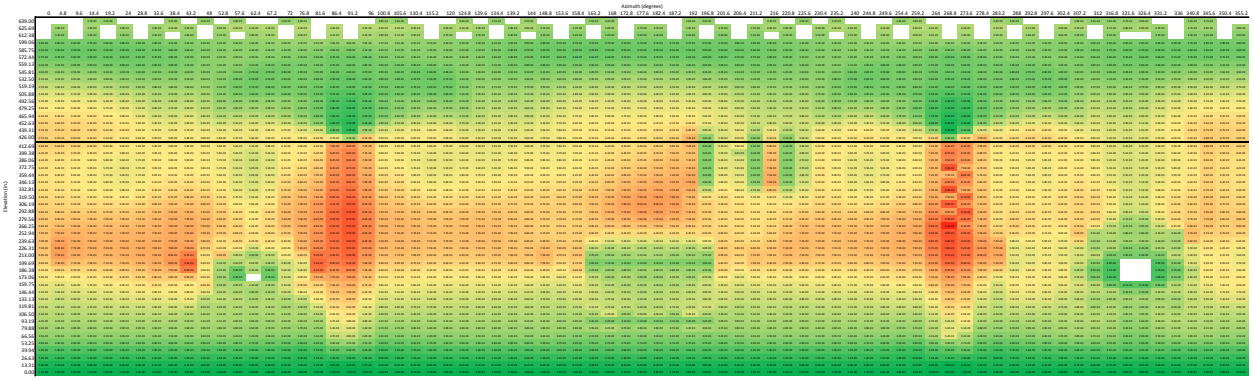

Figure D – 51f: Case 1 liner strain map of entire liner surface at 3.3xPd

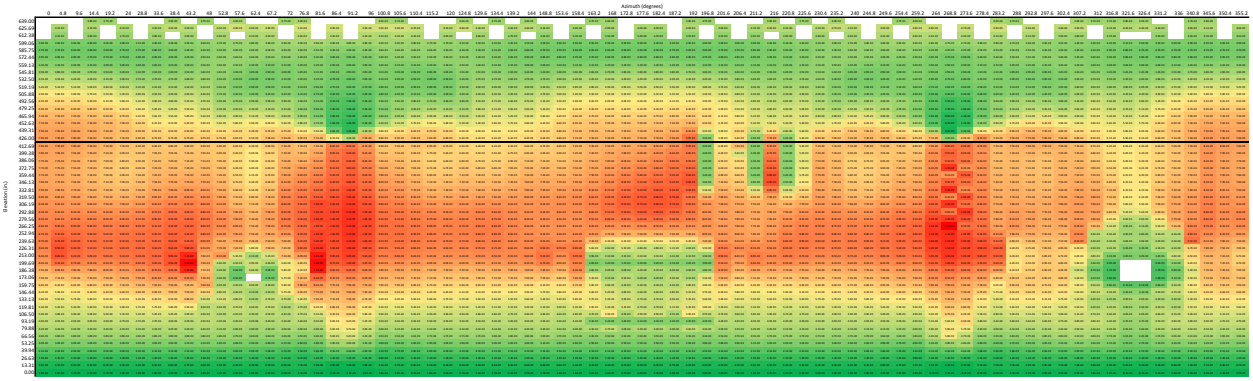

Figure D – 51g: Case 1 liner strain map of entire liner surface at 3.4xPd

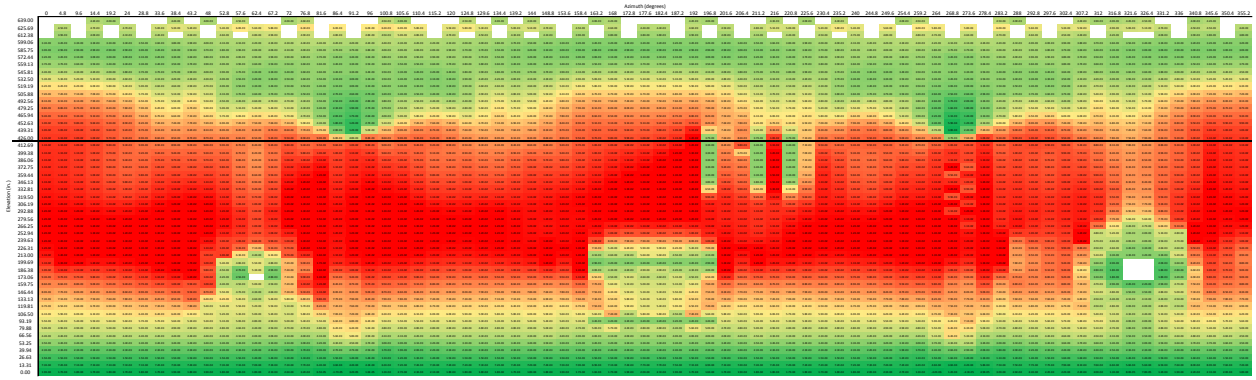

Figure D – 51h: Case 1 liner strain map of entire liner surface at 3.6xPd

Case 2:

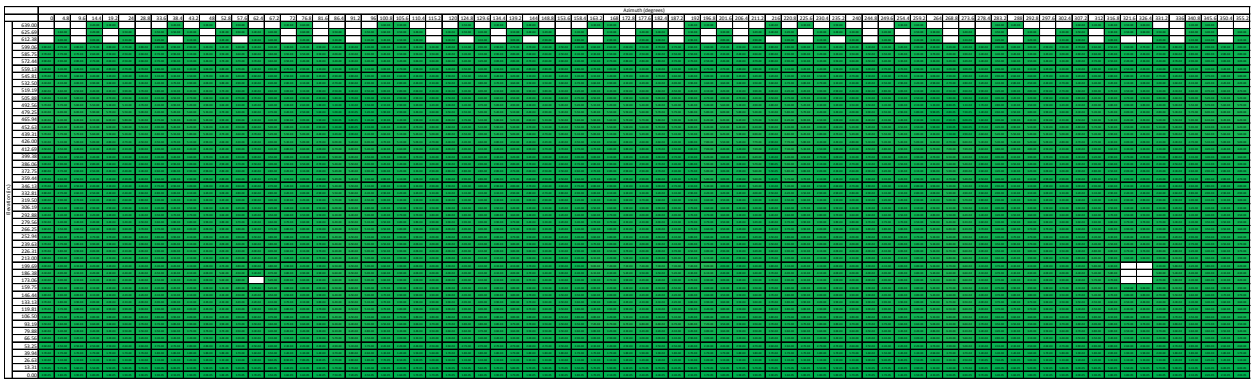

Figure D - 52a: Case 2 liner strain map of entire liner surface at 1.0xPd

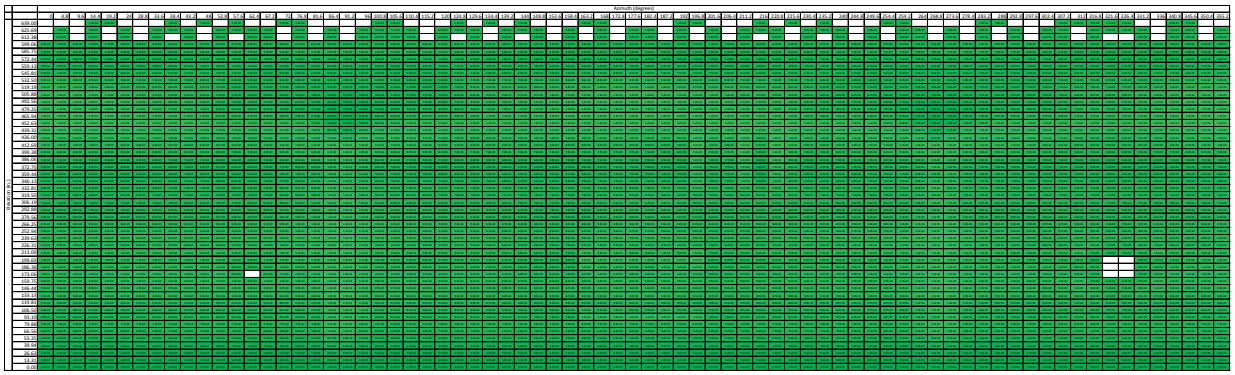

Figure D – 52b: Case 2 liner strain map of entire liner surface at 1.5xPd

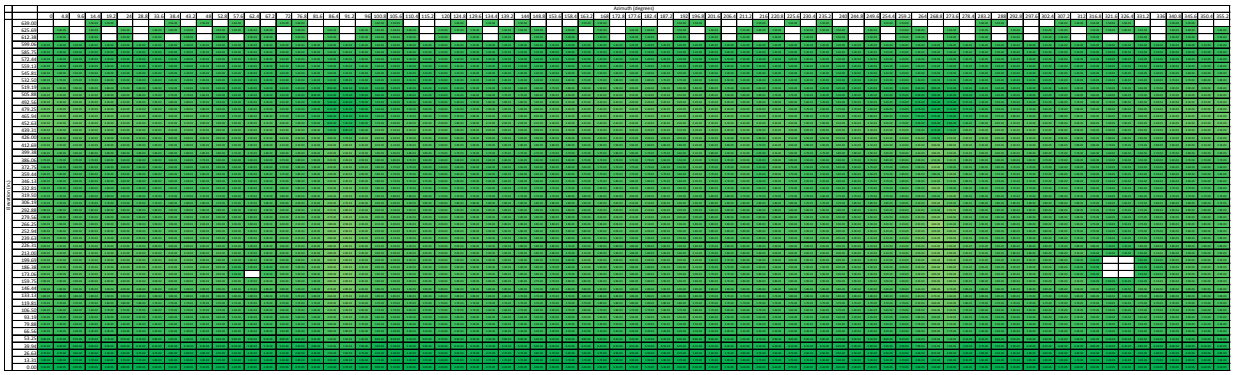

Figure D – 52c: Case 2 liner strain map of entire liner surface at 2.0xPd

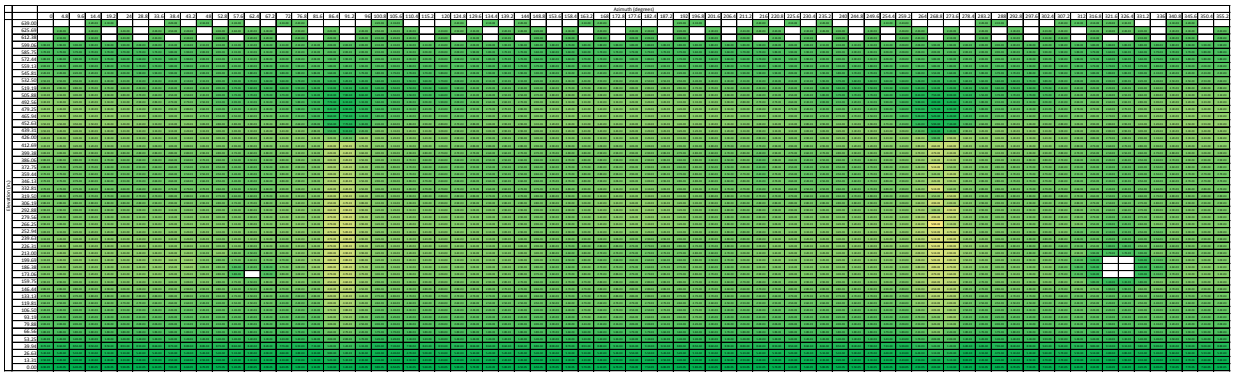

Figure D – 52d: Case 2 liner strain map of entire liner surface at 2.5xPd

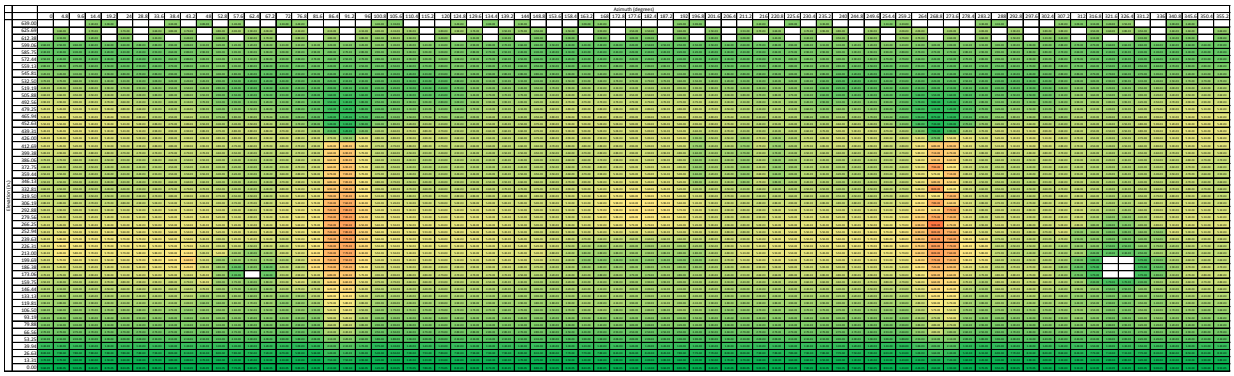

Figure D – 52e: Case 2 liner strain map of entire liner surface at 3.0xPd

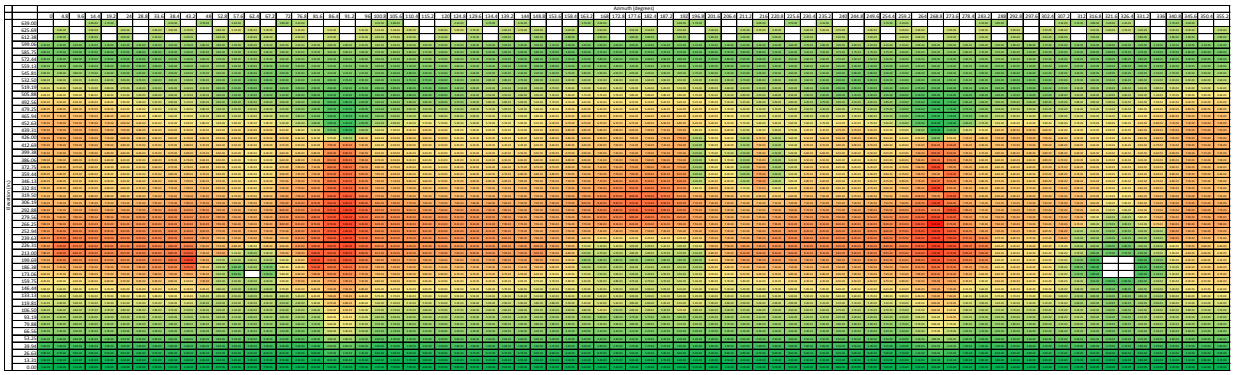

Figure D – 52f: Case 2 liner strain map of entire liner surface at 3.3xPd

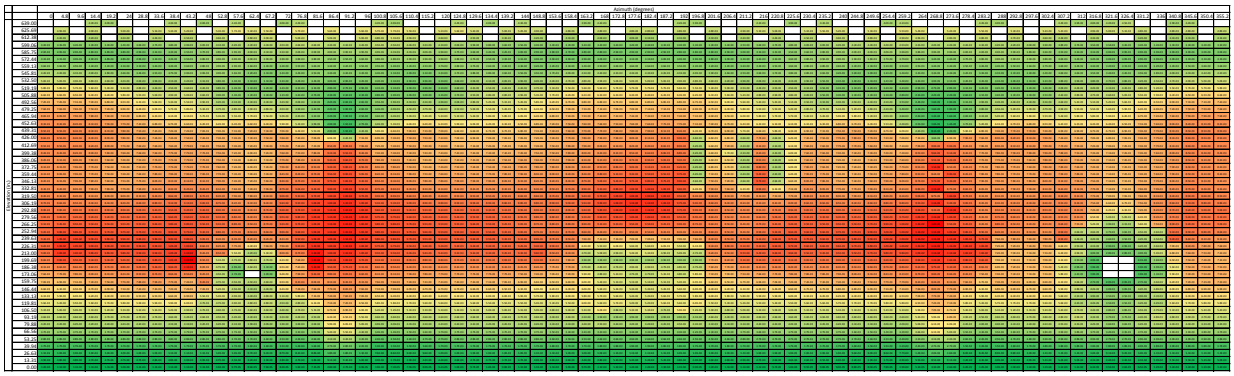

Figure D – 52g: Case 2 liner strain map of entire liner surface at 3.4xPd

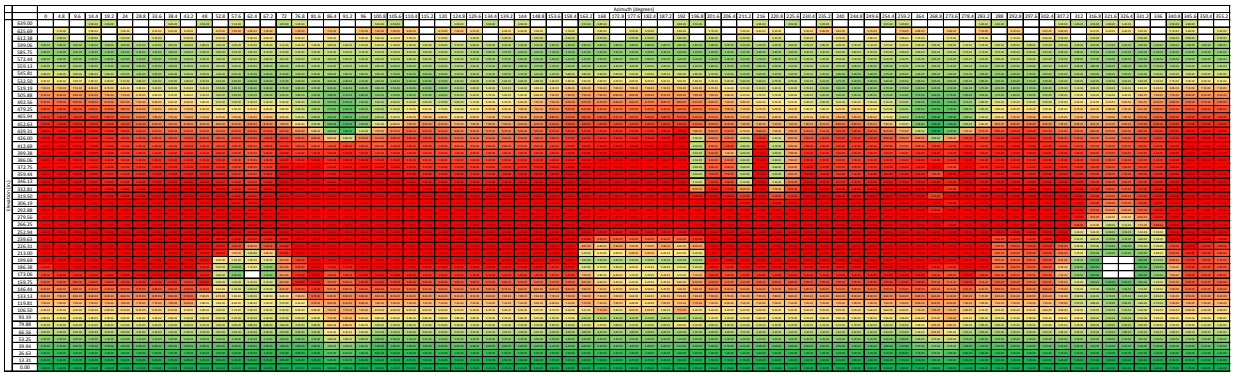

Figure D – 52h: Case 2 liner strain map of entire liner surface at 3.6xPd

Leakage rate

Liner strain is the primary predictor of crack occurrence and liner crack area, as derived in Appendix A. The conversion from liner strain (which is hoop direction strain) to leakage rate is shown in Figures D-53a through D-53h for Model 3, and Figures D-54a through D-54h and D-

55a through D-55h for Model 4 (Case 1 and Case 2). The color codes on the leakage rates are shown in Table D-8.

Table D - 8: Leakage rate color codes.

Color codes	
Leakage rate (ft^3/s)	Color
Q ≤ 0	white
0 < Q < 0.5	green
0.5 ≤ Q < 1.0	yellow
Q ≥ 1.0	orange

Model 3 – Pressure Only Case:

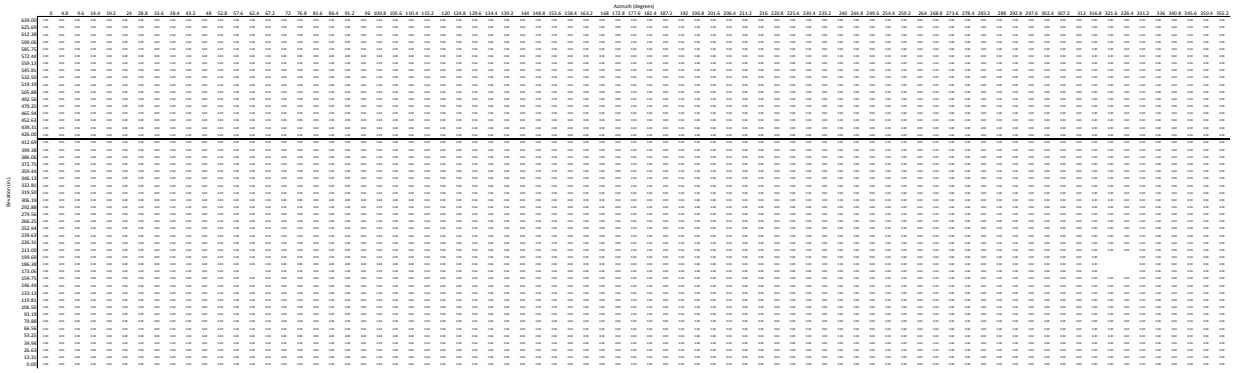

Figure D - 53a: Model 3 mapping of leakage rate of entire liner surface at 2.5xPd

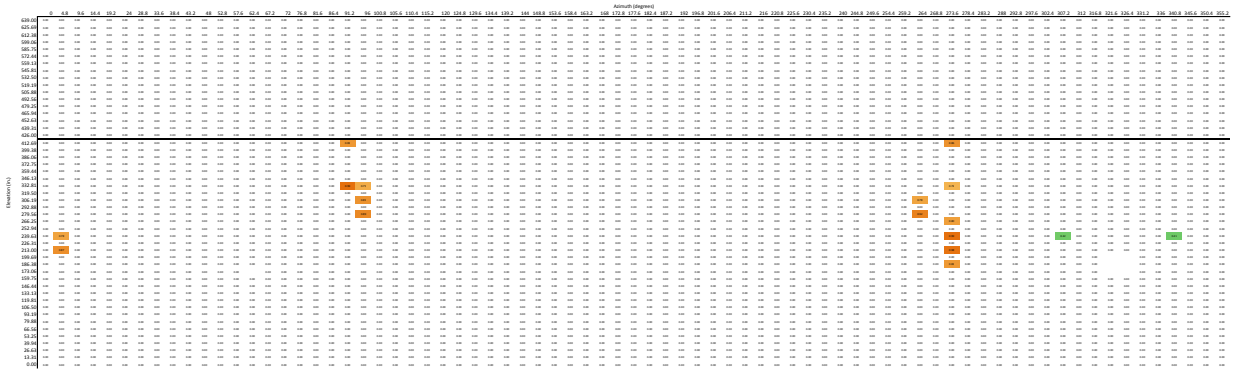

Figure D – 53b: Model 3 mapping of leakage rate of entire liner surface at 3.0xPd

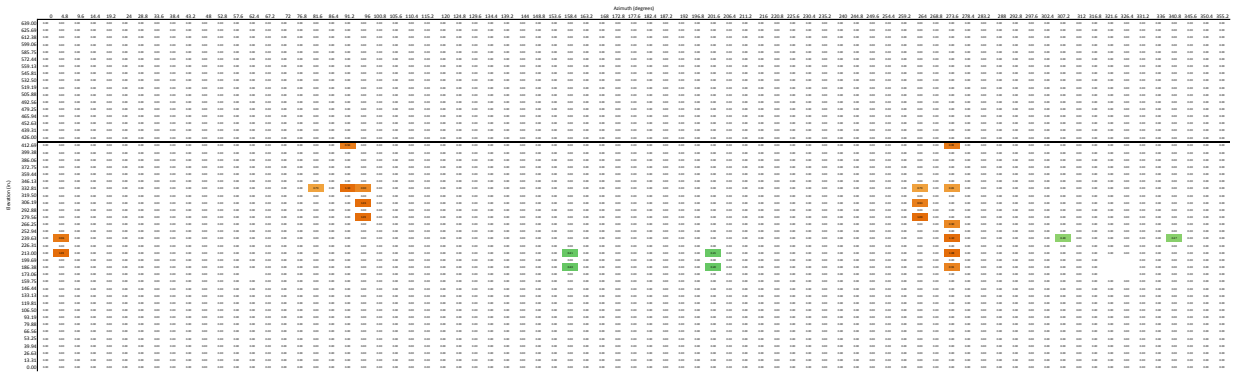

Figure D – 53c: Model 3 mapping of leakage rate of entire liner surface at 3.1xPd

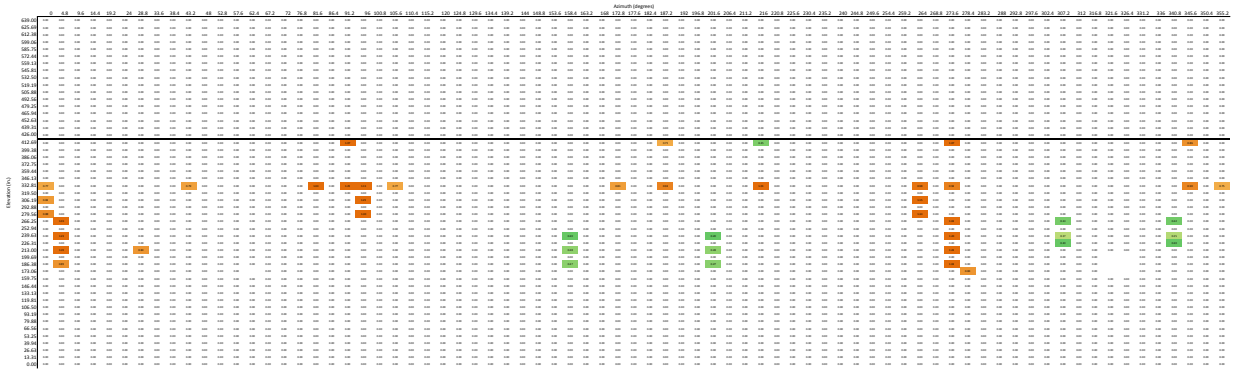

Figure D – 53d: Model 3 mapping of leakage rate of entire liner surface at 3.2xPd

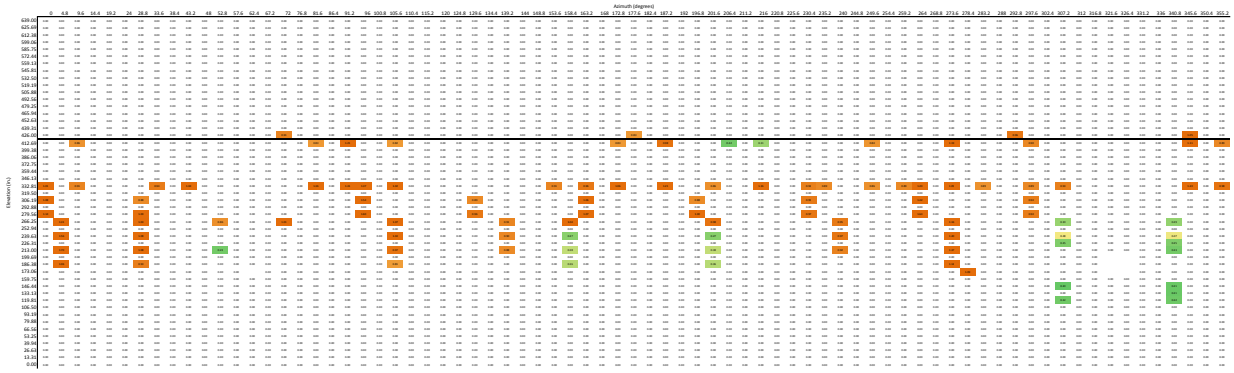

Figure D – 53e: Model 3 mapping of leakage rate of entire liner surface at 3.3xPd

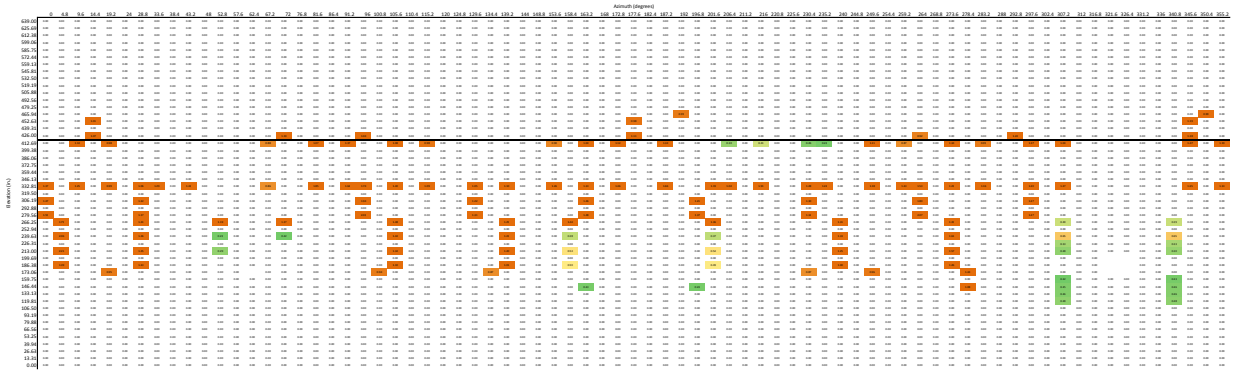

Figure D – 53f: Model 3 mapping of leakage rate of entire liner surface at 3.4xPd

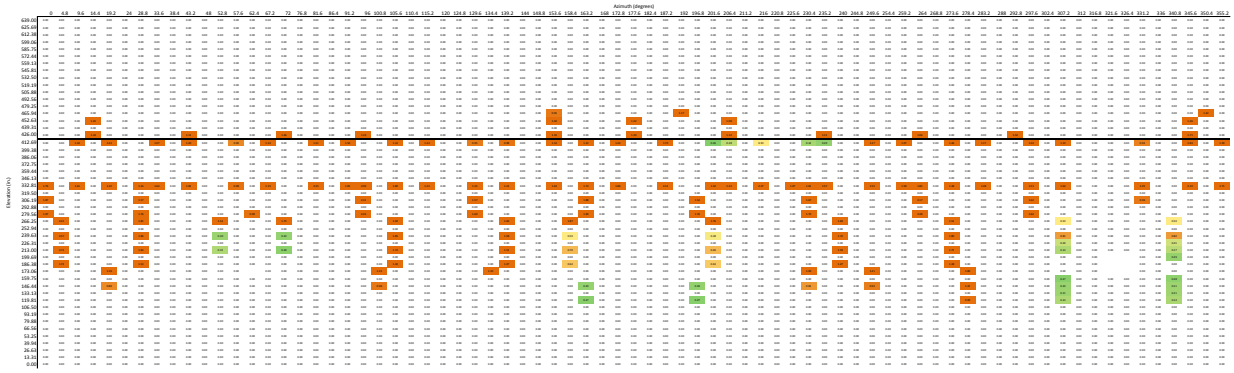

Figure D – 53g: Model 3 mapping of leakage rate of entire liner surface at 3.5xPd

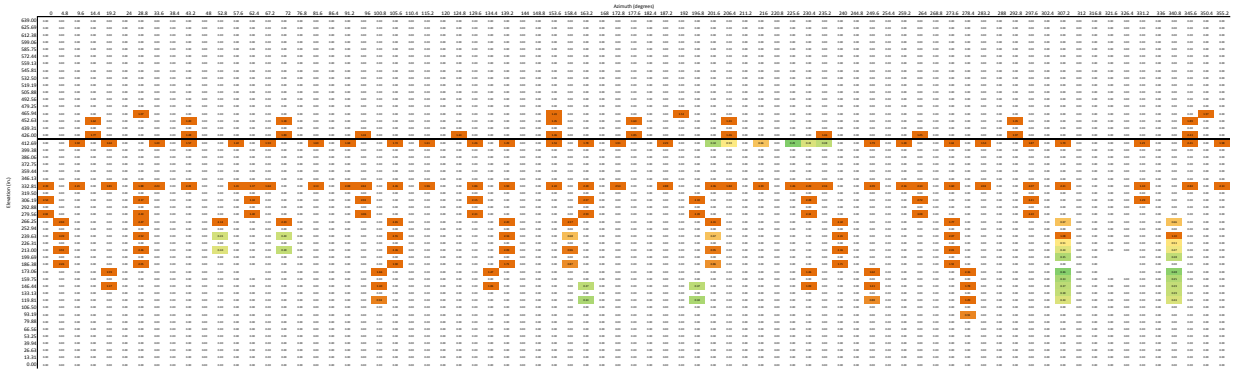

Figure D – 53h: Model 3 Mapping of leakage rate of entire liner surface at 3.6xPd

Model 4 – Case 1:

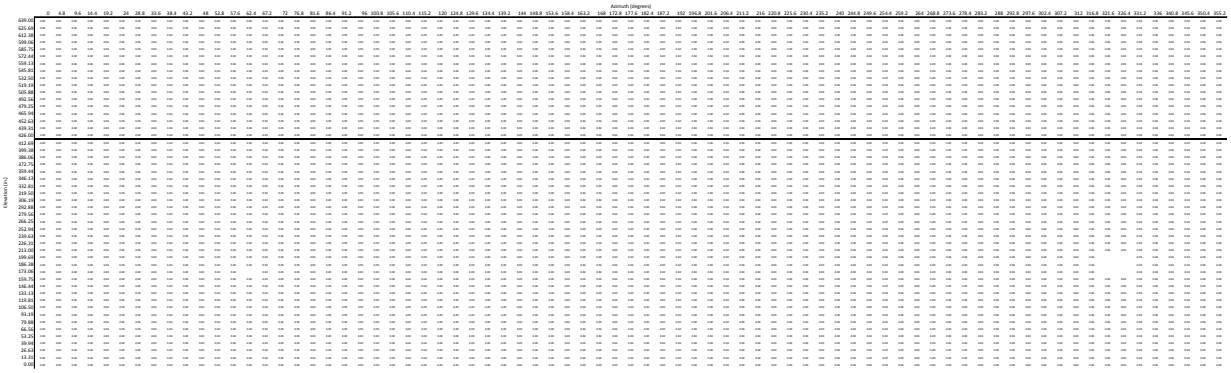

Figure D - 54a: Case 1 mapping of leakage rate of entire liner surface at 2.5xPd

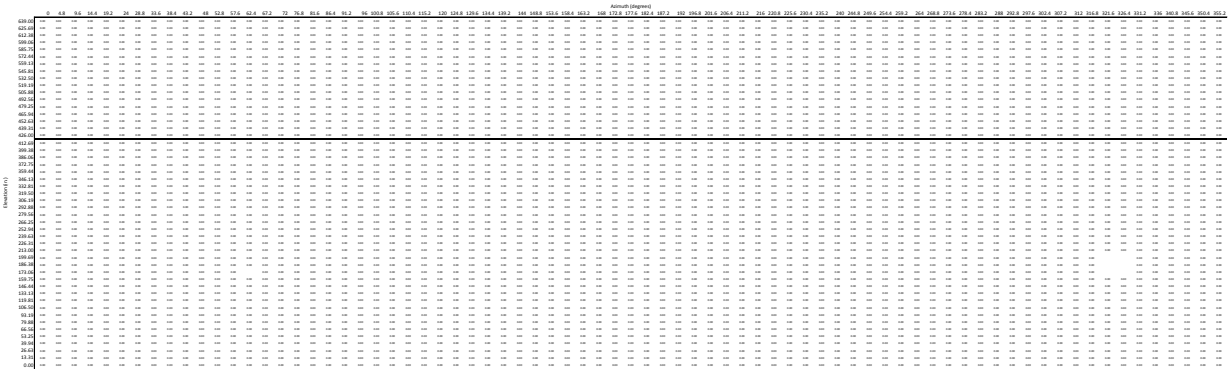

Figure D – 54b: Case 1 mapping of leakage rate of entire liner surface at 3.0xPd

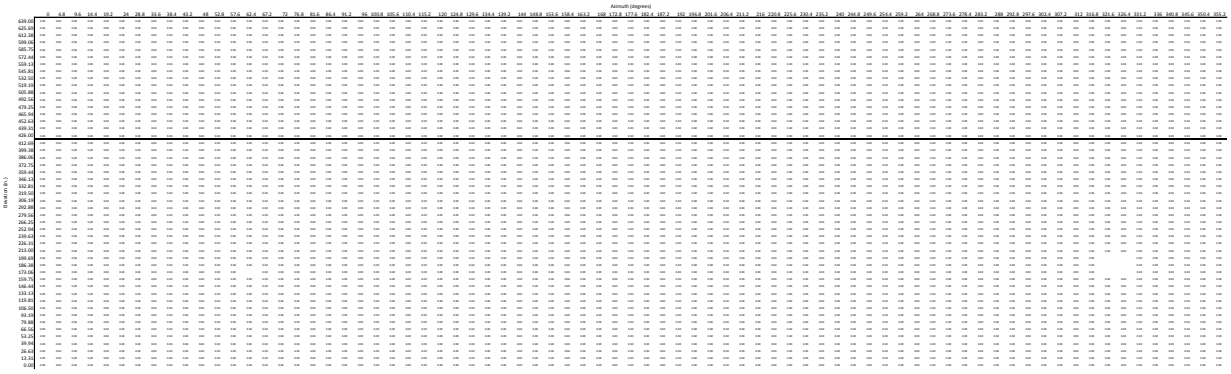

Figure D – 54c: Case 1 mapping of leakage rate of entire liner surface at 3.1xPd

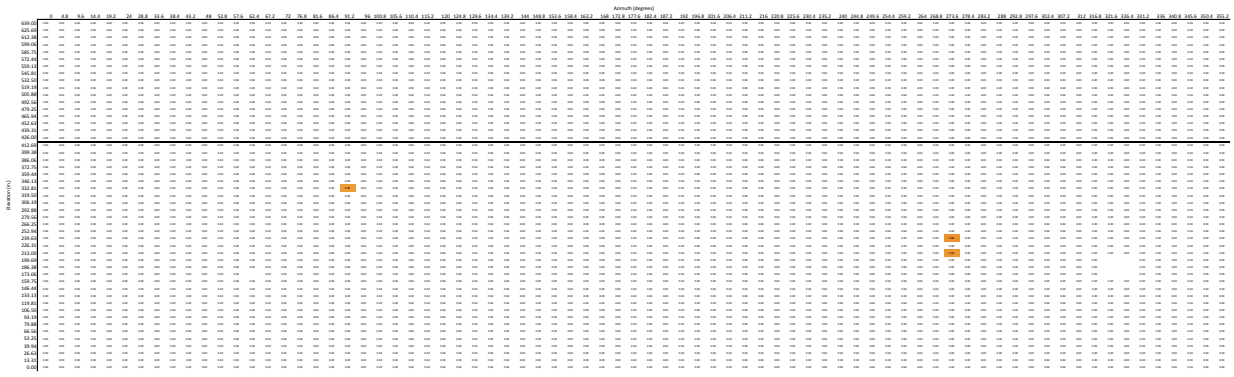

Figure D – 54d: Case 1 mapping of leakage rate of entire liner surface at 3.2xPd

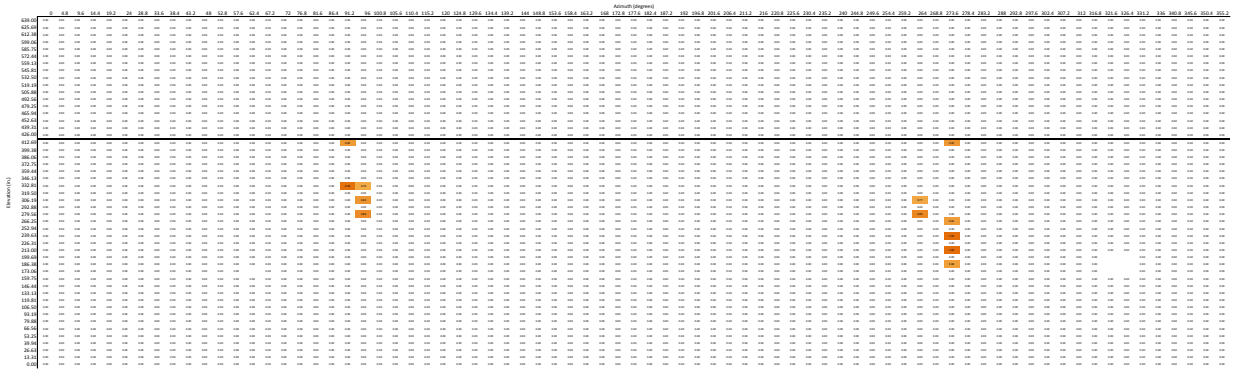

Figure D – 54e: Case 1 mapping of leakage rate of entire liner surface at 3.3xPd

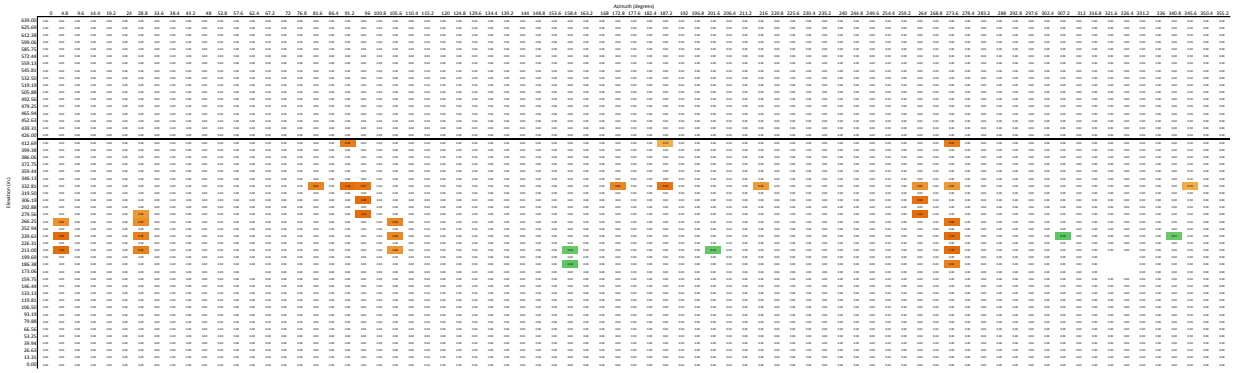

Figure D – 54f: Case 1 mapping of leakage rate of entire liner surface at 3.4xPd

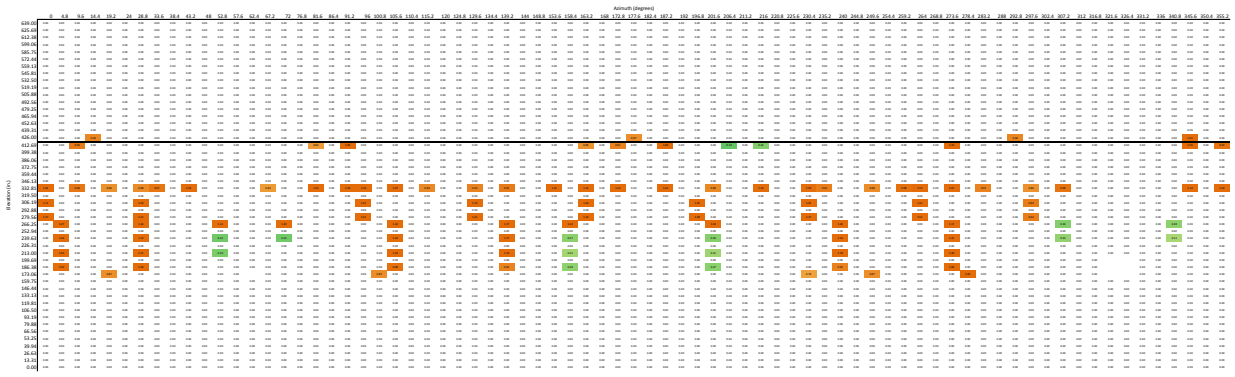

Figure D – 54g: Case 1 mapping of leakage rate of entire liner surface at 3.5xPd

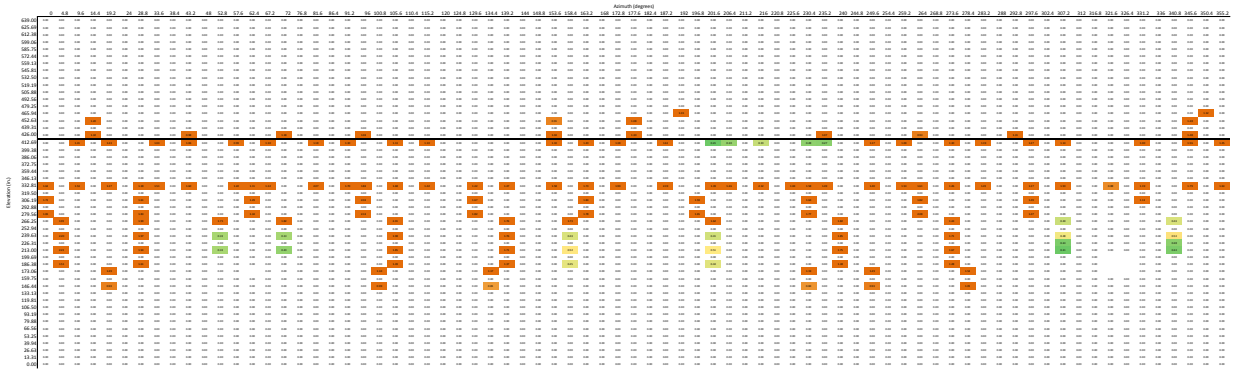

Figure D – 54h: Case 1 mapping of leakage rate of entire liner surface at 3.6xPd

Model 4 – Case 2:

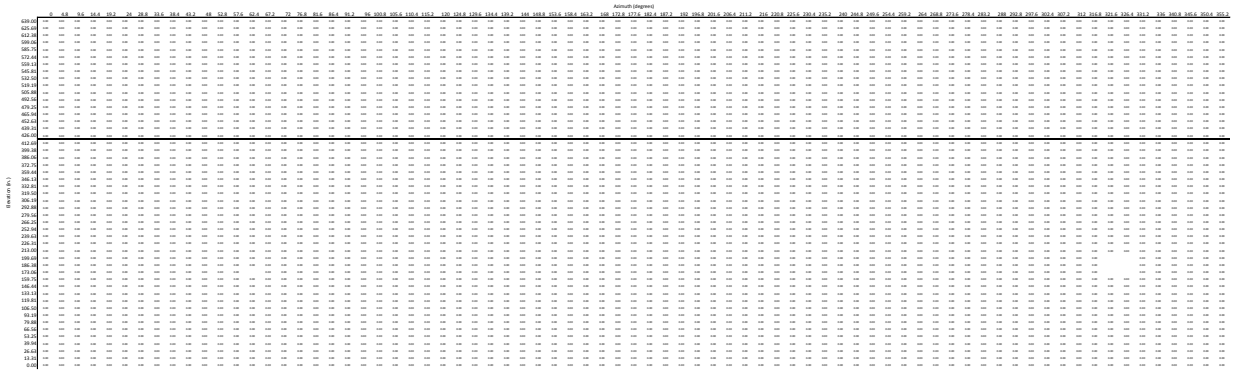

Figure D - 55a: Case 2 mapping of leakage rate of entire liner surface at 2.5xPd

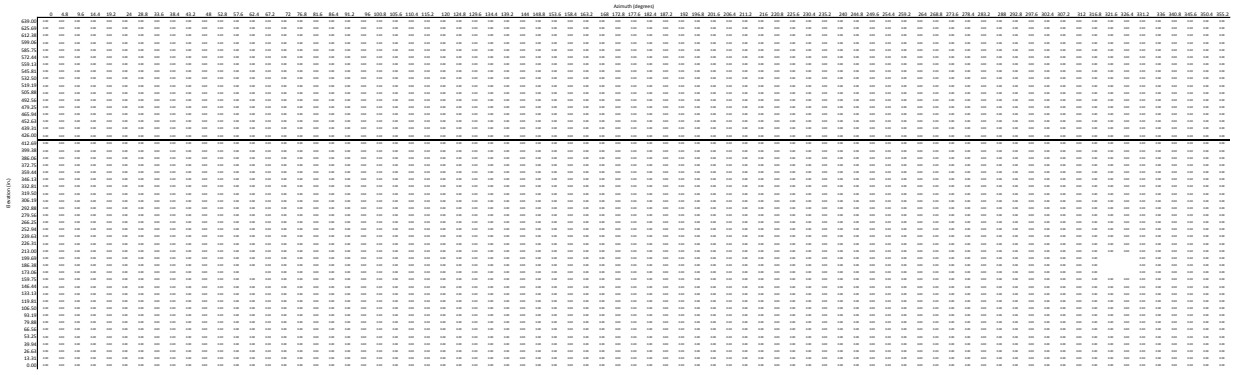

Figure D – 55b: Case 2 mapping of leakage rate of entire liner surface at 3.0xPd

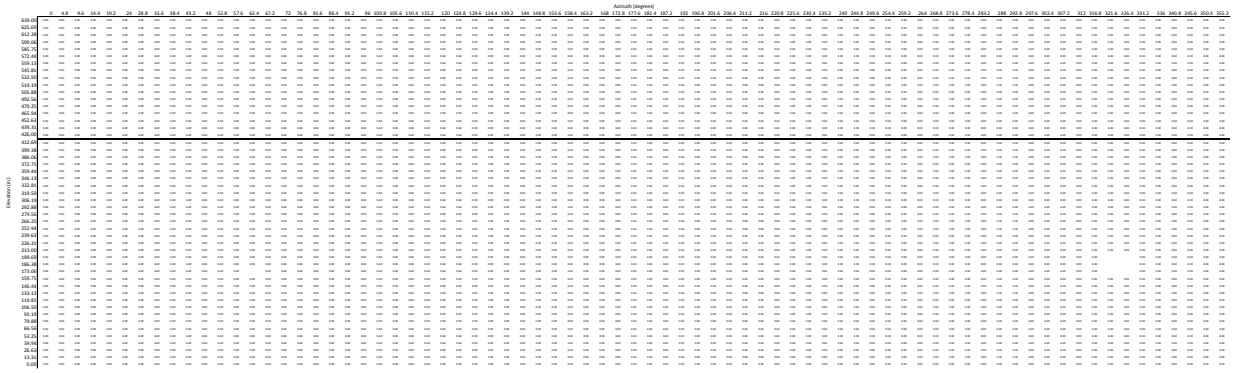

Figure D – 55c: Case 2 mapping of leakage rate of entire liner surface at 3.1xPd

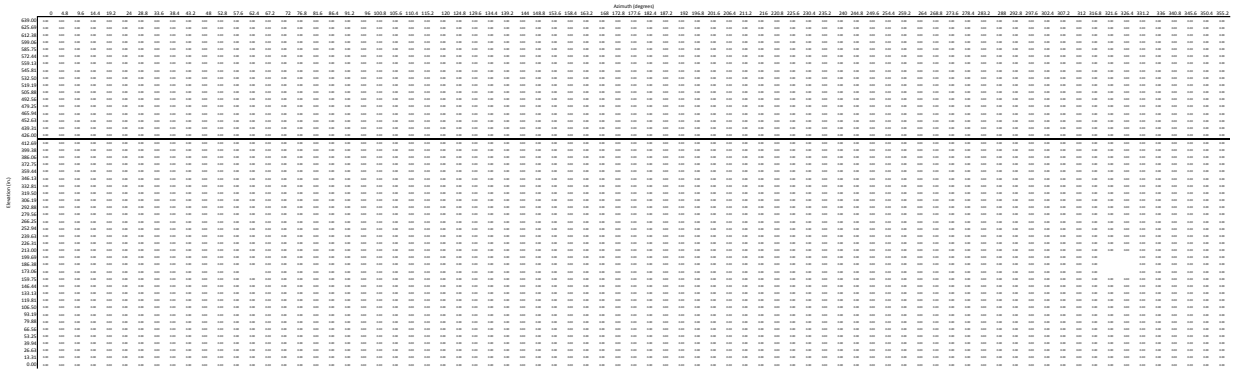

Figure D – 55d: Case 2 mapping of leakage rate of entire liner surface at 3.2xPd

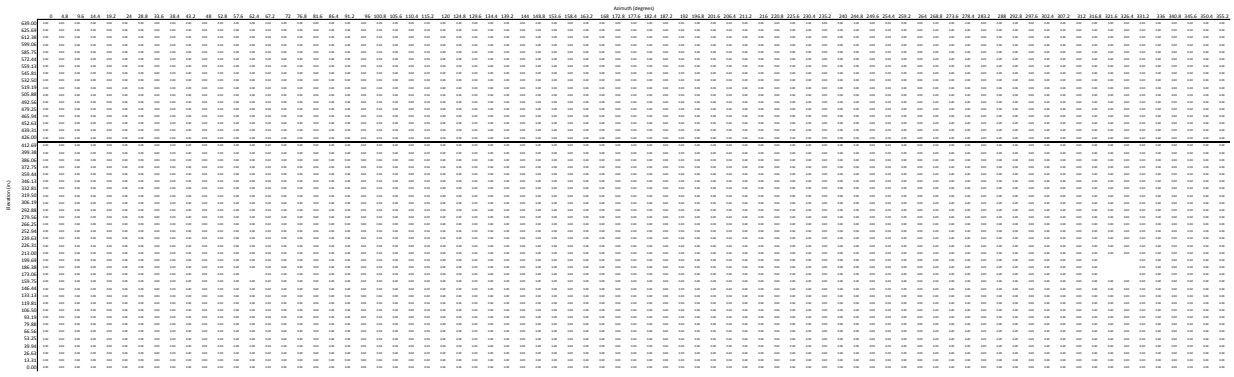

Figure D – 55e: Case 2 mapping of leakage rate of entire liner surface at 3.3xPd

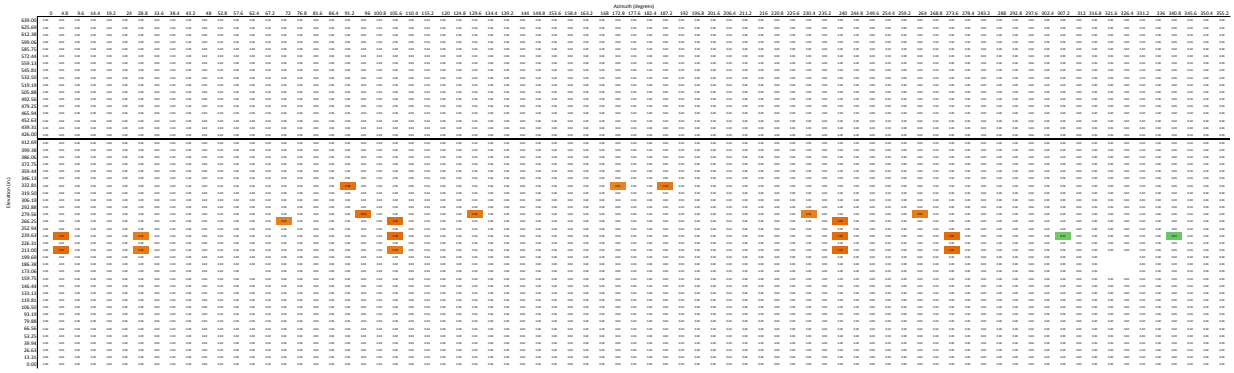

Figure D – 55f:Case 2 mapping of leakage rate of entire liner surface at 3.4xPd

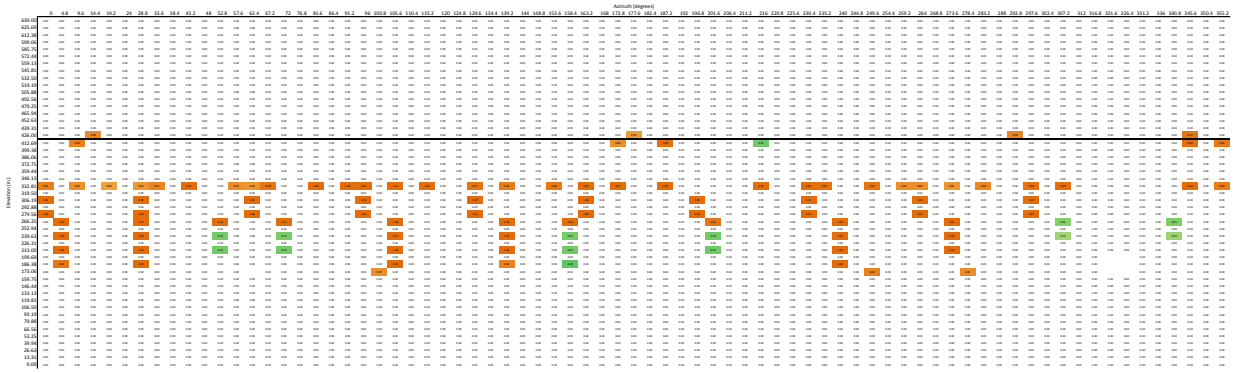

Figure D – 55g: Case 2 mapping of leakage rate of entire liner surface at 3.5xPd

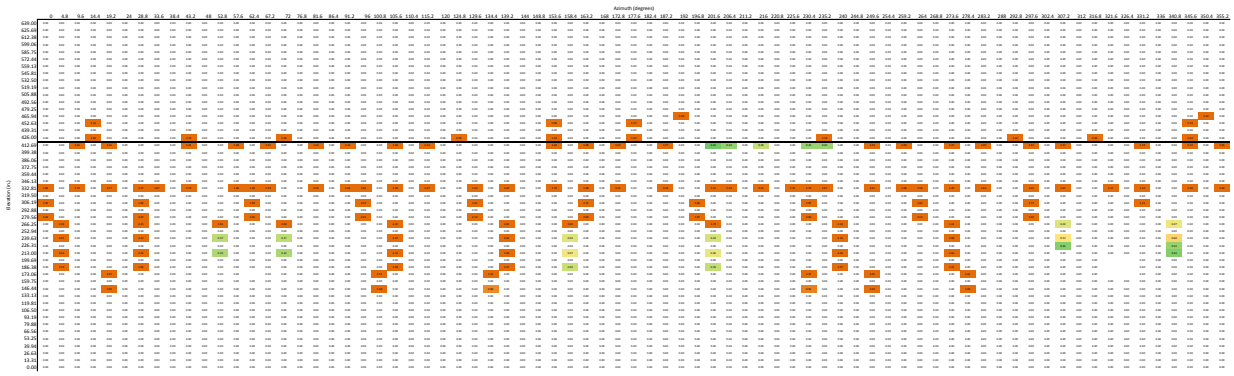

Figure D – 55h: Case 2 mapping of leakage rate of entire liner surface at 3.6xPd

A comparison amongst the three models' leakage rates is outlined in Table D-9. An illustration of leakage rate versus pressure (for Model 3 with no temperature) is displayed in Figure D-57a. Comparisons of this calculation, between Model 3, and Model 4 – Case 1 and Model 4 – Case 2, are shown in Figure D-57b.

As described in Appendix A, liner cracks are driven by liner hoop strain, magnified by a local strain concentration factor, K, and biaxiality (ductility reduction) factor, B. In Figure D-57, K is based on the assumptions summarized in Appendix A; in summary, K occurs at weld-seams which are coincident with stiffness discontinuities (such as stiffener "rat-holes" or penetrations or embossments. But we also know from Ref. [7, 12], that defects in material and construction played a role in the occurrence of tears. This is summarized in the following excerpt from [12]: "All of the 16 tear locations observed were near weld seams, with some variation in the presence or configuration of a rat-hole. Liner welding irregularities were present at almost all of the tear locations. These irregularities included points of extensive repair, such as grinding, points of discontinuous or missing back-up bars, or points with weld and liner seam fit-up irregular geometry.

The liner weld irregularities have been well documented, and are summarized as follows.

- Visual observation showed extensive grinding and weld repair in the liner welds where most of the tears occurred. Ultrasonic measurements showed substantial reductions in thickness near these tears. Measurements showed ~23% thickness reductions in many locations, and more (up to 40% in a few locations). (Several instances were found in which the liner adjacent to repair welds had been completely ground through and subsequently repair welded.)

- Localized plastic deformation occurred in association with many of the vertical field welds, particularly in the vicinity if the tears. No evidence of brittle fracture was seen.

- Photos of the back side of the liner revealed irregularities (missing segments of back-up bars, discontinuous in horizontal stiffeners) associated with a number of the tears.

- Mechanical testing showed only small strain localization in the weld heat affected zones – much less than observed in the liner base metal. Ultimate strength (~72 ksi) was not degraded by welding.

- No evidence was found of material problems that could account for the premature tearing of the liner. Only one tear (1) was associated with a weld defect. This was a lack-of-fusion defect, not porosity in the fusion zone.

- Metallography showed that nearly all of the tear areas had been ground at least 23%, both in preparation repair welding and followed repair welding. The report [19] concluded that most of the tears can be attributed to this excessive grinding."

Appendix A shows that one viable way of incorporating these defects is to modify K; the 1:4 Scale PCCV liner weld defects (grinding, inconsistent back-up bars, etc.) have the effect of approximately doubling "K". To show how this can be implemented, K has been doubled at all the observed tear locations (Figure A-3a superimposed onto the strain map, which produces Figure D-56). The leakage rate is re-calculated and plotted in Figure D-59.

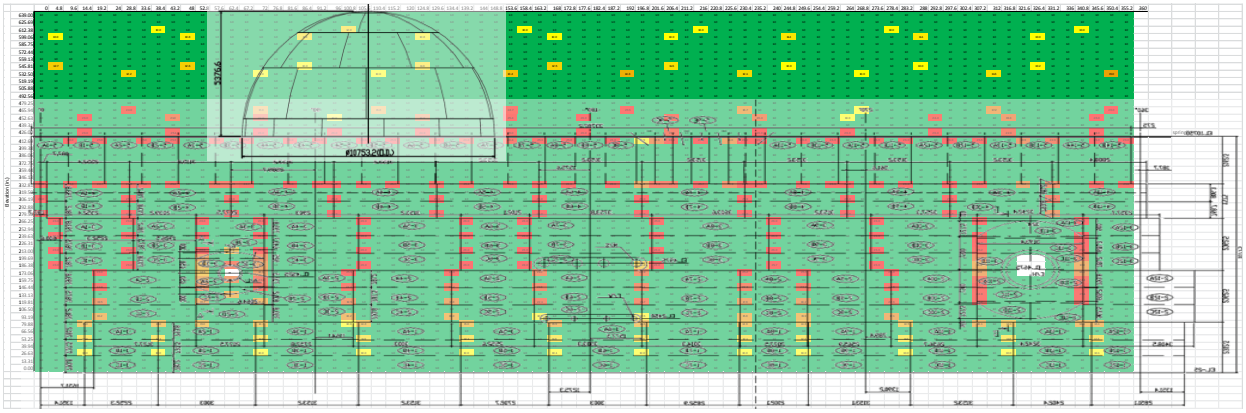

Figure D - 56: Location of liner flaws

Table D - 9: Leakage Rate Comparison

	Q (ft3/s)		
Pressure (xPd)	Model 3 - Pressure Only	Model 4 - Case 1	Model 4 - Case 2
2.5	0	0	0
3.0	13	0	0
3.1	18	0	0
3.2	36	3	0
3.3	95	10	0
3.4	158	29	20
3.5	222	108	101
3.6	308	208	190

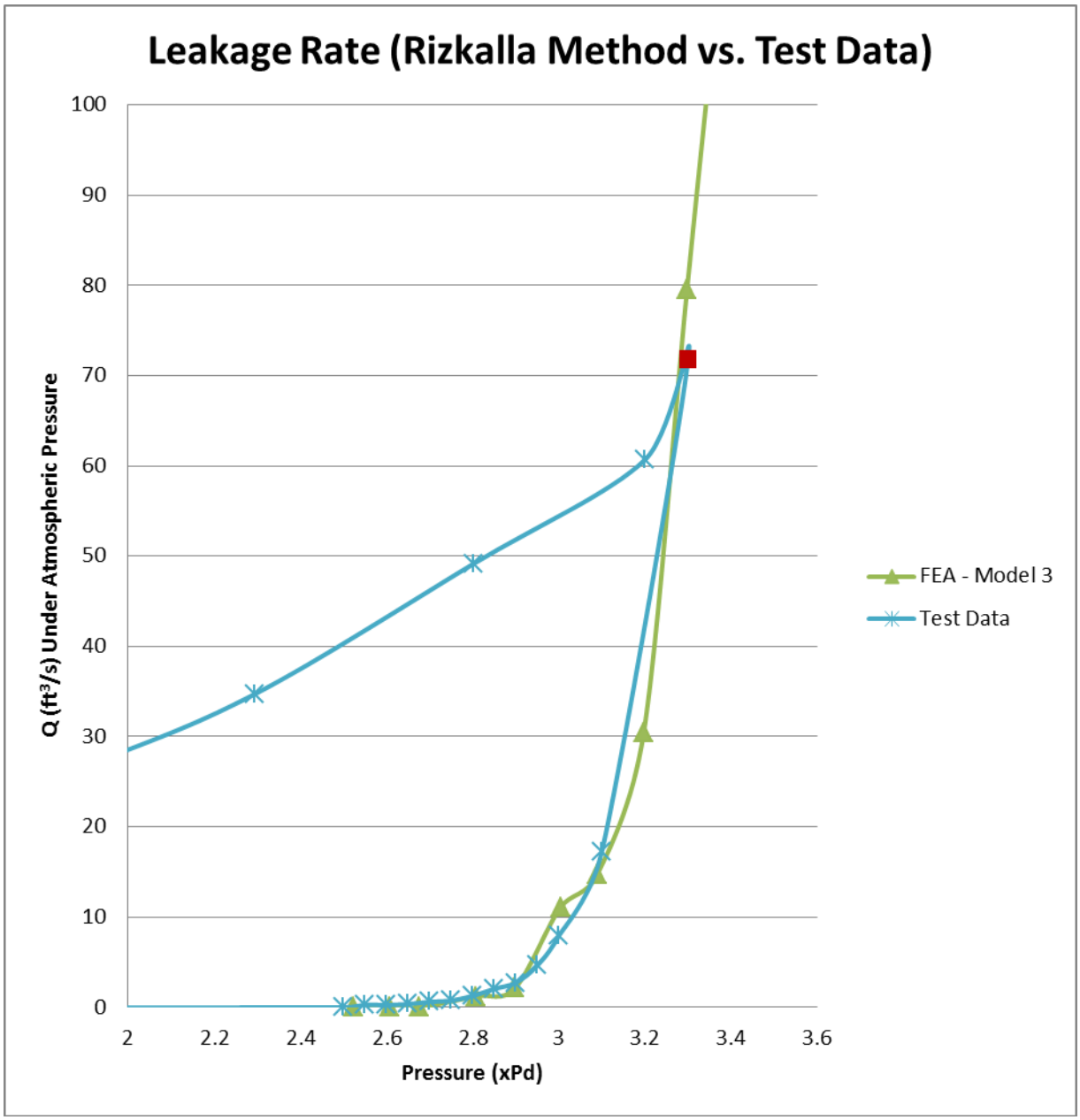

Figure D - 57a: Leakage rate comparison between the Rizkalla Method and Test Data

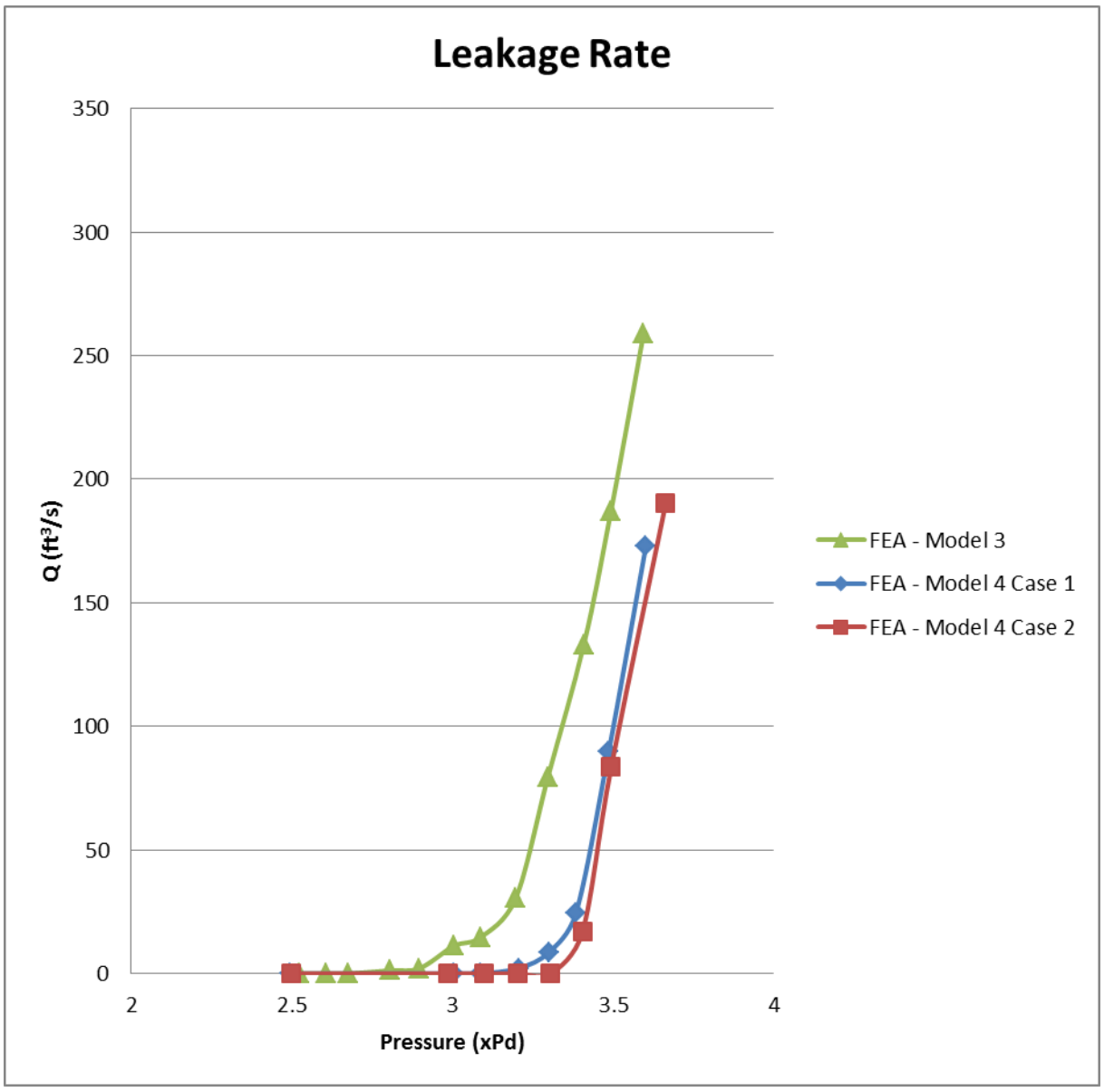

Figure D – 57b: Leakage rate versus pressure

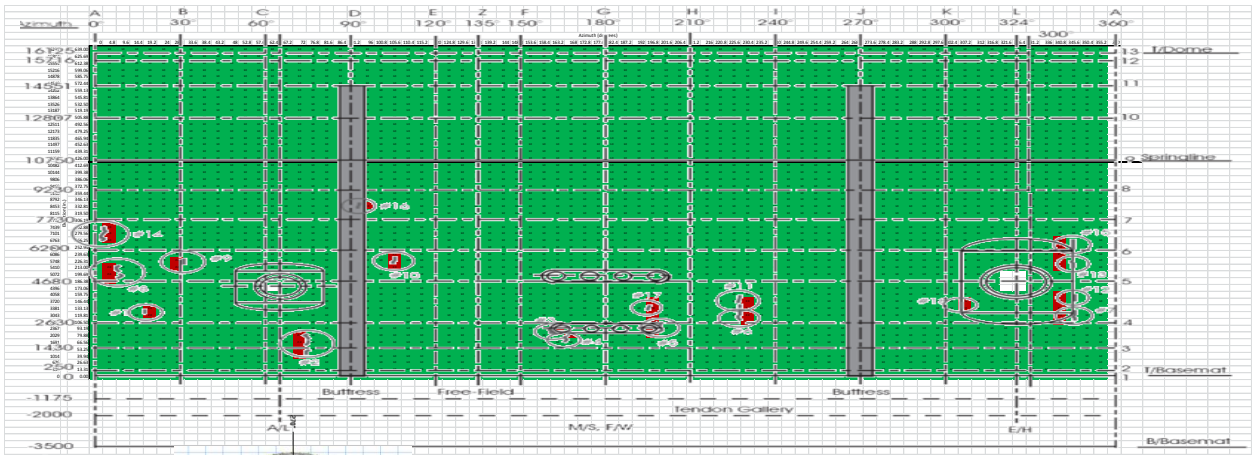

Figure D - 58: Double K Factor for liner flaws

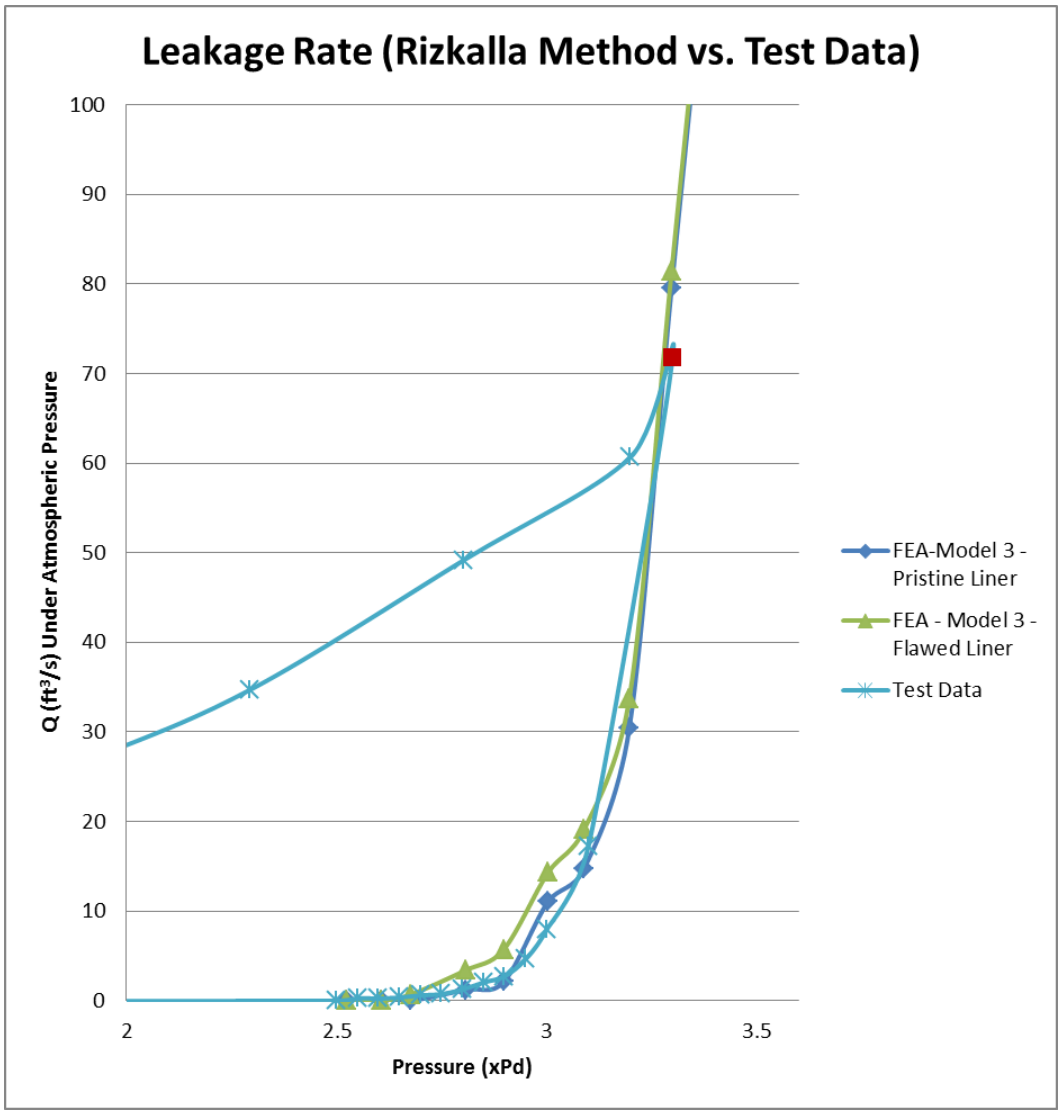

Figure D - 59: Leakage rate comparison with K Factor Adjusted for "Flawed" Liner

Comparing Model 3 with the test data (peak leakage of 70 cu. ft / sec at 3.3xPd), the leakage rate prediction is reasonably close.

For Model 4, the leakage rates actually decrease. We attribute this to the temperature effects. As the temperature increases, the steel liner tries to expand at a faster rate than the concrete. The concrete has a lower coefficient, as well as a lower average temperature, so this retards the liner expansion, thus putting some compression into the liner. The compression helps prevent cracks from opening. (Note that mechanical strains, not thermal strains, have been used in the liner tearing prediction.) This effect is further illustrated in Model 4 - Case 2, where the temperature is higher, and the leakage rate decreases. The temperature range does not significantly degrade the material properties, so material property degradation was not found to have a significant effect on the structure's capacity.

Summary and conclusions

The U.S. Nuclear Regulatory Commission (USNRC) and Sandia (with support from Moffatt & Nichol) have completed analyses documented herein to participate in a round robin analysis with the Atomic Energy Regulatory Board of India (AERB). This analysis is focused on the Standard Problem Exercise (SPE) No. 3, involving the structural analysis of a prestressed concrete containment vessel (PCCV). Phase 1 Results and Discussion were completed in 2011. Phase 2 requires participants to re-investigate Model 3 from Phase 1, with two distinct objectives.

1) The participants are asked to examine the methods to estimate leakage rate as a function of pressure. These methods will be evaluated relative to the PCCV test results, and incorporate lessons learned from Phase 1 of the round robin analysis;

2) Temperature effects modifications will be implemented into Model 3. SPE refers to this additional investigation as Model 4. The participants are to apply two different temperature loading cases to the global Model 4. The two thermal analysis cases under consideration in Part 2 were selected based on the participant's agreement to use the ISP-48 cases, which are considered as representative challenges to typical containments.

The response to the temperature and pressure loadings are provided herein, including comparison of Standard Output Location information between pressure-only and the two pressure-and-temperature cases.

For SPE Phase 2, a key objective of the work was to estimate crack size and leak area. After consideration of alternative methods, it was decided to use the strain-based methodology developed during EPRI research in the 1990's as the basis for the prediction of crack size and occurrence. This also leads to estimation of leakage versus pressure. Some refinements and simplifications to the methodology have been made and are described herein (especially, Appendix A). The Rizkalla forumulation is used to calculate leak rates through postulated liner tear areas. The formulation, when applied to the 1:4 Scale PCCV Model, produces leak rates which are reasonably close to those observed and measured during the test. A significant driver of the formulation is the strain concentration factor K; taking liner-weld-zone-defects into account by increasing the effective "K" might improve predictions of leak rate versus pressure.

A general observation and conclusion can be drawn with respect to temperature response combined with pressure. For the temperature cases considered, while the overall deformation of the PCCV cylinder is larger at a given pressure with the addition of temperature, “failure”, i.e. tearing of the liner and significant leakage, is not reached until a somewhat larger pressure. This conclusion is supported by the following observations:

1. For the liner, which has radial displacement constrained by the concrete to which it is attached, temperature tends to induce compressive mechanical strains. Mechanical strains are used in the liner tear prediction formulation, thus at the same pressure, analysis with internal temperature shows liner tears at higher pressures
2. The temperatures do not climb high enough to substantially degrade the material strengths of the concrete/rebar containment wall. If they did, then pressure + temperature would likely pose a more severe challenge (with lower failure pressure) than with pressure alone.

A final goal of the SPE-3 program was to introduce a probability component to the leakage prediction versus pressure. While work-scope and schedule constraints have not allowed us to pursue this in detail, the framework for this is laid out in the EPRI methodology summarized in [8]. The method consists of the following steps:

a. Assume that prediction of liner strains from a global model, K-factors, B-factors, and liner ductility limit have a lognormal distribution.

b. Through statistical sampling of actual data, use of judgment, or an expert panel, assign parameters of i). Randomness and ii). Uncertainty to liner strains from a global model, K-factors, B-factors, liner ductility limit, and leak rate formula versus leak area.

c. Apply the randomness and Uncertainty parameters to each step of the liner tear prediction versus pressure, and sum these as has been done in the calculations herein. This produces leak rate versus pressure with a lognormal distribution associated with every point on the leak rate versus pressure curve (as shown schematically in Fig. D-60).

d. For any specific plant, other probabilistic aspects related to construction variations (liner thickness variations, weld quality, liner ductility variations, etc.) could also be introduced.

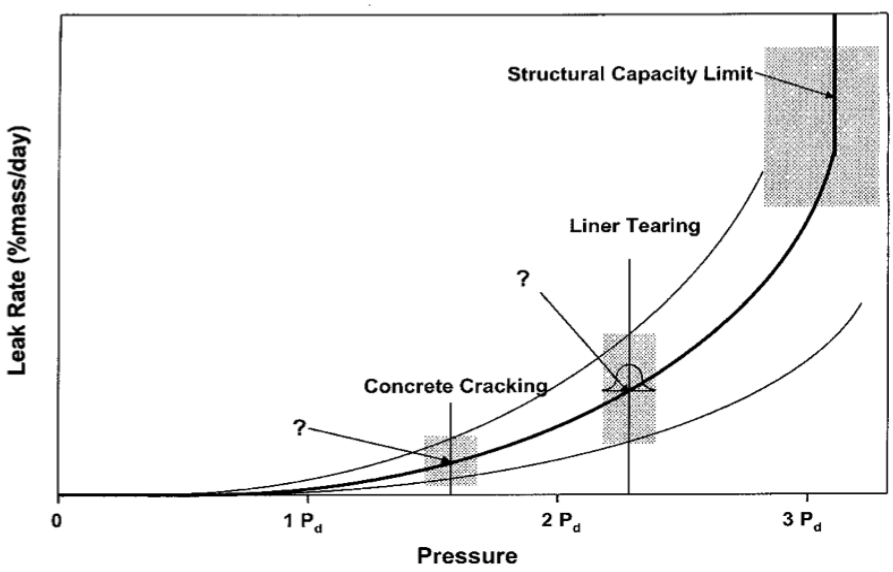

Figure D - 60: Schematic of a containment performance model

References

1. Akin and Dameron, "STANDARD PROBLEM EXERCISE 3 – PHASE 2 on Performance of Containment Vessel Under Severe Accident Conditions," final analysis definition sent to AERB SPE-3 Round Robin Participants, May 23, 2011.

2. Mathet, E., Hessheimer M., Dameron, R., et al, "*International Standard Problem No. 48 – Containment Capacity*", NEA/CSNI Final Report, May, 2005.

3. Hessheimer, M. F., Klamerus, E. W., Rightley, G. S., Lambert, L. D. and Dameron, R. A., "*Overpressurization Test of a 1:4-Scale Prestressed Concrete Containment Vessel Model*", NUREG/CR-6810, SAND2003-0840P, Sandia National Laboratories, Albuquerque NM. March, 2003.

4. NUREG/CR-6810.

5 ASME Boiler and Pressure Vessel Code, Section III, Division I-Subsection NE, Nuclear Power Plant Components-Class MC Components and Section III, Division 2, Code for Concrete Reactor Vessels and Containments, The American Society of Mechanical Engineers, New York, NY.

6. Hessheimer, M. F. and R. A. Dameron, "*Containment Integrity Research at Sandia National Laboratories-An Overview*", NUREG/CR-6906, Sandia National Laboratories, Albuquerque, NM, July, 2006.

7. K. Eckelmeyer, et al, "Metallurgical Analysis of PCCV Liner Tears," Adjunct Report to post-test examination of NUPEC/NRC/Sandia 1:4 Scale Model (Appendix L on SPE-3 website).

8. Dameron, R.A., R.S. Dunham, Y.R. Rashid, and H.T. Tang. "Conclusions of the EPRI Concrete Containment Research Program." *Nuclear Engineering and Design*, 125, 1991, pgs. 41-55.

9. R. A. Dameron et al, Methods for Ultimate Load Analysis of Concrete Containments, Third Phase, 2nd Tier: Procedure Manual and Guidelines for Using Concrete Containment Analysis Software, EPRI Report EPRI NP6263-SD (1989).

10. Klamerus, E. W., et. al., "***Containment Performance of Prototypical Reactor Containments Subjected to Severe Accident Conditions***", NUREG/CR-6433, SAND96-2445, Sandia National Laboratories, Albuquerque, NM, November, 1996.

11. M. J. Manjoine, "Creep-Rupture Behavior of Weldments," Welding Research Supplement, February, 1982.

12. R. A. Dameron, B. E. Hansen, D. R. Parker, Y. R. Rashid, M. F. Hessheimer, ***"Post-test Analysis of NUPEC/Sandia 1:4-Scale Prestressed Concrete Containment Vessel,"*** Sandia National Labs (for USNRC), NUREG CR-6809, March 2003.

13. Rizkalla, S.H., Lau, B.L., Simmonds, S.H., 1984. Air leakage characteristics in reinforced concrete. *J. Struct. Eng. ASCE* 110 (5), pp. 1149-1162.

14. Nagano, T., Kowada, A., Matumura, T., Inada, Y., Yajima, K., 1989. Experimental study of leakage through residual shear cracks on RC walls. *Proc. SMIRT-10,* Session Q, pp. 139-144.

15. Suzuki, T., Takiguchi, K., Hotta, H., Kojima, N., Fukuhara, M., Limura, K., 1989. Experimental study on the leakage of gas trough cracked concrete walls. *Proc. SMIRT-10,* Session Q, pp. 145-150.

16. Suzuki, T., Takiguchi, K., Hotta, H., 1992. Leakage of gas trough concrete cracks, *Nuclear Engineering and Design*, 133, pp. 121-130.

17. Greiner, U., Ramm, W., 1995. Air leakage characteristics in cracked concrete, *Nuclear Engineering and Design*, 156, pp. 167-172.

18. Wang T., Hutchinson T. C., Hamilton C. H., Pardoen G. C., Salmon M. W., 2004, Gas leakage rate through reinforced concrete shear walls: numerical study, *13th World Conference on Earthquake Engineering*, Canada, Paper No. 34.

19. Hessheimer, M. F., Klamerus, E. W., Rightly, G. S., Lambert, L. D. and Dameron, R. A. 2003. *Overpressurization Test of a 1:4-Scale Prestressed Concrete Containment Vessel Model*, NUREG/CR-6810, SAND2003-0840P, Sandia National Laboratories, Albuquerque, NM.

Report	Ref. 10503/R-02	Edition 1

Title

STANDARD PROBLEM EXERCISE PERFORMANCE OF CONTAINMENT VESSEL UNDER SEVERE ACCIDENT CONDITION (PHASE 2)

Abstract

The reactor containment constitutes an important safety barrier between the reactor and the surrounding environment. The main purpose of the containment structure is to ensure tightness at the high overpressure that could occur at an internal accident. At severe accidental conditions, generating overpressure load beyond the design pressure, the response of the containment structures becomes highly non-linear.

This report summarizes studies intended to be included in the Standard Problem Exercise on the performance of containment vessels under severe accident conditions (SPE), phase 2. To verify and validate analytic studies performed in SPE results from a pressurization test carried out on a ¼ scale containment model is used (Sandia ¼).

The main focus in this report is on the steel liner and the prediction of leak rate related to the Sandia ¼ pressurization test. The documentation of Sandia ¼ post-test inspections regarding liner failure (liner tears) are used as basis for the study presented in this report. The size of the tears is analyzed by local models (fracture mechanic) where the global strain, studied in SPE phase 1, is included as load on the liner.

No apparent crack arrest was attained in the FE-analyses. The study using the method of crack propagation according to SPE Final Analysis Definition shows promising results but the accuracy in the current study needs to be improved.

The analyses where the J-integral is studied with respect to interaction between the liner and the containment wall show that both friction and coupling method between the liner and the concrete wall affects the result to a great extent. The J-integral seems very sensitive to the coupling method in particular.

An estimate of the upper bound flow through the liner tears is obtained by using the simple well known expressions for frictionless gas flow through a convergent nozzle. The opening area of the cracks in the Sandia 1:4 test were estimated by assuming that a real crack has a similar deformed shape as the crack studied in the FE-analyses. The estimated gas flow was determined to approximately 4.3 kg/s. The flow rate through the liner measured at 3.3pd in the Sandia 1:4 test was 2.96 kg/s. The flow through the liner is hence overestimated by 45 %.

Edition	Date	Author	Reviewed by	Approved by
1	2012-06-29	Torulf Nilsson / Patrick Anderson	Ola Jovall	Ola Jovall
				

Scanscot Technology AB
Emdalavägen 10, SE-223 69 Lund, Sweden
Telephone: +46.46.276 52 00, *Telefax*: +46.46.276 52 10

Report 10503/R-02

PERFORMANCE OF CONTAINMENT VESSEL UNDER SEVERE ACCIDENT CONDITION (PHASE 2)

LIST OF CONTENTS PAGE

LIST OF REVISIONS

Edition	Date	Revised pages	Revision refers to

0. ABSTRACT

The reactor containment constitutes an important safety barrier between the reactor and the surrounding environment. The main purpose of the containment structure is to ensure tightness at the high overpressure that could occur at an internal accident. At severe accidental conditions, generating overpressure load beyond the design pressure, the response of the containment structures becomes highly non-linear.

This report summarizes studies intended to be included in the Standard Problem Exercise on the performance of containment vessels under severe accident conditions (SPE), phase 2. To verify and validate analytic studies performed in SPE results from a pressurization test carried out on a ¼ scale containment model is used (Sandia ¼).

The main focus in this report is on the steel liner and the prediction of leak rate related to the Sandia ¼ pressurization test. The documentation of Sandia ¼ post-test inspections regarding liner failure (liner tears) are used as basis for the study presented in this report. The size of the tears is analyzed by local models (fracture mechanic) where the global strain, studied in SPE phase 1, is included as load on the liner.

No apparent crack arrest was attained in the FE-analyses. The study using the method of crack propagation according to SPE Final Analysis Definition shows promising results but the accuracy in the current study needs to be improved.

The analyses where the *J*-integral is studied with respect to interaction between the liner and the containment wall show that both friction and coupling method between the liner and the concrete wall affects the result to a great extent. The *J*-integral seems very sensitive to the coupling method in particular.

An estimate of the upper bound flow through the liner tears is obtained by using the simple well known expressions for frictionless gas flow through a convergent nozzle. The opening area of the cracks in the Sandia 1:4 test were estimated by assuming that a real crack has a similar deformed shape as the crack studied in the FE-analyses. The estimated gas flow was determined to approximately 4.3 kg/s. The flow rate through the liner measured at 3.3pd in the Sandia 1:4 test was 2.96 kg/s. The flow through the liner is hence overestimated by 45 %.

1. INTRODUCTION

1.1 Background

The reactor containment constitutes an important safety barrier between the reactor and the surrounding environment. The main purpose of the containment structure is to ensure tightness at the high overpressure that could occur at an internal accident. In many countries it is and has been a common practice to design nuclear containments with an outer concrete structure and an inner sealing consisting of a tight-welded steel liner. The outer concrete constitutes the load bearing part that may be prestressed. The liner is securing the tightness of the containment and has in general no intended bearing function.

At severe accidental conditions, generating overpressure load beyond the design pressure, the response of the containment structures becomes highly non-linear. The nonlinear response originates mainly from concrete cracking and yielding of steel components. The need of verifying the containment load-bearing capacity and leak-tightness in the non-linear range sets high demands on the engineering simulations.

Due to the difficulties related to verifying the non-linear performance, reference tests have been carried out, both overpressurization tests on containment scale models and tests on large wall specimens. Two containment scale model tests have been carried out at Sandia National Laboratories (SNL). The first scale test (Sandia 1:6) was performed in 1987 where a 1/6 scale model of a reinforced containment was pressurized (see [1] and [2]). The second scale test (Sandia 1:4) was performed in year 2000 and in this test a 1/4 scale model of a prestressed containment was pressurized (see [3]). Several experimental studies have been conducted for large scale specimens. An extensive experimental program sponsored by Electric Power Research Institute (EPRI) was performed in the late eighties (summarized in [4]). In this program full-scale or nearly full-scale flat panels, representing the containment wall were tested. The main purpose with the EPRI program was to study the influence of discontinuities and the interaction between the liner and concrete wall.

In the SPE[1] project [5], which this report is a part of, round robin exercises are performed in order to compare structural analysis results with test data from the Sandia 1:4 test (see [3]). The SPE round robin exercise follows up the experiences from previous round robin analyses in the ISP 48[2] project [6]. In the ISP 48 project the main focus was on the global structural behavior and the ultimate capacity. Generally the SPE project will continue the work in the ISP 48 project and focus on the detailed behavior for e.g. prestressing tendons and liner.

The SPE final objective is to determine the containment leakage as function of the internal pressure. The round robin exercise of the SPE project is divided in

[1] Standard Problem Exercise on the performance of containment vessels under severe accident conditions

[2] International Standard Problem 48, Containment Capacity.

two work phases. In *phase one*, which is presented in [7], focus is on examination of local effects including; containment dilation on prestressing force, slippage of prestressing cables, liner-concrete interaction, liner failure mechanisms, and the use of nominal versus in-situ conditions. *Phase two*, which this report refers to, includes two distinct parts. In the first part the leak rate as a function of pressure is examined relative to the Sandia 1:4 test results, incorporating lessons learned from phase one [7]. In the second part methods are developed for predicting leakage as function of pressure and temperature in the probabilistic space.

Our participation in the SPE project has been possible due to financial support from the Swedish / Finnish nuclear power industry and the Swedish Radiation Safety Authority (SSM).

1.2 Scope

The overall scope of the SPE project is to increase the knowledge of the nonlinear response of containment structures exposed to high internal overpressure. This report summarizes studies intended to be included in the SPE phase two exercises (see [5] and [8]).

The main focus in this report is on the steel liner and the prediction of leak rate related to the Sandia ¼ pressurization test, i.e. the main focus is on questions connected to the first part of phase two in the SPE project (see Section 1.1 above). Questions associated with effects due to high temperature are excluded in this report.

The documentation of Sandia 1:4 post-test inspections regarding liner failure (liner tears) are used as basis for the study presented in this report. The size of the tears is analyzed by local models (fracture mechanic) where the global strain, studied in SPE phase 1 (see [7]), is included as load on the liner. Well known expressions regarding gas flow through small openings are then used to estimate the leak rate.

1.3 Outline of report

The next chapter (Chapter 2) describes the containment scale model test (Sandia 1:4), which is used as reference test in this report. Chapter 2 focuses on the steel liner and the post test inspections considering obtained liner failures (liner tearing). In the following chapter (Chapter 3) the analysis of the liner tear size is presented together with estimation of leak rate. In Chapter 4 a comparison is made between the estimated and measured leak rate. Finally, in Chapter 5 the main conclusions are presented.

2. CONTAINMENT SCALE MODEL TEST

2.1 General

The Nuclear Power Engineering Corporation (NUPEC) of Japan and the U.S. Nuclear Regulatory Commission (NRC) jointly funded a Cooperative Containment Research Program at Sandia National Laboratories (SNL), USA, from July, 1991 through December, 2002.

As a part of this program, a ¼ scale model of a pre-stressed concrete containment vessel (PCCV) was constructed and pressurized up to failure. The prototype for the model is the containment building of unit 3 at the Ohi Nuclear Power Station in Japan, an 1127 MW Pressurized Water Reactor (PWR) unit. The design accident overpressure, p_d, of both the prototype and the model containment is 0.39 MPa.

The objectives of the model containment test were to;

- study aspects of the severe accident loads on containment vessels
- observe the model failure mechanisms
- obtain structural response data up to failure for comparison with analytical models

The model incorporated all structural parts important for containment integrity, including all large penetrations (like equipment hatch, personal air lock and pipe penetration). During pressurization the structural response was monitored, giving information on displacements, liner, rebar, concrete and tendon strains and tendon anchor forces. In addition, acoustic monitoring, video and still photography were used to monitor the structural behavior.

A detailed description is given in [3].

2.2 Structural outline

2.2.1 General

The scale model can be divided into three main structural parts, basemat, cylindrical wall and dome (see Figure 2.1).

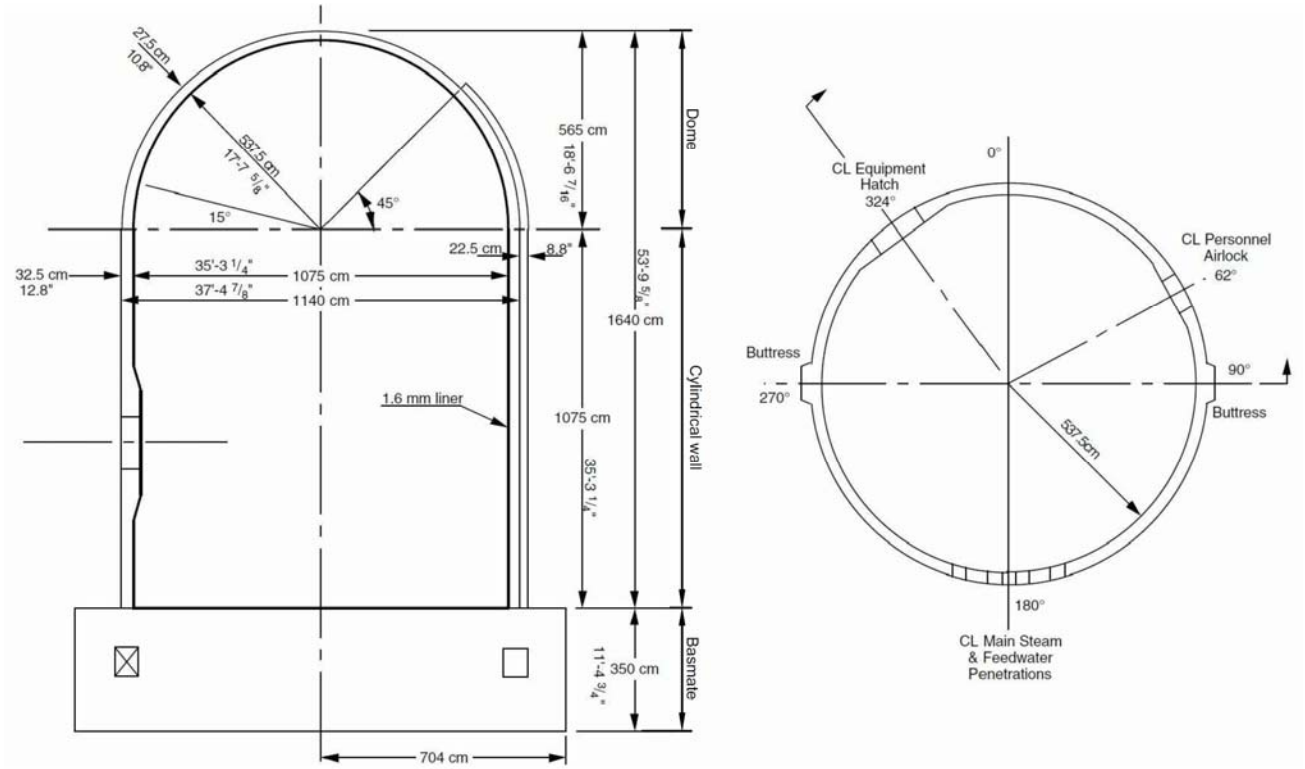

Figure 2.1 Model containment, main structural parts and dimensions [3].

The *containment wall* has a nominal thickness of 0.325 m and is locally thickened at the major penetrations (see Figure 2.1). The wall is prestressed in both the vertical and horizontal directions. The steel liner is placed on the inside of the wall and is anchored to the concrete by means of mechanical anchors, see Section 2.2.2 below. All penetrations through the containment are situated in the cylindrical wall.

2.2.2 Steel liner

The steel liner is fabricated from mild carbon steel and the nominal liner thickness for the prototype containment is 6.4 mm, i.e. 1.6 mm for the scale model containment. The as-built liner is 1.8 mm where the extra 0.2 mm provides fabrication allowance. The nominal yield and failure strength is 230 and 420 MPa respectively.

Panels with different sizes were prefabricated, where liner components like vertical T-anchors and horizontal stiffeners were shop welded onto the liner panels. The liner panels were transported to the construction site including; liner anchors, stiffeners, pipe casing, etc. At site the liner panels where welded together and used as inner formwork for the concrete wall and dome.

These stiffeners had no structural function after the model containment construction was completed. The plates were welded together at site. At penetrations, locally thickened plates were used, connected to the penetration assemblies.

2.2.2.1 Anchors and stiffeners

The vertical T-anchors (see Figure 2.2), continuously welded to the liner, anchors the liner to the concrete. The horizontal stiffeners (see Figure 2.2) have no intended structural function, they are only intended to stiffening the liner panels during transport and at the construction phase. However, the horizontal stiffeners will prevent the liner to slide vertically in relation to the concrete. The vertical anchors will both prevent the liner to separate from and slide in relation to the concrete.

Figure 2.2 Liner anchoring and stiffener details.

The vertical anchors are positioned with a distance of 0.45 m, except regions near discontinuities where they are more closely spaced (distance 0.15 m). The 0.15 m distance represents the accurate scaling from the full-scale containment, while the 0.45 m is three times the accurate scaling (was used to reduce costs). The liner anchor layout is presented in Figure 2.3. The vertical T-anchors are not extended into the dome. Here the liner is instead anchored to the dome with small stud-type anchors.

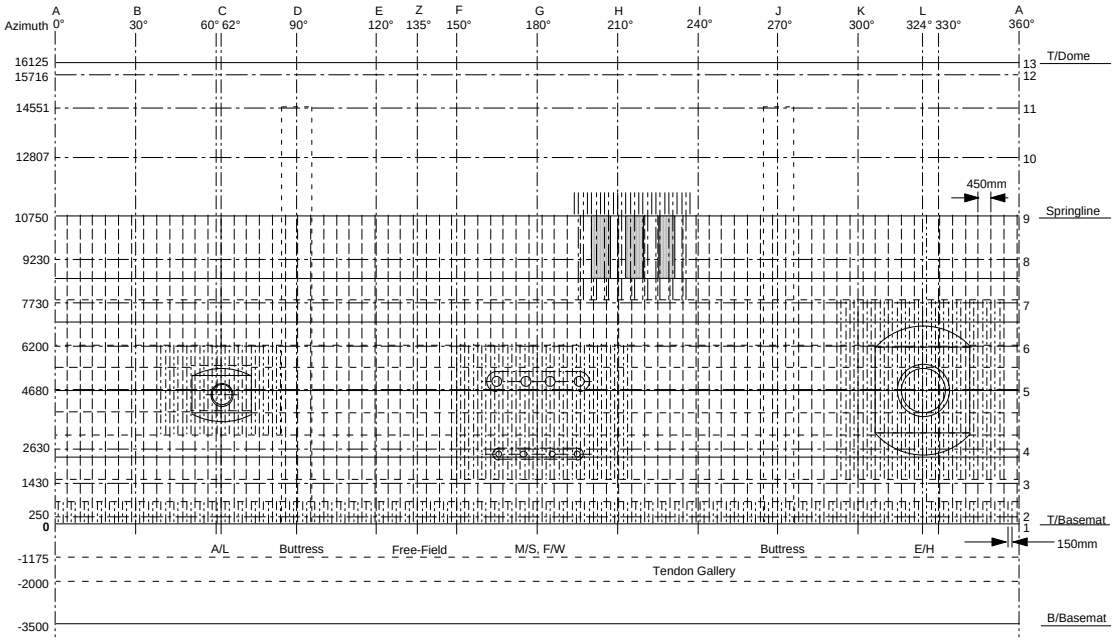

Figure 2.3 Liner anchor layout [3].

2.3 Pressurization test

2.3.1 Test operations

The decision was to perform a static, pneumatic over-pressurization test at ambient temperature. The limit state test (LST) was terminated following a functional failure, i.e. equilibrium leakage was reached and no gross structural failure occurred. Subsequently it was decided to re-pressurize the model containment, prior to demolition, in an attempt to create a global structural failure (Structural Failure Mode Test, SFMT).

Prior to the limit state test (LST), pressure tests at lower pressure levels were conducted. The over-pressurization studies in this report correspond to the limit state test (LST).

A detailed presentation of the overpressurization test is given in [3], also see the summery in [7].

2.3.2 Leak rate

When the model was pressurized to approximately 3 times p_d it became difficult to pressurize the model and the leak rate was estimated to around 100% mass/day (see Figure 2.4). The pressure in the model was increase to 3.1 times p_d which resulted in a more than 2 times increase in leak rate. The nitrogen flow rate was finaly increased to the maximum capacity of the pressurization system, and the pressure was then increased to slightly over 3.3 times p_d. At the final maximum pressure the leak rate was estimated to be on the order of 900% mass/day.

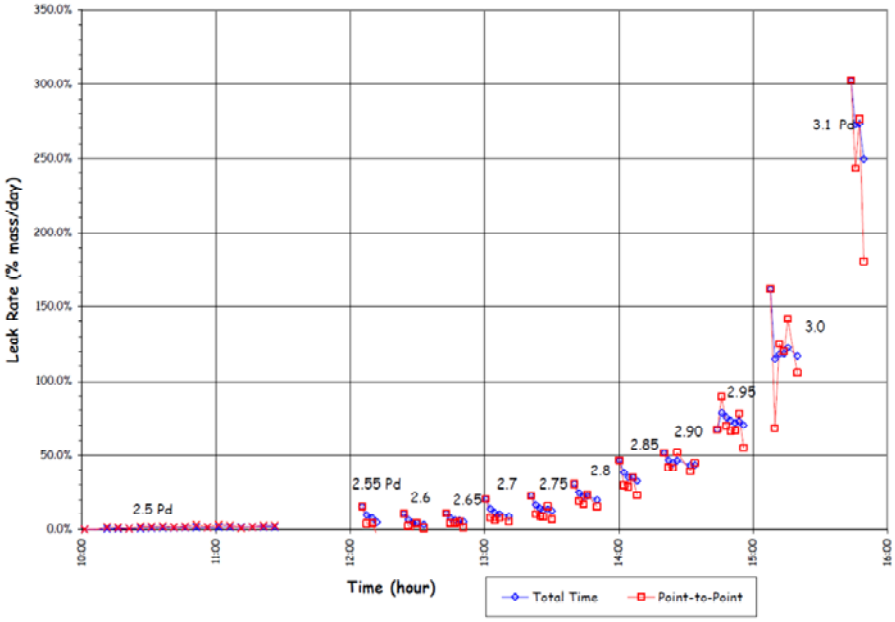

Figure 2.4 LST - Estimated Leak Rates (2.5-3.1 times p_d*) [3].*

2.3.3 Radial displacements

The limit state test was started the 27th of September 2000 and finalized the day after. Figure 2.5 show the midheight radial displacement at different angles. The

start displacement is negative due to prestressing and displacement increases almost linearly up to around 1.5 times p_d (0.59 MPa). At this pressure the concrete can be assumed to start cracking and after this pressure the displacement will increase more rapidly. At 2 times p_d the average displacement is around 3.5 mm, at 3 times p_d around 17.0 mm and finally at 3.3 times p_d around 22.5 mm.

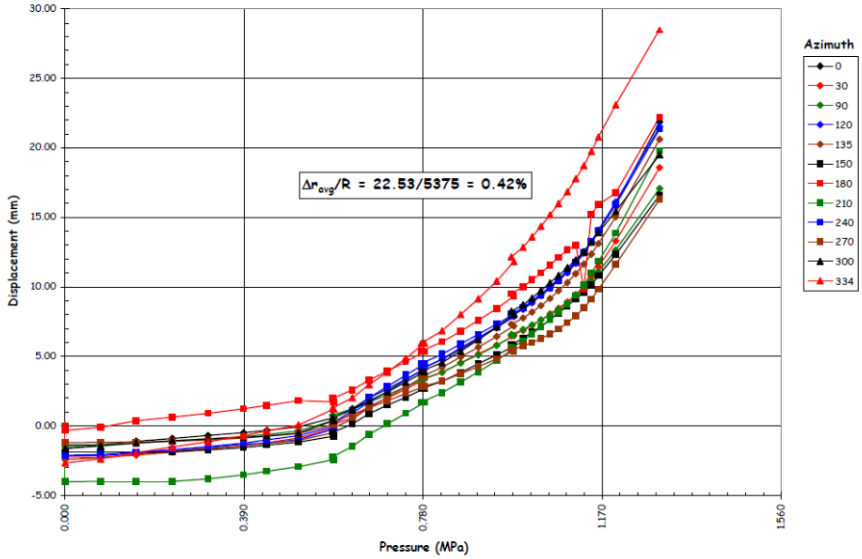

Figure 2.5 Measured radial displacement at midheight (el 4680 mm) [3].

2.3.4 Liner post-test inspections

Figure 2.6 shows a stretch-out sketch of the cylindrical part of the containment model seen from the inside, where liner tears found at the post-test inspections are indicated (#1 to #18[1]). At the overpressurization test, the first leak was detected at an internal pressure 2.5 times p_d (0.98 MPa). At 3.3 times p_d the leak rate exceeded the capacity of the pressurization system and the sources of the leak was a number of tears found in the post-test inspection (see Figure 2.6). An acoustic monitoring system detected the first leak near the penetration E/H (see Figure 2.6).

At the construction stage the liner was grinded in connection with welding, which resulted in localized areas with thinner liner (see Sandia ¼ test report [3]). It was concluded that in the region of almost all tears the liner had been grinded and the liner thickness was reduced up to 50% in some cases[2]. In the region of tear #7 and #15 the liner grinding was concluded to be extensive, between 25 and 50% reduction. The liner grinding was less in the area of tear #12 and #13 and it was concluded that liner tear #12 was the most likely to be caused by a "true structural effect".

[1] "Tear" #18 shown was categorized as localized plastic deformation and not a tear.

[2] Do not reflect the full-scale case. A 50% reduction of the model liner thickness corresponds to a 12.5% reduction for the prototype containment liner.

A detailed description of each tear found in the sandia 1/4 post-test inspection was handed out to the SPE participants. This documentation includes photos where the liner thickness and the tear length are indicated, see Appendix A1.

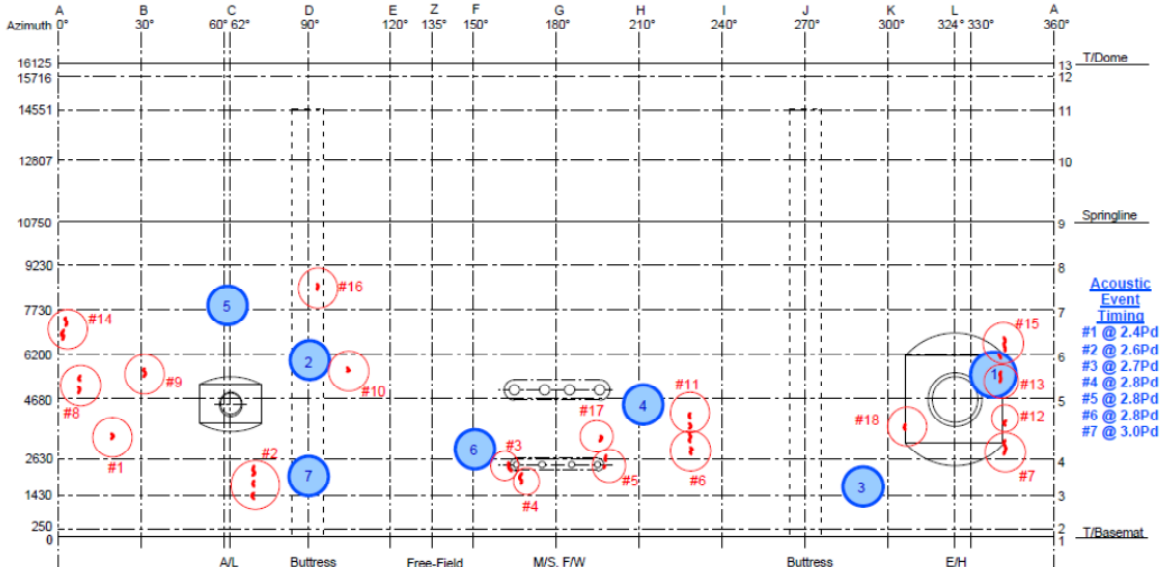

Figure 2.6 Stretched-out sketch, liner in the cylindrical part [3]. Red circles (#1 to #18) indicate tears found at the post-test inspections. Blue circles indicate regions where and at which pressure the acoustic monitoring system detected liner tearing events.

3. ESTIMATION OF LEAKAGE AT PRESSURAZATION

In this chapter an attempt to predict the size of liner tears is presented. A study of how the energy release rate is affected by the interaction with the concrete containment wall is also presented. The leakage through a tear is estimated using simple relations for gas flow through a convergent nozzle.

3.1 Size of liner tears

In the previous report [7] (SPE phase 1), an attempt to predict the size of a liner tear was presented using fracture mechanical calculations for postulated cracks in an FE-model. In this report further effort to achieve reliable estimates of tear lengths is presented.

Two main studies are presented. The first study is an attempt to repeat the method as presented by Robert Dameron in [5]. The second study presents how the interaction between the liner and the concrete containment wall affects the energy release rate at the crack-tip.

3.1.1 Structural models

3.1.1.1 Liner model for crack propagation and arrest

The model used for crack propagation and arrest is essentially the same as in [7]. The model is shown in Figure 3.1 and the applied boundary conditions are shown in Figure 3.2. For further description see [7].

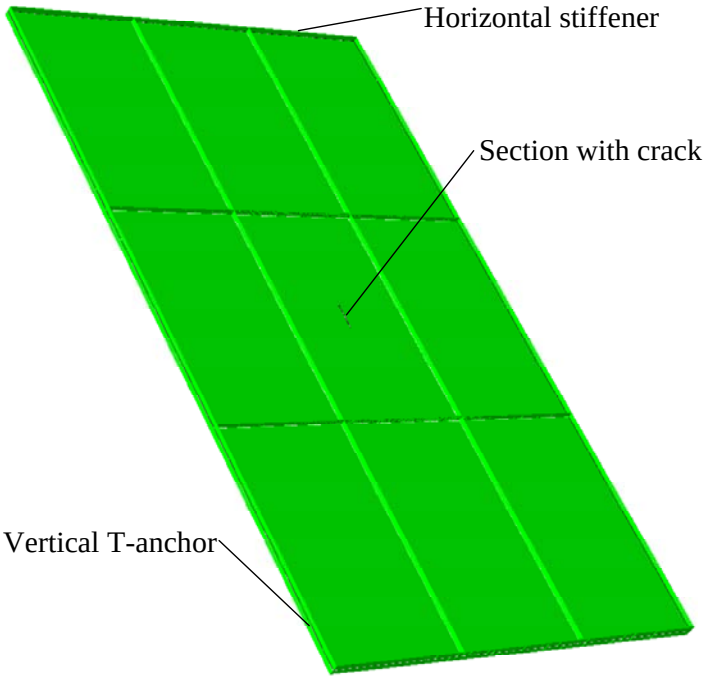

Figure 3.1 Planar model of a part of the liner.

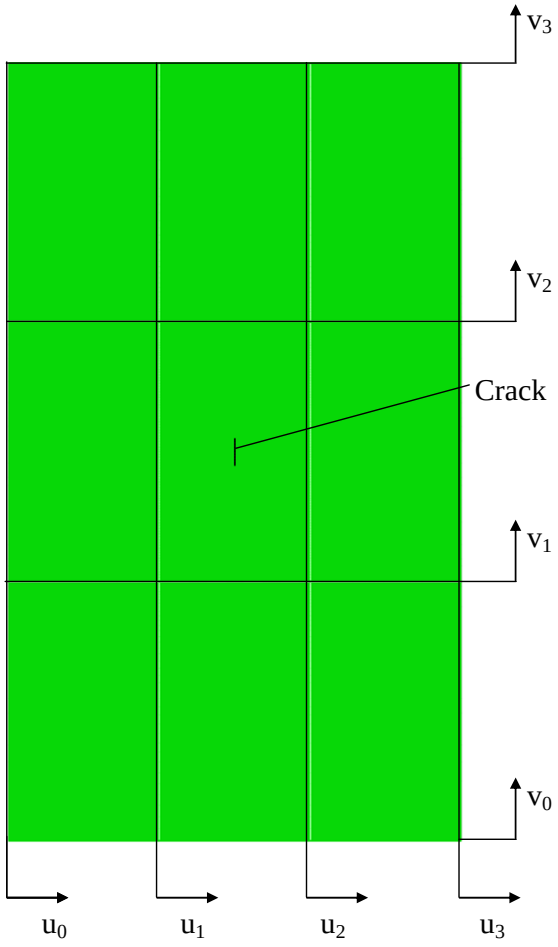

Figure 3.2 Boundary conditions.

3.1.1.2 Liner model for study of interaction with containment wall

The model in this section is slightly modified compared to the model used in [7]. In order to investigate the influence of interaction between the liner and the containment wall, they are modeled as two planar adjacent plates. The interactions investigated are:

1. Friction between the liner and the containment wall.
2. The coupling between stiffeners and T-anchors and containment wall.

Shell elements are used for the containment wall and the liner. The stiffeners and T-anchors are modeled using beam elements. The interaction between the concrete wall and the liner is obtained by applying contact conditions. Moreover, the stiffeners and T-anchors are coupled to the containment by using connector elements with all degrees of freedom constrained. The model is shown in Figure 3.3.

The boundary conditions in the current model are applied at the edges only, i.e. only u_0, u_3, v_0 and v_3 according to Figure 3.4 are prescribed. The "boundary conditions" for the midsection (u_1, u_2, v_1 and v_2) are achieved by the coupling to the stiff concrete containment wall as described above. The boundary conditions at $3.3p_d$ are prescribed as follows:

$u_0 = 0 \cdot 450 \cdot 0.0042 = 0$

$u_3 = 3 \cdot 450 \cdot 0.0042 = 5.67$ mm

and

$v_0 = 0 \cdot 780 \cdot 0.001 = 0$

$v_3 = 3 \cdot 780 \cdot 0.001 = 2.34$ mm

This approach of modeling the coupling of stiffeners and T-anchors to the containment wall is compared to the approach with "hard" boundary conditions as used in [7].

All nodes in the concrete containment wall are constrained in the z-direction.

The contact between the liner and the containment wall is achieved by applying pressure on the liner corresponding to the internal overpressure in the containment. The pressure is increased linearly in accordance with the prescribed boundary conditions. The maximum applied pressure is $3.3p_d$.

The friction coefficient used in the analyses is 0.6 (see e.g. [9]).

The concrete wall is assigned a thickness of 325 mm.

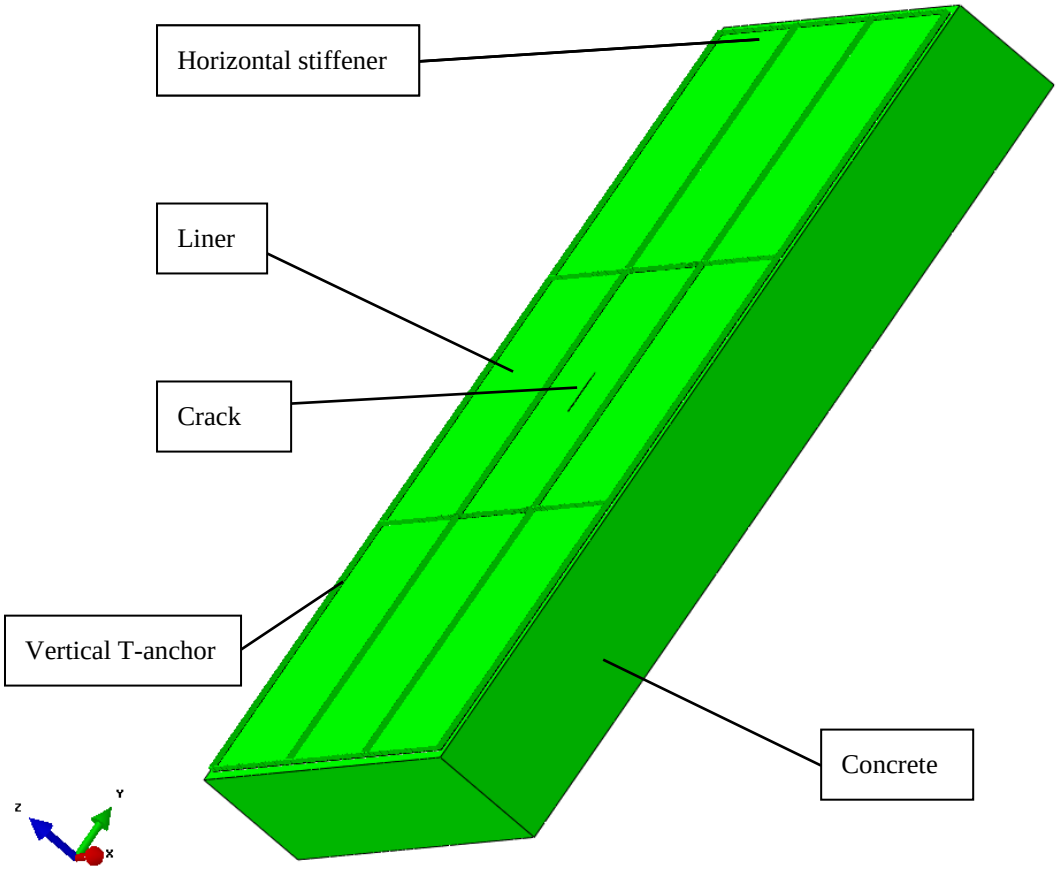

Figure 3.3 Rendered shell element model of liner and concrete.

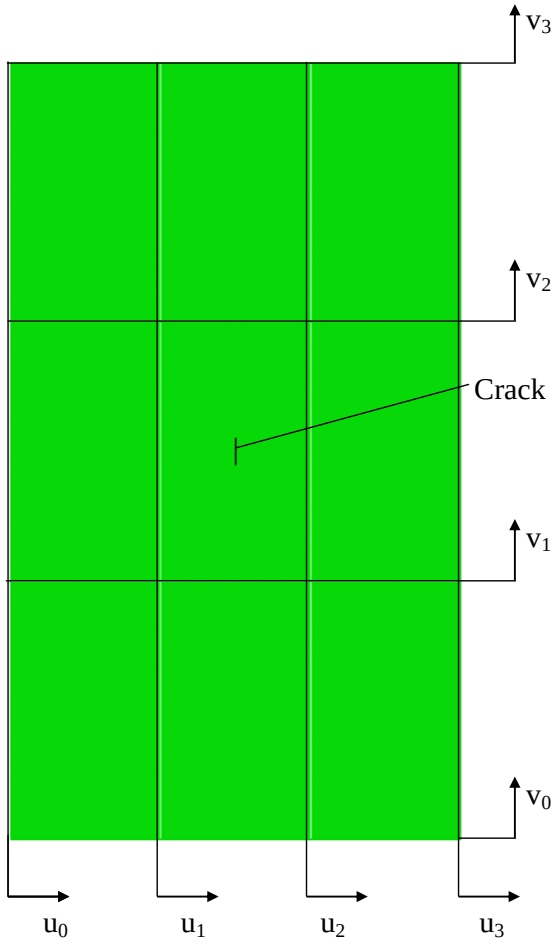

Figure 3.4 Boundary conditions.

3.1.2 Analyses

3.1.2.1 Crack propagation and arrest

The analysis of the model in section 3.1.1.1 is an attempt to reproduce the technique used by Robert Dameron as presented in [5].

The analysis starts out by analyzing a crack of 18 mm length without propagation. The *J*-integral is determined and the global strain level at J_{cr} is established. A close up of the mesh of the initial crack is shown in Figure 3.5.

A new analysis of the model with the initial crack is performed where the global strain obtained in the first analysis is applied. In the next step in the current analysis the crack is propagated by removing elements on both sides of the crack as shown in Figure 3.6 (using *Model change in Abaqus) for the same applied global strain as in the previous analysis step. Equilibrium for the new configuration is obtained at the end of the step and the *J*-integral is extracted for the new equilibrium stress state. In the next analysis step more elements are removed and the actions in the previous step are repeated. This procedure is continued until the *J*-integral is less than or equal to J_{cr}. When this occurs more global strain is applied and the procedure is repeated until the global strain reaches the value at $3.3p_d$ and the *J*-integral is less than or equal to J_{cr}.

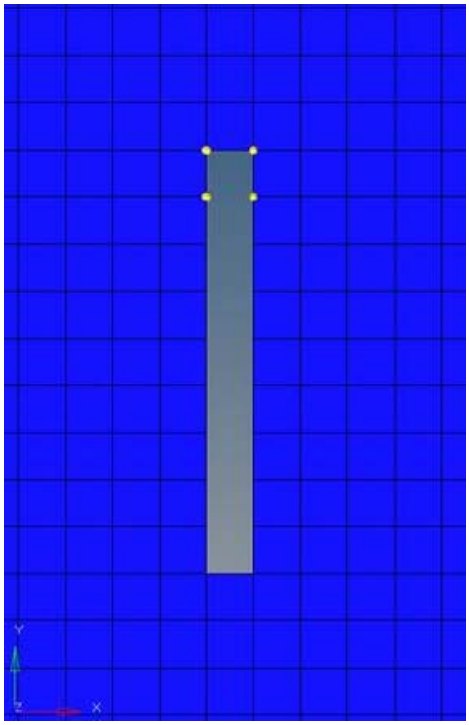

Figure 3.5 Close up of initial crack with highlighted nodes for determination of J-integral.

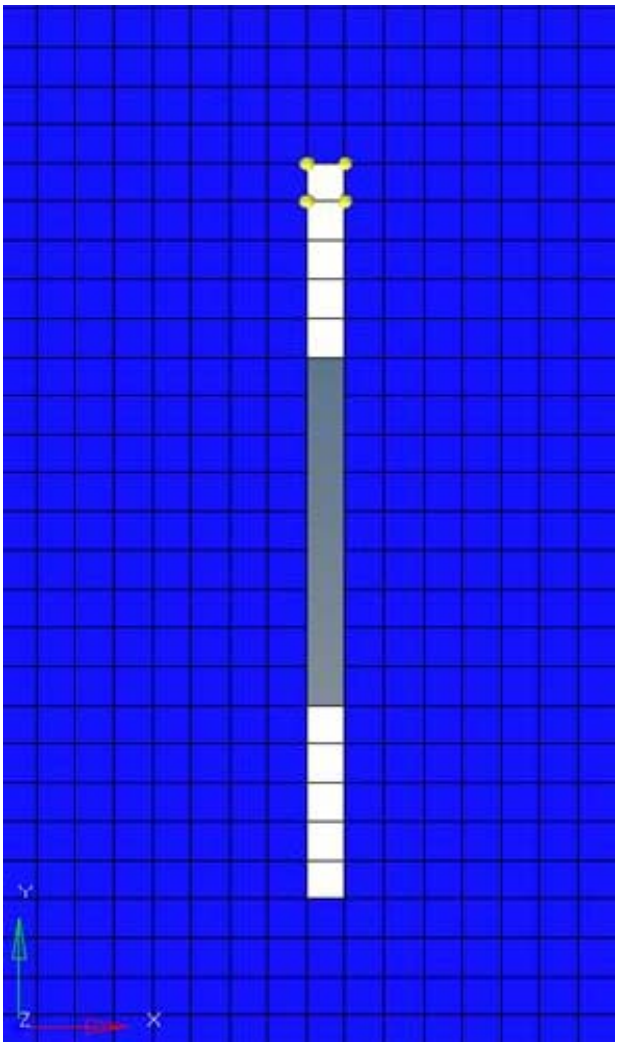

Figure 3.6 Close up of crack at first propagation step. Removed elements highlighted in white.

3.1.2.2 Interaction with containment wall

Analyses are performed in order to investigate the influence of friction and the coupling between liner and concrete containment wall. Analyses have been performed for different crack length. The solution method is described in section 8.3.2.3 in [7].

3.1.3 Result

3.1.3.1 Crack propagation and arrest

The *J*-integral obtained in the first analysis which is performed in order to establish a critical global strain is shown in Figure 3.7. The applied global strain at J_{cr} is obtained to approximately 0.17%.

This value of global strain is applied in the second analysis and the crack is propagated as described in section 3.1.2.1. Figure 3.8 shows how the *J*-integral varies with increased crack length. The crack is advanced to 38, 58, 74, 94, 114 and 126 mm crack length. No further strain has been applied since the *J*-integral

contours do not appear to converge for higher numbers. The tendency is however that the *J*-integral decreases which indicates that the driving strain has been consumed and a crack arrest has been attained at a crack length of 126 mm and a global circumferential strain of 0.17%.

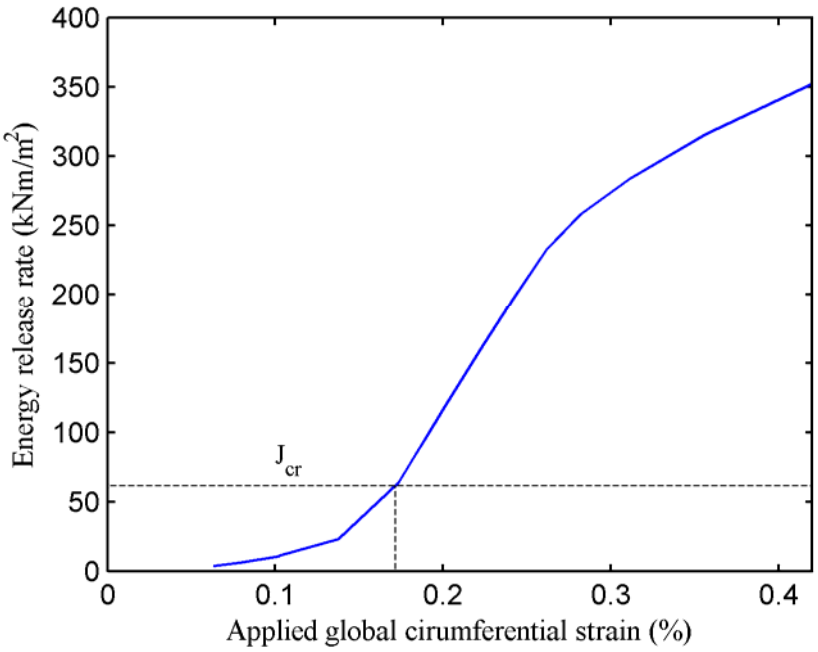

Figure 3.7 J-integral for initial crack versus applied global circumferential strain.

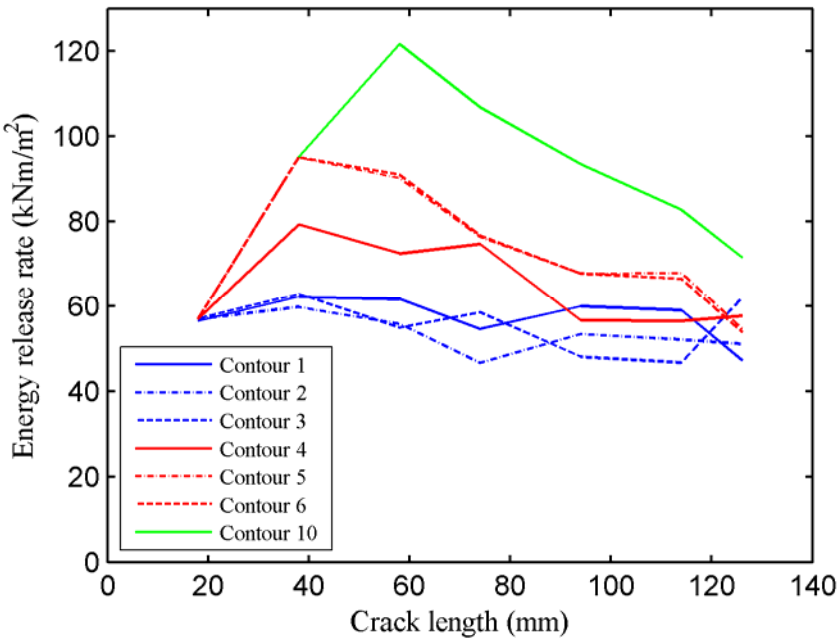

Figure 3.8 J-integral (energy release rate at crack tip) versus crack length.

3.1.3.2 Interaction with containment wall

Figure 3.9-3.12 shows the energy release rate (J-integral) for the analyses with friction, without friction and without friction with “hard” boundary conditions as used in section 3.1.1.1 and in SPE phase 1 [7]. “Hard” boundary condition means that the flexibility of the concrete containment wall is not taken into account. The result is presented for 10, 122, 223 and 423 mm crack length.

The result shows that for shorter cracks the relative influence of friction is significant whereas the relative influence on longer cracks is smaller. The reason is probably that the applied pressure and thereby the friction force is constant. The stress field is reduced with the same amount independent of crack length. Since the *J*-integral increases due to an increasing stress field in the surroundings of the crack the friction force has less relative influence.

The effect of the boundary condition is significant for all crack lengths. The effect of the boundary condition is more evident than the effect of friction. This indicates that the *J*-integral is very sensitive for differences in the stress field and a lot of effort is needed for modeling the coupling between the liner and the concrete containment wall.

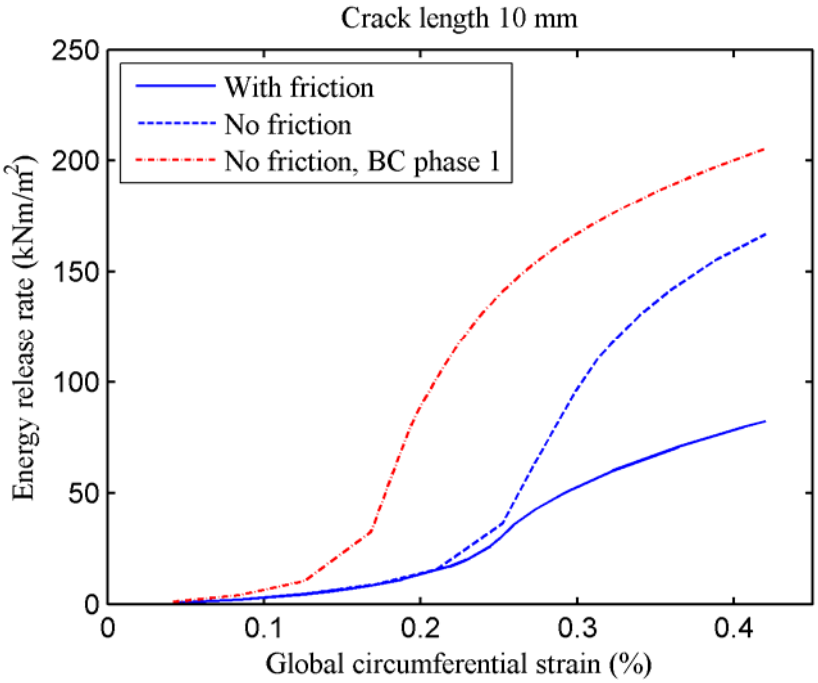

Figure 3.9 Energy release rate versus applied strain for models with friction and no friction, crack length 10 mm.

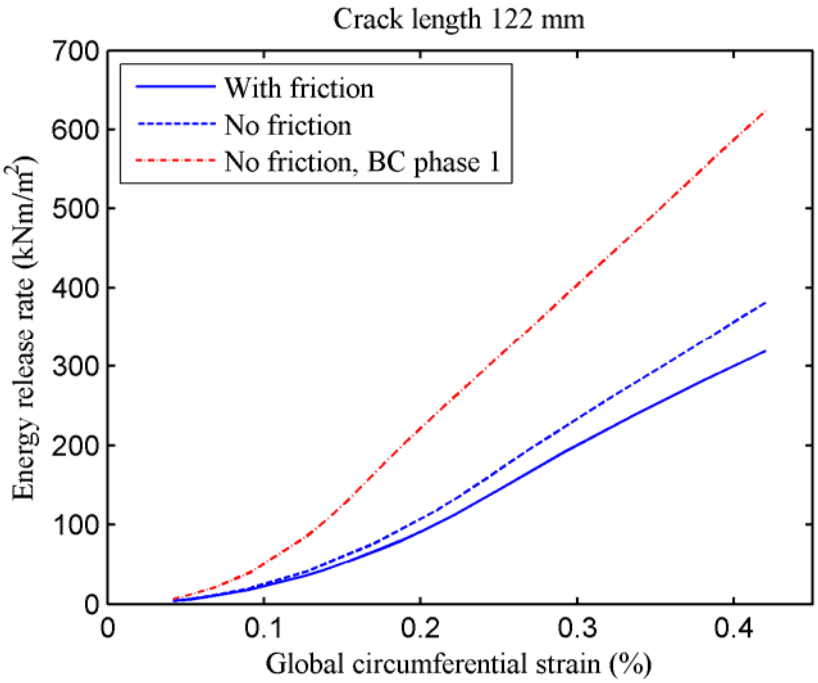

Figure 3.10 Energy release rate versus applied strain for models with friction and no friction, crack length 122 mm.

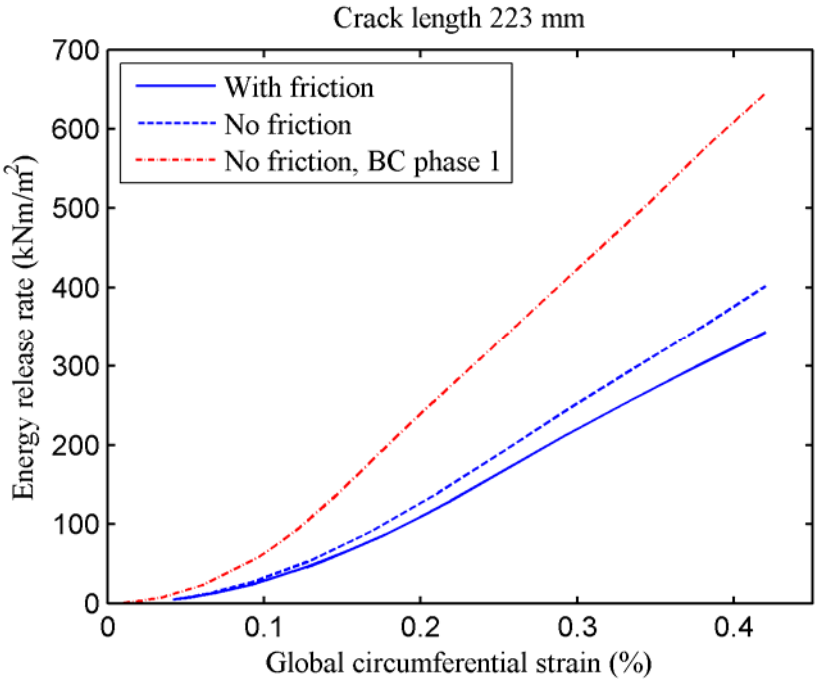

Figure 3.11 Energy release rate versus applied strain for models with friction and no friction, crack length 223 mm.

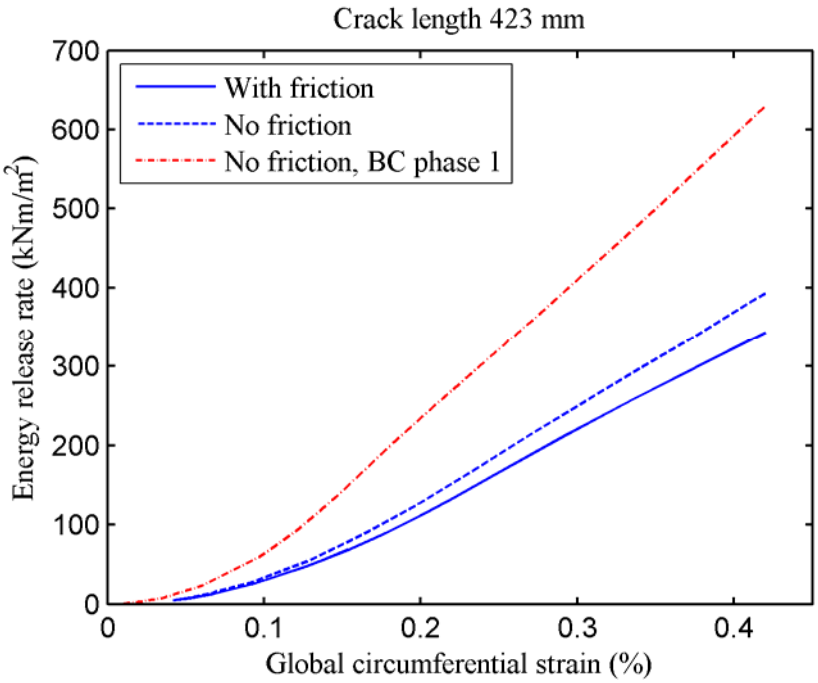

Figure 3.12 Energy release rate versus applied strain for models with friction and no friction, crack length 423 mm.

The energy release rate (*J*-integral) with friction present versus applied global circumferential strain for different crack lengths is presented in Figure 3.13.

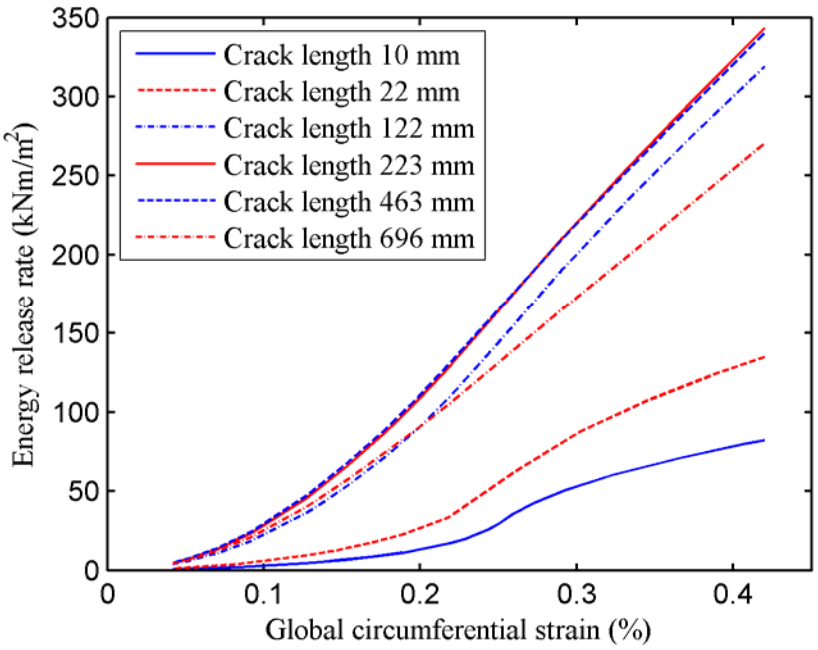

Figure 3.13 Energy release rate versus applied strain for different crack lengths.

Figure 3.14 shows the energy release rate at a global circumferential strain of 0.42 % versus postulated crack length. The result in the current case shows that the

energy release rate increases for a crack length up to approximately 300 mm, increasing the crack length further leads to a decreasing energy release rate. The longest crack with a stable FE solution is obtained at a length of 696 mm. The corresponding value of energy release rate is 270 kNm/m^2.

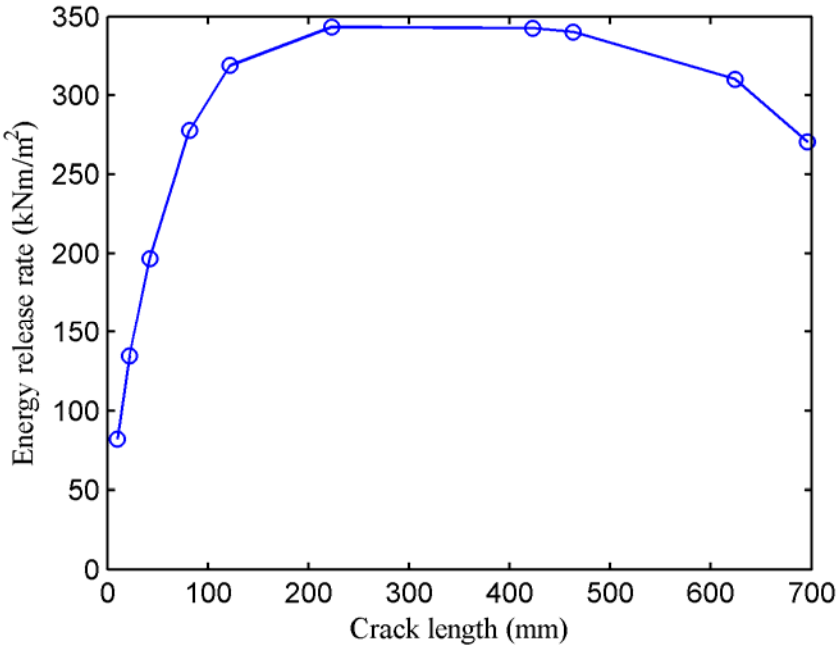

Figure 3.14 Energy release rate at a global circumferential strain of 0.42 % versus crack length.

3.2 Leakage trough liner tears

Since no apparent crack arrest was obtained in the analyses in section 3.1, crack openings found in the Sandia 1:4 test are used for estimation of leakage through liner tears. The length of the different cracks is known but the width of the crack at 3.3p_d is unknown.

The shape of the crack is assumed to be similar to the shape found in the FE-analyses in section 3.1. A crack at 0.42 % global circumferential strain is shown in Figure 3.15.

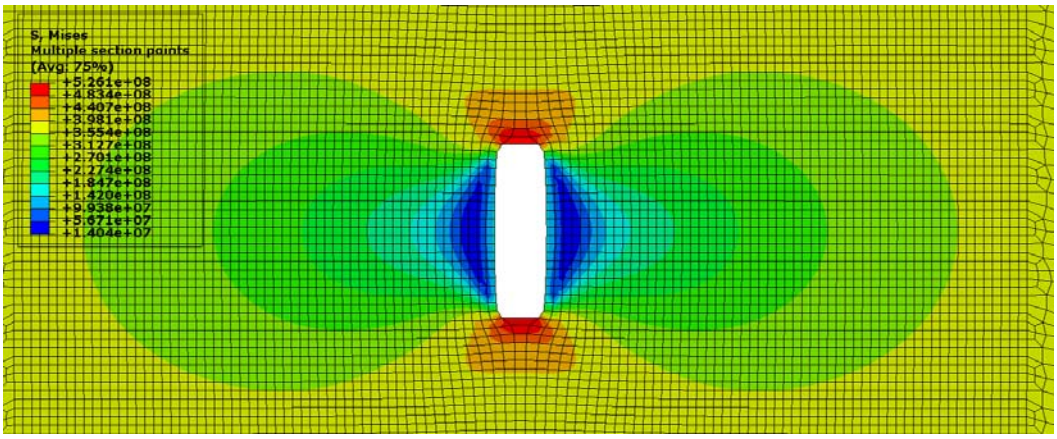

Figure 3.15 Crack shape according to FE-analysis, crack length 42 mm (Deformation magnified 20x).

Following the assumption above, the crack opening area for different postulated crack lengths is obtained from the FE analyses as shown in Figure 3.16. Figure 3.15 shows that the crack shape is similar to a rectangle. For larger postulated cracks the width of the crack is close to the applied deformation. The reason is that the material relaxes between the crack opening and the vertical anchor. Consequently, cracks present in the liner where the distance between the anchors is 150 mm, is assumed to have an opening area of 150/450 = 1/3 of the area presented in Figure 3.16.

The assumed crack shape is to be viewed as an upper bound for estimation of crack opening area. Since the crack shape obtained from the FE-analysis corresponds to a non-arrested crack the deformation close to the crack tip is larger than for an arrested crack. The arrested cracks in the Sandia 1:4 test are likely to be subjected to less plastic strain at the crack tip. A lower bound of the crack opening area is therefore to assume an elliptical crack shape which is the case for a linear elastic analysis.

The estimated upper bound crack opening area of the real cracks at $3.3p_d$ is obtained by entering the graph in Figure 3.16 for the real crack length to get the corresponding opening area from the FE-analysis. Crack lengths, width of liner section and estimated crack opening area are compiled in Table 3.1 for the tears in the liner. The width of the liner section at the location of each tear is found by combining the liner anchor layout (Figure 2.3) and the tears found at the post-test inspections (Figure 2.6) .

The total estimated opening area, i.e. the sum of the values in the right column in Table 3.1 is 1346 mm^2.

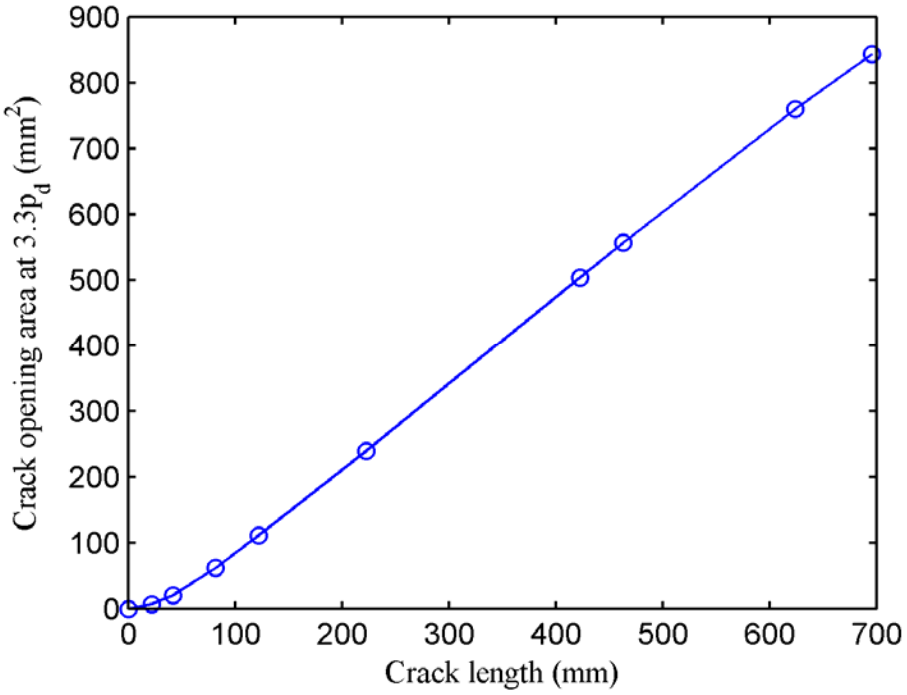

Figure 3.16 Crack opening area versus crack length.

Tear	*Length (mm)*	*Width of liner section (mm)*	*Estimated crack area (mm^2)*
1	28	450	11.0
2-1	68	450	47.2
2-2	73	450	52.4
2-3	157	450	155.7
3	270	150	100.5
4-1	67	150	15.4
4-2	26	150	3.2
4-3	123	150	37.5
5-1	40	150	6.4
5-2	71	150	16.8
6-1	112	450	98.9
6-2	118	450	106.4
7	228	150	82.0
8-1	62	450	41.0
8-2	43	450	21.4
9	123	450	112.6
10	18	450	5.7
11-1	100	450	84.0
11-2	74	450	53.4
12	63	150	14.0
13	92	150	24.7
14-1	77	450	56.5
14-2	120	450	108.8
15	83	150	21.0
16	87	450	67.9
17	15	150	1.6
Sum	-	-	1346.0

Table 3.1 Estimated upper bound of crack opening area.

An estimate of the flow through the liner tears is obtained by using the simple well known expressions for frictionless gas flow through a convergent nozzle[1]. The equations used are described in for instance Elementary Fluid Mechanics by Vennerd & Street [11].

The critical pressure ratio is given by:

[1] In this estimation the flow resistance from concrete is disregarded. At high pressure levels the concrete containment wall will be highly cracked and can be assumed to have small influence on the measured leak rate, see e.g. [4] and [10].

$$\left(\frac{p_2}{p_1}\right)_c = \left(\frac{2}{k+1}\right)^{k/(k-1)}$$

Where p_1 is the pressure in the containment, p_2 is the pressure in the crack (nozzle) and k is the adiabatic exponent.

According to [11] the adiabatic exponent, k = 1.4 for nitrogen gas, which gives:

$$\left(\frac{p_2}{p_1}\right)_c = 0.5283$$

The actual pressure ratio is approximately 101.3/(3.3·390+101.3) = 0.07 which means that the gas flow is sonic and the mass flow through the liner is calculated according to:

$$\dot{m} = \frac{A_2 p_1}{\sqrt{T_1}} \sqrt{\frac{k}{R}\left(\frac{2}{k+1}\right)^{(k+1)/(k-1)}}$$

Where A_2 is the area of the nozzle (in this case the total crack opening area), R is the engineering gas constant and T_1 is the temperature in the containment. According to Table 3.1 A_2 = 1346·10^{-6} m^2 and according to [11] R = 296.5 J/kgK. The containment is exposed to variations in ambient temperature, [3]. A fixed value of T_1 is therefore not available. It is assumed that the mean value of ambient temperature is 20 °C with a variation of ±10 °C. I.e. T_1 = 293±10 K.

With the values above the mass flow through the liner is obtained as:

$\dot{m}$ = 4.34±0.07 kg/s

4. COMPARISON WITH TEST RESULTS

4.1 Size of liner tears

No apparent crack arrest was attained in the FE-analyses. The method for propagating cracks as proposed in [5] shows promising results but the accuracy in the current study needs to be improved.

The analyses where the *J*-integral is studied with respect to interaction between the liner and the containment wall show that both friction and coupling method between the liner and the concrete wall affects the result to a great extent. The *J*-integral seems very sensitive to the coupling method in particular.

The tear lengths as obtained in the Sandia 1:4 test were in the range 18 – 157 mm in the liner sections with a width between the vertical anchors of 450 mm.

Although no crack arrest was obtained in the current study it is important to point out that there are many uncertainties in a comparison between analyzed and experimental results.

There is for instance a large variation in thickness due to grinding of the liner. Stress localizations might lead to that a crack starts to propagate. When the crack tip reaches a thicker region a crack arrest is possible due to lower driving stress.

Another uncertainty is that a weld might stop the crack propagation due to the change in material properties and thickness at the location of the weld.

4.2 Leakage through liner

The mass flow through the liner tears was estimated to approximately 4.3 kg/s.

The maximum nitrogen flow rate through the liner at $3.3p_d$ is assumed to be equal to the maximum capacity of the pressurization system which is stated as 142 std.m^3/min. It is not clear under what standard condition the "standard cubic meter" is specified. It is assumed that the Standard Temperature and Pressure (defined by IUPAC) is used. The standard reference condition used is a temperature of 0 °C and an absolute pressure of 101.325 kPa. At these conditions the density of nitrogen gas is 1.25 kg/m^3. The corresponding mass flow is then easily determined to 2.96 kg/s.

The flow through the liner is hence overestimated by 45 %.

The flow through the liner increases linearly with increasing crack opening area. The crack opening shape shown in Figure 3.15 is to be considered as an upper bound of crack opening area. Since the FE-analyses shows that no crack arrest is present the driving stress is higher than in an arrested crack. This leads to that the shape in an arrested crack more likely is similar to an ellipse as would be the case for a linear elastic solution. An elliptical crack shape leads to that the estimated mass flow through the liner approaches the measured value (2.96 kg/s).

Another possible reason to the overestimation of mass flow is that the friction in the theoretical model of gas flow is neglected.

5. CONLUSIONS

No apparent crack arrest was attained in the FE-analyses. The study using the method of crack propagation according to [5] shows promising results but the accuracy in the current study needs to be improved.

The analyses where the *J*-integral is studied with respect to interaction between the liner and the containment wall show that both friction and coupling method between the liner and the concrete wall affects the result to a great extent. The *J*-integral seems very sensitive to the coupling method in particular.

An estimate of the upper bound flow through the liner tears is obtained by using the simple well known expressions for frictionless gas flow through a convergent nozzle. The opening area of the cracks in the Sandia 1:4 test were estimated by assuming that a real crack has a similar deformed shape as the crack studied in the FE-analyses. The estimated gas flow was determined to approximately 4.3 kg/s. The flow rate through the liner measured at $3.3p_d$ in the Sandia 1:4 test was 2.96 kg/s. The flow through the liner is hence overestimated by 45 %.

6. REFERENSES

[1] Horschel D.S. (1988), Design, construction, and instrumentation of a 1/6-scale reinforced concrete containment building. NUREG/CR-5083, U.S. Nuclear regulatory commission (NRC).

[2] Horschel D.S. (1992), Experimental results from pressure testing a 1:6-scale nuclear power plant containment. NUREG/CR-5121, U.S. Nuclear regulatory commission (NRC).

[3] Hessheimer M. F., Klamerus E. W., Lambert L. D. and Rightley G. S. (2003), Overpressurization test of a 1:4-Scale prestressed concrete containment vessel model NUREG/CR-6810, U.S. Nuclear regulatory commission (NRC).

[4] Hanson N.W., Schults D.M., Roller J.J, Azizinamini A. and Tang H.T. (1987), Testing of large-scale concrete containment structural elements. Nuclear Engineering and Design, v100, pp. 129-149.

[5] SPE, Final Analysis Definition (2010, September), Standard Problem Exercise on performance of containment vessels under severe accident conditions.

[6] ISP-48 (2005, August), International Standard Problem 48 Containment Capacity, Phase 1-3, OECD.

[7] SPE SCTE-report, phase 1 (2011), Standard Problem Exercise on performance of containment vessels under severe accident conditions, 10503/R-01, Scanscot Technology.

[8] SPE - phase 2, Final Analysis Definition (2011, May), Standard Problem Exercise on performance of containment vessels under severe accident conditions.

[9] Rabbat BG and Russell HG (1985). Friction coefficient of steel on concrete or grout. J Struct Eng, v111, pp. 505-515.

[10] Castro, J. C., Dameron R. A., Dunham R. S. and Rashid Y. R. (1993), A Probabilistic approach for predicting concrete containment leakage. EPRI TR-102176, ANATECH research corp..

[11] Vennerd J.K., Street R.L. (1982), Elementary Fluid Mechanics, sixth edition, Wiley, New York.

A1. DETAILED DESCRIPTION OF LINER TEARS

The document included below was prepared for SPE participants (document date; August 9, 2010)

Liner Tears

This document is meant to provide additional information to the participants concerning the liner tears which were found in the PCCV model following the LST. Please refer to Appendix L of NUREG/CR-6810 for a detailed description of each tear. The photos contained here are merely meant to provide the participants additional views of the tears where available. The tear lengths documented in the pictures were initial estimates of the tear length prior to removal of the samples for measurement.

Figure A1.1 Tear Length at Tear #1

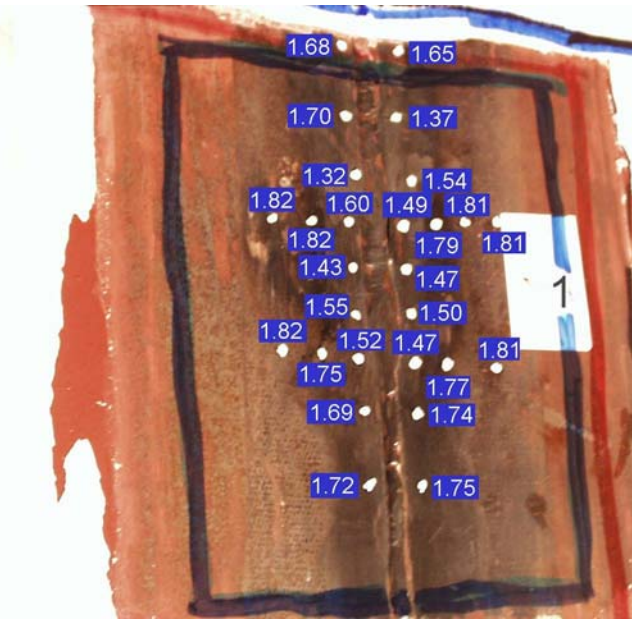

Figure A1.2 Thicknesses At Liner Tear #1.

Figure A1.3 Tear Length at Tear #2.

Figure A1.4 Tear Length at Tear #2

Figure A1.5 Tear Length at Tear #2

Figure A1.6 Tear Length at Tear #3

Figure A1.7 Thicknesses At Liner Tear #3

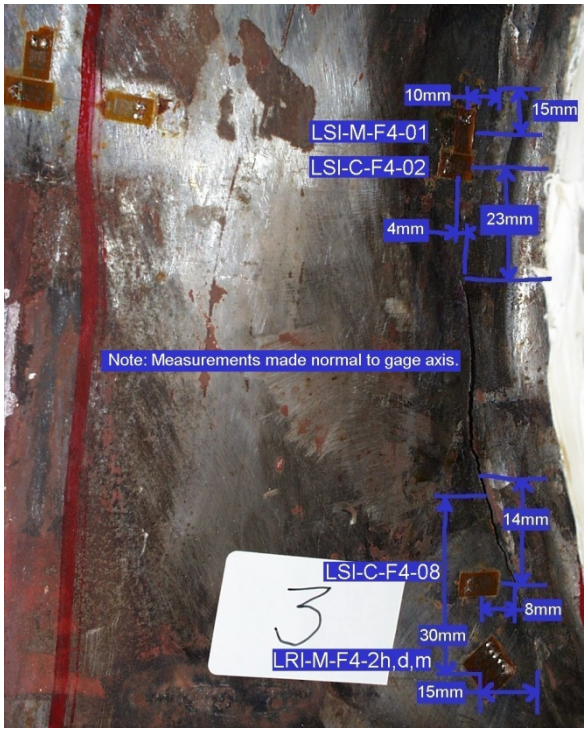

Figure A1.8 Detailed Dimensions of Liner Tear #3

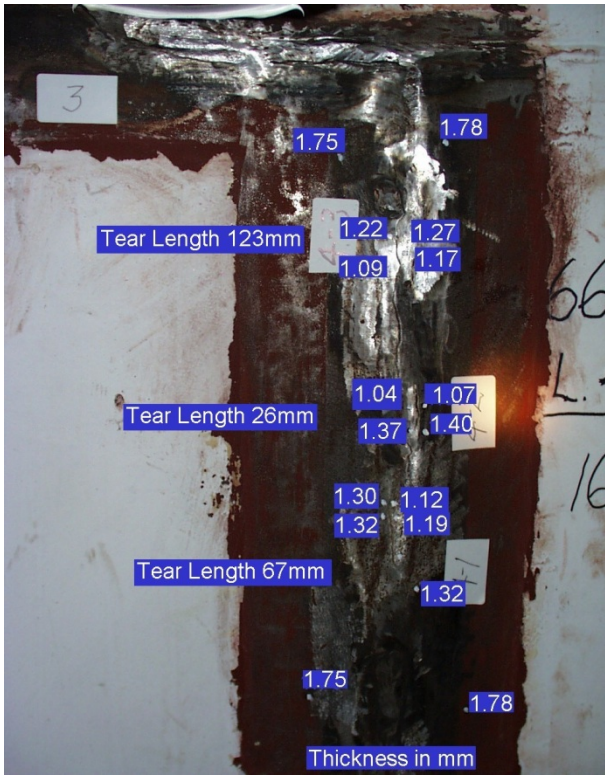

Figure A1.9 Tear Length at Tear #4

Figure A1.10 Tear Length at Tear #5

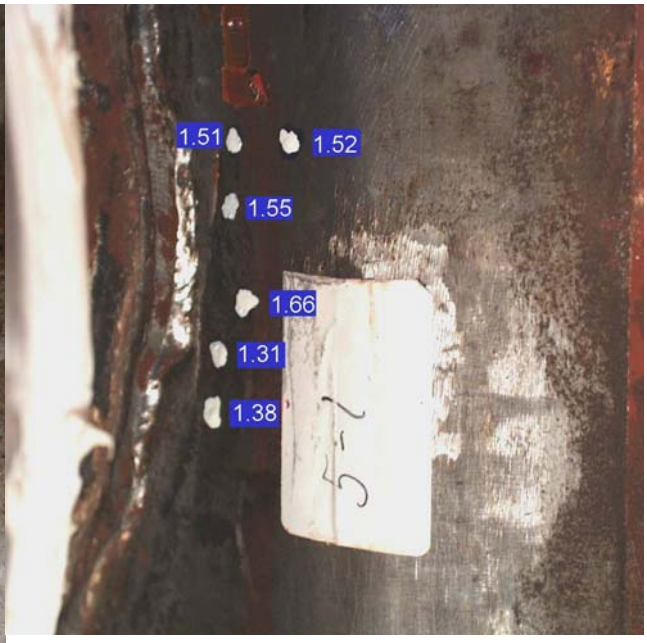

Figure A1.11 Thicknesses At Liner Tear #5-1

Figure A1.12 Tear Length at Tear #5

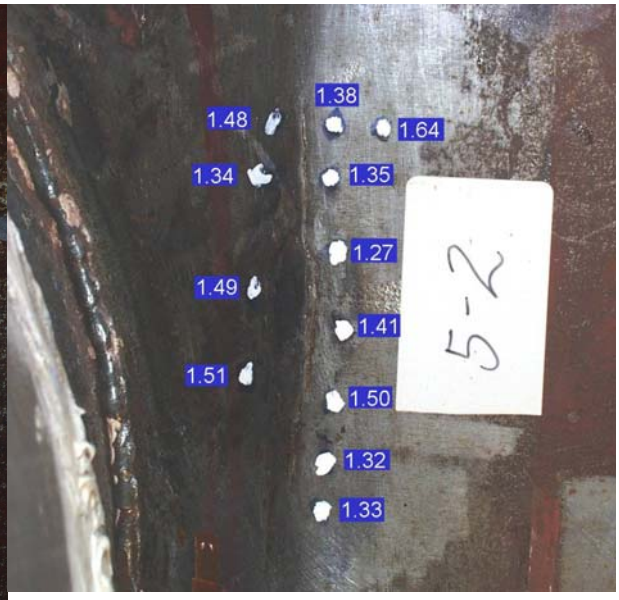

Figure A1.13 Thicknesses At Liner Tear #5-2

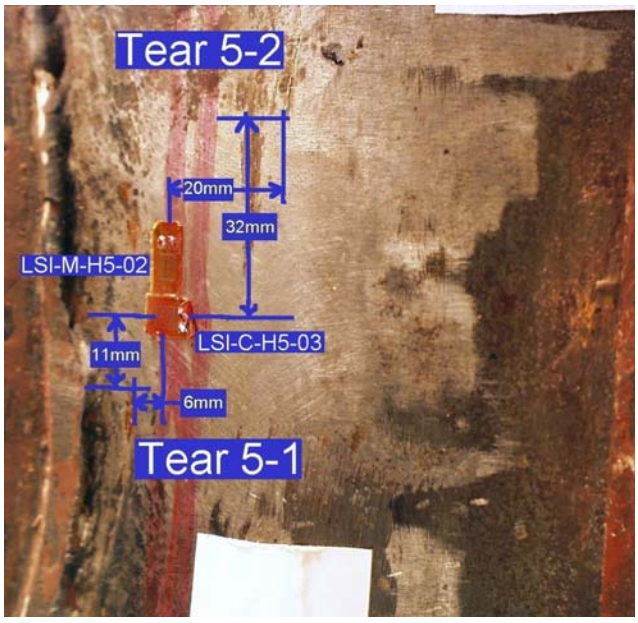

Figure A1.14 Detailed Dimensions of Liner Tear #5

Figure A1.15 Tear Length at Tear #6

Figure A1.16 Liner Thicknesses at Tear #6-1

Figure A1.17 Tear Length at Tear #6

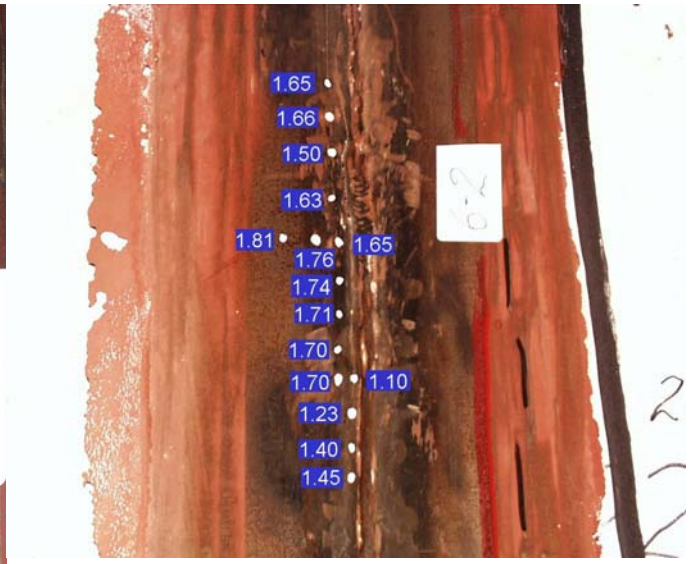

Figure A1.18 Liner Thicknesses at Tear #6-2

Figure A1.19 Tear Length at Tear #7

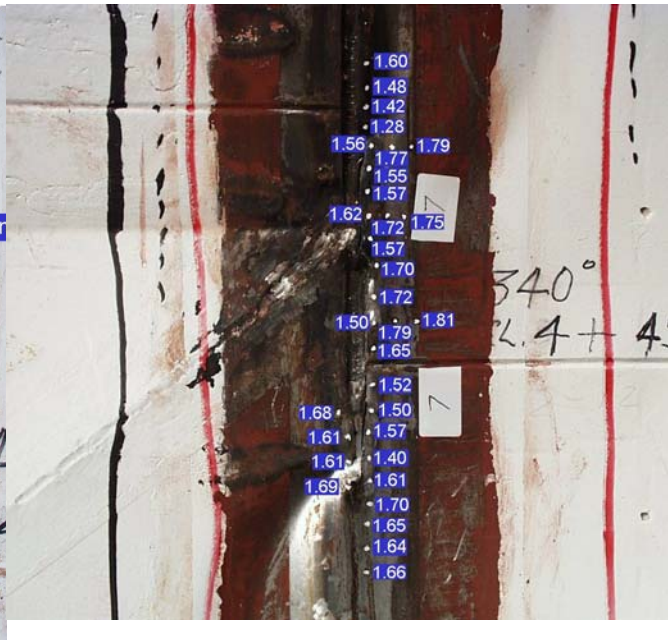

Figure A1.20 Liner Thicknesses at Tear #7

Figure A1.21 Tear Length at Tear #8

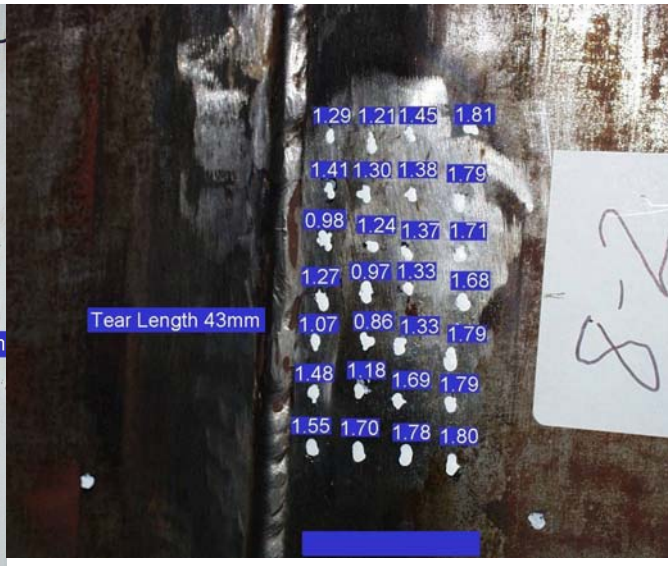

Figure A1.22 Tear Length at Tear #8

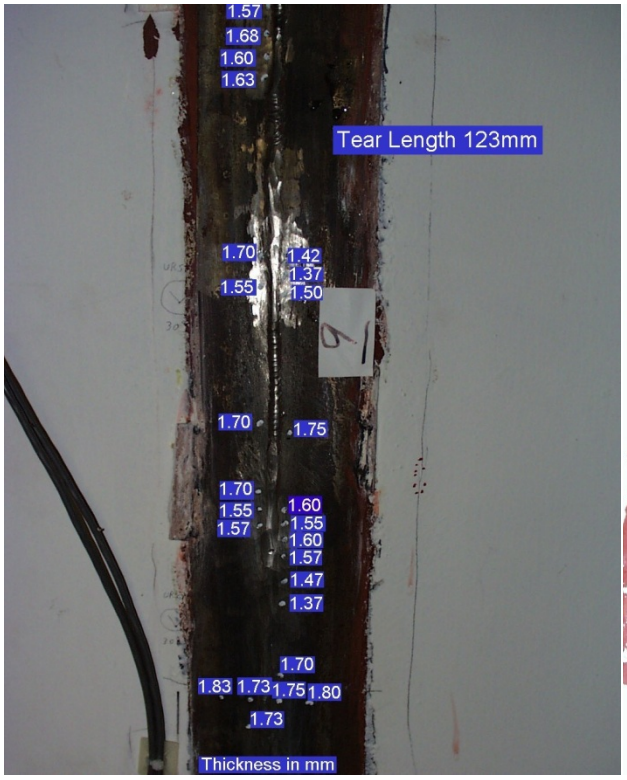

Figure A1.23 Tear Length at Tear #9

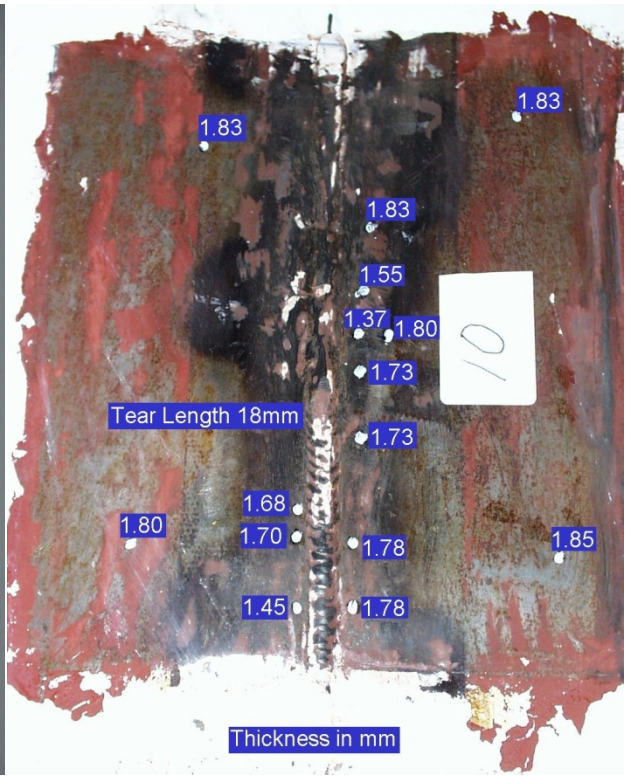

Figure A1.24 Tear Length at Tear #10

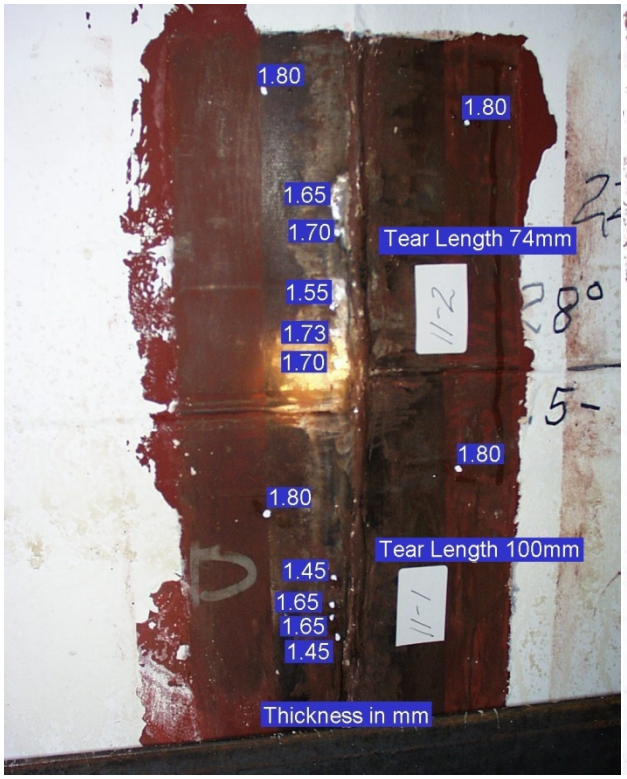

Figure A1.25 Tear Length at Tear #11

Figure A1.26 Tear Length at Tear #12

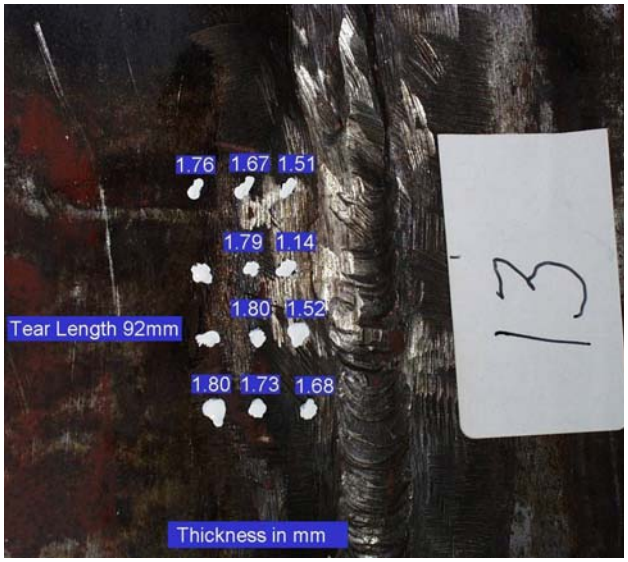

Figure A1.27 Tear Length at Tear #13

Figure A1.28 Tear Length at Tear #1

Figure A1.29 Liner Thicknesses At Tear #14

Figure A1.30 Tear Length at Tear #15

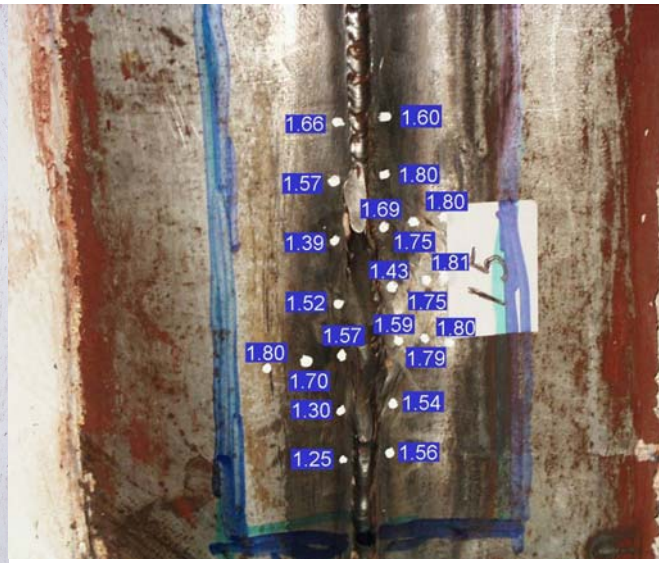

Figure A1.31 Liner Thicknesses At Tear #15

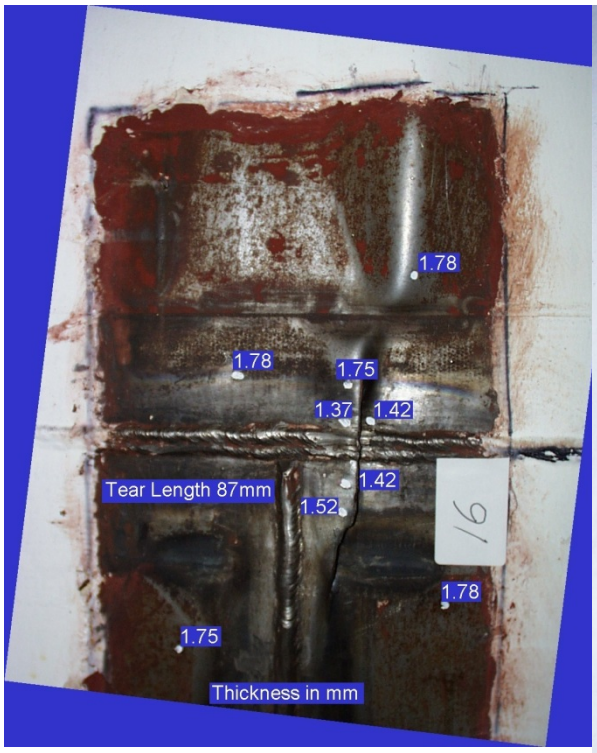

Figure A1.32 Tear Length at Tear #16

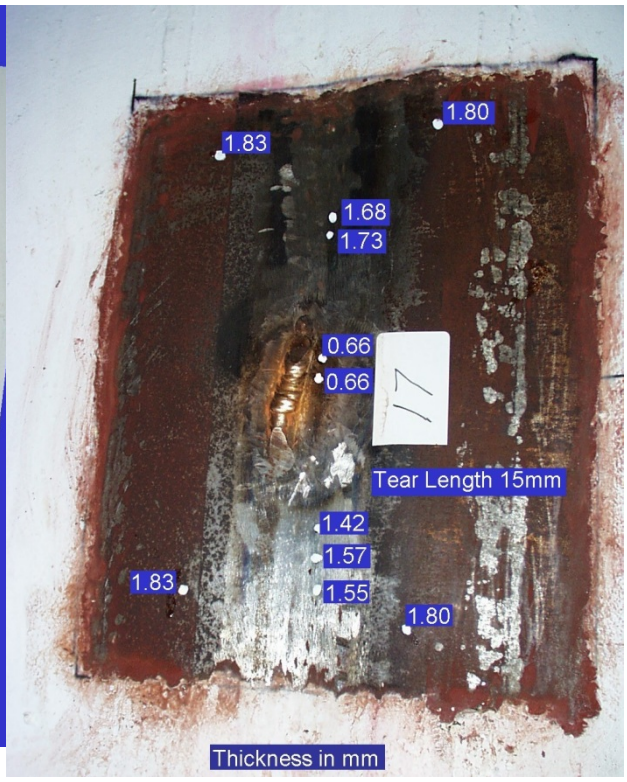

Figure A1.33 Tear Length at Tear #17